SENSORS & TRANSDUCERS

ISSN 1726-5479

vol. 21
Special
5/13

Intelligent Information Process, Automation Technologies and Applications

International Frequency Sensor Association Publishing

IFSA

Sensors & Transducers

International Official Journal of the International Frequency Sensor Association (IFSA) Devoted to Research and Development of Sensors and Transducers

Volume 21, Special Issue, May 2013

IFSA Publishing: Barcelona • Toronto

Printed in the USA.

Sensors & Transducers

Volume 21, Special Issue, May 2013 | **www.sensorsportal.com** | **ISSN 2306-8515 e-ISSN 1726-5479**

Sensors & Transducers Journal

Contents

Volume 21
Special Issue
May 2013

www.sensorsportal.com

ISSN 1726-5479

Research Articles

Authors are encouraged to submit article in MS Word (doc) and Acrobat (pdf) formats by e-mail: editor@sensorsportal.com
Please visit journal's webpage with preparation instructions: http://www.sensorsportal.com/HTML/DIGEST/Submition.htm

Sensors & Transducers, Vol. 21, Special Issue, May 2013, pp. 1-7

Sensors & Transducers

http://www.sensorsportal.com

The Simulation and Optimization of the Electro-Hydraulic Proportional Control System Based on Simulink/SRO

[1] Feilong ZHENG, [1] Liangcai ZENG, [2] Gangsheng KAI, [3] Cong YU, [3] Qianghua XI

[1] Key Laboratory of Metallurgical Equipment & Control Technology, Ministry of Education, Wuhan University of Science and Technology, 947 Heping Road, Wuhan, 430081, P. R. China

[2] Equipment Department of WISCO, Qingshan District, Wuhan City, 430083, P. R. China

[3] Iron Works of WISCO, Qingshan District, Wuhan City, 430083, P. R. China

[1] Tel.: +86-13387573390, fax: +86-027-68862252

[1] E-mail: zfl1984albert@yahoo.com.cn

Received: 26 March 2013 /Accepted: 14 May 2013 /Published: 30 May 2013

Abstract: Nowadays, the electro-hydraulic valves are widely used in industrial manufacture for their low-cost and accuracy. Aiming at electro-hydraulic proportional position system, a model of the system is established in Simulink. The system is simulated respectively as the situation of without PID controller, with the PID controller turned by critical ratio method and SRO optimize module. The results show that: the position control system with electro-hydraulic proportional valve is of good static and dynamic characteristics, and meets the requirements of industrial production fairly, and it also indicates the usage of computer automation optimization technology can design the control system with good performance in a short time and can improve the design efficiency. *Copyright © 2013 IFSA.*

Keywords: Proportional directional valve, Position control system, SRO module, Optimization.

1. Introduction

In order to meet the special requirements of the general engineering systems, the electro-hydraulic proportion control technology has gradually developed as a new branch in the field of fluid power transmission and control since 1960s [1]. Combining with traditional open-loop control and closed-loop servo control, the electro-hydraulic proportional control technology is widely applied with the advantages of high efficiency, relatively inexpensive, adaptive to the high-power and maintenance easily [2].

The commonly used methods of turning the control parameters in the electro-hydraulic proportional control system including trial method, the empirical method, Z-N method, genetic algorithm method, etc.

In this paper, the electro-hydraulic proportional control loop of a steel company is designed and optimized with SRO module, which gets the excellent performance.

2. The Model of Electro-Hydraulic Proportional Control System

This paper studies a proportional directional valve position control system [3-4] and its diagram is shown in Fig. 1.

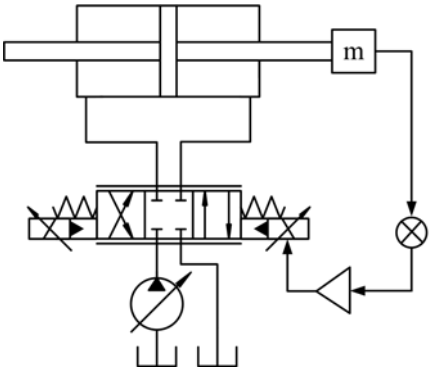

Fig. 1. The proportional directional valve position control system.

The system block diagram is shown in Fig. 2.

3. Dynamic Mathematical Model

Transfer function is the foundation of designing and checking the static and dynamic stability performance of the system. The load in the system is the pure inertia loads, the transfer functions involved is established as followed [5].

The parameters of the PID controller transfer function $W_{pid}(s)$ can be determined after correction, so the PID regulator will not consider temporarily.

The corner frequency of the proportion amplifier gain K_a is much higher than the bandwidth of the system, so it can be regarded as a proportional cycle.

In engineering the proportional directional valve is treated as a second-order cycle, its transfer function will be:

$$W_{pv}(s) = \frac{K_q}{\frac{s^2}{\omega_v^2} + \frac{2\delta_v s}{\omega_v} + 1}, \tag{1}$$

where K_q is the flow gain of the proportional directional valve ($m^3/s \cdot A$ or $m^3/s \cdot V$); ω_v is the relative bandwidth of the proportional directional valve (rad/s); and δ_v is the damping ratio of the proportional directional valve, often ranging from 0.5 to 0.7.

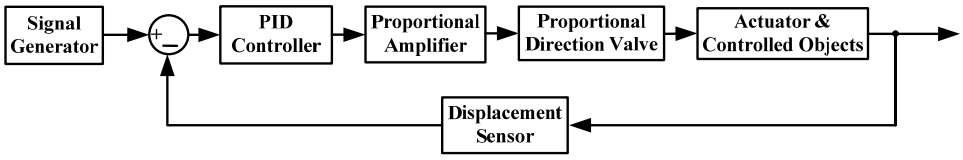

Fig. 2. The system block diagram.

In engineering the actuator which the elastic load is ignored and the controlled objects will be regard as the combination of integrator and a second-order cycle, so the transfer function of the hydraulic cylinder is:

$$W_h(s) = \frac{1/A_h}{s(\frac{S^2}{\omega_h^2} + \frac{2\delta_h s}{\omega_h} + 1)}, \tag{2}$$

where A_h is the effective area of the hydraulic cylinder (m^2); δ_h is the damping ratio of the hydraulic cylinders-load system, ranging from 0.1 to 0.2; and ω_h is the natural frequency of the hydraulic cylinders-load system (rad/s).

$$\omega_h = \sqrt{\frac{K_h}{m_t}} = \sqrt{\frac{4EA_h^2}{m_t V_t}} = \sqrt{\frac{4EA_h}{m_t L}}, \tag{3}$$

where E is the bulk modulus of elasticity of the hydraulic oil (N/m^2); m_t is the total mass of the moving portion including the load and the hydraulic actuator (kg); and V_t is the total volume from proportional control valve to cavities of the hydraulic cylinder (m^3).

The bandwidth of the gain of the position sensor K_m is much higher than that of the system, so it can be regarded as a proportional cycle.

Therefore the open-loop transfer function of this proportional directional valve position control system is:

$$G(s) = \frac{W_{pid} \cdot K_c}{s(\frac{s^2}{\omega_v^2} + \frac{2\delta_v s}{\omega_v} + 1)(\frac{s^2}{\omega_h^2} + \frac{2\delta_h s}{\omega_h} + 1)}, \tag{4}$$

where Kc is the open-loop gain of the closed-loop system, with the dimension of the speed:

$$K_c = K_a K_q K_m / A_h, \tag{5}$$

Analysis shows that the system has the following characteristics:

(1) The system is I type. The main factors affect the dynamic performance of the system are the

frequency of the hydraulic cylinder ω_h and the proportional valve ω_v . δ_h is the damping ratio of hydraulic cylinders, through the experience, it range is 0.1-0.2 as no-load, and it will increased slightly when the load increases.

(2) The steady accuracy, rapidity and stability of the system are mutually restrained. The higher the open-loop gain K_c is, the higher the accuracy of the system will be. As the crossover frequency ω_c rises, the band of the system gets wider, and the rapidity of the control system will be better. Meanwhile, when the open-loop gain of the system K_c increases, the accuracy and bandwidth are both improved, but the amplitude of the stability margin will reduce.

4. Simulation and Analysis

The parameters used in the system are as follows:

The input signal of the proportional amplifier is 4-20 mA, and its output current is 1.2 *A*, so:

$$K_a = 1.2A/(20-4)\times 10^{-3} A = 75\,, \qquad (6)$$

Based on the sample data, the rated flow of the proportional throttle valve is 670 *L/min*, so:

$$K_q = \frac{(670\times 10^{-3})/60m^3/s}{1.2A} = 9.3\times 10^{-3} m^3/(s\cdot A)\,, \qquad (7)$$

The proportional throttle feedback bandwidth is typically 10-70 *Hz*, take 60 *Hz* in this paper:

$$\omega_v = 60\times 6.28 = 376.8 rad/s\,, \qquad (8)$$

The damping ratio of the proportional directional valve $\delta_v = 0.6$.

The effective area of the hydraulic cylinder $A_h = 0.15m^2$, take $E = 1.8GPa$, $m_t = 2.23\times 10^5 kg$ and $L = 0.6m$, the inherent frequency of the hydraulic cylinder- load system according to equation (3) is $\omega_h = 40.36 rad/s$.

The damping ratio of hydraulic cylinder-load system $\delta_h = 0.19$ .The gain of the position sensor is [6]:

$$K_m = (20-4)\times 10^{-3} A/0.15m = 0.11A/m\,, \qquad (9)$$

So the system block diagram without the PID controller is shown in Fig. 3.

And the step response output in the model of Fig. 3 is shown in Fig. 4.

As can be seen from Fig. 4, the rise time is 4.26 s, the adjusting time is 5.83 s, and eventually reaches a steady state value output 1. Judging from the response curve, the time to reach steady state is long, and the accuracy of the system can be further enhanced.

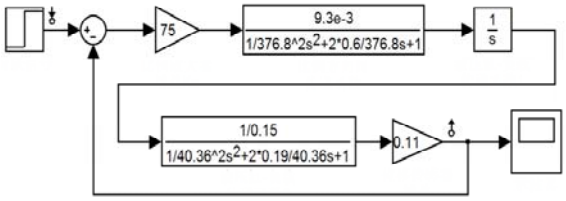

Fig. 3. The block diagram without PID controller.

The Bode diagram of the open-loop system is shown in Fig. 5.

As can be seen from Fig. 5, the amplitude of the system margin (Gain Margin) is 29.2 dB, and the phase margin (Phase Margin) is 89.6°, and the amplitude-frequency and phase-frequency characteristics all display that its stable in the system.

In order to make the system has a good transition process, it usually requires the amplitude margin more than 6 dB and the phase angle reaches 45° to 70°, and to meet this requirement, the slope of the log magnitude-frequency characteristics near the cutoff frequency should be greater than -40 dB, and has a certain width.

The amplitude margin of the system can meet the stability requirements, but the phase margin is greater than 70°, this means its regulating time is too long, and the stability of the system can be further improved.

5. PID Control

5.1. Parameters Tuning of the PID Controller Based on the Ratio Method

Nowadays, the PID control is the most widely used [7], for not only its structure is simple and it's easy to implement, but also it is suitable for the majority of the control object. In some developed countries, such as Japan, the utilization rate of the PID control is 85.4 %.

The PID control system may quite different from using different parameters. The characteristics of the system principally depend on the performance of the PID controller, therefore the adjustment and optimization of the controller parameters determine the control performance of the system, and it is of great significance.

There are many tuning methods to the PID controller, among of which the ratio method can be directly implemented in the process system, and it's simple and easy to calculate. Through calculation, the obtained parameters are: K_p=17.232, K_i=0.08, K_d=0.02. And the step response with these parameters is shown in Fig. 6.

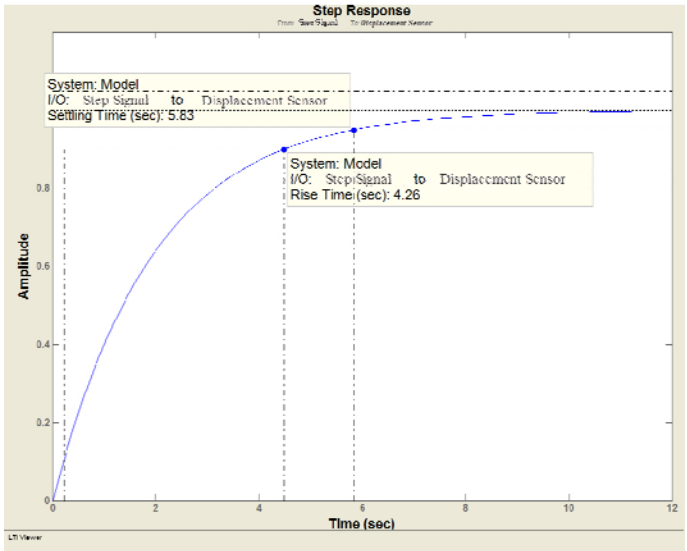

Fig. 4. The step response of the system.

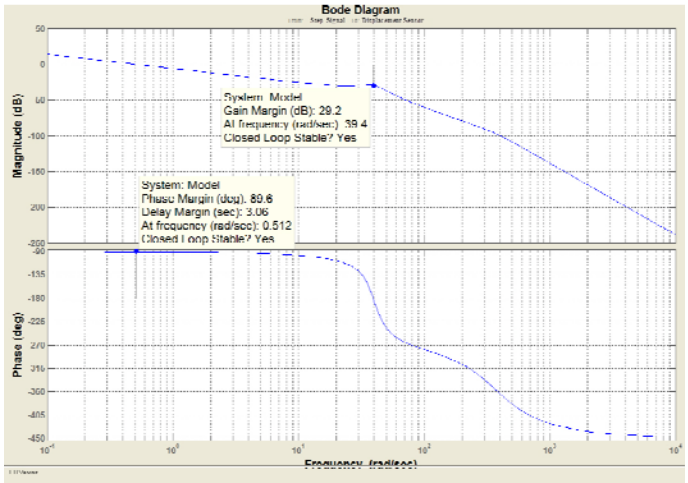

Fig. 5. The Bode diagram of the open-loop system.

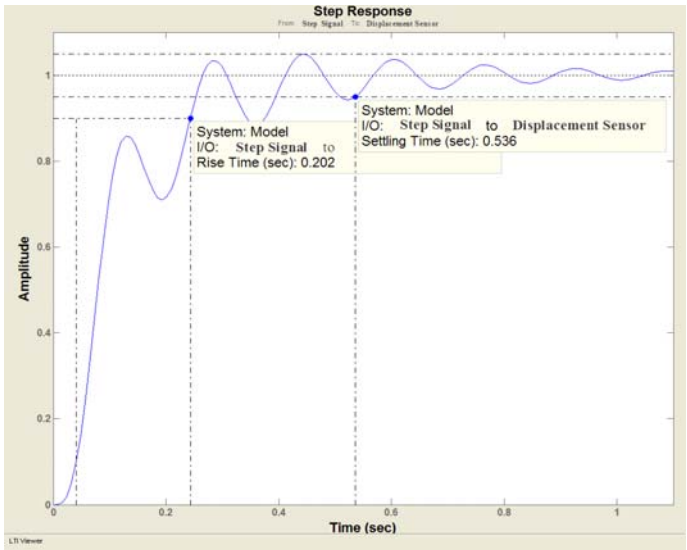

Fig. 6. Step response diagram with PID controller.

It can be seen through the parameters turned by the critical ratio method, the rise time of the system is greatly shortened to 0.202 s from 4.26 s, while regulating time is reduced to 0.536 s. In addition the curve concusses slightly, and the maximum overshoot is 4.91 %. It's clear that after adding the PID controller, the performance of the system has been greatly improved. However, the critical ratio method is the method which only summed through the experience, its parameters is only a reference, and generally can not be directly used for field controlling, and the performance has the room for improvement.

To obtain the control parameters with which the performance is better, there are a variety of methods [8], such as robust PID parameters tuning, ISTE optimal based parameters tuning, relay method, etc. These methods either needs to have sufficient experience in engineering and the takes much time, or requires the knowledge of control theory and mathematics, which is not easily for the technical personnel. Therefore, the computer-aided automatically optimization design technology based on the classical control theory is of a certain practical value.

This article adopts the Simulink Response Optimization (SRO) toolbox to optimize the parameters of PID controller to improve the performance of the system further. Simulink Response Optimization (SRO) is a tool to adjust the design parameters of the Simulink model, it is combined with the Simulink model, can optimize system parameters automatically according to user-defined constraints. With this tool, the variables of scalars, vectors, and the matrix and the constraints of any level model can be optimized. SRO toolbox supports continuous, discrete, and multi-rate model, and could deal with some uncertain values through Monte Carlo simulation in the model.

5.2. PID Parameters Optimization Based on SRO Toolbox

Firstly add the Signal Constraint module to the model, as shown in Fig. 7. Then append the parameters be optimized: K_p, K_i and K_d. To achieve both rapidity and accuracy, set algorithm as "Pattern search" in "Optimization Options", as shown in Fig. 8. Continuously reduce the parameters, such as Rise time, Setting Time and Overshooting, etc., in Goals parameters and simulation repeatedly, as shown in Fig. 9, until a satisfactory result is obtained. Finally, the Simulation results are achieved: K_p = 14.8162, K_i = 4.3761, and K_d = 0.1274.

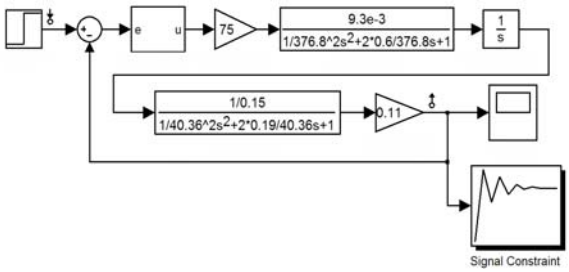

Fig. 7. The diagram within Signal Constraint module.

Apply the parameters optimized above into the PID controller and run the simulation again, and the step response is shown in Fig. 10, which the open loop Bode diagram is also shown in Fig. 11.

Table 1 gives the comparison of the parameters as the situation of without PID controller, PID parameters tuning with the critical ratio method and SRO toolbox.

Table 1. The parameters comparison.

	Rise Time(s)	Adjusting Time(s)	Magnitude Margin(dB)	Phase Margin(°)
Without PID	4.26	5.83	29.2	89.6
Critical Ratio Method	0.202	0.536	—	—
SRO Method	0.206	0.387	39.3	82

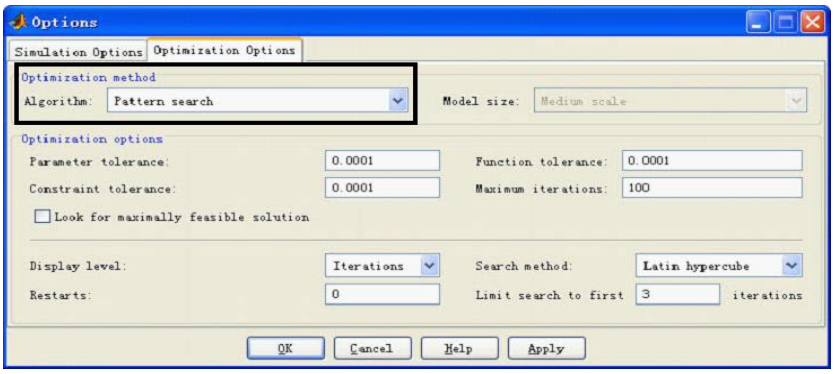

Fig. 8. Algorithm altering.

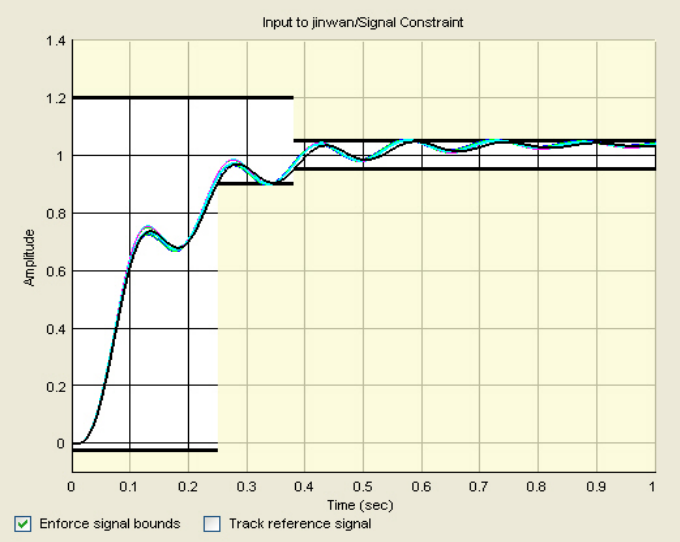

Fig. 9. The curves as optimizing.

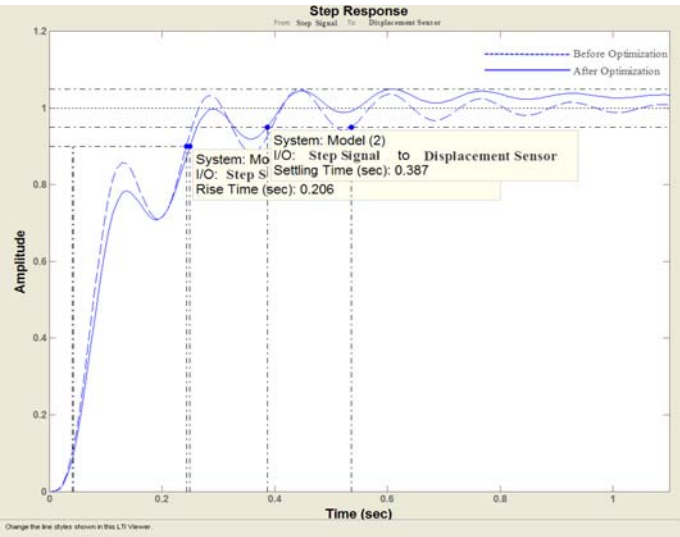

Fig. 10. The comparison of before and after the optimization.

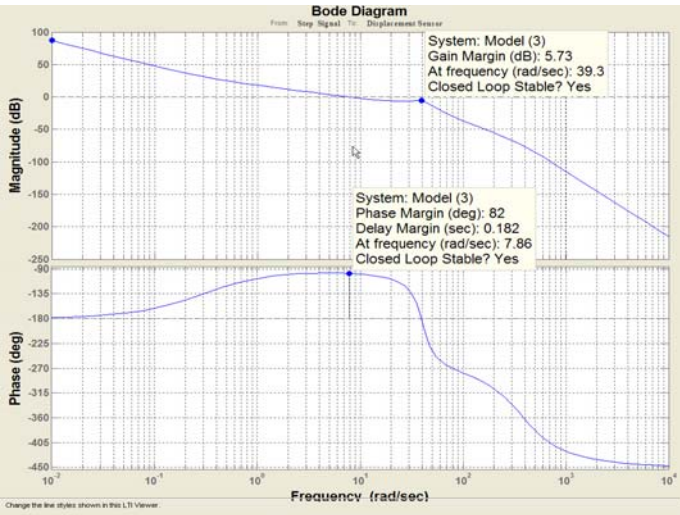

Fig. 11. The open loop Bode diagram after optimization.

As can be seen from Table 1, the rise time of the step response curve after adding PID control is about 5 % of that without PID controller, the adjustment time is also less than 10%; After optimization, the rise time of the step response curve is a little longer, but the adjustment time is shortened by nearly 30 %, and volatile less and the curve is smoother. It means after optimizing the PID parameters, the response performance of the system improves considerably. The amplitude margin of the system after optimization is 5.73 dB and less than previously 6dB but the difference is small; the phase margin decreased 7.6°, and is still greater than the recommended value of 70°, meanwhile, the rapidity and relative stability of the system response improved obviously, and it's acceptable in industrial applications. What's more the design period can be greatly reduced to less than five minutes compared with the original may be more than half an hour.

6. Conclusion

(1) The PID controller plays an important role in improving the system performance, and it is able to reduce the system's response time greatly.

(2) The SRO toolbox has the advantage of friendly to user and easy to operate, it can automatically optimize the parameters of the PID controller and the characteristics of the system can be observed clearly according to the simulation results. In summary, it can improve the working efficiency greatly.

Acknowledgements

The authors would like to offer their gratitude to the National Natural Science Foundation of China for their financial support, grant number 51027002.

References

[1]. Z. F. Peng, R. B. Yung, J. Luo, and R. Li, The research of electro-hydraulic proportional control on copper anode lifting platform, in *Proceedings of the 16th International Conference on Fluid Dynamic and Mechanical and Electrical Control Engineering (FDMECE' 2012)*, Chongqing, China, 10-11 November 2012, pp. 172-176.

[2]. H. Huang, X. Li and Z. W. Sun, Steady hydrodynamic force analysis of non-circular opening hydraulic spool valve, in *Proceedings of the 2nd International Conference on Advanced Design and Manufacturing Engineering (ADME' 2012)*, Taiyuan, China, 16-18 August 2012, pp. 1657-1660.

[3]. R. Sindrey, and G. M. Bone. Position tracking control of a miniature water hydraulic rotary actuator. *Journal of Dynamic Systems, Measurement and Contro, Transactions of the ASME*, Vol. 131, Issue 6, 2009, pp. 1-8.

[4]. F. Rong-Fong, Y. C. Wang, R. T. Yang, and H. Hsing-Hsin, Variable structure control with proportional and integral compensations for electrohydraulic position servo control system. *Mechatronics*, Vol. 7, Issue 1, 1997, pp. 67-81.

[5]. J. Lee, M. Yamazaki, A. Oida, H. Nakashima, and H. Shimizu, Electro-hydraulic tillage depth control system for rotary implements mounted on agricultural tractor: design and response experiments of control system. *Journal of Terramechanics*, Vol. 35, Issue 4, 1998, pp. 229-238.

[6]. C. Subrata, R. Ganesh, and P. Mrutyunjaya, Simple design of a PID controller and tuning of its parameters using LabVIEW software, *Sensors & Transducers*, Vol. 129, Issue 6, June 2011, pp. 69-85.

[7]. R. K. Manjunatha, J. Immanuel, C. S. Parvathi, P. Bhaskar, and L. S. Sudheer, Implementation of PID controller in MATLAB for real time DC motor speed control system, *Sensors & Transducers*, Vol. 126, Issue 3, March 2011, pp. 110-118.

[8]. L. Deng, F. Z. Song and B. Song, Parameters optimization and dynamic characteristic analysis of maglev spindle control system, in Proceedings of the *10th World Congress on Intelligent Control and Automation (WCICA' 2012)*, Beijing, China, 6-8 July 2012, pp. 2403-2406.

Sensors & Transducers, Vol. 21, Special Issue, May 2013, pp. 8-14

Sensors & Transducers

http://www.sensorsportal.com

Design & Test of Radio Communication and Control System for Aquaculture

Fengrong Jia, * Lijia Xu

[1] College of Information Engineering and Technology, Sichuan Agricultural University
Yaan, Sichuan Province, 625014, China
E-mail: jfrfengrong@163.com, lijiaxu13@163.com

Received: 11 March 2013 /Accepted: 14 May 2013 /Published: 30 May 2013

Abstract: Aiming at low automation degree and backward aquatic product management of current aquaculture in China, this paper designed a set of radio communication and control system which consists of 3 parts of information collection module, control module and radio communication module. This system both realizes wireless monitoring of quality parameters of water for aquaculture and realizes wireless control of water level and dissolved oxygen value through radio communication. Test results show that data transfer is more accurate and reliable after adding customized protocol and answer signals in radio communication. The highest error and missing rate within 1000 m is 0.36, the lowest error and missing rate is 0.05 and the longest response time is 49 ms. The dissolved oxygen value detection system designed in this paper is close to the testing value of existing dissolved oxygen value transmitter DO6309. With wireless data transfer mode, it has higher practicality. The wireless control of dissolved oxygen value and water level can be controlled within the appropriate range with stable and precise control. The study results can provide intelligent aquaculture model with simple operation and precise control for enormous aquatic breeders. *Copyright © 2013 IFSA.*

Keywords: Aquaculture, Radio communication, Water level, SCM.

1. Introduction

China is a large agricultural country, while fishery is one of important industries of Chinese agriculture. In despite of Chinese fishery has gone through stable and fast development with considerable increase of total production [1], it is also confronted to challenges in respect of resource, environment, market, S&T and system etc. All of these factors restrict the development of fishery at certain degree. At present, the management of Chinese aquaculture is mainly guided by culture experience such that the production and the safety are hard to be ensured. China's present aquaculture modes are mainly concentrated on two fields that are industrial culture [2] and cage culture [3]. Chinese aquaculture integrally shows following features [4]: decentralized aquaculture operation with unreasonable structure; backward aquaculture facilities with low intelligent degree; and the aquaculture safety needs to be improved.

With people's increasing demand to aquatic products, scaled aquaculture has become a necessary development trend of aquaculture. At present, most of existing scaled culture monitoring systems adopt wired mode for realizing the data communication between the monitoring terminal and the computers of control center [5]. Most of aqua-farms rely on artificial culture experience [6], so the monitoring technology is low and there will be a lot of

Article number P_SI_333

monitoring points and complex wiring when the culture area is larger. Nowadays, some culture monitoring systems have introduced the wireless sensor network technology and partially solved above problems [7]. There are now aquaculture monitoring systems realized automatic monitoring [8] to water level, temperature, pH and dissolved oxygen, which has important significance of scientific culture to farmers, but its cost is high and the intelligent degree and scientific management need to be promoted.

This paper therefore designed a set of radio communication and control system for aquaculture. This design adopts radio communication and sensor networking technology, which has lower cost and easier expansibility than wired, GPRS and GSM data transfer as well as realizes wireless intelligent control to water level and dissolved oxygen value so as to realize more precise and scientific control and reduce energy consumption. This system is mainly suitable for middle and large aquaculture farmers.

2. System Structure

The radio communication control system designed in this paper mainly consists of radio communication module, information collection module and control module. Its structure drawing is shown as Fig. 1. The information collection module collects parameters of the water quality of culture pond in real time and sends the collected information such as water level, dissolved oxygen value, temperature and pH value to the host computer through APC220 after such information are pretreated by single chip micro (SCM) STC89C52; and the host computer will display the collected data on human-machine interface after processing such as temperature compensation and error correction. In the event that the collected parameters are outside the preset range, it will alarm through the alarm promoting circuit; meanwhile, the host computer will send the control information to SCM STC89C52 through APC220 in order to utilize the SCM to control the aerator and the pond's water level and so on.

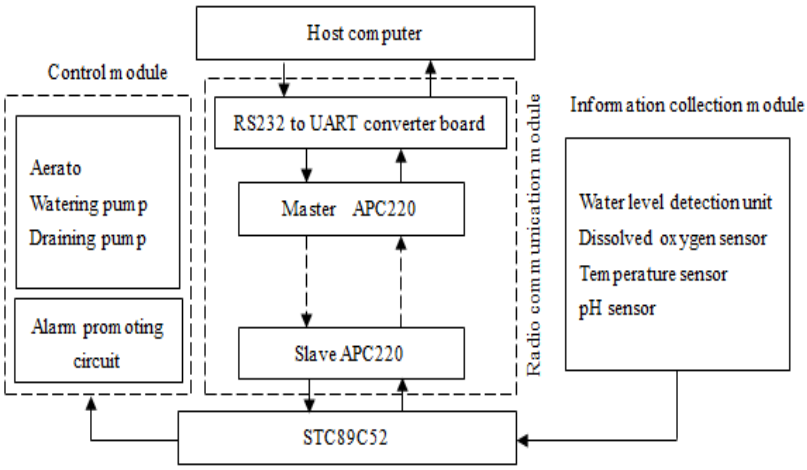

Fig. 1. System structure drawing.

3. Design of Radio Communication

This system adopts APC220-43 multichannel micro-power embedded wireless data transmission module whose communication channel is half-duplex and the module is embedded with high-speed SCM and high-performance radio chip with 1200 m radio transfer range and strong interference rejection. The host computer has to be connected with APC220-43 by RS232 to UART/TTL interface converter board as shown in Fig. 1. The serial port is initialized as 9600 Baud rate, 8 data bits and 0 check bit.

The design of this system demands not less than 2 APC220-43 modules and comprises a master station APC220-43 and multiple slave stations APC220. When the host computer gives information, the master station APC220 will send a set of binary code i.e. a frame of data. According to the function of each part, they are divided into 3 parts that are address code, data code and stop signal code. As a communication station, each APC220 module has a unique address code. When the master station sends signals, all of slave stations unconditionally receives that and compares the received address code with local address code. If the address codes are different from each other, the data will be rejected without response; if the address codes are identical, the data code will be matched with defined ones. When the stop signal code is received after successful matching, it will set corresponding flag bit and simultaneously implement corresponding program and reset flag bit. The flow chart of the slave station receives control command is shown as Fig. 2.

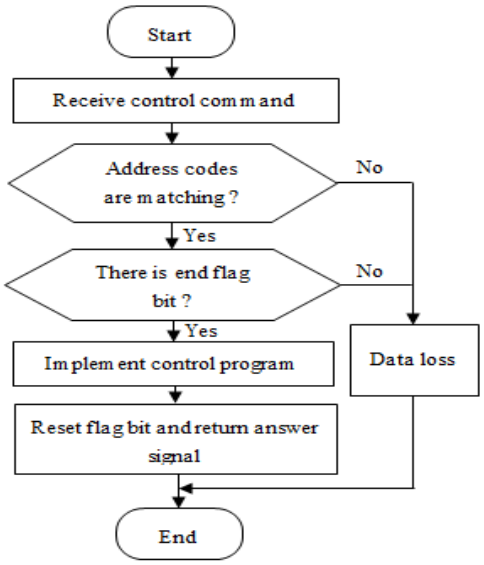

Fig. 2. Flow chart of the slave station receives control command.

In order to strengthen the reliability of the system, answer signal will be returned after all flag bits set by slave stations enter implementation program. The host computer will send the same signal once at 1s interval until it receives the answer signal. If there is no answer signal after sending 3 times, it will give alarm. There are two methods for SCM STC89C52 to send the collected data, of which one is sending collected data once at certain time interval (the time can be customized) to the host computer and display e.g. pH value, dissolved oxygen value and temperature value etc., the other is sending signal when collected signal changes. Taking the water level information for instance, at the beginning of change, it sends normal signal to the host computer for displaying normal water level information, when higher or lower water level is detected, it will send corresponding signal to the host computer for displaying alarm signal until normal signal is received. The mode that the host computer receives collected data is similar to the mode that the lower computer receives control signal. But their difference is that the host computer, upon receiving data, firstly detects the flag bits in data information before reading and displaying data (main functions of flag bit are marking start bit and end bit of data as well as explaining what data value is collected).

4. Design of Control System

4.1. Design & Principle of Water Level Control Hardware

The water control unit consists of watering equipment, draining equipment, water level detection circuit and SCM (STC89C52). The control principle of water level detection is shown as Fig. 3.

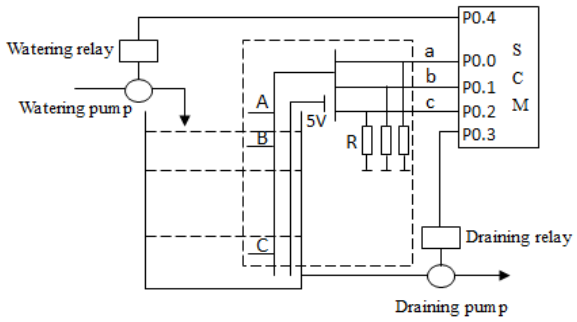

Fig. 3. Schematic of control of water level detection.

The watering equipment comprises of watering relay and watering pump; the draining equipment comprises of draining relay and draining pump; the water level detection circuit is used for detecting the water level of pond; and the SCM is used for implementing water level adjusting commands, controlling open and close of watering relay and draining relay, and then controlling the start and stop of watering pump and draining pump. The water level information obtained is sent to the host computer via APC220-43 module, and then the host computer generates draining command or watering command according to such information.

The water level detection circuit comprises a piece of detecting bar with insulated shell, on which there are detecting points A, B and C that are composed of metal conductor. The three detecting points are respectively connected with ports P0.0, P0.1 and P0.2 of SCM through three conductors a, b and c; the three conductors a, b and c are respectively grounded through a 4 kΩ resistance; SCM respectively exports high and low electrical level to draining relay and watering relay through ports of P0.3 and P0.4 in order to control closing and opening of corresponding pump. When water level is detected, vertically immerse the detecting bar into water and make positions of three detecting points A, B and C respectively on dividing points of high level, normal level and low level. The water to be detected is applied 5 V voltage; utilizing the conducting property of water, when the detecting point is immersed into water, it will be powered by 5 V voltages, and then the port of the SCM connected with such detecting point will input high electrical level, otherwise it will input low electrical level. Therefore, which detecting point is immersed into water can be determined according to high or low of input electrical level of SCM port so as to get the information of water level, and then SCM's P0.3 and P0.4 ports export corresponding high or low electrical level to control actions of two relays in order to control opening or closing of corresponding water pump for adjusting the water level. The relationship between water level detection signals of SCM's P0.0~P0.4 ports and output control is shown as Table 1, of which 0 refers to low electrical level and 1 refers to high electrical level.

Table 1. The relationship between water level detection signals of SCM's P0.0~P0.4 ports and output control.

P0.0(a)	P0.1(b)	P0.2(c)	Water level	P0.3 (Draining relay)	P0.4 (Watering relay)	Function
1	1	1	High water level	0	1	Draining
0	1	1	Normal water level	1	1	No operation
0	0	1	Low water level	1	0	Watering

4.2. Design of Water Level Control Program

The water level control command can be sent by the host computer and the SCM can also self control according to the detected water level information, but the host computer control is preferential. When SCM detects the signal of normal water level, it will send signal of normal water level to the host computer through APC220-43; in case of high water level, it will send signal of high water level to the host computer, meanwhile P0.3 exports low electrical level and P0.4 exports high electrical level to perform drainage operation. When the water level returns to normal, it will send signal of normal water level and stop draining. The control principle for low water level is similar. Water of normal fish pond is changed once per 10~15 days, about 1/3 of pond water amount will be changed each time and massive drainage and irrigation is prohibited [9]. The host computer sends water changing command and the SCM returns water changing answer signal to the host computer and performs drawing action upon receiving such command; when the water level is lower than point C, SCM stops draining and performs watering operation until water level is normal, and then it sends water changing completion information to the host computer; if the host computer receives no water changing answer signal after sending command for 3 times, it will send alarm signal. The flow chart of host computer controls water changing is shown as Fig. 4. The principle that host computer controls draining and watering is similar to that of control of water changing.

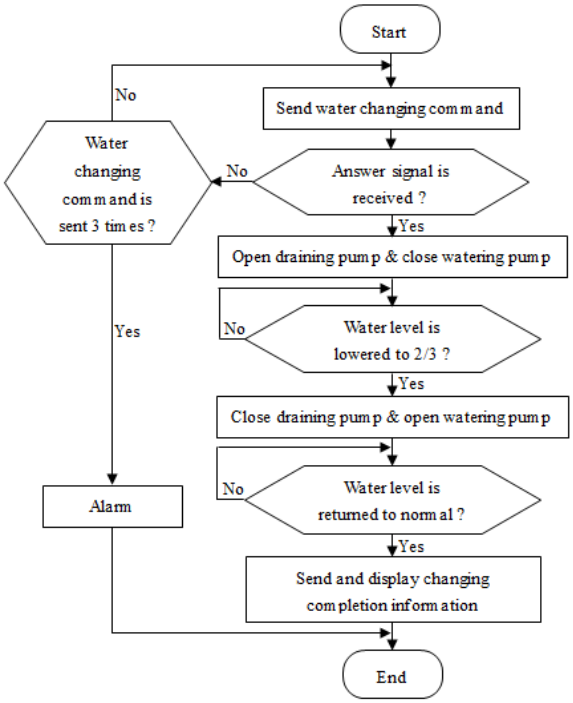

Fig. 4. Flow chart of host computer controls water changing.

4.3. Realization of Detection of Dissolved Oxygen Value

The dissolved oxygen sensor adopted in design of this paper is polarographic oxygen electrode that utilizes galvanometry to determine dissolved oxygen amount. The current value determined on the electrode of dissolved oxygen sensor is at μA level which cannot be directly input into analog-digital conversion (A/D) conversion circuit, but has to be converted into voltage signal by conversion circuit and amplified to 0~5 V voltage before entering A/D conversion. This paper designed a current-voltage conversion circuit by adopting precise amplifier MAX472. The current-voltage conversion circuit is shown as Fig. 5.

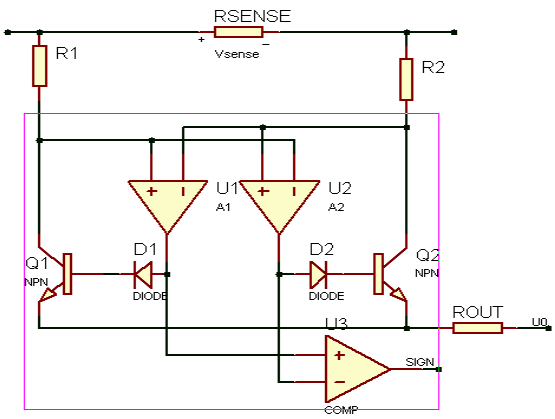

Fig. 5. Current-voltage conversion circuit.

There is internal structure of MAX472 inside the solid line box, of which A1 and A2 are operational amplifiers that forms differential input and can strengthen interference rejection and increase measurement accuracy of low current signal; both Q1 and Q2 are transistors; COMP is comparator; on the outside of the solid box, there is external resistance circuit designed according to system

requirements, of which RSENSE is the current sampling resistance. Due to the impedance of the measuring electrode is very high (normally above meg-ohm) and ordinary amplifying circuit cannot meet requirements of high input impedance, this design uses INA118 to increase the input impedance of amplifying circuit. There is an amplifying structure made up of three operational amplifiers inside INA118 and gain at different levels can be realized through external regulating resistance. The voltage amplifying circuit is shown as Fig. 6. Pins 1 and 8 in the figure externally connect resistance RG for changing gain G of amplifier INA118; pins 2 and 3 respectively connect the cathode and the anode of amplified electric potential signal; pins 4 and 7 respectively connect -5 V and +5 V power source and ground via decoupling capacitors C5 and C4; and pin 5 connects bias voltage. The electric potential signals from pins 2 and 3 can be converted into potential signals within 0~5 V after they are amplified to G times by INA118 and combined with the bias voltage from pin 5; this converted electric potential signal is finally exported by pin 6, and then A/D conversion is performed by ADC0809.

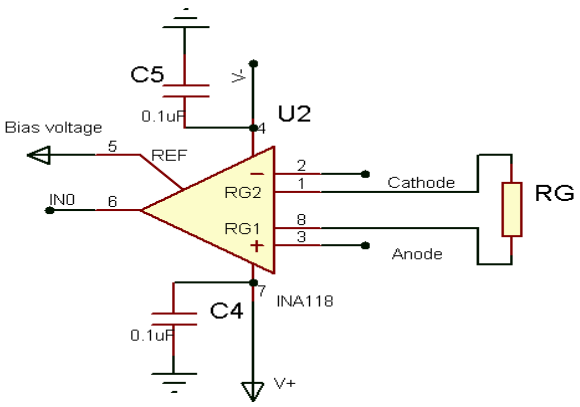

Fig. 6. Voltage amplifying circuit.

4.4. Detection of Dissolved Oxygen Value and Design of Control Program

The electric current signal collected by dissolved oxygen sensor is amplified to 0~5 V voltage signal after passing current-voltage conversion circuit and then passing signal amplifying circuit. The voltage signal enters A/D conversion circuit and preliminarily processed by SCM, and then it is sent to the host computer by APC220-43. The host computer will carry out temperature compensation and error correction to dissolved oxygen value according to the temperature value currently collected. The host computer displays the obtained dissolved oxygen value on human-machine interface and makes comparison with the lower limit set by the system. If the value is smaller than the lower limit, the host computer will send aerator starting command and alarm. Upon correctly receiving such command, the SCM will close the normally open contact terminal of relay to make the aerator operate; when the dissolved oxygen value of pond reaches to the upper limit set by the system, the host computer will automatically give aerator shutting command and SCM will control the aerator to stop working. Dissolved oxygen value detection and control flow chart is shown as Fig. 7.

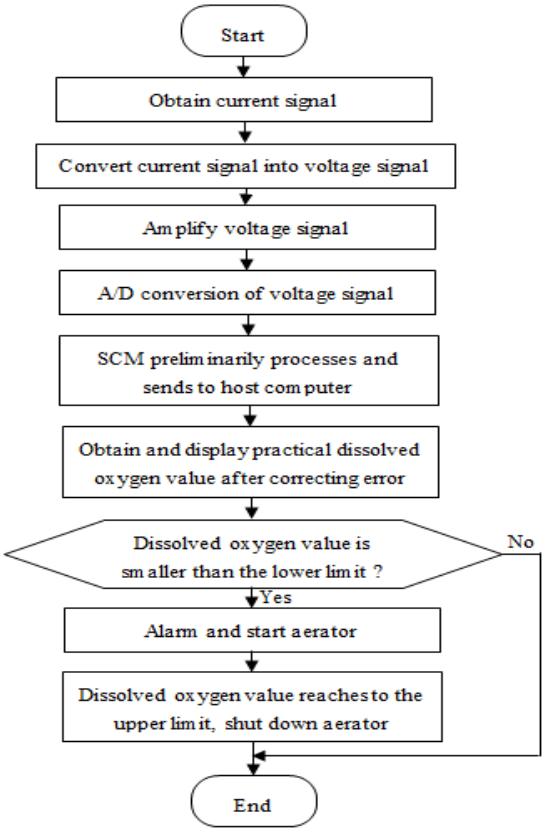

Fig. 7. Dissolved oxygen value detection and control flow chart.

5. Testing & Measurement

5.1. Test Conditions

This system was applied in the fishery experimental park of Sichuan Agricultural University upon completion of design. A 10 m×8 m area and 1.5 m depth pond within the park was taken and 15 kg carp fry was put into the pond. By field survey, the distance between the monitoring room and the fishpond is about 900 m. The radio communication system was tested before testing the system. The test was performed during 1 Jan. 2012 to 2 Jan. 2012 and mainly on missing and error rate of data transfer, response time and transfer distance. The whole system was tested during 1 Mar. 2012 to 30 Sep. 2012 and mainly on system's water quality detection precision and controlling effect of each controlled value.

5.2. Result & Analysis

The performance test of radio communication is shown as Table 2. With respect to data in table under each monitoring distance, each kind of control command was sent 100 times and record the times of sending failure and finally take an average, i.e. the error and missing rate of data transfer in table is the times of error in data transfer of 100 times. It is known from table 2 that the transfer distance of this radio communication system can reach 1000m with short control response time, low and stable data transfer error and missing rate such that the controlling and information communication requirements of this system can be satisfied.

Table 2. Table of performance test of radio communication system.

Monitoring distance /m	Oxygenation response time /ms	Water level control response time /ms	Error and missing rate of data transfer /%
100	16	15	0.05
300	18	19	0.08
500	22	22	0.12
700	27	25	0.18
800	33	35	0.25
900	38	39	0.30
1000	48	49	0.36
1100	53	56	0.52

Dissolved oxygen values under different temperature were tested and the results are shown in Table 3. It can know from data of this table that the test value of dissolved oxygen value detection system is similar to the test value of dissolved oxygen value transmitter DO6309, but the cost of polarographic oxygen electrode adopted is lower and existing dissolved oxygen value transmitter normally collects data by wired method that cannot meet requirements of this system.

Table 3. Test table of dissolved oxygen value detection system.

Temperature	Test value of DO6309 /ppm	Test value of this system /ppm
0 °C	13.55	13.52
5 °C	11.81	11.77
10 °C	10.50	10.51
15 °C	9.52	9.40
20 °C	8.71	8.77
25 °C	7.70	7.82
30 °C	7.00	7.10
35 °C	6.48	6.51

For carp, the suitable temperature is 25°C ~32°C and the optimal dissolved oxygen value is 6.5 mg/L. During continuous 24 h, the dissolved oxygen in water must be above 5 mg/l in more than 16 h and it cannot be under 3 mg/l at any time [10], the water depth is 1.2~1.5 m. Data at 0:00, 8:00, 12:00, 16:00 and 20:00 per day were recorded during the experiment period in order to get average value at each time point for carrying out analysis. Dissolved oxygen value and condition of water level control is shown as table 4. It can be seen from table 5 that the control results of this system during 180 days of experiment were accurate and stable.

Table 4. Dissolved oxygen value and water level control test.

Time	Dissolved oxygen value (mg/L)	Water level (m)
0:00	5.6	1.2
8:00	6.5	1.29
12:00	6.4	1.33
16:00	6.6	1.30
20:00	6.7	1.32

6. Conclusions

Aiming at disadvantages of onsite wired monitoring system that is massively applied at present, the radio communication and control system for aquaculture designed in this paper realized wireless communication and control so as to avoid disadvantages of hard to network, uneasy to expand and high cost. Data transfer is more accurate and reliable after adding customized protocol and answer signal in radio communication. The highest error and missing rate within 1000 m is merely 0.36, the lowest error and missing rate is 0.05 and the longest response time is 49 ms. After temperature compensation and error correction is added to dissolved oxygen value detection system designed in this paper, its measured value is close to the testing value of existing dissolved oxygen value transmitter DO6309 and it adopts wireless data transfer mode that meets the requirement of this system. The wireless control of dissolved oxygen value and water level can be controlled within the appropriate range with stable and precise control.

Acknowledgements

This paper was funded by the Natural Science Project of Sichuan Education Department under Grant 12ZA277 and the interest plan of College student's scientific research training under Grant 2011083.

References

[1]. Xiangzhong Luo, Present situation and trend of Chinese freshwater fisheries, *Journal of Yangtze University (Natural Edition)*, Vol. 2, Issue 5, 2005, pp. 98-102.

[2]. Dazhi Huang, and Jianhua Hu, Study on the detection and control system in the aquaculture industry, *Journal of Agricultural Mechanization Research*, Vol. 31, Issue 11, 2009, pp. 219-222.

[3]. Yongfeng Zhao, Haiyan Hu, and Gaozhong Jiang, Status quo and development trends of facility fishery in China, *Chinese Fisheries Economics*, Vol. 30, Issue 5, 2012, pp. 91-99.

[4]. Xingguo Liu, Zhaopu Liu, and Pengxiang Wang, et al. Aquaculture security guarantee system based on water quality monitoring and its application, *Transactions of the CSAE*, Vol. 25, Issue 3, 2009, pp. 186-191.

[5]. Bing Shi, De'an Zhao, and Xingqiao Liu, et al, Intelligent monitoring system for industrialized aquaculture based on wireless sensor network, *Transactions of the CSAE, Vol.* 27, Issue 9, 2011, pp. 136-140.

[6]. Wei Lu, and Qiuling Wang, Developmental status of fisheries establishments in our country, *Modern Fisheries Information*, Vol. 20, Issue 4, 2005, pp. 13-15.

[7]. Chun Lei, Xiaoyang He, and Shenghui Su, Design and implementation of multipoint temperature acquisition system based on ZigBee, *Automation technology and applications*, Vol. 29, Issue 4, 2010, pp. 43-46.

[8]. Zhang Hongyan, Yongming Yuan, and Yanhui He, et al, Design and Implementation of Water Quality Monitoring System for Pond, *Journal of Agricultural Mechanization Research*, Vol. 33, Issue 10, 2011, pp. 63-65.

[9]. Xin Zhang, Discussion on intensive fishpond water quality control and management technology, *Modern Agriculture*, Vol. 39, Issue 12, 2011, pp. 82.

[10]. GB11607—89, National fishery water quality standard of the People's Republic of China.

Sensors & Transducers, Vol. 21, Special Issue, May 2013, pp. 15-19

Sensors & Transducers

http://www.sensorsportal.com

Application of New Information and Equal Dimensional Grey Model in Industrial Water Consumption

[1, 2] Fang He, [2] Tao Tao, [3] Min Li

[1] College of Urban Construction, Wuhan University of Science and Technology,
Wuhan, Hubei, 430065, China
Tel.: 13886018408

[2] School of Environmental Science and Engineering, Huazhong University of Science and Technology,
Wuhan, Hubei, 430074, China
Tel.: 13908628125

[3] Wuhan Institute of Water Conservancy Planning and Design
Wuhan, Hubei, 430017, China
Tel.: 13871073203

E-mail: hefang@wust.edu.cn, taocaiye@public.wh.hb.cn, 61750935@qq.com

Received: 21 March 2013 /Accepted: 14 May 2013 /Published: 30 May 2013

Abstract: It has always been an important research objective to improve prediction accuracy with limited data. The Grey Model is a typical example in forecasting industrial water c onsumption with a small amount of data. As to the basic grey forecasting models, the prediction accuracy can still be improved. So this paper proposed an improved new information and equal dimensional grey model. The industrial water consumption of Rongchang County in Chongqing is predicted by the basic grey model and the improved new information and equal dimensional grey model. It is tested by residual examination and actual test. The precisions are higher than 95 %. The improved new information and equal dimensional grey forecasting model can greatly improve the prediction accuracy. The relative error is only 0.5 % tested with the actual water consumption in 2012. So it can be used to forecast the long-term industrial water consumption. *Copyright © 2013 IFSA.*

Keywords: Industrial water consumption, Forecasting, Grey model, New information and equal dimensional grey model, Rongchang county.

1. Introduction

Water is the important material base of economic and social development. Industrial water offers important support for production. It is the premise and the foundation of planning decision and economic operation [1]. In recent years it is a paradox between the increased water consumption and the shortage of water resources. Therefore, the prediction accuracy of industrial water consumption has important significance for formulating and implementing industrial development planning, adjusting industrial structure and water structure scientifically. There are different approaches to industrial water consumption forecasting, including long-term forecasts and short-term forecasts. The former is discussed here. The common long-term forecasting methods are the causal method, the Markov method, the linear regression model, the time series model, the artificial neural networks model etc. But each forecasting

model has its own conditions of application [2-7]. For example, the causal method must have enough historical data and enough analysis. The Markov method must know the transition probability between each state. The linear regression model requires a larger number of samples to assume the variables are independent and the samples have normal distribution. The time series model requires stable trends and patterns of historical data. The artificial neural networks model requires long-term, continuous historical data. If there is not a large amount of data, their prediction accuracy is not very high. In a county of China, the industrial water consumption data sequence is short. It also limits the application of some prediction methods. So it's necessary to construct predictive models with high precision to forecast industrial water consumption. The constructed models must be simple and require only a small amount of data.

In recent years, grey theory and grey model are used to predict urban water resources utilization widely. The grey theory is first brought out by Dr. Julong Deng [8]. Yaoguo Dang[9] discussed several advanced models based on the GM (1, 1) model. Fu Xiaoxue and Chen Yijin [10] respectively applied unbiased grey GM (1, 1) model, nonlinear model and combined model of them to calculate water consumption of Beijing from the year 2001 to 2010. The results showed that combination of unbiased grey GM (1, 1) model with nonlinear model had highest accuracy than the other single model. Baoxiang Zhang and Jiaquan Wang [11] discussed GDMG (grey dynamic model group) and made a middle and long term forecast for industrial water demand of Ji'nan city. The predicted results of GMDG are reliable and practical by comparing with actual data and other method results. Faqiang Guo [12] discussed the modeling principle of grey theory and the recognition method of model parameter. The precision test of residual error examination and posterior difference examination showed that the fitting precision reached 98.72 %.

This paper intends to introduce the grey model to forecast industrial water consumption in a fast-growing urban region. Based on the basic grey prediction model GM (1, 1), it is improved to construct the dynamic new information and equal dimensional grey model. The grey models are used to forecast the industrial water consumption of Rongchang County in Chongqing. Compared to the traditional forecasting methods, the improved grey model has great practicability with simple-calculation and better accuracy.

2. Grey System Theory and Model

2.1. Grey System Theory

The grey theory is aimed at questions of "data less and uncertainty". The methods of grey forecasting search for the whole system rules, directly through constructing exponential growth model with grey generating of the original data. The main features are as follows:

(1) It is modeled with the original data generated by the grey sequence. And others are modeled directly with original data sequence.

(2) It belongs to the model of less data, allowing data less to 4. And most other models are based on a large number of sample data.

(3) It is a model with partial difference and partial differential properties. It can describe the essential characteristics of internal changes in data. It can reflect the actual situation of the system better. But general system theory obtains differential model by constructing with recurrence method.

Industrial water consumption is under the influence of economic development, industrial structure, climate, national income level, social activities and so on. There are many random factors. Some factors are determined and other factors are not sure. So it can be treated as a typical grey system. The grey model can be used to forecast industrial water consumption.

2.2. GM (1, 1) Model

At present, the grey system prediction is mainly with the GM (1, 1) model. The procedures of the basic GM (1, 1) are as follows:

Step 1: Establish the original time series of no obvious rule from observed data,

$$x^{(0)} = \{x^{(0)}(1), x^{(0)}(2), ..., x^{(0)}(n)\}, \quad (1)$$

Step 2: Based on the original time series $x^{(0)}$, it is accumulated to generate the regular $x^{(0)}$-AGO series $x^{(1)}$.

$$x^{(1)} = \{x^{(1)}(1), x^{(1)}(2), ..., x^{(1)}(n)\}, \quad (2)$$

Where

$$x^{(1)}(k) = \sum_{i=1}^{n} x^{(0)}(i), \quad (3)$$

Thus the random influence of the original sequence is weakened. Fitting to the weakened white sequence { $x^{(1)}(k)$ }, forecasting model is established.

Step 3: According to the new sequence { $x^{(1)}(k)$ }, calculating the white background value $z^{(1)}(k)$ in the grey model, where

$$z^{(1)}(k) = 0.5x^{(1)}(k) + 0.5x^{(1)}(k-1) \quad (4)$$

Step 4: The grey differential equation and the whitening differential equation of GM (1, 1) are obtained, respectively, as follows:

$$x^{(0)}(k) + az^{(1)}(k) = b \tag{5}$$

$$\frac{dx^{(1)}}{dt} + ax^{(1)} = b, \tag{6}$$

where a is the development coefficient, reflecting the development trend of $x^{(0)}$ and $x^{(1)}$;

b is the grey action.;

a and b are the parameters of the differential equation.

Step 5: Calculate development coefficient a and grey action b.

Where:

$$A = (a,b)^T \tag{7}$$

$$B = \begin{vmatrix} -z^{(1)}(2) & 1 \\ -z^{(1)}(3) & 1 \\ \cdots & \cdots \\ -z^{(1)}(n) & 1 \end{vmatrix} \tag{8}$$

$$Y = \begin{vmatrix} x^{(0)}(2) \\ x^{(0)}(3) \\ \cdots \\ x^{(0)}(n) \end{vmatrix} \tag{9}$$

It can be obtained by least square method:

$$A = (B^T B)^{-1} B^T Y \tag{10}$$

Step 6: The response equation of the white GM(1,1) equation is the solution of differential equation in the initial conditions as:

$$x^{(0)}(1) = x^{(1)}(1) = \hat{x}^{(1)}(1) \tag{11}$$

Then the forecasting model of generate data sequence $x^{(1)}$ is:

$$\hat{x}^{(1)}(k+1) = (x^{(0)}(1) - \frac{b}{a})e^{-ak} + \frac{b}{a} \tag{12}$$

$$\hat{x}^{(0)}(k+1) = \hat{x}^{(1)}(k+1) - \hat{x}^{(1)}(k) \tag{13}$$

In the equation $x^{(0)}(k)$ is the element value of the first k years in the original sequence- $x^{(0)}$;

$x^{(1)}(k)$ is the element value of the first k years in the accumulated sequence- $x^{(1)}$. (k= 1, 2, ..., n);

$\hat{x}^{(0)}(k)$ and $\hat{x}^{(1)}(k)$ are the predicted values at the time of k in the original sequence and the accumulated sequence respectively.

The equation（12）and（13）are time response function models of the basic grey prediction model. They are the specific function equations to predict future data.

2.3. Dynamic New Information and Equal Dimensional Grey Forecasting Model

As for long-term industrial water consumption, some disturbance factors in the future will constantly make intrusions into system and impact the system over time. The GM (1, 1) prediction model can forecast from the initial value to any moment in the future. The farther the future time, the greater the grey space of the predicted value. So only few data next to the first n data in original material has high-precision and practical significance for forecasting.

In the industrial layout, it is necessary to predict industrial water consumption in the future years or longer. But there is only several available data from the past to the present. So usually GM (1, 1) grey forecasting model is constructed to predict a value. In the prediction model new information will be added into data sequence and the old data will be removed at the same time. Then there is the same dimension between the new development sequence and the original sequence.

That is to say:

$$x^{(0)} = \{x^{(0)}(1), x^{(0)}(2), ..., x^{(0)}(n-1), x^{(0)}(n)\} \tag{14}$$

The new data $x^{(0)}(n+1)$ will be joined in the end of the sequence and at the same time the data $x^{(0)}(1)$ will be removed.

So:

$$x^{(0)} = \{x^{(0)}(2), x^{(0)}(3), ..., x^{(0)}(n), x^{(0)}(n+1)\} \tag{15}$$

It is called as dynamic new information and equal dimensional grey model. It can predict life so far by processing data of metabolism, forecasting gradually and filling vacancies in order of precedence.

2.4. Model Test

1) Residual test.

Residual test is to inspect the error of the model value and the actual value by point. For a given sequence- $x^{(0)}$, $\varepsilon(k)$ is the residual of GM (1, 1). $\varepsilon(avg)$ is the average residual. p° is the modeling accuracy of GM(1, 1).

Where

$$\varepsilon(k) = \frac{x^{(0)}(k) - \hat{x}^{(0)}(k)}{x^{(0)}(k)} 100\% \tag{16}$$

$$\varepsilon(avg) = \frac{1}{n-1} \sum_{k=2}^{n} |\varepsilon(k)| \tag{17}$$

$$p^{\circ} = (1 - \varepsilon(avg))100\% \tag{18}$$

2) Actual inspection.

Precisions are obtained by contrasting the actual data to predicted data.

3. Case Analysis

3.1. Modeling

As data to industrial water consumption (Table 1) of Rongchang County in Chongqing from 2006 to 2011, industrial water consumption of 2012 is forecasted. Modeling respectively as GM (1, 1) model and the improved dynamic new information and equal dimensional grey model, forecasting results are in Table 2.

Model 1: GM (1, 1) model sequenced of data from 2006 to 2011:

$$\hat{x}^{(1)}(k+1) = 121.39e^{0.3449763k} - 70.76 \quad (19)$$

Model 2: GM (1, 1) model sequenced of data from 2006 to 2010:

$$\hat{x}^{(1)}(k+1) = 116.43e^{0.3523416k} - 65.80 \quad (20)$$

Model 3: Grey model has equal dimension to model 2, modeling with data of added 2011 and removed 2006:

$$\hat{x}^{(1)}(k+1) = 163.46e^{0.3545656k} - 108.68 \quad (21)$$

3.2. Results Test

(1) Residual test

According to the model prediction and original data, residual is obtained as the following Table 3.

The average residual and model precision are in the following Table 4.

Table 1. Raw data of industrial water consumption in 2006-2012.

Year	2006	2007	2008	2009	2010	2011	2012
Industrial water consumption (10^4 m^3)	50.63	54.78	70.35	97.24	148.87	204.26	288.67

Table 2. Prediction results of three models.

Year	2006	2007	2008	2009	2010	2011	2012
Predicted value of model 1 (10^4 m^3)	50.63	50.01	70.61	99.70	140.77	198.75	280.64
Predicted value of model 2 (10^4 m^3)	50.63	49.18	69.95	99.50	141.53	201.31	286.30
Predicted value of model 3 (10^4 m^3)	-	54.78	69.57	99.16	141.37	201.53	287.30

Table 3. Residual of model.

Year	2006	2007	2008	2009	2010	2011	2012
Residual of model 1(%)	0.0	-8.7	0.4	2.5	-5.4	-2.7	-2.8
Residual of model 2(%)	0.0	-10.0	-0.6	-2.3	-4.9	-1.4	-0.8
Residual of model 3(%)	-	0.0	-1.1	2.0	-5.0	-1.3	-0.5

Table 4. Precision of model.

	model 1	**model 2**	**model 3**
ε (%)	3.94	4.45	2.35
P。(%)	96.06	95.55	97.65

The Table 4 shows that the precision of grey model are more than 95 % and the grey models are suitable for forecasting the industrial water consumption in the county. The precision of modified dynamic new information and equal dimensional grey forecasting model is highest to 97.65 %.

(2) Actual inspection

The prediction results of 2012 are compared to the actual value as the following Table 5. The inspection of predicted results in Table 5 shows that the residual of grey model are under 5 % and the grey models are suitable for forecasting the industrial water consumption in the county. The residual of modified dynamic new information and equal dimensional grey forecasting model for industrial water consumption of 2012 is only 0.5 %. The accuracy is higher than the other two models.

Table 5. Actual inspection table.

	Actual value	Model 1	Model 2	Model 3
Industrial water consumption (m^3)	288.67	280.64	286.30	287.30
Residual (%)	-	-2.8%	-0.8%	-0.5%

4. Conclusions

With the development of society and economy, the industrial water consumption increased constantly. To use water efficiently, it is necessary to forecast the industrial water consumption. Many forecasting models have been proposed, including the time series method, artificial neural networks and grey forecasting model typically. Each forecasting model has its own advantages and disadvantages. Then it is most important to seek ways to improve the forecasting accuracy of prediction models. Influenced by the present water resources, different industry, production process, water price and other factors, the industrial water consumption is of uncertain factors and has no significant statistical law. The statistical data of industrial water consumption in most cities in China is limited. Depending on a large number of historical data to obtain statistically significant results, the traditional forecasting methods cannot be used to predict future industrial water consumption accurately. Therefore, it is important to construct effective predictive models with limited data. So the GM (1, 1) forecasting model is proposed. At the same time, in order to obtain a forecasting model that has highly accuracy with limited data, the traditional GM (1, 1) is improved to the modified dynamic new information and equal dimensional grey model. Using the grey system modeling tool, the industrial water consumption of Rongchang County in Chongqing is predicted from 2006 to 2012. The case study is successful even with limited historical data of industrial water consumption. As for industrial water consumption of 2012, the modified model attains the lowest residual of only 0.5 % and the highest accuracy of 97.65 %. Therefore, the modified dynamic new information and equal dimensional grey model can significantly improve the prediction accuracy of the grey forecasting model. The proposed model is very useful for forecasting the industrial water consumption in Rongchang County. It has certain reference value for the adjustment of industrial structure and water structure scientifically.

Acknowledgements

The authors are grateful for the comments and historical data provided by Rongchang water company in Chongqing.

References

[1]. Schleicha, J., Hillenbrand, T., Determinants of residential water demand in Germany, *Ecological Economics*, Vol. 6, Issue 8, 2009, pp. 1756–1769.

[2]. Cutore P., Campisano A., Probabilistic prediction of urban water consumption using the SCEM-UA algorithm, *Urban Water Journal*, Vol. 5, Issue 2, 2008, pp. 125-132.

[3]. Cheng Qi, Ni-Bin Chang. System dynamics modeling for municipal water demand estimation in an urban region under uncertain economic impacts, *Journal of Environmental Management*, Vol. 9, Issue 2, 2011, pp. 1628-1641.

[4]. Mahmut F., Mustafa E. T., Comparative analysis of neural network techniques for predicting water consumption time series, *Journal of Hydrology*, Vol. 38, Issue 4, 2010, pp. 46–51.

[5]. Mahmut F., Mustafa E. T., Comparative analysis of fuzzy inference systems for water consumption time series prediction, *Journal of Hydrology*, Vol. 37, Issue 4, 2009, pp. 235-241.

[6]. Mehmet A. Y., Mahmut F. T., Adaptive neuro fuzzy inference system approach for municipal water consumption modeling: An application to Izmir, Turkey, *Journal of Hydrology*, Vol. 36, Issue 5, 2009, pp. 225-234.

[7]. Firat M., Yurdusev M. A., Evaluation of artificial neural network techniques for municipal water consumption modeling, *Water Resources Management*, Vol. 23, Issue 4, 2009, pp. 617–632.

[8]. Julong Deng, Introduction to Grey Mathematical Resource Science, *Huazhong University of Science and Technology Press*, 2007.

[9]. Yaoguo Dang, Research of Grey Forecasting and Decision Model, *Science Press*, 2009.

[10]. Fu Xiaoxue Chen Yijin, Modeling for Water Resources Utilization of Beijing, in *Proceedings of the International Conference on Advances in Engineering 2011, Procedia Engineering*, Vol. 24, pp. 629–633.

[11]. Baoxiang Zhang, Jiaquan Wang, Grey dynamic model group and its application in predicting of industrial water demand, *Journal of Water Resources & Water Engineering*, Vol. 16, Issue 3, 2005, pp. 44-47.

[12]. Faqiang Guo, Prediction of City Industrial Water Demand Based on Grey GM (1, 1) model, *Ground Water*, Vol. 32, Issue 3, 2010, pp. 108-110.

Sensors & Transducers, Vol. 21, Special Issue, May 2013, pp. 20-24

Sensors & Transducers

http://www.sensorsportal.com

Stress Distribution Model of Prefabricate Block Electric Furnace Roof

Jia Liu, Gongfa Li, Guozhang Jiang, Jianyi Kong, Liangxi Xie, Shaoyang Shi

College of Machinery and Automation, Wuhan University of Science and Technology, China, 430081

Tel.: 18607185291

E-mail: liujia386691872@163.com

Received: 31 March 2013 /Accepted: 14 May 2013 /Published: 30 May 2013

Abstract: The furnace cover is an important equipment of electric arc furnace steelmaking, the thermal insulation performance and service life directly affects the economic benefits of iron and steel enterprises. Considering the contact between the precast block, this paper establish the CAD/CAE model of high aluminum brick furnace cover and a precast furnace cover (casting three block, eight block, twelve block) , based on heat transfer theory apply the finite element software ANSYS analyzes the stress field of steady state about high aluminum brick furnace cover and a precast block furnace cover in the last stage of melting, which facilitates the analysis of the stress level and distribution of furnace cover, provides the theory support for the production and promotion of precast block furnace cover. *Copyright © 2013 IFSA.*

Keywords: Electric furnace roof, Stress field, Finite element method, Distribution model.

1. Introduction

Arc furnace as a major method of large-scale steel-making, which it makes use of high temperature melting ore and metal that was produced by electrode arc, the advantage of its rich raw material source, power supply and the price is low is a strategic significance for our steel industry to get rid of bad situation and make our country from steel large produced into steel strong.

Electric furnace cover is an important part of electric arc furnace lining, the length of life of the furnace cover and thermal insulation performance, technical and economic indexes of steel production, quality, and consumption has a very close relationship. Domestic and foreign scholars on the furnace cover has taken many measures to reduce the production cost, enhance the thermal stability, such as improving the furnace cover material, improve the content of alumina brick, increase the camber of furnace roof and height of the furnace lid center to the weld pool surface, improvement of operation, using water-cooled furnace cover brick furnace cover. Although these measures have achieved some results, still failed to solve the those problem of refractory brick furnace cover that difficult installation, short service life, the water-cooled furnace cover heat loss and can not meet the needs of development that electric arc furnace turn into large capacity ultra high power. Therefore, it is the main factor of restricting steel benefit that the installation period, thermal insulation performance and the service life, which it has a crucial impact on productivity and economic benefits of the iron and steel enterprise. Therefore, how to shorten the furnace cover the installation period and improve its service life has become an important measure to reduce the production cost and enhance the

competitiveness of electric arc furnace steelmaking technology.

This paper establishes the complete CAD/CAE model of the electric furnace roof with finite element software which it is based on the geometric model of a 30t electric furnace roof of a steel industry, and respectively calculates stress field of the high aluminum brick roof and the prefabricate block roof.

2. Established CAD/CAE Model of the Electric Furnace Roof

High alumina brick furnace cover is formed by moulded high aluminum brick, precast block electric furnace cover is made of fireproof material casting precast block in accordance with the principle of assemble building blocks together, although the manufacturing process is different, the shape and size are same. So during the CAD modeling process, based on a real geometry of a certain steel 30t electric cover (the 3D effect graph as shown in Fig. 1) to establish CAD model of all the furnace cover.

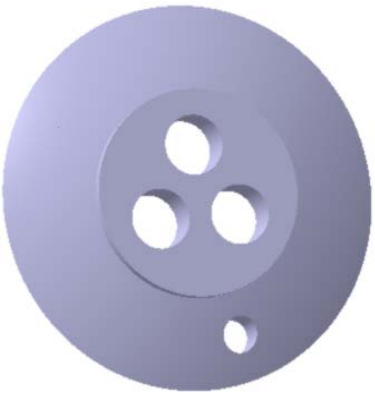

Fig. 1. The entity of electric furnace cover.

Taking into account the thermal cover transfer between center cover and furnace cover, all models were established the complete model which including center cover and furnace cover. Its main dimensions: charging hole diameter is 150 mm, the electrode hole diameter is 250 mm, the circle diameter of electrode hole center is 900 mm, the upside surface of center cover diameter is 1730 mm and the downside surface diameter is 1606 mm, the turning diameter of the outer surface of furnace cover is 3218 mm and inner surface diameter is 3000 mm. Due to the influence of the furnace cover geometry, it is difficult to cast the whole furnace cover, at the same time, according to the demand of the project, this paper set up only block furnace high aluminum brick furnace cover and precast furnace cover (three, eight and twelve) of three kinds of casting solutions.

Established CAD model of two kinds of furnace cover are shown in Figs. 2~5.

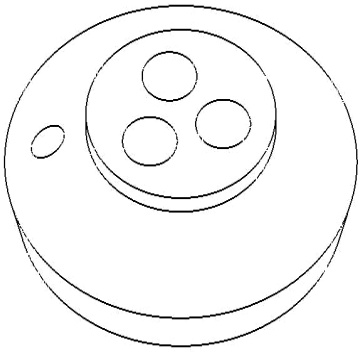

Fig. 2. The CAD model of the whole high aluminum brick furnace cover.

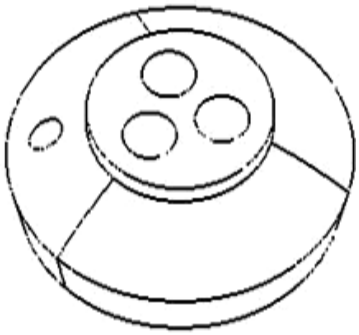

Fig. 3.CAD model of precast block furnace cover (casting three).

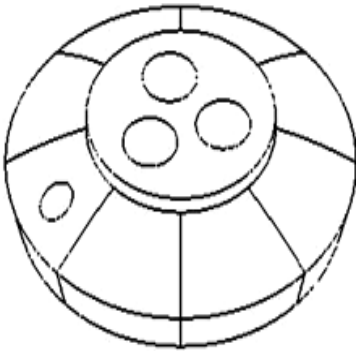

Fig. 4. CAD model of precast block furnace cover (casting eight).

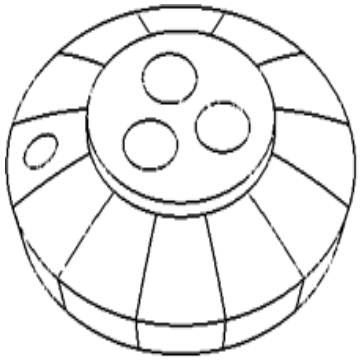

Fig. 5. CAD model of precast block furnace cover (casting twelve).

Applying ANSYS to thermal analysis, first established a geometric model, and then build the finite element model. Create CAD model, then to create CAE model, including the parameter definition of electric furnace cover material, choice of analysis unit type and mesh control.

3. The Stress Field Analysis of Electric Furnace Cover

Only when the material's temperature changes, due to the external constraints and mutual constraints of each part internal, so that it cannot completely free expansion and contraction will lead to the generation of heat stress. In the last stage of melting furnace cover under thermal shock is very strong, so it will produce thermal stress. In this chapter, a furnace cover temperature field as an initial condition ,at the same time, carry out a boundary treatment of structure analysis on the furnace cover in need, make numerical simulation for the stress level and distribution .

Using the sequential coupling method when calculate stress field of the furnace cover, which is mean calculated model of the temperature field at first , then regard the result of temperature field as body load to calculate stress field of it. This paper focuses on precast block of furnace cover whether can withstand temperature shock and not to burst damage, so when processing the stress analysis, just set the node temperature into the model as the body load, Considering the placement situation when assembling the furnace cover and the furnace body, and the locate function of bevel on furnace cover bottom with the cooling water pipe. The boundary condition and the load of stress analysis were treated as follows:

(1) The last brick need external force to push in when build the furnace cover with refractory brick,

(2) Considering a furnace cover deadweight, acceleration of gravity were applied for all models in Z direction (MPA units in 9800);

(3) All nodes that lie in bevel of the bottom of furnace cover were constrained under Descartes coordinates system, and ignore the function of drive, lifting, rotating on the furnace cover;

(4) Regarding the node temperature value of thermal analysis as the body load of structural analysis.

Due to size and shape furnace cover will be changed with thermal shock, it should be according to the fourth strength theory to determine the stress level. The equivalent stress of ANSYS (Von Mises Stress) is calculated according to the fourth strength theory. So, after obtain the calculate destination file, draw the equivalent stress pattern of furnace covers model in ANSYS universal post processor, to show that the variation of stress level in direction (thickness) of charging hole cross section, using ANSYS slice functions split each model along the center symmetry plane of feeding hole, to obtain the equivalent stress slicing image of each furnace cover model, as shown in Figs. 6~9.

The statistics about maximum, minimum and the average stress and contact stress level of each furnace cover model are shown in Table 1; MPA system of units, unit of stress is MPa.

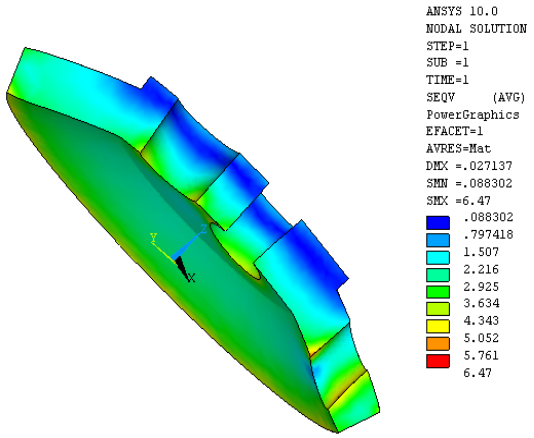

Fig. 6. Equivalent stress slicing image of the whole high aluminum brick furnace cover.

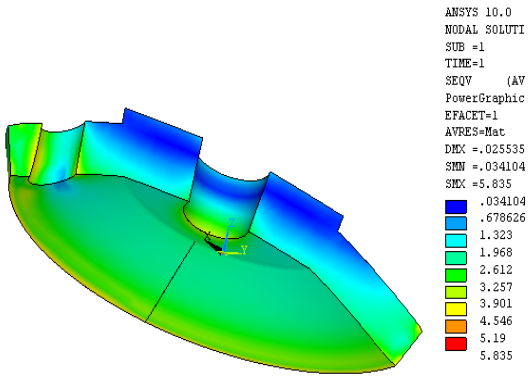

Fig. 7. Equivalent stress slicing image of precast block furnace cover (casting three pieces).

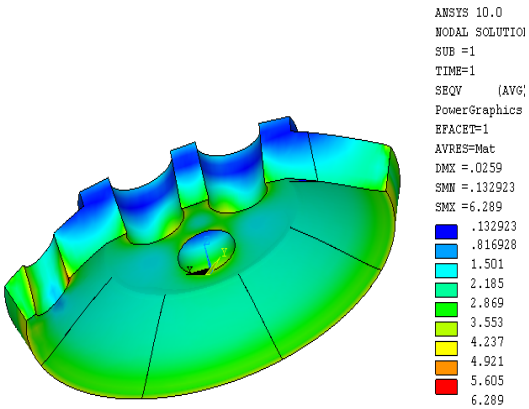

Fig. 8. Equivalent stress slicing image of precast block furnace cover (casting eight pieces).

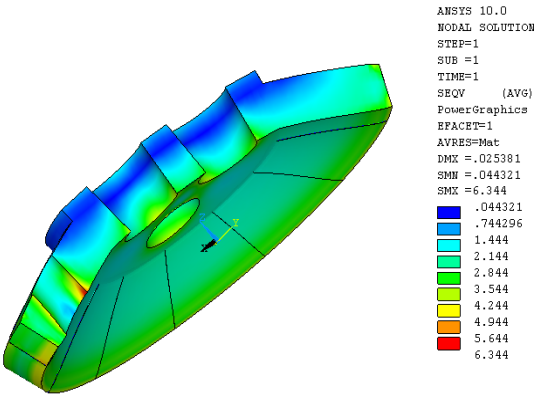

Fig. 9. Equivalent stress slicing image of precast block furnace cover (casting twelve pieces).

Table 1. Statistics of the model of stress level.

Stress	High aluminum brick furnace cover	Precast block furnace cover (casting three pieces)	Precast block furnace cover (casting eight pieces)	Precast block furnace cover (casting twelve pieces)
Maximum	6.47	5.835	6.289	6.344
Minimum	0.088	0.034	0.132	0.044
Average	1.507~ 4.343	1.323~ 3.257	1.501~ 3.553	1.444~ 3.544
Average of contact stress		0.007~ 1.997	0.027~ 1.996	0.012~ 1.95
Maximum of contact stress		3.588	3.57	3.5

The Fig. 6~9 show that it is different equivalent stress level in two kinds of fabrication process of the furnace cover. The maximum equivalent stress of high aluminum brick furnace cover is 6.47 MPa. Most of the stress level of the furnace cover is range from 1.507 MPa to 4.343 MPa, which is higher than precast block furnace cover in maximum and average stress. According to the fourth strength theory, material failure is mainly caused by the deviator strain energy which is equivalent stress, the higher equivalent stress that material bear, then the shorter service life of it. From which we can infer, because the equivalent stress level of precast block furnace cover is low, it has longer service life than the high aluminum brick furnace cover, This is coincide with the experiment that the service life of high alumina EAF arch prefabricated block in a factory is more than 600 [4] furnaces and the high aluminum brick EAF arch is generally 80~120 furnaces. Fully illustrates that precast block furnace cover has longer service life than high aluminum brick furnace cover, shows that simulation results coincide with the test results, which the calculation result is consistent with the theoretical analysis.

The calculated results is not only coincide with experimental results, but also in according with theoretical analysis, which is mean that is reasonable for the established model, load and handle boundary condition, proves the reliability of the simulation, provides theoretical support for the production and promotion of precast block furnace cover.

4. Conclusions

Having simulated the stress field of high aluminum brick cover and precast furnace cover in the final stage of melting. The calculation results have indicated that the general stress level of precast block furnace cover is lower than high aluminum brick furnace, so service life of the precast block furnace cover is longer than high aluminum brick cover, which provides theoretical support for the production of precast block in respect of service life. The stress level of furnace cover present two trend that one is in radical direction which is higher in around of outer circle than center; another is in thickness direction which is higher in inner wall than outer. The around of charge hole in furnace cover which is the most likely to damage parts. For the precast furnace cover, recommended taking measures that changing the size of the feeding hole and set it position to reduce the stress concentration; increased the conical degree of faying surface of center cover and precast block to prevent them separate. the contact stress between furnace cover and precast block will affect the performance of the furnace cover, we recommend change the faying surface of them to groove shape or enforce the fastening device; Among casting solutions, the furnace cover which is assembled by three pieces of casting precast block obtain lower stress levels, has a longer service life, provide a quantitative reference for selection of casting scheme.

References

[1]. Hongxi Zhu, Chengji Deng, etc., Preparation and application of bauxite-based prefabricated block for electric furnace roof, *Steelmaking*, 2, 2008.

[2]. Guozhang Jiang, Jianyi Kong, Gongfa Li etc., Research and application of thermo-mechanical stress model for bottom working lining of 250~300t ladle, *Steelmaking*, 24, 2, 2008, pp. 22-25.

[3]. Gongfa Li, Peixin Qu, Jianyi Kong, etc., Influence of Working Lining Parameters on Temperature and Stress Field of Ladle, *Applied Mathematics & Information*, 7, 2, 2013, pp. 439-448.

[4]. Gongfa Li, Jianyi Kong, Guozhang Jiang, etc., Stress Field of Ladle Composite Construction Body, *International Review on Computers and Software*, 7, 1, 2012, pp. 420-425.

[5]. Gongfa Li, Jianyi Kong, Guozhang Jiang, Simulation research on influence of expansion joint of wall lining inladle composite construction body on thermal stress, Modern Manufacturing Engineering, 10, 2010, pp. 85-88.

[6]. Gongfa Li, Jianyi Kong, Guozhang Jiang, Influence of working lining parameters on temperature field of ladle composite construction body, Manufacturing Engineering, 12, 2010, pp. 77-80.

Conference Announcement

Topic E2: Transportation & Mobility

The Euromat conference series, organised by the Federation of European Materials Societies (FEMS), is one of the largest events of its kind in Europe, covering the full width of materials science and technology. We would like to direct your attention to the following Symposia which are focussing specifically on transport applications:

E2.I: Modeling, simulation, optimization of materials and structures in transportation
Prof. Kambiz Kayvantash, Société CADLM, Massy (F)

E2.II: Intelligent and adaptive materials and structures
Dr.-Ing. Dirk Lehmhus, ISIS Sensorial Materials Scientific Centre, Bremen (D)

E2.III: Energy absorbing and protective materials and structures
Prof. Massimiliano Avalle, Politecnico di Torino, Torino (I)

E2.IV: Production, properties and applications of hybrid materials and structures
Dr.-Ing. Kai Schimanski, Foundation Institut für Werkstofftechnik (IWT), Bremen (D)

DEADLINE CALL FOR PAPERS END OF JANUARY – WATCH OUT FOR DETAILS AT www.euromat2013.fems.eu OR CONTACT

ISIS Sensorial Materials Scientific Centre, University of Bremen

Board of Directors
Prof. Dr.-Ing M. Busse
Prof. Dr. W. Lang
Prof. Dr.-Ing. H.-W. Zoch

Managing Director
Dr.-Ing. Dirk Lehmhus

Wiener Straße 12
28357 Bremen

Fon +49 (0)421 5665 408
Fax +49 (0)421 5665 499

dirk.lehmhus@uni-bremen.de
www.isis.uni-bremen.de

Sensors & Transducers, Vol. 21, Special Issue, May 2013, pp. 25-29

Sensors & Transducers

http://www.sensorsportal.com

Test and Analysis of Metallurgical Converter Equipment

Shan Pang
College of Mechanical and Electrical Engineering,
Xinxiang University, Xinxiang 453007, Henan, China
Tel: 18738533913, E-mail: 9453734@qq.com

Received: 7 April 2013 /Accepted: 14 May 2013 /Published: 30 May 2013

Abstract: Oxygen top-blow converter is the main equipment in steel making, and its work reliability decides the security and economy of steel production. Therefore, how to design and test analysis of convertor has been an important subject of industry research. Geometric modelling and structure analysis of converter tilting device by using Pro/E program .The design Principle, basic design structure were analyzed in detail. The computer simulation software of metallurgical converter equipment and how to use it were introduced .It developed by VC++ software. The position of barycentre and moment curve in No.3 and No.4 are calculated. The converter acceleration down dip can be resolved by comparing the moment curve and center curve.

Keywords: Converter, Three-dimension model, Test, Analysis, Simulation.

1. Introduction

In recent years, the steel industry is developing rapidly, and pneumatic steelmaking is an important component in the steel industry. Therefore, the quality and output of the steel is directly related to the steel industry. To ensure the quality and yield of the steel, first of all ensure the safe operation of the converter equipment, especially the tilting part of the converter, it is not only the focus of the design converter, but also the difficulty. There are four converters in some iron and steel enterprise and the 4 # converter is a 60-ton converter, during the converter tapping or sampling, a lot of problems occur to 4 # converter in the actual production process, such as the accelerating the down – dip of the converter. According to statistics, this situation occurs 1-2 times per year. Once the molten steel poured out, which brings not only the economic losses but also the accidents of life. Many lessons have been learned at home and abroad from the accidents of converter "pouring steel" [1]. Now, the 12.5 planning is carrying out that is to adjust the production structure of excess industry and improve the resource utilization. All these measures are carrier out to make sure the safety of the production.

The slag influent the converter deeply when the converter is tapping and sampling. The slag not only erodes the mouth of the converter, but also accumulates greatly. The slag is a long distance from the trunnion centerline of the converter which has a great influence to the dumping moment. Therefore, the slag is an important consideration when we design the converter.

The content of this paper is the 4 # converter and the goal is to reduce the hidden trouble during the production through the analysis and calculations, finally, the feasibility of the measures are given to make sure the safety of the converter [2].

2. Three-Dimensional Model of the Converter

The converter model is divided into six main parts: the furnace mouth, slag panels, cold water pipe,

and steel plate of the mouth, the furnace body, bottom and internal firebrick. There are many problems about the 4 # converter. This article introduces the 3 #converter as a comparison in order that these problems are analyzed in more detail. 3 # converter is an 80-ton converter, which is similar to the 4 # converter on mechanical structure. Two converters are base on frequency control and the lowest frequency is 50Hz; the difference between the two converters is the bottle of the converter. One is round bottle such as Fig. 1 the other is tip such as Fig. 2.

This document is prepared according to our journal's manuscript instructions. You can use it as a template.

Fig. 1. The structure of the 4# converter.

Fig. 2. The structure of the 3# converter.

3. Converter Simulation Software

3.1. Description

In this paper, the design of the software is base on VC ++ [3], the main function is to imitate the converter operation; describe dynamic center curve of the converter and dumping moment curve and torque curve. The software can quickly and accurately get the center position of converter no matter what state it is, the converter tilting Moment curve is gotten much more easily. Observe dumping moment curve of the converter to find out the reason for pouring steel.

3.2. Basic Design Ideas

The two functions of this software include the static center of mass and dynamic center of mass. The slicing method and integral method is applied to calculate the center position curve of converter dynamically. First determine the intersection position between the steel surface and the furnace wall, and then calculate the center position of the steel, finally the results are obtained by the cumulative.

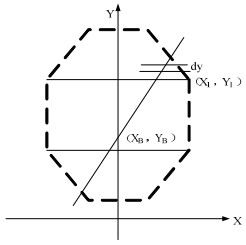

Fig. 3. The brief structure of the converter.

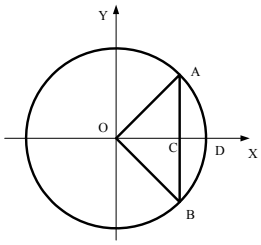

Fig. 4. The converter sections.

First, calculate the weight and center of mass coordinates of the small unit dy. α' is equal to the $\angle COB$, the fan-shaped area of the OAB is S1, the triangle area of the OAB is S2, ρ is the density of steel and ε is the control accuracy, vertical coordinate of the small unit dy is y.

The surface area of the molten steel is S3= (S1-S2), the center coordinates of fan of OAB in the direction of x is $L1 = 2OA \cdot \sin\alpha' / (3\alpha')$, the center coordinates of the triangle OAB in the direction of x is $L2 = 2OC/3$ .so the center of the area of ADBC in the direction of x is $L = (S1 \cdot L1 - S2 \cdot L2)/(S1 - S2)$ .so the weigh of dy is $Z_i = (S1 - S2) \cdot \varepsilon \cdot \rho$, the moments of the x-axis of the center of the small unit dy is $M_{xi} = L \cdot Z_i$. The moments of the y-axis of the center of the small unit dy is $M_{yi} = y \cdot Z_i$ [4].

According to (1) and (2), the center of mass coordinates formula:

$$x = \frac{M_{x1} + M_{x2} + M_{x3} + \cdots + M_{xi}}{Z_1 + Z_2 + Z_3 + \cdots + Z_i} \quad i = 1, 2, 3 \cdots , \qquad (1)$$

$$y = \frac{M_{y1} + M_{y2} + M_{y3} + \cdots + M_{yi}}{Z_1 + Z_2 + Z_3 + \cdots + Z_i} \quad i = 1, 2, 3 \cdots \qquad (2)$$

3.3. Friendly Interface of the Software

It is very easy to run the software, before running the software, please enter the specific parameters of the converter in parameters dialog box as Fig. 5. According to the data stored in TXT files, the curves of the steel center and molten steel dumping moment [5], then the curves are displayed in the view of the software. You can see the picture of molten steel and converter rotation when software is running, which is shown in Fig. 5.

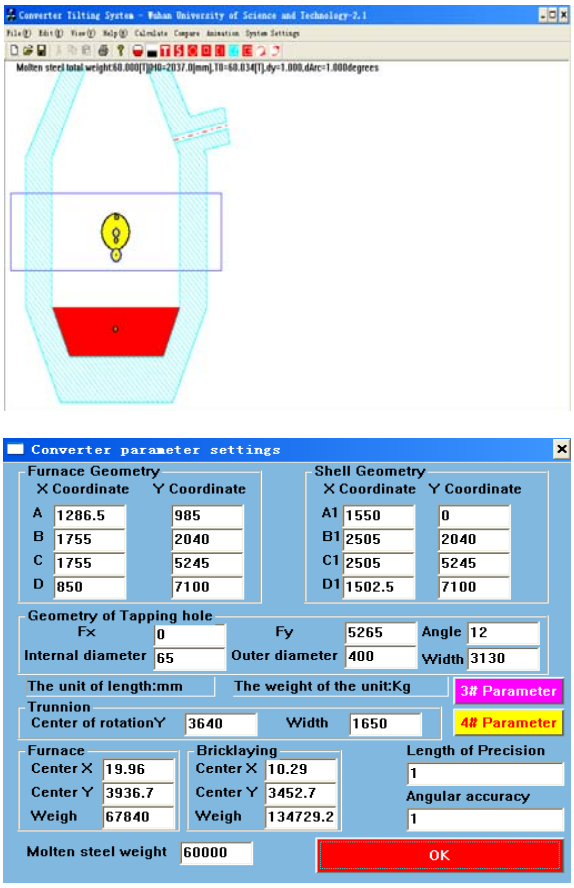

Fig. 5. Software Interface.

4. Calculation and Analysis of Center

Calculation of the software mainly refers to the center of mass of the converter and the center of mass is part of the calculation of dumping moment. Dumping Moment refers to the force acting on the ear axis when the converter is in the oblique. It is the main reference parameters of the converter on designing and calculations. The converter tilting moment is mainly composed of three parts, including empty furnace torque, hydraulic torque and friction torque. Among them, the empty furnace moment is caused by the weight of the converter as well as subsidiary parts, its curve of the rotation can be got by formula; Hydraulic torque is mainly caused by the weight of the molten steel, and its moment is difficult to calculate, and the center position change complexly, because it is the change with the rotation of the converter; The friction torque converter tilting ear axis caused by the friction force on the ear axis when the converter tilts, direction and converter tilting is in the opposite direction, the size remained unchanged.

Friction torque and air furnace torque calculation is very simple, do not repeat them here, the characteristics of the software is the calculation of the hydraulic torque converter which overcomes the previous shortcomings calculation is not fast and inaccurate. The software of the theory is base on the integral method and slicing method.

From the above description, the converter tilting moment is composed of three parts.

$$M = M_K + M_Y + M_M \,, \tag{3}$$

where M_K is the empty furnace torque, M_Y is the hydraulic torque and M_M is the friction torque.

4.1. Static Center Calculation of Converter

The definition of the static center is to calculate the center of main components of the converter. The article describes the method is base on the software which is designed for the converter. First, input the main parameters of the converter to the software, you can get the center curve of the converter that can be in any location. Table 1 shows the calculation results of the 3 # and 4 # converter [6].

Unit of data in Table 1 is mm; the distance is relative to trunnion centerline height of the furnace, in the other words, that means the relative value.

It can be seen from Table 1, the 3 # converter of the center is under the trunnion centerline after masonry the firebrick, 4 # converter of the center is also under the trunnion centerline. But with the slag in the furnace mouth, 4 # converter of the center is above the trunnion centerline. In other words, the converter of the motor torque is zero, it can not automatically reset at the effect of its own gravity and friction. From the above analysis, the slag is the main reason for dumping of the converter [7].

Table 1. The comparison of several cases of two converters.

Converter	4#Converter	3#Converter
With firebrick	-25.2	-248.2
Mouth with steel slag	51.3	-174.5
Weight of 2 tons	15.2	
Loaded 60T steel water	-436.7	-508
Centerline height of the trunnion	3640	3590

4.2. Dynamic Center Calculation

The calculation of the dynamic center of mass means that the change of the molten steel center when the converter is added molten steel. The operation method remains the same. The calculation of the dynamic center of mass is done at the same time, but instructed by two steps in this paper [8]. The center curve and torque curve of the 4# 60 t converter are shown as Fig. 6.

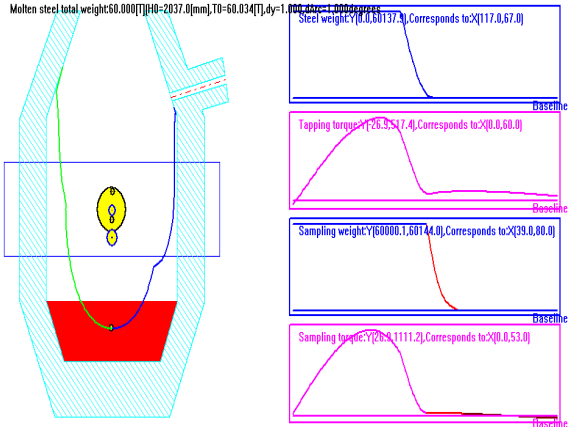

Fig. 6. The Center Curve and Torque Curve.

5. Dumping Moment Curve and Analysis

In the software, the dumping moment curves of 4# converter and 3# converter are got by setting the parameters that are shown as Fig. 7 and Fig. 8.

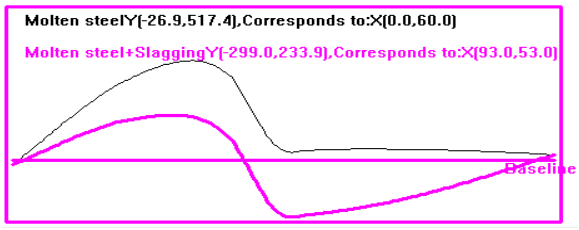

Fig. 7. The dumping moment curves of 4# converter.

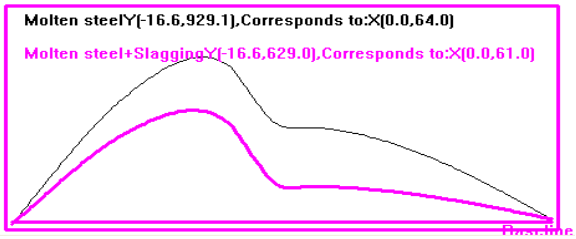

Fig. 8. The dumping moment curves of 3# converter.

Shown as Fig. 7, the thin solid line means the empty converter and the molten steel dumping moment curve, while the thick solid line means the empty converter, the molten steel and the slagging dumping moment curve [9]. The dumping moment curves of 3# converter are shown as Fig. 8.

From Fig. 7, it is got that the dumping moment of converter is positive and the dumping phenomenon is not occurred, when the slagging is not exited. But the dumping moment of converter is positive, if the slagging is exited.

From Fig. 8, Slagging tendency moment is larger than without the slagging tendency moment. However, the dumping moment is positive, so the 3# converter is safer than the 4# converter.

In short, lagging is the main reason which causes the converter to accelerate the down-dip, while the problem can be solved through increasing the weigh on the converter.

6. Conclusion

The software is designed to quickly get the converter dynamic center curve, which can be able to solve the problem of the converter dumping quickly.

The use of software is to observe the dumping torque curves dynamically, contrast and analyze the curves, the conclusion can be drawn that the main reason of 4 # converter "pouring steel" is converter center that is at above of the trunnion centerline, and as time goes on, the slag is accumulated in the converter mouth, all of these would cause the converter dumping quickly.

Therefore, Slag is the main reason for causing the converter dumping quickly, the measures can be taken in the converter bottom to increase the weight so that the total center of the converter is reduced below the trunnion centerline.

References

[1]. Q. M. Huang, The Calculation of Torque Analysis and Dynamic Simulation on Converter, *Heavy Machine*, Vol. 3, Issue 2, 2003, pp. 25-28.

[2]. H. Y. Liu, Q. Qin, The Analysis of the Too Large Tilting Moment of 220t Converter, *Mechanical Engineering and Automation,* Vol. 3, Issue 3, 2009, pp. 151-152.

[3]. David J, Kruglinski, Inside VC++, *Tsinghua University Press*, 2010. 9.

[4]. X. C. Chun, Calculating Hot-metal Ladle's Roll-over Moment by the Formula Method, *Shandong Metallurgy*, Vol. 30, Issue 4, 2008, pp. 41-43.

[5]. G. Q. Wei, D. F. Chen, H. X. Luo, Calculation Model of Converter Tilting Moment, Heavy Machine, Vol. 33, Issue 3, 2009, pp. 537-540.

[6]. W. C. Zhang, Discussion on Calculation Method for the Tilting Torque of ld Converter, *Shanghai Metals*, Vol. 29, Issue 6, 2007, pp. 47-50.

[7]. A. J. Yan, Y. R. Li, The Measure and Fault Diagnosis of the Converter Dumping Device Transmission System, *Metallurgical Equipment*, Vol. 3, Issue 5, 2007, pp. 59-61.

[8]. J. H. Zhang, 3D Finite Element Analysis on Overall Structure of New Basic Oxygen Furnace System, *Computer Aided Engineering*, Vol. 18, Issue 3, 2009, pp. 27-30.

[9]. X. Z. Wang, Analysis and Application of Materials and Heat Balance Calculation of 150t Converter at Angang, *Energy for Metallurgical Industry*, Vol. 29, Issue 3, 2010, pp. 61-64.

Sensors & Transducers, Vol. 21, Special Issue, May 2013, pp. 30-35

Sensors & Transducers

http://www.sensorsportal.com

Research of the L-Type Gantry Crane's System Based on BP Network and Genetic Algorithm

LI Yue, FAN Qin

College of Machinery and Automation of Wuhan University of Science and Technology, Wuhan 430081,China

Tel.: 15926447885

E-mail: liyue.1988@yahoo.com.cn

Received: 20 March 2013 /Accepted: 14 May 2013 /Published: 30 May 2013

Abstract: A kind of parametric finite element analysis system for the L type gantry crane's gate frame is developed by making use of the secondary development on the platform of ANSYS, MATLAB through VC++ programming. The interface technology of VC++, ANSYS, and MATLAB is employed as well as the encapsulation on APDL. To input parameter in the VC++ and to calculate the quality of the L type gantry crane so as to obtain the network training specimens constituted with 20 sets of parameters. The BP network is used to establish the mapping relationship which provides the adaptability function for the genetic algorithm. The genetic algorithm is adopted to accomplish the quality optimization. Then the ANSYS software is employed to simulate the optimized L type gantry crane. The results of the optimization and simulation show that the overall performance of the L type gantry crane is improved dramatically. *Copyright © 2013 IFSA.*

Keywords: L Type gantry crane, Parametric, Finite element method, BP network, Genetic algorithm, Visual C++.

1. Introduction

Gantry crane is widely used in outdoor places such as ports, stations and construction sites [1]. With the rapid development of the economy and trade of our country, crane machines become more effective and bigger.

This will inevitably lead to continuous increase of the size, load and weight of the crane whose performance directly affects its working efficiency [2].

Therefore, based on the object-oriented technology, this paper first uses neural network mapping and the genetic algorithm optimization methods to optimize the main parameters that influence the mechanical properties of gantry crane. Then ANSYS is utilized for parametric modeling. Finally, the calculation results are analyzed to check whether the obtained parameters meet the requirements of strength, stiffness and stability.

2. Setting up Optimized Mathematical Model of L Type Gantry Crane Structure

2.1. Design Variables of Gantry Crane

During the optimization design of L type gantry crane, in order to make the performance indexes of the structure meet the requirements and to minimize its quality, the number of design parameters is large. Moreover, to improve the design efficiency, parameters which greatly influence the structure

analysis are also selected as design variables. Fig. 1 shows the interface for the editing of optimized parameters. There are 16 selected design variables of gantry crane including: upper cover plate width of main girder X1 (initial value is 930); lower cover plate width of main girder X2 (initial value is 930); web height of main girder X3 (initial value is 1500); upper cross section height of outrigger X17 (initial value is 950); upper cross section width of outrigger X18 (initial value is 1520); lower cross section width of outrigger X19 (initial value is 450); lower cross section height of outrigger X20 (initial value is 350); section height of bottom girder X13 (initial value is 600); section width of bottom girder X14 (initial value is 450); cover plate thickness of main girder X4 (initial value is 10); main web thickness of main girder X5 (initial value is 12); vice web thickness of main girder X6 (initial value is 8); cover plate thickness of outrigger X11 (initial value is 8); web thickness of outrigger X12 (initial value is 10); cover plate thickness of bottom girder X15 (initial value is 10); web thickness of bottom girder X16 (initial value is 12). These design variables and the span, outrigger height, cantilever length and cart wheel track as well as some other important sizes basically determine the overall performance and quality of the L type gantry crane.

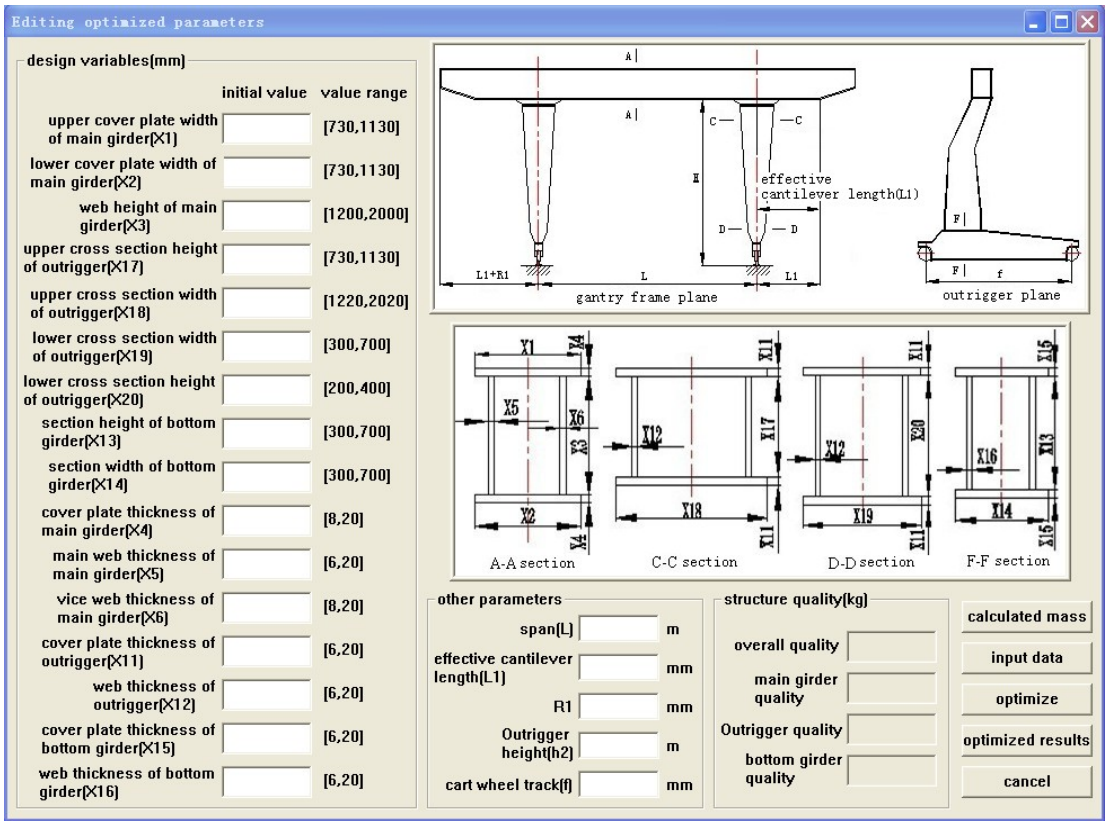

Fig. 1. Interface of editing optimized parameters.

2.2. Objective Function

The minimum quality of the L type gantry crane structure is calculated by the design objective function $f(x)$ on the basis of meeting the overall performance and system reliability requirements. It is described as:

$$f(x) = f(x1) + f(x2) + f(x3), \qquad (1)$$

where $f(x1)$ is the quality of the main girder; $f(x2)$ is the total quality of the outriggers; $f(x3)$ is the total quality of the bottom girders; but the qualities of the wheels and rails are not contained in $f(x)$.

2.3. Constraint Conditions

The establishment of the constraint conditions should fully meet the requirements of strength, stiffness, stability and process size etc. There are two main constraints: performance constraints and geometry constraints. For L type gantry crane, the main constraints are: the maximum static stiffness with main girder span in the middle and span at the end; the maximum static strength with main girder span in the middle and span at the end; the maximum normal stress with span in the middle and cantilever at the end; the maximum shear stress with span in the middle of web and cantilever at the end root; the biggest stress at the joint with cantilever at the end

root of web and cover plate; the maximum stress at the joint with span in the middle of main web and the upper cover plate; the outrigger variable cross-section strength in the gantry frame plane and outrigger plane; the maximum normal stress at the bottom of the girder; the portal frame dynamic stiffness. In addition, aspect ratio of box section, moment of inertia ratio of outrigger related section, width-to-thickness ratio of board and the upper and lower bounds of the design variables, etc. should be considered.

3. Determining the Number of Specimens

Training specimens are vital for the establishment of the neural network. Only when the number and distribution of training specimens are reasonable can they correctly reflect the mapping relationship of the network model. Using orthogonal test method to determine the number of specimens can get sample points which are comprehensive and distributed evenly with less specimens [3].

In this study, the determination of the number of training specimens of neural network model of gantry crane structure makes use of the orthogonal table $L_{20}(2^{19})$, that is to say, the total number of specimens is 20 and the number of factors (design variables) is no more than 19. This design includes 16 factors and each factor has 2 levels. The Orthogonal test factors and their distribution are shown in table 1. For all the twenty specimens, VC++ programming is used to calculate the corresponding quality of the L type gantry crane for each specimens group and the calculation results are regarded as the output variables of the neural network model. Table 2 lists the related parameters of the specimens.

Table 1. Orthogonal test factors and their distribution table.

Factor level	**Upper cover plate width of main girder X1/mm**	**Lower cover plate width of main girder X2/mm**	**Web height of main girder X3/mm**	**Upper cross section height of outrigger X17/mm**	**Upper cross section width of outrigger X18/mm**	**Lower cross section width of outrigger X19/mm**	**Lower cross section height of outrigger X20/mm**	**Section height of bottom girder X13/mm**
1	930	830	1500	950	1520	450	250	450
2	1030	930	1800	1050	1820	600	350	600
Factor level	**Section width of bottom girder X14/mm**	**Cover plate thickness of main girder X4/mm**	**Main web thickness of main girder X5/mm**	**Vice web thickness of main girder X6/mm**	**Cover plate thickness of outrigger X11/mm**	**Web thickness of outrigger X12/mm**	**Cover plate thickness of bottom girder X15/mm**	**Web thickness of bottom girder X16/mm**
1	450	8	10	8	8	8	8	10
2	600	10	12	10	10	10	10	12

Table 2. Data of specimens.

Test number	**X1**	**X2**	**X3**	**X17**	**X18**	**X19**	**X20**	**X13**	**X14**	**X4**	**X5**	**X6**	**X11**	**X12**	**X15**	**X16**	**Self weight (kg)**
1	1030	830	1800	950	1520	450	250	600	600	8	12	10	8	8	10	12	14502.5
2	1030	930	1500	950	1820	600	350	600	450	10	10	10	8	8	8	10	15352.7
3	1030	830	1500	950	1520	600	350	450	600	10	10	8	10	10	10	12	15083.3
:	:	:	:	:	:	:	:	:	:	:	:	:	:	:	:	:	:
20	930	930	1800	950	1520	600	350	600	600	8	12	8	10	8	8	10	14246.3

4. BP Network Modeling

The BP neural network is a kind of multilayer feedforward neural network. It can deal with nonlinear information by increasing back spread error signals on the basis of multilayer perception [13]. The standard BP neural network uses the algorithm of gradient descent and chooses Sigmoid function which is continuous and derivable. It is mainly used for system model identification, prediction, data compression and approximation of function etc.

4.1. Setting up BP Network Model

The structure of BP neural network is simple and has a strong nonlinear mapping ability. It is mainly composed by the input layer, the hidden layer (middle layer) and the output layer. Input signals are first sent to the input layer and then transferred to the hidden layer through weighted processing. The transfer function used by the hidden layer is tansig function. After weighting and threshold value processing, the signals from the hidden layer are then transferred to

the output layer. The transfer function used by the output layer is purelin function. The general form of the transfer function between different layers is:

$$f(x) = 1/(1+e^{-\lambda x}), \quad (2)$$

where x is the input from the previous neurons that has been weighted and threshold value processed; $f(x)$ is the output of the current neuron and also the input of the next panel point.

The 16 factors got by the orthogonal test method are regarded as the input parameters of the neural network; while the quality of L type gantry crane calculated by the parametric interface shown in Fig. 1 is considered as the output parameters of network. A BP neural network simulated model is then established which is composed by the input layer with 16 nodes, the hidden layer with 13 nodes and the output layer with 1 nodes.

4.2. Training BP Network Model

The MATLAB neural network toolbox is called by the VC++ program to train the BP network model in the background and the 20 specimens got by the orthogonal test is implied during this process. Besides, 5 specimens are selected for the testing of the modal. The input and output data is normalized at the beginning of the training. The optimized L-M algorithm is used since it has the fastest convergence speed and lower memory space as compared with other momentum algorithms. Moreover, it can be easily achieved with the trainlm function provided by MATLAB tools. To obtain the learning efficiency of 0.05, the number of training is taken as 1000 and the performance target is taken as 1e-10, and the sim function of toolbox is called as the test function. The training results of the network are shown in Fig. 2. It is found that all the errors are controlled within 1 %, which implies that the establishment of the BP network model is successful.

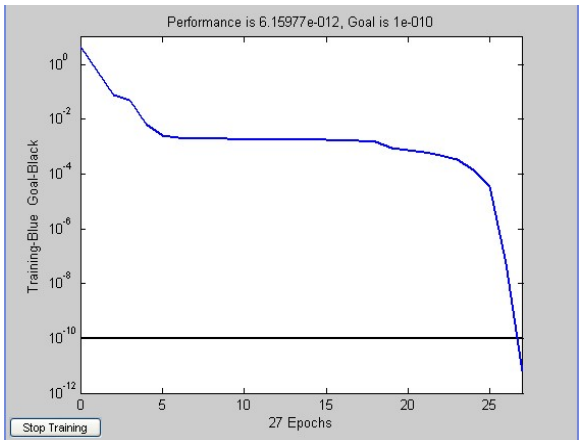

Fig. 2. Results of network training.

5. Optimization of Genetic Algorithm

Genetic algorithm can map implicit functions such as neural network. The advantages of genetic algorithm such as simple calculation, strong robustness, randomness, wholeness and being suitable for parallel processing are used to obtain the best network form and the best weights [4, 14-15].

The genetic algorithm is used to optimize the neural network model and the algorithm toolbox GATBX is employed to carry out optimized calculation. The objective function is described as:

$$ObjV = sim(net, (bs2rv(Chrom, FieldD))')', \quad (3)$$

where sim is the simulated function of neural network; net is trained neural network model; $bs2rv$ is the transferable function which transforms binary string to real value [5, 9-11]. Since the optimization of the L type gantry crane is aimed to get the minimum quality, the fitness function should be $FitnV = ranking(ObjV)$. The optimized flow chart of the L type gantry crane structure is shown in Fig. 3.

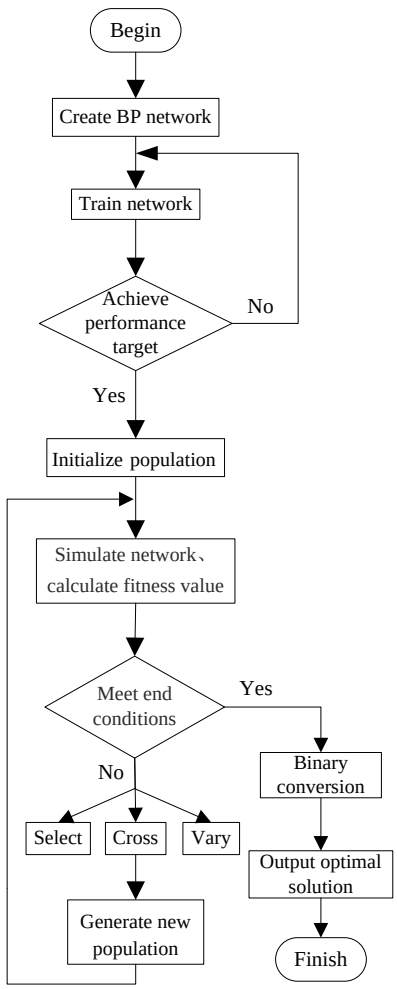

Fig. 3. Optimized flow chart of the L type gantry crane structure.

The design variables are compiled as binary code; the number of population individuals is 40; the largest genetic algebra is 200; the generation gap is 0.9 and the crossover probability is 0.7. Meanwhile, the obtained optimal value and the corresponding design variables need to be converted to the actual value by the counter normalization. Use VC++ calling MATLAB to optimize in the background. The changes of optimal value of the objective function for the first 200 iterations are shown in Fig. 4. After 180 iterations, the objective function almost achieves the optimal value.

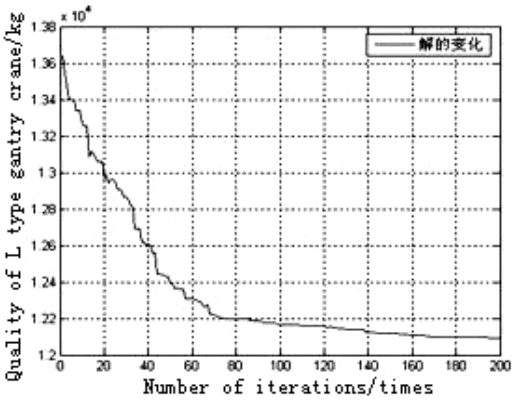

Fig. 4. Changes of optimal value of objective function during 200 times iterations.

The comparison between the optimal design got by the genetic algorithm optimizing and the initial design is shown in Table 3 which demonstrates that the quality of L type gantry crane is reduced by 14.7 % after the optimization design.

6. Finite Element Simulation of Type L Gantry Crane

6.1. Setting up Finite Element Model

After getting the optimal quality of the L type gantry crane, whether its strength and stiffness can meet the requirements should be further considered. The parametric design language APDL of ANSYS is used to construct the parametric model for the L type gantry crane's portal frame; VC++ program is used to compile the graphical user interface and the interface module of VC++ is called to nest VC++ and APDL command stream [6-8]. In order to establish an efficient analysis platform, the APDL macro file encapsulated by VC++ is used to transfer the information [12]. The dialogs are used as human-computer interaction interfaces to set up operation interface for the finite element analysis platform of the L type gantry crane's portal frame.

Table 3. Comparison between initial design and optimal design.

Design	X1	X2	X3	X17	X18	X19	X20	X13	X14	X4	X5	X6	X11	X12	X15	X16	Self weight (kg)
Initial	930	930	1500	950	1520	450	350	600	450	10	12	8	8	10	10	12	14262.2
Optimal	931.6	830	1500.3	951.4	1524.1	451.5	262.6	454.8	450.8	8	10.1	8	8	8	8.1	10	12156.3

Taking the gantry structure analysis of the MGD (L) type single main girder gantry crane (10 t×22 m) of a mechanical co., LTD. as an example, the lifting height is 10m; the lifting speed is 9 m/min; the running speed of the trolley is 35 m/min; the running speed of the cart for 30 m/min; the material is Q235; the safety factor is 1.33 and the working class is A5. After dividing the gantry structure into portal frame plane and outrigger plane, loads are applied on them separately for the simplicity of calculation. Several factors lie in the outrigger plane should be taken into consideration when the cart is breaking, including: the uniformly distributed loads which are caused by the main girder, the outriggers and the self weight of bottom girders; the inertia forces which are caused by the main girder, outriggers, bottom girders, goods and the self weight of the trolley. At the same time, the wind loads which act on the main girder, outriggers, bottom girders, goods and the trolley should also be considered as well as the crane travel mechanism, the cab, the self weight of trolley and the lifting capacity etc. Similarly, most of the above listed factors should also be considered in the portal frame plane when the trolley is braking.

6.2. Analyzing the Results

Through statics analysis the deformation and stress distribution of the L type gantry crane in outrigger plane is obtained. The static rigidity and Von Mises stress distribution of the L type gantry crane are shown in Fig. 5 and Fig. 6 respectively.

Based on the system modeling, we got the maximum stress of the main girder dangerous section is calculated as 143.8 MPa; the static stiffness of the gantry frame is 11.2 mm. In other words,

$$\sigma = 143.8MPa < [\sigma] = 176.69MPa \ ,$$

$$f_j = 11.2mm < \frac{22000}{1000} = 22mm \ ;$$

the strength and stiffness meets the requirements.

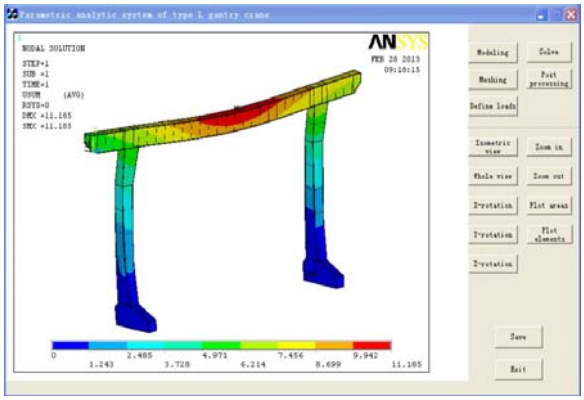

Fig. 5. Result of static rigidity.

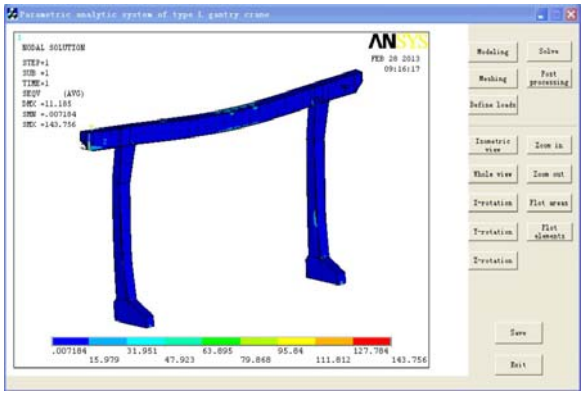

Fig. 6. Result of Von Mises stress.

7. Conclusions

A kind of parametric finite element analysis system for the L type gantry crane is developed by making use of secondary development on the ANSYS and MATLAB software by VC++ programming, and by combining finite element method, BP neural network and genetic algorithm organically. First of all, the design variables and the overall quality calculated by VC++ are selected as the training specimens for the neural network; then the BP neural network model of the L type gantry crane is set up; afterwards, the genetic algorithm is employed to complete the parameter optimization and to analyze the optimal solution by using finite element methods; finally, the optimal solution is tested to meet the requirements of strength and stiffness. The optimized overall quality of the L type gantry crane has decreased by 14.7 % as compared to the quality before the gantry crane is optimized, and its overall performance is obviously improved. This system realizes the visualization of the whole analysis process. Thus, it's possible for the technicians to finish the whole analysis process correctly under the guidance of the dialogs. Moreover, the correctness of the parameters becomes convenient. The operating system can improve the speed of product analysis and shorten the product development cycle. Technicians who are not familiar with the ANSYS software and finite element analysis technology can also use this system easily.

References

[1]. Run Risheng, Wang Zongyan, Wu Shufang etc., Research on Key Technologies for Parametric Design System of Gantry Crane, *Machinery Design & Manufacture*, 1, 2010, pp. 16-18.

[2]. Chen Daonan, Guo Yuqing, Zhou Peide, etc., Hoisting and Conveying Machinery, *Metallurgical Industry Press*, 2003.

[3]. Fu Lijun, Bao Zhongxu, Chen Zezhong etc., Combination of Orthogonal Experimental Method, Combination of Neural Networks and Genetic Algorithms, *Journal of Nanchang University (Engineering & Technology)*, 25, 1, 2003, pp. 79-82.

[4]. Gu Dimin. Construction Crane, *China Building Industry Press*, 1988.

[5]. Lei Yingjie, Zhang Shanwen, Li Xuwu etc., Genetic Algorithm Toolbox Based on MATLAB and Its Applications, *Xi'an University of Electronic Science and Technology Press*, 2005.

[6]. Game Studio, APDL Parametric Finite Element Analysis Technology and Its Applications, *China Water Power Press*, 2004.

[7]. Zhu Xiaohua, Liao Weizhi, Huang Yong' an etc., Collaborative Technology of CAD/CAE/CFD/ VPT/SC, *China Water Power Press*, 2004.

[8]. Gong Shuguang, Xie Guilan, Huang Yunqing. ANSYS Parametric Programming and Command Manual, *China Machine Press*, 2009.

[9]. Goldberg, D. E. Genetic algorithms in search, optimization and machine learning, *MA: Addison-Wesley Publishing Company*, 1989.

[10]. Davis, L., (ed.), Handbook of genetic algorithms, *Van Nostrand Reinhold*, New York, 1991.

[11]. Koza, J. R. Genetic Programming 1. Cambridge, *MA: The MIT Press*, 1992.

[12]. Li Liming. ANSYS Finite Element Analysis and Practical Course. *Tsinghua University Press*, 2007.

[13]. Hou Yuanbin, Du Jingyi, Wang Mei. Neural Network, *Xi'an University of Electronic Science and Technology Press*, 2007.

[14]. Liu Hongjuan. Application of MATLAB Optimal Toolbox in Mechanical Optimal Design, *New Technology & New Process*, 8, 2012, pp. 6-9.

[15]. Cheng Yuansheng, Sun Ying, Yan Guoqiang etc., Optimum Design Method of Structure Based on Neural Network and Genetic Algorithm, *Journal of Guilin University of Technology*, 27, 1, 2007, pp. 128-132.

Sensors & Transducers, Vol. 21, Special Issue, May 2013, pp. 36-41

Sensors & Transducers

http://www.sensorsportal.com

An Efficient Functionalization Method for the Multiwalled Carbon Nanotubes and Their Applications in PMMA Bone Cement

[1] Yongzhi Xu, [*2] Youzhi Wang, [3] Lei Cui

[1,2] School of Civil Engineering, Shandong University, Jing Shi road 17923#, Jinan, 250061, PR China

[3] Shandong Transport Vocational College, Wei Xian road 8#, Weifang, 261206, PR China

[2] Tel.: 13153600920, fax: 0531-88392696

[2] E-mail: xyz2003sdu@163.com

Received: 7 April 2013 /Accepted: 14 May 2013 /Published: 30 May 2013

Abstract: In this work, an efficient procedure for the functionalization of multiwalled carbon nanotube (MWCNTs) based on nitric acid oxidation was presented. The morphologies of MWCNTs oxidized under various conditions were characterized by scanning electron microscopy (SEM) and Fourier transform infrared spectroscopy (FTIR). The FTIR provided clear evidence for the presence of carboxylic groups (–COOH) attached to the surface of MWCNTs resulting from the acid treatment. The unfunctionalised MWCNTs(p-MWCNTs) and carboxy1 functionalized MWCNTs (f-MWCNTs) were successfully applied into the Polymethyl methacrylate (PMMA) bone cement. The resultant mechanical experiment indicated that the f-MWCNTs were a promising additive to improve the compressive strength and bend strength of the PMMA bone cement. The morphology and degree of dispersion of the MWCNTs in the PMMA matrix at different scales were analyzed by SEM. Improvements in mechanical properties were attributed to the MWCNTs arresting or retarding crack propagation through the cement by providing a bridging effect into the crack, normal to the direction of crack growth. *Copyright © 2013 IFSA.*

Keywords: MWCNTs, PMMA, Bone cement, Mechanical properties.

1. Introduction

Since their discovery in 1991 by Iijima [1], carbon nanotubes have attracted considerable interest because of their unique physical, chemical, electronic, and mechanical properties [2]. In order to acquire the optimal performance of MWCNTs in various applications, high-purity carbon MWCNTs are indispensable. Prinstine MWCNTs are generally produced along with amorphous carbon, metal particles and carbon nanoparticle clusters, particularly with a highly hydrophobic surface which seriously hindered their further applications. To date, the removal of impurities and chemical surface modification of carbon materials often processed in the strong oxidant (e.g. HNO_3, HCl or mixtures of H_2SO_4/HNO_3) [3, 4], in which a large amount of acid or a long time of refluxing were used, let alone afterwards wash and separation with high-sped centrifugation. Herein, we report an efficient and simple procedure for the functionalization of MWCNTs based on nitric acid oxidation to overcome the mentioned drawbacks existed in traditional methods.

In the past few decades, the polymethylmethacrylate (PMMA) bone cement is extensively used for primary cemented arthroplasty and orthopaedic surgery [5-7]. Approximately 50 % of all orthopedic implants utilize PMMA-based bone cement to achieve implant fixation [8], such as total hip and total knee replacements (femoral and acetabular parts), etc, where it plays a vital load-bearing function, generating a layer between the artificial polymeric components and the surrounding bone. It is well documented that PMMA bone cement is sensitive to fatigue-related cracking and impact-induced failure [9]. Active or overweight patients with implants fixed with PMMA bone cement are at the risk of cement mantle failure, which occurs in 5 % of all total joint replacement patients by 10 years postoperatively [10]. Failure rates of 67 % have been recorded after 16 years in patients less than 45 years old.

There is a lot of literature reporting methods for improving the mechanical properties of PMMA bone cement. These studies have incorporated various additives into the polymer matrix with the aim of improving mechanical properties. The use of these additives has been less effect due to the poor fibre–polymer matrix bonding, dispersion and distribution. The incorporation of MWCNTs into polymers has been used to improve mechanical properties and to retain the structural capabilities of the polymer matrix. Jin [15] et al. studied multi-walled carbon nanotube/poly(methyl methacrylate) composites fabricated by melting blending and found that the nanotube was well dispersed in the polymer matrix and the storage modulus of the composites was significantly increased. Marrs [10] investigated the influence of MWCNTs in PMMA-based bone cements. They reported moderate improvements (13 % – 24 %) in the static properties when 2 wt% MWCNTs were incorporated into the methyl methacrylate–styrene cement. Marrs also reported significant improvements (>300 %) in the dynamic properties when MWCNTs (2 wt%) were added to the same bone cement. However, these studies used non-clinically relevant methods to ensure optimal dispersion of the MWCNTs into the bone cement. The uniform distribution of MWCNTs within the polymer matrix is critical for maximizing the interfacial bond between the MWCNTs and polymer matrix and therefore achieving optimal improvements in mechanical properties.

In this work, we presented an efficient procedure for the functionalization of MWCNTs based on nitric acid oxidation. PMMA/MWCNTs bone cement nanocomposites with a weight loading of 0.6 % were prepared using 2 different methods of MWCNTs incorporation. The mechanical properties of the resultant nanocomposite cements were characterized in accordance with the international standard for acrylic resin cements. The morphology and degree of dispersion of the MWCNTs in the PMMA matrix at different scales were analyzed using scanning electron microscopy.

2. The Functionalization of MWCNTs

2.1. Experiment Materials and Instruments

The MWCNTs synthesized by Chemical Vapor Deposition (CVD) with a length of 5-15 μm (purity > 95 %, outer diameter 40-60 nm) were purchased from Shenzhen Nanotech Port Co., Ltd. The Prinstine MWCNTs will be referred as p-MWCNTs, and the functionalized MWCNTs will be referred as f-MWCNTs. The concentrated HNO_3 (65~68 wt.%) were purchased from Jinan Le Qi Chemical Reagent Co. Ltd.

The MWCNTs was studied by the following instruments: magnetic stirring apparatus with a temperature controller and a propeller-type agitation system (51450-xx); Thermal gravimetric analyzer (SDT Q600 V8.3); Fourier transform infrared spectroscopy (Nicolet Magna-IR Spectrometer 550, the spectra were run on KBr pellets containing 1 wt.% of MWCNTs sample which were dried in air at 200 °C for 24 h); scanning electron microscopy (SEM, JEOL JSM-7600F); Universal material testing machine (LR10Kplus).

2.2. Purification of MWCNTs

Removal of amorphous carbon, metal catalyst and surface fictionalization of MWCNTs were achieved in one-step as follow: MWCNTs (1 g) and 100 ml concentrated HNO_3 (65~68 wt.%) were poured into a three-necked flask (250 ml). The MWCNTs were refluxed at the temperatures of 120 °C, 160 °C, 200 °C for several hours, respectively. And then, transfer the solution into a wide mouth dish to evaporate the acid and solution, rather than traditional high-speed centrifugation because the used acid is a highly volatile; therefore it is unnecessary to centrifugation. Finally, black piece of powders were obtained and immersing them in de-ionized water for several times to remove dissolved impurities.

2.3 MWCNTs Characterization

2.3.1. Thermal Stability of MWCNTs

The TGA profiles measured in flowing air for p-MWCNTs and f-MWCNTs are shown in Fig. 1, where the samples were heated at a heating rate of 10 °C /min. The figure shows the metal impurities in the f-MWCNTs have been completely removed at 700 °C, however, the residues of p-MWCNTs accounts for about 4 %.

2.3.2. Fourier Transform Infrared Spectroscopy

FTIR spectra were obtained at room temperature in the transmittance mode. The samples were ground

with KBr and pressed into pellets. The FTIR spectra for the p-MWCNTs and f-MWCNTs are shown in Fig. 2.

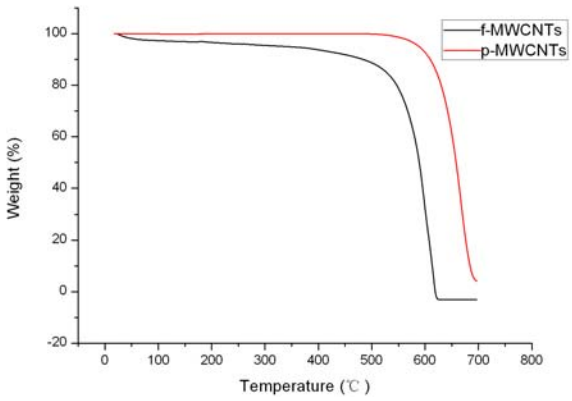

Fig. 1. TG analysis of p-MWCNTs and f-MWCNTs.

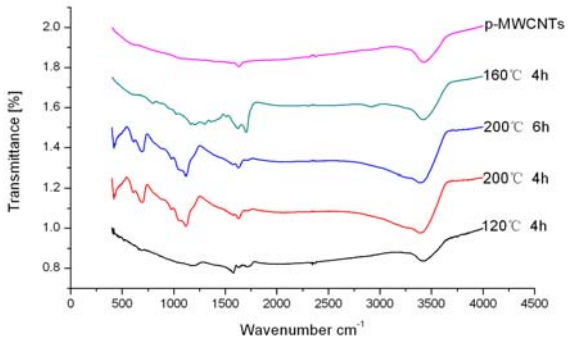

Fig. 2. FTIR spectra of p-MWCNTs and f-MWCNTs.

In the spectrum of p-MWCNTs, the main feature observed at 1580 cm^{-1} is characteristic of the stretching of C=C bonds, related to the expected nanotube phonon modes. The structure at 3440 cm^{-1} can be assigned to vibrational modes of the –OH groups, indicating the presence of functional groups even in the raw material. In the spectrum of the acid treated material, all those bands are enhanced, including a feature at about 1210 cm^{-1} that was not well defined in the spectrum of the raw material. The strong absorption band appearing at 1717 cm^{-1} is related to the carboxylic group (-COOH) vibrations. These results show that the acid treatment is responsible for an increase in the functionalization of the nanotubes.

2.3.3. The SEM of MWCNTs

Fig. 3 shows the SEM images of the p-MWCNTs (Fig. 3 a)and f-MWCNTs (Fig. 3 b~e) oxidized at various temperatures viz 120 °C, 160 °C and 200 °C for 4 hours. Initially, the raw MWCNTs have a very broad length distribution bearing very high average length as shown in Fig. 3a. MWCNTs oxidized at 120 ^{0}C have a larger diameter distribution, starting from 100 to 1000 nm in length (Fig. 3b). However, comparatively thin and short was observed for the oxidation conditions at 160 °C (Fig. 3c) with increasing oxidation temperature. This result indicated that MWCNTs were damaged during oxidation and became shorter. For the oxidation at the temperatures of 200 °C by the oxidation time of 4 hours (Fig. 3d) and 6 hours (Fig. 3e), the length distributions are nearly identical and no significant changes were observed.

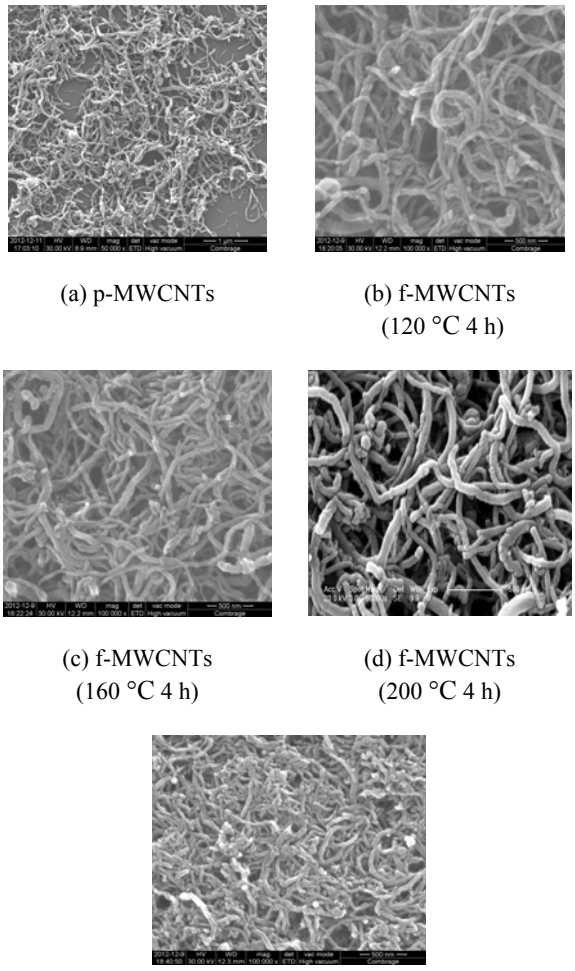

(a) p-MWCNTs (b) f-MWCNTs (120 °C 4 h)

(c) f-MWCNTs (160 °C 4 h) (d) f-MWCNTs (200 °C 4 h)

(e) f-MWCNTs (200 °C 6 h)

Fig. 3. SEM images of p-MWCNTs and f-MWCNTs.

The effects of refluxing temperature during oxidation of MWNTs on properties of nanotubes were investigated. In this research, the changes in length of MWNTs was systematically monitored for various oxidation temperatures and refluxing time. The average length of MWNTs decreased dramatically with increase in the temperature of oxidation. The purification process applied in this work results in a high quality MWCNTs material. The controlled surface modification of MWCNTs was successfully performed by means of a HNO3

hydrothermal functionalization method and the present study allows to draw the following conclusions:

(1)A controlled functionalization using the described HNO_3 hydrothermal method can be achieved by setting with precision the temperature. Fig. 3 shows the best reflux temperature is 200 °C.

(2)The observed dependency in temperature suggests that activation energy is controlling the functionalization process.

(3) The length of MWNTs decreased dramatically when the refluxing time and temperature were increased. The optimal reflux time is 4 hours.

3. Experiment of the PMMA / MWCNTs Bone Cement

3.1. Materials and Preparation of the Bone Cement

The bone cement used was Radiopaque bone cement containing gentamicin (Biomet Orthopaedics Switzerland GmbH), which comprised of PMMA powder (40.8 g) and methyl methacrylate (MMA) liquid monomer (20 mL) (Table1).

Table 1. Composition of PMMA bone cement.

	Constituent	Mass (g)	Volume (ml)
Powder	Polymethyl methacrylate (PMMA)	33.6	
	Benzoyl Peroxide (BPO)	0.3	
	Zirconium dioxide	6.1	
	Gentamicin sulphate	0.8	
Liquid	Methyl Methacrylate (MMA)		19.73
	N,N-dimethyl-p-toluidine (DmpT)		0.27

The PMMA bone cement is created by mixing the solid (powder) components with the liquid, usually in the ratio 2 g powder/1 ml liquid. Basically, PMMA bone cement contains two portions: the powder portion including PMMA and initiator (e.g. benzoyl peroxide, BPO); the liquid portion including methylmethacrylate (MMA) monomer and pr omoter (e.g. N,N-dimethyl-p-toluidine, DmpT). When the two portions are mixed, the initiation is activated by promoters that make the free radicals (initiators). The free radicals react with monomers for polymerization [16].

MWCNTs (0.6 wt%) were incorporated into the precursors prior to mixing the PMMA powder and MMA monomer. The different MWCNTs were incorporated into the bone cement using one of the following methods: (i) magnetically stirring the MWCNTS in the MMA component for 24 h at room temperature; (ii) dispersing the MWCNTs in the MMA monomer using an ultrasonic disintegrator. Subsequently, the bone cements were mixed under ambient conditions according to the manufacturer's instructions. Once mixed the bone cement was injected into the appropriate mould.

Specimens for mechanical testing were prepared by injecting the bone cement into a PTFE mould, which were cured for 24 h. Subsequently, the rough specimen edges were removed by sanding with 1200 μm grit silicon carbide abrasive. Specimens for measuring compressive properties were in the form of cylinders of 12 mm length and 6 mm diameter . The specimens for quantifying the bend properties were in the form of rectangular bars of 75 mm in length, 10 mm in width and 3.3 mm in thickness.

3.2. Mechanical Properties

The mechanical properties of each bone cement mix were determined in accordance with ISO 5833. All tests were conducted using the Lloyds materials testing machine operating at a crosshead speed of 5.0 mm/min. Each compressive specimen was tested to failure. The bend strength for each specimen was determined using a four point bend test arrangement. The load and deflection at mid-span were recorded to failure for each specimen. The mechanical properties are summarized in Table 2 for the control cement and the PMMA/MWCNTs bone cements incorporating functionalised and unfunctionalised MWCNTs.

Table 2. The data from mechanical studies (Mean±SD) of control, unfunctionalised, carboxy1 functionalised MWCNTs loaded cements.

Cement type	MWCNTs type	Mechanical property	
		Compressive Strength (MPa)	Bend Strength (MPa)
Control		74.6±2.5 [a]	51.2±2.6 [a]
Magnetic stirring	Unfunctionalised	76.6±2.3[b]	52.3±2.3[b]
Ultrasonic disintegration	Unfunctionalised	80.6±2.1[c]	54.1±2.4[c]
Magnetic stirring	Functionalised	88.8±2.1[d]	68.2±2.3[d]
Ultrasonic disintegration	Functionalised	92.9±2.2[e]	74.1±2.2 [e]

[a]denotes *p*-values < 0.01, indicating a statistically significant difference between control cement and other cements tested.

[b]denotes *p*-values < 0.01, indicating a statistically significant difference between magnetic stirring (p-MWCNTs) and other cements tested.

[c]denotes *p*-value < 0.01, indicating a statistically significant difference between ultrasonic disintegration (p-MWCNTs) and other cements tested.

[d]denotes *p*-value < 0.01, indicating a statistically significant difference between magnetic stirring (f-MWCNTs) and other cements tested.

[e]denotes *p*-value < 0.01, indicating a statistically significant difference between ultrasonic disintegration (f-MWCNTs) and other cements test

The addition of p-MWCNTs into the cements using magnetic stirring did not have a wholly positive effect on the mechanical properties of the resultant cement. Improvements in the compressive strength (≈2.6 %; p-value < 0.01) and bend strength (≈1.8 %) were observed compared with the control. Incorporating the p-MWCNTs into the monomer using sonication improved the compressive strength (≈8 %; p-value < 0. 01) and bend strength (≈5.8 %). On the contrary, the incorporation of f-MWCNTs into the bone cements presented obvious reinforcement of the mechanical properties of the PMMA/MWCNTs bone cement. By the magnetic stirring, the compressive strength (≈19 %; p-value < 0.01) and bend strength (≈33 %) were observed compared with the control, and by ultrasonic disintegration, the improvements in compressive strength (≈24.5 %) and bend strength (≈45 %; p-value < 0.01) were noted compared with the control cement.

As shown in Fig . 4 and Table 2, we observed that surface modification of the MWCNTs with carboxyl groups could significantly improve the compressive and bend properties of the PMMA/MWCNTs bone cement, especially by the ultrasonic disintegration.

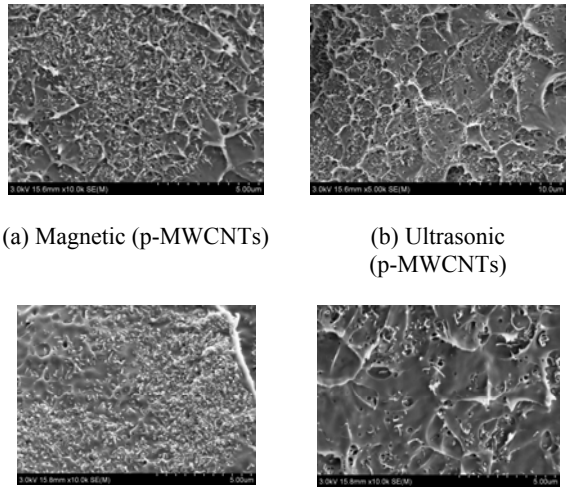

(a) Magnetic (p-MWCNTs) (b) Ultrasonic (p-MWCNTs)

(c) Magnetic (f-MWCNTs) (d) Ultrasonic (f-MWCNTs)

Fig. 4. The fracture surface of the PMMA/ MWNCTs bone cement.

The results of this study demonstrated that adding MWCNTs (0.6 wt%) to the polymer powder or liquid monomer components, prior to cement mixing with a proprietary mixing system, improved the mechanical properties of the resultant cement, provided the appropriate method for incorporating the MWCNTs was used. This is a significant finding because mechanical failure of the bone cement mantle remains a major problem in joint replacement surgery.

4. Conclusions

The surface modification of MWCNTs was successfully performed by means of a HNO_3 hydrothermal functionalization method. The result showed the best reflux temperature is 200 °C and the optimal reflux time is 4 hours. Incorporating 0.6 wt% f-MWCNTs to PMMA bone cement enhanced the compressive strength and bend strength of the resultant nanocomposite, provided the appropriate method for incorporating the MWCNTs was used. This is a significant finding because mechanical failure of the bone cement mantle remains a major problem in joint replacement surgery. The extent of the effect depended on the type of MWCNTs, method of introduction used and the properties being quantified. Improvements in mechanical properties were attributed to the MWCNTs being well dispersed within the PMMA cement, thereby arresting/retarding crack propagation through the cement.

Acknowledgments

The authors would like to thank all editors for their help with the paper proofreading. This study was carried out with financial support from the National Natural Science Foundation of China (50779032), Postdoctoral Foundation of China (20090451330) and Shandong Province Natural Science Foundation Project (ZR2010EM024).

References

[1]. S. Iijima, Helical microtubules of graphitic carbon, *Nature*, 354, 1991, pp. 56–58.

[2]. R. Saito, G. Dresselhaus, M. S. Dresselhaus, Physical properties of carbon nano tubes, *Imperial College Press*, London, 1998.

[3]. H. Hiura, T. Ebessen, T. Tanigaki, Opening and purification of carbon nano tubes in high yields, *Adv Mater,* 7, 1995, pp. 275–276.

[4]. M. Monthioux, B. W. Smith, A. Claye, D. E. Luzzi, Sensitivity of single-wall carbon nano tubes to chemical processing: an electron microscopy investigation, *Carbon*, 39, 2001, pp. 1251–1272.

[5]. Charnley J. Anchorage of femoral head prothesis to the shaft of the femur, *Bone Joint Surg Br*, 42, 1, 1960, pp. 28-30.

[6]. J. Charnley, Acrylic Cement in Orthopaedic Surgery, *The Williams and Wilkins Co.*, Baltimore, 1970.

[7]. P. D. Wilson, H. C. Amstutz, A. Czerniecki, E. A. Salvati, D. G. Mendes, Total hip replacement with fixation by acrylic cement. A preliminary study of 100 concecutive McKee-Farrar prothetic reolacements, *J. Bone Joint Surg Am.*, 1972, 54 (2), pp.207-236.

[8]. Katti, K. S., Verma, D., Katti, D. R., Materials for joint replacement, In: Revell, P. A., Ed., Joint Replacement Technology, Chapter 4, *Woodhead Publishing Limited*, 2008, p. 90.

[9]. Kuehn, K. D., Ege, W., Gopp, U., Acrylic bone cements: Composition and properties, *Orthop. Clin. North Am*., 36, 1, 2005, pp. 17-28.

[10]. Marrs, B., Carbon nanotube augmentation of a bone cement polymer, Ph. D. Thesis, *University of Kentucky*, US, 2007.

[11]. G. Uzun, N. Hersek, T. Tincer, Effect of five woven fibre reinforcements on the impact and transverse strength of a denture base resin, *J. Prosthet. Dent*., 81, 5, 1999, pp. 616–620.

[12]. H. D. Stipho, Effect of glass fibre reinforcement on some mechanical properties of autopolymerizing polymethyl methacrylate, *J. Prosthet. Dent*., 79, 5, 1998, pp. 580–584.

[13]. T. R. Manley, A. J. Bowman, M. Cook, Denture bases reinforced with carbon fibres, *Br. Dent. J.,* 146, 1, 1979, p. 25.

[14]. L. D. Topoleski, P. Ducheyne, J. M. Cuckler, Flow intrusion characteristics and fracture properties of titanium–fibre-reinforced bone cement, *J. Biomath*., 19, 17, 1998, pp. 1569–1577.

[15]. Z. Jin, K. P. Pramoda, G. Xu, S. H. Goh, Dynamic mechanical behavior of melt-processed muti-walled carbon nanotube/poly(methyl methacrylate) composites, *Chemical Physics Letters,* 337, 2001, pp. 43–47.

[16]. Joon B. Park, Roderic S. Lakes, Biomaterials: An Introduction, 2nd edition, *Plenum Publishing Corporation*, New York, NY, 1992.

[17]. Marrs, B., Andrews, R., Rantell, T., Ienkowski, D., Augmentation of acrylic bone cement with multiwall carbon nanotubes, *J. Biomed. Mater. Res.* 77, 2, 2006, pp. 269-276.

Sensors & Transducers, Vol. 21, Special Issue, May 2013, pp. 42-47

Sensors & Transducers

http://www.sensorsportal.com

Path Following Control of a Spherical Robot Rolling on an Inclined Plane

Tao Yu, Hanxu Sun, Qingxuan Jia, Wei Zhao
School of Automation, Beijing University of Posts and Telecommunications, 100876, Beijing, China
Tel.: +861062282571, fax: +861062282571
E-mail: yutaogzm@sohu.com

Received: 31 March 2013 /Accepted: 14 May 2013 /Published: 30 May 2013

Abstract: In this paper, the path following control of a spherical robot rolling without slipping on an inclined plane is discussed. We first study the kinematic constraints of the spherical robot and develop the dynamic model of the robot through the constrained Lagrange method. We then present a state space realization of this constrained system through the null space method and using nonlinear feedback. We investigate the path following control algorithms and develop a variable structure approach to the control of this nonholonomic system. By choosing appropriate output equations for path following, we design the sliding surfaces as the functions of the output tracking errors. Using Lyapunov stability theorem and exponential reaching law, we derive the sliding mode control law. The asymptotic stability of the sliding surfaces is theoretically proved, and the validity of the proposed path following method is further validated through MATLAB simulations. *Copyright © 2013 IFSA.*

Keywords: Spherical robot, Inclined plane, Path following, Sliding mode control, Nonholonomic system.

1. Introduction

Most mobile robots we have today have wheels. That is an obvious choice as there is a considerable amount of knowledge about this type of locomotion. However, more and more possible applications occur where wheeled robots have some flaws. Spherical robots could be a solution to some of these problems. As the robot is encompassed in a ball it is possible to effectively seal everything to enable the robot to withstand exposure to dust, humidity, dangerous substances and other environmental threats. As we can understand, this could be very handy in such applications as planetary exploration, surveillance and others. The above mentioned situations often involve dealing with difficult terrain as well. While wheeled robots can cope with it pretty good, the risk of falling over still persists. A spherical robot, on the other hand, can't fall over at all.

Over the last few decades, there has been considerable interest in the development of powerful methods for motion control of mobile robots. The problems addressed in the literature can be roughly classified into three groups: trajectory tracking, path following and point stabilization [1]. With respect to spherical robots, there have not been established methodologies to resolve these control problems, although many studies have been made during the past. Alves and Dias [2] presented a line tracking method of a spherical robot based on kinematics. Zhan and Liu et al. [3] discussed the trajectory tracking problem of a spherical robot using backstepping approach. Zheng and Zhan et al. [4] investigated the trajectory tracking algorithm for a

Article number P_SI_339

spherical robot based on the RBF-PD controller. Cai and Zhan et al. [5] proposed a real-time fuzzy guidance scheme for trajectory tracking of a spherical robot. Liu and Sun et al. [6] developed a line following controller for a spherical robot based on sliding modes.

Current researches on motion control of spherical robots usually assume that the robot remains strictly on a level plane. As a result, the dynamic model fails to represent the actual motion when the robot rolls up a slope. This paper focuses on practical solutions to trajectory tracking and path following control of a spherical robot rolling on an inclined plane. The main contributions of the paper include two parts. Firstly, the kinematics and dynamics of the robot subject to no-slip and no-spin constraints are derived. Secondly, a sliding mode control scheme for path following of the robot is proposed.

2. Mathematical Model

2.1. System Description

BYQ-VIII is a pendulum-driven spherical robot, the mechanical structure of the robot is illustrated in Fig. 1. The robot is mainly consisted of three parts: the spherical shell 1, the internal gimbals 2 and the pendulum 3. The robot has the internal driving unit mounted inside the spherical shell. The steering motion of the robot is achieved by tilting the pendulum, and the driving motion is performed by swinging the pendulum indirectly through the internal gimbal.

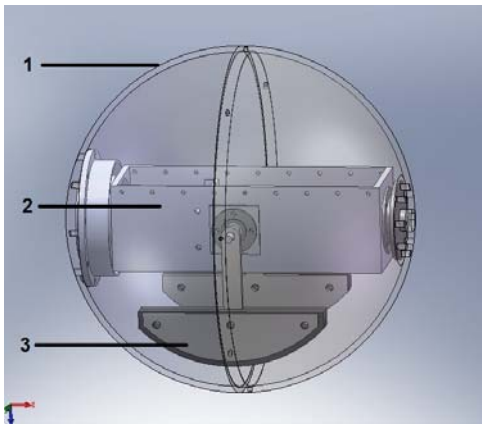

Fig. 1. Three-dimensional model of BYQ-VIII.

2.2. Kinematic Constraints

We first assign two coordinate frames. Let $\sum_O XYZ$ be a fixed inertial frame whose XY plane is anchored to the surface of the incline and Z is the vertical position to the surface. Let $\sum_B X_b Y_b Z_b$ be the body coordinate frame whose origin is located at the center of the sphere B. We denote (ϕ, θ, ψ) to be the ZYX Euler angles from the inertial frame $\sum_O$ to the body coordinate frame $\sum_B$.

Fig. 2 presents the geometrical model of the rolling sphere and definition of necessary variables to deduce the mathematical model. Here R represents the radius of the sphere, C is the contact point between the sphere and slope surface with its coordinates (x_c, y_c) with respect to $\sum_O$, τ_ψ and τ_θ denote the torques exerted on the sphere along the axis X_b and Y_b respectively.

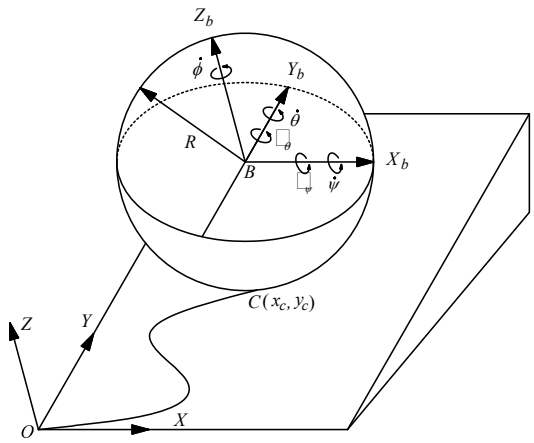

Fig. 2. Definition of system variables for BYQ-VIII.

We now derive the kinematics and dynamics of the spherical robot on the basis of the following assumptions: (i) no-slip constraint: the sphere rolls on the perfectly flat surface of the incline without slipping, (ii) no-spin constraint: rotations of the rolling sphere around the Z axis are not allowed.

Let $\boldsymbol{v}_B$ and $\boldsymbol{\omega}_B$ denote the velocity of the center of mass of the sphere and its angular velocity with respect to the inertia frame $\sum_O$. Then, we have

$$\begin{aligned} \boldsymbol{\omega}_B &= \omega_x \boldsymbol{i} + \omega_y \boldsymbol{j} + \omega_z \boldsymbol{k} \\ \omega_x &= \dot{\psi}\cos\phi\cos\theta - \dot{\theta}\sin\phi \\ \omega_y &= \dot{\theta}\cos\phi + \dot{\psi}\sin\phi\cos\theta\,, \\ \omega_z &= \dot{\phi} - \dot{\psi}\sin\theta \end{aligned} \tag{1}$$

where $\boldsymbol{i}$, $\boldsymbol{j}$, $\boldsymbol{k}$ are the unit vectors of $\sum_O$.

The no-spin constraint can be formulated as

$$\dot{\phi} - \dot{\psi}\sin\theta = 0 \tag{2}$$

The constraint in (2) represents a nonholonomic constraint. The constraints result from the requirement that the sphere rolls without slipping on the incline, i.e., the velocity of the contact point on the sphere is zero at any instant $\boldsymbol{v}_C = 0$. Now we can express $\boldsymbol{v}_B$ as

$$\boldsymbol{v}_B = \boldsymbol{\omega}_B \times r_{BC} + \boldsymbol{v}_C\,, \tag{3}$$

where $r_{BC} = -R\boldsymbol{k}$ represents the vector from point C to B. Substituting (1) into (3) gives

$$\boldsymbol{v}_B = \dot{x}_c \boldsymbol{i} + \dot{y}_c \boldsymbol{j} + \dot{Z}\boldsymbol{k} \tag{4}$$

where

$$\dot{x}_c + R\left(\dot{\theta}\cos\phi + \dot{\psi}\sin\phi\cos\theta\right) = 0 \tag{5}$$

$$\dot{y}_c - R\left(\dot{\psi}\cos\phi\cos\theta - \dot{\theta}\sin\phi\right) = 0 \tag{6}$$

$$\dot{Z} = 0 \tag{7}$$

The constraints in (5) and (6) are nonholonomic, whereas the constraint in (7) is holonomic and can be integrated to obtain $Z = R$.

Therefore the configuration of the robotic system can be described by a vector of five generalized coordinates $\boldsymbol{q} = (x_c, y_c, \phi, \theta, \psi)^T$.

Combing (2), (5) and (6), the nonholonomic constraints can be written as

$$\boldsymbol{A}(\boldsymbol{q})\dot{\boldsymbol{q}} = \boldsymbol{0} \tag{8}$$

where

$$\boldsymbol{A}(\boldsymbol{q}) = \begin{bmatrix} 1 & 0 & 0 & R\cos\phi & R\sin\phi\cos\theta \\ 0 & 1 & 0 & R\sin\phi & -R\cos\phi\cos\theta \\ 0 & 0 & 1 & 0 & -\sin\theta \end{bmatrix}$$

2.3. Robot Dynamics

We study the motion equations by calculating the Lagrangian $L = T - P$ of the system, where T and P are the kinetic energy and potential energy of the system respectively. The spherical shell is assumed to have mass m and the moment of inertia I. Then T and P of the robotic system can be calculated as follows

$$\begin{aligned} T &= \frac{1}{2}m\left(\dot{x}_c^2 + \dot{y}_c^2\right) + \frac{1}{2}I\left(\omega_x^2 + \omega_y^2 + \omega_z^2\right) \\ P &= mg\left(y_c \sin\gamma + R\cos\gamma\right) \end{aligned}, \tag{9}$$

where γ is the inclination angle of the slope.

Using the constrained Lagrangian method, the motion equations of the robotic system are described by

$$\boldsymbol{M}(\boldsymbol{q})\ddot{\boldsymbol{q}} + \boldsymbol{V}(\boldsymbol{q}, \dot{\boldsymbol{q}}) = \boldsymbol{E}(\boldsymbol{q})\boldsymbol{t} - \boldsymbol{A}^{\mathrm{T}}(\boldsymbol{q})\boldsymbol{\lambda} \tag{10}$$

where

$$\boldsymbol{M}(\boldsymbol{q}) = \begin{bmatrix} m & 0 & 0 & 0 & 0 \\ 0 & m & 0 & 0 & 0 \\ 0 & 0 & I & 0 & -I\sin\theta \\ 0 & 0 & 0 & I_s & 0 \\ 0 & 0 & -I\sin\theta & 0 & I \end{bmatrix}$$

$$\boldsymbol{V}(\boldsymbol{q}, \dot{\boldsymbol{q}}) = \begin{bmatrix} 0 \\ mg\sin\gamma \\ -I\dot{\theta}\dot{\psi}\cos\theta \\ I\dot{\phi}\dot{\psi}\cos\theta \\ -I\dot{\phi}\dot{\theta}\cos\theta \end{bmatrix} \quad \boldsymbol{E}(\boldsymbol{q}) = \begin{bmatrix} 0 & 0 \\ 0 & 0 \\ 0 & 0 \\ 1 & 0 \\ 0 & 1 \end{bmatrix}$$

$$\boldsymbol{\lambda} = \begin{bmatrix} \lambda_1 & \lambda_2 \end{bmatrix}^T \quad \boldsymbol{t} = \begin{bmatrix} t_\theta & t_\psi \end{bmatrix}^T$$

To eliminate the Lagrange multipliers [7], we first partition $\boldsymbol{A}(\boldsymbol{q})$ as $\boldsymbol{A} = [\boldsymbol{A}_1 \mid \boldsymbol{A}_2]$, where

$$\boldsymbol{A}_1 = \begin{bmatrix} 1 & 0 & 0 \\ 0 & 1 & 0 \\ 0 & 0 & 1 \end{bmatrix} \quad \boldsymbol{A}_2 = \begin{bmatrix} R\cos\phi & R\sin\phi\cos\theta \\ R\sin\phi & -R\cos\phi\cos\theta \\ 0 & -\sin\theta \end{bmatrix}$$

Let

$$\boldsymbol{C}(\boldsymbol{q}) = \begin{bmatrix} -\boldsymbol{A}_1^{-1}\boldsymbol{A}_2 \\ \boldsymbol{I}_{2\times 2} \end{bmatrix} \tag{11}$$

where $\theta \neq \frac{\pi}{2} \pm k\pi$, $(k = 1, 2, \ldots)$.

It is straightforward to verify that $\boldsymbol{C}(\boldsymbol{q})$ satisfies that $\boldsymbol{A}(\boldsymbol{q})\boldsymbol{C}(\boldsymbol{q}) = \boldsymbol{0}$. If we choose θ and ψ to be the two quasi-coordinates,

$$\boldsymbol{\upsilon}(t) = \begin{bmatrix} \upsilon_1 \\ \upsilon_2 \end{bmatrix} = \begin{bmatrix} \dot{\theta} \\ \dot{\psi} \end{bmatrix}$$

and we can verify that (12) is satisfied.

$$\dot{\boldsymbol{q}} = \boldsymbol{C}(\boldsymbol{q})\boldsymbol{\upsilon}(t) \tag{12}$$

Differentiating (12) yields

$$\ddot{\boldsymbol{q}} = \dot{\boldsymbol{C}}\boldsymbol{\upsilon} + \boldsymbol{C}\dot{\boldsymbol{\upsilon}} \tag{13}$$

Using (10) and (11), we have $\boldsymbol{C}^T\boldsymbol{E} = I$. Substituting (13) into (10), and premultiplying both sides by C^T gives

$$\boldsymbol{C}^{\mathrm{T}}\boldsymbol{M}\boldsymbol{C}\dot{\boldsymbol{\upsilon}}(t) + \boldsymbol{C}^{\mathrm{T}}\boldsymbol{M}\dot{\boldsymbol{C}}\boldsymbol{\upsilon}(t) + \boldsymbol{C}^{\mathrm{T}}\boldsymbol{V} = \boldsymbol{t} \tag{14}$$

Using the state variable $x = (q^T, \upsilon^T)^T$, we have

$$\dot{\boldsymbol{x}} = \begin{bmatrix} \boldsymbol{C}\boldsymbol{\upsilon} \\ \boldsymbol{f}_1 \end{bmatrix} + \begin{bmatrix} \boldsymbol{0} \\ \bar{\boldsymbol{M}}^{-1} \end{bmatrix}\boldsymbol{t}, \tag{15}$$

where $\bar{\boldsymbol{M}} = \boldsymbol{C}^T\boldsymbol{M}\boldsymbol{C}$, $\boldsymbol{f}_1 = -\bar{\boldsymbol{M}}^{-1}\left(\boldsymbol{C}^T\boldsymbol{M}\dot{\boldsymbol{C}}\boldsymbol{\upsilon} + \boldsymbol{C}^T\boldsymbol{V}\right)$.

We apply the following nonlinear feedback [8]

$$\boldsymbol{t} = \bar{\boldsymbol{M}}\left(\boldsymbol{u} - \boldsymbol{f}_1\right), \tag{16}$$

where $\boldsymbol{u} = (u_1, u_2)^T$ represent the new control inputs.

Then the state equation simplifies to the form

$$\dot{\boldsymbol{x}} = \boldsymbol{f}(\boldsymbol{x}) + \boldsymbol{b}(\boldsymbol{x})\boldsymbol{u} \tag{17}$$

where

$$\boldsymbol{f}(\boldsymbol{x}) = \begin{bmatrix} \boldsymbol{C}(\boldsymbol{q})\boldsymbol{\upsilon} \\ \boldsymbol{0} \end{bmatrix} \quad \boldsymbol{b}(\boldsymbol{x}) = \begin{bmatrix} \boldsymbol{0} \\ \boldsymbol{I} \end{bmatrix}$$

3. Path Following

3.1. Controller Design

In the path following task, the controller is given a geometric description of the assigned Cartesian path. For this task, time dependence is not relevant because one is concerned only with the geometric displacement between the robot and path. The path following problem is rephrased as the stabilization to zero of a suitable scalar path error function. Since the robotic system has two control inputs, we may choose two output variables. By appropriately choosing the output variables h_1 and h_2 we can achieve path following control.

Suppose the reference path is

$$\tilde{f}(x_c, y_c) = 0 \tag{18}$$

We define the path error function e_f as

$$e_f = \tilde{f}(x_c, y_c) \tag{19}$$

Then h_1 can be chosen as

$$h_1(\boldsymbol{q}) = e_f = \tilde{f}(x_c, y_c) \tag{20}$$

The other output variable h_2 is chosen to be one of the quasi-velocities of the robotic system.

$$h_2(\boldsymbol{\upsilon}) = \dot{\psi} = \upsilon_2 \tag{21}$$

Differentiating (20) once and twice respectively gives

$$\begin{aligned} \dot{y}_1 &= \frac{h_1(\boldsymbol{q})}{\partial \boldsymbol{q}}\dot{\boldsymbol{q}} = \boldsymbol{J}_{h_1}(\boldsymbol{q})\boldsymbol{C}(\boldsymbol{q})\boldsymbol{\upsilon} \\ \ddot{y}_1 &= \frac{\partial\left(\boldsymbol{J}_{h_1}\boldsymbol{C}\boldsymbol{\upsilon}\right)}{\partial \boldsymbol{q}}\boldsymbol{C}\boldsymbol{\upsilon} + \boldsymbol{J}_{h_1}(\boldsymbol{q})\boldsymbol{C}(\boldsymbol{q})\boldsymbol{u} \end{aligned} \tag{22}$$

where $\boldsymbol{J}_{h_1} = \begin{bmatrix} \frac{\partial \tilde{f}}{\partial x_c} & \frac{\partial \tilde{f}}{\partial y_c} & 0 & 0 & 0 \end{bmatrix}$.

Differentiating (21) yields

$$\dot{y}_2 = \frac{h_2(\boldsymbol{\upsilon})}{\partial \boldsymbol{\upsilon}}\dot{\boldsymbol{\upsilon}} = \boldsymbol{J}_{h_2}\boldsymbol{u}, \tag{23}$$

where $\boldsymbol{J}_{h_2} = \begin{bmatrix} 0 & 1 \end{bmatrix}$.

We define the following sliding surfaces

$$\begin{aligned} s_1 &= \dot{y}_1 + c_1 y_1 \\ s_2 &= y_2 - y_{2d} \end{aligned}, \tag{24}$$

where c_1 is a real positive constant, y_{2d} is the desired value for y_2.

Let $\boldsymbol{S}_1$ be the vector of components s_1 and s_2.

$$\boldsymbol{S}_1 = \begin{bmatrix} s_1 \\ s_2 \end{bmatrix} = \begin{bmatrix} \dot{y}_1 + c_1 y_1 \\ y_2 - y_{2d} \end{bmatrix} = \begin{bmatrix} \boldsymbol{J}_{h_1}\boldsymbol{C}\boldsymbol{\upsilon} + c_1 y_1 \\ y_2 - y_{2d} \end{bmatrix} \tag{25}$$

Differentiating (25) yields

$$\dot{\boldsymbol{S}}_1 = \boldsymbol{f}_2 + \boldsymbol{g}\boldsymbol{u} \tag{26}$$

where

$$\boldsymbol{g} = \begin{bmatrix} \boldsymbol{J}_{h_1}\boldsymbol{C} \\ \boldsymbol{J}_{h_2} \end{bmatrix} \quad \boldsymbol{f}_2 = \begin{bmatrix} \frac{\partial\left(\boldsymbol{J}_{h_1}\boldsymbol{C}\boldsymbol{\upsilon}\right)}{\partial \boldsymbol{q}}\boldsymbol{C}\boldsymbol{\upsilon} + c_1\boldsymbol{J}_{h_1}\boldsymbol{C}\boldsymbol{\upsilon} \\ 0 \end{bmatrix}$$

Let

$$\boldsymbol{\eta}\,\mathrm{sgn}(\boldsymbol{S}_1) = \begin{bmatrix} \eta_1\,\mathrm{sgn}(s_1) & \eta_2\,\mathrm{sgn}(s_2) \end{bmatrix}^T \tag{27}$$

where η_1, η_2 are real positive constants.

We choose the control law $\boldsymbol{u}$ as follows

$$\boldsymbol{u} = \boldsymbol{g}^{-1}\left[-\boldsymbol{\eta}\,\mathrm{sgn}(\boldsymbol{S}_1) - \boldsymbol{K}\boldsymbol{S}_1 - \boldsymbol{f}_2\right] \tag{28}$$

where $\boldsymbol{K} = \begin{bmatrix} k_1 & 0 \\ 0 & k_2 \end{bmatrix}$, k_1 and k_2 are real positive constants.

3.2. Stability Analysis

Theorem 1: Suppose that the system in (17) is controlled by the control law given by (28), then the sliding surfaces s_1, s_2 are asymptotically stable.

Proof: Substituting (28) into (26) yields

$$\begin{aligned} \dot{s}_1 &= -\eta_1\,\mathrm{sgn}(s_1) - k_1 s_1 \\ \dot{s}_2 &= -\eta_2\,\mathrm{sgn}(s_2) - k_2 s_2 \end{aligned} \tag{29}$$

Consider the Lyapunov function candidates

$$V_i = \frac{1}{2}s_i^2, \quad i = 1, 2$$

Differentiating V_i with respect to time gives

$$\dot{V}_i = s_i \dot{s}_i = -\eta_i |s_i| - k_i s_i^2 \le 0 \tag{30}$$

Integrating both sides of (30), we can obtain

$$\begin{aligned} V_i(t) &= \frac{1}{2} s_i^2 \le V_i(0) < \infty \\ \lim_{t\to\infty} \int_0^t \left(\eta_i |s_i| + k_i s_i^2\right) \mathrm{d}\sigma &\le V_i(0) < \infty \end{aligned} \tag{31}$$

From (31), we have $s_i \in L_\infty$, $s_i \in L_2$. From (30), we have $\dot{s}_i \in L_\infty$. Consequently, according to Babalat's lemma we have $\lim_{t\to\infty} s_i = 0,\ i = 1, 2$.

4. Simulation Study

We developed a computer simulation in order to verify the validity of the control algorithms discussed in the previous sections. The dimensions and inertial parameters are representative of the spherical robot. According to the notation introduced before:
$m = 0.85$ kg, $R = 0.14$ m, $I = 0.0111$ kg·m^2, $\gamma = 10$ º.

4.1. Basic Paths

Consider a straight line path $y = x$, as shown in Fig. 3. The initial values of the system configuration variables are such that

$$(x_c, y_c, \phi, \theta, \psi) = (0.4, 0.2, 0, 0, 0)$$

and the initial velocity is zero. For the path following algorithm,

$$h_1 = x_c - y_c,\ y_{2d} = 2.5$$

with the controller parameters

$$c_1 = 4.8,\ k_1 = 4.3,\ k_2 = 4.5,\ \eta_1 = 2.6,\ \eta_2 = 2.2$$

The performance of the robot in straight line path following is shown in Fig. 3. The star marker indicates the starting point of the robot.

Consider a circular path

$$(x - 0.8)^2 + (y - 1)^2 = 0.25$$

as shown in Fig. 4. The initial values of the system configuration variables are such that

$$(x_c, y_c, \phi, \theta, \psi) = (1.2, 1.4, 0, 0, 0)$$

and the initial velocity is zero. For the path following algorithm,

$$h_1 = (x_c - 0.8)^2 + (y_c - 1)^2 - 0.25,\ y_{2d} = 2.5$$

with the controller parameters

$$c_1 = 4.9,\ k_1 = 4.5,\ k_2 = 1.3,\ \eta_1 = 2,\ \eta_2 = 1$$

The performance of the robot in circular path following is shown in Fig. 4.

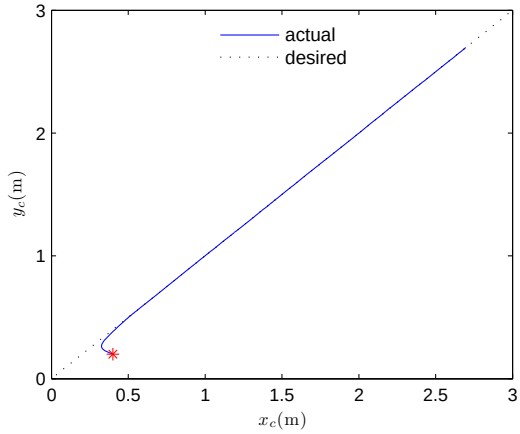

Fig. 3. Control performance in straight line path following.

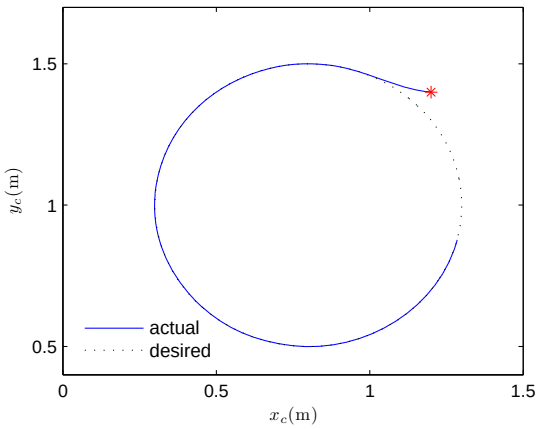

Fig. 4. Performance of the robot in circular path following.

In both cases, the reference point of the robot is able to reach the path and stay on the path. The path following algorithm seems to exhibit a gradual merge, with the path following controller the actual path followed is smooth.

4.2. Piecewise Continuous Paths

An example of a composite path is shown in Fig. 5, which is composed of two circular arcs and a straight line. The performance of the control system is acceptable as seen from the figure. The discontinuities in curvature are negotiated without any difficulty and there is almost no deviation of the actual path from the desired one.

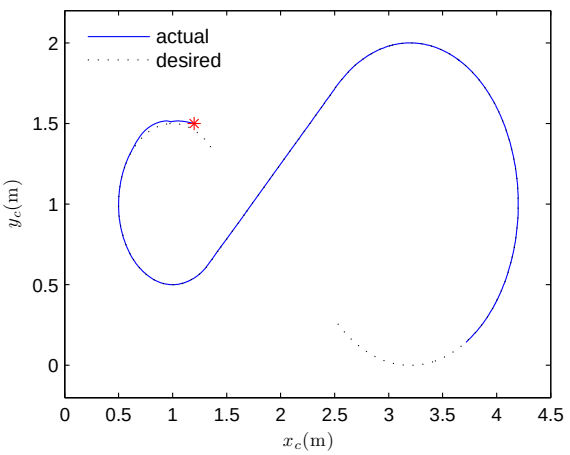

Fig. 5. Control performance in composite path following.

5. Conclusions

We presented a variable structure method for path following control of a spherical robot moving on an inclined plane. We derived the kinematics by imposing the constraint conditions of no-slip and no-spin. We deduced the robot dynamics using the constrained Lagrange formulation. We eliminated the Lagrange multipliers to obtain a state space description of the system. We devised a sliding mode scheme to achieve output tracking. We considered the choice of output variables for path following and derived the sliding mode control laws to satisfy the existence condition of sliding modes. Computer simulation results were presented to illustrate the performance of the proposed control algorithm.

Acknowledgements

The authors wish to acknowledge the financial support provided by the National Natural Science Foundation of China (No. 51175048), the Cultivation Fund of the Key Scientific and Technical Innovation Project, Ministry of Education of China (No. 708011) and Beijing Natural Science Foundation Program and Scientific Research Key Program of Beijing Municipal Commission of Education (No. KZ200810005002).

References

[1]. Soeanto D., Lapierre L., Pascoal A., Adaptive non-singular path-following control of dynamic wheeled robots, in *Proceedings of 42nd IEEE Conference on Decision and Control*, 2, 2003, pp. 1765-1770.

[2]. Alves J., Dias J., Design and control of a spherical mobile robot, in *Proceedings of the Institution of Mechanical Engineers. Part I: Journal of Systems and Control Engineering*, 217, 2003, No. 6, pp. 457-467.

[3]. Liu Z., Zhan Q., Cai Y., Motion control of a spherical mobile robot for environment exploration, *Acta Aeronautica Et Astronautica Sinica*, 29, 2008, No. 6, pp. 1673-1678.

[4]. Zheng M., Zhan Q., Liu J., Cai Y., Trajectory tracking of a spherical robot based on an RBF neural network, in *Proceedings of the IEEE International Conference on Electrical Engineering and Automatic Control*, 7, 2010, pp. 151-154.

[5]. Cai Y., Zhan Q., Xi X., Path tracking control of a spherical mobile robot, *Mechanism and Machine Theory*, 51, 2012, pp. 58-73.

[6]. Liu D., Sun H., Jia Q., Stabilization and path following of a spherical robot, in *Proceedings of the IEEE International Conference on Robotics, Automation and Mechatronics*, 2008, pp. 676-682.

[7]. Bloch A. M., Reyhanoglu M., McClamroch N. H., Control and stabilization of nonholonomic dynamic systems, *IEEE Trans. Aut. Control*, 37, 1992, No. 11, pp. 1746-1757.

[8]. Sarkar N., Yun X., Kumar V., Control of mechanical systems with rolling constraints: application to dynamic control of mobile robots, *International Journal of Robotics Research*, 13, 1994, No. 1, pp. 55-69.

Sensors & Transducers, Vol. 21, Special Issue, May 2013, pp. 48-52

Sensors & Transducers

http://www.sensorsportal.com

Workspace Analysis for Parallel Robot

Ying Sun and Hegen Xiong
College of Machinery and Automation, BOX 242, Wuhan University of Science and Technology, Wuhan, 430081, China
Tel.: +86-027-68862283
E-mail: wustsunying@126.com

Received: 4 April 2013 /Accepted: 14 May 2013 /Published: 30 May 2013

Abstract: As a completely new-type of robot, the parallel robot possesses a lot of advantages that the serial robot does not, such as high rigidity, great load-carrying capacity, small error, high precision, small self-weight/load ratio, good dynamic behavior and easy control, hence its range is extended in using domain. In order to find workspace of parallel mechanism, the numerical boundary-searching algorithm based on the reverse solution of kinematics and limitation of link length has been introduced. This paper analyses position workspace, orientation workspace of parallel robot of the six degrees of freedom. The result shows: It is a main means to increase and decrease its workspace to change the length of branch of parallel mechanism; The radius of the movement platform has no effect on the size of workspace, but will change position of workspace.

Keywords: Parallel robot, Workspace, Mechanism.

1. Introduction

Parallel robot possess such advantages as the accurate orientation, great load-carrying capacity, easy real-time control, etc., its wide application in a great deal of fields, has already caused the great attention of scholars. The workspace of the robot is a job field of the robot-operating device, and it is one of the important indexes of weighing the performance of the robot. During the design of the parallel robot, the workspace is the important index too, and determines the whole size of the parallel robot. The workspace can be divided into accessible workspace and nimble workspace according to the position characteristic of operating device while working. Accessible workspace is an assembly to accessible whole points of some reference point on operation device and it doesn't consider the location of operation. Nimble workspace is an assembly to accessible points from any direction of some reference point on operation device. When the reference point operating device is some point of nimble workspace, the operating device can turn around all lines through this point for a whole circle. The nimble workspace is a part of the accessible workspace, connect the organization in parallel to the space, movement platform can't rotate round some point for 360° generally because the structure restriction of space parallel robot, so the parallel robot lathe does not generally have a nimble workspace. Compared with the serial robot, conformation of the workspace of the parallel robot is too complicated; the reason is that the structure of parallel robot is complexity. This paper will set out from the reverse solution to parallel mechanism, and then study the workspace problem of parallel robot by utilizing the numerical boundary-searching algorithm based on the reverse solution of kinematics and limitation of the link length.

2. Setting-up of the System of Coordinates

In order to discuss conveniently the factors of impacting the workspace of parallel mechanism and the workspace of the parallel robot further, the system of coordinates shown in Fig. 1 is set up. Firstly it sets up the system of coordinates $O_G - X_G Y_G Z_G$ fixed on stationary platform (note by abridging for $\{G\}$) and the system of coordinates $O_H - X_H Y_H Z_H$ fixed on movement platform (note by abridging for $\{H\}$) separately, among them the coordinate origin points O_G and O_H lay on the center of the upper and lower platform separately, axle Z_G and Z_H are perpendicular to the upper and lower platform separately, the axle X_G is through the point B_1, the axle X_H is through the point P_1, the axle Y_G and Y_H are confirmed by the right principle separately. The location matrix of movement platform relative to stationary coordinates system $\{G\}$ is expressed with T, have

$$T = \begin{bmatrix} A_m & Q_m \\ 0 & 1 \end{bmatrix} \tag{1}$$

Among them A_m is called the location matrix of movement platform relative to stationary coordinates system $\{G\}$, if $A_m = I$, then two platforms keep parallel, the change of matrix A_m is called location change; $Q_m = \left(x_{O_H}, y_{O_H}, z_{O_H}\right)^T$ is the coordinate of the origin point O_H of the system of coordinates $\{H\}$ in the coordinate of the system of coordinates $\{G\}$, and it signifies the position of the movement platform, so the change of Q_m value is called position change.

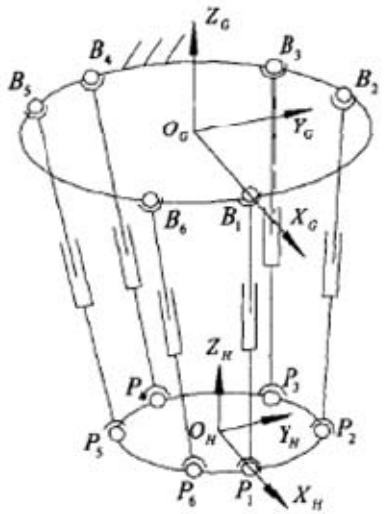

Fig. 1. The system of coordinates of parallel mechanism.

3. Factors of Impacting the Workspace of Parallel Mechanism

There are a lot of factors of impactcting the workspace of parallel mechanism, the main factors among them are: the influence of pole length, the influence of the hinge point position, the influence of restrained in vice corner of sport and the influence of connecting rod interference, etc.

3.1. Influence of Pole Length

Position and posture of platform can be described with posture matrix A_m of movement platform of component relative to stationary platform and translation vector Q_m of two systems of coordinates, while giving the location of the platform definitely, the length and direction of every connecting rod can be expressed with the vector $\vec{l}_i$ $(i = 1, 2, \cdots, 6)$

$$\vec{l}_i = B_i P_i = A_m \vec{P}_i + Q_m - \vec{B}_i \tag{2}$$

Among them $\vec{P}_i = \left\{x_{P_i}, y_{P_i}, 0\right\}^T$ is a vector of hinge point P_i $(i = 1, 2, \cdots, 6)$ of the movement platform relative to system of coordinates $\{H\}$, $\vec{B}_i = \left\{x_{B_i}, y_{B_i}, 0\right\}^T$ is a vector of hinge point B_i $(i = 1, 2, \cdots, 6)$ of the stationary platform relative to system of coordinates $\{G\}$.

The length L_i $(i = 1, 2, \cdots, 6)$ of rod is the modulus of vector $\vec{l}_i$

$$L_i = \left|\vec{l}_i\right| = \left|\mathrm{A_m}\vec{\mathrm{P}}_\mathrm{i} + \mathrm{Q_m} - \vec{\mathrm{B}}_\mathrm{i}\right| \tag{3}$$

The variety of length of rod has a certain limit, and it should meet the following condition.

$$L_{\min} \le L_i \le L_{\max} \tag{4}$$

Among them, $L_{\min}$ and $L_{\max}$ express the minimum length and the maximal length of connecting rod, the expansion & contraction value of rod can be written as $\Delta L = L_{\max} - L_{\min}$. Obviously, when the length of rod is in the limited position, the platform is in the limited position too. The reference point given on movement platform reaches the border of workspace too.

3.2. Influence of the Hinge Point Position

Because the structure of parallel mechanism has nothing in common with each other, there are all kinds of distribution of the hinge point positions of the upper and lower platforms. We can know from Eq.3 that the length of every rod has direct influence on coordinate value of hinge point $\vec{B}_i$ and $\vec{P}_i$, when the hinge point coordinate changes, the length of every rod will change too. So when the limitation length of rod and $L_{\min}$ and $L_{\max}$ are certain, every positions of hinge point have various degree influence on workspace.

3.3. Influence of Restrained in Vice Corner of Sport

Generally speaking, joint linking the upper and lower platform of parallel mechanism with every branch rod is sphere fit or Hooke joint. Whether the joint is sphere fit or Hooke joint, corner ranges of their real structure have certain restriction.

3.4. Influence of Connecting Rod Interference

Generally, the connecting rod has certain size, and the movement of platforms makes the connecting rods interfere each other, which must be avoided. In order to discuss conveniently, supposed that the connecting rod is cylindrical, and its diameter is D. Discussing the question of interference between the connecting rods, is judging the shortest distance d between the two space lines that is greater than the diameter or not. If the condition $d \geq D$ is unsatisfied, then the two connecting rods will be interfered, which will destroy force and balanced condition of the whole mechanism, even can damage the whole mechanism when being serious. Judging the shortest distance between the two space lines is a very complicated problem, which is divided into different situations to judge.

4. Numerical Limited Boundary-searching Algorithm of Parallel Mechanism's Workspace

The Eq. 4 has expressed the length restraint conditions of parallel mechanism, and $L_{\min}$ and $L_{\max}$ in Eq. 4 are the length of the branch rod under the shortest and longest journey respectively. So the length of the group rod corresponding to position matrix of every point can be got by using the reverse solution to kinematics of parallel mechanism, so long as it accords with Eq. 4, the position point can be judged to be in workspace, otherwise outside workspace. If all border points can be hunted out and consist of a surface, then these points between the surface can consist of the workspace of parallel mechanism, which is the principle of the numerical limited boundary-searching algorithm of parallel mechanism's workspace.

Fig. 2 is sketch map of numerical limited boundary-searching algorithm of parallel mechanism's workspace. Firstly along axle z making several sections that can divide workspace into K parts, then limited-border curves in all sections are hunted out one by one, so it is very apt to confirm workspaces of parallel mechanism according to these curves. As for m axle sectional border curve, firstly a foot-path r_step along radial direction further forward in section can be got, then search from up to down along z axle direction until searching out the first limited-border point, then the second limited-border point, and write down them. Using C ++Builder language of programming in this paper can get workspace of various kinds of situations. Using cross section perpendicular to z axle can get the section certainly, and then getting limit border curve of cross section gets workspace. In the whole course of searching, the little step length and the more accurate, but data amounts leap.

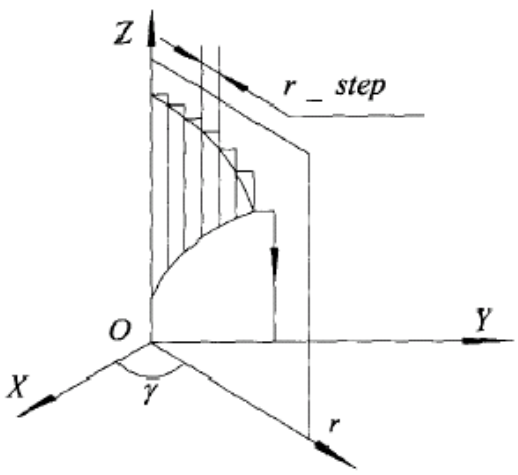

Fig. 2. The sketch map of the numerical limited boundary-searching algorithm of parallel mechanism's workspace.

5. Workspace Analysis of the Parallel Robot

5.1. Position Workspace

To a group of parallel mechanism with regular mechanism parameter, when $A_m = I$, namely stationary platform parallel to movement platform all the time, the workspace of parallel mechanism got is the position workspace. To the robot illustrated in Fig.

1, when the value of $L_{\min} = 730\,mm$, and the value of $L_{\max} = 1130\ mm$, the position workspace tried to get in the $X-Z$ section is shown as curve 3 in Fig. 3. When the length of rod of mechanism is changed, Fig. 3 is the position workspace tried to get in the $X-Z$ section of three groups of length of rod shown in Table 1. We can see from the Fig. 3: The change of mechanism's branch's length has greater influence on the change of the workspace of mechanism. The conclusion can be drawn from the computer emulation and summarizing related documents: It is a main means to increase and decrease the workspace to change the length of branch of parallel mechanism, this conclusion has directive significance to the confirmation of parameter of the robot mechanism.

While changing the radius of the platform, with the change of the hinge point position of the mechanism, has certain influence on the workspace of parallel robot too. Fig. 4 is the position workspace in the $X-Z$ section of three groups of radius of rod shown in Table 2. The conclusion can be drawn from the Fig. 4: The radius of the activity platform has no effect on the size of the workspace, but will change the position of the workspace.

Table 1. Mechanical parameters of different length of branch [mm].

No.	Radius of stationary platform	Radius of movement platform	Scope of expansion & contraction value of rod length
1.	800	200	730-930
2.	800	200	730-1030
3.	800	200	730-1130

Table 2. Mechanical parameters of different radius of platform [mm].

No.	Radius of stationary platform	Radius of movement platform	Scope of expansion & contraction value of rod length
1.	800	150	730-1130
2.	800	200	730-1130
3.	800	250	730-1130

5.2. Orientation Workspace

when $A_m \neq I$, the workspace of parallel mechanism expresses the orientation workspace. The definition of the orientation workspace is when the center O_H of movement platform is in a certain position of regular system of coordinates $O_G - X_G Y_G Z_G$, normal vector n of movement platform becomes the angle θ relative to stationary coordinate parallel to axle Z' (its starting point is through P point), and normal line n' revolves round axle Z' one circle. If the rod length of dispersed points got by reverse solution of kinematics drop on scalable range, this point P is within the orientation space θ, otherwise is outside. Namely position matrix Q_m relative to each point is constant, and its orientation is changed during the dispersed course of winding a certain angle θ with axle Z'. Fig. 5 is namely the orientation workspace under different angles of the third group data listed of Table 1.

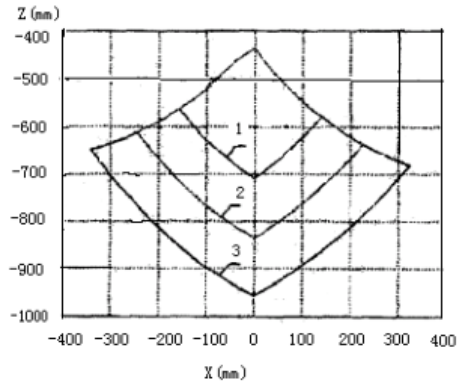

Fig. 3. Position workspace of parallel mechanism and impact of the length of rod on it.

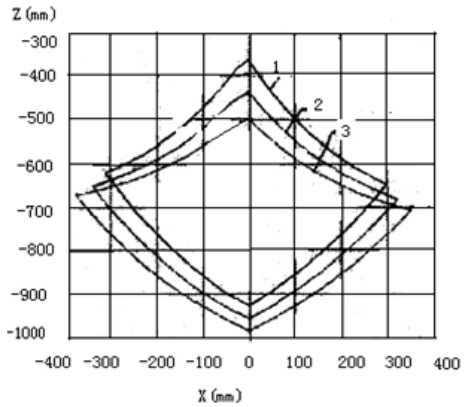

Fig. 4. Position workspace of parallel mechanism and impact of movement platforms on it.

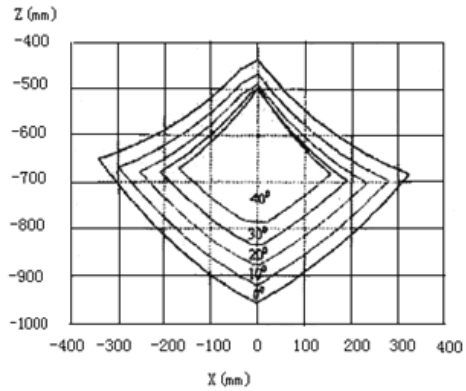

Fig. 5. Orientation workspace of parallel mechanism.

6. Conclusions

This paper has pointed out some factors that influence workspace of the parallel robot, and introduced the numerical boundary-searching algorithm of workspace on the basis of the reverse solution of kinematics of parallel mechanism especially. It has a lot of characteristic, such as simple algorithms, clearing physics meaning and easy programming. These relevant conclusions getting from this algorithm have practical value to the design of the parallel robot. The result shows: It is a main means to increase and decrease the workspace to change the length of branch of parallel mechanism; The radius of the activity platform has no effect on the size of the workspace, but will change the position of the workspace.

References

[1]. Huang Zhen, Mechanics theory and control of parallel robot, Beijing: *China Machine Press*, 1997.

[2]. Zou Hao, Wang Qiyi, Zhao Mingyang, et al., Forward and Inverse Kinematics Analysis of a Parallel Manipulator for Manufacturing, *Journal of Northeastern University (Natural Science)*, 1997, 18, 4, pp. 421 - 425.

[3]. Huang Zhen, Spacing mechanics, *China Machine Press*, Beijing, 1991.

[4]. Wang Qiyi, Zou Hao, Zhao Mingyang, et al., Design and kinematics of a parallel manipulator for manufacturing, *Annals of the CIRP*, 1997, 46, 1, pp. 297 - 300.

[5]. Günter H C, Wust K H., Systematic design of hexapods and other parallel link system, *Annals of the CIRP*, 1997, 46, 1, pp. 291 - 295.

[6]. Zou Hao, Research on mechanical structure and kenematics of Parallel Robot lathe, *Northeastern University*, Dr. 's academic dissertation, 1997.

[7]. Wu Fusheng, Wang Hongbo, Huang Zhen, Research on Workspace of parallel Robot, *Robot*, 1991, 13, 3, pp. 33-39.

[8]. Gosselin C. M., Determination of the Workspace of 6-DOF parallel Manipulators, *J of Mech Des*, 1990C, 112, pp. 331-336.

Sensors & Transducers, Vol. 21, Special Issue, May 2013, pp. 53-57

Sensors & Transducers

http://www.sensorsportal.com

Temperature and Thermal Stress Analysis of Refractory Products

Shaoyang Shi, Gongfa Li, Guozhang Jiang, Liangxi Xie, Jia Liu
College of Machinery and Automation, Wuhan University of Science and Technology,
Wuhan 430081, P. R. China
E-mail: eaglev001@163.com

Received: 1 April 2013 /Accepted: 14 May 2013 /Published: 30 May 2013

Abstract: Firstly current status of temperature and thermal stress research of refractory product at home and aboard are analyzed. Finite element model of two classical refractory products is building by using APDL language. Distribution law of temperature and thermal stress of two typical refractory products-ladles and tundish are analyzed and their structures are optimized. Stress of optimal structure is dropped obviously, and operation life is increased effectively. *Copyright © 2013 IFSA.*

Keywords: Refractory product, Thermal stress, Temperature field, Ladle, Tundish.

1. Introduction

Refractory products (industrial furnaces and all kinds high temperature container, parts) are indispensable part of high-temperature industrial. They are widely used in many industrial sectors, such as metallurgy, machinery, chemicals and building materials, etc. The refractory lining determines their life, thus the normal operation of the entire production process is affected. The damage mechanism of refractory includes two main parts: chemical erosion and thermo-mechanical stress. The former is the refractory is eroded and scoured by the melt, gas, dust, and there have been a lot of research in this regard. The latter refers to result in the lining internal stress is generated due to the expansion caused by the temperature and a certain intrinsic chemical reaction which exceeds its strength to cause damage. Damage by the thermal stress is the main reason for the refractory lining cracking damage. So, it is necessary to analyze the temperature and thermal stress on the refractory products.

2. The Current Situation of Temperature and Thermal Stress of Refractory Products' Research at Home and Abroad

Refractory materials are widely used in the industries of metallurgy, machinery, chemicals, building materials and other high-temperature container pieces, which condition of use determine the service life of these important devices, and ultimately affect the normal operation of the entire production process. And the thermal stress is the main reason for the damage of the refractory products.

At present, thermal stress study has been carried out abroad. For example, Yoshino Ryoichiand and others, Shinagawa Refractories, Japanese, increase the

slide gate's life expectancy of 30-40 %, although they only minor changed skateboard brick after angle based on the thermal stress of the slide gate [1]. Maupin et al, U.S. National Steel, confirmed the reason of its short life due to the lining of thermal stress and shell damage by calculating RH degassing refining equipment [2]. Osamu Nomura and his colleagues, Japanese, has modified converter lining's design according to calculating relations between the coefficient of expansion and thermal stress of the converter lining by finite element method [3]. A Gasser Professor, French, achieved good results through the design of the fluidized bed and the anchorage member lining [4]. Since this approach can extend the life of the product, material savings, which has brought huge economic benefits.

Domestic research has been carried out in this regard. Such as those used in the metallurgical industry converter lining design, converter stress concentration is primarily caused by the incorrect geometric shape and material of the expansion joints, and the areas of stress concentration caused by the traditional ladder masonry is mainly transition zone of the converter. Calculated by the finite element analysis, ladder masonry is replaced by wedge masonry or puzzle arch masonry, which successfully resolved stress concentration problems in converter transition zone [5]. The former Ministry of Metallurgical Industry Building Research Institute has done thermal strain test on refractory, and there is an experimental basis on the case of high temperature refractory test. In recent years, in the study of thermal stress, literature published at home and abroad mainly related to a lot of refractory products used under high-temperature in the blast furnace, converter, skateboards, in package slag dam submerged nozzle and so on, and the study achieved good results, improved production efficiency, reduced production costs.

3. Basic Theory

The stress calculation process can generally be divided into the following steps: firstly, we can calculate the deformation (the deformation displacement of various points within electric furnace roof) under a specific constraint condition, according to the temperature distribution of the electric furnace roof and the various parts of the electric furnace roof's the coefficient of thermal expansion ; then calculate the strain of electric furnace roof points by using geometric equations by the deformation displacement; finally, we calculated stress points of the electric furnace roof by strain based on the physical equation of the material (stress and strain relationships).

The geometry equation of electric furnace roof stress field, which characterize the strain - displacement relations equation. Formula 1 (in matrix form).

$$\varepsilon = \begin{bmatrix} \frac{\partial}{\partial x} & 0 & 0 \\ 0 & \frac{\partial}{\partial y} & 0 \\ 0 & 0 & \frac{\partial}{\partial z} \\ \frac{\partial}{\partial y} & \frac{\partial}{\partial x} & 0 \\ 0 & \frac{\partial}{\partial z} & \frac{\partial}{\partial y} \\ \frac{\partial}{\partial z} & 0 & \frac{\partial}{\partial x} \end{bmatrix} v \quad (1)$$

In the formula, $\varepsilon = \begin{bmatrix} \varepsilon_x & \varepsilon_y & \varepsilon_z & \gamma_{xy} & \gamma_{xz} & \gamma_{yz} \end{bmatrix}^T$ is the strain at any point within the furnace roof; $\upsilon = [u \ v \ w]^T$, u / v / w respectively represent the displacement along the x, y, z direction. According to the above strain - displacement relations, strain of its points within refractories products will be calculated by the displacement of each point of the products (caused by thermal expansion deformation).

The physics equations of furnace roof stress field, which characterize the stress–strain relations equation. Based on Hooke's law, the stress σ of material is proportional to strain ε of material, as Formula 2 shows:

$$\sigma = E\varepsilon \quad (2)$$

For complex solid models, according to the generalized Hooke's law, the relationship between stress and strain can be described for:

$$\sigma = \frac{E(1-\upsilon)}{(1+\upsilon)(1+2\upsilon)} \begin{bmatrix} 1 & \frac{\upsilon}{1-\upsilon} & \frac{\upsilon}{1-\upsilon} & 0 & 0 & 0 \\ \frac{\upsilon}{1-\upsilon} & 1 & \frac{\upsilon}{1-\upsilon} & 0 & 0 & 0 \\ \frac{\upsilon}{1-\upsilon} & \frac{\upsilon}{1-\upsilon} & 1 & 0 & 0 & 0 \\ 0 & 0 & 0 & \frac{1-2\upsilon}{2(1-\upsilon)} & 0 & 0 \\ 0 & 0 & 0 & 0 & \frac{1-2\upsilon}{2(1-\upsilon)} & 0 \\ 0 & 0 & 0 & 0 & 0 & \frac{1-2\upsilon}{2(1-\upsilon)} \end{bmatrix} \varepsilon \quad (3)$$

In the formula, E is the elastic modulus, and υ is Poisson's ratio. According to the above stress - strain relations, any stress of each point is calculated by each point of its inner strain obtained from the previous step, and products are the object of the force, the force meeting the balance equation.

3.1 Stress equilibrium equations

General refractory products is a three-dimensional model, and its inner any point along coordinates x, y, and z-direction of the force balance equation are shown in Formula 4.

$$\begin{aligned} &\frac{\partial \sigma_x}{\partial x} + \frac{\partial \tau_{yx}}{\partial y} + \frac{\partial \tau_{zx}}{\partial z} + f_x = 0 \\ &\frac{\partial \tau_{xy}}{\partial x} + \frac{\partial \sigma_y}{\partial y} + \frac{\partial \tau_{zy}}{\partial z} + f_y = 0 \\ &\frac{\partial \tau_{xz}}{\partial x} + \frac{\partial \tau_{yz}}{\partial y} + \frac{\partial \sigma_z}{\partial z} + f_z = 0 \end{aligned} \quad (4)$$

In the formula, f_x, f_y, f_z are the body force components per unit volume of the furnace cover in the x, y, z direction.

In the work process, the inner wall of the refractory products are not in direct contact with molten steel, so thermal shock which is exposed to should be derived from the thermal radiation of the molten steel and arc, therefore, this effect should be considered to in the finite element analysis. In this article, the ANSYS software is used for numerical simulation of temperature and stress field of refractory products, and its basic analysis process is shown in Fig. 1.

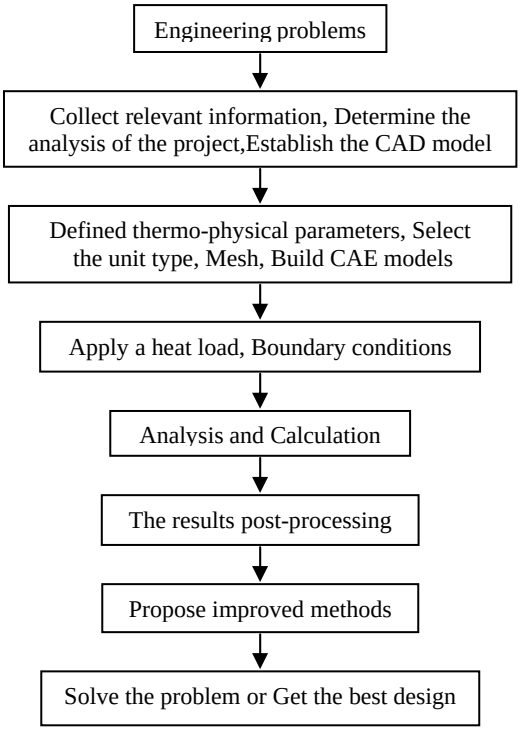

Fig. 1. ANSYS thermal analysis flowchart

4. The Ladle Heat Stress Analysis

The ladle is an important container in the metallurgical industry, and used to store and transport molten steel, also conducted secondary refining, etc. Ladle in the process of using, the most common failure is the pitting and bursting of the refractory lining, resulting in the penetration of the molten steel. The causes of refractory lining damage include chemical erosion, thermal mechanical stress. And the cause of the breakdown of the refractory lining is the thermo-mechanical stresses.

4.1. The Original Ladle Thermal Stress Distribution

250 ton ladle in a steel mill was selected as the analysis object. Ladle was lined by a variety of materials and the structure of the ladle bottom and ladle wall lining was adjusted without changing the texture, and the structures of the smaller level of stress distribution in ladle bottom and ladle wall lining could be obtained. The program of finite element model could be written in APDL language generated, then ladle model was analyzed. The stress distribution of the original ladle bottom structure is shown in Fig. 2.

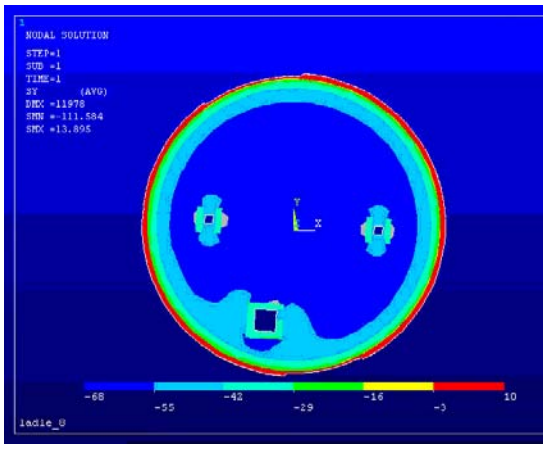

Fig. 2. The original ladle thermal stress distribution cloud.

4.2. The Thermal Stress Distribution of Ladle after Optimization

The ladle bottom hot surface stress in radius is generally higher than that near the center part, because the heat loss close to the wall of the ladle is bigger than that close to the center portion, and caused the premises the temperature gradient larger than close to the central portion, thus creating a greater thermal stress. Thermal expansion coefficient of micro-expansion high alumina bricks in ladle lining material permanent layer is small, so increasing a circle of high aluminum lining in the ladle bottom peripheral will help to reduce the package bottom thermal stress value.

Ladle will be subject to the molten steel's impact when the molten steel is poured into it, first which come into contact with molten steel is the impact block, and installing high aluminum lining around it can also reduce lining bricks instant expansion which causes the thermal stress value increasing. As increasing circle of high aluminum lined brick in the periphery of the package bottom nozzle brick, which is the optimization of the ladle, and reduce the compressive stress of nozzle brick subjected. Its stress distribution cloud is shown in Fig. 3.

By the thermal stress analysis, the circle high aluminum lining bricks with smaller coefficient of thermal expansion are increased the periphery original ladle bottom, so the thermal stress value and the

compressive stress value in this region is smaller than the stress value of the lined region of the intermediate aluminum-magnesium carbonous 10 MPa. Ladle bottom structure after optimization reduced the stress around the nozzle brick, and effectively alleviated the nozzle brick extent of the damage.

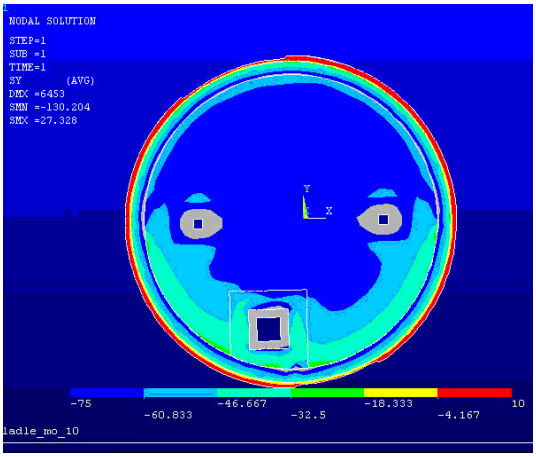

Fig. 3. The ladle after optimization thermal stress distribution cloud.

5. The Law of the Tundish Temperature Distribution

The early stages of development in the Continuous Casting Technology, the tundish just used as storage and distributor of liquid steel. The role of tundish is not only the distribution of liquid steel. but also temperature and composition can be uniformly, and remove inclusions. The flow of molten steel in the tundish may be a non-isothermal flow state under many conditions. The study of the flow characteristics of the molten steel in the tundish non-isothermal state is a very significant problem of research topics in the flow within the tundish.

5.1. Temperature Distribution of the Molten Steel in the No Flow Control Device within the Tundish

Fig. 4 is a temperature distribution of the tundish liquid steel that without any flow control device. From the analysis shows, no flow control device, isotherms of the liquid steel in tundish in the form of horizontal push forward, which is consistent with characteristics of “less reflux "and" more than a short circuit flow” of tundish flow field. And the temperature of the liquid steel in the tundish is very unevenly distributed, in the figure, the proportion of the "Green Line" is more, and the liquid steel between note orifice and the outlet of is quite different. When casting for a long time, the molten steel will be stratified in this case, that the high and low temperature layer. The tundish temperature instability will exacerbate mold shell growth in homogeneity, which is not conducive to the floating separation of the inclusions in the tundish liquid steel, even lead to serious pull leakage. So it is necessary to make the appropriate improvements to the tundish.

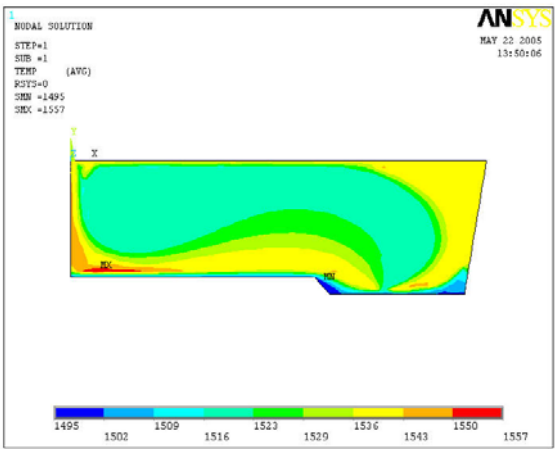

Fig. 4. The temperature isoline of molten steel in the no flow control device tundish.

5.2. The Temperature Distribution of the Liquid Steel inside Tundish after Optimization

Due to the temperature difference between the liquid steel tundish and outside heat, the temperature of the molten steel in the tundish enabled would drop, but when the tundish was taken certain measures, the temperature distribution would be greatly improved. Fig. 5 is a temperature distribution of the liquid steel in the tundish after setting the weir dam, compared to Fig. 3, we can found that the temperature of the molten steel are more evenly distributed, and the temperature at the outlet is the lowest, at the entrances to the temperature difference between the liquid steel is reduced to 12 °C. A layer of fluid near the wall, the temperature is very low, annular, because of the presence of the fluid reflux.

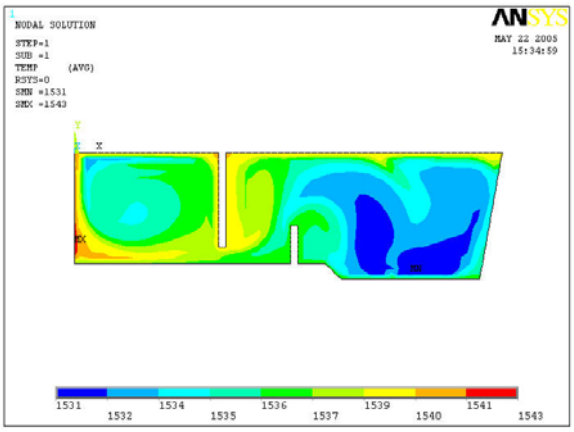

Fig. 5. The temperature isoline of molten steel in the tundish after setting the weir dam.

6. Conclusion

Refractory products are widely used in high-temperature industries, and its service life directly affects the normal operation of the entire production process. The damage to the thermal stress is the direct cause of the refractory lining cracking damage. Using Finite element model of two classical refractory products is building by using APDL language, and the analysis showed that temperature and thermal stress of two typical refractory products-ladle and tundish had its special distribution pattern. It is a good reference to explore ways and means to reduce the thermal stress, to optimize the structure of refractory products, and to provide guidance for the actual production.

References

[1]. Yoshikazu Yoshino, Improvement of Plate Brick Shape for Slide Gate Valve, *Shinagawa Technical Report*, 1997, pp. 35-39.

[2]. Michael W. Maupin, Finite-Element Study of A Degasser Bottom and Throat Area, *National Steel*, 1997, pp. 369-378.

[3]. Osamu Nomura, Shigeru Uchida, Heat-Transfer Analysis of Various Ladle Refractory Linings, *Shinagawa Technical Report*, 2000, pp. 23-34.

[4]. A. Gasser, P. Boisse, Experimental and Numerical Analyses of Thermomechanical Refractory Lining Behaviour, *Proc Instn Mech Engrs*, 2001, pp. 41-53.

[5]. Changxing Lv, Jianfeng Lang, Gang Niu, Ladle permanent layer structure and the masonry design of a method. *Refractories*, 1997, pp. 151-153.

Sensors & Transducers, Vol. 21, Special Issue, May 2013, pp. 58-65

Sensors & Transducers

http://www.sensorsportal.com

Design of Control System for Kiwifruit Automatic Grading Machine

Xingjian Zuo, * Lijia Xu

College of Information Engineering and Technology, Sichuan Agricultural University
Yaan, Sichuan Province, 625014, China
* E-mail: lijiaxu13@163.com

Received: 31 March 2013 /Accepted: 14 May 2013 /Published: 30 May 2013

Abstract: The kiwifruit automatic grading machine is an important machine for postharvest processing of kiwifruit, and the control system ensures that the machine realizes intelligence. The control system for the kiwifruit automatic grading machine designed in this paper comprises a host computer and a slave microcontroller. The host computer provides a visual grading interface for the machine with a LabVIEW software, the slave microcontroller adopts an STC89C52 microcontroller as its core, and C language is used to write programs for controlling a position sensor module, push-pull type electromagnets, motor driving modules and a power supply for controlling the operation of the machine as well as the rise or descend of grading baffle plates. The ideal control effect is obtained through test, and the intelligent operation of the machine is realized.

Keywords: Kiwifruit automatic grading machine, Control system, STC89C52 microcontroller, C language.

1. Introduction

The kiwifruit automatic grading machine is an important intelligent grading machine, and the automatic grading can not only improve the grading efficiency, but also reduce the labor amount, and also increase the market value-added of products, thus grading plays an important role before kiwifruit enters the market. The control system thereof is the core of realizing automation. Kiwifruit grading is all along as a weak link of China's fruit production industry, at this stage the Chinese kiwifruit grading mainly includes manual grading and semi-mechanical grading, wherein the former has the obvious disadvantages that the grading standards are greatly affected by human factors, and the grading efficiency and grading accuracy cannot be compared with those in an automatic grading machine [1]; the latter is carried out only according to some characteristics. At present, few devices researched and developed at home and abroad are specially used for kiwifruit grading, the fully-automatic grading equipment machinery has a complex structure, the price is usually expensive [2-4], and the situation of kiwifruit grading directly leads to a big minus in quality. As one of the largest country in kiwifruit production, the research on how to improve the automatic grading level and increase the market competitiveness of Chinese kiwifruit has far-reaching significance. Therefore, the control system for the kiwifruit automatic grading machine designed in this paper adopts an STC89C52 microcontroller as the main control chip, which can accomplish various functions such as automatic running, automatic stopping and automatic control of grading baffle plates, and also provide a solution for the kiwifruit automatic grading machine.

2. Hardware Structure of Control System

The kiwifruit automatic grading machine designed in this paper is shown in Fig. 1. A hardware system is composed of six parts: a storage box, a single-row positioning conveying system, an image acquisition system, a grading conveying system, a grading executive system and a control system; the storage box is mainly used for temporarily storing kiwifruits to be graded, the single-row positioning conveying system is used for separating the kiwifruits in the storage box into single rows of single kiwifruits at certain intervals for making preparations for image processing and grading of single kiwifruits; the image acquisition system is used for providing a stable light source for a CCD camera, so as to ensure the clear kiwifruit information extracted from the system and accurate kiwifruit grading; the grading conveying system is used for conveying the kiwifruits after image processing to specified grading boxes; the grading executive system is used for executing the signal of the control system for controlling the rise or descend of a grading baffle plate, so as to ensure the kiwifruits to enter into the corresponding grading boxes in the direction of the grading baffle plate; the control system is used for allowing the whole mechanical system to realize intelligent operation.

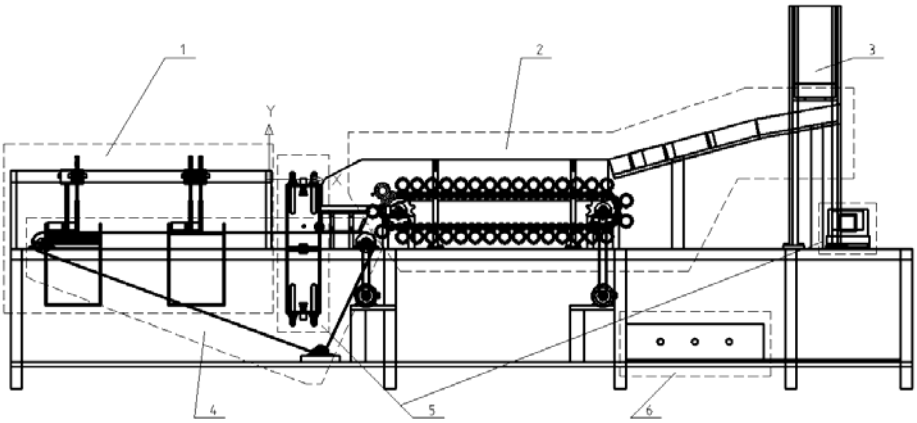

1-Grading executive system; 2-Single-line positioning system; 3-Material storage bin; 4-Grading conveying belt; 5-Image capture system; 6-Control system.

Fig. 1. Structure sketch of grading equipment.

3. Module Design Scheme of Control System

The control system adopts a host computer and an STC89C52 microcontroller as its core, a friendly man-machine interface for data acquisition, analysis, display and serial port control is designed by writing program with LabVIEW 8.6 software, and the exchange of data streams between subsystems of a grading system is further realized. First, the grading system is started through the man-machine interface, the initialization of the microcontroller and the connection between the microcontroller and the host computer are realized at the same time, and after receiving a kiwifruit positioning signal from a position sensor, the microcontroller transmits the kiwifruit positioning signal to the host computer through serial communication; cameras on the upper and lower sides of a transparent conveyer belt start collecting kiwifruit images, the images are transmitted to the host computer for storage trough a USB data line, then the labVIEW8.6 software invokes an MATLAB image processing program for image processing, so as to obtain quality characteristic parameters of kiwifruit, a BP neural network gives grades of kiwifruit according to the quality characteristic parameters, and then the host computer transmits the grading signals to the microcontroller through serial communication; the microcontroller controls the actions of corresponding grading baffle plates according to the grading signals for purpose of grading kiwifruits. The structure of the whole control system is shown in Fig. 2.

3.1. Position Sensor Module

The position sensor module is composed of an LE18S-A30NAD3 diffuse photoelectric switch and a supporting structure. The position sensor is positioned on the wall of a light box. After the grading system is started, the kiwifruits are conveyed through the single-row positioning conveying system and the conveyer belt, when the kiwifruits reach the vertical line of the camera, the light path of the position sensor is blocked, the kiwifruit positioning signal is transmitted to the microcontroller, and the microcontroller starts to communicate with the host computer. The circuit diagram of the position sensor is shown in Fig. 3.

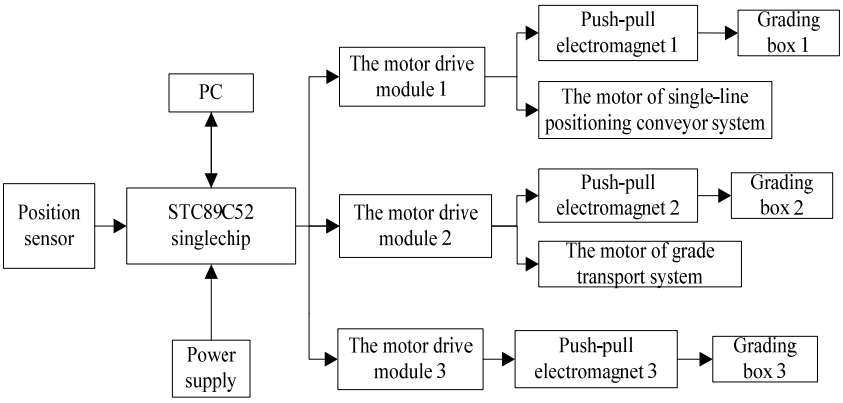

Fig. 2 The control block diagram showing the overall structure of the system.

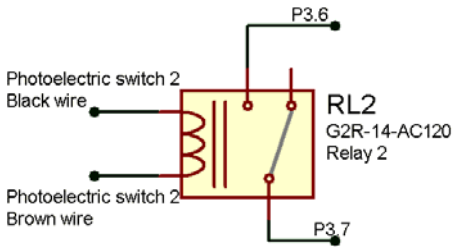

Fig. 3. Position sensor circuit.

3.1.1. Design of Position Sensor

The positioning information of kiwifruits on the transparent grading conveyor belt is monitored in real time, and determining the execution state of a grading program of the microcontroller according to the detection result is the inherent requirement of realizing the grading function of the system. During the running process of the hardware system, the microcontroller needs to monitor whether the kiwifruits are put in place in real time and transmits the signal to the host computer, thus the detection signal is only required to be changed when the kiwifruits reach the specified position, and a photoelectric switch is a commonly used device for realizing this function. In view of the blocking or reflection of a detected object to the light beam, the photoelectric switch is used for detecting whether an object exists through a gating circuit of a synchronous circuit. The object is not limited to metal, and all objects capable of reflecting light can be detected. The photoelectric switch transforms the input current into an optical signal emitted through an emitter, a receiver is used for detecting the target object according to the intensity of the light received or the presence or absence of light.

According to the demands of the system to the positioning of kiwifruits, the LE18S-A30NAD3 diffuse photoelectric switch is selected as the core of the position sensor, and the position sensor is a three-wire single-part position sensor with switching value output, which can detect whether an object exists according to the reflection of the detected object to infrared rays. The structure of the position sensor is shown in Fig. 4.

In Fig. 4, a brown wire is connected to a positive electrode of a power supply, a blue wire is connected to a negative electrode of the power supply, and a load is connected between a black wire and the brown wire. When the transmit path of an infrared emitter is blocked by the arrival kiwifruits, and light is reflected and received by an infrared receiver, the on-off state of the sensor is changed, and the load is powered on.

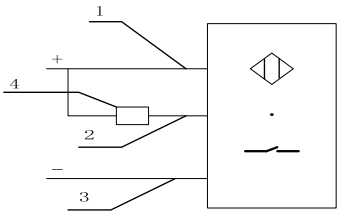

1-Blue wire; 2-Black wire; 3-Load; 4-Brown wire.

Fig. 4. Photoelectric switch diagram.

3.1.2. Electromagnetic Relay

The SRD-12VDC-SL-C electromagnetic relay is an automatic electric appliance, and used as an intermediate member for the position sensor and the microcontroller in the system. The operation characteristic curve and the structure of the electromagnetic relay are shown in Fig. 5 and Fig. 6 respectively.

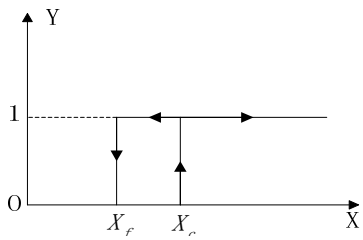

Fig. 5. The characteristic curve of the relay.

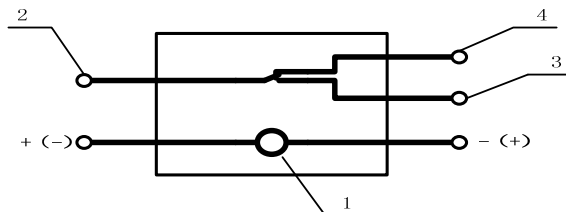

1-Coil; 2-COM port; 3-Normally closed contact;
4-Normally open contact.

Fig. 6. Relay structure diagram.

In Fig. 5, X represents the input voltage of a coil, Y represents the logic output quantity of a relay switch, X_f represents release voltage, and X_c represents pull-in voltage. When $X < X_f$, an armature does not move, the output quantity Y=0; when $X = X_c$, the armature gets absorbed, the switch is closed, the output quantity is changed from 0 to 1, and at the moment, normally closed contacts are opened, and normally open contacts are closed; the output quantity is continued to be increased, when $X > X_c$, the output quantity Y=1. When the output quantity is decreased, although the pull characteristic is lowered during the process of $X > X_f$, the suction force of the armature is still greater than the counterforce in the suction state, so the armature is not released, and the output quantity Y=1. When $X = X_f$, because the suction force is smaller than the counterforce, the armature is released, the output quantity is changed into 0 from 1, and the relay is restored.

In Fig. 6, two ends of the coil are connected to positive and negative terminals of the power supply, and the requirement of polarity is not required. A COM terminal is a common terminal, which can generally input signals which can be selectively output. The rest two contacts of a normally open contact and a normally closed contact are connected with the input end of a device required to be controlled.

3.1.3. Connection of Photoelectric Switch and Microcontroller

In the system, the photoelectric switch is in signal connection with the microcontroller through a relay, but not in direct physical contact with the microcontroller, and the connection between the both is shown in Fig. 7.

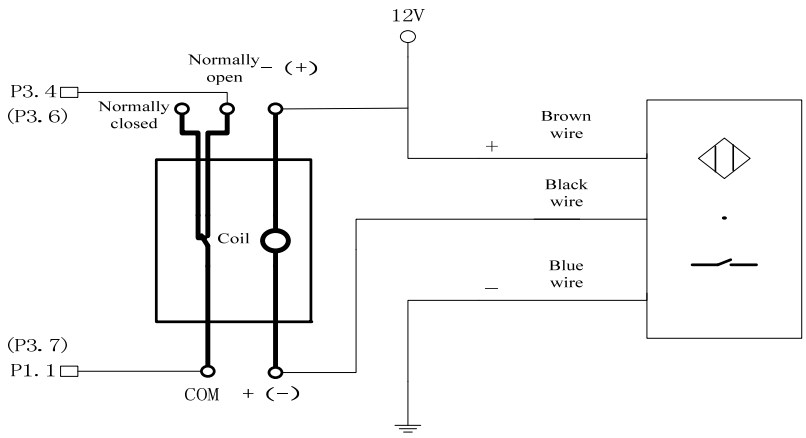

Fig. 7. Photoelectric switch with SCM physical connection diagram.

In Fig. 7, a brown wire of the photoelectric switch is connected to a positive electrode of a 12V power supply, and a blue wire is connected to power line ground; a black wire is connected to any contact of a relay coil, and then led to another contact of the relay coil from the brown wire; a P3.7 in a parallel port of the microcontroller is connected with the COM terminal, and a P3.6 is connected with a normally open contact of the relay. In the system, the position sensor is connected with the microcontroller. During the initialization of the microcontroller, the P3.7 is in high level, the P3.6 is in low level, when kiwifruits are conveyed to the position sensor module through the transparent grading conveyor belt, and the optical path of the photoelectric switch is blocked, the relay coil is powered on, the P3.6 is pulled to high level by the P3.7, when this state is detected through a program, the kiwifruit positioning information is sent to the host computer, and this process is defined as “kiwifruit positioning”. The overall structure of the position sensor module is shown in Fig. 8.

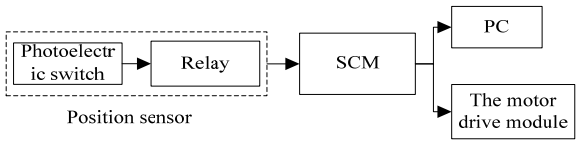

Fig. 8. The overall configuration diagram of the position sensor module.

3.2. Motors, Push-pull Type Electromagnets and Driving Modules

The system comprises two motors and three push-pull type electromagnets, wherein the motor 1 drives the single-row positioning conveying system to move, and the motor 2 drives the transparent grading conveyor belt to move; the push-pull type electromagnet 1 pulls a grading baffle plate 1 to rise or descend, the push-pull type electromagnet 2 pulls a grading baffle plate 2 to rise or descend, and the push-pull type electromagnet 3 pulls a grading baffle plate 3 to rise or descend. The microcontroller controls the working states of the push-pull type electromagnets through motor driving modules according to the received kiwifruit positioning signal, so as to realize the rise or descend of the grading baffle plates 1, 2 and 3 as well as the successful grading of kiwifruits.

3.2.1. Push-pull Type Electromagnets

The system adopts an inclined plane blocking type grading method, and the grading baffle plates are driven to move up and down by the push-pull type electromagnets. When the push-pull type electromagnet is powered off, the grading baffle plate is in the highest position, and kiwifruits can smoothly pass through the grading baffle plate; when the push-pull type electromagnet is in the suction state, the grading baffle plate is in the lowest position, and kiwifruits are blocked by the grading baffle plates, and slide into the corresponding grading boxes in the direction of the grading baffle plate. Based on this requirement, the push-pull type electromagnet with stroke of 3.5 cm and rated DC voltage of 12 V and with automatic resetting function is selected to drive the grading baffle plate.

3.2.2. L298N Motor Driving Modules

In the control system, three sets of motor driving modules [6] are used, a 5 V onboard power supply is enabled, and an external 5 V power supply is not used; a channel A of the motor driving module 1 is used for controlling the motor 1 for realizing the control of the single-row positioning conveying system; a channel B of the motor driving module 1 is used for the push-pull type electromagnet 1 for realizing the control of the grading baffle plate 1; a channel A of the motor driving module 2 is used for controlling the motor 2 for realizing the control of the transparent grading conveyor belt; a channel B of the motor driving module 2 is used for controlling the push-pull type electromagnet 2 for realizing the control of the grading baffle plate 2; a channel A of the motor driving module 3 is used for the push-pull type electromagnet 3 for realizing the control of the grading baffle plate 3. The p1.0, P1.7 and P1.2, the p1.0, P1.6 and P1.3, the p1.0, P1.5 and P2.1 as well as the p1.0, P2.2 and P1.4 and the p1.0 and P3.5 of the microcontroller are used as the logic output ends of the single-row positioning conveying device, the grading baffle plate 1, the grading baffle plate 2, the grading baffle plate 3 and the transparent grading conveyor belt respectively, during the working process, of the two logic input ends is only required to be set to “1”, the corresponding motor or push-pull type electromagnet is driven, and when different logic input ends are set to “1”, the rotating direction of the driven motors is different. The circuit connection is shown in Fig. 9.

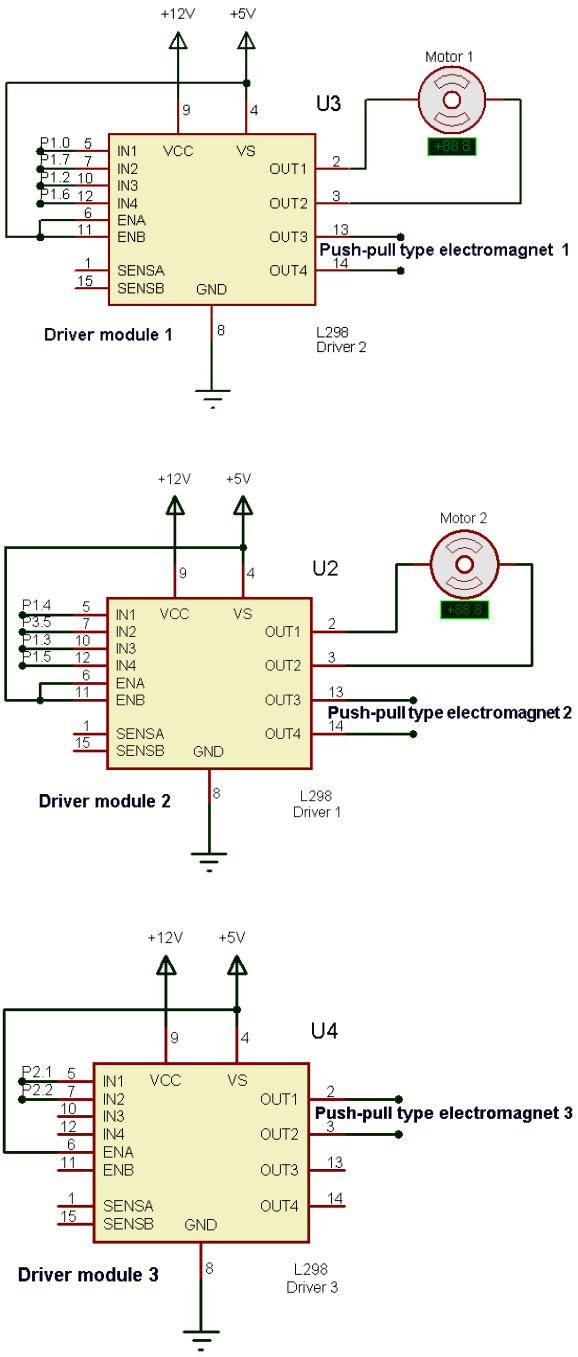

Fig. 9. A circuit diagram of motor and its drive modules.

3.3. Power Supply Module

The power supply of the slave microcontroller in the control system is completed through a USB power line communicated with the host computer, and the power supply of other parts is provided by an ST-122 type DC power supply. The power supply of lighting equipment is provided by a domestic 220 V AC power supply.

4. Serial Communication

4.1. Serial Port Setting

The baud rate of the serial port is set at 9600 bps. The control system is connected with the host computer through an RS232-TTL line, and instructions of the host computer are sent to the slave microcontroller through serial communication.

The instructions sent to the slave microcontroller from the host computer include start, suspend and stop instructions as well as four grading signals. Workers can send the start, suspend and stop instructions to the slave microcontroller from the man-machine interface according to the situation at the scene; after receiving the kiwifruit positioning information sent from the slave microcontroller, the host computer controls the camera to finish the work of image acquisition, the collected images are stored in the host computer, and after the images are processed through the host computer, the grading signal is sent to the slave microcontroller.

The instruction sent to the host computer from the slave microcontroller only includes a kiwifruit positioning signal. When receiving the signal, the host computer starts to control the camera for finishing image acquisition and storing and processing the images, and then sends the grading signal corresponding to the processing result to the slave microcontroller through a serial port. The working flow of the serial port is shown in Fig. 10. The codes for signal connection between the host computer and the slave microcontroller are shown in Table 1.

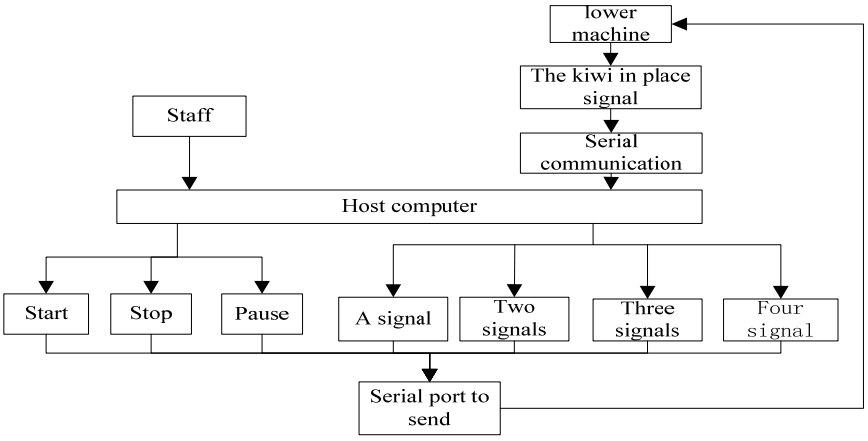

Fig. 10. Serial workflow.

Table 1. Signal connection of upper machine and lower machine.

Signal	The sending code
Kiwi in place	0X55
The first grade	0X31
The second grade	0X32
The third grade	0X33
The fourth grade	0X34
Start	0X30
Pause	0X35
Stop	0X36

5. Design of Software Structure of Host Computer

The software of the host computer mainly comprises an operation control part and an interaction part, wherein the operation control part comprises a starting device, a halt device and a stopping device, and used for implementing various functions of monitoring the grading progress, storing the grading results, performing error message warning and automatic processing, etc.; the interaction part comprises a landing device control system and a help system, and used for viewing the record files and reporting operation, setting the related parameters of equipment, changing passwords, etc. By adopting a graphic programming method [7], LabVIEW software with lots of functions can conveniently finish various operations of data acquisition, analysis and display, instrument control, measurement and test and industrial process simulation and control, and has good expansibility with other programming languages. Therefore, the software adopts labVIEW8.6 for programming, the image processing adopts MATLAB, and the

operating system adopts Windows XP. Programming is carried out in the labVIEW8.6 according to the nodes and sequence. The flow chart of the software structure is shown in Fig. 11.

6. Experimental Test

In the system, aiming at the common kiwifruit lesion symptoms, the image approximate component features are obtained through wavelet transformation, the statistic features are extracted as the input parameters of BP neural network and the recognition of surface faults of kiwifruits is realized through training. The images obtained after the quantization encoding of approximate component of the third layer in wavelet transformation are compressed into a 100×100 dimension matrix, the median value, maximum value, minimum value and the difference between the maximum and minimum values in the matrix are extracted as the input parameters of the BP neural network for grading verification. The test results are shown in Table 2.

Table 2. Test results.

No	Defect or no defect	Desired output	Actual output	No	Defect or no defect	Desired output	Actual output
1.	Y	1	1.020484	41	Y	1	1.021066
2.	N	0	-0.05528	42	Y	1	0.820555
3.	Y	1	0.873705	43	Y	1	0.952468
4.	Y	1	1.024353	44	N	0	-0.07435
5.	N	0	-0.0635	45	Y	1	1.009494
6.	Y	1	1.018292	46	N	0	-0.05734
7.	Y	1	0.806659	47	Y	1	1.020465
8.	N	0	-0.06322	48	N	0	-0.06632
9.	N	0	-0.0635	49	N	0	-0.0227
10.	Y	1	0.108156	50	Y	1	1.021066
11.	N	0	0.129774	51	N	0	0.030735
12.	N	0	-0.05632	52	Y	1	0.424307
13.	N	0	-0.05734	53	Y	1	1.022928
14.	Y	1	1.022928	54	N	0	0.319255
15.	Y	1	1.020548	55	Y	1	1.021495
16.	Y	1	1.046718	56	N	0	-0.06567
17.	Y	1	1.021495	57	Y	1	1.020465
18.	Y	1	1.022086	58	N	0	-0.06739
19.	Y	1	1.024353	59	Y	1	0.806659
20.	N	0	-0.06567	60	N	0	-0.0635
21.	N	0	0.095904	61	Y	1	1.022473
22.	N	0	-0.02521	62	Y	1	0.873705
23.	N	0	-0.0436	63	Y	1	1.020142
24.	N	0	0.85327	64	N	0	0.095904
25.	N	0	-0.05794	65	Y	1	1.003501
26.	N	0	0.135731	66	Y	1	0.584572
27.	N	0	0.275656	67	N	0	-0.05678
28.	Y	1	1.010871	68	Y	1	1.022086
29.	N	0	-0.04454	69	N	0	1.303887
30.	Y	1	1.022633	70	Y	1	1.02661
31.	N	0	0.014773	71	N	0	-0.05933
32.	N	0	0.021012	72	Y	1	0.977687
33.	N	0	-0.04039	73	N	0	-0.03514
34.	Y	1	1.01912	74	Y	1	1.016991
35.	Y	1	0.890394	75	N	0	-0.06493
36.	Y	1	1.023574	76	N	0	-0.05672
37.	N	0	-0.0513	77	N	0	-0.04773
38.	Y	1	1.022517	78	Y	1	0.017276
39.	Y	1	1.003501	79	N	0	0.411776
40.	N	0	-0.03772	80	Y	1	0.667191

Note: Defective--Y, No defects--N

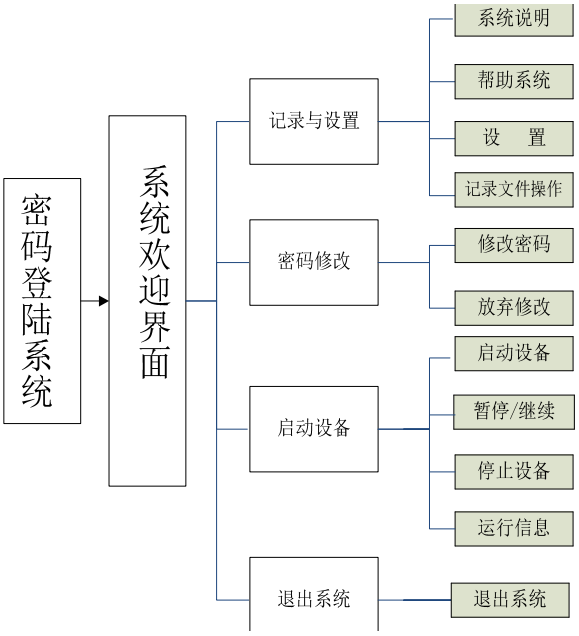

Fig. 11. PC software diagram.

7. Conclusions

With the comprehensive utilization of rich software and hardware resources of the STC89C52 microcontroller, the system realizes the intelligent control of the kiwifruit automatic grading machine through the visual monitoring running by being combined with the host computer. The position sensor module, push-pull type electromagnets and motor driving modules are combined organically, thus the operation control of the grading machine is realized through programming with C language. By adopting the modular design, the system has good expansibility and upgradeability. The experiments show that the design can realize the intelligent operation of the grading machine, but has deficiency in control accuracy, thus it needs to be improved and explored continuously in the practice.

Acknowledgements

This paper was funded by the Natural Science Project of Sichuan Education Department under Grant 12ZA277 and the interest plan of College student's scientific research training.

References

[1]. Feng Bin, Wang Maohua, Computer Vision Classification of Fruit Based on Fractal Color, *Transactions of the Chinese Society of Agricultural Engineering*, Vol. 18, Issue 2, 2002, pp. 141-44.

[2]. Abedini J. Post harvest physiology and technology of kiwi, *Danesh-Negar Publishers*, Tehran, Iran, 2004.

[3]. An Aiqin, Yu Zetong, Wang Hongqiang, The Method of automatic apple hierarchy based on machine vision, *Journal of Agricultural Mechanization Research*, Vol. 29, Issue 4, 2008, pp. 163-166.

[4]. Wu Rongsen, Wu Baokui, Research on grading apple size and defect based on computer vision, *Journal of Nantong Vocational College*, Vol. 23, Issue 4, 2009, pp. 74-77.

[5]. Wu Rentao, Jiang Yunhai, Zuo Jianyong, Vision acquisition based on LabVIEW and USB camera, *Industrial Instrumentation & Automation Magazine*, Issue 3, 2011, pp. 80-83.

[6]. Sun Xucai, The Application of L298N in DC Motor PWM Speed Regulation System, *Journal of Weifang University*, Vol. 9, Issue 4, 2009, pp. 19-22.

[7]. Yuan Yuan, Li Shaowen, Wang Weiwei, et al, Application of LabVIEW to remote monitoring system for orchard environment, *Transactions of the Chinese Society of Agricultural Engineering*, Vol. 23, Issue 6, 2017, pp. 186-188.

Sensors & Transducers, Vol. 21, Special Issue, May 2013, pp. 66-72

Sensors & Transducers

http://www.sensorsportal.com

Design of Remote Power Plant Monitoring System Based on LabVIEW and VC++ Software

Dawei Tan, Gongfa Li, Dan Meng, Xiao Xiao
College of Machinery and Automation,
Wuhan University of Science and Technology, Wuhan 430081, Hubei, China
Tel.: 086-02768862283
E-mail: 804570163@qq.com

Received: 30 March 2013 /Accepted: 14 May 2013 /Published: 30 May 2013

Abstract: This study designs a real-time remote monitoring system based on LabVIEW and Microsoft Visual C++ for Plant Units. The server written in LabVIEW uses for data acquisition and storage. The server adopts the TCP and DataSocket to communicate with the VC client. The remote VC client can accept real-time data and process data, enabling remote monitoring. *Copyright © 2013 IFSA.*

Keywords: LabVIEW, Online monitoring, VC++, Mixed programming, DataSocket.

1. Introduction

Through field investigation and research, at present the plant power plant production systems exist the following problems: geographic distribution is wide, handan power plant production points is much, workload is very big to connect the control system. With long relied on manual pickup, manual meter reading statistics, it is less access to production information , slow the transmission speed, long processing cycles, not conducive to the discovery of the hidden problem, at the same time it will cause fluctuations and energy waste in production. With the production process more and more complex, the factory workshop each other incomplete coordination is worsening contradictions. Online monitoring has been taken for the main equipment in the existing units in power plant, such as gas turbine, steam turbine, generator. After data processing in mean way, once fault occurs, the machine will shut down immediately. The cause of the failure cannot be determined, and data can't be long-term preservation.

This paper designs a set of power plant real-time remote monitoring system monitoring and recording the key data (displacement, vibration, and differential expansion, pressure, temperature, and other real-time data) of the main equipment of the unit based on C/S mode.

Remote real-time monitoring system designed in this paper a set of C/S mode Plant Units monitoring and recording the key data (displacement, vibration, and differential expansion, pressure, temperature, and other real-time data) of the main equipment of the unit, as well as a failure occurs, it is convenient to call the historical data to determine the cause of the malfunction for engineering and technical personnel.

2. Server Design

The power plant includes 10 units. There are 618 measurement points among units (224 acceleration measurement points, 52 displacement measurement points, 56 rotational speed measurement points, 186 temperature measurement,

90 flow measurement points and 10 differential expansion measurement points). Due to the wide geographical distribution of units and so much the measuring points, if all the collected data centralizes storage and processing on one server, it would be a very heavy burden on the server. According to the geographical distribution of the 10 units, all acquisition signals are processed with three servers. Each server has the following five functions: data acquisition, data storage, warning judgment, monitoring database, remote communication.

2.1. Data Acquisition

Shown in Fig. 1, the measurement signal from the sensor after signal conditioning is transferred to the computer by DAQ card [1]; finally the programs written in the LabVIEW extracts the data [2]. Shown in Fig. 2, it's a high-frequency signal acquisition task.

2.2. Data Storage

For signals such as temperature, speed, differential expansion, pressure and flow, the sampling frequency is low; all the original data stored will not take up a lot of space, so a direct storage. However Acceleration and displacement signals with higher frequencies save the data in event-triggered and time-triggered Control ways [3]. It saves characteristic values of the signals in Time-Triggered Control ways (Fig. 3) and save original data of the signals in event-triggered control ways (Fig. 4). For example, an acquisition task which sampling frequency is 3.2 kHz and it has 16 channels extracted once data each second, the number of the original data is 51200. After transforming the original data into characteristic values which contains the average, maximum and minimum values, the data amount is reduced to 0.09375 % of the amount of original data. If the average value exceeds the warning threshold, then the server save the raw data of the measuring points to provide the basis for the failure analysis. After pretreatment (Fig. 5), it ensures that the useful data is long-term storage without affecting the online monitoring.

2.3. Early Warning Judgment

Shown is Fig. 6, compared with the alarm threshold characteristic data from the database, if the average exceeds the warning threshold, the alarm signal is sent to the client, while raw data collected is stored.

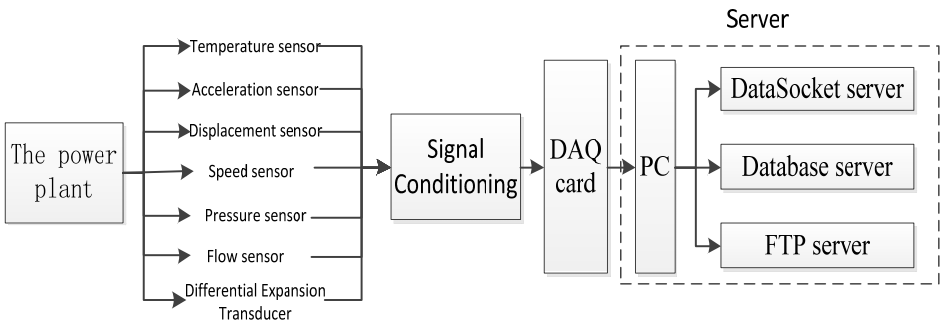

Fig. 1. The diagram of the data acquisition.

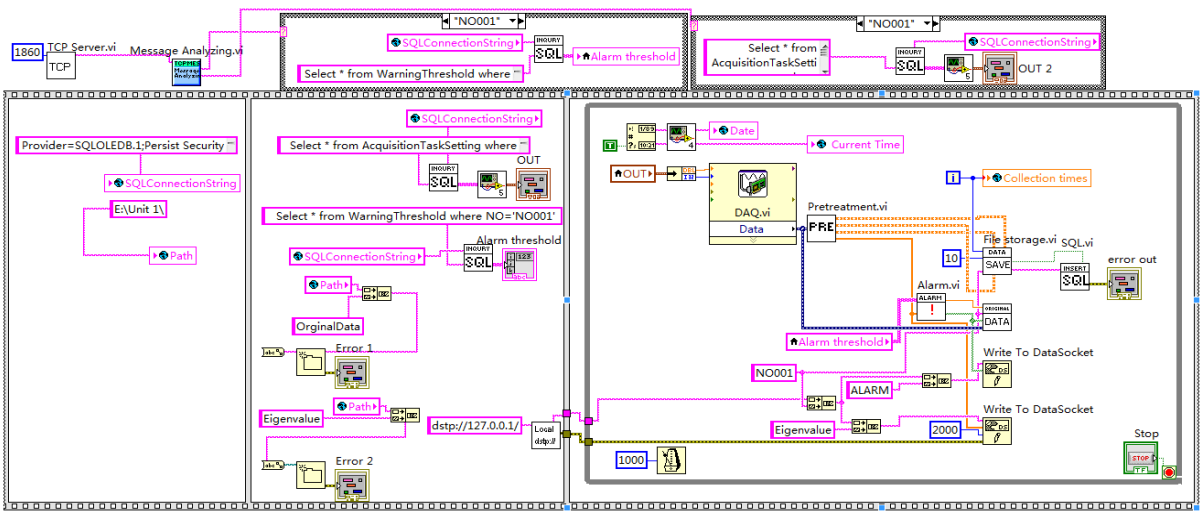

Fig. 2. A high-frequency signal acquisition task.

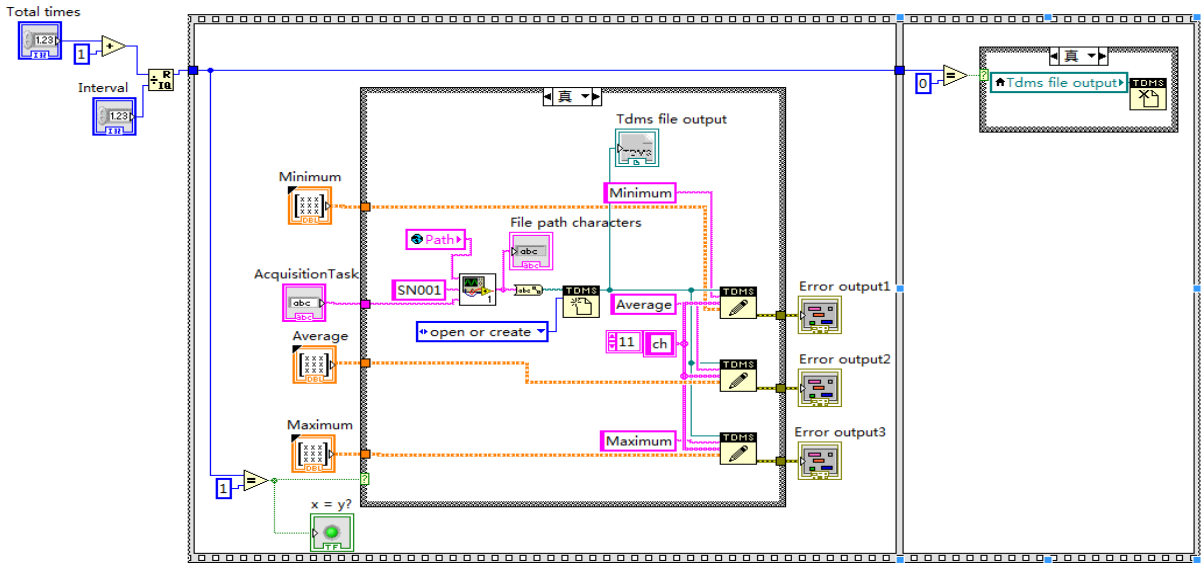

Fig. 3. The characteristic data storage.

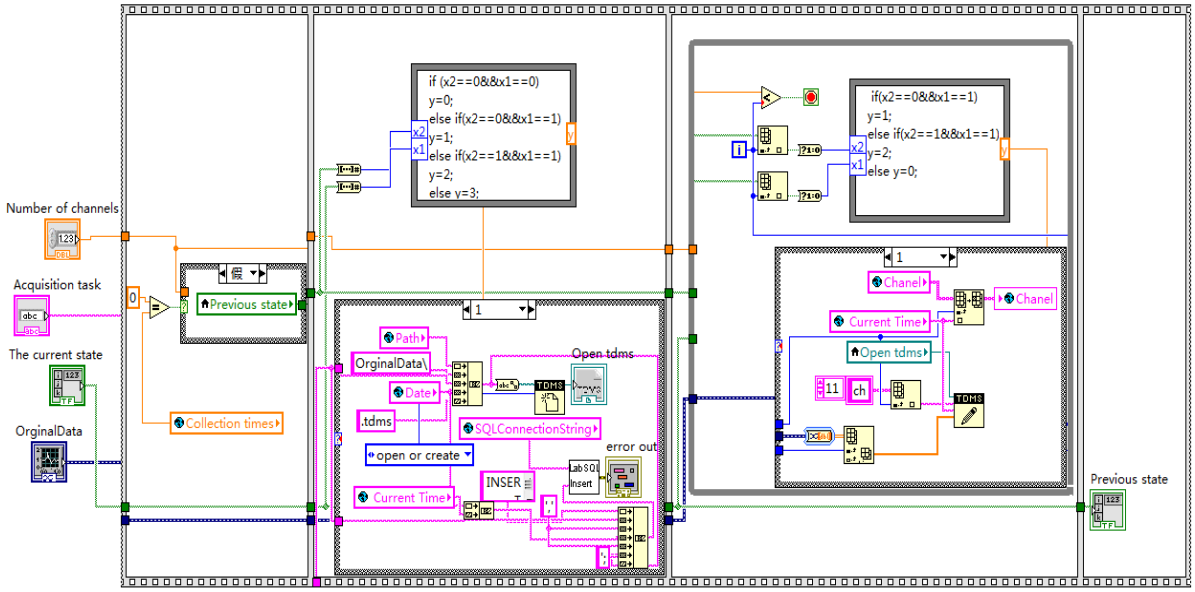

Fig. 4. Store the original data according to the alarm signal.

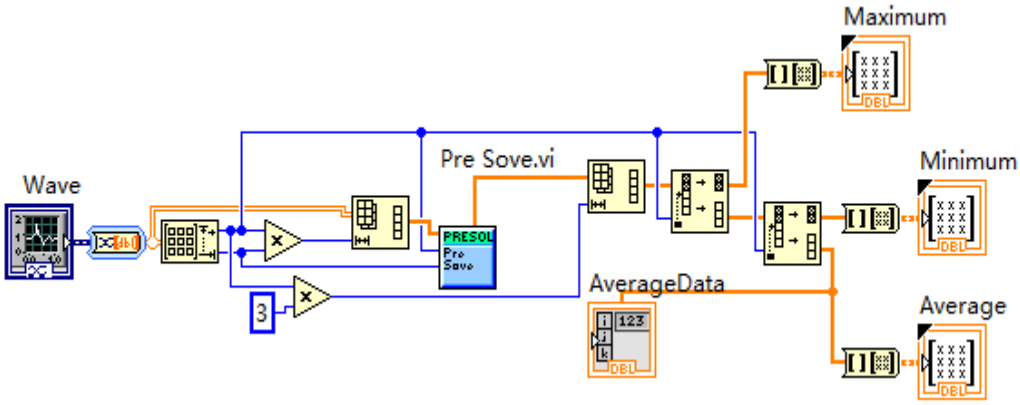

Fig. 5. The Pretreatment of the high-frequency signal.

2.4. Monitoring Database

The acquisition system uses SQL Server as the back-end storage database, the database system has three main functions [4]: (1) static data storage including the unit number of the design parameters, sensor information, the measuring point, the transmission of data communications (FTP address, TCP port connection Datasocket Server URL); (2) dynamic data storage including channel sampling parameters, alarm thresholds; (3) real-time data storage including the characteristics of data storage information, failure data storage information, condition information, message log. Structure of the database relations is shown in Fig. 7, and the procedure of database query operation is shown in Fig. 8.

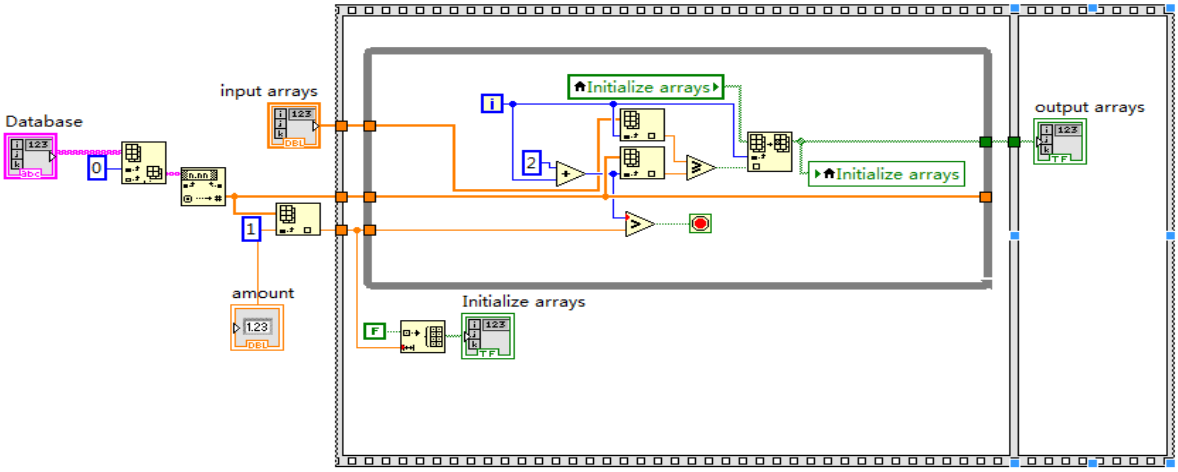

Fig. 6. Warning judge.

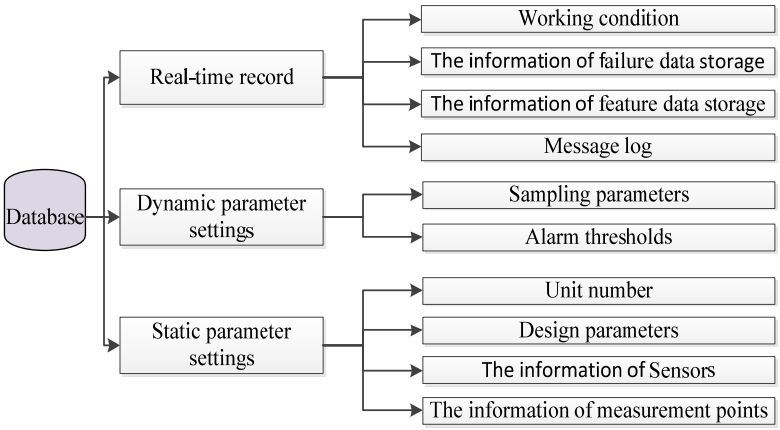

Fig. 7. The relation of database structure

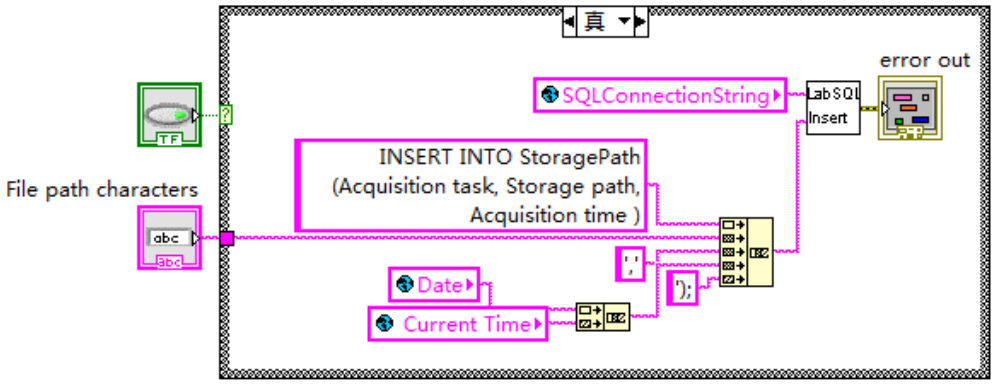

Fig. 8. Database query operation.

2.5. Remote Communications

The remote communication includes real-time data communication, message communication and file communication. Real-time data communication is based on DataSocket Server [5]. All data is passed from publishers to subscribers through the DataSocket server. The DataSocket server is identified on the network using a Uniform Resource Locator (URL). URL sets as “dstp: // native IP/ unit number + acquisition signal type number + acquisition card number”, so that each acquisition task corresponds to a unique URL. The corresponding information of acquisition card and data channel of all URLs is stored in the server database. Clients can acquire the information from the server through the TCP. Clients can connect to DataSocket Server through the URL, in order to obtain the feature data corresponding to the point. According to the corresponding information of acquisition card and data channel, the clients can have knowledge of the equipment operation. Clients can have access to data stored in the server through the FTP server [6]. The structure diagram of C/S communication is shown as in Fig. 9.

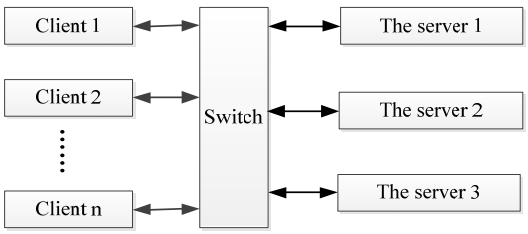

Fig. 9. The structure diagram of C/S communication

3. Client Design

The advantages of the C / S structure is able to give full play to the client PC's processing power, a lot of work are processed in the client-side and then submitted to the server [7]. The functions of customer service are divided into the following sections: system settings module, real-time signal display module, and signal monitoring and analysis module, Fault diagnosis module, recalling the accident module.

3.1. The System Settings Module

When using this module, the system requires a password to obtain the appropriate permissions to set system parameters.

The function is that the settings of power plant critical equipment's sensors and the settings of the upper and lower threshold of important parameters such as vibration, voltage, displacement, temperature. It ensures timely detection of equipment failure and reduces the economic losses caused by equipment failure.

3.2. Real-time Signal Display Module

Client uses the control of DataSocket communicate with the server to obtain real-time signal data. The date of power plant critical equipment, like voltage, vibration, displacement, the gap, the temperature and flow of acquired signals, would be displayed according to the user's requirements. The client can conduct real-time display and real-time status analysis according to the user's requirements.

3.3. Signal Monitoring and Analysis Module

Signal detection analysis module is applied to field data analysis and processing, in order to provide data support for intelligent fault diagnosis module and field staff‘s Judgment [8].

Function: signal time-domain waveform analysis: using different equipment to obtain the characteristics of signals in time domain diagram, auto-correlation, cross-correlation, probability density, time-domain envelope, and for time domain analysis .Signal frequency domain analysis: the analysis of equipment acquisition signal such as amplitude spectrum, phase spectrum, cross-power spectrum, envelope spectrum and cepstrum. Signal three-dimensional spectrum analysis: using the three-dimensional spectrum observed the rotor’s dynamic response process under its many frequency components. Analysis of the signal amplitude: Signal acquisition, including the mean, maximum, minimum, rms value and kurtosis, etc. Signal trend graph: historical data for the use of statements (day\month\year), observing whether there is a significant change in trend on the magnitude of the equipment‘s key parameters and then predict the possible failure of a position.

3.4. The Intelligent Fault Diagnosis Module

Data using real-time signal data acquisition module and the detection analysis module, key equipment working condition of the power plant, the failure mechanism, the cause of the failure to make judgments and to provide a reference for the engineering staff to provide troubleshooting measures. Function: failure mechanism analysis: acquisition signal analysis using fuzzy mathematical principles to judge the malfunction site conditions. The main reason for the failure: the main reason for equipment failure, the decision to provide a scientific basis for people whether the failure of the unit and take safeguard measures. Fault Analysis of the salient features: equipment failure occurs, especially scene gathering the salient features of the signal [9].

3.5. Recall the Accident Module

Recall the accident module stores the historical accident data of power plant critical equipment, and offers a variety of ways to search for the engineering staff.

Function: direct inquiries can carried out through the use of workshop, equipment name, time, accidents name .etc. Providing the indirect way input keyword fuzzy query. By clicking on the using name of the equipment, you can link to all historical accident records of this equipment, and view all incidents information this equipment recorded. Simultaneously having the modifying permissions of the user can conduct modified operation

4. Software Test

A waveform of the client from the server to obtain real-time data is shown in Fig. 10. The servers use collection procedures written by LabVIEW to get real-time signal from the scene, while they store and post the data. Local clients can selectively receive data according to their own needs, and display the data in the form of a waveform on client [10].

When the device fails, the client can download the raw data from the server to find faults, and give diagnostic results back to the server in the form of a data file, enabling data sharing between other clients.

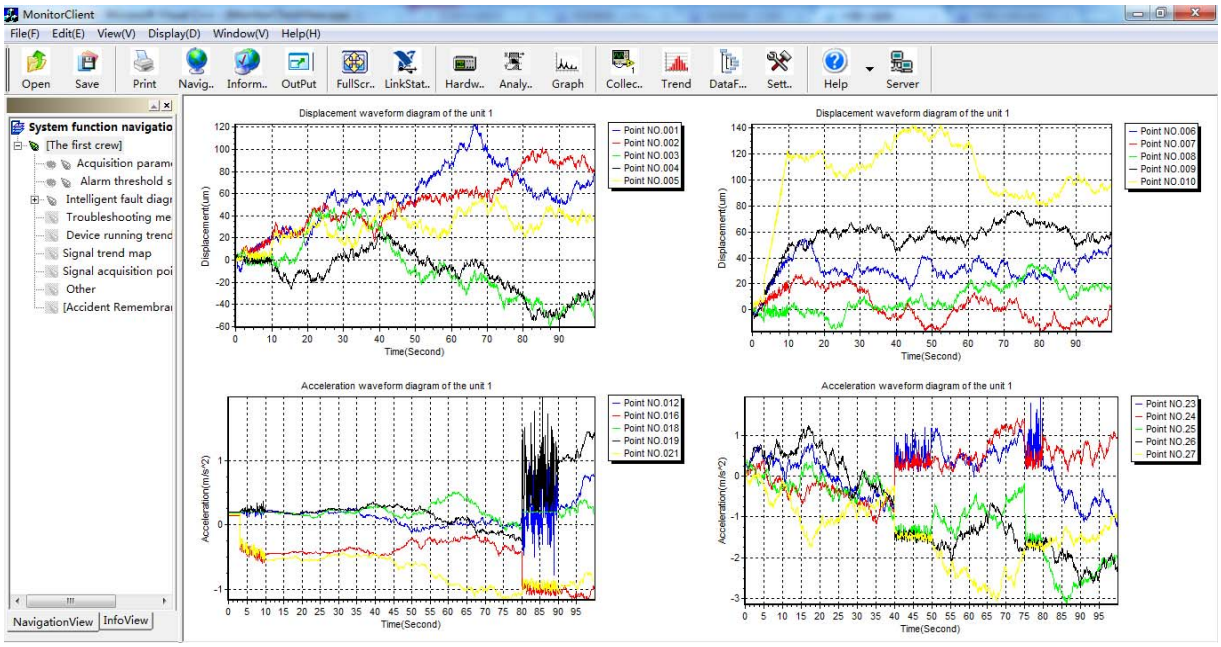

Fig. 10. Client monitoring interface.

5. Conclusions

This article by LabVIEW and VC communication, design a set of C/S mode multi-unit multi-points remote monitoring system. The system uses DataSocket, TCP and FTP communication to make the remote real-time data communication, information communication and file communication come true. It makes sure engineers and technicians to easily understand the operation of the various units. Once a device comes to failure, engineers and technicians can download the original data which acquired from the corresponding measuring points on the event of a failure from the server to carry out fault diagnosis. Clients can take full advantage of the server publishing feature data and raw data provided, and use a variety of knowledge and experience (including knowledge of the equipment and parts failure or failure mechanism, as well as the principle of the device structure, kinematics and dynamics design, manufacture, installation, operation, and maintenance of knowledge),to make identification and diagnosis of the state of the equipment and to make prediction and forecast of its development trends for providing the technical basis for troubleshooting and equipment maintenance decision. Continuously improving the equipment operation quality and state control level to make maintain the equipment high precision, high efficiency, low failure and low operation cost is of great significance to realize the equipment's life and cost optimization.

References

[1]. Hao Li, Zhao Wei, Logical relationship between MAX, DAQ assistant and DAQmx VI, *Research and Exploration in Laboratory*, 2012, 31 (6), pp. 82-85.

[2]. Wu Xiao, Development of Comprehensive Laboratory with Virtual Instrument, *Precise Manufacturing & Automation*, 2006, (1), pp. 27-31.

[3]. Yan Yan, Ma Zengqiang, Yang Ming, Programming Skill of Data Acquisition and Processing Based on LabVIEW, *Control & Automation*, 2005, (5), pp. 25-26.

[4]. Wang Peng, Pan Weijia, Qi Lijun, Database System for ST Vibration Monitoring and Fault Diagnosis Based on LabVIEW, *Power System Engineering*, 2008, 24 (1), pp. 63-64.

[5]. Ma Junxiu, Remote temperature measurement system based on virtual instrument technology, *Science & Technology Information*, 2011, 21, pp. 102-104.

[6]. Yang Yanli, Miao Changyun ,Wind power multi-unit remote monitoring based on multiple sampling rate, *Journal of Vibration Measurement & Diagnosis*, 2012, 32 (3), pp. 498-501.

[7]. David J. Kruglinski, Inside VC++, Beijing, *Tsinghua University Press*, 2009, 4.

[8]. Lei Zhenshan, Wei Li, Zhao Chenguang, Tang Xiaojiao, Advanced Programming based on LabVIEW and Engineering Applications of Virtual Instrument, Beijing, *China Railway Press*,2009. 5

[9]. Cui Bowen, Ren Zhang, Chen Jian, et al. Real-time fault detection of inverter-fed motor drive systems, *Electric Machines and Control*, 10, 1, 2006, pp. 52-56.

[10]. Chen Changzheng, Li Qing, Liu Yifang, et al., Intelligent fault diagnosis method for turbo-generator unit, in *Proceedings of the CSEEM*, 22, 5, 2002, pp. 121-124.

Sensors & Transducers, Vol. 21, Special Issue, May 2013, pp. 73-77

Sensors & Transducers

http://www.sensorsportal.com

Anti-fatigue Performance Analysis on Steel Crane Beam

Yuanmin Xie
College of Machinery and Automation,
Wuhan University of Science and Technology, Wuhan 430081, Hubei, China
Tel.: +86-027-68862283
E-mail: wustxie@126.com

Received: 31 March 2013 /Accepted: 14 May 2013 /Published: 30 May 2013

Abstract: Loads and working conditions of the trapezoidal cross-section of 36 m span crane beam can be analyzed by finite element method. Firstly, analysis of the stress and deformation is completed under the dangerous condition of crane beam based on the ANSYS software; secondly, find out the stress concentration and fatigue crack sensitive area of the bearing; finally, capture the position of fatigue crack. All these methods can provide strong basis for implementing effective monitoring to the state of the crane beam stress. Thus, ensure safe operation of equipment and improve equipment utilization rate in work. *Copyright © 2013 IFSA.*

Keywords: Fatigue cracks, Crane beam, Stress concentration, Finite element analysis.

1. Introduction

In recent years, the steel structure is widely used in industry and civil construction. Steel structure of crane beam is one of them which are used in industrial workshop electric hoist of wall or bridge supporting beam, wall cranes and other type of cranes. In industrial workshop, cross section of the crane beam is needed to be changed at joints as well as the production technology and economy requirements. So, designers can use a variety of ways that can be summarized up as: cross-section of the end trapezoidal, cross-section of the end Angle variable and cross-section of the end arc variable. Trapezoid transition of variable cross-section bearing is widely applied in engineering practice because of its relatively high anti-fatigue performance.

The stress of steel crane beam structure is complex; the repeated actions of vertical wheel crane pressure often does not meet the design stress, so fatigue crack happened at the parts. China has begun to pay attention to study the cause of the cracks, the prevention and control method since the 1990 s. But until now, someone haven't seen a effective measures to stop this kind of crack, the current specifications for design of steel structure in our country has not explicitly put forward to prevent the cracks of concrete calculation method and construction measures [1].

Now, more and more crane beam fatigue cracks of heavy duty welded steel have been discovered, especially more serious on large tonnage of heavy duty steel crane beam. Because the early cracks that is tiny and more hidden, often ignored by people. Dozens of crane beams cracking in the original rough rolling mill of a steel plant in 2003, feeding oblique beam fatigue cracking in iron in 2007. All of these caused by fatigue crack or damage, are directly or indirectly affect the safety in production. So the unit should census earnestly to deal with this kind of heavy duty welded steel crane beams, who find the problem and deal with as soon as possible to ensure the safe use of this important component. So in this paper, the variable cross section of the crane beam should be simulated to find out the static characteristics and fatigue performance by

application of finite element analysis software ANSYS, which can determine the trapezoidal variable cross-section stress concentration, produce the detection of cracks and establish an effective monitoring system. It can avoid unnecessary loss. The cracks often appear in the section of trapezoidal variable crane beam in actual engineering such as Fig. 1.

Fig. 1. The actual cracks of crane girder.

2. Overall Layout of Crane Beam

Crane beam is mainly composed of main girder and end beam, main beam and side beam is rigid connection, on both ends of the beam is equipped with wheel, in order to support bridge running on crane beam. Crane beam is generally designed as simply supported beam, whose characteristic is force clear, simple structure and convenient construction. The different column spacing in the workshop leads to the different heights of the adjacent crane beams. And to make the same column rail surface elevation at the same height, the crane beam is trapezoidal mutation type bearing, the beam end using the trapezoidal cross section.

Steel structure design specification [2, 3] is in accordance with the crane use status and level of work, divided the work level as 4 working system such as light, medium, weight and heavy duty. Crane design specification [4] and the crane load code divided crane work level into grade A1~A8. The crane beam span of this study is 36 meters, work level for the A7, namely the structure of heavy duty.

3. Finite Element Analysis

Finite element method [5] is a method of structural analysis; its basic idea is to disperse solving continuous area to unit assembly which is composed of a finite number of units connected together in a certain way to analyze. The current finite element software analysis function covers almost all engineering field; the use of the program is also very convenient. Currently, finite element analysis software which is widely used and very popular in Chinese engineering field contain: ANSYS, Abaqus, Marc and Algor etc.

Finite element equation principle: by the known element stiffness matrix and equivalent node load array assembled into the whole stiffness matrix of the whole structure and load array, assisted by a total stiffness matrix [K], total load vector {F} and integral nodal displacement vector $\{\delta\}$ showed balance equations.

$$[K]\{\delta\} = \{F\}, \tag{1}$$

The overall nodes displacement vector is obtained after introducing displacement boundary conditions. The finite element discrete equation is an algebraic system of equations, the symmetric stiffness matrix after introducing boundary conditions is a definite sparse equation, algebraic equations of such a can be solved by using a variety of methods.

ANSYS is one kind of engineering analysis software [6], mainly in the mechanical structure system by external load of reaction, such as displacement, temperature stress. The state of mechanical structure system can be got according to the reaction by external loads. General geometry of mechanical structure system is very complex; the load is considerable, so theory analysis often can not be conducted. In order to answer the analysis, the structure should first simplified by using the numerical simulation analysis method. Finite element software ANSYS has strong treatment before solving and post-processing function [7]. It has reliable calculation and high efficiency, and it also is a powerful tool in structural analysis. It is widely used in engineering, which can reduce the design cost and shorten the design time.

The calculation of crane girder structure was introduced by using the finite element analysis software ANSYS. The local stress state of the cross-section is investigated and the stress concentration position of variable cross-section is found, which can provide a theoretical basis for the establishment of monitoring system.

3.1. Load Analysis

The calculation load of the crane beam is shown in Fig. 2, including: vertical loads generated by the crane, transverse horizontal loads and longitudinal horizontal loads. The longitudinal horizontal load is along the direction of crane rail, which is supported by column crane beam. So it can be ignored when calculating. Transverse horizontal load is mainly composed of crane beam on the flange of the directly to the brake structure, relative to the vertical load, its effect on crane beam is smaller, for which the influence of the flange and its nearby area is much smaller than top flange and bearing variable

cross-section is generally close to the flange. Therefore, in order to simplify the calculation, only the vertical load on the web need considering.

Considering a variety of adverse conditions, the most dangerous situation of crane beam is when the bending moment is maximum. Then the crane is not located in the center of the crane beam, but located in the position shown in Fig. 3.

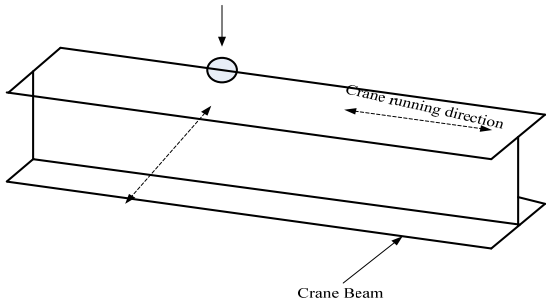

Fig. 2. Calculation load of the crane beam

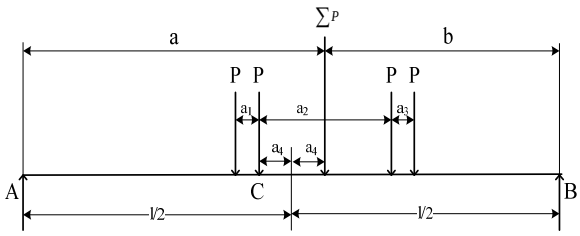

Fig. 3. The most dangerous situation.

Steel Design Manual pointed out the force of beam when four wheels act on the beam.

(1)The location of the maximum bending moment point (C):

$$a_4 = \frac{2a_2 + a_3 - a_1}{8}, \tag{2}$$

(2)The maximum bending moment:

$$M_{\max}^{c} = \frac{\sum p\left(\frac{l}{2} - a_4\right)^2}{l} - Pa_1, \tag{3}$$

where l is the span of crane girder, P is the wheel pressure which was distributed in the form of concentrated force, a is the distance from the application point of join forces to the A-side.

When $a_3 = a_1$, $a_4 = \frac{a_2}{4}$.

The maximum bending moment $M_{\max}^{c}$ is the same as the formula (3), while a_4 in the formula should be replaced by $\frac{a_2}{4}$.

The mechanical model should be loaded as the case shown in Fig. 4.

The length of the entire crane girder is 36 meters. When the bending moment is the maximum, the distance from application point of join forces to one end of crane girder is: $a = 19.275m, b = 16.725m$.

3.2. Material Setting and Modeling

The material setting of the crane beam is shown as Table 1.

Table 1. The material setting.

Material	Elastic Modulus (MPa)	Poisson Ratio	Density (t/mm^3)
Q235	2.1×10^5	0.3	7.85×10^{-9}

Steel crane beam is composed of web plate, flange plate, stiffener and many other small plates. It is very complicated if all parts are considering, and parts or less important small ribs can make the ANSYS calculation inaccurate even not able to be calculated. So it is necessary to make model simplified, the reasonableness of finite element model of the crane girder structure directly affects the accuracy of the finite element results. Therefore, in this paper, the finite element model of the crane girder is drawn by the three-dimensional mapping software of PROE, then change into IGES format and import into ANSYS. The selected units of PROE is mm/N/s, coordinate origin is fixed at the center of the bottom flange.

3.3. Load Case of the Crane Girder

(1) Meshing. The entire structure meshed by solid element (Solid 45). The meshed map of crane girder is shown as Fig. 4.

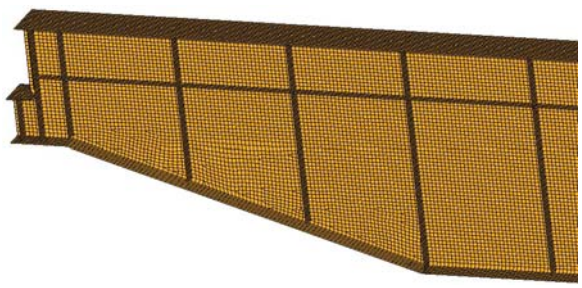

Fig. 4. The meshed map of crane girder.

(2) Constraint. Because the size of crane girder is large, the structure is complex, so it is simplified to simply supported beams. One side is fixed hinged bearing and the other is horizontal movable hinged bearing [8].

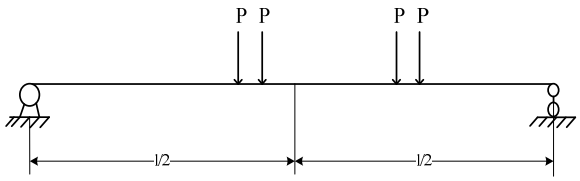

Fig. 5. Simplified as simply-supported beam.

(3) Loading. In static analysis, the weight of crane girder is not considered, only hanging wheel pressure is considered. So the calculated stress is the stress amplitude. There are four small wheels on each side, whose maximum wheel pressure is 272 KN. The wheel pressure distribution is shown as Fig. 6. The concentrated load of each wheel is evenly distributed to the corresponding nodes nearby, direction is vertically downward.

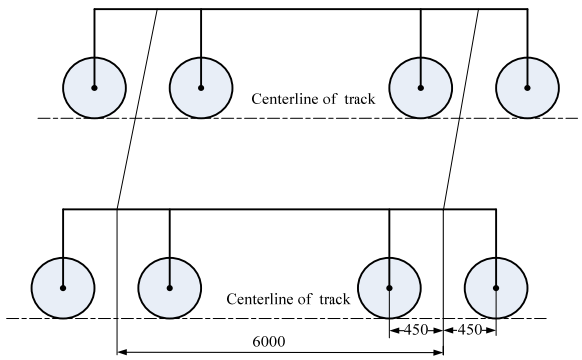

Fig. 6. The wheel pressure distribution

4. Calculation Results

Deformation of crane girder belongs to elastic deformation, using finite element method can calculate the stress and strain after loading. In order to reflect the characteristics of the crane beam more intuitively, the deformation of the vertical direction of the crane beam and Von Mises stress equivalent diagram are drawn out. Von Mises stress equivalent diagram of crane girder is shown in Fig. 7.

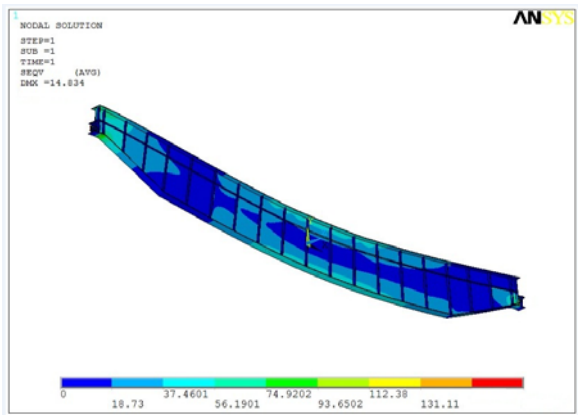

Fig. 7. Von Mises stress of crane girder.

Through finite element static analysis of 36 meters span crane girder structure with trapezoidal variable cross section, the following conclusions can be drawn:

When the crane beam is in the most dangerous conditions, the maximum vertical deflection of the crane beam is 14.834 mm (L/2427), while allowable value is 30 mm (L/1200); crane beam on the bottom flange is relatively weak because of the uneven distribution of crane beam stiffness, and the Von Mises stress is 55.163 MPa; the maximum Von Mises stress of variable cross-section is 119 MPa. The stress concentration phenomenon appears on variable cross-section of crane girder, because of residual stress due to the shrinkage of the weld, so crane girder easily fracture due to fatigue of variable cross-section.

The physical quantities of crane beam generated in the course of work are important test parameters of the monitoring system, such as stress, strain and others, which also can directly reflect working conditions. Determined by static analysis, the monitoring locations are the trapezoidal variable cross section and the middle of the bottom flange. The monitoring locations are shown in Fig. 8.

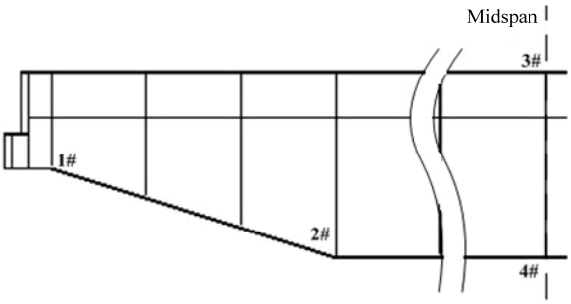

Fig. 8. The monitoring locations.

5. Conclusions

By static analysis of crane beam with trapezoidal variable cross section, the stress levels and performance indicators of the dangerous parts of crane beam are obtained. The welded crane girder destruction is mainly fatigue failure, and stress concentration is the main reason of fatigue failure [10]. The results show that stress concentration phenomenon appears on ladder variable cross section. Under repeated loads, fatigue crack appears easily. So the real-time monitoring of trapezoidal variable cross section is conducted to prevent fatigue failure. At the same time, the crane beam should be checked regularly in use process, which can contribute to find obvious deformation and steel plate cracking of the crane beam. These problems should be timely reported, and then take the necessary measures to avoid certain losses and damage.

In order to ensure the safe use of the crane girder with trapezoidal variable cross section, the real-time monitoring system is established by using advanced sensor technology, which can monitor the crane beam timely and effectively. Especially the trapezoidal variable cross section and the middle of the bottom flange are focal monitoring areas. Therefore, the flange and web connection strength should be strengthened in the process of design and manufacturing under, especially the welding quality of these parts, which can improve the fatigue life of crane beam, reduce the accident rate and promote safety production.

References

[1]. Y. Huang. Analysis and Treatment of Cracks of Steel Crane Beam, *Nanjing Science and Management,* Vol. 1, Issue 3, 2007, pp. 37-39.

[2]. B. F. Luo, M. Z. Wei, etc., Steel Structure Design Manual Beijing, *China Building Industry Press*, 1989, pp. 379-446.

[3]. Y. J. Wang etc., Steel Structure Design Manual (Third Edition), *China Building Industry Press*, Beijing, 2004, pp. 318-393.

[4]. Z. W. Zhang, H. Q. Yu, etc., the Manual Design of Crane, *China Railway Publishing House*, 1998.

[5]. Y. F. Hong, The Basic Principle and Application of Finite Element Method, *Higher Education Press*, 2010.

[6]. X. J. Gao, H. H Zhao, Brief Introduction to the Finite Element Analysis Software ANSYS, *Journal of Liaoning Shihua University*, Vol. 24, Issue 3, 2004, pp. 94-97.

[7]. Y. F. Ding, ANSYS12.0 Finite Element Analyses, Beijing, *Electronic Industry Press*, 2011.

[8]. J. Chen, Z. H. Lu, F. Xu, Q. X. He, Performance Analysis of the Arc and Right-Angle Type Mutation Bearing of Cross-Section Crane Beam, *Structural Engineer*, Vol. 26, Issue 1, 2010, pp. 22-26.

[9]. J. Dai, Three Kinds of Variable Cross-Section Crane Beam Analysis by Finite Element, *The Structure of the Steel*, Vol. 26, Issue 11, 2011, pp. 44-46.

[10]. G. J. Xia, The Reason for Web Cracking of Welded Crane Girder and Prevention Measures, *The Structure of the Steel*, Vol. 25, Issue 4, 2010, pp. 65-68.

.

Sensors & Transducers, Vol. 21, Special Issue, May 2013, pp. 78-84

Sensors & Transducers

http://www.sensorsportal.com

Application of Theory and Technology of Wireless Sensor Network System for Soil Environmental Monitoring

[1,2,3] Xu Xi, [3] Xiaoyao Xie, [4] Zhang Hai

[1.] School of Computer Science and Technology, Guizhou University, China
[2.] School of Information and Electrical Engineering,
Hunan University of Science and Technology, China
[3.] Key Laboratory of Information and Computing Science, Guizhou Normal University, China
[4.] Guizhou Transportation Research Institute Company, China
Tel.: +8618673330543, fax: +8618673330543
E-mail: xebox@sohu.com

Received: 10 April 2013 /Accepted: 14 May 2013 /Published: 30 May 2013

Abstract: With the environment problem increasingly high degree of attention, need for environmental data acquisition is also more and more, the emergence of wireless sensor networks to provide convenience for the study of random access to data, and can also avoid invasive traditional data collection methods for environmental damage. For example, researchers at Intel research laboratory had 32 small sensor is connected to the Internet, to read the main "great duck island" on climate, used to evaluate a sea Yanchao conditions. Migration of wireless sensor network can also keep track of birds and insects, effects of environmental change on crops, monitoring the ocean, atmosphere and soil components. In addition, it can also be used in precision agriculture, to monitor crop pests, soil pH and fertilization. In this article, according to the application demand of farmland environment monitoring, based on the composition and application conditions of wireless sensor network technology, we design a soil energy consumption monitoring system with the JN5121 wireless microprocessor as the core, which has the advantages of low cost, high stability, multiple functions function characteristics, and we have carried on the corresponding technical test, the results show that it can achieve effective environmental monitoring of soil in the monitored regional. *Copyright © 2013 IFSA.*

Keywords: Soil environmental monitoring system, Wireless sensor network, Theory, Technology, Application.

1. Introduction

Wireless sensor network technology has attracted more and more attentions of the researchers, and especially as a large agricultural country, its application in farmland soils has become an inevitable trend. In view the advantages of the wireless sensor, as well as the important significance of real-time monitoring of soil moisture and temperature, it is necessary to promote the rapid development of China's agriculture, and to develop a low cost, high stability, strong application farmland environment monitoring system based on wireless sensor network technology.

2. Composition and Application Conditions of Wireless Sensor Network System in Soil Environmental Monitoring

Compared with the traditional means of environmental monitoring, environmental monitoring has three significant advantages of using sensor networks: firstly, the sensor node is small in size and the whole network only needs to be deployed at a time, so the deployment of sensor networks has very small impact on the human environmental monitoring; secondly, the number sensor nodes are with large quantity and high density of the distribution, and each node can gather the detailed information of local environment detected the base station, so the sensor network is with the characteristics of large quantity of data collecting and high precision; third, the wireless sensor node itself has a certain degree of computing power and storage capacity, and it can conduct more complex monitoring according to changes in the physical environment, and the sensor node is also with wireless communication capability, which can carry out the cooperative control among the nodes.

2.1. Composition of Soil Environmental Monitoring System

Implementation of wireless sensor network technology function, is through a series of technical support of the routing, location, synchronization, security, network management, and energy saving. And on the soil environment, in view of the actual application value for monitoring soil, while the farmland soil has the following characteristics: 1. monitoring environment requires the knowing ability; 2. the soil needs plenty of sunlight, namely the solar energy resources; 3. the crop is with fixed growth cycle; 4. the monitoring environment will change according to the natural and human factors; 5. in farmland, the infrastructures with the scientific and technological content is less.

2.2. Application Conditions of Soil Environmental Monitoring System

In view of the above characteristics, the soil environment monitoring system can be divided into the two parts of wireless sensor network and remote data center. Between them, the remote data center functions are receiving, storage as well as the corresponding spatial analysis of relevant monitoring data, namely remote operation can be completed in the interior. While the wireless sensor network is installing a plurality of intelligent sensor nodes in the field, and the network formed by the connection of these nodes is wireless sensor network, which is responsible for the real-time acquisition of soil temperature, humidity, moisture and other data.

3. The Design of Wireless Sensor Network for Soil Environmental Monitoring System

According to the characteristics of the soil, the key to effective application of wireless sensor network to soil environmental monitoring, is to establish remote data transmission and effective data transmission of each node, namely to establish the Mesh network based on ZigBee wireless communication protocol, to ensure all the node data can go through the gateway node of routing transportation belt, then the data will be transmitted to the remote data center by a gateway node through GPRS wireless communication mode, in order to realize the real-time monitoring of soil for the remote data center, and in view of the consideration of saving energy and reducing consumption, all the monitoring nodes use solar power supply mode. According to the principle above, now the analysis of the design of wireless sensor network is as follows.

3.1. Design Requirements of Wireless Sensor Network

In view of the consideration of advantages and applicability of the application of wireless sensor network, in the design it should be mainly taken its economy and technicality two aspects into consideration: 1. The economy, soil environment is closely related to agricultural production, and given the agricultural income level is relatively low, so big cost of input is not practical, and we must reduce the cost, namely we should adopt products of relatively low prices in a variety of hardware and software related to the nodes of wireless sensor network, and for monitoring in the field, the objective conditions of large-scale power system generally does not exist, so we use the solar power, and use the common battery for standby power supply as the main way. 2. The technicality, on the basis of considering the economic cost, monitoring the effect is not affected, to ensure the accuracy of the corresponding data index monitoring for the system, namely under the premise of considering the cost, and in case of great influence of the environmental changes on the field monitoring data, to get the accuracy of the data as far as possible, of course, this process allows some error in it; Real-time characteristic of monitoring process, we must ensure that the information of each monitoring node can be instantaneously transmitted to the remote data center, so that the users can timely master the corresponding changes of indexes of soil of the monitoring area; The stability of the system, in addition to the corresponding maintenance and supervision of hardware and software of the remote data center, the key is to monitor every node module in the field, and to keep them in the normal work in the change range of soil environment, and these three aspects are also the basic demand of the wireless sensor network system.

3.2. Structure Design of Network Sensor Network

3.2.1. The Hardware Design

In this article, the sensor nodes adopted are on the basis of using the JN5125 wireless microprocessor module as the core component, and the communication interface, bus interface, power supply interface, and the sensor interface are with developed corresponding design. In view of the integrated features of the JN5125 module, which has 32 bits, 16MHz processor, and ADC input, DAC input, asynchronous serial port, SPI interface, hardware design reliable and effective to achieve system integration. Network structure design of the sensor node structure is shown as in Fig. 1.

In the picture below, the power supply adopts the solar power components for power supply, and it supports data acquisition of six sensors after extending, and the remote data center realize the corresponding receiver design and program downloading function through the serial port. For the sensor network data local storage, we use the USB interface storage mode, which has the advantages of large capacity, extensible and hot-swap. For the power input, the part of the power supply adopts the solar power, and because the gateway node is with large amount of energy consumption, we select the power of solar power components of 8 W, and also need for the corresponding hardware optimization, to reduce energy consumption.

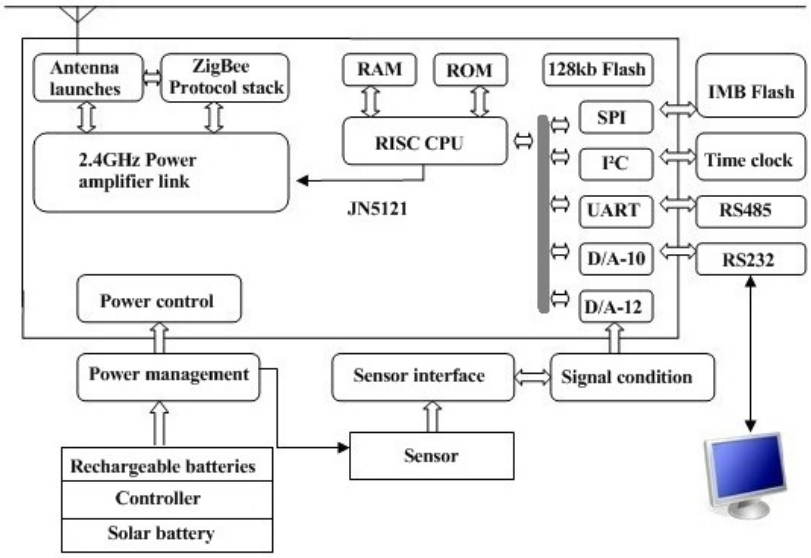

Fig. 1. The sensor nodes structure.

In addition, the sensor for the monitoring of soil moisture is through a flat frequency domain technique to collect the data of soil water mixture; Sensor for temperature monitoring is based on the principle of measurement of the semiconductor PN level, and the effective measuring range is between -20 °C - 50 °C, while the measuring accuracy is ± 0.5 °C. After completing of the design of the two kinds of soil environmental monitoring, the node of each sensor and the sensor interface of the corresponding control board can be connected, and then connected to the A/D channel in the JN5121 module through the corresponding signal adjustment, and then we can obtain the specific measurement parameter values of the corresponding soil moisture and temperature through the determination of the curve transformation. So, we complete the process of "sensor nodes collection in monitoring area, each node autonomously to form a wireless network, each node information gathered to the sink node or network coordinator, remote data center", so as to realize the real-time monitoring of the moisture and temperature of the soil in monitoring area.

It should be noted that, in the deployment of sensor nodes, it should ensure all sensors in the pre-planning monitored area, and forming multi-hop network in the self-organized way, and among them, the sink node may be artificially arranged, because the sink node has to handle many tasks, and is responsible for the activities of the whole wireless sensor network, and consumes more energy, so it needs artificial arrangement and adopts the artificial method to replace the battery if necessary. For ordinary nodes, because it is only responsible for the collection of soil environmental data, we do not have too much trouble, but the routing node is responsible for forwarding the data acquisition information of other nodes in addition to data collection, so it will transmit it to the sink node or network coordinator in the multi-hop way, so as to realize the purpose of transmitting the monitoring data of all the nodes in the whole region to the remote data center by long

distance link. In addition, the wireless sensor network adopts the topological structure, so even there is individual node failure of the application, the system can network again by changing the topological structure, which effectively improves the robustness of the system.

3.2.2. The Software Design

Compared with the hardware design, the software design of wireless sensor network is relatively simple, because it uses the mesh topology, and the JN5121 module embedded in the gateway node is the network monitoring coordinator under ZigBee protocol, while for the JN5121 module, its development company has introduced the software development platform and network stack, so in the system software design part, we only need to design the corresponding target, and input specific regulating parameters, and specific procedures are as follows: 1. After sensor nodes are deployed, the nodes start, and wait the command to join the wireless sensor network. 2. The gateway sends start commands to each sensor nodes in the network. 3. The node joins the network after receiving the start command, acquires the address information of the network, configures the local link address, and creates the routing. 4. The node collects data according to the data acquisition cycle set in advance, and transmits the data information in the form of data packets to the network coordinator (Gateway) and monitoring equipments.

According to the working process of the system, the brief work flow of the data transmission is shown as in Fig. 2.

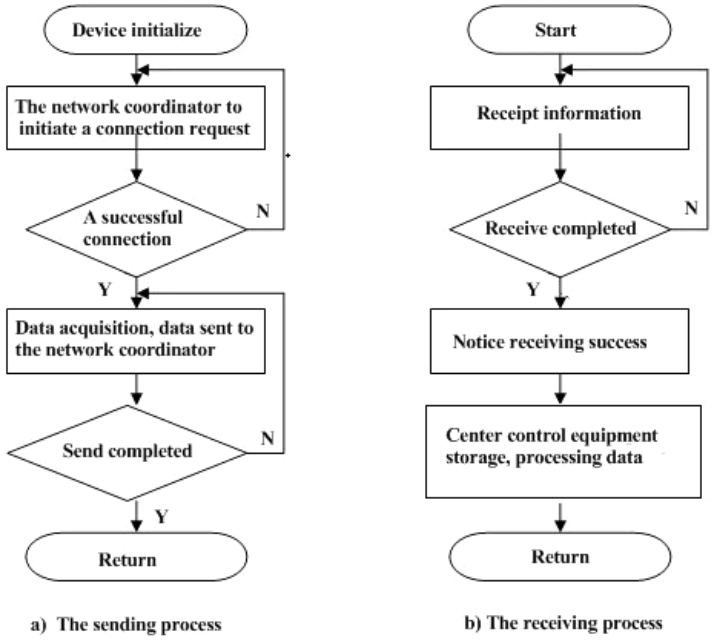

Fig. 2. Data transmission work flow.

3.2.3 GPRS remote Data Transmission

The communication module of Siemens MC35i is connected through another asynchronous serial port, and to realize GPRS remote data communication needs from bottom to top to complete the designs of the driving layer, protocol layer and the application layer. In the configuration of embedded Linux kernel, we select the equipments supporting the serial port to drive the MC35i module; The embedded Linux kernel supports the PPP (Pointto Point Protocol) protocol and TCP/IP protocol, and we select to support these options in compiling the Linux kernel; The application layer realizes the particular function of forwarding data to the remote data center after the network is connected.

3.3. Design of Wireless Sensor Network Node

3.3.1. The Sensor Node Design Principles

From the above known, sensor nodes generally can be divided into the network nodes and the sink nodes, which is the body to realize the sensing function of the wireless sensor network, and its position in the system is very important, and the nodes based on the sensor will receive limits of many conditions in practical application, therefore in the design, we must comply with the following principles. 1. The node needs low power consumption, and under normal circumstances, the nodes use disposable batteries, while in the application of wireless sensor network, because of a

number of nodes, and the broader regional distribution, and the current situation of more difficult for the artificial replacement battery operation, in the design of the sensor node, we must hold the pass of the power consumption, namely reducing the power consumption in the two aspects of hardware and software, and using the chip of low voltage and low power consumption as far as possible in the hardware, and correspondingly adding the power management function in the software, in order to effectively control the capacity allocation. 2. Optimization of the radio frequency performance, improving the radio frequency performance of the node can improve the network capacity, for example, under the same power consumption, if the distance is further, the practicability of the node will be stronger. 3. Nodes miniaturization, the node size should be small enough to ensure that it will not constitute influence on the target system itself, and it is simple and convenient in terms of the actual deployment. 4. The node should be low cost. As already stated above, if it costs a lot for the measurement of soil environment, then the study itself will lose some value, so as to make it widely used, we must control the number of nodes in the design, and the structure of the network topology should be simple and clear as the original intention, not too complex. 5. The node should have expandability. 6. The node should have expandability, namely using the modular design, and adding different function modules at any time according to different needs, such as connecting different types of sensor boards in different applications, or connecting other corresponding modules for other needs, or connecting the coprocessor through the general interface and so on. Of course, in addition, it needs to ensure the accurate transmission of data and safety of the transmission process, assuming the node likely to work in harsh environments, to ensure the stability of the node in the work.

3.3.2. Specific Design of the Sensor Nodes

We will design the sensor nodes in accordance with the wireless sensor node design principles above. From the above known, the sensor node is the basic unit of wireless sensor network, so the design is good or bad will directly affect the quality of whole network. The sensor node is the main unit of composing the soil moisture and temperature acquisition system, which besides in charge of collecting the information of the environment and processing the information, also needs to transfer other nodes to the gateway information and in the specific application environment, it also needs to cooperate with other nodes to complete certain tasks. Therefore, the stable operation of the sensor node is the basic guarantee for the reliability of the network. Generally, sensor nodes can be regarded as a miniature embedded system, whose processing power, storage capacity, as well as communication capability are relatively weak, and in different applications, the components of the sensor nodes are not the same, in terms of soil environmental monitoring in this article, which consists of the sensor module, processor module, wireless communication module, and the energy supply module four parts, and the diagram below is the structure of the sensor node.

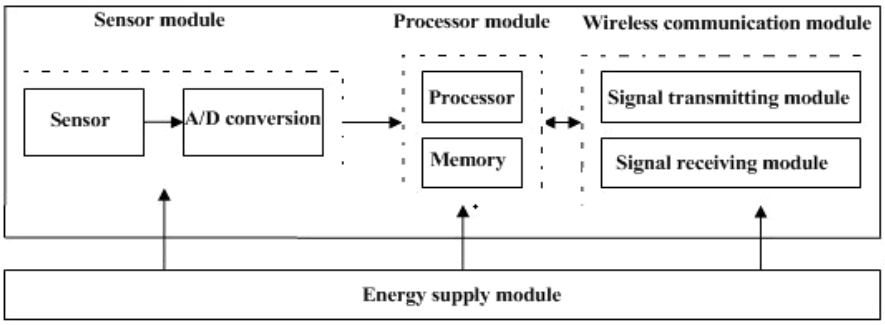

Fig. 3. Sensor nodes structure after specific design.

4. Technology Application of Wireless Sensor Networks

Application of wireless sensor network in the soil environmental monitoring system mainly includes the construction of development environment, data receiving, storage module selection, monitoring data analysis three aspects, and the concrete application steps are as follows.

4.1. Create the Development Environment

We choose the Microsoft Visual C++ 6 as the development tool for base station data management software, and use the database operation to achieve the node data storage and reading. In addition, for the effective implementation of real-time monitoring data in farmland soil, it integrates the function of geographical information system, which uses ArcGIS

Engine embedded component library of the ESRI Company. ArcEngine is composed of the ArcObjects core package, and it can call in various programming interfaces, and without the need to install the ArcGIS desktop platform. Compared with the traditional map control, on the basis of the drawing, data editing and the function of GIS, the ArcEnginec adds the space and 3D analysis and other advanced operation functions.

4.2. Data receiving and Storage Module Selection

4.2.1. The Function Module Selection

The C/S client server mode is used between the gateway node and the base station, based on Socket programming technique; it can listen to the bound ports of the local IP address, after confirming the connection request of the gateway node it will work on data receiving, reading and parsing.

4.2.2. The Data Storage Module Selection

According to the data acquisition time, and the corresponding period data storage divisions, the data after analysis will be stored in the corresponding table.

4.3. Analysis of Monitoring Data

4.3.1. The Time Change Analysis

After extracting the monitoring data from the database table, we use the time T as the abscissa axis, to draw the change curve of the monitoring data according to the time change, and then analyzes the characteristics of monitoring contents.

4.3.2. The Spatial Variation Analysis

The management and analysis functions of GIS are integrated into the design of wireless sensor network applications, and then through the ArcEngine spatial analysis module to realize spatial interpolation, and to obtain the spatial distribution of monitoring for any period. Then using the corresponding function algorithm can get the spatial variation of real-time monitoring data.

5. Wireless Sensor Network Communication Test

Because wireless sensor will appear the phenomenon of obvious path loss in transmission, it needs to verify whether the sensor node layout is reasonable, and we must carry on the distance transmission text on the JN5121 module. In view of the influence of the antenna height of the sending end and receiving end of on signal transmission, as well as the influence of the gradual growth of the crops on farmland soil environment, for example, if the general plant height of the wheat is 60 cm, in this farmland, the antenna height of 150 cm, then the effective transmission distance of low power module is only 50 meters, and high power module can only reach 150 meters, so in the arrangement of the wireless sensor networks, special attention should be paid to the following points. First of all, in the same area of farmland, if all it using are low power modules, it should be appropriate to raise the arrangement density of effective monitoring case. Secondly, if there are cover crops in the farmland, a node antenna should be designed suitable for raising the placing height, to reduce the signal transmission path loss. Finally, attention should be paid in the design of network topology, and each sensor node should communicate with more than two nodes in the effective communication range, to ensure that after the occurrence of a single link fault, it does not affect the normal monitoring of the entire network.

5. Conclusions

In the process of the design and implementation of wireless sensor network with JN5121 wireless microprocessor module as the core, not only the development cycle is short, but also it achieves the desired purpose of effectively reducing the economic cost, guaranteeing the system effective and steady operation, and it is a kind of soil environmental monitoring system worth widely popularizing. Of course, in the process of the practical application, it is believed that there will be a better and more optimized wireless sensor optimization network developed.

References

[1]. S. Qiao X. Q, Zhang X, Wang C. The application of wireless sensor networks in agriculture, *Journal of agricultural engineering, Vol. 21, Is*sue 2, 2005, pp. 55-58.

[2]. S. Li X. H, Huang T. C, Sun Z. F. Embedded environment monitoring system based on GPRS/SMS, *Journal of Jilin University: Engineering Science*, Vol. 37, Issue 6, 2007, pp. 23-26.

[3]. S. Zhu S. J, Nan Z. T. GIS software framework construction based on agriculture engineering, *Remote Sensing Technology and Application*, Vol. 25, Issue 4, 2006, pp. 49-52.

[4]. A. Theodore S. R, Principles and Applications of Wireless Communication (2nd edition), Zhou W. A, *Beijing Electric Industrial Publisher*, 2006.

[5]. S. Lu Z. Q, Huang M. C, Du Z, Liu F., Greenhouse planting temperature monitoring system based on

ZigBee wireless network, *Anhui Agricultural Science*, Vol. 48, Issue 13, 2008, pp. 13-16.

[6]. S. Peng Y, Wang J. X., Orchard environment wireless sensor network monitoring system, *Anhui Agricultural Sciences*, Vol. 50, Issue 09, 2010, pp. 44-48.

[7]. S. Wang X. C, Yan Y. Y, Liu J. G., Design of wireless meter reading terminal based on AVR MCU, *Journal of Changsha University*, Vol. 25, Issue 02, 2011, pp. 33-36.

[8]. S. Zou N, Han G. Y, Cao L., Application of ZigBee technology in the automatic detection of air power car, *Testing Technology*, Vol. 42, Issue 06, 2010, pp. 66-68.

Sensors & Transducers, Vol. 21, Special Issue, May 2013, pp. 85-88

Sensors & Transducers

http://www.sensorsportal.com

Influence Factors on Temperature Distribution of Electric Furnace Roof

Chongwu Lei, Guozhang Jiang, Gongfa Li, Jianyi Kong, Liangxi Xie, Zheng Li

College of Machinery and Automation, Wuhan University of Science and Technology, Wuhan 430081, P. R. China

Tel.: 13995696931

E-mail: haolei0725@163.com

Received: 1 April 2013 /Accepted: 14 May 2013 /Published: 30 May 2013

Abstract: Electric furnace roof is an important device for electric steel making, whose heat preservation performance and life-span have a direct impact on the economic benefits of iron and steel enterprise. This paper investigates the effect between the temperature level of electric furnace roof and the material parameters. Research indicates that they have a trend to change in the same direction. *Copyright © 2013 IFSA.*

Keywords: Electric furnace roof (EFR), Temperature field, Finite element method, Influence factors.

1. Introduction

EFR is an important part of the lining of electric arc furnace. The lifetime and insulation performance of EFR have a close relation with the production, quality, consumption, etc of steel. Domestic and foreign scholars had taken many measures to decrease its production cost and enhance its thermal stability. For instance, improving material, content of the alumina in brick, camber of bricklaying EFR, height between EFR center and molten pool surface, operation, using whole water cooling EFR. Although these measures had acquired certain effect, it failed to solve the problem that the difficulty of firebrick EFR's installation ,short service life, being unable to meet the requirement that the electric arc furnace is approaching to the large capacity and UHP ones and the great heat loss of whole water cooling EFR. So the installation time of EFR, heat insulation performance and service life become the main restrictive factors of steel plant benefit, which have important effects on the productivity and economic benefit of steel enterprises. So the measures to shorten the installation time of EFR and improve its service life are very important to reduce production cost and enhance competitiveness. Take the steel mill's 30t EFR as research projects. This paper studied the steady temperature field of high aluminum brick EFR and prefabricate block of EFR in typical operating condition and the influence law of EFR temperature field affected by material properties and the shape of prefabricate block. We try to compare the temperature level of high aluminum brick EFR and prefabricate block of EFR to provide theoretical support for scheme of prefabricate block of EFR.

2. Building the CAD Model of EFR

The high aluminum brick EFR is constructed by molding high aluminum brick. Prefabricate block of EFR is assembled from prefabricate blocks casted by refractory material according to fight blocks principle.

Although there is difference in manufacturing process, its shape and geometry size are the same. So in the process of model building, we build all the CAD model of EFR based on the real geometry size of 30t EFR of a steel mill (The 3D effect graph is shown in Fig. 1). On one hand, we take the structure of EFR and real situation in load into consideration, for another hand, we neglect the steps that are relatively small and don't influence the whole. The assumptions are as follows.

1) All the geometry models are built according to Fig. 1. All the models are completely built like that which include central cover and EFR. The main sizes are as follows. The diameter of feeding hole is 150 mm. The diameter of electrode hole is 250 mm. The diameter of circle where the center of the circle of electrode hole is 900 mm. The diameter of upper end face of central cover is 1730 mm. The diameter of lower end face is 1606 mm. The swing diameter of external end face of EFR is 3218 mm. The swing diameter of internal EFR is 3000 mm.

2) Because the fabrication process is different. High aluminum brick EFR is structurally one integrated mass. There is no interface in the internal EFR; prefabricate block EFR consist of many bulks, so there exist interface between prefabricate block EFR. In the process of building model, we take different Boolean operation. Namely, taking GLUE operation to the high aluminum brick EFR, bonding EFR and central roof for a whole, which guarantee that the node of physical interface coincide; for the prefabricate block EFR, according to the different number of prefabricate block, setting the VGEN command parameter to guarantee that there is interface between prefabricate block and take preparation for creating contact pair between prefabricate block. Meanwhile, taking that it is close from the bottom of EFR to molten steel and arc , circumferential expansion is larger than radial expansion when in thermal shock .Contact between prefabricate and central roof can be neglected, taking GLUE operation for prefabricate block and central roof, eliminating composition plane to guarantee the node of prefabricate block and central roof interface coincide. The two CAD models of EFR are shown in Fig. 2.

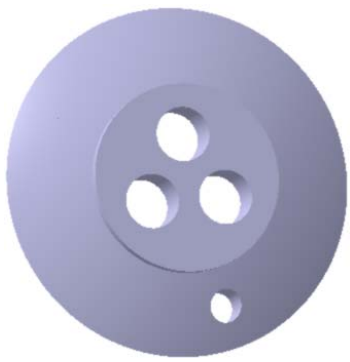

Fig. 1. Graph together of EFR.

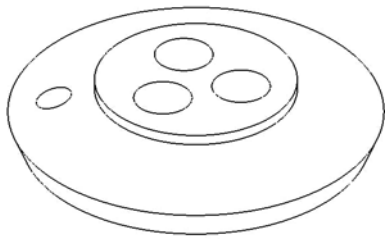

Fig. 2. CAD model of the whole high aluminum brick EFR.

After building CAD model, build the CAE model, it includes the definition the material parameters of EFR, selection of element type and control of mesh generation. High aluminum brick EFR and prefabricate block of EFR are made of refractory material in different production process. Its main ingredients are AL_2O_3. Definition of material properties in the finite element model is treated according to the same material. The finite element model of high aluminum brick EFR is shown in Fig. 3.

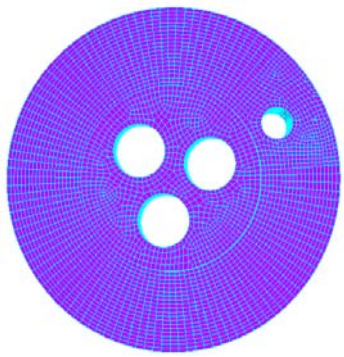

Fig. 3. CAE model of High aluminum brick EFR.

3. Temperature Field of EFR

After setting Loads and boundary conditions as the previously described, running LG.mac macro file, setting N value operation analysis to respectively obtain the calculation result file for each model. In order to display the temperature change of EFR on the cross section of the feeding hole, Cutting along the central symmetry plane using ANSYS working plane and draw the temperature contour section nephogram of high aluminum brick EFR and prefabricate block EFR. It is shown in Fig. 4. Because the final working plane origin is on the axis of the feeding hole in the CAD modeling, the Z axis is the height direction of the feeding hole, so the YZ plane is rotated by 90 degrees; meanwhile, the electrode hole are uniformly set in the circumferential direction of central roof, the amount of prefabricate blocks of EFR is different, the location ranges from feeding hole to electrode hole, the cross-section of the three electrode holes and feeding hole can't be shown simultaneously, therefore only one or two of the electrode hole can be shown.

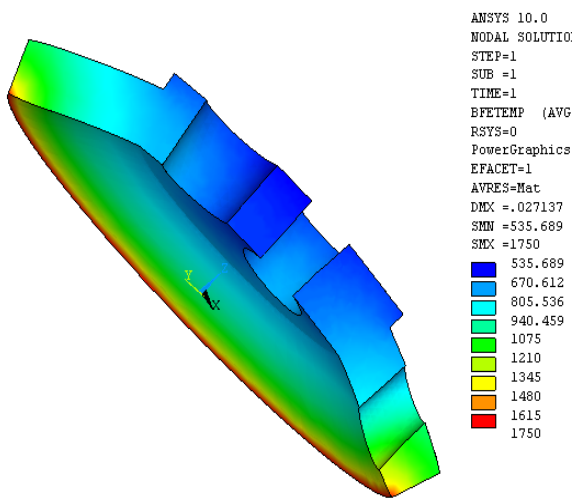

Fig. 4. Temperature contour section nephogram of the whole high aluminum brick EFR.

As can be seen from Fig. 4 in the melting end stage of the same working conditions, the central roof temperature distribution is between 535.689 °C - 670.612 °C, however, the temperature distribution of the most area of furnace roof is between 805.536 °C - 1210°C.

4. Analysis of Influence Factors on Temperature Field of EFR

By the physics knowledge, the material properties of the model will directly affect the value of the physical quantity. Aiming at EFR model of this article, the thermophysical properties parameters and the mechanical properties of EFR material will have a direct impact on EFR of the temperature and stress level; from the equivalent integral form of finite element theory foundation-differential equations, the geometry and structure of model directly affect the solving domain and boundary conditions, thus also affect the distribution law of physical quantities.

1) Material parameters of EFR.

EFR is all made by the high aluminum material in different manufacturing process, its finite element model only contains high aluminum material. Therefore the coefficient of thermal conductivity of the high aluminum material directly affect the heat conduction matrix of EFR model, thus it will affect the temperature field of EFR. For high aluminum brick, the percentage of raw material quota has been standardized by industry regulations. Once sintering and taken out of kiln, its physical parameters will be identified, so the temperature field of high aluminum brick roof can be considered immutable.

2) Structure of EFR.

Geometric relationships of EFR of the internal structure have a great impact on the temperature field, there exist high thermal resistance owing to the interface between the prefabricate block inside of the prefabricate block EFR, it hinders the heat transfer, so the temperature level of prefabricate block EFR is integrally low than the one of high aluminum EFR; meanwhile, the electrode hole pore size and its setting position, the feeding hole pore size and its layout position, the opening diameter of the EFR thickness and the thickness dimension will all affect the distribution of the temperature level of the EFR. circumferential size of EFR which is related to the production capacity of electric furnace has been standardized, it follows that the circumferential size of EFR is not allowed to change for the electric furnace of specific production capacity, the thickness dimension could be reduced and analyze its temperature and stress. We don't study in-depth aiming at the analytical purpose of this article, comparing to influence of material properties the structure size is relatively small.

Comprehensive consideration, the castable thermal conductivity of prefabricate block EFR has a greater impact on the temperature field. The physical meaning of thermal conductivity is for the unit thickness of the object having a unit temperature difference, within a unit time per unit area of heat conduction. Its magnitude is related to the material composition structure, density, moisture content, temperature and other factors.

When in analysis, despite the thermal conductivity of material parameters, the thermal conductivity is respectively set from the original 20 w/(mgK) to 10 w/(mgK), 40 w/(mgK). The loads and boundary conditions are all set in accordance with the previous. Running LG.mac, setting the KX values of 10 w/(mgK), 40 w/(mgK) in the main macro file running window, counting twice, then calculation result documents can be obtained when the thermal conductivity is 10 w/(mgK), 40 w/(mgK). As the structure, loads and boundary conditions of EFR don't change. So the changes of material parameters only affect the magnitude of the physical quantities. It will not affect the qualitative distribution law. The temperature counter maps are shown in Figs. 5-6.

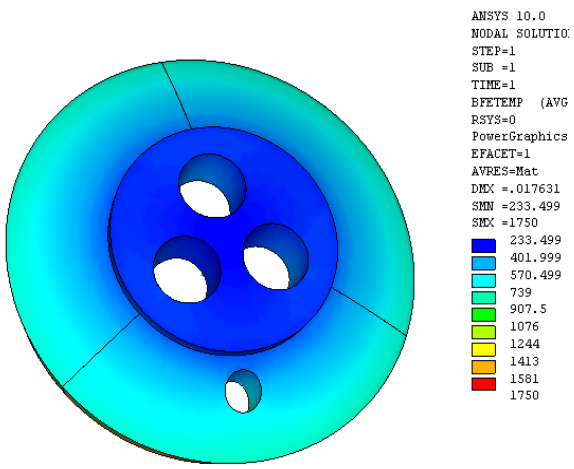

Fig. 5. Temperature contour map of EFR when thermal conductivity is 10 w/(mgK).

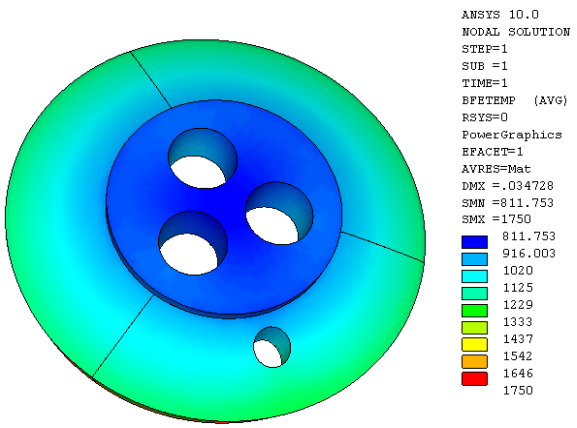

Fig. 6. Temperature contour map of EFR when thermal conductivity is 40 w/(mgK).

As can be seen from Fig. 5. We only change the thermal conductivity of casting material in case that other parameters and conditions remain unchanged, its value decrease from 20 w/(mgK) to 10 w/(mgK), the exine temperature of prefabricate block EFR is about 233.499°C. The temperature of the most EFR is 401.999 °C – 1076 °C; as can be seen from Fig. 6, when the thermal conductivity of casting material is 40 w/(mgK). The exine temperature of EFR rises which is about 811.753 °C. The temperature of the most EFR is 916.003 °C - 1333°C.

The change of thermal conductivity does not affect the law of temperature distribution, but it has a large impact on the temperature level of EFR. With the increase of thermal conductivity, the overall temperature level will increase, the heat absorbed by EFR increases, namely, the heat insulation performance of EFR will decline. Therefore, the temperature level of EFR changes in the same direction with thermal conductivity, however, there is a reverse change between the heat insulation performance of EFR and thermal conductivity. Above all, the temperature level of EFR increase with the increasing thermal conductivity, decrease with the decreasing thermal conductivity in the same direction variation; the heat insulation performance and service life of EFR show the reverse variation law into the thermal conductivity.

5. Conclusion

It studies that the influence of casting material thermal conductivity on temperature field of prefabricate block EFR. Studies have shown that the temperature level of EFR changes in the same direction with thermal conductivity. There is a reverse change between the heat insulation performance of EFR and thermal conductivity. Service life of EFR shows the reverse variation law into the thermal conductivity.

References

[1]. Hongxi Zhu, Chengji Deng, etc., Preparation and application of bauxite-based prefabricated block for electric furnace roof, *Steelmaking*, Vol. 24, Issue 2, 2008, pp. 50-58.

[2]. Guozhang Jiang, Jianyi Kong, Gongfa Li, etc., Research and application of thermo mechanical stress model for bottom working lining of 250~300 t ladle, *Steelmaking*, Vol. 24, Issue 2, 2008, pp. 22-25.

[3]. Gongfa Li, Peixin Qu, Jianyi Kong, etc., Influence of Working Lining Parameters on Temperature and Stress Field of Ladle, *Applied Mathematics & Information Sciences*, Vol. 7, Issue 2, 2013, pp. 439-448.

[4]. Gongfa Li, Jianyi Kong, Guozhang Jiang, etc., Stress Field of Ladle Composite Construction Body, *International Review on Computers and Software*, Vol. 7, Issue 2, 2012, pp. 420-425.

[5]. Guozhang Jiang, Jianyi Kong, Gongfa Li, Simulation research on influence of expansion joint of wall lining in ladle composite construction body on thermal stress, *Modern Manufacturing Engineering*, Vol. 10, 2010, pp. 85-88.

[6]. Guozhang Jiang, Jianyi Kong, Gongfa Li, Influence of working lining parameters on temperature field of ladle composite construction body, *Modern Manufacturing Engineering*, Vol. 12, 2010, pp. 77-80.

Sensors & Transducers, Vol. 21, Special Issue, May 2013, pp. 89-94

Sensors & Transducers

http://www.sensorsportal.com

Finite Element Analysis on Crane Girder with Variable Cross Sections Based on ANSYS

Dan Meng, Gongfa Li, Dawei Tan, Shulin Yang
College of Machinery and Automation,
Wuhan University of Science and Technology, Wuhan 430081, Hubei, China
Tel.: 15671676471
E-mail: mengdan1023@163.com

Received: 20 March 2013 /Accepted: 14 May 2013 /Published: 30 May 2013

Abstract: To the 36 meters crane girder with trapezoidal variable cross-section in a steel plant, finite element model is established reasonably according its actual size. The calculation of crane girder structure was introduced by using the finite element analysis software ANSYS. The local stress state of the cross-section is investigated and the stress concentration position of variable cross-section is found, which can provide a theoretical basis for the establishment of monitoring system. At the same time, the former 6 natural frequencies and the corresponding vibration patterns of the crane beam are extracted in modal analysis of crane girder, which is to provide a basis and reference for the structure design of crane girder. *Copyright © 2013 IFSA.*

Keywords: Crane girder, Finite element analysis, Trapezoidal cross-section, ANSYS.

1. Introduction

Steel crane girder is a member which supports various types of cranes in factory buildings. Due to the complexity of crane girder stress, the metal structure of crane is easy to discover crack, propagation, and sudden rupture under cycles of alternating loads. Especially crane girder with trapezoidal variable cross-section, due to the poor fatigue resistance of the mutation of cross-section, fatigue fracture appears frequently in the practical engineering which results in reduced reliability and security of the crane beam as well as the increase of service life.

In recent years, the situation of fracture of crane beam caused by fatigue often appears in a steel mill. Such as dozens root crane beam cracking in the steel billet library of original rough rolling mill in 2003, crane girder at the top of the platform in iron making plant cracking because of fatigue in 2007, main span 22 # crane beam in iron making plant cracking suddenly in 2011.All of these are directly or indirectly affect the safety in production caused by fatigue crack or damage. Therefore, the stress test and modal analysis of the crane beam which has long service cycles and use of high frequency has important practical significance.

If the crane girder with trapezoidal variable cross section is calculated by using the traditional mechanical calculation method, the relevant parameters should be estimated and simplified, and then inaccurate calculation result is reflected. To this end, the static characteristics and the dynamic characteristics of the crane girder are simulated by using the finite element analysis software of ANSYS [1]. Through analytical data, the state of deformation and stress distribution of crane girder is researched, the stress concentration position of variable cross-section is found, the distribution of bending

rigidity and torsional rigidity of crane girder is determined. The comparative analysis of analytical data and field results is performed, which can provide a theoretical basis for the establishment of monitoring system and maintenance and reinforcement of the crane girder. Finally, the rate of accidents can be reduced and the safe production can be promoted. 36 meters span crane girder structure with trapezoidal variable cross-section is shown as Fig. 1.

Fig. 1. Crane girder structure with trapezoidal variable cross-section.

2. Static Analysis of the Crane Girder

2.1. Establish the Model of Crane Girder

The reasonableness of finite element model of the crane girder structure directly affects the accuracy of the finite element results. Therefore, in this paper, the finite element model of the crane girder is drawn by the three-dimensional mapping software of PROE, then change into IGES format and import into ANSYS. The selected units of PROE is mm/N/s, coordinate origin is fixed at the center of the bottom flange. The material of crane girder is Q235, isotropic material, the elastic modulus E = 2.1E5 MPa, Poisson ratio $\mu = 0.3$, density $\rho = 7.8E\text{-}9$ t/mm^3. The entire structure meshed by solid element (Solid 45). The schematic plan and the three-dimensional model of crane girder in PROE are shown as Fig. 2 and Fig. 3. The meshed map of crane girder is shown as Fig. 4.

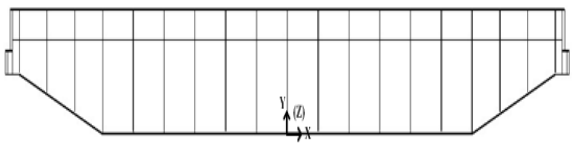

Fig. 2. The schematic plan of crane girder.

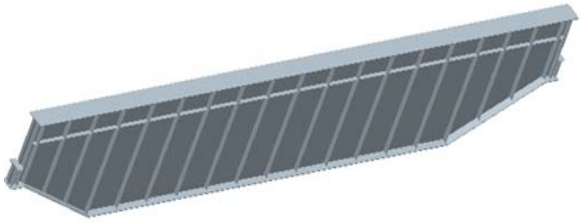

Fig. 3. The three-dimensional model of crane girder in PROE.

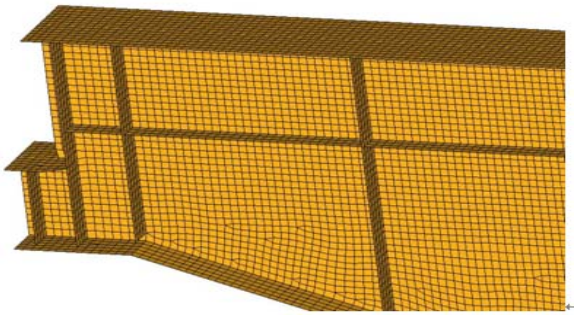

Fig. 4. The meshed map of crane girder.

2.2. Load Case of the Crane Girder

Because the size of crane girder is large, the structure is complex, so it is simplified to simply supported beams. One side is fixed hinged bearing and the other is horizontal movable hinged bearing [2]. In static analysis, the weight of crane girder is not considered, only hanging wheel pressure is considered. So the calculated stress is the stress amplitude. The working-level of crane is A7, there are four small wheels on each side, whose maximum wheel pressure is 272KN. The wheel pressure distribution is shown as Fig. 5.

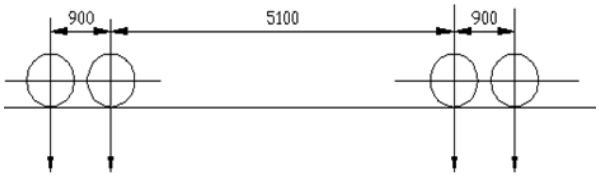

Fig. 5. The wheel pressure distribution.

Because the wheel pressure which acts on the beam is dynamic loads, the most unfavorable load position of the crane girder should be pointed, which produce maximum bending moment. According to the crane running and Steel Design Manual [3]: when the bending moment is maximum, the crane is not located in the center of the crane beam, but located in the position shown in Fig. 6.

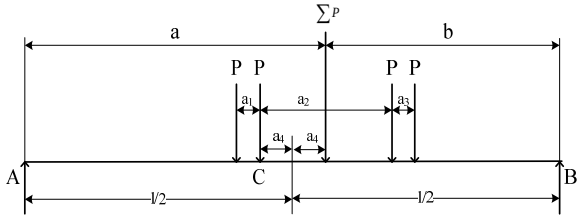

Fig. 6. The location of crane when the bending moment is the maximum.

Steel Design Manual [4] pointed out the force of beam when four wheels act on the beam.

1) The location of the maximum bending moment point (C):

$$a_4 = \frac{2a_2 + a_3 - a_1}{8}, \tag{1}$$

2) The maximum bending moment:

$$M_{\max}^{c} = \frac{\sum p\left(\frac{l}{2} - a_4\right)^2}{l} - Pa_1, \tag{2}$$

3) Radiation formula:

$$V^{c} = \frac{\sum p\left(\frac{l}{2} - a_4\right)}{l} - P, \tag{3}$$

where l is the span of crane girder, P is the wheel pressure which was distributed in the form of concentrated force, a is the distance from the application point of join forces to the A-side.

When $a_3 = a_1$, $a_4 = \frac{a_2}{4}$.

The maximum bending moment $M_{\max}^{c}$ and its corresponding shear V^{c} are all the same as the formula (2) and formula (3), while a_4 in the formula should be replaced by $\frac{a_2}{4}$.

The mechanical model should be loaded as the case shown in Fig. 6.

The length of the entire crane girder is 36 meters. When the bending moment is the maximum, the distance from application point of join forces to one end of crane girder is: $a = 19.275m, b = 16.725m$.

2.3. Calculation Results and Analysis of the Static Characteristics

Deformation of crane girder belongs to elastic deformation, using finite element method can calculate the stress and strain after loading. The finite element analysis software of ANSYS has powerful pretreatment, solving and post-processing functions. It has reliable calculation, high efficiency, and is a powerful tool in structural analysis [5]. The deformation of the vertical direction of the crane beam is shown in Fig. 7, Von Mises stress equivalent diagram of variable cross-section is shown in Fig. 8, and Von Mises stress contours of variable cross-section is shown in Fig. 9.

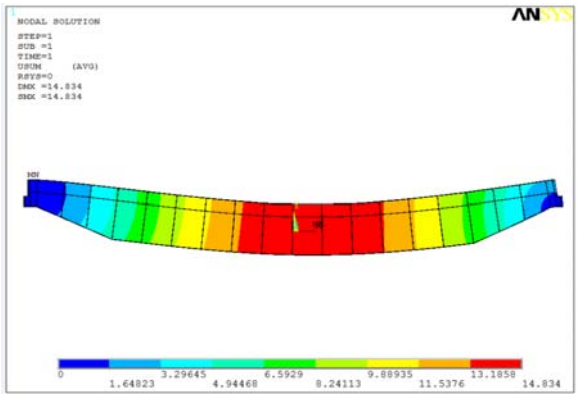

Fig. 7. The deformation of the vertical direction.

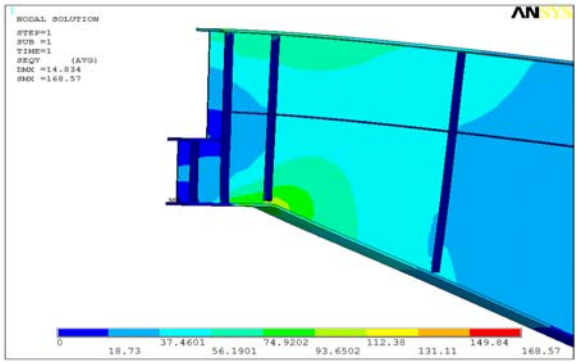

Fig. 8. Von Mises stress equivalent diagram of variable cross-section.

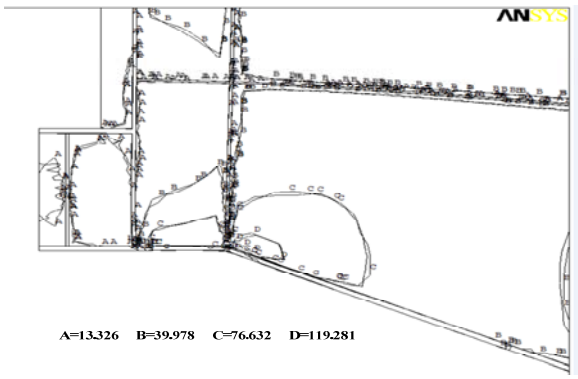

Fig. 9. Von Mises stress contours of variable cross-section.

When the crane is located in the position shown in Fig. 6, the maximum vertical deflection of the

crane beam is 14.834 mm (L/2427), while allowable value is 30 mm (L/1200); and the maximum Von Mises stress of variable cross-section is 119 MPa. The stress concentration phenomenon appears on variable cross-section of crane girder, so crane girder easily fracture due to fatigue of variable cross-section. Under the effect of dynamic loads of the crane whose working-level is A7, crack of trapezoidal variable cross-section is generated. The crack is the same as the judgment of calculation result. The actual crack of trapezoidal variable cross-section crane girder is shown in Fig. 10.

Fig. 10. The actual cracks of trapezoidal variable cross-section crane girder.

3. Modal Analysis of the Crane Girder

3.1. The Theory of Modal Analysis

Finite element modal analysis is the progress to establish the modal model and conduct numerical analysis [7]. For the general structure system with multi degree of freedom, any movement can be synthesized by its free vibration modal. For one linear system with multi degree of freedom, the vibration equation can be represented as:

$$M\ddot{u}(t) + C\dot{u}(t) + Ku(t) = P(t), \quad (4)$$

where M is the mass matrix; C is the damping matrix; K is the stiffness matrix; they are all n order square. $\ddot{u}(t)$ is the acceleration vector; $\dot{u}(t)$ is the velocity vector; $u(t)$ is the displacement vector; $P(t)$ is the dynamic load vector.

The essence of the modal analysis is to solve the modal vector of motion equation with a finite number of degrees of freedom without external load. Structural damping can be ignored, the effect of it on its modal frequencies and mode shapes is small [8]. In the process of modal analysis, undamped free vibration equation is:

$$M\ddot{u}(t) + Ku(t) = 0, \quad (5)$$

ANSYS offers six modal extraction methods [9], the Block Lanczos method is selected to conduct modal analysis [9]. Block Lanczos method is the acquiescent solution method of ANSYS, it uses the Lanczos algorithm, which realizes recursive algorithm by a set of vectors. Its characteristic is that using sparse matrix equation solver which turns n*n order matrix by similar transformation into three diagonal matrix to get characteristic value. It is also with less input parameters, faster convergence speed and higher accuracy of characteristic value and characteristic vector solution. It is suitable for solving the problem of large symmetric matrix [10].

3.2. Calculation Results of Modal Analysis

In order to understand the dynamic characteristics of crane girder, natural frequencies and mode shapes, modal analysis of the crane girder is carried out. In modal analysis, unit types and constraints loaded remains the same as parameters of static stress analysis. As crane beam is low-frequency vibration structure, engineering value in use is several previous order nature frequencies. The 1st to 6th vibration modes are extracted in modal analysis of crane girder, and the results are shown as Table 1.

Table 1. The modal results of the top 6 steps.

SET	1	2	3	4	5	6
FREQ(HZ)	1.50	3.28	4.29	7.35	8.43	10.51

The vibration diagrams of 1st to 6th are shown as Fig. 11.

Known by the calculation results, because of the uneven distribution of crane beam stiffness, crane beam on the bottom flange is relatively weak. When the excitation frequency reaches its natural frequency, it produces resonance and cause jitter. However, within the scope of our analysis, the mode vibration deformation amount of crane beam is very small, and general resonance frequency is relatively high, so resonance is not produced, it is always consistent with requirements.

4. Conclusions

The results of the static analysis of crane beam show that stress concentration phenomenon appears on ladder variable cross-section. Under repeated loads, fatigue crack appears easily and the calculation result is consistent with the actual working condition. So the crane beam should be checked regularly in use process, which can contribute to find obvious deformation and steel plate cracking of the crane beam. These problems should be timely reported, and then take the necessary measures to avoid certain losses and damage.

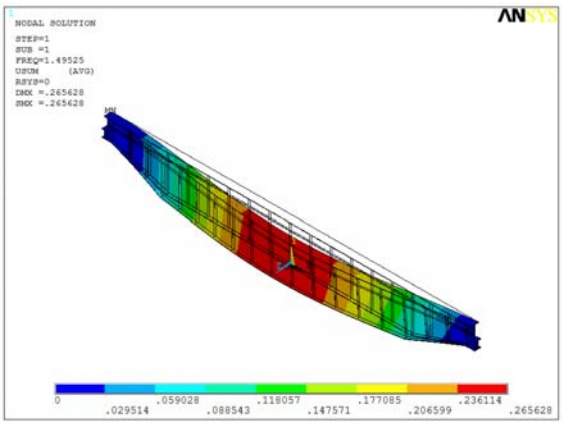

(a) The 1st vibration mode.

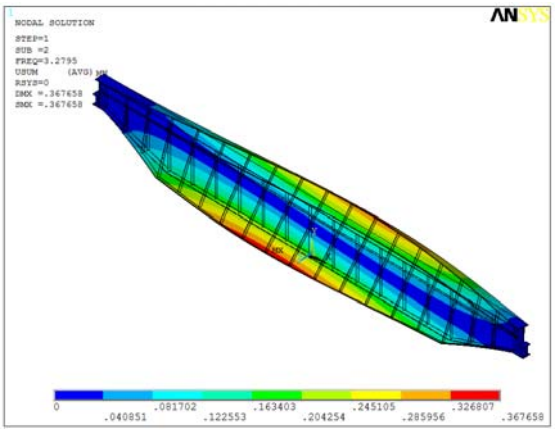

(b) The 2nd vibration mode.

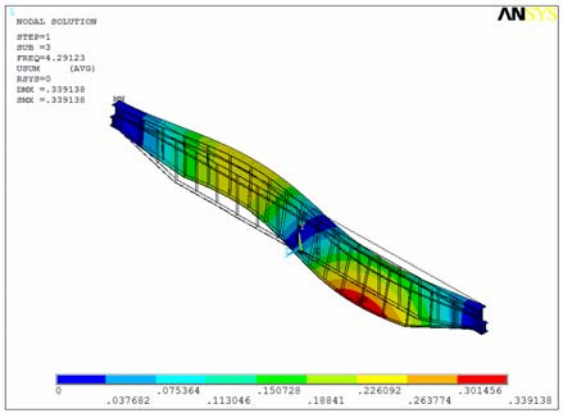

(c) The 3rd vibration mode.

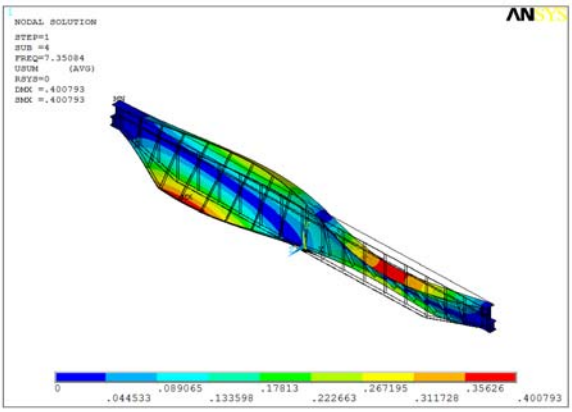

(d) The 4th vibration mode.

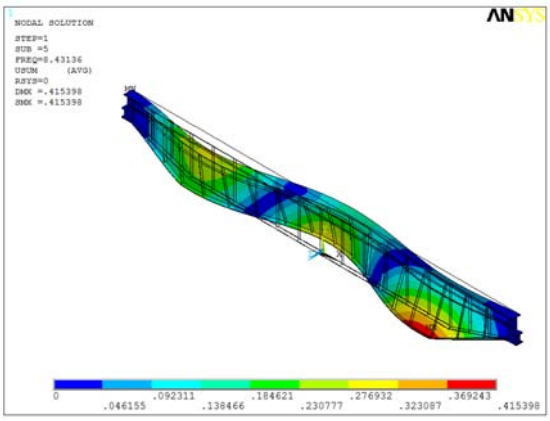

(e) The 5th vibration mode.

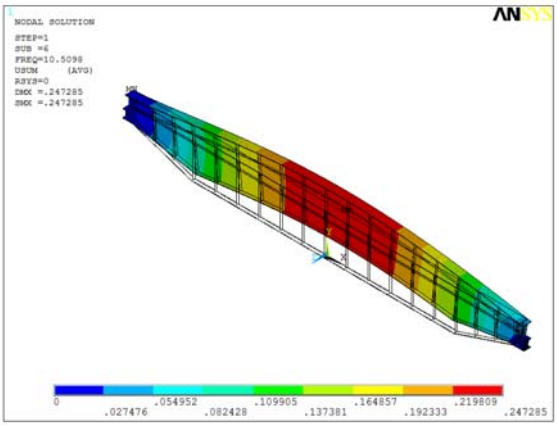

(f) The 6th vibration mode.

Fig. 11. The vibration cloud modes of 1st to 6th.

Through modal analysis of the crane beam, the distribution of bending rigidity and torsional rigidity of crane beam can be determined. In order to ensure the safe use of trapezoidal cross-section of crane beam, the flange and web connection strength should be strengthened in the process of design and manufacturing under, especially the welding quality of these parts. At the same time, special attention should be paid to the working conditions of these areas in the daily maintenance of crane beam, especially to the detection of weld, which can improve the fatigue life of crane beam, reduce the accident rate and promote safety production.

References

[1]. H. S. Xu, ANSYS Application in Construction Projects, *Machinery Industry Press*, Beijing, 2005.

[2]. J. Chen, Z. H. Lu, F. Xu, Q. X. He., Performance Analysis of the Arc and Right-Angle Type Mutation

Bearing of Cross-Section Crane Beam, *Structural Engineer,* Vol. 26, Issue 1, 2010, pp. 22-26.
[3]. Y. J. Wang, Steel Structure Design Manual (Third Edition), *China Building Industry Press*, Beijing, 2004.
[4]. B. F . Luo, M. Z. Wei, Steel Structure Design Manual Beijing, *China Building Industry Press*, 1989.
[5]. H. M. Wang, Z. S. Liu, Dynamic Characteristics Analysis of the Four Hot Mill Rack, *Journal of Hefei University of Technology,* Vol. 32, Issue 3, 2009, pp. 40-45.
[6]. Y. F. Ding, ANSYS12.0 Finite Element Analyses, *Electronic Industry Press*, Beijing, 2011.
[7]. Y. Y. Cao, D. F. Zhao, Analysis Theory and Its Application of the Finite Element Modal, *Mechanical Engineering & Automation,* Vol. 1, Issue 1, 2007, pp. 352-354.
[8]. A. F. Yuan, J. Chen, The Application of Modal Analysis in ANSYS, *Manufacturing Technology & Machine Tool,* Vol. 1, Issue 8, 2007, pp. 102-105.
[9]. K. Chen, Modal Analysis of PCR-80 Cold Rolling Machine and Multiple Objective Optimization of Total Machine Rigidity, *Journal of Hefei University of Technology,* Vol. 1, Issue 1, 2005, pp. 26-27.
[10]. H. L. Jia, P. F. Du, X. P Ren, Modal Analysis of Crane Beam Structure Based on the ANSYS, *Industrial Buildings,* Vol. 40, 2010, pp. 406-408.

Sensors & Transducers, Vol. 21, Special Issue, May 2013, pp. 95-99

Sensors & Transducers

http://www.sensorsportal.com

Research on Temperature Distribution Model of Electric Furnace Roof

Zheng Li, Guozhang Jiang, Gongfa Li, Jiangyi Kong, Liangxi Xie, Chongwu Lei

College of Machinery and Automation, Wuhan University of Science and Technology,
Wuhan 430081, Hubei, China
Tel.: +86-027-68862283
E-mail: 626106183 @qq.com

Received: 30 March 2013 /Accepted: 14 May 2013 /Published: 30 May 2013

Abstract: Electric furnace roof is an important device for electric steel making, whose heat preservation performance and life-span have a direct impact on the economic benefits of iron and steel enterprise. Considered contact behavior between prefabricate block, this paper establishes the complete CAD/CAE model of the electric furnace roof with finite element software based on the theory of transferring heating subject, and respectively calculates the stable temperature and stress field of the firebrick roof and the prefabricate block roof in last melting stage, as is advantageous to analyze the level and the distribution of temperature and stress of electric furnace roof. *Copyright © 2013 IFSA.*

Keywords: Electric furnace roof, Temperature field, Finite element method, Distribution model.

1. Introduction

Electric furnace roof is an important component of the electric furnace lining, whose heat preservation performance and life-span have a close relationship with the productivity, quality, consumption and many other technical-economic indicators of steel. Many scholars, at home or abroad, have adopted various of measures on the furnace roof to lower production costs and enhance its heat preservation performance, such as improving the material, increasing alumina content of the brick, increasing camber of furnace roof and the height between center of furnace roof and weld pool surface, improving operation, adopting full water cooling furnace roof, etc. These measures do have some effect, but they do not really solve many problems. It is hard to install refractory brick furnace roof. Service life of furnace roof is too short. The develop trends of larger capacitance and high power density of furnace roof cannot be satisfied. Full water cooling technology produces too much heat loss. So the installation period of electric furnace roof, heat preservation ability and the life-span main become the main reasons that restrict the benefit of steel enterprise, which make great influence on its productivity and economic benefit. As the result, the measures that shorten the installation period of furnace roof and raise the life-span are significant for electric steel making technology to reduce production costs and improve its competitiveness.

Electric furnace roof is an important device for electric steel making, whose heat preservation performance and life-span have a direct impact on the economic benefits of iron and steel enterprise. Considered the disadvantages of firebrick roof like

its short life-span, bad thermal stability and difficult installing, the prefabricate block roof is made. This paper establishes the CAD/CAE model of the two furnace roofs based on a 30t electric furnace roof real model of a steel factory, simulates the temperature and stress field of the firebrick roof and the prefabricate block roof with ANSYS.

2. Modeling

The firebrick roof is made with high alumina bricks. The prefabricate block roof is assembled with prefabricate blocks casted by refractory material like building toy blocks together. Although they are manufactured with different methods, their appearance and geometrical dimension are identical. So all furnace roof CAD models can be built according to the real geometrical dimensions of a 30 t furnace roof from a steel factory. The main dimensions are below: the diameter of the charging hole is 150 mm, the diameter of the electrode hole is 250 mm, the diameter of the circle that with the center of the electrode hole on is 90 mm, the diameter of the upper end face of the center roof is 1730 mm, the diameter of its lower end face is 1606 mm, the diameter of the external end face circle is 3218 mm, the diameter of the inner end face circle is 3000 mm. Because of the effect of the geometrical dimensions, it is not operable to cast the whole furnace roof. This paper only establishes the CAD model of the firebrick roof and three kinds of prefabricate roof casted by different pans.

The CAD models of the two furnace roof are established in Fig. 2-5.

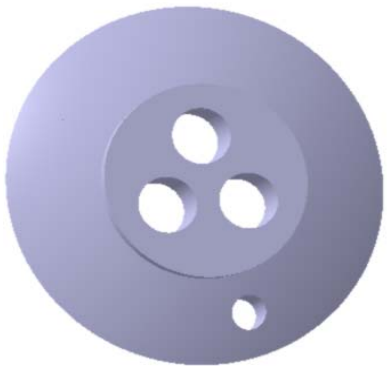

Fig. 1. Electric furnace roof model.

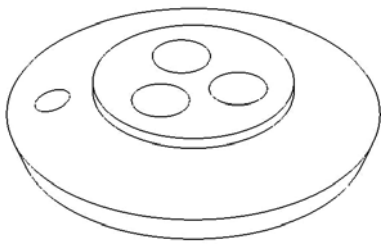

Fig. 2. Firebrick roof CAD model.

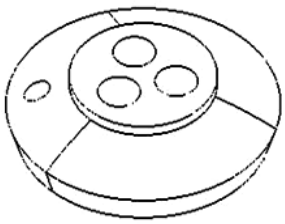

Fig. 3. Prefabricate block roof model (3 blocks).

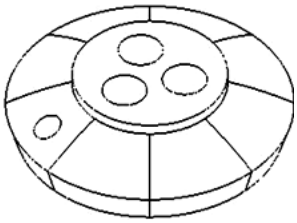

Fig. 4. Prefabricate block roof model (8 blocks).

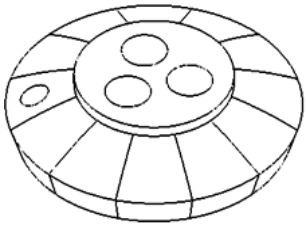

Fig. 5. Prefabricate block roof model (12 blocks).

To do thermal analysis with ANASY, the CAD model should be built firstly, then establish the finite element model. After building the CAD model, the CAE model should be established mainly including the definition of the material of the electrical furnace roof, the choice of the type of analytic elements and the control of mesh dividing.

The finite element model of firebrick roof is established in Fig. 6 and the model of prefabricate roof is the shadow zone of Fig. 6. The number of the elements and nodal points are in Table 1, and prefabricate roof model contains contract elements.

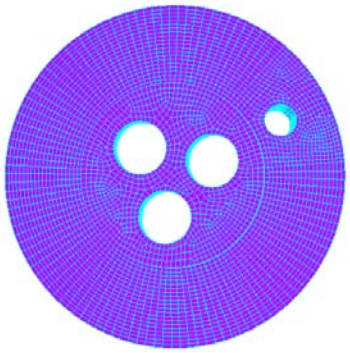

Fig. 6. Firebrick roof CAE model.

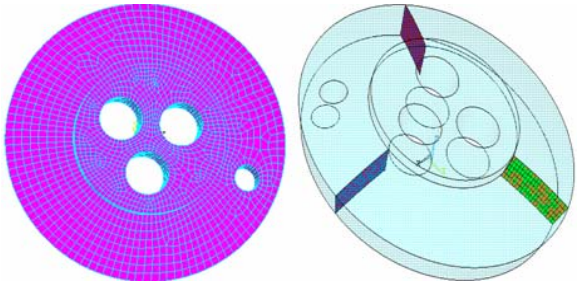

(a) (b)

Fig. 7. Prefabricate block roof CAE model (3 blocks) and its contract pairs.

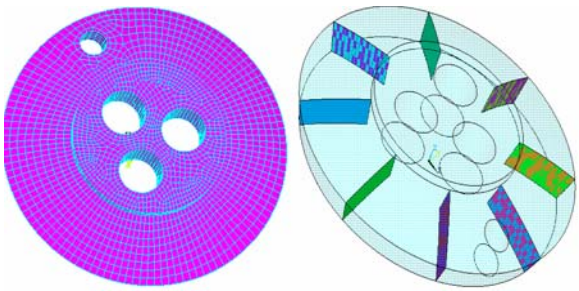

(a) (b)

Fig. 8. Prefabricate block roof CAE model (8 blocks) and its contract pairs.

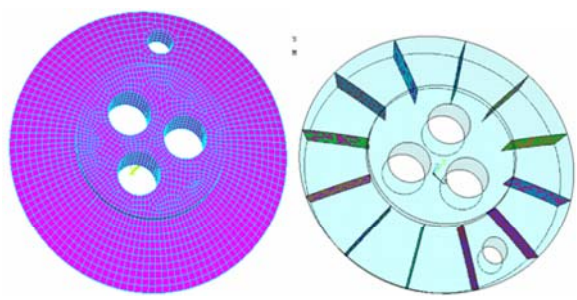

(a) (b)

Fig. 9. Prefabricate block roof CAE model (12 blocks) and its contract pairs.

Table 1. The ACE parameters of the furnace roofs.

Part	Firebrick roof	Prefabricate block roof (3 blocks)	Prefabricate block roof (8 blocks)	Prefabricate block roof (12blocks)
Center roof	535.68~ 670.612	480.874~ 621.888	488.592~ 628.748	479.145~ 620.351
Furnace Roof	670.612 ~1210	621.888~ 1186	628.748~ 1189	620.351~ 1185

3. Temperature and Stress Field of the Electrical Furnace Roof

After setting the loads and boundary conditions, run the macro document LG.mac, get the calculated results of each models. To show the temperature variation of the furnace roof on section of the charging hole, slice the firebrick roof and prefabricate roof along the center symmetry plane by the ANASY work plane, the temperature equivalent slices contours are in Figs. 10-13.

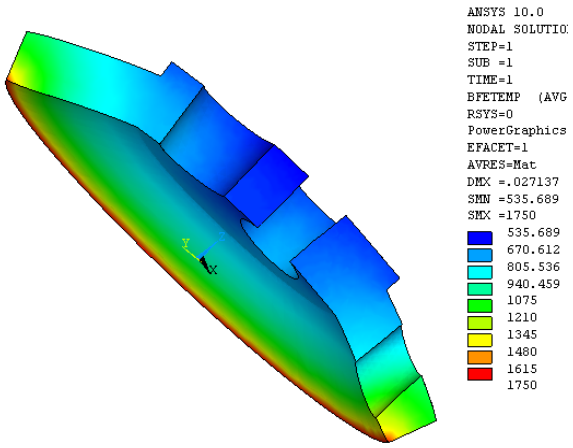

Fig. 10. Isograms slice image of firebrick roof temperature.

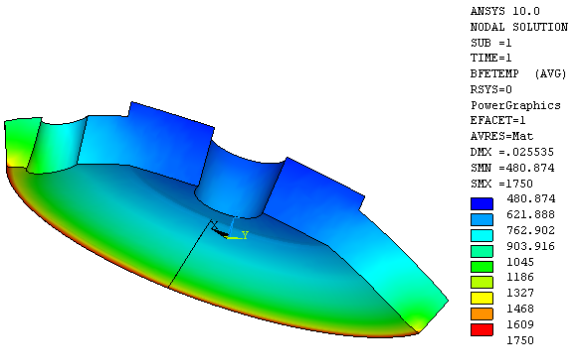

Fig. 11. Isograms slice image of prefabricate block roof (3 blocks).

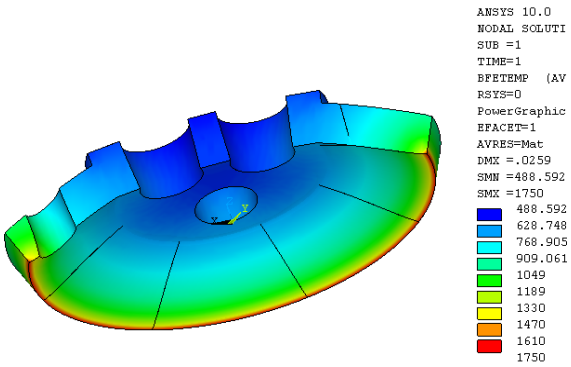

Fig. 12. Isograms slice image of prefabricate block roof (8 blocks).

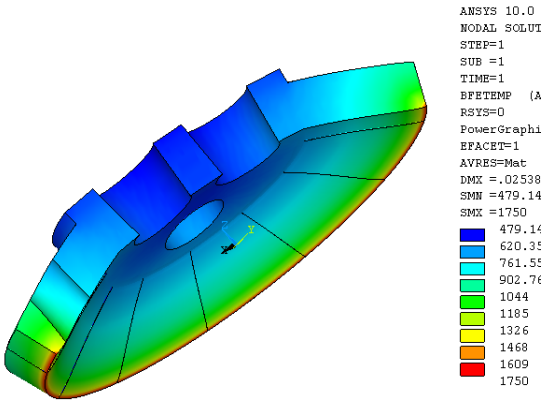

Fig. 13. Isograms slice image of prefabricate block roof (12 blocks).

As the origin point of the last work plane of the CAD model is on the axis of the charging hole, the Z axis is the height direction of the charging hole, so rotate the YZ plane by 90 degrees; meanwhile since the charging holes are set uniformly on the center roof circle, on furnace roof with different number of prefabricate bricks, the relative positions of electrode holes and charging holes are different on roof with different number of prefabricate bricks. The section of the three electrode holes and charging holes can not be shown at the same time. So there are only 1 or 2 of the electrode holes that can be shown.

The Figs. 10-13 indicates that, in last melting stage, the center roof temperature of the firebrick roof ranges from 535.689 °C ~ 670.612°C, but the temperature of the other zone is 805.536 °C ~ 1210 °C; the temperature of center zone of the roof composed with three prefabricate bricks ranges from 480.874 °C ~ 621.888 °C, the temperature of the most part of the roof is 621.888 °C ~ 1186 °C; the temperature of center zone of the roof composed with eight prefabricate bricks ranges from 488.592 °C ~ 628.748 °C, the temperature of the most part of this roof is 628.748 °C ~ 1189 °C; the center zone temperature of the roof composed with twelve prefabricate bricks ranges from 479.145 °C ~ 620.351 °C, the temperature of the most part of this roof is 620.351 °C ~ 1185 °C. All the temperatures along the roof thickness gradually decrease and their maximum values are 1750 °C, at the bottom of these roofs. This paper equalizes the thermal radiation absorbed by roof to temperature degrees of freedom, so the maximum temperature distributions are at the same area of each roof; this area is closest to molten steel of the high temperature zone and electric arc, squaring to the fact; and cause there are differences between the overall structures of the firebrick roof and the prefabricate block roof as the different manufacturing technology, there is no interface in the firebrick roof, but the prefabricate block roof has interface as its making up with several blocks. So the heat transfer rates of each roof at diameter direction and in thickness direction are different, so the temperatures are different.

In the diameter direction, temperature is higher on the outer circumference of the roof and lower in the center of the roof. In the thickness direction, temperature of the roof is higher on the inside wall of roof and lower on the surface of roof. This is because the bottom and inside wall of the roof are closer to the steel water, these areas will absorb more heat radiation. The result is consistent with the reality. The average temperature distribution statistics of each roof model are in Table 2.

Table 2. The average temperature distribution statistics of each roof model (°C).

CAE model	Fire-brick roof	Prefabricate block roof (3 blocks)	Prefabricate block roof (8 blocks)	Prefabricate block roof (12 blocks)
Number of element points	18906	19305	20122	21400
Number of nodal points	22068	23278	24070	25140

The calculated results indicates that, in last melting stage, the average temperature of firebrick roof is higher than prefabricate block roof and the temperature distribution law of each roof are basically the same.

The result indicates that, in last melting stage the average temperature of firebrick roof is higher than prefabricate block roof and the temperature distribution law of each roof are basically the same.

4. Conclusion

This paper simulates the stable temperature and stress field of firebrick roof and the prefabricate block roof in last melting stage. The result corresponds to the theory of transferring heating subject, indicating that the simplification of model and the operation to boundary are reasonable, proving the responsibility of the temperature analysis. The result shows that the heat preservation performance of prefabricate block roof is better than that of firebrick roof, providing theory support for prefabricate block roof from heat preservation perspective.

References

[1]. Hongxi Zhu, Chengji Zheng, etc. Preparation and application of bauxite-based prefabricated block for electric furnace roof, *Steelmaking*, 2, 2008.

[2]. Guozhang Jiang, Jianyi Kong, Gongfa Li, etc., Research and application of thermo-mechanical

stress model for bottom working lining of 250-300 t ladle, *Steelmaking*, 24, 2, 2008, pp. 22-25.

[3]. Gongfa Li, Peixin Qu, Jianyi Kong, etc., Influence of Working Lining Parameters on Temperature and Stress Field of Ladle, *Applied Mathematics & Information Sciences*, 7, 2, 2013, pp. 439-448.

[4]. Gongfa Li, Jianyi Kong, Guozhang Jiang, etc., Stress Field of Ladle Composite Construction Body, *International Review on Computers and Software*, 7, 1, 2012, pp. 420-425.

[5]. Gongfa Li, Jianyi Kong, Guozhang Jiang, Simulation research on influence of expansion joint of wall lining in ladle composite construction body on thermal stress, *Modern Manufacturing Engineering*, 10, 2010, pp. 85-88.

[6]. Gongfa Li, Jianyi Kong, Guozhang Jiang, Influence of working lining parameters on temperature field of ladle composite construction body, *Modern Manufacturing Engineering*, 12, 2010, pp. 77-80.

Sensors & Transducers, Vol. 21, Special Issue, May 2013, pp. 100-104

Sensors & Transducers

http://www.sensorsportal.com

A Measuring Method of Steel Plate Defect Uncertain Correlation Information based on Rough Set and Functional Dependency

Junwei LIU, Jianyi KONG, Xingdong WANG
College of mechanical automation, Wuhan University of Science and Technology,
Wuhan 430081 P. R. China
Tel.: +8613657290532, fax: +8602768862830
E-mail: liujunwei@wust.edu.cn, 15697188659@wo.com.cn, xingdongwang@163.com

Received: 31 March 2013 /Accepted: 14 May 2013 /Published: 30 May 2013

Abstract: There are multitudinous, multispecies, nonlinearity, multiphase and so on complex system time and space scales characteristics in steel plate production process, whose defects are divided into dominant defects and hidden defects. Real-time dynamic steel plate defects information can not be effectively and quickly converted, it is difficult to find the relationship among defects facts, defects reasons and defects controls in production elements. To reduce steel plate defects as the research object, through building-up steel plate defect information database, we can get a uncertain correlation information measurement method between steel plate defect and the production process elements by study associated information concept model of steel plate defects, measurement of uncertainty defects associated information based on Rough Set theory and mapping membership calculation based on Functional Dependency, which provides a useful theoretical support for reducing defects, improving the finished product rate. *Copyright © 2013 IFSA.*

Keywords: Steel plate defects, Correlation information, Uncertainty, Rough set, Functional dependency.

1. Introduction

According to the statistics, the total output global crude steel is 1.5478 billion tons in 2012, and the output of Chinese mainland crude steel is 716 million tons, which is 46.3 % of global production. Deeply influenced by downstream demand growth reduced drastically, productivity and yield continued promoting, and the contradiction of trade credit is sharpened, the iron and steel industry sales margins down, reach 0.13 % in 2012, which is at the lowest level in the national industry. In steel products output stage, the high defect rate, lower finished product rate caused enormous losses, which become one of the main factors that restrict iron and steel industry profits.

Steel plate defects stems from its production process's complex features, iron and steel metallurgy production process including sintering, iron making, steelmaking, continuous casting, rolling and etc. The whole production process is a typical hybrid industrial process integrated by chemical and physical process. It has multitudinous, multi-species, nonlinearity, multiphase and so on complex system time and space scales characteristics. Defect is very informative and heterogeneity exists. How to min the association rules of steel defect 'Fact- Reasons-Controls' (*FRC*), analysis reasons that cause the defects, and explore the feasible solutions to control defects become the difficult problems confused iron and steel industry.

Article number P_SI_349

2. Pretreatment of Steel Plate Defect Information

2.1. The Classification and Description of Steel Plate Defect Information

2.1.1. The Classification of Steel Plate Defect Information

Steel defects are classified based on defects characteristics in steel production process, defects can be divided into major classification and small classification. Major classification is the total classification of defects, such as surface defects, internal defects, shape defects, bad SPEC, bad SIZE, single weight shortage and others, which can be expressed in English letters as (A, B... V). Small classification is detailed defects classification, which can be expressed with Arabic numerals.

2.2.2. The Description of Steel Plate Defect Information

In order to describe the associated attributes of defect information effectively, the defect information in defect information database is described, whose description method is shown in Table 1. There are two types of defects in steel plate production process, the first kind of defect is dominant which can be discovered by existing detection technology, the second kind of defect is hidden defects that remains from previous process or hidden in the engineering and technical personnel. Hidden defects is hysteretic and remain to be domination, the dominant defects should be further quantitative in order to implement control.

Table 1. Description method of the defect facts.

Defect Information access	Storage location	Defect type	Attribute counter-measures
The existing detection technology	Defect information warehouse	Dominant defects	Reasons controls quantization
Experience	Engineering technicians	Hidden defects	Reasons controls domination

2.2. The Space Model of Steel Defect Information Resources

To improve efficiency of plate defect information storage and retrieval, the space model of steel defect information resources is build as Fig. 1 [1]. The model is composed by defect information level, defects types and storage location of defect information. Each point in the space model determines one or one type of defect information [2], and the storage location in defect information database is determined.

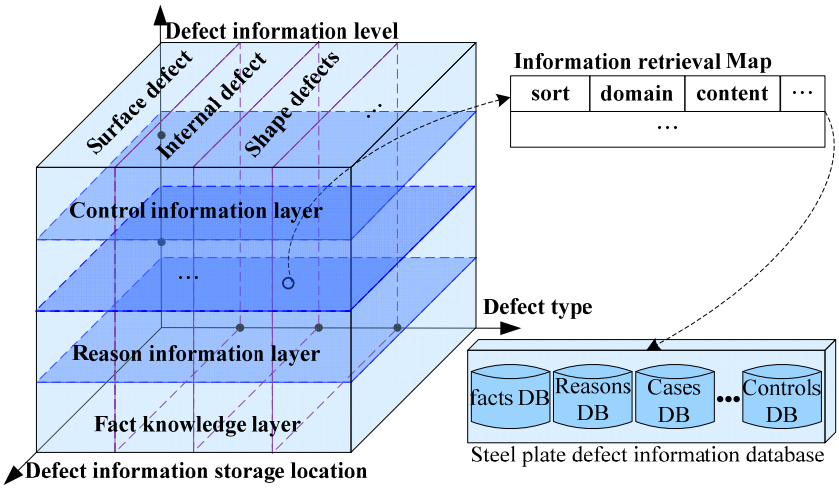

Fig. 1. The space model of steel defect information resource.

2.3. The Logic Relationship of Steel Defect Associated Information

After classifying, express, coding, sorting and other structured treatment, massive defect information is stored at specified location. Steel defect facts is stored in real-time defects database or historical defects database, steel defects reasons is stored in defect reasons database or defect dynamic reasons databases, steel defects controls is stored in defect control cases database or defect dynamic control measures databases. In addition, defect information relationship database is build based on uncertainty steel plate defect information measurement method. The logic relationship of steel defect associated information is shown as Fig. 2.

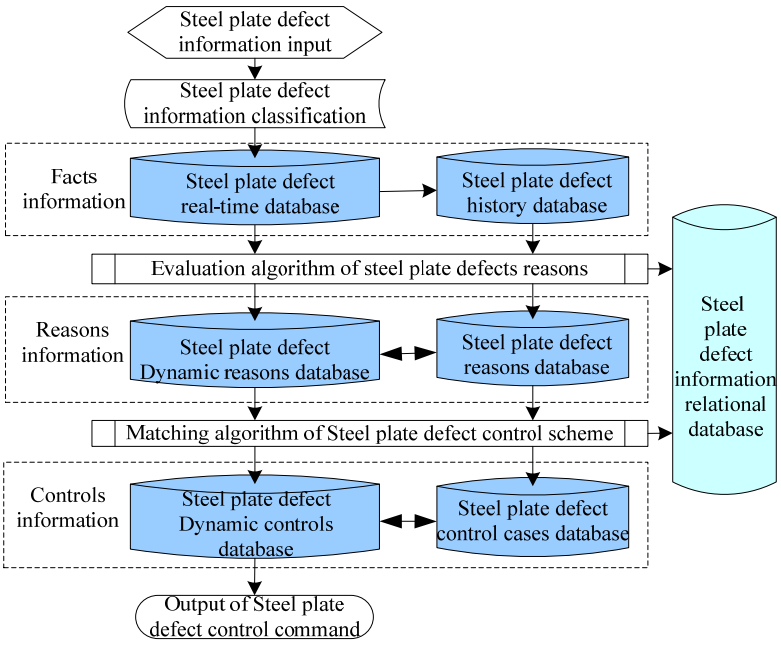

Fig. 2. The logic relationship of steel defect associated information.

3. Measurement Methods about Uncertainty Associated Information of Steel Plate Defects

Measurement about uncertainty associated information of steel plate defects is a creative activity based on knowledge processing and operation. It is a reasoning process from qualitative to quantitative, from uncertain information to determinate information [3]. And it is also a mapping process from defects facts to the defects reasons and from the defects reasons to defects control measures [4].

3.1. Associated Information Concept Model of Steel Plate Defects

In order to reveal the FRC association rules between plate defects and production process elements effectively, an associated information concept model of steel plate defects is build as Fig. 3.

Where, $\sum_{i=1,2,\cdots n} i = 100$, $\sum_{j=1,2,\cdots p} ij = 100$.

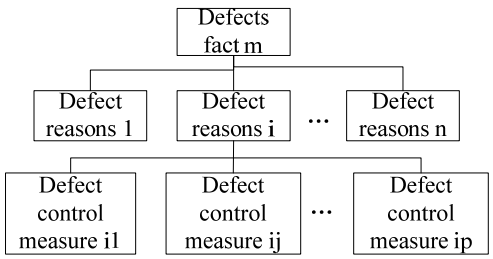

Fig. 3. Associated information concept model of steel plate defects.

3.2. Measurement of Uncertainty Defects Associated Information based on Rough Set Theory

Assume $\varphi = (F, R)$ is a defect information system, F is a finite object collection about defects facts, which is called the domain, X is a subset of the domain $X \in F$. R is a limited attribute collection of defect causes, B is a subset of R, $B \subseteq R$. The lower approximation and upper approximation of B are denoted as $B^{-}(X)$, $B_{-}(X)$ respectively. Set $BN_B = B^{-}(X) - B_{-}(X)$ boundary region of X. If boundary of X is empty set, that is $BN_B(X) = \phi$, set X is a precise set of B, otherwise X is rough set of B [5, 6].

Assume $S = \{X_1, X_2, \cdots X_n\}$ is a classification of F, which is independent of R. The sub collection $X_i (i = 1,2,\cdots,n)$ is a classification of S. According to defects facts, $F(X)$ is a collection of objective reality defects information which all can be conclude to x, and $R(X)$ is collections of goal knowledge which may be reduce to defects reasons mapping collection x. The R lower approximation and the R Upper approximation of S are defined as $R_{-}(X)$ in formula (1), $R^{-}(X)$ in formula (2).

$$R_{-}(F) = \{R_{-}(X_1), R_{-}(X_2), \cdots, R_{-}(X_m)\}, \quad (1)$$

$$R^{-}(F) = \{R^{-}(X_1), R^{-}(X_2), \cdots, R^{-}(X_n)\}, \quad (2)$$

The approximate classification accuracy of S is as formula (3).

$$d_F(R) = \sum_{i=1}^{m} \left| R_-(X_i) \right| \Big/ \sum_{i=1}^{n} \left| R^-(X_i) \right| , \quad (3)$$

Because vague concept is border, the mapping degree of defects facts - reasons is uncertain. Indiscernibility relation is used to define rough set membership function as formula (4).

$$\mu_x^B(x) = \left| X \cap B(x) \right| \Big/ \left| B(x) \right| , \quad \mu_x^B(x) \in [0,1] , \quad (4)$$

The value of the membership function $\mu_x(x)$ can be interpreted as conditional probability of defect facts - reasons mapping, which is certainty degree of x belongs to X . Membership value can be calculated by dependent function data.

3.3. The Mapping Membership Calculation based on Functional Dependency

The similarity matching input of defect 'fact-reason' is defined as defect facts F , defect reasons R , and candidate matching set K of each defect fact in 'fact-reason' model. The Similarity matching output is defined as mapping relationship $M(F,R)$ between defect facts F and defect reasons R [7]. The computational steps are as following.

1). Create the mode pattern $G(F)$ and $G(R)$ of defect facts F and defect reasons R .

2). For each candidate matching (f,r) , calculate the father structure similarity $asim(f,r)$ and the substructure similarity $csim(f,r)$. $asim(f,r)$ and $csim(f,r)$ are transmit According to the mode pattern $G(F)$ and $G(R)$.

Defect 'fact-reason' information is representing by mapping membership, for the candidate match (f,r) , generates function of element f in model F about function dependence set S_F , and decides elements closure $F_{R_f}^+$. Then generates function of element r in model R about function dependence set S_r , and decide elements closure $r_{S_f}^+$. And then we can calculate similarity $\delta(f,r)$ according to formula (5).

$$\delta(f,r) = \frac{\left| \begin{matrix} \{x \mid x \in f_s^+ \wedge \exists y \in r_s^+, y \in K(X) \cup \} \\ \{x \mid x \in r_s^+ \wedge \exists y \in t_s^+, y \in K(X)\} \end{matrix} \right|}{f_s^+ \cup r_s^+} , \quad (5)$$

After getting similarity φ , qualitative analysis the relationship among similarity $\delta(f,r)$, stability factor m and the substructure similarity $csim(f,r)$, their quantitative relationship can be represent by formula (6).

$$csim(f,r) = (\delta(f,r))^2 \times (\frac{m}{m+\alpha}) , \quad (6)$$

In the formula, the smaller the parameter α , the influence of stability factor m is smaller to substructure similarity. On the contrary, the influence of stability factor m is bigger to substructure similarity.

3). Create probability $psim(f,r)$ according to the adjusted $asim(f,r)$ and $csim(f,r)$.

For any element in the defects facts set, the higher the total value of all candidates matching similarity, the probability of actual matching degree to the defect reason is higher. Instead it is low. For any defect fact element x and the candidates match defect reason $K(x)$, the matching probability of x in defects reason can be calculated through formula (7).

$$P(x) = \frac{\sum_{y}^{y \in K(x)} sim(x,y)}{\sum_{y}^{y \in K(x)} sim(x,y) + d} , \quad (7)$$

In the formula, d is parameter in the same situation, the bigger the numeric of d , the candidate match probability is lower, where the probability similarity is lower. The smaller the numeric of d , the candidate match probability is higher, where the probability similarity is higher.

4). Mapping relationship collection M between models is chosen according to similar probability.

The inference method between defect reason R and defect control C is similarity.

4. Conclusions

In steel products output stage, the high defect rate, lower finished product rate caused enormous losses, which becomes one of the main factors that restrict iron and steel industry profits. Steel plate defects stems from its production process's complex features, defect is very informative and heterogeneity exists. Take the research object as enhancing conversion efficiency of steel plate real-time dynamic defects information, find the relationship among defects facts, defects reasons and defects controls in production elements. Through building-up steel plate

defect information database, we can get a uncertain correlation information measurement method between steel plate defect and the production process elements by study associated information concept model of steel plate defects, measurement of uncertainty defects associated information based on Rough Set theory and mapping membership calculation based on Functional Dependency, which provides a useful theoretical support for reducing defects, improving the finished product rate.

References

[1]. Junwei Liu, Jianyi Kong, Min Zhou, Xingdong Wang, Hegen Xiong, Gongfa Li, Study on Intelligent Manufacturing System Model of Iron & Steel Enterprises in Ubiquitous Information Environment, *Advanced Materials Research*, Vol. 328-330, 2011, pp. 416-420.

[2]. Zhen Lu, Knowledge supply theory and technology Based on knowledge grid, Doctoral Dissertation, *Shanghai Jiaotong University*, 2008.

[3]. Slobodan Ribaric, Tomislav Hrkac, A model of fuzzy spatio-temporal knowledge representation and reasoning based on high-level Petri nets, *Information Systems*, 37, 3, 2012, pp. 238-256.

[4]. Eugene Santos Jr., Deqing Li, Eunice E. Santos, John Korah, Temporal Bayesian Knowledge Bases – Reasoning about uncertainty with temporal constraints, *Expert Systems with Applications*, 39, 17, 2012, pp. 12905-12917.

[5]. Wang Xiang Yang, Study on pattern recognition method of Uncertainty reasoning and data analysis, Doctoral Dissertation, *Shanghai Jiao Tong University*, 2006.

[6]. Wang Yu, Research on key technologies of knowledge measuring, reasoning and fusing in knowledge engineering, Doctoral Dissertation, *Fudan University*, 2004.

[7]. Du Xiaokun, Research on Database schema matching algorithm, Doctoral Dissertation, *Huazhong University of Science and Technology*, 2010.

Sensors & Transducers, Vol. 21, Special Issue, May 2013, pp. 105-110

Sensors & Transducers

http://www.sensorsportal.com

Vibration Analysis and Test of Backup Roll in Temper Mill

Yuanmin Xie
College of Machinery and Automation,
Wuhan University of Science and Technology, Wuhan 430081, Hubei, China
Tel.: +86-027-68862283
E-mail: wustxie@126.com

Received: 11 April 2013 /Accepted: 14 May 2013 /Published: 30 May 2013

Abstract: Based on experimental researches on chatter marks on the strip steel and backup roll of a 1700 temper mill, test and analysis the vibration on the vibration mode and work mode vibration of the temper mill, then the formation of the chatter mark on the roll surface is relation to the natural frequency of the temper mill, tension, assembly space between the rolling system and the rack post, the roller bearing support and the rack arch. The forming reasons and the characters of the chatter marks are grasped, so the suppression method is proposed and considerable effects are achieved. *Copyright © 2013 IFSA.*

Keywords: Temper mill, Vibration analysis, Test, Chatter mark, Strip steel, Suppression method.

1. Introduction

A supporting roller is replaced once every 25 days according to the original design of temper mill. Outside of support roll and the strip surface began to appear light and shade spacing rules of mark which have obvious cycle characteristics in practical work in about 7 days. Vibration mark on the surface of the support roll rapidly increase, which leads to light and shade spacing rules of mark on strip surface. In order to guarantee the quality of steel strip, the trimming machine every seven days or so will need to replace a supporting roller and grinding was carried out on the change of supporting roller before using. This measure not only seriously affects the production efficiency and greatly increases the equipment and maintenance costs.

The vibration characteristics of temper mill and the possible cause of vibration should be find out through mark of vibration detection and analyzing of the support roll and the strip steel products according to the vibration problems of temper mill in the practical work. Through the vertical vibration, the horizontal vibration and displacement test and analysis of roll system of temper mill, the vibration characteristics and proven source of the temper mill should be find. Explore the vibration transmission mechanism and set up vibration model through finite element analysis of structure, natural frequency and vibration mode of temper mill. According to analysis influence of temper mill process parameters and equipment structure on the temper mill mark problem, find out the improvement scheme to inhibit vibration of temper mill system. So as to improve the machine dynamic performance and stability peace of the work roll and extend the support roller service life of temper mill.

2. Analysis of Support Roller Marks Formation on the Surface of Root

2.1. The Characteristics of Marks on Support Roll Surface

There is light and shade spacing rules of mark on support roll surface which is shown as Fig. 1.

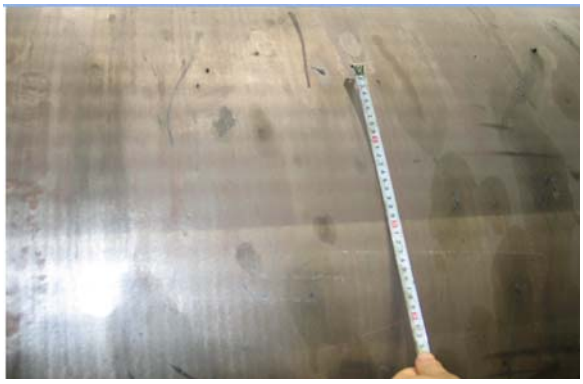

Fig. 1. The shape of marks on support roller surface.

2.2. The Influence of Tension to Vibration of Roll System

According to the control characteristics of temper mill shown as Fig. 2, the longer distance between the tension rollers is, the bigger vibration trace spacing is. The thicker the material is, the smaller the spacing is at the same circumstances. The greater the tension setting is, the smaller time space is. Horizontal component of the rolling force caused by tension difference is bigger which lead unstable to the work roll.

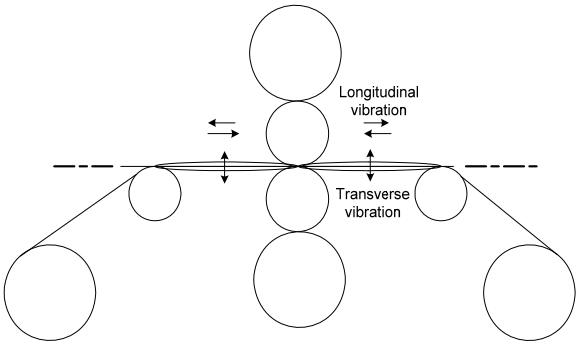

Fig. 2. The vibration of temper mill.

2.3. Assembly Clearance Effect on the Vibration of Roll System

The horizontal force of the work rolls point to the export side when the work roll of temper mill shifts towards exports relative to its supporting roller. Considering the inevitable existence assembling clearance between frame arch column and bearing seat of the working roller and supporting roller, the work roll could have a horizontal scroll at a direction of exports side to mill and support roll have a horizontal scroll at a direction of entrance side to the mill. Periodic collision between work roll and support roll at the same time can make the size and properties of contact friction between working roller and supporting roller surface change periodically, which cause periodicity uneven wear. Periodic vibration is formed on the surface of supporting roller. If the assembly gap is too big, the offset of work roll increases more than the level of support roll and horizontal and vertical vibration of roll system will be more intense.

2.4. The Analysis of Source Vibration of the Roll System

Analysis shows that the vibration source of the temper mill is the horizontal vibration of temper mill roll system, which causes the vertical vibration of roll system, while the fluctuations in pressure between the rollers caused by vertical vibration. Friction condition cyclically changes in the presence of relative sliding between the roll surfaces leading to the marks of roll surface. And marks on the surface of the support roller as excitation source further intensifies the formation of the marks which has promoting effect on the vibration of the system.

2.5. State Analysis of Temper Mill

Analyze the 3d model in ANSYS which is combined with the drawing size to establish three-dimensional model of temper mill in Pro/E. 3d model and finite element model are shown in Fig. 3.

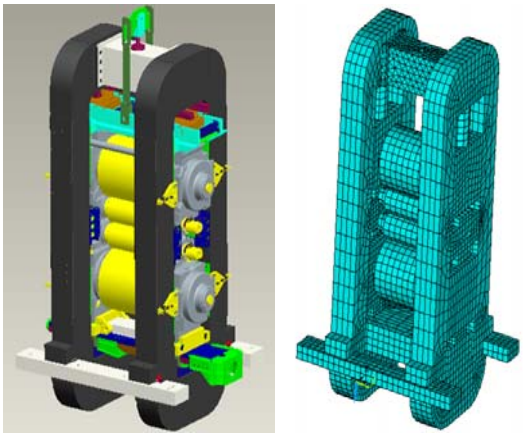

Fig. 3. 3d model and finite element model of temper mill.

The modal analysis of ANSYS software is a linear analysis, any nonlinear characteristics, such as

elastic, plastic and contact gap element, even if consideration will also be ignored. These nonlinear will be directly converted into linear by software to calculation and post-processing of modal analysis do not consider nonlinear. The first six order modal results in the Table 1.

Table 1. Results of each order modal.

Order number	f_1	f_2	f_3	f_4	f_5	f_6
Frequency	88.5	116.4	168.9	325.2	414.8	533.6

3. The Composition of the Test and Analysis System

3.1. Test Methods of Vibration and Displacement

Use acceleration sensor to acquire horizontal and vertical vibration signal of temper mill roll system by using VC to write collection procedures to observe and record each measuring point signal in real time. There are a total of 16 measuring point vibration signal and as shown in fig 4. Use displacement sensor to acquire displacement signals of temper mill roll system. There are a total of four displacement signal measuring points and as shown in Fig. 4.

Acquisition system choose to use Taiwan company PCI bus acquisition card PCI-1741-U which is the high-resolution multi-function and use multithreading drivers to complete acquisition program to call inquiry under the VC development environment. Its architecture is shown in Fig. 5.

The measured data by Acquisition process is stored in text to analyze by Matlab program.

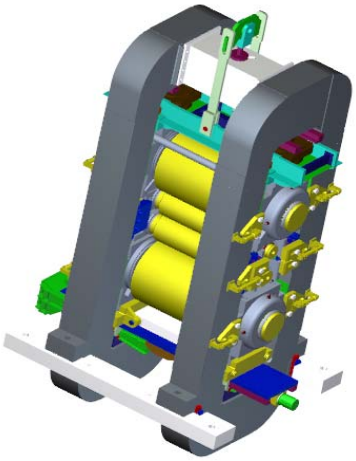

Fig. 4. 3d layout of the sensor.

3.2. The Composition of the Test System

3.3. Analyze the Test Result

Upper and lower support roll signal analysis and vibration power spectrum of the transmission side and working side is shown in Fig. 6 and Fig. 7 by using of Matlab to draw signal frequency spectrum analysis According to the measured data.

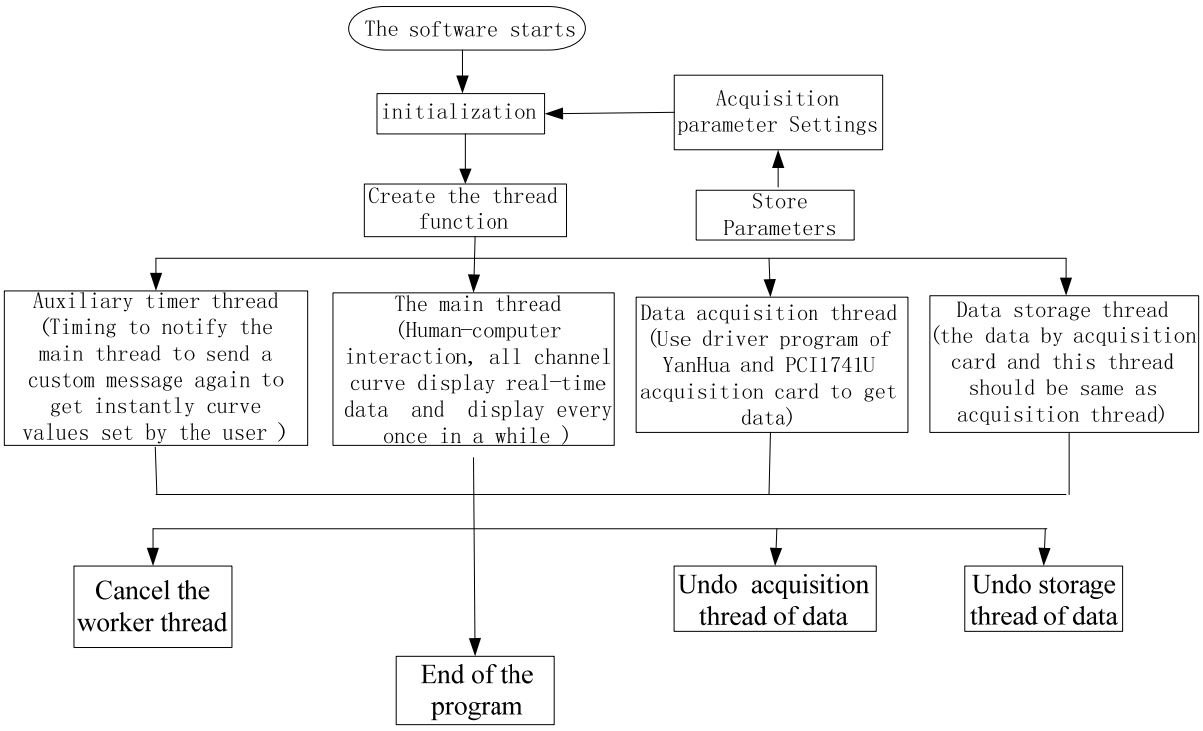

Fig. 5. The software process of vibration and displacement signal of temper mill roll system.

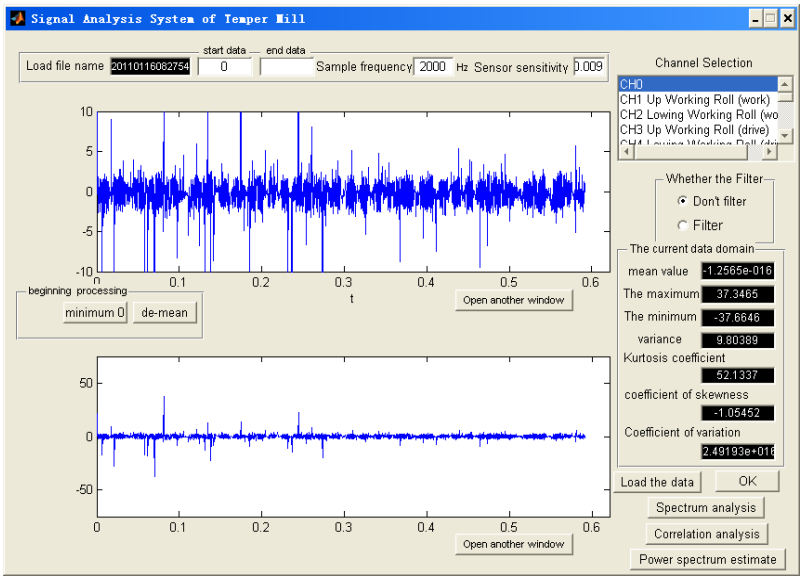

Fig. 6. Signal analysis.

A conclusion can be draw according to the signal power spectrum chart of test and changing the assembly clearance and other process parameters on the vibration mark.

(1) Main frequency of Energy maximum and amplitude maximum is 547.7 Hz and 750 Hz and they all have small wave. The frequency of 547.7 Hz is between 547 Hz and 549.6 Hz.

(2) The frequency of 547.7 Hz occurs very frequently. Almost each channel in each test has appeared. And the frequency is very close to X natural frequency of the temper mill.

(3) From comparing between the working roll and supporting roll amplitude, work roll amplitude is greater than the support roll and supporting roller changes gently, amplitude is greater than the support roll and work roll is most significant. Comparison between drive side and working side find: vibration amplitudes of Work roll under the roller drive side is significantly greater than the working side which is driven roll; vibration amplitudes of The support roll and working roll under drive side is not less than working side, but horizontal vibration amplitude of supporting roller under working side is slightly greater than the drive side. Vibration amplitude of the upper support roller and the lower support roller: On the drive side, the changing of vertical and horizontal vibration amplitude of upper supporting roller and lower support roller is not obvious. Vertical and horizontal vibration amplitude changes more significant in the work side at the up and down side of the backup roll and horizontal vibration amplitude is the greatest. The vibration of the lower support roller is strong than on supporting roller. Vibration condition of the upper work roll and lower work roll (driven roller): vibration amplitude of the upper work roll is greater than the lower work roll. Vibration of the lower work roll should be stronger than the upper work roll. Vibration of the work roll at the drive side is significantly stronger than work side. The frequency of 547.7 Hz of the vibration of each roll system occurred on temper mill and the frequency fluctuations within certain range. The energy of frequency of 547.7 Hz accounts a considerable advantage in each roll system of vibration.

The vibration source of temper mill oscillation is horizontal vibration of temper mill roll system through theoretical analysis, which causes the vertical vibration of roll system, while the fluctuations in pressure between the rollers caused by vertical vibration. The relative sliding between roll surfaces caused the cyclical change friction condition. At the same time the frequency 547.7 HZ is close to the 6th natural frequency with temper mill, the frequency corresponding to the vibration mode is easy to cause the marks of the surface.

When the work roll of temper mill shift towards exports that is relative to its supporting roller, the horizontal force to rolling mill work roll suffered the export side. The inevitable existence assembling clearance between the working roller or supporting roller bearing seat and frame arch column can make the work roll horizontal direction exporting to mill side; At the same time supporting roller appear the inlet side of the horizontal direction.

Reduce the assembling clearance between working rollers or supporting roller bearing seat and the frame arch pillar. Reduce level relative to one another between rolling work roller and back-up roller of the skin pass in the process of moving, which try to ensure that horizontal offset of the work roll system relative to the support roll roller is meet the design value 6 mm.

The width dimension of upper and lower support roller bearing seat (with both sides of skateboard) and the top and bottom work roll bearing seat belt (both sides of skateboard) and the assembly size between the inside of the frame window pillar size should meet the design requirements to reduce the assembly clearance between the bearing seat and stud.

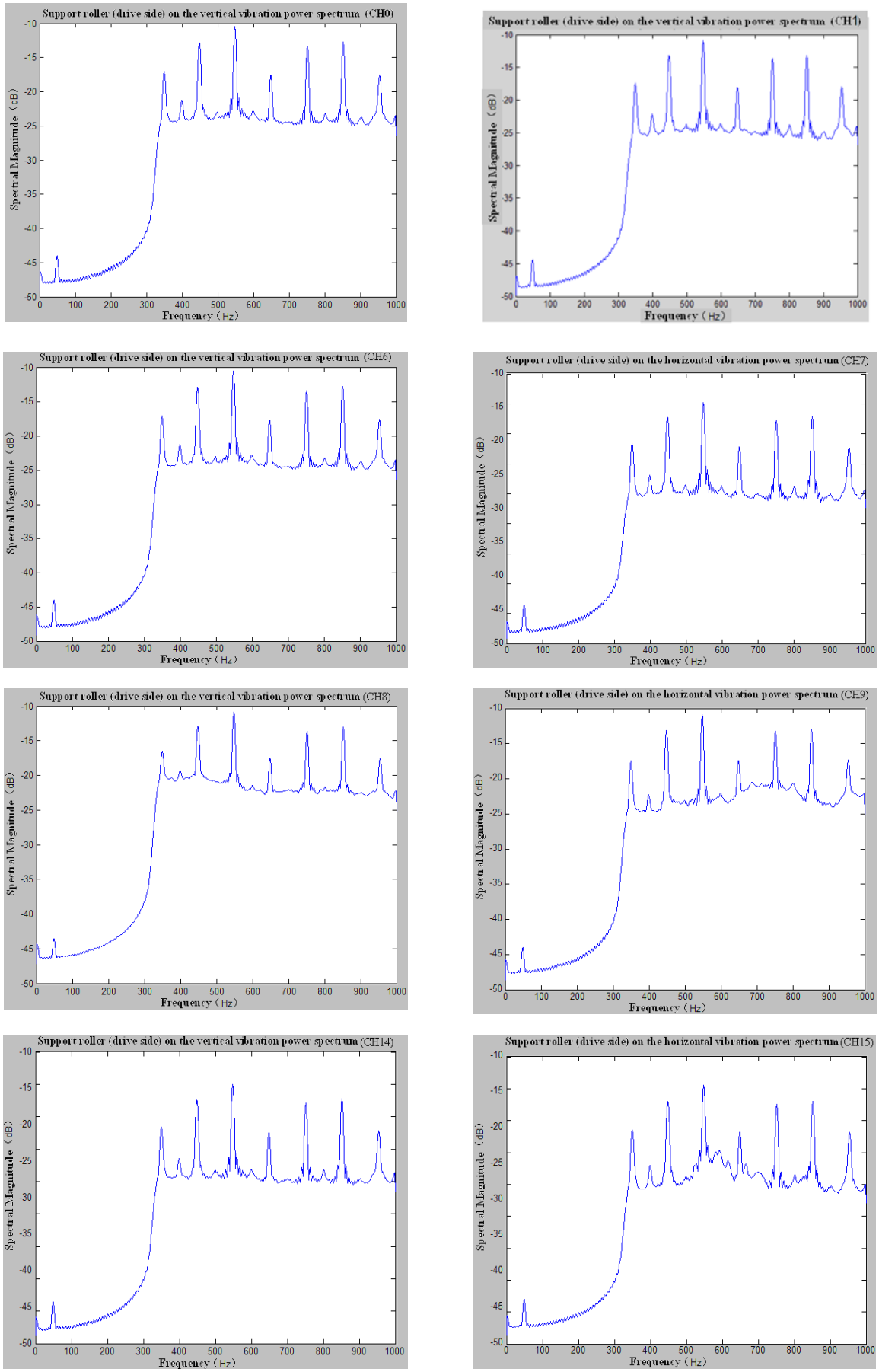

Fig. 7. Power spectrum diagram of support roller.

4. Targets and Effect

4.1. Goals and Implementation

Based on the above analysis, determine the total target of inhibition. Work roll such as making support roller life have obvious improve after taking measures as adjustment on the memorial arch system clearance and the hardness of supporting roll and so on, which strive for the using time of support roller more than 25 days. Adjust the concrete content as follows:

(1) The size of frame window without lining on the inside of the supporting roller was not measured. Please take measures during the maintenance, which is a basis for the adjustment compared with drawing size.

(2) Frame window on the inside of the column plate (panel) were measured after removal which is a basis for the adjustment.

(3) All the width size, up and down the size of slide of roll (including work roller and back-up roller) bearing without slide and width size with belt slide must be measured which is into form as a basis for the adjustment.

(4) Thickness of the support roller bearing seat board on the inlet side slightly changes to big and the export side changes to small or appropriate changes according to the standard size processing.

4.2. Corrective Effect

Take the adjustment on arch series and the hardness of roll gap because the formation of the marks has direct relationship with the assembly clearance by mentioned before. From the information of the scene production, the support roller life has improved significantly which has reached 25 days and the service life is 7 days before the adjustment, so the result is obvious changes and reaches the original design life.

5. Conclusions

According to the test plan and the measured vibration and displacement signal data, the effect of process parameters on vibration mark is analyzed, through the MATLAB software and analysis of signal data acquisition, draw the corresponding sensor test signal spectrum and power spectrum diagram. Analysis shows that the vibration source of the temper mill is the horizontal vibration of temper mill roll system, which causes the vertical vibration of roll system, while the fluctuations in pressure between the rollers caused by vertical vibration. The relative sliding between roll surfaces caused the cyclical change friction condition leading to the roll surface of the marks, which is the Frequency of 547.7 Hz for the vibration frequency of supporting roll and the strip surface. Tension and the working roll and supporting roll bearing seat and the clearance between frame arch pillars has a great promoting effect on the formation of the marks. Above analysis for subduing the supporting roller surface marks and extending the life of the supporting roller has certain significance.

References

[1]. X. Fu, J. Zhang, X. L. Shi, etc., Research on the Forming Reason and Control of Chatter Marks on Backup Roll of Temper Mill, *Metallurgical equipment*, 2006, 4, pp. 37-40.

[2]. P. L. Chen, Z. J. Wang, Cause and Control of Chatter Marks on Steel Strip Surface, *Iron & Steel*, Vol. 41, Issue 5, 2006, pp. 49-52.

[3]. F. X. Hou, J. Zhang, X. L Shi etc., Horizon chatter in a single-roll driving temper rolling mill system. *Journal of University of Science and Technology,* Vol. 28, Issue 10, 2006, pp. 973-976.

[4]. F. G. Liu, Z. S. Qi, H. B. Xie, Analysis of the surface crack of backup roll on temper mill, *Heavy Machinery,* Vol. 1, Issue 3, 2010, pp. 64-66.

[5]. J. J. He, L. Y. Li, X. Li, T. Q. Wang, The signal analysis of self-shielded flux-core welding based on Matlab, *Material Science and Technology,* Vol. 1, Issue 17, 2009, pp. 195-198.

[6]. Garcia, Thomas R., Communication signal analysis using MATLAB, *Frontiers in Education Conference, Vol.* 2, Issue 1, 1996, pp. 616-619.

[7]. J Xiang, Batch signal processing using Matlab and excel, in Proceedings of the International Conference on Signal Processing, Vol. 3, Issue 1, 2004, pp. 2514-2517.

[8]. Mazid Abdul Md, Martin Ryan, Automation of compressor test procedure using Advantech data acquisition module, in *Proceedings of the International Conference on Control, Automation, Robotics and Vision*, 2008, pp. 2266-2271.

Sensors & Transducers, Vol. 21, Special Issue, May 2013, pp. 111-116

Sensors & Transducers

http://www.sensorsportal.com

A Research of Cement Energy-Saving KM System Based on CBR and BP Neural Network

An Ji-Yu, Zhu Xiao-Hui, Ma Yong-Qiang
Lab. of Service Science and Technology, Henan Polytechnic University,
Jiaozuo, 454000, China
E-mail: anjiyu@yeah.net

Received: 23 March 2013 /Accepted: 14 May 2013 /Published: 30 May 2013

Abstract: The level of enterprise knowledge management is becoming an important means to measure their competitiveness. Inside the cement companies, the efficient and comprehensive management is come from the encoded data with a high degree of structure. But for that hard-to-codified tacit knowledge, the enterprise lacks of effective organization. This paper analyzes the advantages of case-based reasoning and BP neural network in case retrieval, and combines the features respectively to design the BP-CBR case retrieval model. The model joins BP neural network technology to the case organization index and retrieval stage of case-based reasoning, which makes up for the defect of traditional case-based reasoning. Through using the retrieval instance of a cement energy program, it verifies the effective application of knowledge management in the field of energy-saving reconstruction. *Copyright © 2013 IFSA.*

Keywords: Cement enterprise, Knowledge management, Energy-saving reconstruction, Case-based reasoning, BP neural network.

1. Introduction

With the intensification of the energy crisis, many of the high energy consumption enterprises are committed to implement their own energy-saving reconstruction. As the basis of national construction, the cement production enterprises should finish the integration of system resources and implementation of knowledge management (KM) well, which is an important factor to reshape its core competitiveness. Due to the complex process and diverse energy consumption of cement production, we need a different energy-saving program to complete the different implementation direction. How to improve the organization and management level of cement enterprise case knowledge in the field of energy-saving reconstruction, and complete the retrieval of energy-saving programs efficiently, is particularly important to the implementation of the enterprise KM.

The traditional case-based reasoning (CBR) is often combined with the rule-based reasoning (RBR) technology, so that is able to avoid the bottleneck of knowledge acquisition and take advantage of the RBR technology to achieve the case adaptation and correction [1]. The literature [2] using the BP neural network pattern matching capacity to make up for the CBR technology defects, implement the classification function of case retrieval, but failed to give full play to its retrieval advantage in CBR processing.

In this paper, based on systematic analysis of the technical characteristics of the CBR and BP neural network, we using the BP neural network to replace the part of stage during CBR process to improve the

efficiency. Not only did we figure out a way to make up for the defects of the CBR treatment system in case index as well as the definition of similarity, but also avoid the problem of BP neural network, the reasoning process is not visible, and the lack of explanation mechanism. Then, we establish the BP-CBR case retrieval model, and utilize the powerful pattern recognition and self-learning ability of the BP neural network to achieve the index classification in case-base, reduce the search space, and improve the retrieval speed. More than that, we also realized the case similarity retrieval algorithm by the good feature extraction of BP neural network. Before the case retrieval, we established the knowledge frame network of energy-saving reconstruction and divided cases into different rank. Finally, we verified an enterprise-class energy-saving retrieval instance of the cement industry, and confirmed the validity of the BP-CBR case retrieval model.

2. CBR and BP Neural Network

2.1. CBR

The case-based reasoning technology simulates the cognitive psychological process of human being, and solves the current problems by using past practical experience. When faced with a new problem, the CBR will compare differences of occurred background and relevant parameters between the old and new problem, and make some proper adjustments and amendment to similar problems, that is, to re-use the previous information and solve the current problems [3].

CBR technology does not need to master the explicit domain knowledge model, thus avoiding the bottleneck of knowledge acquisition during the traditional RBR. And the incremental self-learning mode will allow coverage of the CBR case base continues to improve with continued use, and get a better reasoning effect. A typical CBR process is mainly composed of case retrieval, case reuse, case correction and case preservation, as shown in Fig. 1.

2.2. BP Neural Network

The artificial neural network (ANN) is a simulation of the structure and function of biological neural networks, which is used to deal with some problems that general mathematical model difficult or impossible to solve. The BP neural network model is the most commonly used network with one-way transmission and multi-layer feed-forward. The learning ability of hidden layer unit inside the BP network model can ensure its powerful information processing capacity, and the model is simple and practical and is widely used in pattern recognition, pattern classification, pattern matching and other fields.

BP neural network model is powerful, but there are also problems such as learning slowly, local minimum value, and network structure determination without scientific theory guidance. At present, the ANN is being developed a large-scale application form, using automatic, efficient network structure design methods will be able to enhance the efficiency of project [4]. A typical three-layer BP neural network model is shown in Fig. 2. It includes an input layer, an output layer and a hidden layer, and the node unit activation function is usually a sigmoid type. BP neural network can be regarded as a highly nonlinear mapping from input to output.

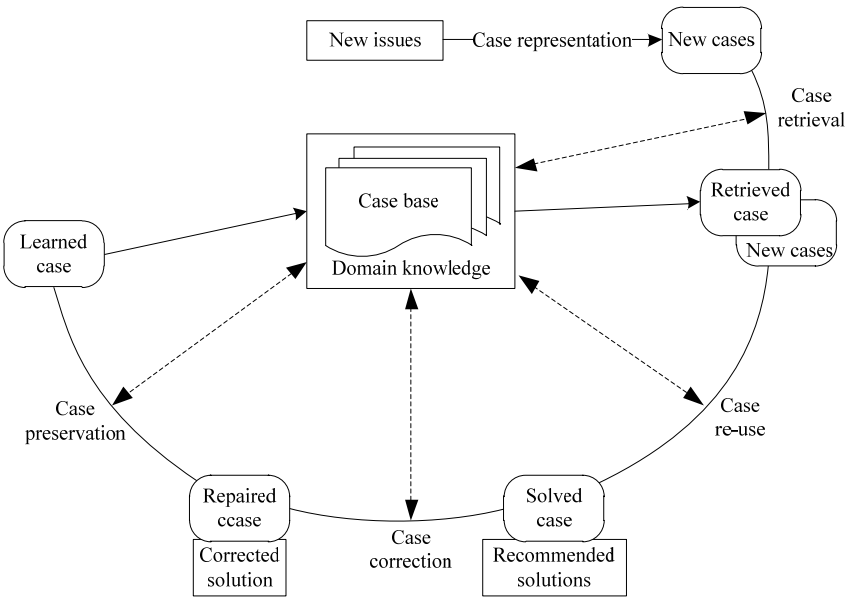

Fig. 1. Case-based reasoning process.

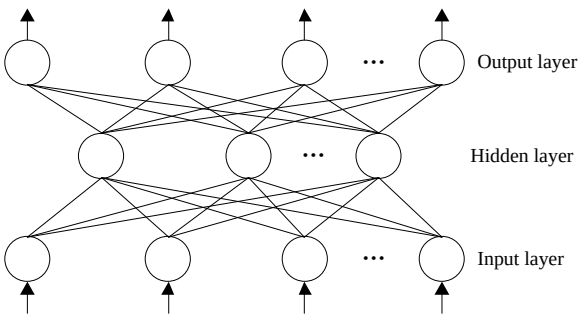

Fig. 2. BP neural network structure.

3. The Design Ideas of the Case Retrieval in Cement Enterprise KM

At present, the effective implementation of KM has become an important factor of the enterprise to reshape its core competitiveness. Inside the cement companies, the efficient and comprehensive management is come from the encoded data with a high degree of structure. But for that hard-to-codified tacit knowledge, the enterprise is lack of effective organization and management. This tends to make the enterprise in the face of new problem, even before have encountered and treated the same or similar circumstances, but because of the lack of platform support, failed to save the full case records, resulting in problems processing mode cannot go on. Obviously, this situation will lead to a duplication of investment in enterprise human, material and financial, even make the efficiency and effectiveness of the problem solving stranded in a lower level [5, 6]. Therefore, improving the level of case knowledge organization and management, completing the case retrieval efficiently is an important way to solve the above problems.

The traditional CBR model can make up for many of the shortcomings of the conventional knowledge processing system, but there are inadequacies: the case indexing difficulties; difficult to complete the definition of case similarity; the size of the case base affects retrieval efficiency; the reasoning process ignores the statistical information. The BP neural network model also has limitations: high require for the typicality and quantity of case data; reasoning process is not visible; the knowledge processing outside the system “boundary” is very inefficient. While both have flaws, but at the same time there are complementary. BP neural network has strong robust and feature extraction capabilities, so it can be part of the stage into the CBR.

This article uses the BP neural network to establish the index classification of case base, reducing the search space and improving the retrieval speed. Then, we realize a case similarity retrieval algorithm with BP neural network to improve the case retrieval capabilities of traditional CBR.

4. The Case Retrieval Model of Energy Saving Reconstruction

4.1. The Case Representation of Energy Saving Reconstruction

The case representation is the premise and foundation of the entire CBR research. The article uses the frame to extract the properties characteristic of the case. The frame name, a number of grooves and sides are forming a complete frame. Each groove describes a part of case, a side in this part describes a group of characteristic attributes, a groove value or side value is a particular feature value. The feature value may be either a specific value, and may be an operation or process, can also be the name of another frame, which enables the lateral calls between the frames and create a complex frame network. In the frame network, the lower frame can inherit the public groove from the upper frame, and can also be supplemented or modified, so not only reduce the redundancy and ensure the consistency of knowledge [7].

Cement enterprise case content of energy-saving relates to the different production processes and implementation direction, so we use the frame network to describe the case composition, as shown in Fig. 3. The energy-saving knowledge frame (KF) described a complete enterprise-class energy program. The frame contains a public groove and a feature groove, used to describe the general knowledge and characteristics knowledge of the case known part. The feature groove value is set to a specific frame name for the feature KF group, horizontal linkages between the feature frames. The feature KF group by seven independent frames, each frame has a dedicated inherited groove used to store public properties inherited by the upper frame. So far, we have established horizontal and vertical ties between the frames, achieved the calls between different frames, and the channels that upper to lower frame.

4.2. BP-CBR Case Retrieval Model

Based on the above idea, we combine the respective advantages of the BP neural network with CBR to create the BP-CBR case retrieval model, as shown in Fig. 4.

First of all, using the BP neural network pretreat the energy-saving case sample to achieve the classification of the case index. There are feature properties inside the vector of the input layer, and typical energy-saving cases inside the vector of the output layer. The case index process is divided into model-learning and retrieval classification. Model-learning is input training sample to the BP neural network for training network model, and then use the trained network to establish the index classification of sub-case base. The case index

classification is shown in Fig. 5. Index classification is input the target case to the trained classification network model, and gets the corresponding sub-case base. Then the system retrieves similar cases from the sub-case base, and makes better retrieval efficiency even when a larger scale case base.

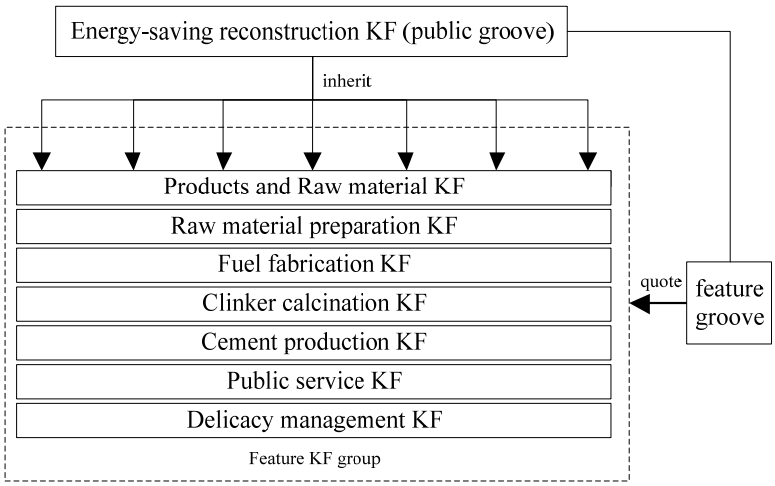

Fig. 3. The KF network of energy-saving reconstruction case.

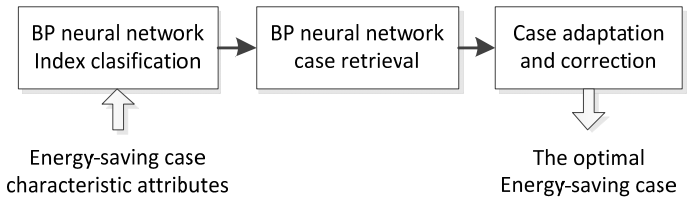

Fig. 4. BP-CBR case retrieval model.

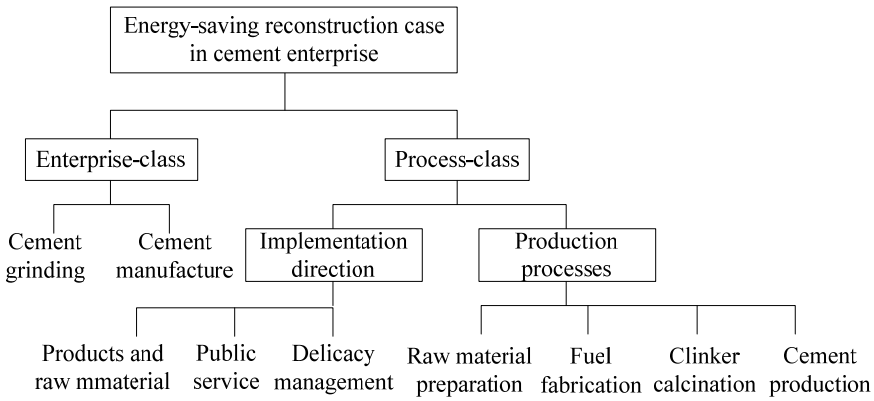

Fig. 5. The index classification of Energy-saving reconstruction case.

Second, the system can use the BP neural network algorithm to retrieve similar cases in the sub-case base in order to get the optimal energy-saving case. BP neural network has the advantages of distributed storage, and feature extraction function, but there is also exists some drawback. So, we can use the genetic algorithm to learn the weights of BP network, and make weights generating automatically and efficiently. Then, we will be able to meet the computing requirements to build a three-layer BP network structure, as shown in Fig. 6. The input layer nodes composed of two parts, one each for the characteristic properties of the input target case T and source case S. The output layer node gets the similarity value of the two cases after the characteristics extracted and parallel processing through the hidden layer. The number of hidden layer nodes is determined by analyzing the experimental data.

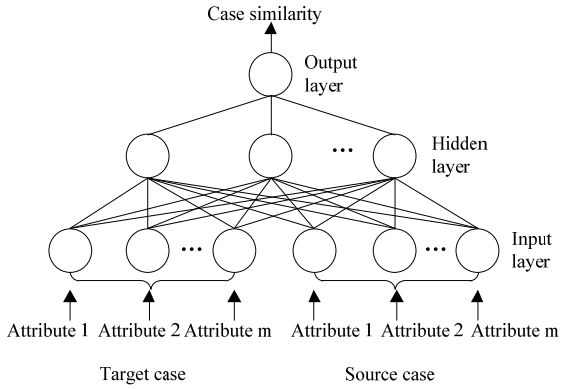

Fig. 6. Case retrieval structure based on BP neural network.

Before the sample input of target case T and source case S, you need to use the membership function to pre-process the data, and ensure that the input range in [0, 1]. The characteristic information with two values can be directly assigned to 0 or 1. The activation function takes the sigmoid function:

$$y_k = \varphi(v_k) = a \cdot \frac{1-\exp(-bv_k)}{1+\exp(-bv_k)}, \quad (1)$$

In the equation, v_k represents the neuron nodes input-weighted sum, y_k represents the node output. The control parameter a values 1.72 and the control parameter b values 0.67. Disposed there are n source cases in sub-case base, and input the target case, the single calculated output of the network is the similarity p_i between the target case T and the i-th source case s_i, i = 1, 2, 3…n. The BP neural network retrieved to get the similarity vector $p = \{p_1, p_2 ..., p_n\}$, and the vector represents the case similarity the step membership function value complete works. It is represented by a set of discrete values, such as (0.35, 0.5, 0.7, 0.85). Then, we choose a collection of similar cases from the sub-case that meet the threshold requirements. The collection called candidate set C of search results.

Assumptions there are t similar cases in the candidate set C, the each similar case corresponding to the energy-saving program output is a one-dimensional vector f_i composed by different energy-saving measures. The retrieval function of the neural network is not the simple sum of output results, but by the respective weights w_i of the sum of the final energy-saving program output F:

$$F = \sum_{i=1}^{t} w_i \times f_i, \quad (2)$$

Among them, the calculation of the energy-saving program output weight vector $w = \{w_1, w_2 ..., w_t\}$ by the similarity of each case, the proportion of computing [8].

5. The Case Retrieval Instance of Energy Saving Reconstruction

Based on the above, the case of energy-saving reconstruction consists of different characteristics KF, and the different frame corresponding to the data sample format will also be different. Therefore, we need to adopt a dynamic neural network structure generated model used to distinguish between the different data samples. The following background to research case retrieval process based on the BP-CBR model for enterprise-class energy-saving case.

We selected a cement enterprise's basic information as the sample vectors input to the trained BP neural network. The basic properties characteristic includes: enterprise status, firm size, region, production process, materials structure, product range, energy varieties, kiln type, heat generation, purchase and sale of electricity and clinker, compressive strength, mill types, power structure, standard type, energy-saving target, and so on. For binary information, such as purchase and sale of electricity (presence of purchase and sale or does not exist), can be directly assigned to 0 or 1 state.

After the trained BP neural network classification pre-processing, the output of the sample results is the index number of the corresponding sub-case base. Samples information shown in Table 1.

Table 1. The classification index samples.

Sample input						Sample output			
Properties						Sample result			Sub
1	0.4	0.5	0.6	0	…	0.03	0.14	0.91	1#
1	0.7	0.5	0.7	1	…	0.21	0.89	0.02	2#
0	0.8	0.7	0.8	1	…	0.84	0.07	0.05	3#

For sample 1, the neural network output (0.03, 0.14, 0.91), match the desired output (0, 0, 1), it should be into the 1# sub-case base for similar cases retrieved, and then start the new retrieval in the sub-case base.

Still focus on sample 1, we input the target case sample to the trained BP neural network that meet the requirements of the sub-case base four candidate set. The similarity of the candidate sets and the target case, and the energy-saving measures vectors of candidate set, as shown in Table 2.

The corresponding entry of the vector of energy-saving measures in the table cannot be fully listed, the part is: composite Portland cement production, waste alternative to traditional fuels, use

of iron and steel enterprises arc slag instead of limestone, the raw materials process control systems, mechanical and pneumatic hybrid delivery system, to increase the amount of fan air intake, optimizing insulation refractories, using far inverter technology, low (high) temperature warm-up power generation, to increase the preheater preheating stage, the use of advanced mill, improved grinding media, using the factory lighting control system, to strengthen heat recovery measures, corporate the meticulous management program content, and so on.

Table 2. Candidate set of energy-saving case samples.

Num	Similarity	Energy-saving measures vectors					
1	0.53	0.13	0.00	0.52	0.00	0.61	…
2	0.67	0.00	0.00	0.75	0.11	0.00	…
3	0.82	0.10	0.00	0.63	0.06	0.00	…
4	0.41	0.08	0.17	0.67	0.00	0.00	…

The similarity vector of the candidate set is shown as (0.53, 0.67, 0.82, 0.41) in table, then we can calculate the corresponding weight vector $w =$ (0.22, 0.28, 0.34, 0.17). Through the formula 2, we can get the output vector of the energy-saving solution F = (0.077, 0.029, 0.652, 0.051, 0.134…), seen by the principle of maximum degree of membership the third corresponding energy-saving measures in the table may be the most suitable in the case to be solved, that is the use of iron and steel enterprises arc residue instead of limestone.

It should be noted that the case retrieval model based on the BP-CBR, the network training and retrieve are two separate processes, meaning that training does not retrieve, retrieving when not training.

6. Conclusions

In the context of knowledge-based economy, how to integrate existing system resources quickly, and implement knowledge management within the enterprise effectively, which are the important factors of the enterprise to reshape their core competitiveness. This article uses the BP neural network to establish the index classification of case base, reducing the search space and improving the retrieval speed. And realize a case similarity retrieval algorithm with BP neural network to improve the case retrieval capabilities of traditional CBR. Finally, through a case instance of cement energy-saving reconstruction to achieve the BP-CBR retrieval process, and received a good retrieval effect.

References

[1]. Man Xu, Haiyan Yu, Jiang Shen. New algorithm for CBR-RBR fusion with robust thresholds, *Chinese Journal of Mechanical Engineering*, Vol. 25, Issue 6, 2012, pp. 1255-1263.

[2]. Tao Liang, Xiaoyan Ma, Ruijuan Yang, Wei Cheng. Study on Radar Fault Diagnosis Systems based on ANN and CBR, *Journal of Air Force Radar Academy*, Vol. 24, Issue 2, 2010, pp. 91-93.

[3]. Jiankang Liu, Bing Jiang. The Building of Decision Support System using Case-based Reasoning Techniques and Its Application in Rural Surplus Labor Problem, *JDCTA: International Journal of Digital Content Technology and its Application*, Vol. 6, Issue 14, 2012, pp. 220-227.

[4]. Xuefeng Jiang, An Effective Decision Support System based on Neural Networks and Its Application, *IJACT: International Journal of Advancements in Computing Technology*, Vol. 5, Issue 1, 2013, pp. 37-45.

[5]. Alavi M, Leidner D., Knowledge Management and Knowledge Management Systems: Conceptual Foundations and Research Issues, *Mis Quarterly*, Vol. 25, Issue 1, 2009, pp. 107-136.

[6]. Junjie Zhang, The System Architecture and Fulfilling Thought of Case-Based Reasoning for Enterprise Knowledge Management, *Journal of Intelligence*, Vol. 30, Issue 5, 2011, pp. 130-133.

[7]. Wuhua Wei, Research on Knowledge Management System with Intelligence based on CBR and XML, *Computer Engineering and Design*, Vol. 27, Issue 14, 2006, pp. 2608-2610.

[8]. Lungen Wang, Zhiqiang Yang, Study on Fault Diagnosis of Equipment Based on BP Neural Network and CBR, *Ship Electronic Engineering*, Vol. 32, Issue 6, 2012, pp. 118-120.

Sensors & Transducers, Vol. 21, Special Issue, May 2013, pp. 117-121

Sensors & Transducers

http://www.sensorsportal.com

Study on Hickory Plant Environment Management Based on Web-GIS

[1] Nuoqianjin HU, [*2,3] Jiajia YU

[1,] Department of Resource Environment & Urban and Rural Planning, Zhejiang Gongshang University, Hangzhou, 310018, China

[*] Zhejiang Institute of Mechanical & Electrical Engineering, No. 528 Binwen Road, Hangzhou, 310053, China

[3] College of Biosystems Engineering and Food Science, Zhejiang University, 866 Yuhangtang Road, Hangzhou, 310058, China,

[1] E-mail: nuoqianjinhu@163.com, jiajiayu163@163.com

Received: 23 March 2013 /Accepted: 14 May 2013 /Published: 30 May 2013

Abstract: In this paper, Web-GIS is imported to manage hickory environment condition date, which can make the date visualize and direct-viewing, and also can easily give advises to the farmers where is good for hickory growing. The data including longitude, latitude, altitude, PH value, hydrolysable nitrogen, Olsen P and available K, which was measured by every 5 kilometers in Lin'an City (a city in Zhejiang province in China). These data were converted into map file format - .shp by ArcView. Then geo-spatial interpolation techniques - Kriging were applied to infer the value of unknown points in Lin'an's map. The Web-GIS-Based Information System was developed by Mapserver (one of the open source WebGIS) and C# in Visual Studio 2008. The hickory plant environment management system can help farmers easily find the environment condition and give advises whether the place is suitable for hickory's growing. *Copyright © 2013 IFSA.*

Keywords: Hickory, Web GIS, Information system, Mapserver.

1. Introduction

Hickory nuts is a kind of dried fruit, belong to Juglandaceae Carya (Carya Nutt), there are 18 species and 3 varieties in the world [1]. In China, Hickory mainly grow in Zhejiang and Anhui provinces at the junction of Tianmushan area, located in north latitude 29° -31°, longitude 118° -120°, with particular reference to Lin'an hickory-based. Hickory is a kind of neutral to slightly overcast plants, has high demands to the climate of growth environment, hi cool and humid climate, require an altitude of 200 to 900 meters of hills, slope less than 25°, between the soil pH 5.5-7 (slightly acidic to neutral) as well as the appropriate content of organic matter [2-4].

Carry out the hickory WebGIS Management Information System has become a concern of society and the focus of government who is eager to carry out research and the important issue to be addressed. The system's research has contributed to increasing the production of hickory, making raising income of the farmers in hickory-producing areas, and promoting the local government's fiscal revenue,balancing the expected benefits between social and environmental which can effectively minimize the natural factors harm on the hickory .So to carry out the hickory

WebGIS Management Information System really has a broader application prospects.

At present, WebGIS has been widely used in various areas, including wetlands [5], landslide monitoring [6], and the regional air quality observations [7-9]. There are many WebGIS platforms such as ARCIMS, GeoMedia, MapServer, OpenMap, and GeoServer, etc. So it is easy for us to develop this idea for hickory WebGIS Management Information System.

2. Technical Support for the Hickory WebGIS MIS

In our hickory Web-GIS MIS, three main technical support were used, which refers to the developer platform—MapServer, the geo-spatial interpolation technique - Kriging and the web developer platform - Visual studio 2008 with C#.

2.1. The Developer Platform—MapServer

MapServer is an open-source WebGIS developed by University of Minnesota (university of Minnesota, UMN) in the 20th century in 1990s, the core is programmed by C script, which can be easily used in Windows, Lunix, MacOSX and other operating systems. MapServer has many advancements:
1) Advanced graphics capabilities; 2) Supporting a variety of popular scripts and application environments, including PHP, Python, C #, Perl, Ruby, Java, and. NET, etc.; 3) Supporting for the operating system interoperability; 4) Supporting for multiple open Geospatial Consortium OGC (Open Geospatial Consortium) standards such as WMS (C/S), non-operational, WFS (C/S), WMC, WCS, Filter of decoding (Encoding), LD, GML, SOS, and OM, etc.; 5) Supporting a variety of vector and raster data sources, and supporting sub-block vector and raster data; 6) Support projection transformation and the standard TrueType fonts. Is precisely because of the strong MapServer portability, openness and security, has been widely used in the industry.

2.2. Geo-spatial Interpolation Technique-Kriging

The Kriging technique is a linear inter- polator which belongs to the best linear un- biased estimator (BLUE) family estimators. Thus, the main purpose of the Kriging technique is to estimate a certain unknown variable $\boldsymbol{X}^*$as a linear combination of the known values $\boldsymbol{X}_i$:

$$X^* = \sum_i \omega_i X_i \tag{1}$$

In this formula $\boldsymbol{\omega}_i$ being the weights computed by the Kriging equations.

3. Design for the Hickory WebGIS MIS

3.1. Data Sources

The data primarily get from our research and the survey data by Zhejiang Forestry College in China. including the altitude, soil hydrolase N, quick-K, the effective P, organic matter, pH value in Lin’an area by every 5 kilometers; Lin'an’s 2002-2007 hickory production; 2007 hickory production in the towns of Lin'an regions; the knowledge of hickory diseases and insect.

3.2. The Flow of the Hickory WebGIS MIS

In this MIS we used vector file as the format of date source, it can be ensure the hickory WebGIS MIS’s basic information, as well as the efficiency of system implementation. The system flowchart is shown in Fig. 1. To achieve the functions of different modules, we have established 9 layers: 3 polygon layers which used to achieve production distribution, weather warning, administrative divisions; 5 point layers which according to altitude, soil hydrolase N, quick-K, the effective P, organic matter, PH value and one line layer (administrative boundaries).Some attribute parameters’ format is shown is Table 1.

The data primarily get from our research and the survey data by Zhejiang Forestry College in China. including the altitude, soil hydrolase N, quick-K, the effective P, organic matter, pH value in Lin’an area by every 5 kilometers; Lin'an’s 2002-2007 hickory production; 2007 hickory production in the towns of Lin'an regions; the knowledge of hickory diseases and insect.

Table 1. The Parameters In hickory WebGIS information management system.

Parameter	Caption
Soil hydrolase N	Units--mg/kg
The effective P of soil	Units --mg/kg
Soil quick-K	Units --mg/kg
PH value of soil	National Standard GB
Organic matter of soil	Units --g/kg
Altitude	Units --meter
Production	The production in 2007 in rural as a unit

3.3. System Architecture for Hickory WebGIS MIS

System mainly includes hickory plant suitable analysis system, weather warning system, yield forecasting system, pest and disease expert decision-making system.

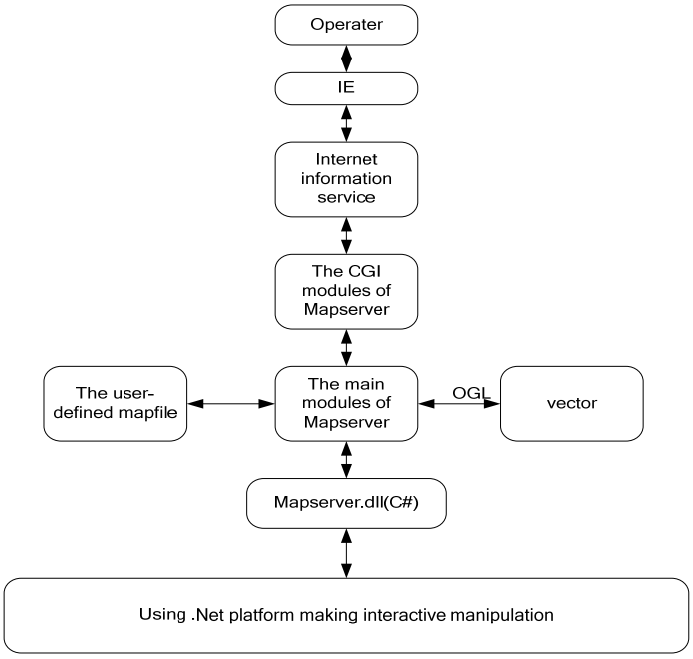

Fig. 1. The flowchart of hickory WebGIS information management system.

Hickory plant suitable analysis system, that is, mainly make analysis of altitude and soil organic matter to ensure if the surroundings is suitable for hickory plant , through the operator entered the region to assess whether it is a large area suitable for planting hickory cultivation.

Weather warning system, that is, according to the season and the region to give an advice of early warning forest protection rating, and warning levels for different suggestions for actions.

Pest and disease expert decision-making system, that is, the operator depending on the chosen forest hickory tree symptoms may be given to the prevalence of pests and diseases, and to give treatment advice.

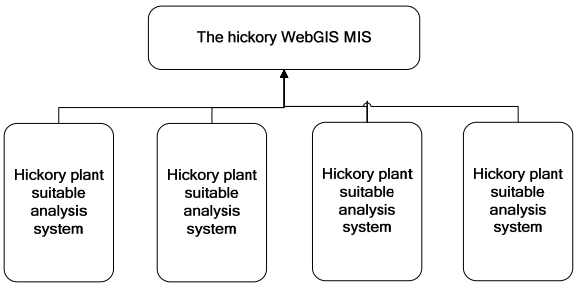

Fig. 2. The overall structure of hickory WebGIS information management system.

4. The Hickory WebGIS MIS

Hickory plant suitable analysis system (Fig. 3). From this sub-system, in addition to the basic operation of the map such as zoom, the alternative view different properties of the distribution of parameters which include altitude, soil hydrolase N, quick-K, the effective P, organic matter, PH value and so on. Operator can also after enter into the sub-system, click on the map in any one area, the left column will also be prompted to give information to the point of information and the results of the analysis given to whether suitable for planting hickory rating criteria.

Weather Warning System (Fig. 4). From this sub-system, Operator can find the current season, and then the system will give different temperature grades warning.

Yield forecasting system (Fig. 5). From this sub-system, operator can fill the in the need to the year, and click OK, Fig. 5b will show the results. Clicking the button of view or view the graphical trend charts can show the historical data of Linan hickory in different ways.

Pest and disease expert decision making system (Fig. 6) From this sub-system, the operator clicks on the incidence of symptomatic plants in different locations, and selects it, then clicks Next to start the decision-making, or chooses to re-select the Empty the contents and re-select the previous selection.

5. Conclusion

This article was based on WebGIS, using .Net platform and the open-source WebGIS- Mapserver to achieve the Hickory WebGIS management information system .Make an implement on the remote control of hickory production and the protection of cultivation; a networked system for information transmission and dissemination; an information analysis and processing model; the visualization of information services and decision-making.

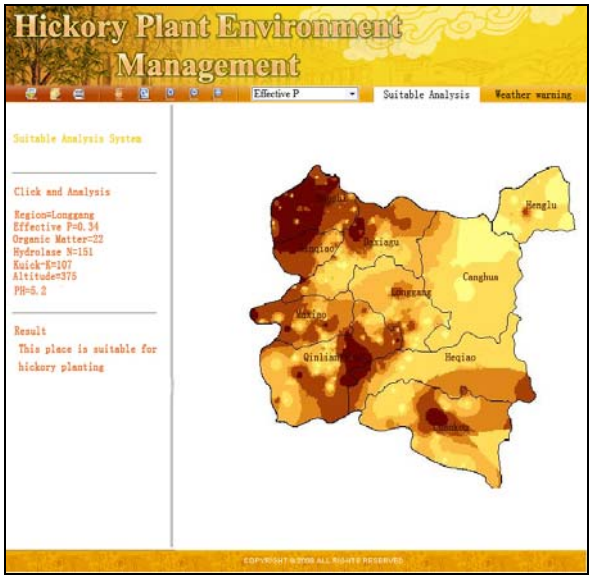

Fig. 3. Hickory plant suitable analysis system.

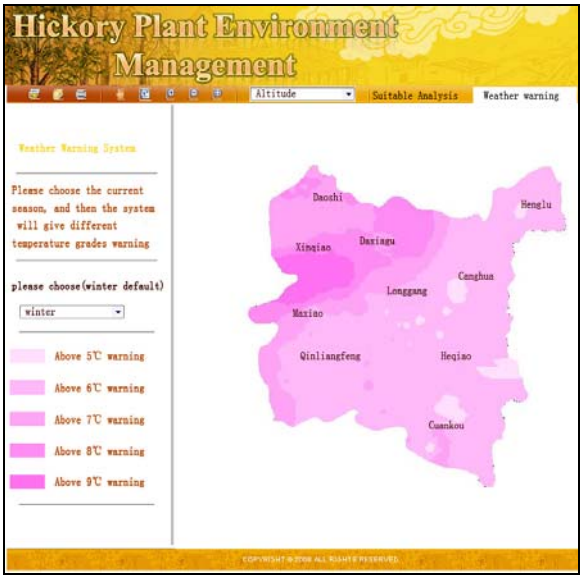

Fig. 4. Hickory Weather Warning System.

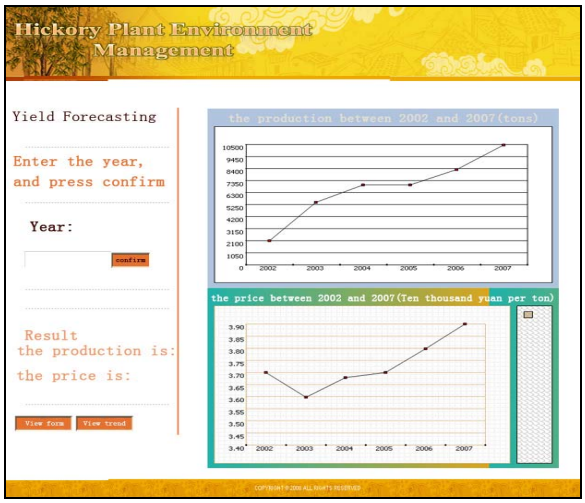

(a)

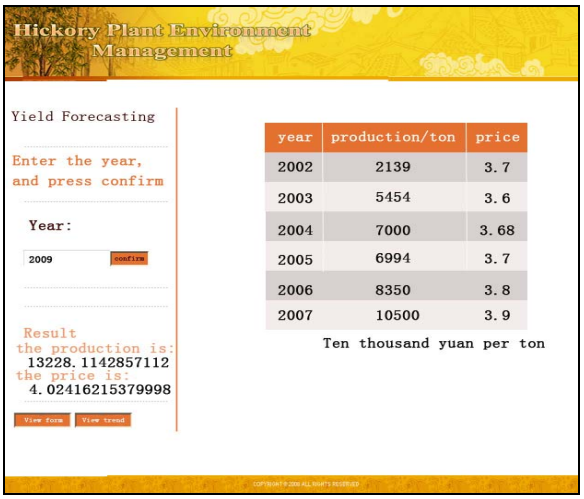

(b)

Fig. 5. Hickory yield forecasting system.

(a)

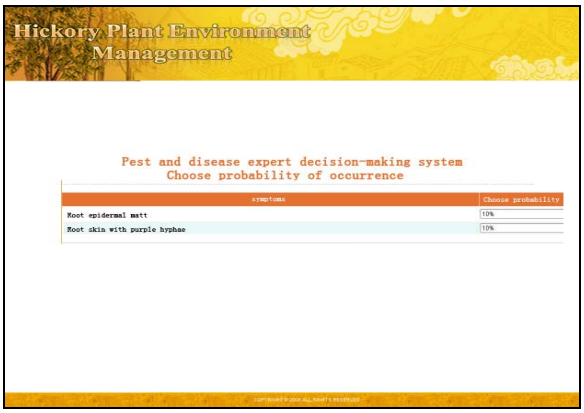

(b)

Fig. 6 (a-b). Expert decision-making system of diseases and insect pests.

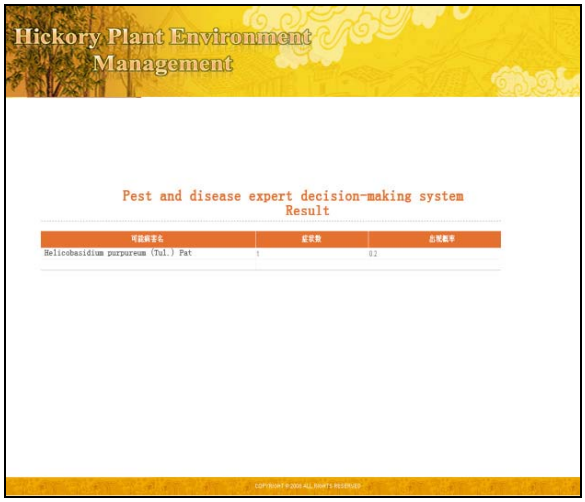

Fig. 6c. Expert decision-making system of diseases and insect pests.

References

[1]. F. Lv, J. Huang, Advances in study of Carya Nutt, *Economic Forest Researches*, Vol. 23, Issue 2, 2005, pp. 72-75.

[2]. C. Guo et al., Study on correlation between soil property and fruit quality of carya cathayensis, *Anhui Agricultrual Science Bulletin*, Vol. 14, Issue 21, 2008, pp. 122-123, 188.

[3]. H. Xie, Y. Huang, X. Xue, C. Xu, L. Liu, Growth and development of the carya cathayensis nut, *Journal of Zhejiang Forestry College*, Vol. 25, Issue 4, 2008, pp. 527-531.

[4]. Y. Jia, H. Zhao, C. Niu, Y. Jiang, et al., A WebGIS-based system for rainfall-runoff prediction and real-time water resources assessment for Beijing, *Computers & Geosciences*, Vol. 35, Issue 7, 2009, pp. 1517-1528.

[5]. V. Mathiyalagan, S. Grunwald, K. R. Reddy, S. A. Bloom, A WebGIS and geodatabase for Florida's wetlands, *Computers and Electronics in Agriculture*, Vol. 47, Issue 1, 2005, pp. 69-75.

[6]. K. Karatzas, E. Dioudil, N. Moussiopoulos, Identification of major components for integrated urban air quality management and information systems via user requirements prioritization, *Environmental Modelling & Software*, Vol. 18, Issue 2, 2003, pp. 173-178.

[7]. Y. Luo, S. Fu, L. Zhang, Y. Zhou, Effects of altitude on growth and yield in Carya cathayens, *Economic Forest Researches*, Vol. 26, Issue 1, 2008, pp. 71-73.

[8]. D. A. Cobb, A. Olivero, Online GIS service, *The Journal of Academic Librarianship*, Vol. 23, Issue 6, 1997, pp. 484-497.

[9]. Q. Zhang, M. Li, W. Zhang, H. Zhang, et al., Research on log management system of geographical information sharing platform based on WebGIS, *in Proceedings of the Conference on '2012 20th International Conference on Geoinformatics'*, Hong Kong SAR, China, 15-17 June 2012, pp. 1-5.

Sensors & Transducers, Vol. 21, Special Issue, May 2013, pp. 122-127

Sensors & Transducers

http://www.sensorsportal.com

Using Energy Difference for Speech Separation of Dual-microphone Close-talk System

[1] Yi Jiang, [2] Ming Jiang, [3] Yuanyuan Zu, [3] Hong Zhou, [1] Zhenming Feng

[1] Department of Electronic Engineering, Tsinghua University, Beijing, 100084, P. R. China

[2] Deparment of optoelectronic science and engineering, Huazhong University of Science and Technology, Wuhan, Hubei, 430074, P. R. China

[3] Quartermaster Equipment Research Institute, Beijing, 100010, P. R. China

E-mail: yijiang2013@yeah.net

Received: 23 March 2013 /Accepted: 14 May 2013 /Published: 30 May 2013

Abstract: Using the computational auditory scene analysis (CASA) as a framework, a novel speech separation approach based on dual-microphone energy difference (DMED) is proposed for close-talk system. The energy levels of the two microphones are calculated in time-frequency (T-F) units. The DMEDs are calculated as the energy level ratio between the two microphones, and used as a cue to estimate the signal to noise ratio (SNR) and ideal binary mask (IBM) for mix-acoustic of the close-to-mouth microphone. The binary masked units are grouped to generate the target speech. Test with speeches and different noises show that the algorithm is more than 95 % accurate. As the T-F units' length increase, the accuracy increase as well. Using automatic speech recognition (ASR) analysis, we show that the proposed algorithm improves speech quality in actual close talk system. *Copyright © 2013 IFSA.*

Keywords: Speech separation, Computational auditory scene analysis (CASA), Ideal binary mask (IBM), Close-talk system, Dual-microphone energy difference (DMED).

1. Introduction

Given the popularity of portable devices, people can communicate anywhere and anytime. Background noise is one of the primary factors in decreasing the performance of portable communication systems and robust automatic speech recognition (ASR) systems. Close-talk equipment, such as mobile phones or headsets, often uses a nearby microphone to improve the quality of speech collection. Even if the microphone is close enough to the mouth, obtaining clean speech is also difficult in complex auditory scenes, especially in noisy environments such as railway stations, airports and the subway.

In recent years, great progress has been made in the study of the computational auditory scene analysis (CASA) algorithm for speech separation [1], ASR [2], and robust speaker identification [3] from mixture acoustic signals. Using CASA as the framework, the acoustic input is divided into auditory segments as time frequency (T-F) units by gammatone filters. Each T-F unit likely comes from one single source [4]. Wang proposes the ideal binary masks (IBM) as the critical computational goal for a CASA based system. Many studies have confirmed the good performance of IBM in different noise conditions and low SNR conditions [5]. The key point of CASA methods is to find proper cues to assign each T-F unit to different sources. The main cues in the monaural speech segregation system include pitch [6] and onset/offset [7], which are too complex or sensitive to be used in real live application systems. An inter-aural time

differences (ITD) and inter-aural intensity differences (IID) cues of dual-microphone system is used as a locator to estimate the IBM [8]. The dual-microphone system based on CASA attempts to explain the mechanism of the human ears other than speech enhancement.

Another distinguished class of dual-microphone speech enhancement techniques is the coherence-based algorithm. In a dual-microphone hearing aids system, the energy level difference and coherence function are used to get the front target sound in noisy environment [9, 10]. The aids system estimates the power spectral density (PSD) of the noise, which makes it hard to reduce the non-stationary noise. The distance between the two microphones in hearing aid system is also small, which make it hard to be used in close-talk system. A dual–microphone mobile phone system uses spectral subtraction to get the target speech [11]. The noise difference between the two microphones reduces the mobile phone's performance.

In the close-talk system, one microphone is near the mouth. The present study positions another microphone far from the mouth. Both the theoretical calculations and the experiments indicate that the energy difference between the two microphones increases substantially for a lateral sound source as distance decreases. Then, the DMED difference between the close talk and far noise can be used to separate the target speech from the noise.

2. Dual-microphone Speech Separation

The structure of the dual-microphone system is shown in Fig. 1. Two microphones in different positions are used to independently collect the target speech and noise. Using the energy level difference as separation cue, the complex audio scene can be viewed as two sound sources: a close target speech and a far environment noise. The aim of the system is to separate the target speech signal from the mixture signal of the close microphone A.

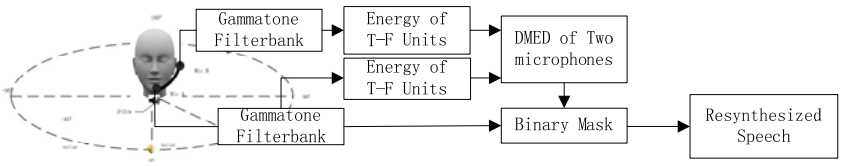

Fig. 1. Schematic diagram of the dual-microphone system.

With the framework of computational auditory scene analysis (CASA), the proposed closed-talk speech segregate processing consists of two parts: the same auditory filter bank is used to decompose the input mixture signal. Then energy is calculated in each frame as T-F units respectively. Then the energy difference between microphone A and B is used as cue to generate the binary mask. Subsequently, the binary masks are affected on the decomposed signal of microphone A to group the target speech.

3. Binary Mask Estimation

Background noise acoustically mixed with clean speech is additive in this paper. This assumption is described by the following equation:

$$X_A = S_A + N_A, \tag{1}$$

$$X_B = S_B + N_B, \tag{2}$$

where x_A and x_B refers to the mixture signal obtained by the dual-microphone A and B, respectively, which compose of target speech and environment noise. In this paper, the position of microphone A is close to the target speech. s_A and s_B refers directly to the target speech signal reaching microphone A and B, respectively. N_A and N_B is the noise signal received by microphones. The distance between A and B is less than 10 cm. the time delay of the sound between the two microphones is less than 0.3 ms, and is omitted in the energy calculation.

The energy of the mixture signal can be calculated as

$$\|X_A\|^2 = \|S_A\|^2 + \|N_A\|^2 + 2\|S_A\|\|N_A\|\cos\theta_A, \tag{3}$$

$$\|X_B\|^2 = \|S_B\|^2 + \|N_B\|^2 + 2\|S_B\|\|N_B\|\cos\theta_B, \tag{4}$$

where θ_A and θ_B indicate the angle between the vector of target speech and noise in microphones, respectively. Based on CASA, the signals received by microphones are divided into a time sequence of T-F units by gammatone filterbank and subsequent time windowing. In each T-F unit k points or k-dimensional vectors are present in time sequence. The signal of microphone A can be described as

$$X_A(t, f) = [x_1 x_2 ... x_k], \tag{5}$$

where t and f index are the time and frequency dimension. The energy of one T-F unit can be calculated as

$$\|X_A(t,f)\|^2 = \|S_A(t,f)\|^2 + \|N_A(t,f)\|^2 + 2\|S_A(t,f)\|\|N_A(t,f)\|\cos\theta_A \quad (6)$$

$$\|X_B(t,f)\|^2 = \|S_B(t,f)\|^2 + \|N_B(t,f)\|^2 + 2\|S_B(t,f)\|\|N_B(t,f)\|\cos\theta_B , \quad (7)$$

In practice, $\cos\theta_A$ and $\cos\theta_B$ is usually small, $2\|S_A(t,f)\|\|N_A(t,f)\|\cos\theta_A$ and $2\|S_B(t,f)\|\|N_B(t,f)\|\cos\theta_B$ can be ignored, especially with the increase of dimension k . Then the energy in the system is equal to

$$\|X_A(t,f)\|^2 = \|S_A(t,f)\|^2 + \|N_A(t,f)\|^2 , \quad (8)$$

$$\|X_B(t,f)\|^2 = \|S_B(t,f)\|^2 + \|N_B(t,f)\|^2 , \quad (9)$$

The value of DMED calculates as

$$DMED_{AB}(t,f) = \frac{\|X_A(t,f)\|^2}{\|X_B(t,f)\|^2} = \frac{\frac{\|S_A(t,f)\|^2}{\|N_A(t,f)\|^2} + 1}{\frac{\|S_B(t,f)\|^2}{\|N_A(t,f)\|^2} + \frac{\|N_B(t,f)\|^2}{\|N_A(t,f)\|^2}} , \quad (10)$$

The DMED value of the target speech signal and noise can be described separately as

$$DMED_S(t,f) = \frac{\|S_A(t,f)\|^2}{\|S_B(t,f)\|^2} , \quad (11)$$

$$DMED_N(t,f) = \frac{\|N_A(t,f)\|^2}{\|N_B(t,f)\|^2} , \quad (12)$$

The $DMED_S(t,f)$ indicate the DMED value of the close sound in frame t and frequency f , and the $DMED_N(t,f)$ indicate the DMED value of the far noise in framea. In close-talk system, they can be fixed to certain value as $DMED_S$ and $DMED_N$. Then the dual-microphone energy difference is.

$$DMED_{AB}(t,f) = \frac{\|X_A(t,f)\|^2}{\|X_B(t,f)\|^2} = \frac{\frac{\|S_A(t,f)\|^2}{\|N_A(t,f)\|^2} + 1}{\frac{\|S_A(t,f)\|^2}{\|N_A(t,f)\|^2}\frac{1}{DMED_S} + \frac{1}{DMED_N}} , \quad (13)$$

where $\frac{\|S_A(t,f)\|^2}{\|N_A(t,f)\|^2}$ indicates the SNR in each microphone A T-F units. Thus $DMED_{AB}(t,f)$ relates to the SNR.

In CASA, the single microphone IBM is generated based on the signal energy and noise energy in the mixed signal. The output of CASA segregation is in the form of a binary T-F mask that indicates whether a particular T-F unit is dominated by speech or background noise.

$$M(t,f) = \begin{cases} 1 & if\ \|S_A(t,f)\|^2 \ge \|N_A(t,f)\|^2 \\ 0 & others \end{cases} , \quad (14)$$

where $M(t,f)$ is the binary mask value to the T-F unit. The variable "1" indicates T-F unit that belongs to the target speech. The variable "0" indicates that the T-F unit is dominated by noise and belongs to the noise.

In this paper, we use the cues of DMED to estimate the IBM of the nearby microphone A, and $\|S_A(t,f)\|^2 = \|N_A(t,f)\|^2$ is also the separation threshold of the T-F units of microphone A. The separation threshold would be

$$DMEDT_{AB} = \frac{2}{\frac{1}{DMED_S} + \frac{1}{DMED_N}} , \quad (15)$$

This indicates that in the dual-microphone system, the harmonic mean of the DMED can be used to generate the binary mask.

The difference of the two microphones can also be described as

$$DMED_{AB}(t,f) = DMED_S + \frac{1 - \frac{DMED_S}{DMED_N}}{\frac{\|S_A(t,f)\|^2}{\|N_A(t,f)\|^2}\frac{1}{DMED_S} + \frac{1}{DMED_N}} \quad (16)$$

Combined with the result of HRTF and microphone location of the close-talk system, $\frac{DMED_S}{DMED_N} > 1$. The value of $DMED_{AB}(t,f)$ increases with the increasing of $\frac{\|S_A(t,f)\|^2}{\|N_A(t,f)\|^2}$ in each T-F unit.

The binary mask for close microphone is estimated

$$DM(t,f) = \begin{cases} 1 & if\ DMED_{AB}(t,f) \ge DMEDT_{AB} \\ \gamma & others \end{cases} , \quad (17)$$

γ sets to zero to estimate the IBM. In common application, we can adapt the value from zero to one to retain part of the noise mainly units.

4. Performance and Comparison

The DMED based separation algorithm transfers the IBM of one microphone system to the dual-microphone system.

A testing corpus is employed, which created with one clean speech and different noises. The speech materials are chosen from TIMIT corpus, and noise materials come from noise 92. The mask accurate between IBM and DMED is compared in different SNR conditions. We also use actual recordings to evaluate it performance with standard ASR system.

4.1. Testing Corpus Setup

1) A simulated testing corpus.

A simulated testing corpus is created as follows to conduct an SNR evaluation:

$$X_A = S_A + N_A, \tag{18}$$

$$X_B = \frac{S_A}{a} + N_A, \tag{19}$$

where A and B is the index of two microphones. $a > 1$ indicates weakening of the target speech energy between microphone A and microphone B, which is 10 in this paper. The noise is always far away from microphone A and B, and so the energy level is almost the same to microphones A and B. The time delay or the time difference of the two microphones is therefore not considered.

The mixture signal of microphone A with different SNRs is generated to test the performance of the DMED-based algorithm.

$$SNR_A(t) = 10\log_{10}{}^{\sum_t S_A^2(t)/\sum_t N_A^2(t)}, \tag{20}$$

The S_A is certain and fixed at "sx198" and is chosen from TIMIT test sets. Then the power of NA is adjusted to generate the mixture signal in different SNRs. The NA and weaken speech signal are used to generate the mixture signal of microphone B as equation (19).

2) Actual recordings of a dual-microphone system.

The actual close-talk recording system with two-microphone is set up as shown in Fig. 1. Microphone A is about 2 centimeters away from the mouth. Microphone B is posed near the left ear on one head-set. The distance between microphone A and B is almost 10 cm. A noise source is placed about 1.5 m away from the test person.

4.2. Binary Masks Estimation

IBM is one goal of CASA system. Thus, the proposed algorithm is evaluated by SNR estimation and IBM comparison.

1) SNR estimation.

The main principle of IBM is to calculate the SNR of each T-F units. We use the DMED to estimate the SNR in each T-F units.

The actual SNR of the mixture is 0dB with babble noise. The true SNR is calculated by the target signal and far noise signal directly. The predicted SNR is calculated by the equation (13), and the $DMED_S$ is 100, $DMED_N = 1$. As shown in Fig. 3, the DMED based algorithm provides a good estimate (prediction) of the true SNR value.

2) IBM estimation.

The similarity between IBM and the binary masks is calculated as classification accuracy:

$$\text{Accuracy} = \frac{\sum_t \sum_f (DM(t,f) == M(t,f))}{\sum_t \sum_f 1} \times 100\%. \tag{21}$$

where $M(t,f)$ refers to the binary masks generated by equation (14). $DM(t,f)$ refers to the binary masks generated by the algorithm proposed as equation (17), where γ is equal to zero. $\sum_t \sum_f 1$ is the number of total units. The variable t and f, indicates the time frame and frequency channel of the T-F units. A higher accurate would result in better separate performance.

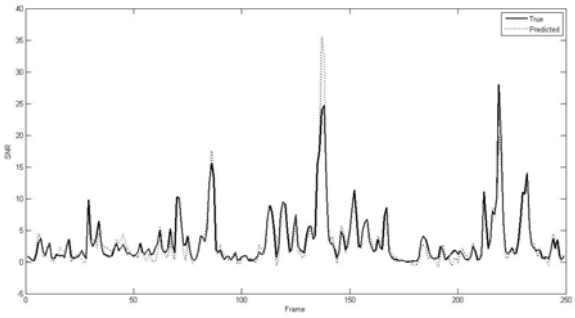

Fig. 3. Comparison between the true SNR values and its' predicted values in T-F units. The channel center frequency of the T-F units is 1000 Hz.

The similarity of the binary mask between the two algorithms is shown. Four types of noise signal are used to generate the mixture signals, which SNR levels various from -30 dB to 30 dB at -5 dB intervals. The accuracies are more than 95 % in all conditions.

The differences between the IBM and DMED-based binary masks are less than 5 % in all conditions. The cue of DMED is robust in different SNRs, especially in higher or lower SNR conditions. Fig. 4 shows that DMED performs better with machine gun noise than with babble, si762, and m109 noise. Stronger correlation between target source and noise, a larger effect of the additional factor $2\|S_A(t,f)\|\|N_A(t,f)\|\cos\theta_A$ and $2\|S_B(t,f)\|\|N_B(t,f)\|\cos\theta_B$, and greater difficulties in separating the mixture signals.

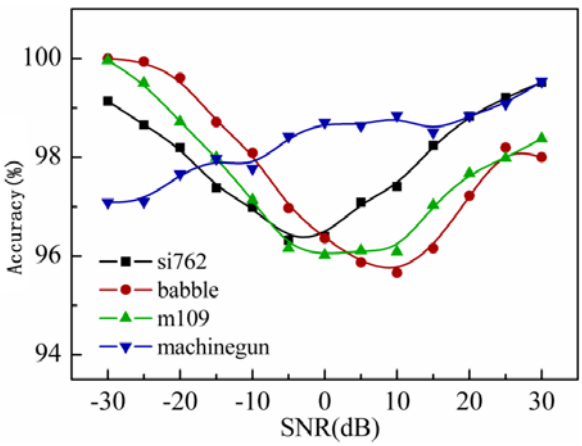

Fig. 4. Accuracy of the DMED-based binary mask.

3) System Performance with various lengths of T-F units

The performance of the proposed method with different lengths of T-F units is given in Fig. 5. Four types of noise and speech "sx198" were used to generate the mixture signal at the SNR level of -5 dB.

By increasing the frame length from 2 ms to 256 ms, Accuracy is increased as well. The best performance is obtained at 256 ms above 97 %. Given the T-F units' increase in length, the correlation between signal and noise are decreased. The smaller the value of $2\|S_A(t,f)\|\|N_A(t,f)\|\cos\theta_A$, $2\|S_B(t,f)\|\|N_B(t,f)\|\cos\theta_B$.

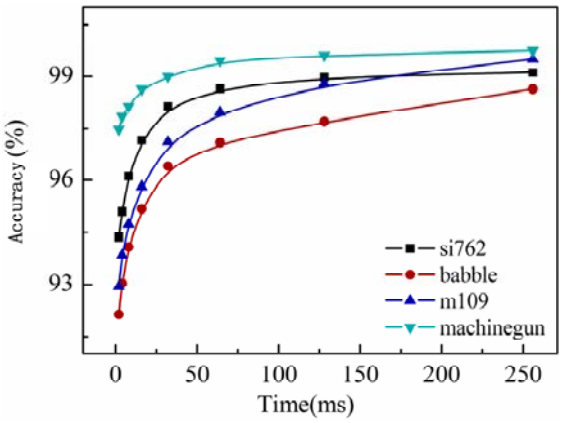

Fig. 5. DMED Performance with various T-F units' lengths.

4.3. ASR Performance with Actual Recordings of a Dual-microphone System

The training dataset is from the standard Mandarin speech database collected under the state-sponsored 863 research program, which involves 127 hours of reading speech data. The test data consist of recordings of two male speakers and one female speaker, which collected in office rooms with babble noise 1.5 m away from the speaker. Each speaker speaks 600 short Chinese utterances involving 200 Chinese names, 200 stock names and 200 Chinese place-names. The acoustic model of the ASR baseline system is based on the structure of GMM-HMM and cross-word mono-phones modeled in 3 states left-to-right HMMs. Each state density is 10 component Gaussian mixture models with diagonal covariance. The baseline acoustic model is trained by the standard HTK3.4 toolkit.

The two microphones system was used to collect the signal as section 4.1. We got 3734 test sentences.

Table 1 shows results of ASR accuracy over 3734 sentences. For this evaluation, the SNR of the mixture signals are from -5 dB to 20 dB with babble, m109 and single speech noise. The sentence accuracy and word accuracy is improved almost 10 % as average by the proposed algorithm. The wiener and spectral subtract algorithm has the lower accuracy, and they would damage the target speech when remove the noise. The dual-microphone PLD algorithm improves the ASR accuracy with the coherence between two microphones.

Table 1. ASR accuracy (%) of the actual recordings.

Algorithm	Sentence Accuracy (%)	Word Accuracy (%)
Original Mixture	64.70	70.78
Spectral subtract [12]	63.63	71.32
Wiener [13]	52.89	61.09
PLD [10]	69.04	76.20
Proposed	73.67	80.28

In Fig. 6. The SNR is estimated from the mixture signal of microphone A. The data of wiener and spectral subtract is got from the close microphone A. power level difference based Dual-microphone algorithm is named as PLD.

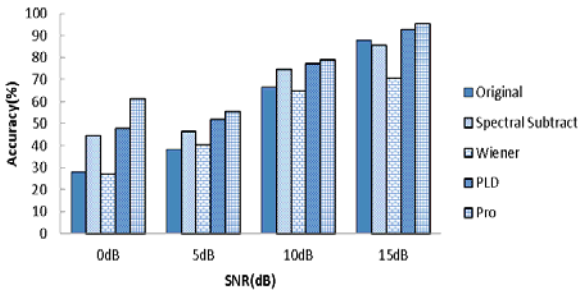

Fig. 6. Recognition accuracy with babble noise.

We observe the proposed algorithm outperforms the single channel wiener and spectral subtract algorithm and the dual-microphone PLD, especially in low SNR conditions. The proposed algorithm can improve the intellective of target speech in noisy environments.

6. Conclusions

An extended algorithm to separate the target speech from far noise is proposed. Compared with the IBM for single microphone, the DMEDs can be used to obtain the optimal binary masks for two microphone systems. Systematic evaluation shows that the proposed algorithm based on DMED performs similarly well to the IBM. In all conditions, the accuracies are more than 95 %. Better performance can be obtained by increasing frame length, which would be a problem in the real-time application. ASR test shown that the proposed algorithm performance better than the other system in babble noisy environments. Obtaining DMED of the target sound

and noise is the key point. Fortunately, in the close-talk system, the great difference of DMED between the close target speech and far noise sound source make it simplify. More work should be done to get more accurate DMED value to improve the performance of this algorithm.

References

[1]. Chao Ling Hsu, De Liang Wang, J. S. R. Jang, Ke Hu, A Tandem Algorithm for Singing Pitch Extraction and Voice Separation From Music Accompaniment, *IEEE Transactions on Audio, Speech and Language Processing*, Vol. 20, No. 5, 2012, pp. 1482-1491.

[2]. Narayanan, A., Xiaojia Zhao, De Liang Wang, Fosler-Lussier, Robust speech recognition using multiple prior models for speech reconstruction, in *Proceedings of the IEEE International Conference on Acoustics, Speech and Signal Processing (ICASSP'2011)'*, Prague, Czech Republic, 22-27 May 2011, pp. 4800-4803.

[3]. Xiaojia Zhao, Yang Shao, De Liang Wang, CASA-Based Robust Speaker Identification, *IEEE Transactions on Audio, Speech and Language Processing*, Vol. 20, No. 5, 2012, pp. 1608-1616.

[4]. G. J. Brown, and Martin Cooke, Computational auditory scene analysis, *Computer Speech And Language*, Vol. 8, No. 4, 1994, pp. 297-336.

[5]. Yi Jiang, Hong Zhong, Zhenming Feng, Performance analysis of ideal binary masks in speech enhancement, in *Proceedings of the 4th International Congress on Image and Signal Processing (CISP' 2011)'*, Shanghai, China, 15-17 October 2011, pp. 2422-2425.

[6]. Guoning Hu, Deliang Wang, A Tandem Algorithm for Pitch Estimation and Voiced Speech Segregation, *IEEE Transactions on Audio, Speech, and Language Processing*, Vol. 18, No. 8, 2010, pp. 2067-2079.

[7]. Guoning Hu, Deliang Wang, Auditory Segmentation Based on Onset and Offset Analysis, *IEEE Transactions on Audio, Speech, and Language Processing*, Vol. 15, No. 2, 2007, pp. 396-405.

[8]. N. Roman, D. L. Wang, and G. J. Brown, Speech segregation based on sound localization, *Journal Of The Acoustical Society of America*, Vol. 114, No. 41, 2003, pp. 2236-2252.

[9]. N. Yousefian, A. Akbari, and M. Rahmani, Using power level difference for near field dual-microphone speech enhancement, *Applied Acoustics*, Vol. 70, No. 11, 2009, pp. 1412-1421.

[10]. N. Yousefian, and P. C. Loizou, A Dual-Microphone Speech Enhancement Algorithm Based on the Coherence Function, *IEEE Transactions on Audio, Speech, and Language Processing*, Vol. 20, No. 2, 2012, pp. 599-609.

[11]. F. Kallel, M. Frikha, M. Ghorbel, A. Ben Hamida, and C. Berger-Vachon, Dual-channel spectral subtraction algorithms based speech enhancement dedicated to a bilateral cochlear implant, *Applied Acoustics*, Vol. 73, No. 1, 2012, pp. 12-20.

[12]. D. S. Brungart, W. M. Rabi Nowitz, Auditory localization of nearby sources: Head-related transfer functions, *Journal of The Acoustical Society of America*, Vol. 106, No. 3, 1999, pp. 1465-1479.

[13]. D. O. Kim, B. Bishop, S. Kuwada, Acoustic Cues for Sound Source Distance and Azimuth in Rabbits, a Racquetball and a Rigid Spherical Model, *Jaro-Journal of the Association for Research in Otolaryngology*, Vol. 11, No. 4, 2010, pp. 541-557.

Sensors & Transducers, Vol. 21, Special Issue, May 2013, pp. 128-134

Sensors & Transducers

http://www.sensorsportal.com

Optimization of Cone Beam CT Reconstruction Algorithm Based on CUDA

[1] Wang LI-Fang, [2] Zhang Shu-Hai

[1] School of Electronics and Computer Science Technology, North University of China
Taiyuan 030051, China

[2] School of Chemical Engineering and Environment, North University of China
Taiyuan 030051, China

E-mail: wanglifang2013@yeah.net

Received: 23 March 2013 /Accepted: 14 May 2013 /Published: 30 May 2013

Abstract: In CBCT, image reconstruction is difficult to meet the requirements of the user real-time reconstruction because data amount of image reconstruction is large, operation complexity is high and the time of reconstruction is long. CUDA based on GPU launched by NVIDIA is very suitable for large-scale parallel computing problem. This paper optimizes cone beam CT reconstruction algorithm by CUDA and improves the speed of weighted back-projection and filtering, and shortens the data access time by using the texture memory and constant memory in CUDA to respectively store the kernel function and the filtered data. The experimental results show that the reconstruction speed and the reconstruction quality are obviously improved compared with the reconstruction method based on GPU. *Copyright © 2013 IFSA.*

Keywords: Cone beam CT, Reconstruction algorithm, Computer unified device architecture, Graphic processing unit, Texture memory, Constant memory.

1. Introduction

Cone beam CT (Cone-Beam Computed Tomography, CBCT) compared with conventional CT system has scanning speed, low amount of radiation, better spatial resolution and other advantages. So it is widely used in medical imaging and industrial testing field [1]. The calculation amount is large and time-consuming is long of the reconstruction algorithm of three-dimensional cone beam CT. Such as Feldkamp-Davis-Kress (FDK) algorithm without any acceleration measures reconstruction the body data of 5123 needs about 90 min. The algorithm is very difficult to satisfy the application requirement. So how to improve the reconstruction speed is the urgent problem to be solved [2].

In recent years many domestic research institutions and scholars have done a lot of research on the acceleration problems of cone beam CT reconstruction algorithm. In literature [3] Fang Xu and Klaus Mueller realized the accelerate of FDK reconstruction algorithm completely in graphics and solved the transmission bottleneck between the CPU-GPU. However due to the operation of floating pipeline is about five times slower than the ordinary texture pipeline, Fang Xu and Klaus Mueller proposed the joint use of floating pipeline and normal pipeline to improve the quality and the speed of image reconstruction and achieved satisfactory results [4]. Literature [5] used multiple textures mapping to improve back-projection speed and reduced the storage amount of intermediate data and the accumulation number of floating point, and used

vertex color channel to realize the distance weighted computing, and used the extension methods to increase the texture units of parallel back-projection, so as to improve the reconstruction speed. Literature [6] used multi-threading technology to achieve the fast parallel of cone beam CT on multi-core platforms. Literature [7] proposed a voxel density modeling based on projection data and realized the fast imaging of cone beam CT. The implementations of these methods need to use API and the implementation processes are more complex.

In 2006, the United States NVIDIA company putted forward a graphics processor based on CUDA (Computer Unified Device Architecture, CUDA) and could bring reconstruction algorithm as general multiprocessor task performed in the GPU by unified programming technology of CUDA. Holger Scher1 etc proposed an accelerating image reconstruction algorithm to the unified architecture[8]. Literature [9] used stream processors in CUDA graphics processors to accelerate the filtering and back-projection calculation and realized the reconstruction acceleration of FDK. But the methods in Literature [9] has high complexity and large calculation amount. For the large computation of FDK algorithm in filtering and back-projection process, this paper rearranges the pre-filtered data by the CUFFT function library in CUDA and computes back- projection by two-dimensional thread block and speeds up the speed of the filter and back-projection. And this paper uses the texture memory and constant memory in CUDA model to respectively store the kernel function and the filtered data, shortens the data access time and realizes the acceleration of FDK algorithm.

2. FDK Algorithm

The FDK algorithm which was proposed by Feldkamp, Davis and Kress in 1984 for the cone beam geometry circular scan trajectory is a kind of three-dimensional image reconstruction algorithm based on a circular orbit scanning filtering back-projection. Compared with the iterative reconstruction algorithm, FDK algorithm belongs to the analytic reconstruction algorithm. The main advantages of this algorithm are as follows. First, the mathematical form of the algorithm is simple and easy to realize for computer hardware system. Secondly in the case of the small rag beam cone angle, this algorithm can obtain satisfactory reconstruction effect and can satisfy the need of practical application. Finally, the mechanical structure of hardware system is simple. FDK algorithm is a general algorithm in engineering practice.

The principle diagram of FDK cone beam reconstruction algorithm is shown in Fig. 1. Ray source S is rotated around the central axis Z. R is turning radius. β is fan angle. θ is the intersection angle of the ray source and the axis X positive direction. For the convenient of computing, the detector in Fig. 1 is a virtual detector. $y'oz$ is virtual detector plane. In the rotation angle θ, the projection position corresponding point of a reconstruction point X in object is Q and the coordinates is (Y, Z). Thus the projection data of the object point can be expressed as $p_\theta(Y, Z)$.

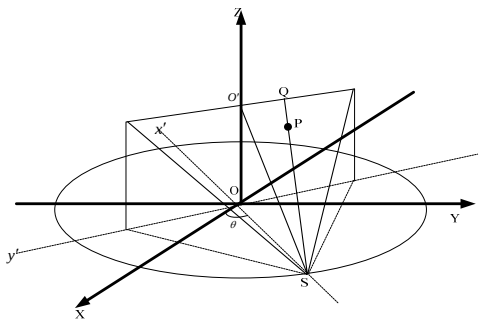

Fig. 1. Principle diagram of FDK.

FDK reconstruction algorithm mainly includes three steps: weighted, filtering and back- projection. The concrete realizations are as follows:

1) Projection data are weighted.

$$p'_\theta(Y,Z) = p_\theta(Y,Z)\frac{R}{\sqrt{R^2+Y^2+Z^2}}, \quad (1)$$

where $\frac{R}{\sqrt{R^2+Y^2+Z^2}}$ is modified weight coefficient, which is the cosine of the intersection angle between any ray and center ray. $p'_\theta(Y, Z)$ is weighted result of projection data.

2) The revised projection data are filtered.

$$p^*_\theta(Y, Z) = p'_\theta(Y, Z) * h(Y), \quad (2)$$

where $h(Y)$ is filtering kernel function and $p^*_\theta(Y, Z)$ is the result of filtered projection data.

3) Weighting and back- projection computing.

$$f(x,y,z) = \int_0^{2\pi} \frac{R^2}{V(x,y,\theta)^2} p^*_\theta(Y(x,y,\theta), Z(x,y,\theta))d\theta, \quad (3)$$

where

$$V(x, y, \theta) = Yr(x, y, \theta) + R, \quad (4)$$

$$Y(x, y, \theta) = \frac{Xr(x, y, \theta)}{V(x, y.\theta)} R \quad (5)$$

$$Z(x, y, \theta) = \frac{R \bullet z}{V(x, y, \theta)} \quad (6)$$

$$Xr(x, y, \theta) = -x\sin\theta + y\cos\theta \quad (7)$$

$$Yr(x, y, \theta) = -x\cos\theta - y\sin\theta \ , \qquad (8)$$

where V is the weighting factor and (Y, Z) is the coordinate of ray source through the rebuilt point $f(x, y, z)$ in detector plane.

In the equation (3), FDK algorithm separately deals with each angle data in the process of filtering and back- projection. The data are independent under different angles. The different reconstruction point is also independent of each other for the data under the same angle. So the parallel degree of this algorithm is high.

3. CUDA Basics

CUDA is NVIDIA's general parallel computing architecture. The C language is used to be development language in CUDA. CUDA don't need to use API in graphics. Its purpose is to make the GPU as a general parallel computing equipment, and to solve the complicated calculation problem. At present, its application has gradually beyond the computer graphics, and has been widely used in all kinds of computation intensive research field.

3.1. CUDA Programming Model

CUDA programming model makes GPU as parallel computing device to run multiple threads. And GPU is the coprocessor of main CPU. The CUDA program compiled by the compiler NVCC is divided into two parts: one part is the host code run on CPU and the other part is device code run on GUP. The host code is generally serial calculation program which controls process. The device code is parallel program for intensive computing.

The parallel computing function on the GPU is called Kernel. Kernel is organized by grid. The internal of each grid is composed by several blocks. Each block is composed by some thread. Essentially, Kernel is executed in the unit of block. Each block is executed in parallel. Blocks can't communicate with each other and also haven't the order of execution. In actual operation, the block is divided into smaller thread group which composes warp. And the warp is the real execution unit. CUDA programming model is shown in Fig. 2 [10].

3.2. CUDA Memory Model

In addition to programming model and execution model, CUDA also has specific memory model which is shown in Fig. 3.

In Fig. 3 each thread has its own registers and local memory. Each block has a piece of shared memory. When thread is executed, it can access to data in different storage spaces. All threads in grid can access global memory. And there are two kinds of read-only memory which can be accessed by all threads: constant memory and Texture Memory. The data of local storage and global memory are be stored in video memory and not stored in register or cache, so the access speed is very slow. Registers and shared memory are cache memory on the GPU and execution unit can be accessed with very low delay. Constant memory and texture memory have cache acceleration which can save bandwidth and have faster access speed.

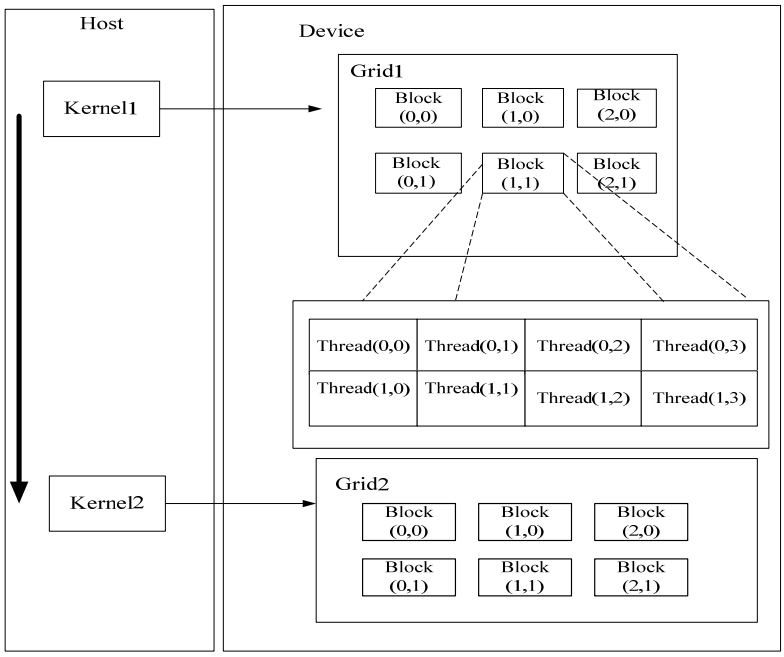

Fig. 2. Programming model of CUDA.

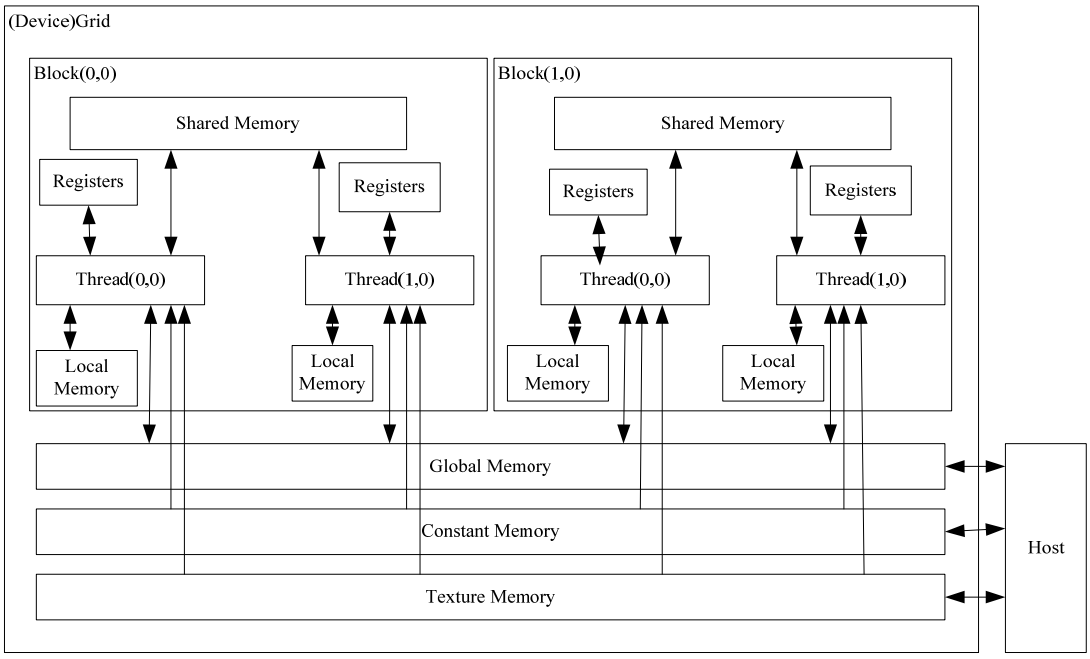

Fig. 3. Storage model of CUDA.

4. Optimizing the FDK Algorithm with CUDA

In the realization process of FDK algorithm, calculation amount of filtering and back-projection is large and the time complexity of calculation is high. Therefore optimizing FDK algorithm is mainly to accelerate the filtering and back-projection. For these problems such as large amount CT data and time-consuming to access, this paper rationally uses constant memory and texture memory in CUDA memory model to access data, and improves the access efficiency.

4.1. The Optimization of FDK Algorithm

The filtering computing on the projection data, which is equivalent to the convolution computation, can be realized by FFT algorithm. NVIDIA's CUFFT for calculating FFT provides some simple interface. Using cores in Nvidia GPU, CUFFT realizes the FFT computation of single precision floating point number in GPU. But because FFT function of CUFFT library can only be applied to complex, the projection data before filtered needs be rearranged. Thus two rows data which real part and imaginary part corresponds to can be simultaneously filtered. This row data rearranged by the two rows is calculated Fast Fourier Transform (FFT) and Inverse Fast Fourier Transform (IFFT).Then the row data is rearranged to the corresponding two rows. This method can reduce filtering operation time to half of the original. The execution process is shown in Fig. 4.

In the projection reconstruction process, the back-projection of all voxels in each angle can be simultaneously calculated, and each thread calculates the back-projection of a voxel. So a three-dimensional thread block is necessary. But the same z axis point (x, y) coordinates are the same, the three-dimensional thread block can lead to formula (5) and (8) repeatedly calculated which reduces calculation efficiency. This paper calculates back-projection by a two-dimensional thread, and each thread completes the reconstruction of series of voxels in the Z axis. In this way, the reconstruction point handled by each thread has same x, y and Y . The formula (9) can be drawn by the formula (6) and (7).

$$Z(x_0,y_0,z_1,\theta)=\frac{R}{V(x_0,y_0,\theta)}\Delta z+Z(x_0,y_0,z_0,\theta) \qquad (9)$$

In formula (9), $Z_1 = Z_0+\Delta Z$. This method can make full use of the z axis correlation of voxels, effectively reduce the complexity of the algorithm, and easy to be expanded. The way that thread is divided is shown in Fig. 5.

Such as formula (9), this new division way makes that every single thread only uses formula (5) to calculate the z of each voxel corresponding, and then uses formula (9) to simply the projection index calculation of other voxels. And this division way also optimizes the access order of the two-dimensional texture, makes full use of the texture cache, and can reduce the register consumption.

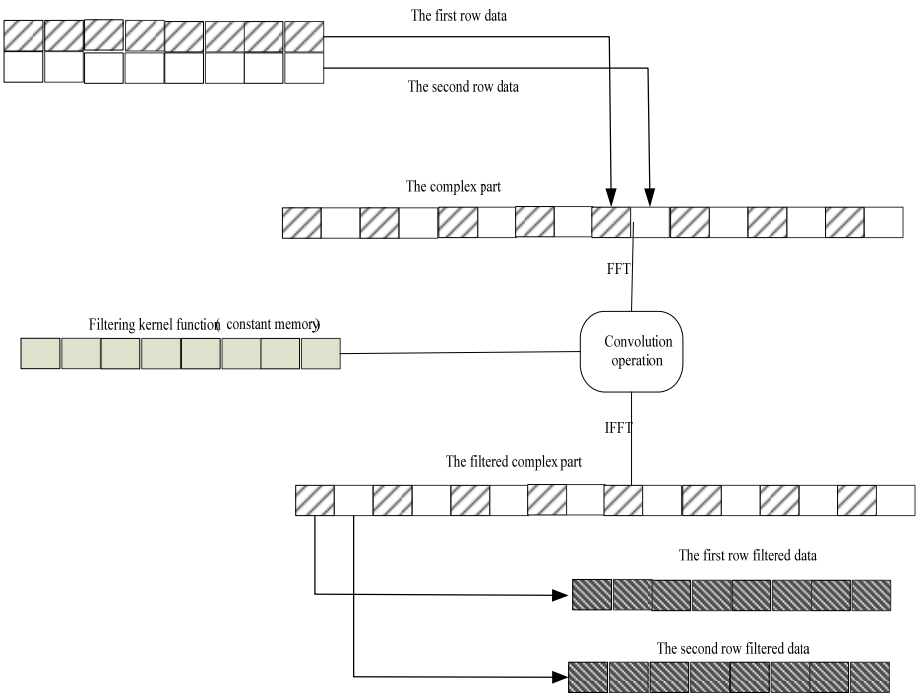

Fig. 4. Implementation process of filtering.

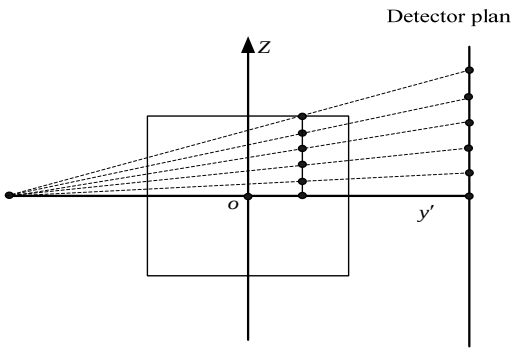

Fig. 5. Thread division of reverse projection.

4.2. Memory Type Optimization

Filtering is that the back-projection data in reconstruction process are made one dimensional filtering. The filtering kernel functions are the same in each row. If the filtering kernel function is stored in the global memory, each row filtering data needs to be read from the global memory. But the global memory in GPU is common memory and furthest away from the arithmetic execution unit, and has no cache. The global memory access requires 400-600 clock cycles and access speed is relatively slow. Due to the constant memory in GPU has cache which access speed is fast, the fixed filtering kernel function can be stored in the constant memory in GPU to improve the access speed. The back-projection process of the FDK algorithm is the part which has the largest calculation amount and most time-consuming. In using CUDA technology, each thread calculates the back-projection of one pixel in the slice image and adds the calculation results to the corresponding pixel. First each thread calculates its projection coordinates (Y, Z), and then interpolates its back- projection. Due to projection data is random accessed in the interpolation process, direct picking pretreated data in video can cause an access violation and increase memory access latency and reduce memory access efficiency. The back-projection only read-only accesses the pretreated data, and in view of this the filtered data can be bound to the texture memory which has good acceleration for large amount random access to increase the efficiency of memory access. At the same time the texture memory also has linear filtering processing functions which doesn't occupy the programmable computing unit and directly calls the hardware resources, and eliminates the interpolation time to improve the computing efficiency.

4.3. Instruction Stream Optimization

Due to Various instructions in the program have different execution time, those instructions which occupy less execution time can be used as far as possible to improve the execution speed. Instruction-level optimization of program code that needs to run multiple times can effectively improve the throughput of the instruction stream which refers to the performed operation number of each multi-processor in one clock cycle.

Each pixel of each angle in the back-projection process is required to calculate the formula (4), (5), (7) and (8), and these formulas include the division and

the trigonometric calculation. In CUDA, the instruction stream throughput of single-precision floating-point addition is 0.88 operating per clock cycle. The throughput of the built-in function $\_\_fdivide(x)$ in CUDA is 1.6 operating per clock cycle. Therefore, using the built-in function $\_\_fdivide(x)$ can increase the throughput of the instruction stream. For the instruction operation computation amount to $\sin x$ and $\cos x$ corresponding, this paper uses the built-in functions sin(x) and cos(x) to improve the throughput of the instruction stream in the high-speed version of CUDA.

5. The Experimental Results of Accelerating Reconstruction

The experimental platform configuration is as follows: AMD5200+ CPU, 2G memory of Kingston, GTX550 graphics card, XP operation system, Visual Studio 2005+CUDA 3.0 development environment. The data model is Shepp – Logan, scanning mode is circular locus, the effective detector size is 512×512, the rotation angle is 360 degrees, scanning interval is 1 degree, the distance between the ray source and the rotation center is 850 mm, the distance between the object center and the probe is 150 mm, the FDK algorithm is respectively rebuilt by GPU and CPU and the reconstruction size is 512×512×512. The reconstruction results by GPU and CPU are respectively shown in Fig. 6 and Fig. 7.

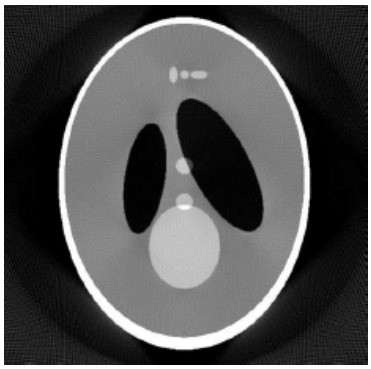

Fig. 6. GPU Reconstruction.

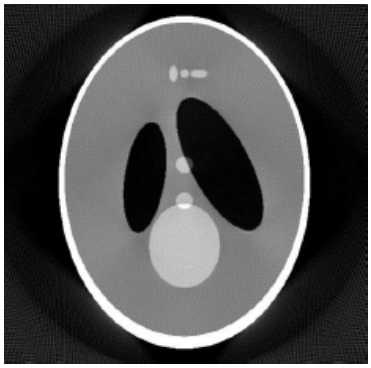

Fig. 7. CPU Reconstruction.

The comparison of reconstruction time of the optimized FDK algorithm and the original CUDA method is shown in Table 1.

It can be seen from Fig. 6 and 7 that the reconstruction experimental results respectively by GPU and CPU are basically the same and within the scope of the allowable error. From Table 1 it can be seen that after the memory optimized, the reconstruction speed compared with the original CUDA method can be increased nearly 3.6 times. This is because that global memory access latency is long and the speed of accessing data from global memory is slow. After optimized by the algorithm and directive, the reconstruction speed can be increased by about 10 times. From the reconstruction schedule of Table 2, it can be seen that the GPU reconstruction time compared with the CPU can be increased 84 times and the back-projection process can be increased nearly 89 times, and the reconstruction speed has been significantly improved.

Table 1. The reconstruction contrast of original CUDA and optimized FDK (unit: second).

Algorithm	Algorithm execution process			
	Optimization mode	**Filtering time**	**Back -projection time**	**Total time**
Original CUDA	Null	2.5	112.5	115.0
Optimized FDK	Memory optimization	1.5	30.4	31.9
	Algorithm optimization	0.7	10.7	11.4
	Instruction optimization	0.8	10.5	11.3

6. Conclusion

This paper puts forward a method which can accelerate FDK algorithm by CUDA. This method improves the FDK respectively from the memory optimization, algorithm optimization and instruction optimization. Experimental results show that the speed can reach 11.4 s with the projection data of 360 degrees 512 × 512, and the reconstruction speed compared with CPU improves 84 times. After the circle of projection data is collected, the reconstructed voxel data can be obtained. Due to the limitations of instruction and memory bandwidth, the computing performance of filtering and back-projection needs to be further improved. How to take advantage of asynchronous processing and stream processing mechanism to improve the speed of the reconstruction algorithm is the content of the future research.

Acknowledgements

The Work is supported by Natural Science Foundation of Shanxi Province of China (N0.20110011053)

References

[1]. A. V. Narasimhadhan, Kasi Rajgopal, FDK-Type Algorithms with No Backprojection Weight for Circular and Helical Scan CT, *International Journal of Biomedical Imaging*, Vol. 2012, Issue 11, 2012, pp. 1-12.

[2]. M. Abella, J. J. Vaquero, A. Sisiega, J. Pascau, A. Udias, V. Garcia, etc, Software architecture for multi-bed FDK-based reconstruction in X-ray CT scanners, *Computer Methods and Programs in Biomedicine*, Vol. 107, Issue 2, 2012, pp. 218-232.

[3]. Nitin Jain, M. S. Kalra, Characteristic Signature of Specimen Using an Approximate Formula for 3D Circular Cone-Beam Tomography, *Research in Nondestructive Evalation*, Vol. 22, Issue 3, 2011, pp. 169-195.

[4]. Dai Zhisheng, Chen Zhiqiang, Xing Yuxiang, Accelerated 3-D T-FDK reconstruction Algorithm using the commodity graphics hardware, *Journal of Tsinghua Univ. (Sci & Tech)*, Vol. 46, Issue 9, 2006, pp. 1589-1592.

[5]. Ma Cheping, Zeng-Li, Fast 3D CT reconstruction with multitexture of GPU, C*omputer Engineering and Applications*, Vol. 44, Issue 7, 2008, pp. 227-228.

[6]. Zhang Shunli, Zhang Dinghua, Li Xiaolin, Fast Calculation of Simulation Projection for Cone-beam CT Based on Shepp-Logan Head Phantom, *Computer Science*, Vol. 39, Issue 5, 2012, pp. 257-260.

[7]. Qian Ying, Yang Wenfeng, Cone-beam CT Perfusion Imaging Method on Image-guided Radiation Therapy, *Journal of Computer Applications*, Vol. 31, No. 5, 2011, pp. 1242-1248.

[8]. Scherl H., Keck B., Kowarschik M., Fast huGPU-Based CT reconstruction using the common unified device architecture(CUDA), *Nuclear Science Symposium and Medical Imaging Conference*, Paris, France, 18-20 August 2009, pp. 4464 -4466.

[9]. Wang Jue, Cao Siyuan, Zhou Yongning, Fast Cone-beam CT Reconstruction with CUDA, *Nuclear Electronics & Detection Technology*, Vol. 30, Issue 3, 2012, pp. 315-318.

[10]. Wang Cianchao, Hu Guoen, Yan Bin, etc, Fast low-dose reconstruction from truncated data in dental CT, *IEEE Transactions on Nuclear Science*, Vol. 60, Issue 1, 2013, pp. 174-181.

Sensors & Transducers, Vol. 21, Special Issue, May 2013, pp. 135-141

Sensors & Transducers

http://www.sensorsportal.com

Equilibrium Sediment Transport and Evolution Trend Simulation of the Lower Yellow River

[1,2*] Shaolei GUO, [2] Dongpo SUN, [1] Xiuru WANG

[1] College of Soil and Water Conservation, Beijing Forestry University, Beijing 10008, P. R. China

[2] North China University of Water Resources and Electric Power, Henan Zhengzhou 450011, P.R China

[*]E-mail: guo_shaolei@163.com

Received: 23 March 2013 /Accepted: 14 May 2013 /Published: 30 May 2013

Abstract: The non-equilibrium development of the scouring and silting evolution of the Lower Yellow River is caused by the different characteristics of river channel. On the basis of the water and sediment data of the Lower Yellow River between 1960 and 2008, statistic method was used to analyze the sediment transport of different discharges flow. The combination of 2500 $m^3/s < Q < 4000$ m^3/s and 20 $kg/m^3 < S < 60$ kg/m^3 is considered a better combination for the Lower Yellow River. Combined with the model experiments data, the evolution trend of the Lower Yellow Rive channel in the later sediment-retaining period of Xiaolangdi Reservoir were analyzed, and the importance of the equilibrium development of the upper and lower reaches in the later sediment-retaining period of Xiaolangdi Reservoir was pointed out. *Copyright © 2013 IFSA.*

.

Keywords: Model test, Lower yellow river, Equilibrium sediment transport, Regulation value.

1. Introduction

In the Lower Yellow River, there are three types of river channels: wandering, transitional, bending. When the flow transmits in the Lower Yellow River (Fig.1), the scour and silting characteristic of the three reaches which are different because of the different characteristics of river channels often result in the disadvantageous phenomenon that upstream scour and downstream silt or upstream silt and downstream scour. The sediment transporting capacity of some reaches can not be fully which influence the effect of sediment transporting, and that is caused by the non-equilibrium development scour and silting evolution of the Lower Yellow River. Facing with increasingly scarce water resources, the channel of the Lower Yellow River can develop equilibrium at what water and sediment condition, and how can achieve this condition by joint operation of reservoirs. Those have great help to solve the problem of silting and flood control of the Lower Yellow River.

It is well-known that the water and sediment condition of the Lower Yellow River is complicated and variable. Many scholars have given different regulation values of the water and sediment condition from different aspects based on the condition of balance sediment transport [1-11]. However, it is difficult to achieve balance sediment transport because of the complicated relationship of sediment transport, scouring and silting, the rapid change of the boundary condition of the riverbed under the influence of the flow, the changeable river channel and water and sediment condition. Moreover, balance is relative in nature, unbalance is absolute. So Equilibrium sediment transport, an approximate balance sediment transport, is more feasible in the Lower Yellow River [12, 13]. In this condition the scouring and silting variation is not serious (< 10 %), and in a long period of time the sediment transport is balanced. Han proved it from theory [12].

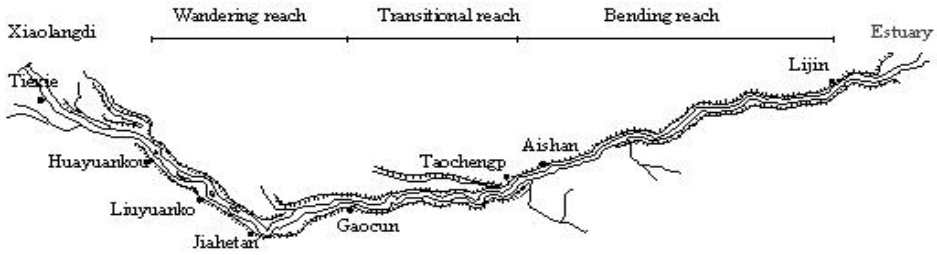

Fig. 1. Schematic diagram of the Lower Yellow River.

In order to find the controllable relation between discharge and sediment in which condition equilibrium sediment transport could be achieve in the Lower Yellow River, statistic method would be used to analyze the different discharge and the sediment concentration of flow on the basis of water and sediment data of the Lower Yellow River between 1960 and 2008. Also the scouring and silting trend would be forecasted in the later sediment-retaining period of Xiaolangdi Reservoir on the basis of the Lower Yellow River physical model tests. All of these would provide theoretical support to equilibrium sediment transport of different reach in the Lower Yellow River.

2. Materials and Methods

2.1. Measured data and Methods

The Lower Yellow River measured data of Huayuankou hydrologic station, Jiahetan hydrologic station, Gaocun hydrologic station, Aishan hydrologic station and Lijin hydrologic station between 1960 and 2008 are used in this article. And all the data is in the condition that the discharge and sediment concentration have not large change (<20 %) in 3-5 days, no overflow, no hyper-concentrated flow and the average discharge of flow is more than 1000 m^3/s.

During the analysis, the Lower Yellow River is divided into four reach: Huayuankou–Jiahetan, Jiahetan–Gaocun, Gaocun–Aishan, Aishan–Lijin. Huayuankou–Jiahetan and Jiahetan–Gaocun are wandering reach. Gaocun–Aishan is transitionalreach. Aishan–Lijin is bending reach. First the data of Huayuankou hydrologic station are selected. Then other hydrologic station's data are selected on the basis of flow velocity. Transport rate method, which is based on the data of sediment transport rates, is used to calculate the sedimentation amount. Statistic method is used to analyze the different magnitude and the sediment concentration of flow of the Lower Yellow River.

2.2. Model Test

The model is built to study the fluvial process in the different use period of Xiaolangdi Reservoir. The main model scales are in Table 1. The model has been used during the beginning sediment-retaining period of Xiaolangdi Reservoir. Its reliability has been verified.

After the beginning sediment-retaining period of Xiaolangdi Reservoir, the reservoir is changed over to sediment-retaining period for the designed usage. In order to forecast the evolution trend of the Lower Yellow Rive channel in the that period, the discharge and sediment process which is designed by the actual data of 1990-2008+1956-1960 is used in the model. And cross section method which is based on the cross section data is used to calculate the scouring and silting.

Table 1. The Main Model Scale.

Scale name	Model Scale	Remark
Horizontal scale λ_L	600	According to the site conditions and test requirement
Vertical scale λ_H	60	Meet the geometry deformation limit condition, etc.
Geometry deformation D_t	10	$D_t = \lambda_L / \lambda_H$
Velocity scale λ_V	7.75	$\lambda_V = \lambda_H^{1/2}$
Roughness scale λ_n	0.626	$\lambda_n = \lambda_R^{2/3} \lambda_V^{-1} \lambda_J^{1/2}$
Time scale of flow movement λ_{t_1}	77.5	$\lambda_{t_1} = \lambda_L / \lambda_V$
Sediment diffusion scale λ_ω	1.38	$\lambda_\omega = \lambda_V \left(\lambda_H / \lambda_L\right)^{3/4}$
Grain-size scale λ_d	0.81	$\lambda_d = (\lambda_V \lambda_\omega / \lambda_{\gamma_s - \gamma})^{1/2}$ Little adjustment with water temperature
Sediment concentration scale λ_S	1.8	$\lambda_s = \lambda_{s_*}$ and with the verification test(λ_{s_*} is suspended sediment)
Time scale of riverbed deformation λ_{t2}	83	$\lambda_{t_2} = \lambda_{\gamma_0} \lambda_L / (\lambda_s \lambda_V)$ and with the verification test

3. Results and Discussion

In order to analysis the scouring and silting law in channel with different discharge, channel scouring-silting rate of reach was introduced. Channel scouring-silting rate for the reach was the ratio of scouring and silting amount to incoming sediment amount.

The Figs. 2-5 was given after analyzing the relationship of channel scouring-silting rate and sediment concentration when the discharge was between 1000 m^3/s and 5000 m^3/s in the years 1960-2008. The correlation of channel scouring-silting rate and sediment concentration in the four reaches could be expressed in the formula 1-12.

3.1. The Discharge Between 1000m^3/s and 2000 m^3/s

$$\Delta W_S/W_S = 37.72\ln S - 115.53 \quad (1)$$

$$\Delta W_S/W_S = 40.73\ln S - 122.4 \quad (2)$$

$$\Delta W_S/W_S = 46.86\ln S - 130.51 \quad (3)$$

$$\Delta W_S/W_S = 68.28\ln S - 186.2 \quad (4)$$

Here ΔW_S is scouring or silting amount of the reach, W_S is incoming sediment amount of the reach and S is sediment concentration.

As shown in the Fig. 2, the channel scouring-silting rate of the four reaches increased with the increase of sediment concentration. The channel scouring-silting rate of Huayuankou–Gaocun was close to 0 when the sediment concentration of Huayuankou and Jiahetan was about 18 kg/m^3. The channel scouring-silting rate of Gaocun-Lijin was close to 0 when the sediment concentration of Gaocun and Aishan was about 15 kg/m^3.

3.2. The Discharge between 2000m^3/s and 3000 m^3/s

$$\Delta W_S/W_S = 43.62\ln S - 150.75 \quad (5)$$

$$\Delta W_S/W_S = 55.17\ln S - 201.74 \quad (6)$$

$$\Delta W_S/W_S = 33.21\ln S - 113.86 \quad (7)$$

$$\Delta W_S/W_S = 48.81\ln S - 164.87 \quad (8)$$

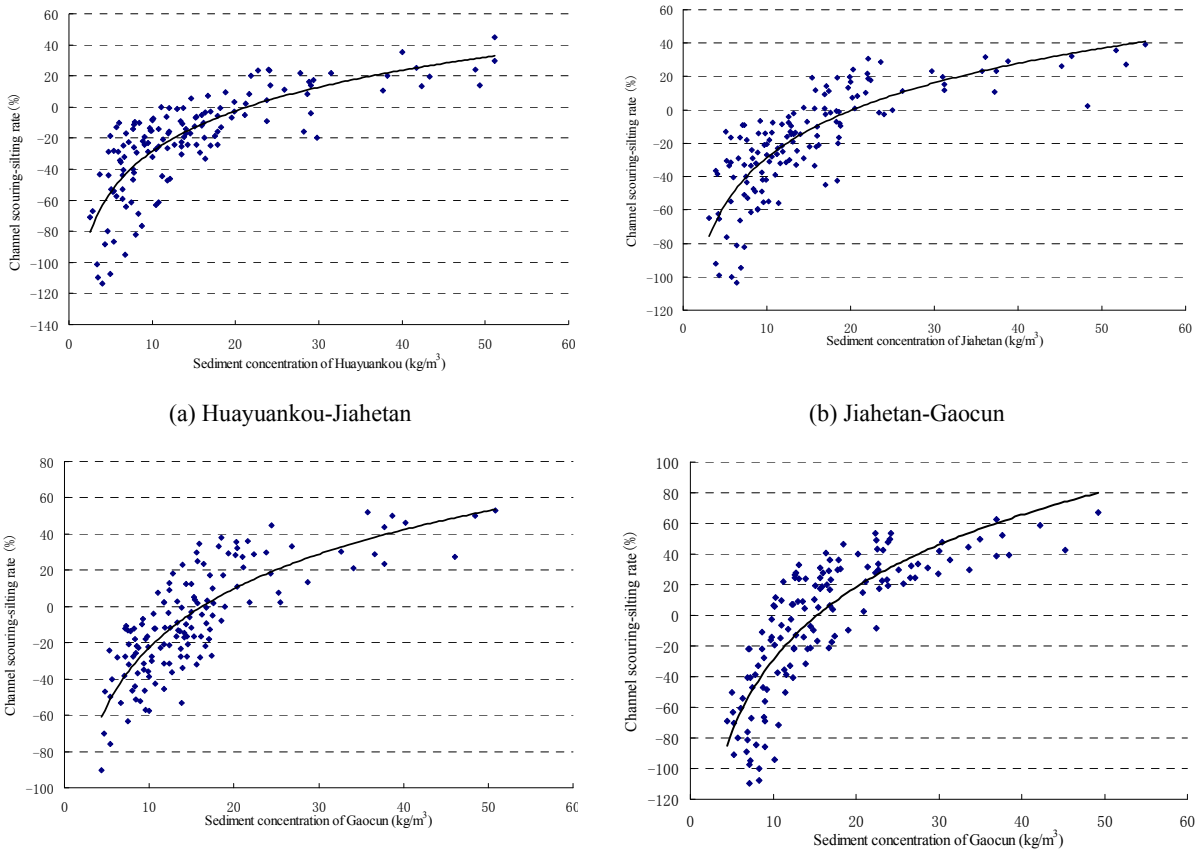

(a) Huayuankou-Jiahetan

(b) Jiahetan-Gaocun

(c) Gaocun-Aishan

(d) Aishan-Lijin

Fig. 2. The relation of Sediment Concentration and the channel scouring-silting rate in the lower Yellow River between 1000 m^3/s-2000 m^3/s.

According to the Fig. 3 presented, the channel scouring-silting rate of the four reaches increased with increase of sediment concentration. The channel scouring-silting rate of Huayuankou–Jiahetan was close to 0 when the sediment concentration of Huayuankou was about 30 kg/m^3. The channel scouring-silting rate of Jiahetan–Gaocun was close to 0 when the sediment concentration of Jiahetan was about 30 kg/m^3. The channel scouring-silting rate of Gaocun–Aishan was close to 0 when the sediment concentration of Gaocun was about 30 kg/m^3. The channel scouring-silting rate of Aishan–Lijin was close to 0 when the sediment concentration of Aishan was about 28 kg/m^3.

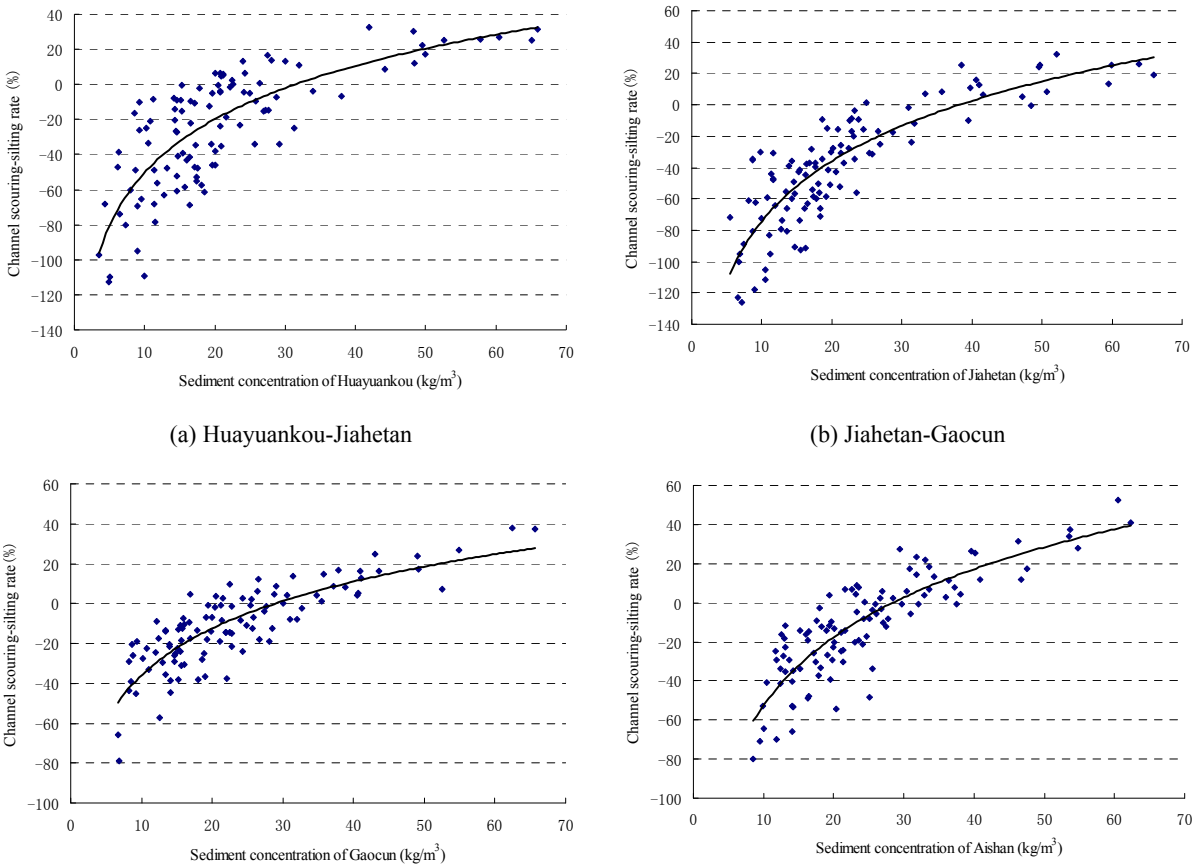

(a) Huayuankou-Jiahetan

(b) Jiahetan-Gaocun

(c) Gaocun-Aishan

(d) Aishan-Lijin

Fig. 3. The relation of Sediment Concentration and the channel scouring-silting rate in the lower Yellow River between 2000 m^3/s-3000 m^3/s.

3.3. The discharge between 3000m^3/s and 4000 m^3/s

$$\Delta W_S/W_S = 29.31\ln S - 118.77 \quad (9)$$

$$\Delta W_S/W_S = 32.25\ln S - 120.43 \quad (10)$$

$$\Delta W_S/W_S = 37.82\ln S - 144.97 \quad (11)$$

$$\Delta W_S/W_S = 26.86\ln S - 108.28 \quad (12)$$

According to the Fig. 4 presented, the channel scouring-silting rate of the four reaches increased with increase of sediment concentration. All the reaches were scouring except the larger sediment concentration.

3.4. The discharge between 4000 m^3/s and 5000 m^3/s

$$\Delta W_S/W_S = 42.56\ln S - 158.36 \quad (13)$$

$$\Delta W_S/W_S = 37.43\ln S - 138.13 \quad (14)$$

$$\Delta W_S/W_S = 55.29\ln S - 204.1 \quad (15)$$

$$\Delta W_S/W_S = 44.47\ln S - 167.71 \quad (16)$$

As could been seen in the Fig. 5, all the reaches were scouring when the discharge was more than 4000 m^3/s.

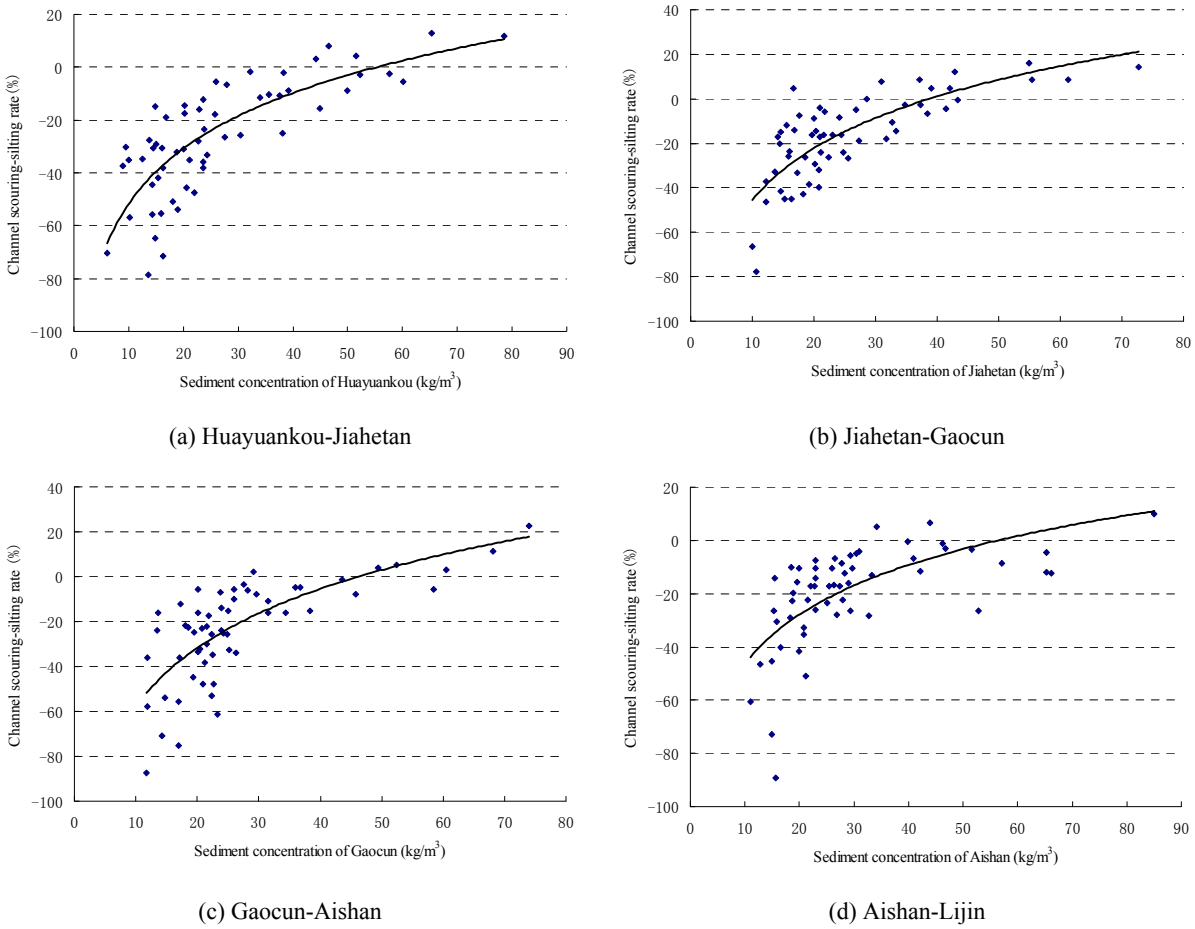

(a) Huayuankou-Jiahetan

(b) Jiahetan-Gaocun

(c) Gaocun-Aishan

(d) Aishan-Lijin

Fig. 4. The relation of Sediment Concentration and the channel scouring-silting rate in the lower Yellow River between 3000 m^3/s-4000 m^3/s.

It could be seen from the Figs. 2-5 that when the combination of discharge and the sediment concentration was different, the scouring-silting of the four reaches has different. But when the combination of discharge and the sediment concentration changed in the range of 2000 $m^3/s < Q < 3000$ m^3/s and 20 $kg/m^3 < S < 60$ kg/m^3, the scouring-silting of the four reaches were close to 0 (<10 %).

Combining the cognition to the sediment carrying capacity and the actual discharge and the sediment concentration of the lower Yellow River, the combination of $2000m^3/s<Q<3000m^3/s$ and $20kg/m^3<S<60kg/m^3$ was considered a better combination for the Lower Yellow River equilibrium sediment transport in long period of time. It could be used as the control condition of Hayuankou. Considering the decrease of the flow when the flow flowed Hayuankou to Lijin, the control discharge could be $2500m^3/s<Q<4000m^3/s$. In this condition, the four reaches might be scouring or silting in a short period of time. According to the adjustment of the flow and channel in a long period of time, Equilibrium sediment transport could be achieved. Also single combination of discharge and the sediment concentration should be avoided when the Xiaolangdi Reservoir was used to regulate the discharge and the sediment concentration.

3.5. The Forecast of Scouring and Silting Trend in the Later Sediment-retaining Period of Xiaolangdi Reservoir

It could be seen from graph 6 that silting distribution increased generally from Tiexie to Taochengpu. That was because some river training works which decrease the wandering range of channel were built up between Tiexie and Huayuankou. And in the initial operation stage of Xiaolangdi Reservoir, the channel geometry of that reach became better and better. Overflow of that reach became less in the later sediment-retaining period of Xiaolangdi Reservoir and the main channel was scouring. Between Huayuankou and Jiahetan, river training works were also built up, overflow was not too much. The silting in that reach was not serious. Between Jiahetan and Taochengpu, the silting was very serious. As was shown in Fig. 6, the deposition amount increased sharply in that reach. That was because overflow was too much and there were three big floodplain areas. The sediment that carried by the overflow deposited in quantity on the floodplain area.

It could be seen from the analysis that the sediment transporting capacity of upstream and downstream in the Lower Yellow River had great difference. If the

quondam discharge and the sediment concentration were used in the later sediment-retaining period of Xiaolangdi Reservoir, silting is inevitable below Jiahetan. Equilibrium sediment transport could solve this problem if the combination of 2500 $m^3/s < Q <$ 4000 m^3/s and 20 $kg/m^3 < S <$ 60 $kg/m^3$was used.

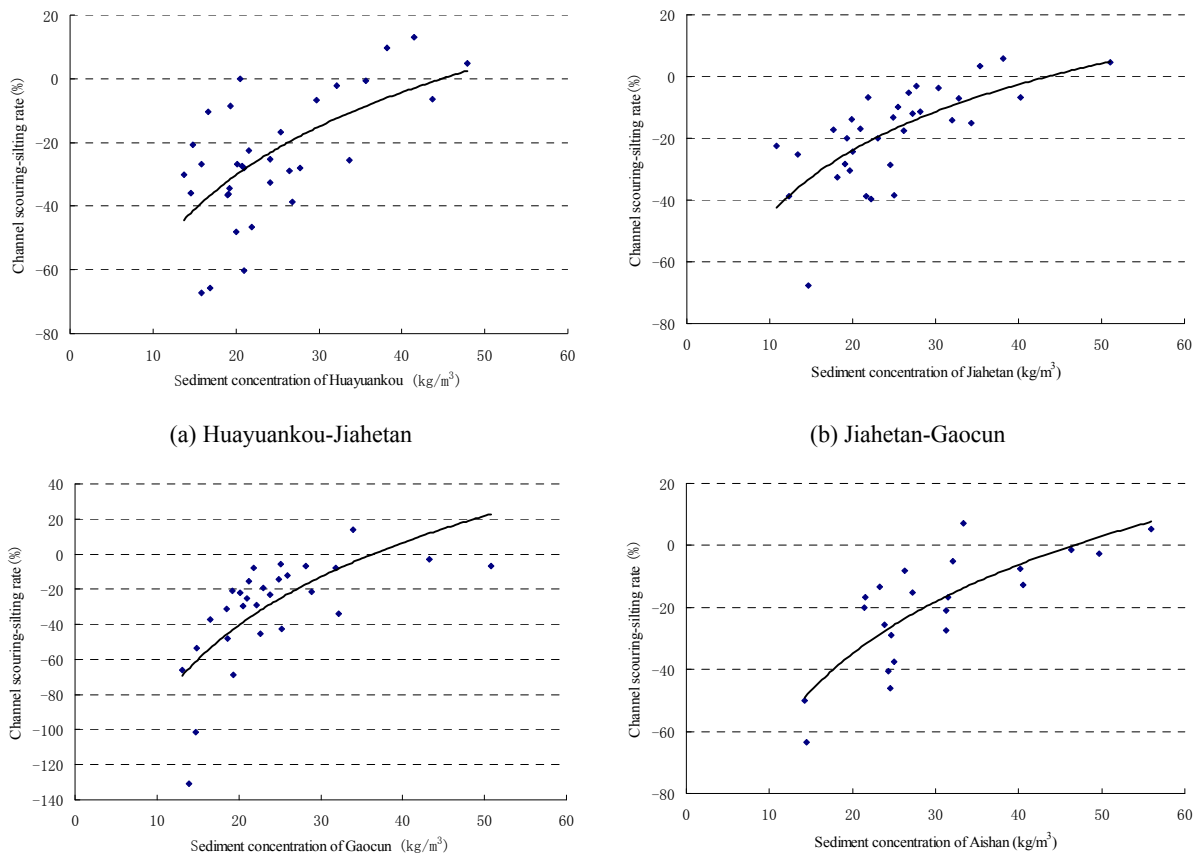

(a) Huayuankou-Jiahetan

(b) Jiahetan-Gaocun

(c) Gaocun-Aishan

(d) Aishan-Lijin

Fig. 5. The relation of Sediment Concentration and the channel rate of silting in the lower Yellow River between 4000 m^3/s-5000 m^3/s.

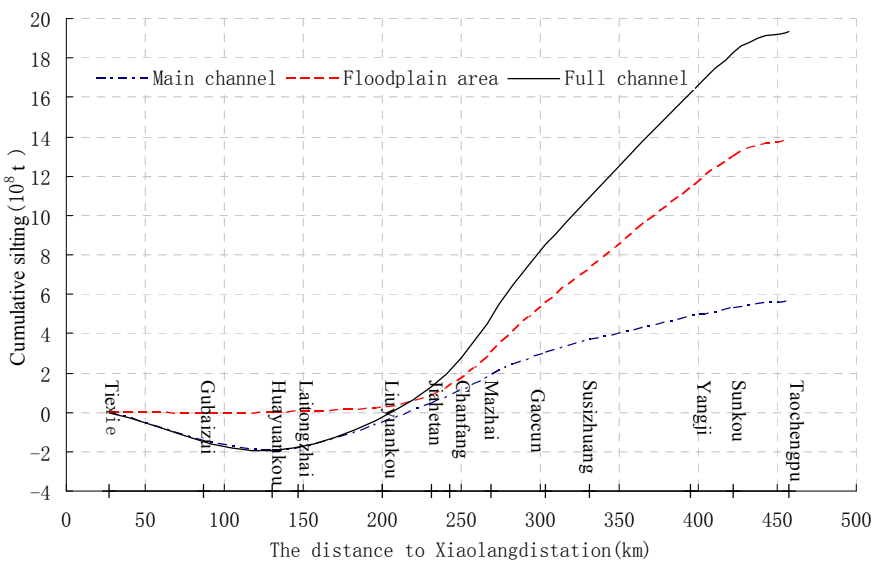

Fig. 6. The accumulated scour of the model test between Tiexie and Taochengpu.

4. Conclusions

The analysis of model test results shows that the sediment transporting capacity of upstream and downstream in the Lower Yellow River had great difference. If the quondam discharge and the sediment concentration were used in the later sediment-retaining period of Xiaolangdi Reservoir, silting is inevitable below Jiahetan. But equilibrium sediment transport can solve this problem. The combination of discharge and the sediment concentration changed in the range of 2500 $m^3/s < Q <$ 4000 m^3/s and 20 $kg/m^3 < S <$ 60 kg/m^3 is considered a better combination for the Lower Yellow River equilibrium sediment transport in long period.

Acknowledgement

The study is financially supported by the National Natural Science Foundation of China (No.51039004, No.51079055).

References

[1]. Hu, C. H., Chen, J. G., and Guo, Q. C. Shaping and maintaining a medium-sized main channel in the Lower Yellow River, *International Journal of Sediment Research,* 27, 3, 2012, pp. 259-270.

[2]. Ma, Y. X., Huang, H. Q., Nanson, G. C., Li, Y. and Yao, W. Y. Channel adjustments in response to the operation of large dams: The upper reach of the lower Yellow River, *Geomorphology,* 147, SI, 2012, pp. 35-48.

[3]. Xia, J. Q., Lin, B. L., Falconer, R. A., and Wang, Y. P. Modelling of man-made flood routing in the lower Yellow River, *Proceedings of the Institution of Civil Engineers-Water,* 165, 7, 2012, pp. 377-391.

[4]. Chen, J. G., Zhou, W. H., and Chen, Q. Reservoir Sedimentation and Transformation of Morphology in THE Lower Yellow River during 10 Year's Initial Operation of the Xiaolangdi Reservoir, *Journal of Hydrodynamics*, 24, 6, 2012, pp. 914-924.

[5]. Fu, X. D., Jiang, L. W., and Wu, B. S. Sediment delivery ratio and its uncertainties on flood event scale: Quantification for the Lower Yellow River. *Science China-Technological Sciences,* 53, 3, 2010, pp. 854-862.

[6]. Liu J.-X., Gao G.-M., Study on Characteristics of Scouring and Deposition of lower channels of the Yellow River, *Yellow River,* 22, 8, 2000, pp. 11-12.

[7]. Liang Z.-Y., Liu J.-X., Zhang H.-J., Relation between scour siltation and flow sediment combination for floods in the lower Yellow River, *Journal of Hydroelectric Engineering*, 24, 2, 2005, pp. 52-55.

[8]. Liang Z.-Y., Li C.-P., Critical discharge between scour and siltation in alluvial rivers, *Journal of Hydroelectric Engineering,* 3, 2003, pp. 79-82.

[9]. Liang Z.-Y., Yang L.-F., Relations of channel geometry to water and sediment rate for the lower Yellow River, *Journal of Hydroelectric Engineering*, 24, 6, 2005, pp. 68-71.

[10]. Han Q.-W., Some rules of sediment transportation and deposition-scouring in the lower Yellow River, *Journal of Sediment Research*, 3, 2004, pp. 1-13.

[11]. Han Q.-W., Huge Sediment Transporting Capacity and Trend of Equilibrium of t he Lower Yellow River, *Yellow River,* 30, 2, 2008, pp. 1-3.

[12]. Han Q.-W., Equilibrium trend of sediment transportation and river morphology, *Journal of Sediment Research,* 4, 2011, pp. 1-14.

[13]. Peng R.-S., River Training and Equilibrium Sediment Transport of the Lower Yellow River, *Yellow River*, 33, 3, 2011, pp. 3-7.

Sensors & Transducers, Vol. 21, Special Issue, May 2013, pp. 142-146

Sensors & Transducers

http://www.sensorsportal.com

Convergence Analysis of Multi-innovation Learning Algorithm Based on PID Neural Network

[1] Gang Ren, [1,2] Pinle Qin, [2] Minmin Sun, [1] Yan Lin

[1] Ship CAD Engineer Center, Dalian University of Technology, Liaoling, China

[2] Department of Computer Science, North University of China, Shanxi, China

[1] E-mail: pinleqin@126.com

Received: 26 March 2013 /Accepted: 14 May 2013 /Published: 30 May 2013

Abstract: In order to improve the identification accuracy of dynamic system, multi-innovation learning algorithm based on PID neural networks is presented, which can improve the online identification performance of the networks. The multi-innovation gradient type algorithms use the current data and the past data that make it more effective than the BP algorithm in view of accuracy and convergence rate. Simulation results showed that the proposed algorithm is effect. *Copyright © 2013 IFSA.*

Keywords: Multi-innovation, PID neural networks, System identification, Nonlinear system.

1. Introduction

As we have known, the model-based control techniques are usually implemented under the assumption of good understanding of process dynamics and they are the dependence on mathematical model of controlled plant. These techniques, however, can not provide satisfactory results when applied to poorly modeled processes. Therefore, how to design adaptive control system only based on information from the I/O data of the plant is great significance both in theoretic and application. Now, one successful method of the model-free control approaches is Proportional Integral Derivative neural network (PIDNN) control [1, 2].

PIDNN is a new kind of networks. It utilizes the advantages of both PID control and neural structure. But the method has some shortcomings, such as slow convergence, easy to fall into local minimum and forget the samples [3, 4].

In order to overcome these shortcomings, this paper improves the convergence by using multi innovation theory [5, 6] and proofs the fast convergence of the improvement method by supermartigale theory.

2. PID Neural Network Model and Multi-innovation Identification Algorithm

2.1. PID Neural Network Model

Consider a time-invariant stochastic system described by a linear regression model [7, 8]:

$$y(t) = \phi^T(t)\theta + \nu(t), \tag{1}$$

where $\theta \in R^n$ is the parameter vector of system, $y(t) \in R^1$ is the system output, $u(t) \in R^1$ is the system input, $\nu(t) \in R^1$ is a stochastic noise with zero mean, $\phi(t) \in R^n$ is the information vector consisting

of the system observation (input-output) data, the superscript T denotes the transpose.

As it is shown in Fig. 1, PID neural network has a simple feed forward neural network which consists of 2-3-1 structure, so it has three layers [7-9]. Let $W=(w_{ij})_{2\times 3}$ be the weight matrix between the input layer and the hidden layer and $V=(v_1,v_2,v_3)$ be the weight matrix between the hidden layer and the output layer. u_i, u'_j and u'' are the inputs of the input layer, the hidden layer and the output layer. x_i, x'_j and x'' are the outputs of them. The actual output of the PID neural network is d.

We can use Fig. 1 to approximate the process described by expressing (1).

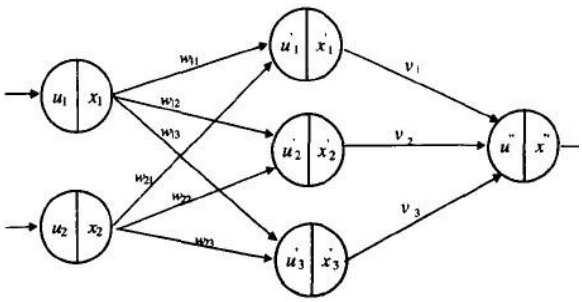

Fig. 1. Structure of PIDNN.

2.2. Multi-innovation Identification Algorithm

The following single innovation identification algorithm can be used to estimate the parameter θ of system (1) [10].

$$\hat{\theta}(t)=\hat{\theta}(t-1)+\frac{\phi(t)}{r(t)}e(t) \tag{2}$$

$$e(t)=y(t)-\phi^T(t)\hat{\theta}(t-1) \tag{3}$$

$$r(t-1)=r(t-1)+\|\phi(t)\|^2,\quad r(0)=1, \tag{4}$$

where $e(t)$ is a single innovation.

In multi-innovation identification algorithm [5], the single innovation $e(t)\in R^1$ is extended to multi-innovation vector $E(p,t-1)\in R^p$, the information vector $\phi(t)\in R^n$ is also extended to $\Phi(p,t)\in R^{n\times p}$ for scalar system. From here, the algorithm can be expressed as

$$\hat{\theta}(t)=\hat{\theta}(t-1)+\frac{\Phi(p,t)}{r(t)}E(p,t) \tag{5}$$

$$E(p,t-1)=[e(t-1),e(t-1),\cdots,e(t-p)]^T\in R^p \tag{6}$$

$$\Phi(p,t)=[\phi(t),\phi(t-1),\cdots,\phi(t-p+1)]\in R^{n\times p} \tag{7}$$

where $p\geq 1$ represents the innovation length. As $p=1$, the multi-innovation identification algorithm reduces to the single innovation identification algorithm.

3. Multi-innovation Learning Algorithm based on PID Neural Network

Considering p groups of input-output data from time $t-p+1$ to time t, the output vectors of the ith input node is

$$X_i(p,t)=[x_i(t),x_i(t-1),\cdots,x_i(t-p+1)],\quad i=1,2$$

The output vector of the output node is

$$D(p,t)=[d(t),d(t-1),\cdots d(t-p+1)]^T$$

The expected vector of PID neural network is

$$Y(p,t)=[y(t),y(t-1),\cdots,y(t-p+1)]^T$$

Define a cost function [10]:

$$J(p,t)=\frac{1}{2}\|Y(p,t)-D(p,t)\|^2 \tag{8}$$

Thus, we proceed to refine the weights by the training iteration as follows:

$$v_j(t+1)=v_j(t)-\eta\frac{\partial J(p,t)}{\partial v_j}$$

$$w_{ij}(t+1)=w_{ij}(t)-\eta\frac{\partial J(p,t)}{\partial w_{ij}} \tag{9}$$

where $\eta>0$ is the learning rate.

$$\begin{aligned}\frac{\partial J(p,t)}{\partial v_j}&=\frac{\partial X''(p,t)}{\partial v_j}\frac{\partial J(p,t)}{\partial X''(p,t)}\\&=X'_j(p,t)[\frac{\partial J(p,t)}{\partial x''(t)},\cdots,\frac{\partial J(p,t)}{\partial x''(t-p+1)}]^T\\&=X'_j(p,t)[\frac{\partial J(p,t)}{\partial d(t)},\cdots,\frac{\partial J(p,t)}{\partial d(t-p+1)}]^T\\&=X'_j(p,t)[-e(t),\cdots,-e(t-p+1)]^T\\&=-X'_j(p,t)E(p,t)\end{aligned}$$

by defining the vector $X'_j(p,t)$ as

$$X_j'(p,t) = [x_j'(t), x_j'(t-1), \cdots, x_j'(t-p+1)]$$

and

$$\begin{aligned}\frac{\partial J(p,t)}{\partial w_{ij}} &= \frac{\partial U_j'(p,t)}{\partial w_{ij}} \frac{\partial J(p,t)}{\partial U_j'(p,t)} \\ &= X_i(p,t)[\frac{\partial J(p,t)}{\partial u_j'(t)}, \cdots, \frac{\partial J(p,t)}{\partial u_j'(t-p+1)}]^T \\ &= X_i(p,t)[-e_1(t), \cdots, -e_1(t-p+1)]^T \\ &= -X_i(p,t)E_1(p,t)\end{aligned}$$

the vector $X_j'(p,t)$ and $e_1(t)$ may be expressed as

$$X_i(p,t)=[x_i(t), x_i(t\text{-}1), \cdots, x_i(t-p+1)]$$

$$\begin{aligned}e_1(t) &= -\frac{\partial J(p,t)}{\partial d(t)} \frac{\partial d(t)}{\partial x_j'(t)} \frac{\partial x_j'(t)}{\partial u_j'(t)} \\ &= e(t)v_j(t)sign\frac{x_j'(t)-x_j'(t-1)}{u_j'(t)-u_j'(t-1)}\end{aligned}$$

So we have

$$v_j(t+1) = v_j(t) + \eta X_j'(p,t)E(p,t)$$

$$w_{ij}(t+1) = w_{ij}(t) + \eta X_i(p,t)E_1(p,t) \tag{10}$$

4. Convergence Analysis of multi-Innovation Learning Algorithm

For the identification of nonlinear dynamical systems, PID neural network can be treated as a dynamical system described by (1). Its adjustable parameters $\theta = (w_{ij}, v_j)$ which is made of $W = (w_{ij})_{2\times 3}$ and $V = (v_1, v_2, v_3)$ can be written as (5).

Reference [11, 12], convergence analysis of the proposed algorithm be given as fellows.

Theorem 1. For the system in (1), assume that a stochastic white noise with zero mean $v(t)$ is uncorrelated with $u(t)$

(A1) $E[v^2(t)] \le \sigma_v^2 < \infty$.

if there exist constants $0 < \alpha \le \beta < \infty$ and the innovation length $p \ge n$ such that the following persistent excitation condition holds,

(A2) $\alpha I \le \frac{1}{p}\sum_{i=1}^{p}\phi(t-i+1)\phi^T(t-i+1) \le \beta I$.

Then the parameter estimation $\hat{\theta}(t)$ given by Eq.(5) is uniform bounded.

Proof. Define the estimation error $\tilde{\theta}(t) = \theta(t) - \theta$, assume θ is real value. Subtracting θ from the two sides of Eq.(5), we have

$$\begin{aligned}\theta(t) - \theta &= \theta(t-1) - \theta + \frac{\Phi(p,t)}{r(t)}[\Phi^T(p,t)\theta + \\ &\quad V(p,t) - \Phi^T(p,t)\theta(t-1)] \\ &= \theta(t-1) - \theta + \frac{\Phi(p,t)}{r(t)}[V(p,t) - \\ &\quad \Phi^T(p,t)(\theta(t-1)-\theta)]\end{aligned} \tag{11}$$

Substituting $\tilde{\theta}(t)$

$$\begin{aligned}\tilde{\theta}(t) &= \tilde{\theta}(t-1) + \frac{\Phi(p,t)}{r(t)}[-\Phi^T(p,t)\tilde{\theta}(t-1) + V(p,t)] \\ &= \left[I - \frac{\Phi(p,t)\Phi^T(p,t)}{r(t)}\right]\tilde{\theta}(t-1) + \frac{\Phi(p,t)V(p,t)}{r(t)}\end{aligned} \tag{12}$$

By using A2, taking the trace gives

$$p\alpha \le \frac{1}{p}\sum_{i=1}^{p}\|\phi(t-i+1)\|^2 \le p\beta$$

$$np\alpha \le \sum_{i=1}^{p}\|\phi(t-i+1)\|^2 \le np\beta$$

Hence, we have

$$np\alpha \le \|\phi(t)\|^2 \le np\beta$$

According to the definition of $r(t)$ in (4), we have

$$\begin{aligned}r(t) &= \sum_{j=1}^{t}\|\phi(j)\|^2 + r(0) \\ &\le \sum_{j=0}^{\lfloor (t-1)/p \rfloor}\sum_{i=1}^{p}\|\phi(jp+i)\|^2 + r(0) \\ &\le \sum_{j=0}^{\lfloor (t-1)/p \rfloor} np\beta + 1 \\ &\le (\lfloor (t-1)/p \rfloor + 1)np\beta + 1 \\ &\le (t+p-1)n\beta + 1\end{aligned}$$

$$\begin{aligned}r(t) &= \sum_{j=1}^{t}\|\phi(j)\|^2 + r(0) \\ &\ge \sum_{j=0}^{\lfloor t/p \rfloor - 1}\sum_{i=1}^{p}\|\phi(jp+i)\|^2 + r(0) \\ &\ge \sum_{j=0}^{\lfloor t/p \rfloor - 1} np\alpha + r(0) \\ &\ge (\lfloor t/p \rfloor - 1 + 1)np\alpha + 1 \\ &\ge tn\alpha + 1\end{aligned}$$

Then, the following inequality has been obtained

$$tn\alpha + 1 \le r(t) \le (t+p-1)n\beta + 1$$

$$I - \frac{\Phi(p,t)\Phi^T(p,t)}{r(t)} \le \left[1 - \frac{p\alpha}{(t+p-1)n\beta+1}\right] I$$

Here, using assume A1, we have

$$\begin{aligned} E(\|\Phi(p,t)V(p,t)\|) &\le \sqrt{E(\|\Phi(p,t)V(p,t)\|^2)} \\ &\le \sqrt{p\beta E(\|V(p,t)\|^2)} \\ &\le \sqrt{p\beta p\sigma_v^2} \\ &\le p\sigma_v\sqrt{\beta} \end{aligned} \tag{13}$$

Taking the expectation and norm of (12) and using (13) give

$$\begin{aligned} \|\tilde{\theta}(t)\| &= \left\| \left[I - \frac{\Phi(p,t)\Phi^T(p,t)}{r(t)} \right] \tilde{\theta}(t-1) + \frac{\Phi(p,t)V(p,t)}{r(t)} \right\| \\ &\le \left\| \left[I - \frac{\Phi(p,t)\Phi^T(p,t)}{r(t)} \right] \tilde{\theta}(t-1) \right\| + \left\| \frac{\Phi(p,t)V(p,t)}{r(t)} \right\| \\ &\le \left\| 1 - \frac{p\alpha}{(t+p-1)n\beta+1} \right\| \|\tilde{\theta}(t-1)\| + \frac{\|\Phi(p,t)V(p,t)\|}{r(t)} \\ &\le \left\| 1 - \frac{p\alpha}{(t+p-1)n\beta+1} \right\| \|\tilde{\theta}(t-1)\| + \frac{\|\Phi(p,t)V(p,t)\|}{r(t)} \\ &\le \left\| 1 - \frac{p\alpha}{(t+p-1)n\beta+1} \right\| \|\tilde{\theta}(t-1)\| + \frac{\|\Phi(p,t)V(p,t)\|}{tn\alpha+1} \end{aligned}$$

$$\begin{aligned} E\left(\|\tilde{\theta}(t)\|\right) &\le \left\| 1 - \frac{p\alpha}{(t+p-1)n\beta+1} \right\| E\left(\|\tilde{\theta}(t-1)\|\right) + \\ &\quad \frac{1}{tn\alpha+1} E\left(\|\Phi(p,t)V(p,t)\|\right) \\ &\le \left\| 1 - \frac{p\alpha}{(t+p-1)n\beta+1} \right\| E\left(\|\tilde{\theta}(t-1)\|\right) + \frac{p\sigma_v\sqrt{\beta}}{tn\alpha+1} \end{aligned}$$

If we select suitable parameter α and β, it follows that

$$0 < 1 - \frac{p\alpha}{(t+p-1)n\beta+1} \le d < 1$$

where d is a constant. Thus,

$$E\left(\|\tilde{\theta}(t)\|\right) \le dE\left(\|\tilde{\theta}(t-1)\|\right) + M \tag{14}$$

where M is a constant. Repeating using the formula (14)

$$\begin{aligned} E\left(\|\tilde{\theta}(t)\|\right) &\le dE\left(\|\tilde{\theta}(t-1)\|\right) + M \\ &\le d^{t-1}E\left(\|\tilde{\theta}(1)\|\right) + \frac{1-d^{t-1}}{1-d} M \end{aligned}$$

This completes the proof of Theorem 1.

5. Examples

To illustrate the effectiveness of the proposed algorithm, this paper compares its accuracy with the traditionaly BP algorithm with the following example.

Example 1. Considering the nonlinear dynamical systems described by the following function.

$$y(t) = 0.4y(t-1) + 0.54y(t-2) + f[u(k-1)]$$

where $y(t)$ is the output system, $u(t)$ is the input system,

$$f(u) = u^3 + u^2 - 2.5u$$

The test signal used for the example is

$$u(t) = 0.2\sin\frac{2\pi t}{25} + 0.3\sin\frac{\pi t}{75}$$

The initial weight matrix in output layer $W(0) = [1, 0.1, 1; -1, -0.1, -1]$, the initial weight matrix in hidden layer $V(0) = (0.1, 0.1, 0.1)$, the innovation length $p = 2$, the learning rate $\eta = 0.175$. The system responses are shown in Fig. 2 and Fig. 3.

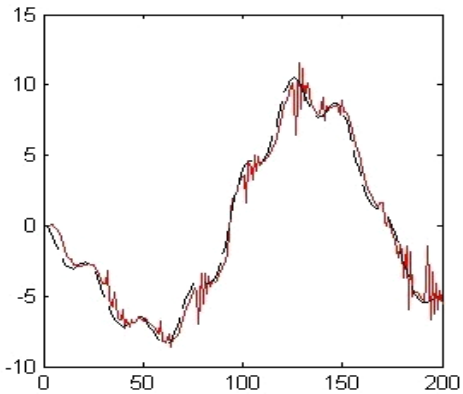

Fig. 2. Identification effect of the unmodified algorithm.

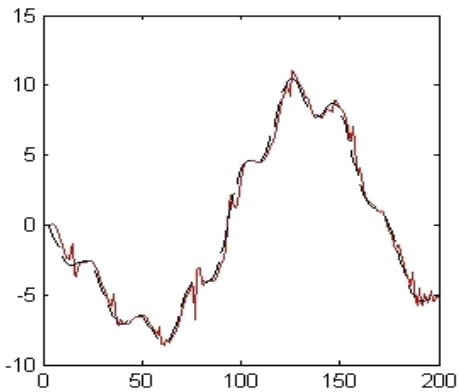

Fig. 3. Identification effect of the proposed algorithm.

Example 2. Considering the nonlinear dynamical systems described by the following function.

$$y(t+1) = f[y(t)] + g[u(k)]$$

where $f[y(t)] = \dfrac{5y(t)}{2.5 + y^2(t)}$, $g[u(t)] = u^3(t)$

The test signal used for the example is

$$u(t) = 0.6\sin\frac{2\pi t}{50} + 0.4\sin\frac{2\pi t}{75}$$

Here, the initial weight matrices of PID neural network be the same as the above example, the innovation length $p = 3$, the learning rate $\eta = 0.015$. The system responses are shown in Fig. 4 and Fig. 5.

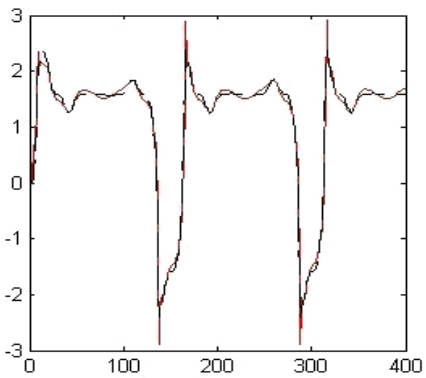

Fig. 4. Identification effect of the unmodified algorithm.

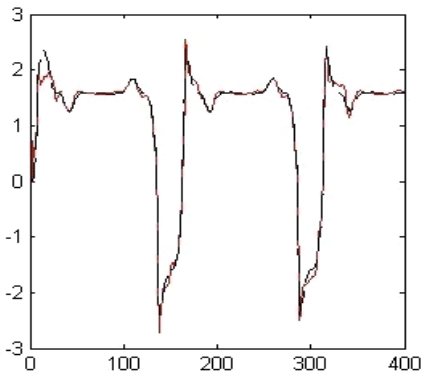

Fig. 5. Identification effect of the proposed algorithm.

6. Conclusions

This paper proposed a multi-innovation learning algorithm based on PID neural network and analyses the convergence of the algorithm. From the simulation example, it is shown that the proposed algorithm has fast convergence rate and good tracking ability.

References

[1]. Huailin Shu, Youguo Pi, PID neural networks for time-delay systems, *Computers and Chemical Engineering*, Vol. 5, 2000, pp. 859-862.

[2]. Shu Huai-Lin. Identification of Nonliner Systems Based on PID Neural Networks, *Acta Automatica Sinica*, Vol. 28, Issue 3, 2002, pp. 301-305.

[3]. Shou-Ju Li, Ying-Xi Liu, An Improved Approach to Nonlinear Dynamical System Identification using PID Neural Networks, *International Journal of Nonlinear Sciences and Numerical Simulation*, Vol. 7, Issue 2, 2006, pp. 177-182.

[4]. Xu Shaoyun, BP learning algorithm of online mode and batch mode, in *Proceedings of Chinese Intelligent Automation Conference Papers*, China Beijing, 15-17 May 1996, pp. 501-505.

[5]. Feng Ding, Tongwen Chen, Performance analysis of multi-innovation gradient type identification methods, *Automatica*, Vol. 43, Issue 1, 2007, pp. 1-17.

[6]. Liu Ying-Yu, Shen Dong-Ri, Chen Yi-Jun, Li Rong, Multi-innovation stochastic gradient identification algorithm based on feedforward neural networks, *Journal of Harbin University of Commerce (Natural Sciences Edition)*, Vol. 22, Issue 2, 2006. pp. 78-86.

[7]. Shu Huailin, On the Ability the PID Neural Networks in Nonlinear System Indentification, *Automation & Information Engineering*, Vol. 4, 2001, pp. 14-20.

[8]. Huailin Shu, Youguo Pi, Decoupled Temperature Control System Based on PID Neural Network, in *Proceeding of the ACSE' 05 Conference*, China Shanghai 14-16 August 2005, pp. 19-21.

[9]. Fardadi M., Selk Ghafari A., Hannani S. K., PID neural net-work control of SUT building energy management system, in *Proceedings of the IEEE/ASME International Conference on Advanced Intelligent Mechatronics*, China Changsha 24-26 May 2005, pp. 682-686.

[10]. Qin Pinle, Lin Yan, Chen Ming, Improvement of Tracking Performance in Model-Free Adaptive Controller Based on Multi-innovation and Particle Swarm Optimization, *International Journal of Innovative Computing, Information and Control*, Vol. 5, Issue 5, 2009, pp. 1367-1377.

[11]. Lei Guo, Time-Varying Stochastic Systems-Stability, Estimation and Control, *Changchun: Jinlin Science and Technology Press*, 1993.

[12]. Yanjun Liu, Li Yu, Feng Ding, Multi-innovation extended stochastic gradient algorithm and its performance analysis, *Circuits Syst. Signal Processing*, Vol. 29, Issue 4, 2010, pp. 649-667.

Sensors & Transducers, Vol. 21, Special Issue, May 2013, pp. 147-152

Sensors & Transducers

http://www.sensorsportal.com

Research on Automatic Identification for the Leakage Signal of Petroleum Pipeline

[1] Wei Liu, [2] Hongzhao Liu

[1] School of Mechanical and Precision Instrument Engineering, Xi'an University of Technology, Xi'an, Shaanxi, 710001, China

[2] Department of Computer Science and Technology, Shaanxi Xueqian Normal University, Xi'an, Shaanxi, 710001, China

E-mail: yuancongwang@yeah.net

Received: 26 March 2013 /Accepted: 14 May 2013 /Published: 30 May 2013

Abstract: The waveform of dynamic pressure wave contains the safety information of petroleum pipeline. The complete automatic identification program for the leakage signal of petroleum pipeline was proposed based on the characteristics of the dynamic pressure wave signal from the point of view of the signal processing. Wavelet and empirical mode decomposition method were adopted to deny the signals collected by dynamic pressure transmitter respectively. We tried to use the statistical characteristics of the one-dimensional digital sequence to describe the signal. Support vector machine method which is suitable to small size sample was selected to automatically identify the leaked signal of petroleum pipeline. And a relatively high signal identification rate was acquired. *Copyright © 2013 IFSA.*

Keywords: Dynamic pressure wave, Statistical characteristic, EMD, SVM.

1. Introduction

Pipeline transport is an important mode of transportation that is related to the national economy, life, environment and safety, as one of the five major modes of transportation. Due to aging pipes, naturally corrosion, vandalism and other reasons, pipeline breaks happens occasionally. The pipeline leak not only caused a waste of energy, but also a threat to the safety of the surrounding people's lives. The present detection methods for petroleum pipeline leaks are mainly divided into two categories, including the hardware-based detection methods such as observation method, the cable method for leak detection, tracer detection method and the leak detection method for optical fiber as well as the software methods[1] such as negative pressure wave method, the pressure gradient method, real-time model method, the mass balance method, statistical decision-making method, stress wave method and acoustic emission method. Negative pressure wave method is often used in pipeline leak detection in view of easy construction and low-cost. Negative pressure wave method is taken as the theoretical basis of the study in this paper. Due to the sensitivity of the dynamic pressure transmitter for the weak variation of pressure, dynamic pressure transmitter replaced the pressure sensors in the negative pressure wave experiments to analyze and process the dynamic pressure variation signals. In addition, support vector machine method was adopted to automatically identify and classify the acquired signals.

2. Dynamic Pressure Wave Signals

Negative pressure wave method [2] measures the absolute pressure on the pipeline. The pressure

variation signals caused by leakage are usually small and low signal noise ratio. The weak pressure variation is difficult to capture due to the sensitivity of the pressure sensor. Thus the pressure variation can't be captured when leakage and small leakage occurs. The research data of this paper is the internal pressure variation in the pipeline, coming from the piezoelectric dynamic pressure transmitters [3] installed at both ends of the pipeline. The dielectric surface in the piezoelectric sensor generated the electrical charge, caused by the internal pressure variation in the pipeline. The charge signals were enhanced through the charge amplifier and multi-stage amplifier. Therefore, the obtained signals not the actual value of the pressure variation, merely reflecting the trend of the signal variation. Dynamic pressure transmitter has higher sensitivity for the instantaneous pressure variation in the pipeline compared with pressure sensor.

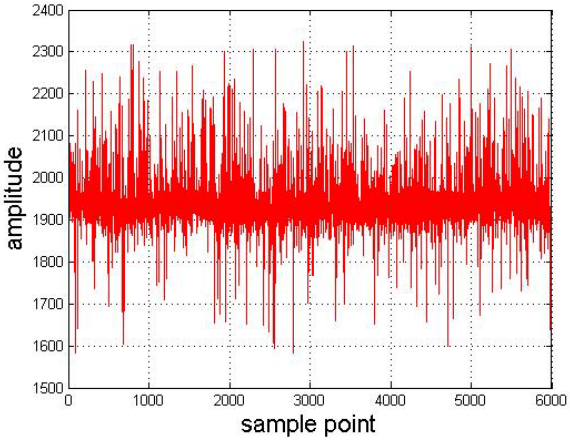

Fig. 1. Normal signals of the pipeline.

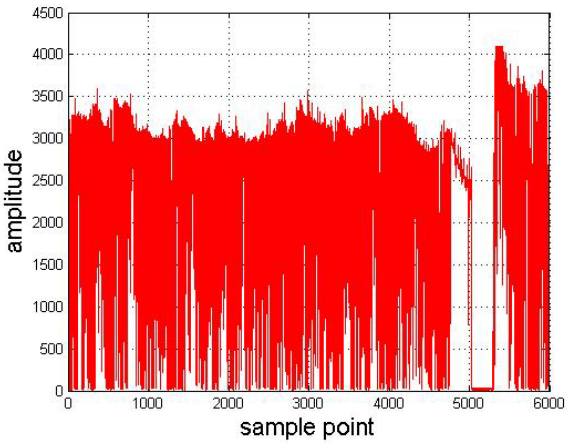

Fig. 2. Abnormal signals of the pipeline.

The periodic operation of the centrifugal pump, the characteristics of the pipeline, friction, etc. would cause the straight fluctuations of the internal pressure variation in the pipeline with the normal running of the oil transportation. The obtained signals are shown in Fig. 1. Leakage occurred, triggering a rapid decline of the pressure at the leak. Afterwards, the pressure rebounded, tending towards the new pressure balance after a period of fluctuation. The signal variation is shown in Fig. 2. The sampling interval of the experimental signal is 20 ms. The sampling frequency is 50 Hz. The sampling total duration is 2 minute each time. 6000 sampling points are obtained. Seen from the above figure, the obtained signal of the dynamic pressure sensor is the linear superposition of the useful signal and noise signal. The waveform character of the useful signal reflects the security status of the pipeline. The useful signal can be extracted from the mixed signals to make analysis through signal processing. The problems that we are concerned about are how to remove the noise and how to make the demised signal not distorted and maintain the physical meaning of the signal itself completely.

3. Filtering

Sensor detection and signal processing are the two ways to obtain the useful signal. Since the circumstance of the pipeline inspection is usually relatively complex, the obtained measured signal and its interference signal are often the non-stationary signals. Thus it is difficult to eliminate the noise by filtering the measured data directly. Next, wavelet and EMD (Empirical Mode Decomposition) method are adopted to process the signals respectively.

3.1. Waveform Denoising based on EMD Method

EMD (Empirical Mode Decomposition) method [4] is a new processing method of non-linear and non-stationary signals presented by U.S. NASA Chinese American Dr. Huang E and his research team in 1998. It has been successfully applied to the turbulence, earthquake and atmospheric sciences well as engineering fields such as zoology, environment, economic and biomedicine. The method adaptively selects the decomposed signal band based on the time-scale characteristics of the data itself. The resolution of the signal in the different frequency bands is determined. The signal is gradually decomposed into several intrinsic mode components IMF (Intrinsic Mode Functions) and a residual amount in accordance with the scale (Frequency). IMF is arranged in descending order according to the rate of the frequency. Each IMF component is a stationary signal with nonlinear characteristics. The local feature of the signal is protruded. Every decomposed IMF must satisfy: the number of the extreme points and the zero crossing points in each component are equal, or at most a difference of one; the component curve can meet the symmetry criterion

and the mean of the maximum value and the minimum value is zero in any position.

The steps of EMD method to decompose IMF components are as follows:

(a) Find all the local maximums and minimums in the signal. The cubic spline function is used to connect the maximums and minimums respectively. Then the upper and lower envelopes are generated. Set the original signal $x(t)=h_0(t)$.

(b) The mean of the upper and lower envelope is obtained, symbolized by m0. And the difference between the source signal and the mean of the envelope is obtained.

$$h_j(t)=h_{j-1}(t)-m_{j-1}(t), \tag{1}$$

(c) h_j is checked to see if it meets the IMF conditions. If not, then go back to step 1, take $h_j=h_{j+1}$ as the original signal and restart the screen. If satisfied, then $imf_i(t)=h_j(t)$.

$$SD=\sum_{i=0}^{r}\frac{\left|h_j(t)-h_{j-1}(t)\right|^2}{h_j(t)^2}\le\varepsilon \tag{2}$$

(d) Eliminate the intrinsic mode components.

$$r_i(t)=r_{i-1}(t)-imf_i(t), \tag{3}$$

(e) If the extreme points of $r_i(t)$ are greater than 2, then $i=i+1$. Continue to decompose.

EMD method is used to decompose the dynamic pressure wave signal. The 12-layer IMF components arranged in accordance with the frequency from high to low are acquired. For Fig. 2 signal, the highest and lowest frequency components are removed based on experience. The 4-9 layer reconstructed signals are used, shown in Fig. 3(a). The processed signal protrudes the oscillation characteristics of the leakage.

3.2. Waveform Denoising based on Wavelet Method

Wavelet transform [5] is a time–scale method for signal analysis, which conducts translation and scaling on the finite or rapidly decaying oscillation waveform of the mother wavelet to match the input signal. It is different from Fourier transform. Fourier transform, established in linear system theory, takes the sinusoidal wave that extends infinitely in both directions as the orthogonal basis function. Fourier transform can only partially characterize signal infrequency domain and is not suitable for processing the non-stationary signal. But wavelet transform has the ability to characterize the local characteristics of the signal in both time domain and frequency domain. It is a common method to process the non-stationary signal. The frequency resolution is high and the time resolution is low in the low-frequency part; the frequency resolution is low and the time resolution is high in the high-frequency part. It is known as the microscope for signal analysis, being widely used in the field of astrophysics, seismology, optics, biomedicine, etc. Wavelet transform is suitable for detecting the abnormal signal entrained in the normal signal. For transient signal or highly localized signal, since its components are not similar to any Fourier basis functions and the transformation coefficients are not compact, the traditional Fourier transform can't be used to conduct the time-frequency analysis. Therefore, the more mature wavelet method is selected to conduct the denoising. The results are taken as the baseline compared to EMD method.

The signal in Fig. 3 (b) is the dynamic pressure wave signal after the decomposition and reconstruction of the 4 layer of db9 wavelet basis. The signal extracted by the wavelet method can be seen to retain the oscillation characteristics of the original signal, protruding the local oscillation characteristics of the leaked signal. In addition, the denoised signals of the two methods share some similarities in waveform to some extent. Which method is more appropriate to process the dynamic pressure wave signal should be determined by the effect of the waveform identification.

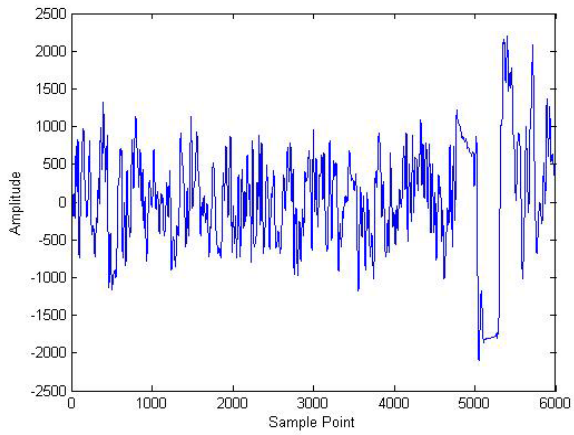

Fig. 3 (a). EMD denoising.

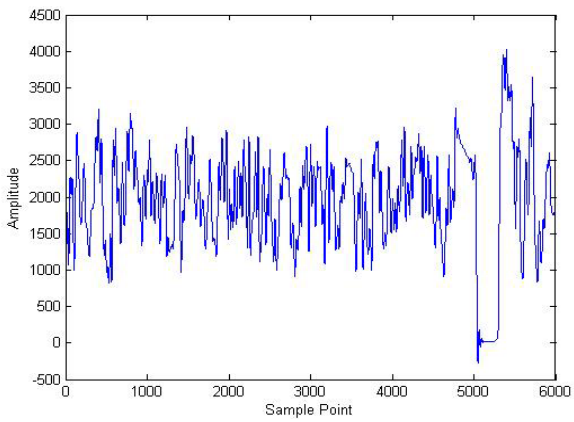

Fig. 3 (b). Wavelet denoising.

4. The Extraction of the Waveform Character

The dynamic pressure wave signal after the denoising is a one-dimensional digital sequence. The statistical characteristic is the common method to describe digital sequences. The extraction of the statistical characteristics for one-dimensional digital sequence is described in detail in the literature 6. Herein, the statistical characteristics of the extracted signal of the two noise reduction methods are calculated respectively. The 9 eigenvalues such as mean value, three mean, and variance, and standard deviation, coefficients of variation, range, quartile range, skewness and kurtosis. The formulas are shown as follows:

Mean value:

$$J_i = \frac{1}{6000}\sum_{k=1}^{6000} a_k \tag{4}$$

Three mean:

$$\acute{M}_i = \frac{1}{4}M_{i_{0.25}} + \frac{1}{2}M_i + \frac{1}{4}M_{i_{0.75}} \tag{5}$$

Variance:

$$s_i^{\,2} = \frac{1}{6000-1}\sum_{k=1}^{6000}\left(a_k - \bar{a}\right)^2 \tag{6}$$

Standard deviation:

$$S_d = \sqrt{S_i^{\,2}} \tag{7}$$

Coefficients of variation:

$$V_i = s_i / J_i \tag{8}$$

Range:

$$R_i = max(a) - min(a) \tag{9}$$

Quartile range:

$$Q_R = Q_3 - Q_1 \tag{10}$$

Skewness:

$$p_{d_i} = \frac{6000^2 u_{3_i}}{(6000-1)(n-2)s_i^{\,3}} \tag{11}$$

Kurtosis:

$$f_{d_i} = \frac{6000^2 u_{4_i}}{(6000-1)(6000-2)s_i^{\,4}} - \frac{3(6000-1)^2}{(6000-2)(6000-3)} \tag{12}$$

Extract the 9 statistical characteristics from 30 groups of pressure wave signals obtained in the normal state and 10 groups of pressure wave signals in the leakage state respectively. The result is shown in Fig. 4. Seen from Fig. 4, although there are several differences in the statistical characteristics extracted from the two methods, it is obvious that the statistical characteristics of the latter 10 groups of abnormal data in the two methods change significantly.

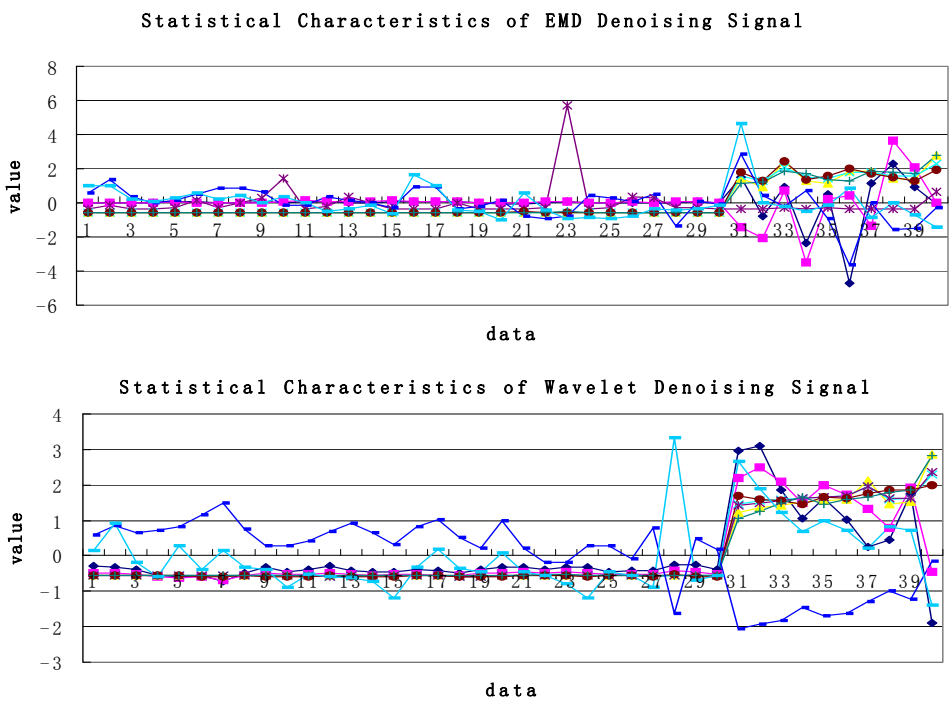

Fig. 4. Test data.

5. SVM Method to Identify Leaks

Support vector machine method is a new method of machine learning based on statistical learning theory, which is developed in the mid-1990s. The minimization of empirical risk and confidence interval is achieved by using structural risk minimization principle to improve the generalization capability of the learning machine. Good statistical regularities can be acquired when the statistical sample size is small. The topological structure of the method is determined by support vectors. It overcomes the problems such as the network structure of artificial neural networks, etc. is difficult to confirm, over-fitting and under-fitting as well as the local minimum. The curse of dimensionality does not exist. The generalization capability is high. The method has been hailed as the best method to deal with the classification problems for tiny samples at present [7]. SVM method maps the training data nonlinearly into a high-dimensional space via kernel function instead of the inner product. The optimal separating hyper plane is constructed in the high-dimensional space via the determination of the support vectors, so that the distances between each support vector and the optimal separating hyper plane is the minimum. The classification problem is transformed to the problem of finding the optimal separating hyper plane in high-dimensional space. The essence of the problem is solving a convex quadratic optimization problem, so that the local optimal solution is certainly the global optimal one.

The work site is difficult to obtain leakage data, so the automatic identification of the dynamic pressure wave signal is a small-sample problem. As the identification of the pipeline dynamic pressure wave signal is a binary classification, i.e. the normal signal and abnormal signal, the C-SVM method of the SVM toolbox of Matlab 7.6 software was used in this paper. Kernel_Function was selected as rbf and RBF_Sigma was selected as 5. The modeling of the characteristic data obtained in the above two methods was conducted respectively. Moreover, 5 groups of normal data and abnormal data were prepared. EMD and wavelet method were used to conduct the denoising respectively. The denoised data was taken as the experimental data. The experimental results were: EMD method, modeling data was used for cross-validation, the classification accuracy: 95 %. 10 groups of experimental data were used for validation, accuracy: 70 %. Wavelet method, modeling data was used for cross-validation, the classification accuracy: 100 %. 10 groups of experimental data were used for validation, accuracy: 70 %.

6. Conclusions

The wavelet transform is a common method of processing non-linear and non-stable signal. However, the wavelet basis is usually selected based on experience during the wavelet transform of the signal. The selection of wavelet basis has a direct impact on the effect of the signal processing. Furthermore, wavelet basis can't transform in the process of signal processing. EMD method decomposes the signal into several IMF components based on the time-scale local characteristics of the signal. Each IMF component contains the information of the local characteristics of the original signal, being able to characterize the physical significance of the instantaneous frequency of the actual signal. Therefore, the adaptively of EMD method is stronger than wavelet method. At first, EMD and wavelet method were adopted to conduct the signal denosing in this paper. Then the statistical characteristics of the signal processed by the two methods are extracted. And the C_SVM method is adopted classify the dynamic pressure wave signal after the processing. The experimental results show that relatively good identification results can be obtained by using the statistical characteristics to describe the pressure wave signal. C_SVM method is suitable for the automatic identification of the dynamic pressure wave signal in petroleum pipeline. Although the method of the automatic identification for dynamic pressure wave signal has been proposed completely in the experiment, there are some aspects that can also be improved: 1) The number of the signal is relatively small. A large amount of data is required to verify the method; 2) The number of the normal signals and abnormal signals in the experimental data for modeling is not balanced. The identification accuracy may be influenced due to the restrictions of the C_SVM algorithm itself; 3) The effectiveness of the feature extraction method should be compared with other methods. 4) The selection of the modeling data will affect the identification results.

Acknowledgements

The study is funded by the youth projects (2012KJ042) of Shaanxi Xueqian Normal University.

References

[1]. Lin Weiguo and Zheng Zhishou, Research on detection technology for pipeline leak based on dynamic pressure signal, *Chinese Journal of Scientific Instrument*, Vol. 27, Issue 8, 2006, pp. 907-910.

[2]. Silva R. A., Bu Iatti C. M., Crvz S. L., et a1., Pressure wave behavior and leak detection in pipe line, *Computers Chem. Engng*, Vol. 20, 1996, pp. 491-496.

[3]. Jia Jingkun, Research on detection technology for natural gas pipeline leak based on voiceprint comparison, M. S. Thesis, *Beijing Institute of Chemical Technology*, 2012.

[4]. Huang N. E. , Shen Z. and Long S. R., The Empirical mode decomposition and Hilbert spectrum for nonlinear and non-stationary time series analysis, *Proc. Roy. Soc*, Vol. 454, 1998, pp. 903-995.
[5]. The Feisi technology R & D center, The wavelet theory and MATLAB7 achievement, *Beijing: Publishing House of Electronics Industry*, 2005.
[6]. Li Yihua, The assist of MATLAB for modern engineering digital signal processing, *Xidian University Publishing House*, 2010.
[7]. Li Bonian and Wu Libin, MATLAB data analysis methods, *Machinery Industry Press*, 2012.
[8]. ABE S. Support vector machine for pattern classification, *Springer-Verlag*, 2005.

Sensors & Transducers, Vol. 21, Special Issue, May 2013, pp. 153-158

Sensors & Transducers

http://www.sensorsportal.com

Adaptive Watermarking Algorithm in DCT Domain Based on Chaos

Wenhao Wang
Computer Engineering Faculty, Huaiyin Institute of Technology,
Huaian, Jiang Su, 223003, China
E-mail: wenhaowang2013@sina.com

Received: 26 March 2013 /Accepted: 14 May 2013 /Published: 30 May 2013

Abstract: In order to improve the security, robustness and invisibility of the digital watermarking, a new adaptive watermarking algorithm is proposed in this paper. Firstly, this algorithm uses chaos sequence, which Logistic chaotic mapping produces, to encrypt the watermark image. And then the original image is divided into many sub-blocks and discrete cosine transform (DCT).The watermark information is embedded into sub-blocks medium coefficients. With the features of Human Visual System (HVS) and image texture sufficiently taken into account during embedding, the embedding intensity of watermark is able to adaptively adjust according to HVS and texture characteristic. The watermarking is embedded into the different sub-blocks coefficients. Experiment results haven shown that the proposed algorithm is robust against the attacks of general image processing methods, such as noise, cut, filtering and JPEG compression, and receives a good tradeoff between invisible and robustness, and better security. *Copyright © 2013 IFSA.*

Keywords: Watermarking, Chaotic encryption and decryption, DCT, Human visual system, Texture, Attack test.

1. Introduction

With the rapid development and wide application of the multimedia and network technology, the storage, replication and transmission of digital media become very convenient, which has made a serious social problem of the ownership of products. As the time requires, digital watermarking develops rapidly as a copyright protection technology. At present, there are mainly the space domain algorithms and transform domain algorithms [1, 2]. The spatial domain algorithm is that watermark information is embedded directly into the pixels of the image. This algorithm is simple, but robustness is poor a. As for the transform algorithm, such as discrete wavelet transform (DWT) and discrete cosine transform (DCT), it can make the energy distribute to all the pixel space, so the algorithm has good robustness and application prospect [3, 4].

The key techniques of the watermark algorithm are the degree of image scrambling and the location and intensity of embedding. In scrambling aspects, there is mainly Arnold transform at present. The essence of Arnold shuffling is an iterative process, which needs high time complexity, and this shuffling has periodic. So the algorithm is poor security and easily cracked. Now many scholars study on the chaos systems characteristics. The watermark data encrypted by chaos can ensure the security of the transmission. In the aspect of watermark embedding location, research results have shown that humans' eyes are more sensitive to the parts of the low frequency. If the watermark information should be embedded into the high frequency parts of the image, it will lose information because of the attacks of noise, filter, and compression. So the watermark information is embedded into the intermediate frequency part of the image. In terms of the watermark embedding strength, research results have shown that the higher watermark energy is embedded, the watermark imperceptibility will be worse. But the robust will be better .On the contrary, the lower watermark energy is embedded;

the watermark imperceptibility will be much better. But the robust will be worse. So the embedding strength should be adjusted with the luminance and image texture.

In view of this, this paper presents an adaptive watermarking algorithm based on Chaos in DCT domain. Firstly encrypt the watermark image with the logistic chaos technology, and then make sure embedding strength according to the features of Human Visual System (HVS) and image texture, finally, the watermark is embedded into the DCT intermediate frequency coefficients.

2. Encryption Based Chaos

2.1. Chaotic Encryption

The Chaos is a kind of complicated dynamics system. Chaos is the process of the determining and random in the nonlinear dynamic system, and the process is neither periodic nor convergence, and it has extremely sensitive dependences to initial value. It is often used to encrypt the image to improve the security performance of image [5, 6]. The chaotic systems mainly include: Logistic Mapping, Tent-Map Mapping, Rosslea System, Lorenz System, Chen System, Lu system and so on. Logistic mapping is the simplest mapping among these mapping. The formula is described as follows:

$$x_{k+1} = ux_k(1 - x_k) \tag{1}$$

When $3.5699456....<u\leq 4$, the Logistic function will work in a chaotic state, and will generate the neither periodic nor convergence sequence $\{x_k : k = 0,1,2,...\}$. So the security of watermarking information can be greatly improved, if watermark image is encrypted by Logistic chaotic sequence.

2.2. Chaotic Encryption Based on Logistic

Suppose that $\{P_n\}$ is a plaintext information sequence, $\{K_n\}$ is the key information sequence, $\{C_n\}$ is the cryptograph information sequence.

The encryption algorithm based on the chaos is described as follows:

$$\{C_n\} = \{P_n\} + \{K_n\} \tag{2}$$

As shown Fig. 1 is the principle of the encryption and decryption based on chaotic:

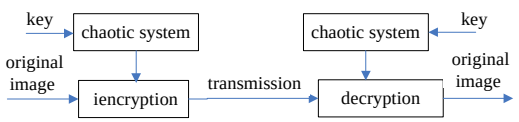

Fig. 1. The encryption and decryption based on chaotic.

The key is freely chosen by the user in Fig. 1. It makes decryption more difficult. Besides, so very small initial errors will transmit to the relevant domain space quickly. This feature also increases the difficulty of decryption. The specific algorithm is as follows:

(1) Input the original image, the key u and $Xstart$.

(2) According to Logistic function, calculate N times again and again (The N value is random number), Final function value is referred to y and $Xstart = y$.

(3) Compute chaos byte. Reading each pixels information, Computing 8 times again and again according to the Logistic function, Each times generates a bit of $chaos$ value, which this value rests with the size of y and $u/6$. If $y \geq u/6$, $chaos = 1$. Otherwise $chaos = 0$. Finally, they will be assembled into a byte. The new value will be generated through this chaos value XOR pixel value.

(4) Continue reading the next pixel, computing the next chaos byte, and carrying on XOR operation, such as deals with all the pixels in the image, finally, the encrypted image will be got.

This algorithm is the symmetric algorithm. The decryption is the same key with the encryption. As long as keys are correct, the encrypted image can be correctly decrypted. As shown Fig. 2 is the test results, when $u = 3.9$ and $Xstart = 0.7$; as shown Fig. 2 (a) is the original image; as shown Fig. 2 (b) is the encrypted image; The original image information has been scrambled, which has achieved the better visual effect; as shown Fig. 2(c) is the correctly decrypted result; as shown Fig. 2 (d) is the decrypted result, when $u = 3.9000001$, $Xstart = 0.7$. Although the error is very small, Fig. 2 (b) can be the correctly decrypted. As shown Fig. 2 (e) is the histogram of Fig. 2(a). As shown Fig. 2 (f) is the histogram of Fig. 2 (b); Obviously, the histogram of the watermark image can be changed by chaotic encryption, which makes it uniform distribution and avoids the possibilities that attacker may detect the watermark using statistical methods.

3. Adaptive Watermarking Algorithm

3.1. DCT Transform

Suppose the image is denoted as $f(x, y)$, $0 \leq x \leq N-1$, $0 \leq y \leq N-1$, $f_m(i, j)$ is a 8×8 sub-block. $0 \leq i \leq 7$, $0 \leq j \leq 7$, $m = 0,1,2,..,(N^2/64)-1$. The formula of DCT transform is as follows:

$$F(u,v) = \frac{1}{4}C(u)C(v)\sum_{i=0}^{7}\sum_{j=0}^{7} f_m(i,j)\times\cos\left[\frac{(2i+1)u\pi}{16}\right]\cos\left[\frac{(2j+1)v\pi}{16}\right] \tag{3}$$

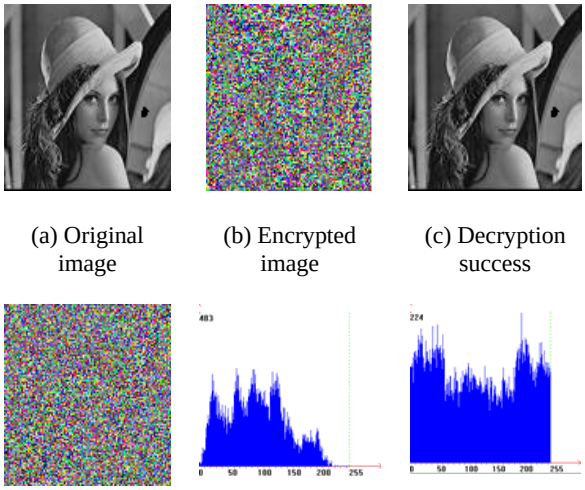

(a) Original image (b) Encrypted image (c) Decryption success

(d) Decryption failure (e) Fig (a) histogram (f) Fig (b) histogram

Fig. 2. The encrypted and decrypted based on Logistic

The formula of IDCT transform is as follows:

$$f_m(i,j)=\frac{1}{4}C(u)C(v)\sum_{u=0}^{7}\sum_{v=0}^{7}F(u,v)\times\cos\left[\frac{(2i+1)u\pi}{16}\right]\cos\left[\frac{(2j+1)v\pi}{16}\right] \quad (4)$$

$$C(u)=C(v)=\begin{cases}\frac{1}{\sqrt{2}} & u=v=0\\ 1 & other\end{cases}, \quad (5)$$

where $f_m(i,j)$ is the grey value of the pixel (i,j), $F(u,v)$ is the DCT coefficient, $F(0,0)$ is the DC coefficient, the other is AC coefficient. Research results have shown that humans' eyes are more sensitive to the low-frequency noise. So the watermark should be embedded into the high frequency part of original image. However, it will lose information because of the attacks of noises, filter, and compression. It will have influence on the robustness of the watermark. In order to solve this contradiction, in this paper, watermark is embedded into the intermediate frequency of the original image.

3.2. Adaptive Embedding Strength

The formula, which watermarking is embedded based on DCT, is as follows

$$F^{'}(u,v)=F(u,v)+\alpha_k w_i \quad (6)$$

The higher brightness of the background (The DC coefficient is bigger) becomes, and the higher the watermark embedding strength will be; the more complex image texture is (the greater variance of image is), and the higher watermark embedding strength will be [7]. In this paper, the embedding strength based on the luminance masking and texture characteristic is adaptively adjusted. The calculation of the embedding strength factor is described as follows:

(1) The original image $f(x,y)$ is divided into $K\times 8\times 8$ sub-blocks, each sub-blocks is denoted as $f_k^{'}(x^{'},y^{'})$ $0\le x^{'},y^{'}\le 7$, ($k=0,1,2...,K-1$), where K is the number of sub-blocks. DCT transform is applied to each sub-block. Sub-blocks coefficients through the DCT transform are denoted as $F_k(u,v)$. The calculation formula of the mean value and variance is as follows:

$$u_k=\frac{1}{64}\sum_{i=0}^{8}\sum_{j=0}^{8}F_k(u,v) \quad (7)$$

$$\sigma_k=\frac{1}{64}\sum_{i=0}^{8}\sum_{j=0}^{8}(F_k(u,v)-u_k) \quad (8)$$

(2) Calculate the embedding strength factor of each sub-block. Suppose $min\sigma_k$ is the minimum variance, $max\sigma_k$ is the maximum variance, $minL_{DC}$ is the minimum value of DC coefficient; $maxL_{DC}$ is the maximum value of DC coefficient. The formula is as follows:

$$\alpha_1\frac{\sigma_k-min\sigma_k}{max\sigma_k-min\sigma_k} \quad (9)$$

$$\alpha_2=\frac{L_{Dc}-minL_{DC}}{maxL_{DC}-minL_{DC}} \quad (10)$$

So embedding strength factor is described as follows: $\alpha_k=\alpha_1+\alpha_2$, $i=0,1,2,...K-1$ .The embedding strength can be changed with the characteristic of the illumination and image texture. Namely, the embedding strength is adaptive.

(3) Calculate the threshold of the embedding factor α_k. According to the signal-to-noise ratio (SNR) and formula (6), the formula is as follows:

$$SNR=20\lg\frac{\sqrt{\sum_{k=0}^{K-1}F_k(u,v)^2}}{\sqrt{\sum_{k=0}^{K-1}(F_k^{'}(u,v)-F_k(u,v))^2}}=20\lg\frac{\sqrt{\sum_{k=0}^{K-1}F_k^2(u,v)}}{\alpha_k\sqrt{\sum_i(w_i)^2}} \quad (11)$$

$$\alpha_k=\frac{\sqrt{\sum_{k=0}^{K-1}F_k^2(u,v)}}{\alpha_k\sqrt{\sum_i(w_i)^2}}10^{-\frac{SNR}{20}} \quad (12)$$

The single-to-noise ratio (SNR), is often in above 20 dB. it will affect the visual effect of image below 20 dB. The SNR in the formula (12) was replaced with a 20; the following threshold value is as follows:

$$\bar{\alpha} = \frac{\sqrt{\sum_{k=0}^{K-1} F_k^2(u,v)}}{10\sqrt{\sum_i (w_i)^2}} \tag{13}$$

If $\alpha_k < \bar{\alpha}$, Revise DCT coefficient with α_k , otherwise revise DCT coefficient with $\bar{\alpha}$

4. Watermark Embedding and Extraction

4.1. Algorithm of the Watermark Embedding

Suppose the size of the watermark image W is $P \times Q$. The size of the original image I is $M \times N$. The embedding procedure is as follows:

(1) Encrypt the watermark image W based on the chaotic encryption algorithm; the watermark sequence which length is $P \times Q \times 8$ bytes will be obtained.

(2) The original image $I(M \times N)$ is divided into 8*8 sub-blocks, each sub-block is denoted as $f_m(x, y), x = 0,1,2...7,\ \ y = 0,1,2...7$, k=0, 1. . . $\frac{M \times N}{8 \times 8} - 1$, DCT transform is performed on each sub-blocks, the result is $F_k(u,v)$, $u = 0,1,2...7, v = 0,1,2...7$.

(3) According to formula (7 and formula (8) calculate the mean value and variance of the gray image. Get the DC coefficient ($F_k(0,0)$) of the each sub-block. Calculate FI_k of the sub-block according to $FI_k = F_k(0,0) + \sigma_k$. The value reflects the comprehensive illumination characteristics and texture characteristics of each sub-block.

(4) Sort FI_k of the all sub-blocks. Select the l sub-blocks that their FI_k values are the biggest. Where l is number of the sub-blocks. Then, sort the intermediate frequency coefficient of each selected sub-blocks, Select the first q biggest intermediate frequency coefficients, where q is number of intermediate frequency which will be modified.

(5) Calculated threshold $\bar{\alpha}$ and the embedding strength α_k . The watermark embedding formula is described as follows: $F_k^{'}(u,v) = F_k(u,v) + \alpha_k w_i$; If $\alpha_k < \bar{\alpha}$, revise DCT coefficient with α_k , otherwise revise DCT coefficient with $\bar{\alpha}$.

(6) Using IDCT transform to $F_k(u,v)$, the watermarked image will be abstained.

4.2. Algorithm of the Watermark Extraction

The watermark extraction process is the inverse process of watermark embedding. The specific steps are as follows:

(1) The original image and watermarked image are divided into the 8×8 sub-blocks, and DCT transform is performed on each block. Suppose their Coefficients are respective $F_k(u,v)$ and $F_k^{'}(u,v)$ after DCT transformation

(2) Sort FI_k of the all sub-blocks, Select the l sub-blocks that their FI_k value are the biggest.

(3) Sort the intermediate frequency coefficients of each selected sub-blocks; select the first q biggest intermediate frequency coefficient. Use the inverse process of watermark embedding formula. Watermark ($W_k^{''}$) sequences are got. The method is as follows:

$$W_k^{'} = \frac{F_k^{'}(u,v) - F_k(u,v)}{\alpha_k} \tag{14}$$

$$W_k^{''} = \begin{cases} 1, \left| W_k^{'} - \lfloor W_k^{i} \rfloor \right| > 0.5 \\ 0, \left| W_k^{'} - \lfloor W_k^{i} \rfloor \right| < 0.5 \end{cases} \tag{15}$$

(4) Decrypt the one-dimensional watermark sequence; we can get the watermark image sequence.

(5) The watermark sequences reformulate 2D watermarking matrix. The watermark image can be obtained immediately.

5. Experimental Result

The gray image Lena (512×512) is used as the original image (Fig. 3(a)). As shown Figure 3(b) is the watermark image (32×32), the simulation experiments are tested on the platform of Matlab7.0.

Fig. 3. Original image and Watermark image.

As shown in Fig. 4(a) is the encrypted watermark image. As shown Fig. 4(b) is the effect of original image embedded by watermark. As shown Fig. 4(c) is extracted watermark from Fig. 4(b). The peak signal-to-noise ratio ($PSNR$) value is 40.25. Obviously, the algorithm ensures the invisibility of watermark embedding.

(a) Encrypted watermark (b) Host image (c) Extract watermark

Fig. 4. Watermark embedded and extracted image.

In order to test the robustness of the algorithm, the watermarked image is attacked by added noise, filtered and JPEG compression respectively. The experimental results are as shown in Table 1:

Table 1. Test result of some common attacks

No.	Attack type	PSNR/dB	NC
1.	No attack	40.25	1.0
2.	Salt & pepper noise (0.01)	24.23	0.9035
3.	Gaussian noise (0.01)	20.63	0.9476
4.	Gaussian low pass filter	36.53	0.9635
5.	Median filter (3×3)	30.33	0.8248
6.	JPEG compression (90 %)	36.82	0.9883
7.	JPEG compression (80 %)	34.62	0.9801
8.	JPEG compression (70 %)	33.37	0.9712
9.	JPEG compression (60 %)	32.40	0.9402
10.	JPEG compression (50 %)	31.69	0.9204

The Table 1 shows that the algorithm is robust against the attacks of general image processing methods such as noise; filtering and JPEG compression. The algorithm in this paper is applied to Peppers, Boat, Balloon, three gray images (512×512) again. after they are suffered from various image attacks, the watermark information is respectively extracted from them. Table 2 gives the correlation coefficient NC.

Table 2. Test results of different original image.

No.	Attack type	Peppers (NC)	Boat (NC)	Baloon (NC)
1.	No attack	1.0	1.0	1.0
2.	Salt & pepper noise (0.01)	0.8559	0.8597	0.8587
3.	Gaussian noise (0.01)	0.9348	0.9367	0.9513
4.	Gaussian low pass filter	0.9705	0.9541	0.9642
5.	Median filter(3×3)	0.8611	0.8309	0.8485
6.	JPEG compression (90 %)	0.9864	0.9813	0.9891
7.	JPEG compression (80 %)	0.9752	0.9810	0.9834
8.	JPEG compression (70 %)	0.9703	0.9638	0.9719
9.	JPEG compression (60 %)	0.9337	0.9315	0.9406
10.	JPEG compression (50 %)	0.9305	0.9286	0.9304

In order to test algorithm's character of against geometric attack, this paper make a Scaling, cropping and rotation test to the watermarked image. The test results are shown in Fig. 5: The NC and PNSR values are shown in Table 3:

(a) Scale (0.5,2) and extracting watermark.

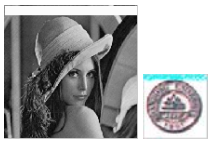

(b) Cropping attract and extracting watermark.

(c) Rotation 23 angle and extracting watermark.

Fig. 5. Geometric attack test.

Table 3. Test result on Geometric attack.

No.	Geometric distortion	PSNR/dB	NC
1.	Scale (0.5,2)	25.67	0.9298
2.	Cropping	29.53	0.9593
3.	Rotation 23 angle	27.52	0.9047

6. Conclusions

In analyzing the foundation of the characteristic of the Chaos system, the watermark image is encrypted through Logistic mapping to improve the security of the watermark, and then encrypted watermark information is embedded into the sub-blocks DCT medium frequency coefficients Based on the feature of human visual system and image texture. The advantage of this algorithm is simple and easy. Experiments show this algorithm can achieve the desired effect.

References

[1]. Xuehua Jiang, Digital Watermarking and its Application in Image Copyright Protection, in *Proceedings of the Conference on ' Intelligent Computation Technology and Automation (ICICTA'2010)'*, Changsha, China, 11-12, May, 2010, pp. 114-117.

[2]. Pei-Yu Lin, Jung-San Lee, Chin-Chen Chang, Dual Digital Watermarking for Internet Media Based on

Hybrid, *Circuits and Systems for Video Technology*, Vol. 19, Issue 8, 2009, pp. 1169-1177.

[3]. Geng-Ming Zhu Shao-Bo, Zhang, Research and Implementation of DCT-Based Image Digital Watermarking Algorithm, in *Proceedings of the Conference on Electronic Commerce and Security (ISECS' 2009)*, Nanchang, China, 22-24, May 2009, pp. 195-198.

[4]. Zhi-Yong Meng, Ping-Ping Yu, Guo-Qing Yu, Copyright protection for digital image based on joint DWT-DCT transformation, in *Proceedings of the Conference on Wavelet Analysis and Pattern Recognition (ICWAPR' 2012)*, Xian, China, 15-17 July, 2012, pp. 11-14.

[5]. Zhao Song, Li Hengjian, Yan Xu, A new chaotic algorithm for image encryption, in *Proceedings of the Conference on Young Computer Scientists (ICYCS'2008)*, Zhang Jia Jie, Hunan, China, 18-21, November, 2008, pp. 889-892.

[6]. Zhang Yunpeng, Zuo Fei, Zhai Zhengjun, Cai Xiaobin, A New Image Encryption Algorithm Based on Multiple Chaos System, in *Proceedings of the Conference on Electronic Commerce and Security (ISECS' 2008)*, Guangzhou, China, 3-5, August, 2008, pp. 347-350.

[7]. Zheng, Jiangyong, Dong Hongling, Jiang Zengliang, Milo Jin, A DCT-BASED Digital Watermarking Algorithm for Image, in *Proceedings of the Conference on Industrial Control and Electronics Engineering, (ICICEE' 2012)*, Xian, China, 23-25, August 2012, pp. 1217-1220.

[8]. Xiao-Li Zhang, Xin Lv, A Novel Watermarking Algorithm Resist to Geometrical Attacks, in *Proceedings of the Conference on Electronic Commerce and Business Intelligence, (ECBI' 2009)*, Beijing, China, 6-7, September, 2009, pp. 503-506.

[9]. Lin Yu-Tzu-T, Huang C.-Y, Lee Greg C. Rotation, Scaling and Translation Resilient Watermarking for Images, *Image Processing*, Vol. 5, Issue 4, 2010, pp. 328-340.

[10]. Yin Thu Win, Nitin Afzulpurkar, Chumnarn Punyasai, Hla Thar Htun. Ultrasonic System Approach to Obstacle Detection and Edge Detection, *Sensors & Transducers*, Vol. 127, Issue 4, 2011, pp. 56-68.

Sensors & Transducers, Vol. 21, Special Issue, May 2013, pp. 159-163

Sensors & Transducers

http://www.sensorsportal.com

Experimental Research on Oxygen-enriched Air Supply System for Gasoline Engine

[1,2] Yahong Li, [3] Lixi Zhang, [1] Zelu Sun

[1] School of Chemistry & Chemical Engineering, Xi'an Shiyou University, Xi'an 710065, China
[2] School of Materials Science and Engineering, Xi'an Jiaotong University, Xi'an 710049, China
[3] Institute of Air-Conditioning & Solar Energy, Northwestern Polytechnical University, Xi'an 710068, China
E-mail: yahongli8@163.com

Received: 26 March 2013 /Accepted: 14 May 2013 /Published: 30 May 2013

Abstract: The paper designs and establishes a set of membrane oxygen-enriched air supply system. Experimental research is conducted for LTV-PS roll-type oxygen-enriched membrane module, results of which show that oxygen-enriched concentration is on the rise with the increase of pressure and air flow. Under normal operating temperature, the concentration of O_2 in membrane enriched air can reach 28.3 % when the operating pressure and air flow are respectively 102.7 kPa and 24 m^3/h. *Copyright © 2013 IFSA.*

Keywords: Membrane separation, Oxygen enrichment, Air supply system, Experiment.

1. Introduction

Power of automobile comes from heat energy emitted by fuel combustion within engine cylinder. When fuel combustion's heat energy provides power for engine, waste gas after the combustion will cause air pollution [1, 2]. In recent years, because of skyrocketing of oil price and environmental pollution caused by exhaust emission of automobiles, high requirements are imposed on combustion technology of engine. Therefore, from the perspective of engine combustion technology, experts and scientific research academies and institutes of all countries now make great effort to find out the most effective method that can improve engine power, reduce fuel consumption and exhaust pollution [3-6].

During combustion process of engine, the fuel can give off all heat only when it is under complete oxidation and combustion. It is easy to provide cylinder with sufficient fuel, but it is difficult to provide cylinder with sufficient oxygen for combustion. Therefore, it is believed that main factor for power level of engine lies in air (oxygen) amount instead of fuel supply for combustion. In this way, focusing on characteristics of engine combustion, certain technology that increases oxygen content in total air amount entering the cylinder can meet requirements of complete fuel combustion on oxygen content without change of engine displacement. Such technology will improve power performance and economic efficiency of engine without deteriorating emission, which is endowed with important research significance.

The paper applies the method of membrane separation to produce oxygen-enriched air and carries out experimental research on membrane oxygen-enriched air supply system so as to promote complete fuel combustion in engine and improve power performance and economic efficiency of the engine.

2. Experimental System

Oxygen-enriched air supply membrane experiment system applies one Φ100×1000 mm LTV-PS roll-type oxygen-enriched membrane module. Membrane material is polysulfone-silane rubber composite membrane, which brings better effect of oxygen enrichment. Ventilation property of oxygen enrichment is 1.0×10^{-12} $m^3/(m^2\cdot s\cdot Pa)$. Oxygen enrichment membrane apparatus is operated under vacuum conditions. Differential pressure of operation at two sides of the oxygen enrichment membrane will be maintained by air blower and vacuum pump. Experiential equipment can be seen in Fig. 1.

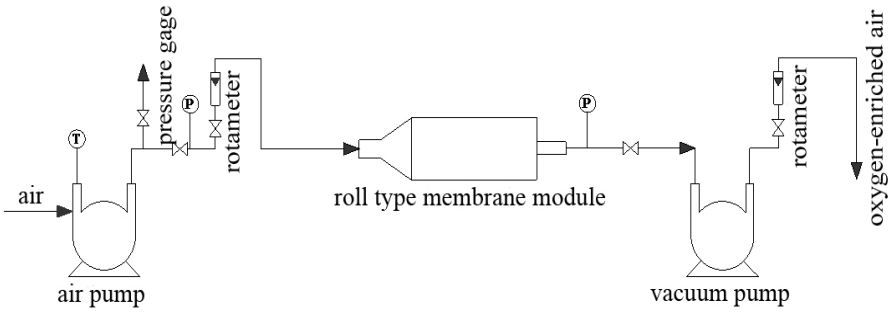

Fig. 1. Schematic diagram on oxygen-enriched air supply membrane experiment system.

When fresh air passes through filter, it will be transported to surface of high-pressure side of membrane module after mechanical impurity is removed. Vacuum pump is used for suction at low-pressure side of oxygen enrichment membrane. Gas discharged by vacuum pump is oxygen -enriched air. Impermeable gas discharged by membrane module is nitrogen-enriched air, which will be directly emitted into the atmosphere.

3. Experimental Results

Feed of experiment will be provided by air in the environment. Certain content of air enters membrane module and oxygen-enriched air will be obtained through membrane separation. After measurement, mass fractions of air are N_2 80.233 % and O_2 19.767 %. Feed quantity of air is 15 m^3/h.

Table 1. Oxygen enrichment operating parameters under different operating conditions after calibration.

Pressure for entering membrane, kPa	Pressure for exiting from membrane, kPa	Pressure ratio	Oxygen-enriched concentration, %	Flow for entering membrane, m^3/h	Amount of oxygen-enriched air, m^3/h
97.672	61.472	0.629	20.015	6.131	5.705
97.872	61.472	0.628	21.769	9.241	5.753
98.472	61.472	0.624	22.615	12.359	5.788
98.972	61.472	0.621	23.888	15.504	5.842
100.172	61.472	0.617	24.040	18.604	5.858
101.272	62.472	0.614	25.134	21.792	5.921
102.672	62.472	0.608	26.320	24.965	5.966
103.472	62.472	0.606	27.272	28.107	6.037
103.872	63.472	0.605	28.269	31.299	6.077

3.1. Relations of Pressure Ratio with Oxygen-Enriched Concentration and Amount of Oxygen-enriched Air

It can be seen from Fig. 2 and Fig. 3 that pressure ratio of pressure at two sides of oxygen enrichment membrane can vary with the vacuum degree under vacuum conditions for operation. When the pressure ratio decreases, flow of passing air (oxygen-enriched air) increases accordingly, but oxygen-enriched concentration firstly increases and then decreases slightly. The reason is that increase of vacuum degree causes greater differential pressure at the front and rear side of membrane module, resulting in increase of permeability and decrease of selectivity of the membrane, which causes increase of permeable air amount that affects oxygen-enriched concentration. Therefore, in order to improve oxygen-enriched air or concentration, differential pressure at two sides of separation membrane can be appropriately improved, but if the differential pressure is too high, it will result in increase of equipment power and power consumption.

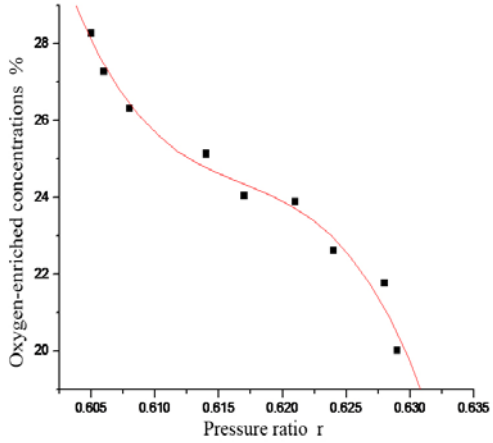

Fig. 2. Relations of pressure ratio with oxygen-enriched concentration.

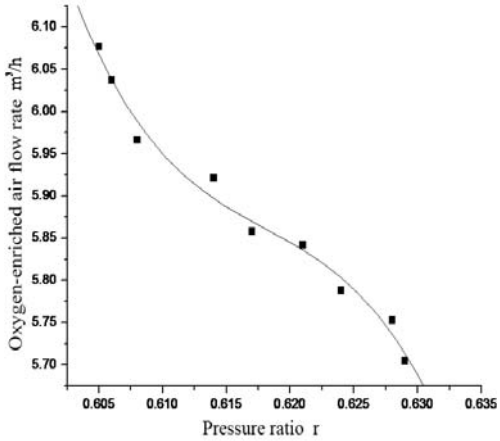

Fig. 3. Relations of pressure ratio with amount of oxygen-enriched air.

3.2. Relations of Air Supply Amount with Oxygen-enriched Concentration and Amount of Oxygen-enriched Air

It can be seen from Fig. 4 that change of flow supplied by air pump has little effect on the amount of oxygen-enriched air (in a certain range of air supply amount), but the change still affects oxygen content in oxygen-enriched air. With the increase of air supply amount, amount of oxygen-enriched air increases accordingly, but oxygen-enriched concentration firstly increases and then decreases slightly. The main reason is that under vacuum conditions for operation, limit of vacuum pump's characteristics and increase of air supply amount result in greater differential pressure at the front and rear side of membrane module, causing increase of permeability and decrease of selectivity of the membrane, which leads to the increase of permeable air amount that affects oxygen-enriched concentration. Actually, after oxygen-enriched concentration increases to a certain degree with the increase of air supply amount, it will be free from effect of air supply amount and it will mainly be controlled by vacuum degree. However, increase of air supply amount will still result in low recovery rate and high power expense.

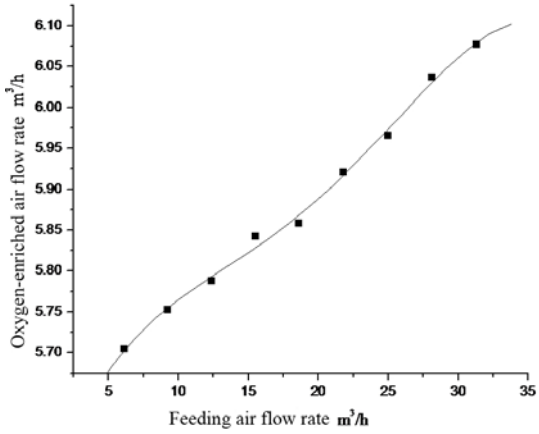

Fig. 4. Relations of air amount of feed with amount of oxygen-enriched air.

3.3. Permeation Coefficient and Separation Coefficient [7]

Gas permeation coefficient and separation coefficient are the main performance indexes of oxygen enrichment membrane. They respectively indicate the separation property and permeability of the membrane and they are both related to membrane materials.

Permeation coefficient of oxygen enrichment membrane can be obtained through calculation in accordance with active area of membrane module, flow of permeable gas and differential pressure at two sides of membrane. The formula is as follows:

$$P = \frac{Q_2}{(\Delta P \cdot A)} \tag{1}$$

where P refers to permeation coefficient of oxygen enrichment membrane, $cm^3/(m^2 \cdot s \cdot MPa)$;A refers to active area of membrane, m^2; Q_2 refers to amount of oxygen-enriched air, m^3/s; ΔP refers to differential pressure of gas at two sides of membrane, MPa.

Separation coefficient can be calculated through following formula in accordance with oxygen concentration of gas supplied and permeable gas as well as pressure ratio for two sides of oxygen enrichment membrane.

$$\alpha = \frac{X_2[1 - X_1 - \gamma(1 - X_2)]}{(1 - X_2)(X_1 - \gamma X_2)} \tag{2}$$

where α refers to separation coefficient of oxygen enrichment membrane; γ refers to pressure ratio for two sides of oxygen enrichment membrane; X_1 is

the oxygen concentration of gas supplied; X_2 is the oxygen concentration of permeable gas.

The first group of data in Table 1 will be used as calculation example and other data calculation will applies the same method. Calculation results will be listed in Table 2.

According to experimental data, average permeation coefficient of the oxygen enrichment membrane is 8.14×10^{-9} $cm^3/(m^2\cdot s\cdot MPa)$ after being calculated with Formula (1) and (2). The value is larger than theoretical permeation coefficient (which is $1\times10^{-9}cm^3/(m^2\cdot s\cdot MPa)$ of the membrane. The main reason is that the vacuum degree of vacuum pump is too large. Average separation coefficient is 1.397 that is lower than theoretical separation coefficient (which is 2) of the membrane. The reason is that there is bias current, slight concentration polarization and loss of pressure in oxygen-enriched membrane module.

Table 2. Data for performance experiment of oxygen enrichment membrane apparatus.

ΔP [kPa]	Q_2 [m^3/h]	X_2	γ	$P\times10^{-9}$ [$m^3/(m^2\cdot s\cdot MPa)$]	α
36.200	5.705	20.015	0.629	8.44	1.045
36.400	5.753	21.769	0.628	8.41	1.188
37.000	5.788	22.615	0.624	8.38	1.375
37.500	5.842	23.888	0.621	8.32	1.440
38.700	5.858	24.040	0.617	8.09	1.468
38.800	5.921	25.134	0.614	8.05	1.497
40.200	5.966	26.320	0.608	7.92	1.530
41.000	6.037	27.272	0.606	7.86	1.522
41.400	6.077	28.269	0.605	7.82	1.510

3.4. Main Factors Affecting the Oxygen-enriched Concentration

Influence of oxygen enrichment membrane performance. For oxygen enrichment by means of membrane, it is very important to improve the oxygen-enriched performance; the performance of oxygen enrichment membrane is measured by the permeability coefficient and separation coefficient [8]. However, the permeation coefficient and separation coefficient are mainly influenced by the fore-and-aft differential pressure, pressure ratio of membrane module, the effective area of the membrane, the amount of oxygen-enriched air, and oxygen-enriched concentration. This experiment is mainly affected by influence of the vacuum pump characteristics; the degree of vacuum does not achieve the requirements of the experiment; the degree of vacuum is too high so that the pressure ratio is too high, which leads to the permeability coefficient of membrane becomes large, and the separation factor becomes smaller, that is to say, the increasing amount of passing air will reduce the concentration of oxygen enrichment. We can see from the above analysis, if the permeability coefficient and separation factor of membrane are increased, it will not only reduce the motive power of the device, but also reduce the cost of the oxygen-enriched air, and make the oxygen-rich device miniaturization at the same time.

Influence of operating condition. The running state of oxygen enrichment membrane experimental apparatus is closely related to the operating condition; its operating condition mainly includes pressure ratio (differential pressure) and feed air quantity. Seen from the data analysis of the experimental results, the oxygen-enriched concentration increases with the increasing of pressure, feed flow capacity in a certain operating temperature; but this experiment is operated under vacuum conditions; the influence of the vacuum pump is particularly serious; the oxygen-enriched concentration has a slight decrease with their increasing, that is because the degree of vacuum is too large, which makes the differential pressure before and after the membrane module becomes large and permeation of gas is increased; this leads to the deterioration of the efficiency of membrane separation, thereby reducing the oxygen-enriched concentration. In a word, changes in the degree of vacuum have great impact on the experiment. So in the experiment, the amount of feed air should be appropriate, in order to fully reflect the performance of oxygen enrichment membrane, this not only can get a higher oxygen-enriched concentration and oxygen-enriched air volume, but also reduce the running power costs of oxygen-rich membrane apparatus, making the best of economic benefits.

4. Conclusions

(1) This paper designs and establishes a membrane oxygen-enriched air supply experimental system; the system is running under vacuum conditions.

(2) Through experimental research on separation characteristics of LTV-PS membrane module, we understand that: with the increase of pressure and air

flow, oxygen-rich concentration tends to increase. Under operation in normal temperature and pressure (under the test condition, the atmospheric pressure is 102.7 kPa), when the air flow rate is 24 m^3/h, the concentration oxygen in membrane enrichment air is up to 28.3 %.

(3) In the research, we have analyzed that the main reasons that influenced the oxygen enrichment concentration are oxygen enrichment membrane performance and operating conditions; with the improvement of separation performance of domestic membrane, the performance of the existing oxygen-enriched air supply process program will subsequently be improved and enhanced.

References

[1]. Li Shengqin, Guan Qiang, et al., Study of the Interior Process of Oxygen-enriched Combustion on Mini-type Gasoline Engine, *Journal of Small Internal Combustion Engine and Motorcycle*, Vol. 37, Issue 2, 2008, pp. 22-26 (in Chinese).

[2]. Perez P. L., Boehman A. L., Experimental study of oxygenenriched diesel combustion using simulated exhaust gas recirculation, *Journal of Engineering for Gas Turbines and Power*, Vol. 131, Issue 4, 2009.

[3]. Li Sheng-Qin, Guan Qiang et al., Test Study on Combustion Process of Oxygen-enriched Gasoline Engine, *Journal of Highway and Transportation Research and Development*, Vol. 25, Issue 3, 2008, pp. 143-158.

[4]. Wartinbee W. J. Jr., Emissions study of oxygen-enriched air, *SAE Paper*, 710606.

[5]. Jia Zhonghui, Li Hongjun, Liu Gang, Membrane process oxygen-enriched local oxygen jet combustion system in vacuum furnace, *Journal of Refining and Chemical Industry*, Vol. 22, Issue 6, 2011, pp. 32-34.

[6]. Peter L. P., Andre L. B., Performance of a single – cylinder diesel engine using oxygen-enriched intake air at simulated high-altitude conditions, *Journal of Aerospace Science and Technology*, Issue 8, 2009, pp. 1-12.

[7]. Huanlin Chen, New-type Separation Technology, *Chemical Industry Press*, Beijing, 2005, pp. 83-87 (in Chinese).

[8]. Guanglin Shen, Advances in the application of membrane technology of oxygen enrichment in China, *Journal of Cryogenic Technology*, Issue 1, 2006, pp. 1-6.

Sensors & Transducers, Vol. 21, Special Issue, May 2013, pp. 164-168

Sensors & Transducers

http://www.sensorsportal.com

The Design of Multi-channel Signals Source with High-speed and High-precision Based on FPGA

[1] Xiao-Dan DU, [2] Qing HU, [1, 3] Tao YAN, [1, 3] Yong-Hong LIU

[1] College of Information Science & Technology of Chengdu University, Sichuan, Chengdu, 610106, China

[2] College of Electronic and Information Engineering of Chengdu University, Sichuan, Chengdu, 610106, China

[3] Key Laboratory in Colleges for Pattern Recognition and Intelligent Information Processing of Sichuan Province, Sichuan, Chengdu, 610106, China

[1] E-mail: xiaodandu@yeah.net

Received: 26 March 2013 /Accepted: 14 May 2013 /Published: 30 May 2013

Abstract: The multi-channel signals source that the structure is simple and flexible control is proposed in the article, with FPGA and high-speed D/A as its core. The choice of parts of apparatus, hardware constitution and design of software of the signals source are recommended here. Before the hardware designed, detailed theoretical analyses and quantitative description for the key factors on effecting the precision of signal source are given, and when debugging in hardware circuit is completed, on the base of analysis, errors estimation were verified with experimental results. It has provided high-precision signal related to the static and dynamic characteristics test accuracy of measured system for encoder and memory. By experiment and application it can meet the system requirements and has some theoretic and practical value. *Copyright © 2013 IFSA.*

Keywords: Multi-channel, Signals source, FPGA, High-speed, High-precision.

1. Introduction

There are more requirements to the output amplitude accuracy of the source signal, to the frequency accuracy and stability, to the number outputs and controllability of signals in modern electronic measurement. So we must design a signals source with producing large amounts of the standard signal and guarantee the high accuracy, high stability, maneuverability and operability of signals. The signals, with continuous phase transformation and frequency stability, can be controlled real-time in frequency, phase and amplitude.

The traditional signals source is an independent source, depending on hardware mainly, without computer participating in. It has complex hardware design and hasn't played software functional fully. In the system, the signals source is programmed by software. By that, these Standard signals' waveform are quantified and the quantitative data are preset in memory. The Communications between the system and computer rely on USB2.0.

2. Analysis of Accuracy of the Signals Source

Provided high-precision signals, it related to the static and dynamic characteristics test accuracy of measured system. Generally, the factors that affect

the accuracy of the sources are in the following mainly: a variety of circuit noise, static and dynamic parameters of DA converter, Operational Amplifier's zero-drift and static and dynamic accuracy, resistance deviation and resistance drift in resistor network, shut-off and conduction delay of electronic switch, no synchronization between electronic switch and DA conversion and so on.

2.1. The Electronic Switch's Effect in Accuracy

Signal output accuracy is required to reach 0.01 % in the system. So signal amplitude of capacitance C in a channel after t1charging should be greater than full range of 99.99 %.And in other channel switching process, the leakage voltage in the channel after t2 discharging should be less than full range of 0.01 %.

In the design we use ADG506 as electronic switch. It's contact resistance is about 400 Ω in the working and is more than 1kM in the else. We can Use the capacitance for polypropylene capacitor, their leakage resistance is greater than 1 kM. LM324, the input impedance is greater than 250 M, is adopted as Operational amplifier in the design. Therefore, the whole leakage resistance of the total device is about 250 M. The equivalent circuit is shown Fig. 1.

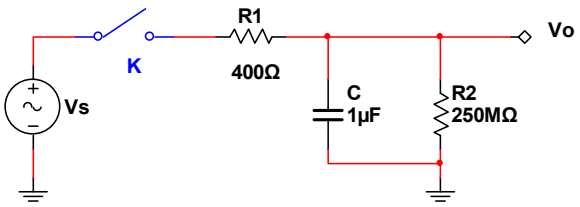

Fig. 1. The equivalent circuit.

From the Fig. 1, we can know that capacitance C can be charged through R_1 when the switch is turn-on; otherwise, capacitance C will discharge through Leakage resistance R_2. The charging process is:

$$U_O = (U_S - U_O^{'})(1 - e^{-\frac{t_1}{\tau_1}}) + U_O^{'}, \quad (1)$$

When Corrugated coefficient is 1‰, there is $1 - e^{-\frac{t_1}{\tau_1}} \geq 0.999$. In ADG506, Not synchronized and the switching delay time should be less than 400ns. So $t_S \approx 0.4\mu s$, Then there is:

$$C \geq \frac{-4\mu s}{R_1 \times \ln 0.001} = \frac{-4\mu s}{400 \times 6.9} = 1449\, pF$$

and

$$C \geq \frac{-64 \times 4\mu s}{R_2 \times \ln 0.999} = \frac{-256\mu s}{10^{13} \times \ln 0.999} = 2.56\, pF$$

To meet the design requirements, we choose 102 capacitance.

2.2. The PCB's Effect in Accuracy

Crosstalk is a Noise voltage signal that is brought owing to electromagnetic coupling between adjacent signals line, namely, the energy is coupled by a line to another line. To the higher signal accuracy system, crosstalk noise can further reduce signal quality and margin to other transmission line, taking into account accuracy, this paper focuses on the peak output voltage of crosstalk noise.

$$V_{FE} = \frac{1}{2} L_S (Z_0 C_m - \frac{L_m}{Z_0}) \frac{d\upsilon_s}{dt} \quad (2)$$

$$V_{NE} = K_{EN} \upsilon_0 \quad (3)$$

Young-Soo Sohn has brought out experience formula of C_S, L_S, C_m and L_m and approximate impedance formula of single line in PCB. As follows formula (4), (5), (6), (7), (8).

$$\frac{C_t}{\varepsilon} = [1.15(\frac{W}{H})^{0.963} + 1.07(\frac{T}{H})^{0.049}] + exp(-3.52\frac{S}{H})[0.75(\frac{W}{H})^{0.25} + 2.7(\frac{T}{H})^{1.34}], \quad (4)$$

$$\frac{C_m}{\varepsilon} = 1.17(\frac{W}{H})^{0.083}(\frac{S}{H} + 0.402)^{-0.78} + (\frac{S}{H} + 1.32)^{-0.8}[-1.36(\frac{W}{H})^{0.037} + 0.227(\frac{T}{H})^{0.98}], \quad (5)$$

$$\frac{L_s}{\mu_0} = 3.71(\frac{H}{W})^{0.041} + 0.018(\frac{H}{W})^{-0.73} - 3.39(\frac{H}{T})^{-0.0006} + exp(-1.89\frac{S}{H})[0.75(\frac{H}{W})^{-0.0052} - 0.84(\frac{H}{T})^{-0.0026}], \quad (6)$$

$$\frac{L_m}{\mu_0} = [-0.415(\frac{H}{W})^{-0.16} - 2.38(\frac{T}{W})^{1.18}] + (\frac{S}{H} + 1.07)^{-2.6} + (\frac{S}{H} + 0.89)^{-2.03}[0.418(\frac{H}{W})^{0.13} + 1.37(\frac{T}{W})^{1.09}], \quad (7)$$

$$Z_0 = \sqrt{L_s / C_t} \quad (8)$$

Therefore, from the formula (4), (5), (6), (7), (8), we can see distal crosstalk interference will be eliminated when $Z_0 C_m - L_m / Z_0 = 0$ and $Z_0 = \sqrt{L_s / C_t}$ or $L_m / C_m = L_s / C_t$. So we are not layout line between the pin of integrated chip in the PCB and should add earth wire or use wide wire around in easy interference parts. Do not forms a loop in any signal, if inevitable, must be allowed to loop area as small as possible. To improve anti-interference ability of the system we use 4 layer boards in PCB in the design.

2.3. The DA Effect in Accuracy

Based on high-precision, we must select a high-resolution, high-precision D/A Converter in the design. As is known to all, D/A converter the analog output rely ultimately on voltage reference source Predictably, voltage references of the output voltage is directly influence to the precision and stability.

We use A/D768AR, a high-speed 16-bit digital-to-analog converter, as AD In the system. The AD768 may be used in either current-output mode with the output connected to a virtual ground, or voltage-output mode with the output connected to a resistive load.

In current output mode:

$$I_{out} = (DACCODE / 65536) \times (I_{REFIN} \times 4), \quad (9)$$

In voltage output mode:

$$V_{out} = I_{out} \times R_{LOAD} // R_{LAD}, \quad (10)$$

I_{REFIN} is the current applied at the I_{REFIN} pin, determined by V_{REF} / R_{REF}. Substituting for $\boldsymbol{I_{out}}$ and I_{REFIN},

$$V_{out} = -V_{REF} \times (DACCODE / 65536) \times 4 \times [(R_{LOAD} // R_{LAD}) / R_{REF}] \quad (11)$$

For application flexibility and multiplying capabilities, the reference amplifier is design to offer adjustable bandwidth that can be reduced by connecting an external capacitor from the NR node to the negative supply pin, $\boldsymbol{V_{EE}}$. This capacitor lim it's the bandwidth and acts as a filter to reduce the noise contribution from the reference amplifier. The voltage output is then a function of the ratio of $(R_{LOAD} // R_{LAD}) / R_{REF}$, allowing for cancellation of resistor drift by selection of resistors with matched characteristics.

3. The Programmer of System and Hardware Constitution

This system has put forward a new method of signal source realization. Using the principle of DDS, computer technology is been into the signal source implementations Through the USB bus. The hardware design will be softened using the power of computer. FPGA is used as center logic control. Hardware circuit principle diagram Fig. 2.

The basic principle for the signal source: Computers send forth Commands and waveform number to FPGA by the USB interface module. Then the FPGA receive computer orders and accomplish the following two tasks according to different command. The first, in the controlling of FPGA the waveforms are read form FIFO and are stored to SRAM. The second is to control the waveform read an SRAM data to the D/A converter, and control the D/A converter finishes conversion.

In the D/A conversion process, the advancement of the memory address pointer should be synchronized with the multi-switch forward address pointer. AD824 is chosen in the design, the AD824 is a quad, FET input, single supply amplifier, featuring rail-to-rail outputs. Its slew rate is $2V / \mu s$, the ability of the output to swing rail-to-rail enables designs to build multistage filters in single supply systems and maintain high signal-to-noise ratios. When peak-to-peak value occurs in adjacent two channels signal to overact next channel stable output demands $(8V / 2V) / \mu s = 4\mu s$, so electronic switch must be opened after $4\mu s$ in the D/A conversion ending, otherwise channel interference will arise.

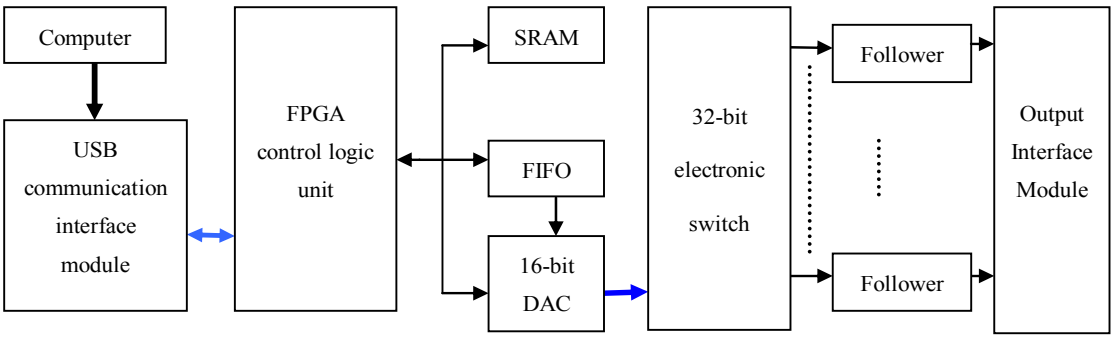

Fig. 2. Source hardware principle diagram.

4. The Design of Logical Control Unit in FPGA

As the center logic control devices of the signal source, FPGA has the following functions: to analyze Communication Protocol between the system and PC; to control storage and read of waveform data; to control DA conversion and electronic switch address propulsion; to control signal generator; to control impedance test and so on. The program control flow chart is as shown in Fig. 3.

Limited by the USB data transfer, each received 18 valid data which is truly effective data bits D_7 ~ D_0. Because there are 16 bit waveforms data in the signals source, the device must receive two effective data to synthesize a 16-bit waveform data which is sent in accordance with the first low 8 bits, then the high order 8 bits. The PC issue data in accordance with the address-Command-Data. So, when the system is working, to determine whether the received address matches the address for the system, if it is , then to judge the specific order form of the second 18-bit data. If the data are download command flag, to set write signal of FIFO is valid, the valid data has been received at this time is the waveform data. And, a 16-bit waveform data, integrating the before low 8-bit data and the after low 8-bit data, will be written into FIFO.

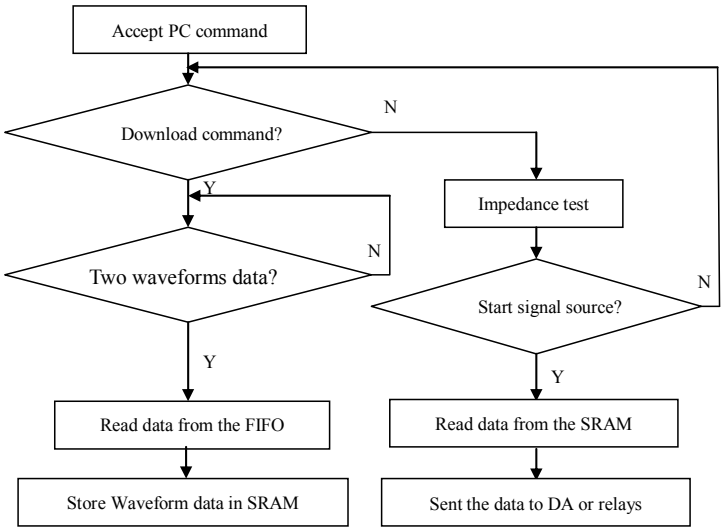

Fig. 3. Program flow chart of FPGA.

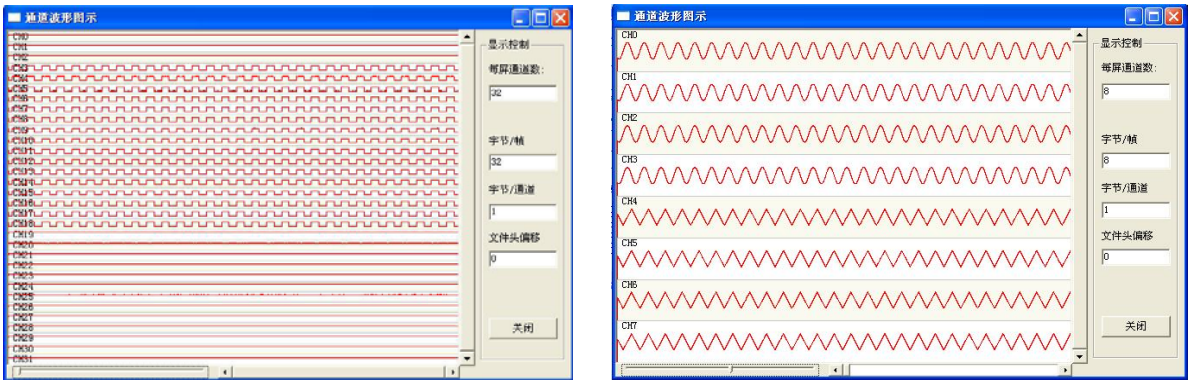

Fig. 4. Self-test wave of signal source.

5. Conclusion

The system has been put into use, and is involved in some large test. In the experimental process, it has provided high-precision signal for encoder and memory. It provides the basis for developing high-accuracy encoder and memory. Fig. 4 is self-test wave of signal source; we can be seen the design can conform to the system requirements.

Acknowledgements

Fund Project: 1. Scientific Instrument Shared System of Southwest. The project is supported by Educational Department of China. 2. Research and Application of QoS Real-time Video Stream (NO.09ZB114). 3. Research on the Key Technology of Intelligent Campus Network Construction Based

on the Internet of Things. The project is supported By Educational Department of China (NO.11ZB278).

References

[1]. Young-Soo Sohn, Jeong-Cheol Lee, Hong-June Park, et al., Empirical Equations on Electrical Parameters of Couple Microstrip Line for Crosstalk Estimation in Printed Circuit Board, *IEEE Transactions on Advanced Packaging*, Vol. 24, Issue 4, 2001, pp. 521-527.

[2]. Cheng Gao, Wei Guo, Jiaoying Huang, Single-Event-Upset (SEU) Mitigation Techniques for Routing Resources of SRAM-FPGA, *IJACT*, Vol. 4, Issue 20, 2012, pp. 205-213.

[3]. Chao Huang, Li-Xiang Ren, Er-Ke Mao, A systematic frequency planning method in Direct Digital Synthesizer (DDS) design, *IEEE Wireless Communications & Signal Processing*, 2009, pp. 1-4.

[4]. Yuzhong Li, Research and Design on a Novel Optoelectronic Current Transformer Based on FPGA and DSP, *JDCTA*, Vol. 6, Issue 7, 2012, pp. 206-215.

[5]. Zhou Libo, Bai Na, Research of High-speed Image and Number' s Recognition System Based on FPGA, *JDCTA*, Vol. 6, Issue 19, 2012, pp. 239-245.

[6]. T. Nandha Kumar, Haider A. F, Almurib, New Chin-Ee, Fine grain faults diagnosis of FPGA interconnect, *Microprocessors and Microsystems*, Vol. 37, Issue 1, 2013, pp. 33-40.

[7]. Vinay B. Y. Kumar, Siddharth Joshi, Sachin B. Patkar, H. Narayanan, FPGA Based High Performance Double-Precision Matrix Multiplication, *International Journal of Parallel Programming*, Vol. 38, Issue 3, 2010, pp. 322-338.

[8]. Qinglin Zhang, Shuzhen Chen, Yijun Luo, Shan Wang, High-speed parallel matched filter designing and FPGA implementation, *Wuhan University Journal of Natural Sciences*, Vol. 15, Issue 4, 2010, pp. 335-339.

[9]. Meher P. K., Chandrasekaran S., Amira A., FPGA Realization of FIR Filters by Efficient and Flexible Systolization Using Distributed Arithmetic, *IEEE Transactions on Signal Processing*, Vol. 56, Issue 7, 2008, pp. 3009-3017.

[10]. Jia Hui-Juan, Research on the Technology of RS485 over Ethernet, *The International Conference on E-Product, E-Service and E-Entertainment (ICEEE' 2010),* 2010, pp. 1-3.

[11]. NI Haiyan, HU Chao, MA Changwang, Research on a 485-serial network architecture in intelligent uptown management, *2006 IEEE Conf on Mechatronics and Automation. Luoyang: IEEE Press*, 2006, pp. 400-405.

[12]. Shihong Qin, Design of the Multi-computer communication system based on RS485, *2011 International Conference on Electric Information and Control Engineering (ICEICE)*, 2011, pp. 1318-1320.

[13]. Gao Zhen-Bin, FPGA implementation of a multi-channel HDLC protocol transceiver, *2005 International Conference on Communications, Circuits and Systems, 2005*, pp. 1200-1203.

[14]. Bin Huang, Design of a multi-channel high speed FIFO applied to HDLC processor based on PCI bus, *IEEE 2002 International Conference on Communications, Circuits and Systems and West Sino Expositions*, 2002, pp. 1476-1480.

Sensors & Transducers, Vol. 21, Special Issue, May 2013, pp. 169-174

Sensors & Transducers

http://www.sensorsportal.com

A Study of the Influence of L-Cut on Resistance of Chip Resistor Based on Finite Element Method

Wang Zhijuan
College of Information Engineering, Minzu University of China,
Minority Languages Branch, National Language Resource Monitoring & Research Center
No. 27, South Street of Zhongguancun, Haidian District, Beijing, China, 100081
E-mail: wangzhijuan2000@yeah.net

Received: 26 March 2013 /Accepted: 14 May 2013 /Published: 30 May 2013

Abstract: The resistance increase by transverse cutting is more quickly than by ordinate cutting when using laser trimming. Therefore, the precision and efficiency of laser trimming can be improved at low cost through reasonable design of the L-cut. In this paper, the finite element method is used to study the influence of L-cut on the resistance of chip resistor. Experiments proved that the qualitative and quantitative conclusions of the influence of L-cut on the resistance obtained by the finite element method are consistent with the experimental results. Thus, using the conclusions of the influence of L-cut on the resistance obtained by the finite element method can provide the control basis for improving the trimming precision and trimming efficiency.

Keywords: Laser trimming, Trimming precision, Resistance of chip resistor, L-cut, Finite element method.

1. Introduction

Laser trimming is the most precise method to adjust resistance of chip resistor [1]. The scanning path of laser on the resistive film is called cutting path, which is relative to the laser trimming precision. Due to the influence of control difficulty of the laser beams, the laser cutting path is generally straight line or combinations of straight lines. The common laser-cutting paths are shown in Fig. 1.

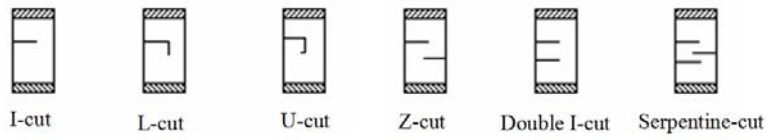

Fig. 1. The basic laser cutting paths.

As shown in Fig. 2, the laser-cutting path that is vertical to the current flow is called transverse cutting. It increases the resistance quickly. The laser-cutting path that is parallel to the current flow is called ordinate cutting. It increases the resistance slowly. L-cut can guarantee the trimming precision based on guaranteeing the trimming efficiency, and therefore is broadly applied in the laser trimming. Through mastering the influence of L-cut on the resistance of chip resistor, the precision and efficiency of laser

trimming can be improved at a low cost through reasonable design of L-cut.

At present, there are only independent studies on the influence of the transverse cutting length and the ordinate cutting length on the resistance of chip resistor [2-9]. There is no the study on the influence of L-cut on the resistance of chip resistor. A method based on the finite element is introduced to study the relationship of L-cut and resistance in this paper. Then the relationship between L-cut and resistance of chip resistor is studied applying this method. Finally, the experimental data are applied to prove the qualitative and quantitative conclusions gotten by the finite element method.

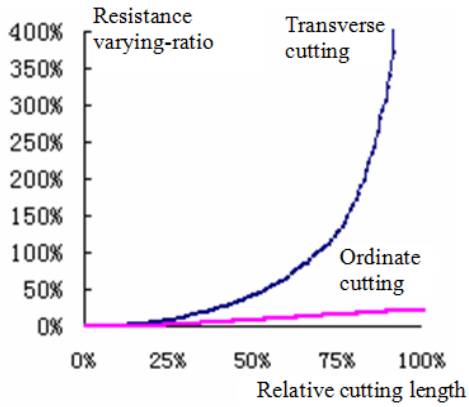

Fig. 2. The influence of transverse and ordinate cutting length on the resistance of chip resistor.

2. Introduction of Research Method based on Finite Element Method [10]

Formula (1) is the calculation formula of the resistance of chip resistor. Rt is the resistance. U is the voltage applied on two electrode of the resistor. E is the electric field intensity. l is any line section within the region of the resistor. $\rho_s = \rho / h$, h is the thickness of resistive film and ρ is the resistivity.

$$R_t = \rho_s \frac{U}{\int_l E \bullet dl} \tag{1}$$

The method to solve the resistance of chip resistor trimmed by L-cut is introduced in following paragraphs.

Firstly, the finite element analysis software ANSYS with the electric field analysis and calculation module is applied to divide the chip resistor trimmed by L-cut path into lots of small resistors. The finite element node diagram of chip resistor is shown in Fig. 3.

Secondly, the electric field intensity of every small resistor under certain voltage action is solved. As shown in Fig. 4, the electric field intensity of each finite element can be calculated using ANSYS. The arrow color shows the size of electric field intensity of each finite element and the arrow points to the direction of the electric field intensity of each finite element.

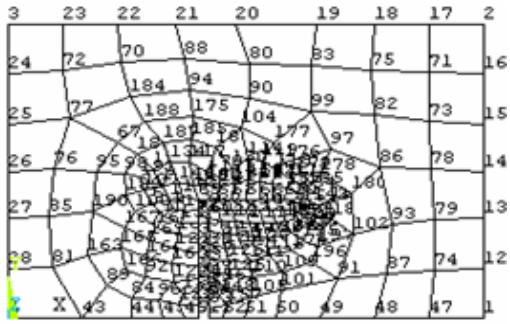

Fig. 3. Finite element node diagram of chip resistor.

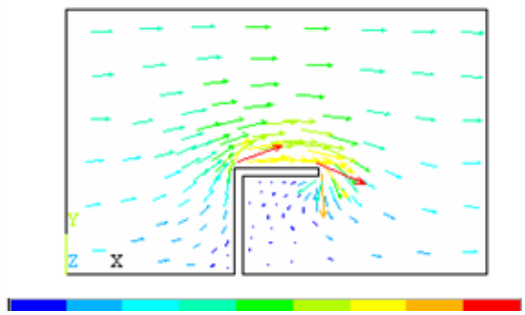

Fig. 4. Electric field intensity diagram of chip resistor.

Thirdly, solve the line integral of electric field intensity of all small resistors on a certain line. Using formula (1), the resistance of resistor trimmed by the L-cut can be calculated. Fig. 5 is the solution diagram of the resistance through ANSYS.

Finally, the relationship between different L-cut and corresponding resistance can be analyzed through the data analysis software Excel and Origin. And the qualitative and quantitative relationships between L-cut and the resistance of chip resistor can be obtained.

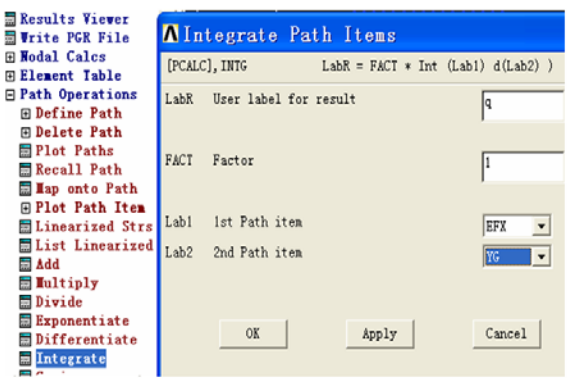

Fig. 5. The Path Operations of the ANSYS.

3. Influence of L-cut on the Resistance based on Finite Element Method

The chip resistor trimmed by L-cut is shown in Fig. 6. L_1 and W_1 respectively represent the length and the width of the chip resistor. L_2 is the distance from the left electrode to the begin position of L-cut. W_2 is the transverse cutting length. L_3 is the ordinate cutting length and C is the diameter of laser beam.

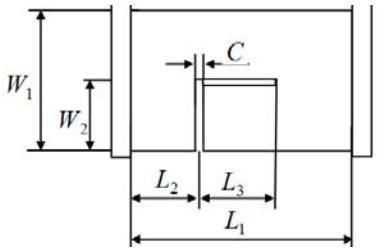

Fig.6. Chip resistor trimmed by L-cut.

R_k is the varying ratio of resistance, it can be expressed in formula (1). R_{t0} is the initial resistance of before laser cutting, $R_{t0} = \rho_s L_1 / W_1$. R_t is final resistance of the resistor trimmed by laser. $L_{initial}$ is the relative begin position. L_{kx} is the relative transverse cutting length. L_{ky} is the relative ordinate cutting length.

$$R_k = \frac{R_t - R_{t0}}{R_{t0}} \times 100\% \quad (2)$$

$$L_{initial} = L_2 / L_1 \quad (3)$$

$$L_{kx} = W_2 / W_1 \quad (4)$$

$$L_{ky} = L_3 / L_1 \quad (5)$$

The influence of L-cut on the resistance is very complicated. So, R_{kx} and R_{ky} are used to study the influence of L-cut on the resistance. As shown in Formula (6) and (7), R_{kx} is the varying ratio of resistance caused by transverse cutting and R_{ky} is varying ratio of resistance caused by ordinate cutting. R_{tx} is the resistance when the transverse cutting is over.

$$R_{kx} = \frac{R_{tx} - R_{t0}}{R_{t0}} \times 100\% \quad (6)$$

$$R_{ky} = \frac{R_t - R_{tx}}{R_{tx}} \times 100\% \quad (7)$$

So the relationship between R_k and R_{kx}, R_{ky} is shown in Formula (8).

$$R_k = R_{kx} + R_{ky} + R_{kx} R_{ky} \quad (8)$$

3.1. The Influence of $L_{initial}$ and L_{kx} on R_{kx}

Fig. 7 is the relationship diagram of R_{kx} and L_{kx}, $L_{initial}$ of 0603 1K resistor when $L_{initial}$ is respectively 0.125, 0.25, 0.5, 0.75 and 0.875.The influence of $L_{initial}$ and L_{kx} on R_{kx} will be introduced in following.

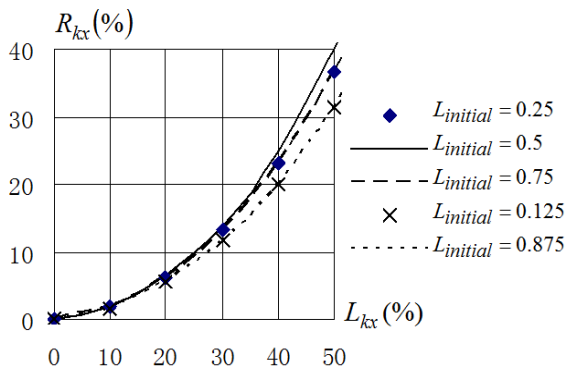

Fig. 7. The relationship between R_{kx} and $L_{initial}$, L_{ky}

3.1.1. The Influence of L_{kx} on R_{kx}

When $L_{kx} \leq 0.5$, the relationship between R_{kx} and L_{kx} is an approximate quadratic function. And their relationship can be expressed with Formula (9). C_1 is a constant related to the resistor type and $L_{initial}$. $C_1 > 0$.

$$R_{kx} = C_1 L_{kx}^2 \, (L_{kx} \leq 0.5) \quad (9)$$

3.1.2. The Influence of $L_{initial}$ on R_{kx}

The begin position of L-cut influences the increase speed of the resistance.

(1) When $L_{initial} = 0.5$, R_{kx} increases at the quickest speed with the increase of L_{kx}.

(2) When the begin positions of L-cut are symmetric, the two R_{kx} increase at the same speed with the same increase of L_{kx}.

(3) The closer the begin position of L-cut is to two electrodes, the slower the increase speed of R_{kx} is with the same increase of L_{kx}.

3.2. The Influence of $L_{initial}$, L_{kx} and L_{ky} on R_{ky}

3.2.1. The Influence of L_{ky} on R_{ky}

For the influence on the edge effect of the resistor, the influence of ordinate cutting length L_{ky} on R_{ky} is divided into the linear section and nonlinear section. Fig. 8 shows the relationship diagram of R_{ky} and L_{ky} of the 0603 1K resistor gotten by finite element method when $L_{initial} = 0.5$ and $L_{kx} = 0.5$.

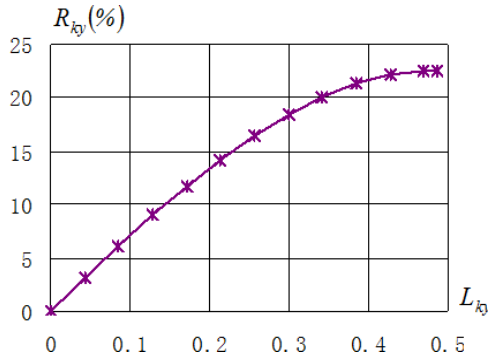

Fig. 8. Relationship diagram of R_{ky} and L_{ky}.

When $L_{ky} \le a_i$, R_{ky} and L_{ky} have a linear relationship, and the linear relationship can be expressed in Formula (10). C_3 is a constant related to $L_{initial}$ and L_{kx}. $C_3 > 0$.

$$R_{ky} = C_3 L_{ky} \ (L_{ky} \le a_i) \tag{10}$$

When $L_{ky} > a_i$, R_{ky} and L_{ky} have a nonlinear relationship and a_i is a constant related to the resistor type and cutting path.

3.2.2. The Influence of L_{kx} on R_{ky}

Fig. 9 shows the relationship diagram between L_{kx} and R_{ky} - L_{ky} of 0603 1K resistor when $L_{initial} = 0.5$.

The larger L_{kx} is, the quicker the increase speed of R_{ky} with the increase of L_{ky} is. Meanwhile, for same ordinate cutting length, with the increase of L_{kx}, the increase of R_{ky} is same with the increase of L_{kx}. So the influence of L_{kx} on R_{ky} is a linear relationship which can be expressed in Formula (11). C_4 is a constant that relates to the resistor type, $L_{initial}$ and L_{ky}. $C_4 > 0$.

$$R_{ky} = C_4 L_{kx} \ (L_{kx} > 0) \tag{11}$$

The relationship between R_{ky} and L_{kx}, L_{ky} is shown in Formula (12). C_2 is a constant related to the resistor type and $L_{initial}$. $C_2 > 0$.

$$R_{ky} = C_2 L_{kx} L_{ky} \ (L_{kx} > 0, \ L_{ky} \le a_i) \tag{12}$$

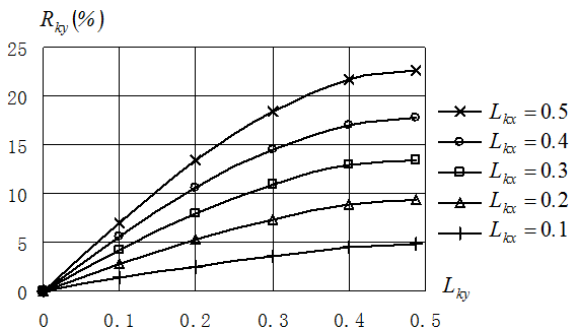

Fig. 9. Relationship diagram of L_{kx} and R_{ky} - L_{ky}.

3.2.3. The Influence of $L_{initial}$ on R_{ky}

Fig. 10 shows the relationship diagram of R_{ky} and L_{ky} of 0603 1K resistor gotten by the finite element method when $L_{kx} = 0.2$ and $L_{initial} = 0.25,\ 0.5,\ 0.75$. The closer the begin position of L-cut is to two electrodes, the quicker the increase speed of R_{ky} is with the same increase of L_{ky}.

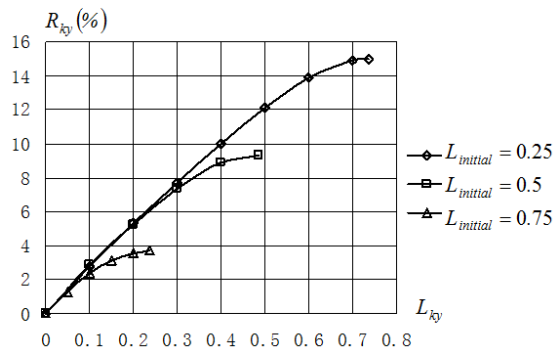

Fig. 10. Influence diagram of $L_{initial}$ on R_{ky}.

3.3. The Influence of L-cut on R_k

3.3.1. The Influence of L_{kx} and L_{ky} on R_k

According to the analysis in 3.2, 3.3, the relationship between R_k and L_{kx}, L_{ky} is shown in

Formula (13) within certain L_{kx} and L_{ky} ($0 < L_{kx} \le 0.5,\ L_{ky} \le a_i$).

$$R_k = C_1 L_{kx}{}^2 + C_2 L_{kx} L_{ky} + C_1 C_2 L_{kx}{}^3 L_{ky} \tag{13}$$

C_1, C_2 are two constants related to the resistor type and $L_{initial}$. a_i is the relative ordinate cutting length when the relation between R_{ky} and L_{ky} is liner. a_i is a constant related to the resistor type and $L_{initial}$.

From formula (13), when $L_{kx} \le 0.5,\ L_{ky} \le a_i$, the relationship between R_k and L_{kx} is cubic function, the relationship between R_k and L_{ky} is liner.

3.3.2. The Influence of $L_{initial}$ on R_k

Fig. 11 shows the relationship diagram of R_k and L_{ky} of 0603 1K resistor gotten by the finite element method when $L_{kx} = 0.5$ and $L_{initial} = 0.3,\ 0.5,\ 0.7$.

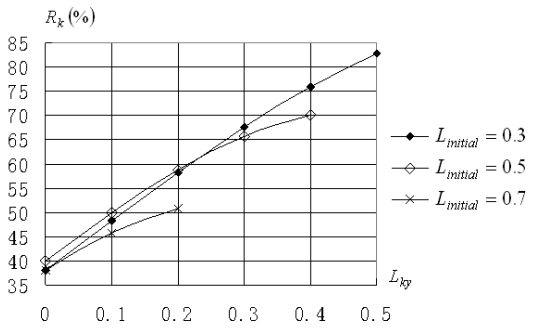

Fig. 11. The relationship diagram of R_k and L_{ky} .

According to Fig. 11, the influence of $L_{initial}$ on R_k can be expressed in two cases.

(1) When $L_{ky} \le b_i$, the influence of $L_{initial}$ on R_{kx} is prevailing. That is, when $L_{initial} = 0.5$, R_{kx} increases at the quickest speed with the increase of L_{ky} .

(2) When $L_{ky} > b_i$, the influence of $L_{initial}$ on R_{ky} is prevailing. That is, the closer the begin position of L-cut is to left electrodes, the quicker the increase speed of R_k is with the same increase of L_{ky} . b_i is a constant related to the resistor type and L_{kx} of L-cut.

4. Experiments

The experimental data are gotten by using Laser Trimming System that is made by Changchun Institute of Optics, Fine Mechanics and Physics, Chinese Academy of Sciences. Let Laser Trimming System trim the resistor at certain step and measure the resistance using resistance measuring system. R_{ke} is the varying ratio of resistance gotten by experiment. 0603 type 1K resistors are used in experiment.

The influence of L-cut on the resistance is very complicated. So, we take two steps to study the influence of L-cut on the resistance based on experiments.

4.1. The Influence of $L_{initial}$ and L_{kx} on R_{ke} when $L_{ky} = 0$

Fig. 12 is the influence diagram of $L_{initial}$ and L_{kx} on R_{ke} when $L_{ky} = 0$. The following conclusions can be reduced.

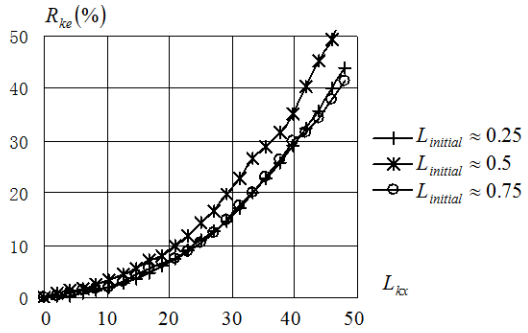

Fig. 12. Influence diagram of $L_{initial}$ and L_{kx} on R_{ke} .

When $L_{initial} = 0.5$, R_{ke} increases at the quickest speed with the increase of L_{kx} . When the begin positions of L-cut is symmetric, the two R_{ke} increase at the same speed with the same increase of L_{kx} . The closer the begin position is to two electrodes, the slower the increase speed of R_{ke} is with the same increase of L_{kx} . These conclusions are consistent with the conclusions gotten by finite element method.

When $L_{initial} \approx 0.5$ and $L_{kx} \le 0.5$, the relationship between R_{ke} and L_{kx} gotten by experiment data can be expressed with Formula (14). And Formula (15) is the relationship between R_k and L_{kx} gotten by finite element method .They are almost same.

$$R_{ke} \approx 1.66 L_{kx}{}^2 \tag{14}$$

$$R_k \approx 1.62 L_{kx}{}^2 \tag{15}$$

4.2. The Influence of L_{ky} on R_{ke}

Fig. 13 is the relationship diagram of R_{ke} and L_{ky} when $L_{initial} \approx 0.3$ and $L_{kx} \approx 21\%$ .The relationship

of R_{ke} and L_{ky} is nearly liner when $L_{ky} < 40\%$, their relationship is nonlinear when $L_{ky} > 40\%$. These conclusions are consistent with the conclusions gotten by finite element method in 3.2 and 3.3.

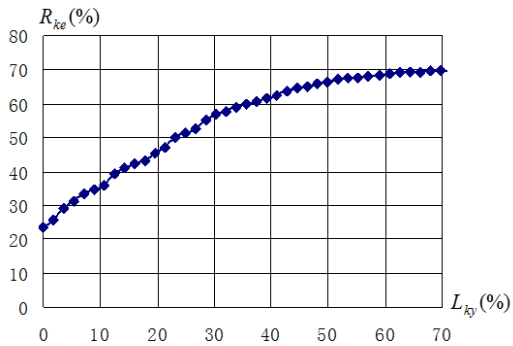

Fig. 13. The relationship diagram of R_{ke} and L_{ky}

4.3. The Influence of L_{kx} on R_{ke} when $L_{ky} \neq 0$

Fig. 14 is the relationship of R_{ke} and L_{kx} when $L_{initial} \approx 0.3$, $L_{kx} \approx 0.21, 0.42, 0.63$ and $L_{ky} \leq 0.2$. The relationships of R_{ke} and L_{kx} are consistent with the conclusions gotten by finite element method.

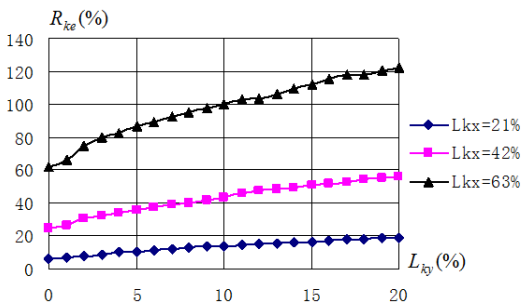

Fig. 14. The relationship diagram of R_{ke} and L_{kx}

5. Conclusions

The influences of L-cut on resistance of chip resistor are following:

(1) As shown in formula (13), the relationship of R_k and L_{ky} is liner. The relationship of R_k and L_{ky} is nonlinear.

(2) The influences of $L_{initial}$ on R_k can be expressed in two cases. The closer $L_{initial}$ is to 0.5, the quicker the increase speed of R_k with the increase of L_{kx} is when $L_{ky} \leq b_i$. The smaller $L_{initial}$ is, the quicker the increase speed of R_k with the increase of L_{kx} is when $L_{ky} > b_i$. b_i is a constant related to the resistor type and $L_{initial}$.

Experiments proved that the qualitative conclusions of the influence of L-cut on the resistance obtained through the finite element method are consistent with the experimental results. So the L- cut can be designed reasonably according to the relationship of L-cut and resistance of chip resistor. And the precision and efficiency of laser trimming can be improved at a low cost.

6. Acknowledgment

This work is supported by National social science fund (No: 11CY016), and Open Project of National Language Resource Monitoring & Research Center (No: NMLR201104).

References

[1]. Bu Shoupeng, Stationary resistor, Chen Yaozu, *Electronic Industry Publishing Company*, 1995.

[2]. Wang Jiajin, Laser-processing technology, Guo Xiaoguang, *Chinese Metric Publishing Company*, 1992.

[3]. Jaime Ramirez-Angulo, Improvement of Laser Trimmed Film Resistor Stability by Selection of Optimal Trim Paths, in *Proceeding of the IEEE International Symposium on Circuits and Systems*, Las Cruces, USA, 11-14 June 1991, Vol. 4, pp. 2188 – 2191.

[4]. Klaus Schimmanz, Film Resistor Design for High Precision Laser Trimming, *IEEE Transactions on Computer-aided Design of IC and Systems*, Vol. 17, Issue 5, 2001, pp. 207-212.

[5]. Takashi Mitsuhashi, A Resistance Calculation Algorithm and Its Application to Circuit Extraction, *IEEE Transactions on Computer-aided Design*, Vol. 6, Issue 3, 1987, pp. 337-345.

[6]. Zhijuan Wang, The experimental study of the dependence of resistance on ordinate-cutting length of chip resistor based on resistor-subsection method, *Chinese Journal of Electron Device*, Vol. 27, Issue. 3, 2004, pp. 432-436.

[7]. WANG Zhi-Juan, Experimental Study of the Effect of Laser Transverse-cutting Length on Resistance of Chip Resistor, *Laser Journal*, Vol. 26, Issue 13, 2005, pp. 125-129.

[8]. Wang Zhi-Juan, The Influence Study of Laser Cutting Path on the Resistance of Chip Resistors, *SPIE*, 2004, Vol. 5629, pp. 253-262.

[9]. Wang Zhi-Juan, The Influence of Laser Transverse Cutting on the Resistance of Chip Resistors Based on the Finite Element, *Chinese Journal of Electron Devices*, Vol. 31, Issue 3, 2008, pp. 791-794.

Sensors & Transducers, Vol. 21, Special Issue, May 2013, pp. 175-181

Sensors & Transducers

http://www.sensorsportal.com

Experimental Investigation and Comparison of Nonlinear Kalman Filters

[1,2] Yingjun Zhou, [1] Feng Gu, [1] Yuqing He, [1] Jianda Han

[1] State Key Laboratory of Robotics, Shenyang Institute of Automation, Chinese Academy of Sciences, Shenyang,110016, China

[2] University of Chinese Academy of Sciences, Beijing, 100049, China

E-mail: zhouyingjun2000@163.com

Received: 26 March 2013 /Accepted: 14 May 2013 /Published: 30 May 2013

Abstract: One of the most important problems when designing controller is how to deal with all kinds of uncertainties, which, along with the high nonlinearities of most real systems, makes it difficult to guarantee the desired closed loop performance. Recently, nonlinear Kalman-class filter has been extensively researched and several well-known algorithms, including Extended Kalman Filter (EKF), Unscented Kalman Filter (UKF) and Adaptive Unscented Kalman Filter (AUKF), have been reported to be applicable in some cases. In this paper, on the basis of the moving target cooperative observation problem, performances of these nonlinear filter algorithms are analyzed and tested on a multi-flying-robot testbed, and the experimental results are listed to show the advantages and disadvantages of them. *Copyright © 2013 IFSA.*

Keywords: Nonlinear Kalman Filter, Moving target observation, Flying robots.

1. Introduction

Since Kalman Filter was proposed by Kalman R. E. in 1960 [1], linear Kalman filters have been extensively utilized in many real systems. However, when nonlinearities are unavoidable, the performance of linear Kalman filter can only be guaranteed locally, which make many researchers turn their attentions to the topic of nonlinear Kalman filter.

Extended Kalman Filter (EKF) and Unscented Kalman Filter (UKF) are two typical nonlinear Kalman-class filters. Among them, EKF is the earliest and most often referred-to one. Its basic idea is to linearize the nonlinear term using Taylor series expansion, and then linear Kalman filter algorithm is directly used with respect to the linearized system model [2]. While in UKF, a set of samples are used to approach the nonlinear system model. It has been proved that UKF algorithm is equivalent to using the second order Taylor expansion to replace the nonlinear terms, thus it is of much better performance compared to EKF algorithm. It should be noted that the performance of both EKF and UKF rely much on accurate prior noise distribution [3], which is difficult to be obtained in most real applications. Therefore, adaptive Kalman-class filtering algorithms which are able to regulate the noise covariance online have been discussed [4-7]. For example, Jiang [7] proposed an MIT based adaptive UKF (MIT-AUKF), in which the noise covariance is updated adaptively to minimize a cost function and the updated covariance is then fed back into normal UKF to compensate the inaccurate prior information.

Theoretical and experimental comparison study on these three kinds of nonlinear Kalman-class filter, in this paper, are conducted with respect to the problem of moving target Motion Estimation using Mobile Robot (MEMR). MEMR is a typical application and

key problem in the field of robotics [8-9]. Besides, the high nonlinearity in system and measurement model, the uncertainty of moving targets and unpredictable time-varying noise and disturbance, make it fit to test the performance of nonlinear Kalman-class filters.

2. Problem Description

Moving target observation is a typical nonlinear estimation problem can be modeled as follows,

$$\begin{aligned} x_k &= f(x_{k-1}, w_{k-1}) \\ y_k &= h(x_k, n_k) \end{aligned}, \tag{1}$$

where $x_k \in R^n$ are states of the moving target (or the relative states between moving target and robot); w_k and n_k are process noise and measurement noise; $y_k \in R^p$ are measurements. The aim of "moving target observation" is to design an algorithm to estimate the real-time system states x_k based on known y_k as accurately as possible.

3. Nonlinear Kalman Filtering Algorithms

Kalman-class filter is usually composed of two steps, called prediction step (or time update) and correction step (or measurement update). These two steps are conducted iteratively and form a closed-loop as in Fig. 1.

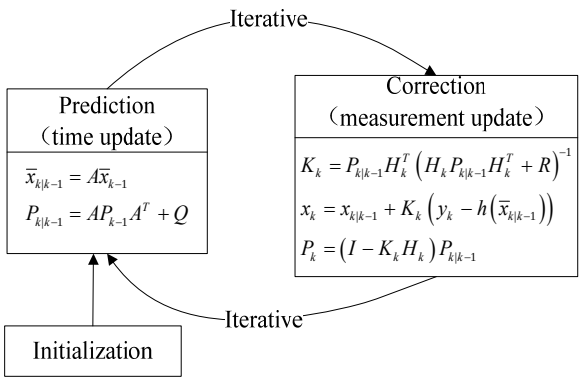

Fig. 1. Basic idea of Kalman filter.

In prediction step, the current states are predicted using the states in last time step and their statistical covariance using system model. While in correction step, based on the measurement, the Kalman gain K_k is updated according to measurement models and the pre-known measurement noise covariance.

EKF is a linear approximation method which is based on Taylor expansion with only linear terms being used. The system can be described by Eq. (2).

$$\begin{aligned} x_k &= A(x_{k-1})x_{k-1} + w_{k-1} \\ y_k &= H(x_k)x_k + n_k \end{aligned}, \tag{2}$$

where

$$A(x_{k-1}) = \partial f / \partial x\big|_{x=x_{k-1}}, H(x_k) = \partial h / \partial x\big|_{x=x_k}$$

It can be seen in Eq. (2) that EKF reserves first order Taylor expansion of nonlinear models to convert it to linear. That leads to: 1) Local linearization may produce prediction errors, and thus deteriorate the estimation accuracy. 2) Performance of EKF depends much on the noise covariance, which is difficult to be obtained before-hand.

Different from the EKF, UKF uses similar distribution, called Unscented Transfer (UT), to approach the suboptimal filtering performance. The principle of UT is to take the distribution of sample points as the approached distribution of the random variables. According to the prior estimated states means and variances, a set of discrete sample points are generated as sigma points. These points are transferred by the nonlinear models so that the posterior means and variances can be obtained iteratively.

There are analysis showing that UKF has an equal calculation complexity to EKF and equal precision to two-stage EKF [7]. Therefore UKF is considered more suitable for system of stronger nonlinearity. However, the performance of UKF still depends on the initial statistical characteristics of noise, which should be estimated accurately to avoid divergence.

Aiming at the problem that noise covariance is difficult to obtain, adaptive Kalman-class filters have been researched. For example, in preceding study, we proposed an MIT-based adaptive UKF (MIT-AUKF) [7]. In MIT-AUKF algorithm, taking the deviation of the actual and estimated value of innovation as the adaptive index function J_r as Eq. (4), an MIT adaptive rule, i.e., the parameters are updated in the negative gradient direction of the criterion function, is used to regulate the noise covariance online as Eq. (5). Then in each iterative step, the renewal noise variances are substituted into the new UKF so as to improve the estimation performance while the noise is unknown or time-variant.

$$J_r = tr\left(\left(diag\Delta S_k\right)^2\right) = tr\left(\left(diag\left(S_k - S_k'\right)\right)^2\right), \tag{4}$$

$$q_k^m = q_{k-1}^m - \eta_k \frac{\partial J_k}{\partial q_k^m} T_0, \tag{5}$$

where $tr(*)$ is the trace of the matrix(*), $diag(*)$ obtains a diagonal matrix, S_k is the mean of innovation in a moving N-size window, q_k^m is the m_{th} diagonal element of Q^n at time k, T_0 is sample time, η_k is the tuning rate of converging, and

y_k-$y'_{k|k-1}$ is the estimation of S'_k, which is defined as follows,

$$S_k = \frac{1}{N}\sum_{i=k-N+1}^{k}\left(y_k - y'_{k|k-1}\right)\left(y_k - y'_{k|k-1}\right)^T,$$

$$S'_k = \sum_{i=0}^{2n} w_i^c\left(r_{i,k|k-1} - y'_{k|k-1}\right)\left(r_{i,k|k-1} - y'_{k|k-1}\right)^T + Q^n$$

Reference [7] has a detailed introduction about MIT-AUKF algorithm.

4. Experimental Platform

In this paper, a kind of indoor multi-flying-robots testbed and an extended vision based measurement system on it are used to test performance of the three nonlinear Kalman filters.

4.1. Introduction of the Experimental Platform

The whole multi-flying-robot testbed structure is as Fig. 2. It contains a vertical main shaft and 3 horizontal mechanic arms. Each arm has two passive joints driving the yaw and pitch. A flying robot is installed on the end of each arm. In order to avoid robots crashing, the pitch freedom is limited to rang in (-15°, 15°). On the other end of the arms, adjustable balance weight stacks are used for canceling out the extra load generated by flying robots taking off. Besides, encoders are assembled on each rotary joint to get position information [11-12].

In our experiments, two arms are used, as shown in Fig. 2. Arm-1 carried an LED with 850 nm wavelength as the moving target to be observed. While on Arm-2, an industrial camera is installed vertically to observe the optical target. In order to simplify the image processing, we propose a target-enhance solution to identify the target. In brief, an 850 nm narrow band filter was installed in front of the camera lens so that the complex background on the images can be removed a lot, and there would only be the target light source on the images as shown in Fig. 3. In that way the focus can be concentrated on the realization and efficiency of the experiments.

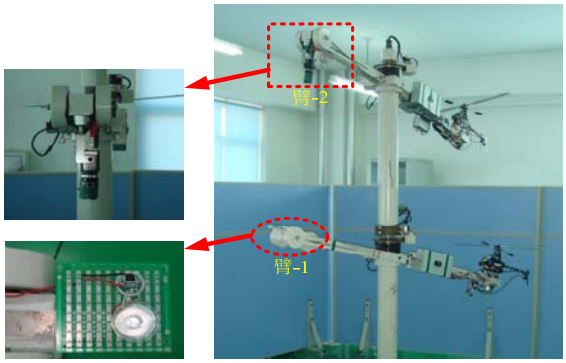

Fig. 2. Multiple Rotated Flying Robots Testbed.

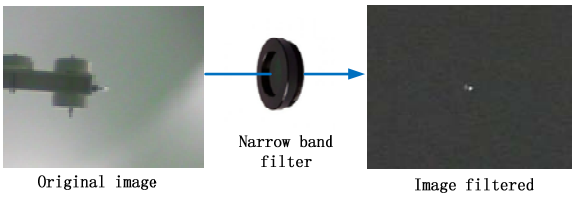

Fig. 3. Effect of Optical Filter.

4.2. Observation Model of Dynamic Target

In this sub-section, the moving target observation model is given out. Firstly, two main coordinates are defined as Fig. 4: 1) Image pixel coordinate system *uOv*: the left up corner of the image is the origin, *u* and *v* are the row and the column of the image; 2) World coordinate system X^w: the bottom center of testbed is origin, z_w is the upward direction of the main shaft, x_w is along the arm when $\beta=0$.

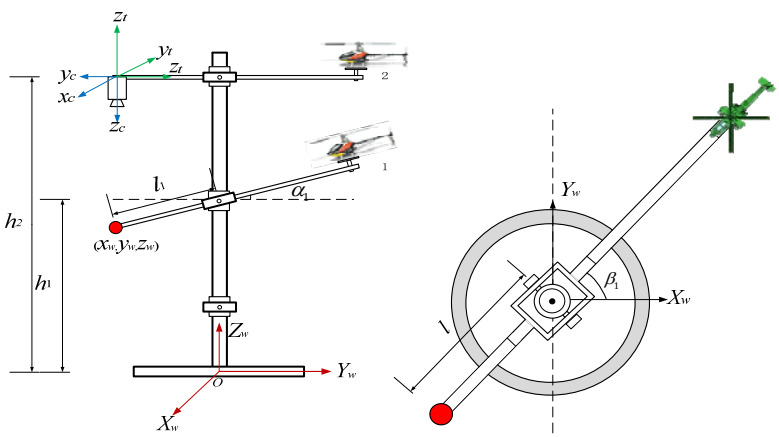

Fig. 4. Definition of Ordinate on the Platform.

In this platform, the position of each robot is denoted uniquely as the angles of α and β which can be measured using the encoders. It means that (α_1, β_1) needs to be estimated. Furthermore, the output of the system is (u, v), the pixels position on the image of the objective source. Define Q^w as the variance of system state noise w_k, and the system and measurement equation are as follows,

$$\begin{pmatrix}\beta_{1,k+1}\\ \alpha_{1,k+1}\end{pmatrix}=\begin{pmatrix}1 & 0\\ 0 & 1\end{pmatrix}\begin{pmatrix}\beta_{1,k}\\ \alpha_{1,k}\end{pmatrix}+w_k$$
$$\begin{cases} u=\dfrac{r_{11}x_w+r_{12}y_w+r_{13}z_w+T_x}{r_{31}x_w+r_{32}y_w+r_{33}z_w+T_z}+u_0 \\ v=\dfrac{r_{21}x_w+r_{22}y_w+r_{23}z_w+T_x}{r_{31}x_w+r_{32}y_w+r_{33}z_w+T_z}+v_0 \end{cases} \tag{6}$$

where u_0, v_0, f_x, f_y are calibration parameters of camera, r_{ij} and T_i are factors of R and T, as Eq. (7). And (x_w,y_w,z_w) and (α_1,β_1) satisfies Eq. (8).

$$R=\begin{bmatrix} r_{11} & r_{12} & r_{13}\\ r_{21} & r_{22} & r_{23}\\ r_{31} & r_{32} & r_{33}\end{bmatrix}=\begin{bmatrix} c\alpha_2 c\beta_2 & c\alpha_2 s\beta_2 & s\alpha_2\\ -s\beta_2 & c\beta_2 & 0\\ -s\alpha_2 c\beta_2 & -s\alpha_2 s\beta_2 & c\alpha_2\end{bmatrix}$$
$$T=\begin{pmatrix}(l_2-h_2 s\alpha_2)c\varphi c\theta-h_2 c\alpha_2 c\varphi s\theta\\ (l_2-h_2 s\alpha_2)s\varphi c\theta-h_2 c\alpha_2 s\varphi s\theta\\ -(l_2-h_2 s\alpha_2)s\theta-h_2 c\alpha_2 c\theta\end{pmatrix} \tag{7}$$

$$x_w=-l_1 c\alpha_1 c\beta_1,\ y_w=-l_1 c\alpha_1 s\beta_1,\ z_w=h_1-l_1 s\alpha_1 \tag{8}$$

where $c\alpha$ indicates $cos(\alpha)$, $s\alpha$ indicates $sin(\alpha)$, l_i and h_i are the length and height of manipulator i.

5. Experimental Results and Analysis

In this section, EKF, UKF and AUKF are applied to the moving target observation system to estimate the target's position. The estimated results are then compared with the real position measured by the encoders bonded on the manipulator to evaluate the estimation precision.

Experimental parameters are listed out in Table 1. The target is controlled to move along the trajectory as Eq. (9).The purpose to design such a trajectory is to fully reflect the nonlinearity so that the performances of three nonlinear filters could be best tested.

Table 1. Parameters of platform and vision system.

l_1	l_2	h_1	h_2	u_0	v_0	f_x	f_y
600	700	1275	2185	345	315	618	674

$$\begin{cases}\alpha_1=0\\ \beta_1=0\end{cases}(t\le t_s),\begin{cases}\alpha_1=0\\ \beta_1=\varpi(t-t_s)\end{cases}(t>t_s)\ , \tag{9}$$

5.1. Analysis of Noise Characteristics

Noise distribution matters much to performances of filters (even for linear KFs, its optimality can be realized only if the noise characteristics are known). So we firstly analyze the measurement noise statistical characteristics.

The measurement noise (n_u,n_v) can be defined as,

$$n_u=u-u_s,\ n_v=v-v_s, \tag{10}$$

where (u,v) are the measurement; (u_s,v_s) are the real values based on encoders output.

The noise distribution is as Fig. 5(a) and Fig. 5(b). Furthermore, Curve Fitting Tool Box in Matlab is used to obtain the noise PDF as the red line in Fig. 5(b) (95 % degree of confidence). It can be seen from Fig. 5(b) that n_v can be modeled by a standard Gaussian noise, whose PDF is described by Eq. (11) while n_u is approached by a triple-mixed Gaussian noise, whose PDF is Eq. (12). All the parameters of $p_v(x)$ and $p_u(x)$ are shown in Table 2.

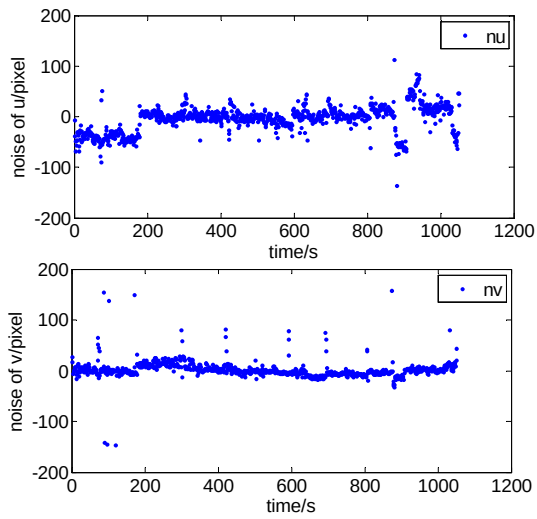

(a)

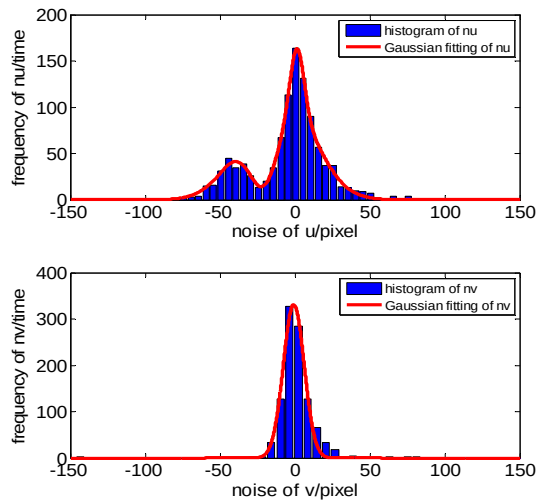

(b)

Fig. 5. (a) Noise in time domain; (b) distribution histogram.

Table 2. Parameters for the fitting function.

a_1	70.6	b_1	1.419	c_1	6.475
a_2	-106.9	b_2	-19.75	c_2	15.28
a_3	131	b_3	-12.32	c_3	31.32
a_v	311.5	b_v	-0.8402	c_v	9.85

$$p_v(x) = a_v e^{-((x-b_v)/c_v)^2} \tag{11}$$

$$p_u(x) = a_1 e^{-(x-b_1/c_1)^2} + a_2 e^{-(x-b_2/c_2)^2} + a_3 e^{-(x-b_3/c_3)^2} \tag{12}$$

According to the analysis above, the measurement noise distribution of u is clearly not standard Gaussian. In the following sub-sections, we will test the performance of the three nonlinear Kalman filters (EKF, KF, MIT-AUKF) when the noise is as Eq. (11) and (12).

Supposing the noises of n_u and n_v are uncorrelated, that is, the off-diagonal elements of the covariance matrix are all zeros, and q_1 and q_2, the diagonal elements of measurement noise covariance matrix Q^n, could be approached using the following equations,

$$q_1 = \sum_{k=1}^{n} \left(n_k^u - n_0^u\right)^2 / \left(n-1\right) = 495, \quad q_2 = \sum_{k=1}^{n} \left(n_k^v - n_0^v\right)^2 / \left(n-1\right) = 57 \tag{13}$$

5.2 Experimental Results

The parameters of EKF algorithm can be designed as

$$(\alpha, \beta)^T = (0, 0.8727)^T, \quad Q^w = diag([0.01, 0.1]^T), \tag{14}$$

The estimation results using EKF are given in Fig. 6 (a). From Fig. 6(a), it can be seen that estimation of β using EKF is bias, and estimation of α is even not convergent. The main reasons on the phenomenon can be explained from the following two aspects: Firstly, because of local linearization, EKF uses only the first order of Taylor expansion, which results in possible prediction errors. Furthermore, the noises distribution in the experiments are not Gaussian distributed, which destroy the basic assumption of EKF.

The parameter of UKF is as follows. The estimation results are shown in Fig. 6(b). From Fig. 6(b), we can conclude that the estimation performance of UKF is clearly better than that of EKF. However, the estimation result of α is still bias. This is mainly because the noise distribution in the experiment is complicated, while the UKF algorithm has no adaptive ability with respect to the possible varying of the noise covariance.

The estimation results of MIT-AUKF are shown in Fig. 6(c). From Fig. 6(c), it can be seen that for both angles, the estimated values are unbiased, and high precision of the estimation can be ensured. This presents the strong adaptability of MIT-AUKF to noise.

5.3 Comparison of EKF, UKF and AUKF

In order to quantitatively compare the estimation performances of these three different algorithms, the following evaluating index are defined,

$$\mu = \sum_{i-1}^{n} (\bar{x}_i - x_i), \quad \sigma = \sqrt{\sum_{i-1}^{n} (\bar{x}_i - x_i)^2 / (n-1)}, \quad t = t_x / t_{EKF} \, (t_x = t_{EKF}, t_{UKF}, t_{AUKF}) \tag{15}$$

where μ ,σ is the mean and square of estimation error; t is the average execution time for each iterative step. The comparison results are shown in Fig. 6(d) and Table 3.

From Fig. 7(d), we can conclude that the estimation errors of AUKF are smaller than that of UKF, and both of them are better than EKF. Table 3 gives out the similar results. About the executive time, EKF needs the least time because it needs actually run a linear Kalman filter program. Determined by the sampling strategy, although UKF does not need to calculate the complex Jacobian matrices, but the computation of sigma points and the unscented transfer will increase the processing workload, thus UKF runs a little more slowly than EKF algorithm. Finally, because of the additional adaptive computation, AUKF takes more time than both UKF and EKF.

Table 3. Statistical performance comparison.

Index	μ_α	μ_β	σ_α	σ_β	t_n
EKF	0.1373	2.8909	0.1068	1.6717	1.000
UKF	0.0017	2.8059	0.0085	1.6689	3.460
AUKF	0.0003	2.7074	0.0033	1.6679	15.75

6. Conclusions

In this paper, taking the moving target cooperative observation problem as an example, performances of three kind of nonlinear Kalman filters, including Extended Kalman Filter (EKF), Unscented Kalman Filter (UKF), and MIT based Unscented Kalman Filter (MIT-AUKF) are analyzed, compared and tested on a multi-flying-robot testbed, which has a typical non-Gaussian measurement noise.

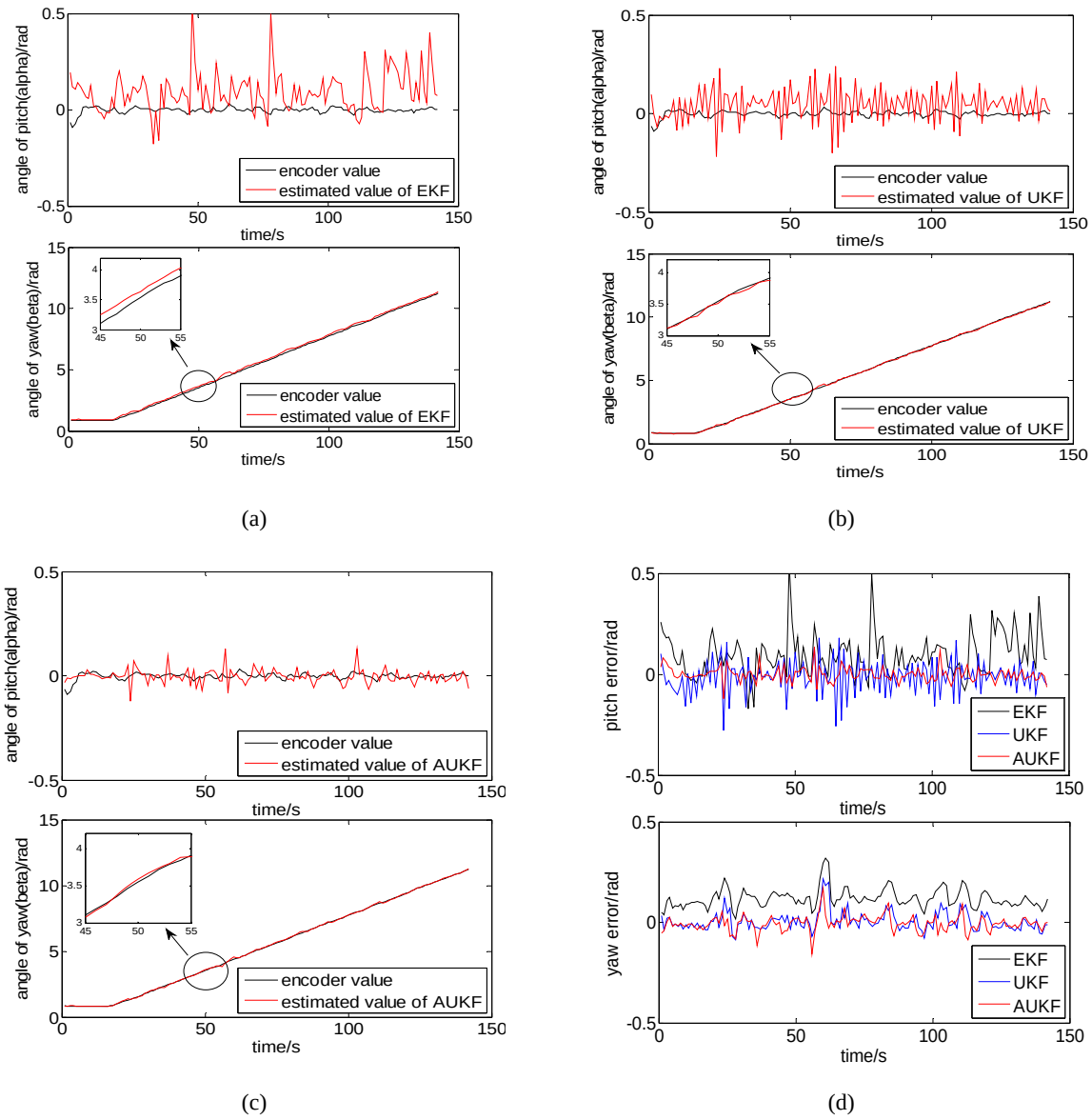

Fig. 6. (a) Estimation by EKF; (b) Estimation by UKF; (c) Estimation by AUKF; (d) Error Comparison.

The experimental results show that: 1) The MIT-AUKF presents the best estimation performance. This is mainly because it can adaptively regulate the noise covariance online based on the realities. The estimation performance of UKF is better than that of EKF because the latter use only first-Taylor-expansion to approach the nonlinear term in system model. 2) In the aspect to executive time, the EKF algorithm is better than both UKF and MIT-AUKF. Although MIT-AUKF presents good estimation performance, it takes most time because of the computational burden from both unscented transfer and adaptive scheme.

References

[1]. R. E. Kalman, A new approach to linear filtering and prediction problems, *Transactions of the ASME--Journal of Basic Engineering*, Vol. 82, Issue 1, 1960, pp. 35-45.

[2]. Ito K., Xiong K., Gaussian filters for nonlinear filtering problems, *IEEE Transactions on Automatic Control*, Vol. 5, Issue 5, 2000, pp. 910-927.

[3]. S. J. Julier, J. K. Uhlmann, H. F. Durrant-Whyte, A new approach for the nonlinear transformation of means and covariance in filters and estimators, *IEEE Transaction on Automatic Control*, Vol. 45, Issue 3, 2000, pp. 477-482.

[4]. R. Rahbari, B. W. Leach, J. Dillon, C. W. De Silva, Adaptive tuning of a Kalman filter using the fuzzy integral for an intelligent navigation system, *Proceedings of the 2002 IEEE International Symposium on Intelligent Control*, Vancouver, Canada, 27-30 October 2002, pp. 252-257.

[5]. D. Lee, K. T. Alfriend, Adaptive sigma point filtering for state and parameter estimation, *AIAA/AAS Astrodynamics Specialist Conference and Exhibit*, RI, USA, 16-19 August 2004, pp. 1-20.

[6]. D. Loebis, R. Sutton, J. Chudley, W. Naeem, Adaptive tuning of a Kalman filter via fuzzy logic for an intelligent AUV navigation system, *Control Engineering Practice*, Vol. 12, Issue 12, 2004, pp. 1531-1539.

[7]. Z. Jiang, Q. Song, Y. Q. He, J. D. Han, A novel adaptive unscented Kalman filter for nonlinear estimation, in *Proceedings of the IEEE Conference on Decision and Control*, New Orleans, LA, USA, 12-14 Dec. 2007, pp. 4293-4298.

[8]. J. C. Wang, T. M. Wang, Y. Yang, L. Hu, Robot hand-Eye calibration using unscented Kalman, *Robot*, Vol. 33, Issue 5, 2011, pp. 621-627.

[9]. M. Wu, J. Ma, J. W. Tian, J. Liu, An adaptive UKF algorithm and its application to geomagnetic navigation, *Information and Control*, Vol. 40, Issue 4, 2011, pp. 558-562.

[10]. N. J. Gordon, D. J. Salmond , A. F. M. Smith, A novel approach to nonlinear/non-Gaussian Bayesian state estimation, *Radar and Signal Processing, IEE Proceedings F*, Vol. 140, Issue 2, 1993, pp. 107-113.

[11]. F. Gu, Z. Wang, Y. Q. He, J. H. Han, Y. C. Wang, Theoretical and experimental study of uncertain set based moving target localization using multiple robots, *IEEE International Conference on Robotics and Biomimetics*, Karon Beach, Phuket, 7-11 Dec. 2011, pp. 1646-1651.

[12]. F. Gu, Z. Wang, Y. Q. He, J. D. Han, Y. C. Wang, Experimental study of vision sensor based multiple robots active cooperative observation using multi-RFRs testbed, *IEEE International Conference on Robotics and Biomimetics*, Karon Beach, Phuket, 7-11 Dec. 2011, pp. 2417-2418.

Sensors & Transducers, Vol. 21, Special Issue, May 2013, pp. 182-187

Sensors & Transducers

http://www.sensorsportal.com

Ecological Environment Monitoring System of Litopenaeus Vannamei Farming Based on Neural Network

[1] Ajin Zou, [2*] Shilong Zhang, [1] Xiuchun Xiao

[1] College of Information, Guangdong Ocean University, Zhanjiang 524088, China

[2] School of Information Science and Technology, Zhongkai University of Agriculture and Engineering, Guangzhou 510225, China

[1,2] E-mail: ajinzou@126.com, shilongzh@163.com

Received: 30 March 2013 /Accepted: 14 May 2013 /Published: 30 May 2013

Abstract: One ecological environment monitoring system of Litopenaeus vannamei farming has been developed in order to protect and regulate the ecological environment of Litopenaeus vannamei farming, halt and reverses the situations in the ecological environment deterioration of Litopenaeus vannamei farming and the little farming success rate. The early warning information of ecological environment degradation is automatically generated by means of the generalized polynomial neural network so as to prompt the user to take effective measures to improve farming ecological environment in a timely manner and effectively increase the success rate of shrimp farming. *Copyright © 2013 IFSA.*

Keywords: Litopenaeus vannamei, Ecological environment, Early warning, Neural network.

1. Introduction

Litopenaeus vannamei is of many advantages, such as high temperature resistance, miscellaneous diet, low dietary protein requirements, euryhaline, short growth cycle, big individual, high-yield, strong disease resistance, delicious meat and easy to transport [1]. Its processing meat rate is up to 67 %, and it is an excellent desalination breeding variety and has become a major shrimp species cultured in southern China [2, 3]. Its appropriate ecological environment factors are as follows [4-6]:

Optimum water temperature: 22~32 °C;
Adaptive salinity: 5 % ~ 45 % ;
PH value range:7.5 ~ 8.6 ;
Dissolved oxygen: > 2 mg/L ;
Chemical oxygen demand: 5 ~ 30 mg/L ;
Transparency: 0.2 ~ 0.9 m ;
Ideal water colors: dark brown and yellowish green;
Phosphate content: 0.1 ~ 0.3 mg/L ;
Silicate content: 0.2 mg/L ;
Ammonia nitrogen content: < 0.3 mg/L.

But the aquaculture pond is both feeding pond and metabolic pond of shrimp as well as the oxidation decomposition pond of organic matter for shrimp aquaculture ways, so there exists a few problems, such as weak aquaculture pond ecosystem and low self-purification capacity [7] so as to worsen the aquaculture ecological environment, even trigger shrimp disease occurrence, and impede the normal growth of farmed shrimp to seriously hamper the improvement of feeding efficiency.

The neural network theory [8-10] is applied to the dynamic change tracking and forecasting of ecological environment factors of Litopenaeus vannamei farming in order to solve the above problems to build the predictive models of ecological environment factors and set up the early warning mechanism of ecological environment factors degradation to achieve the ecological environment real-time monitoring of Litopenaeus vannamei farming.

2. Research Methods

The ecological environment key factors to impact Litopenaeus vannamei farming were screened out by reference to the ecosystem research achievements of Litopenaeus vannamei farming. The polynomial neural network was applied to the overall quality evaluation of shrimp farming ecological environment to build the forecasting models of shrimp farming ecological environment factors and quantificationally work out the change results of aquaculture environment factors to accurately track and forecast the dynamic change trends of ecological environment of Litopenaeus vannamei farming. Thus, farmers can visually understand the changes in the environment of Litopenaeus vannamei farming; farmers are prompted to timely take effective measures and adjust ecological indicators to help to improve shrimp production against sudden ecological indicators degradation so as to effectively improve the success rate of shrimp farming.

A dynamic ecological environment monitoring system of Litopenaeus vannamei farming was developed by combining the theory and methods of neural networks and aquaculture, and it has friendly interface and is easy to operate. The technical route flow chart is shown in Fig. 1.

3. System Development Environments

CPU: configuration of above Pentium III; Memory: more than 512 M; Monitor resolution: above 1024×768.

Operating system: higher than Windows Server 2003; Browser: higher than IE 6.0; Database: higher than Sql Server 2005; higher than Net Framework 2.0; higher than IIS 6.0.

Programming language: HTML/javascript/css/ T-SQL/C#.

4. System Design

4.1. System Function Module

The system functions are shown in Fig. 2, including industry dynamic; historical monitoring data and analysis; disaster history; early warning information of disaster; shrimp picture library; shrimp farming knowledge base; introduction to neural networks and system back-stage management.

4.2. Database Design

Entity E-R model was built as a basis for completing the table structure design of system through needs analysis, and the system possessed a total of nine data tables, where Table 1 shows the table structure of warning information:

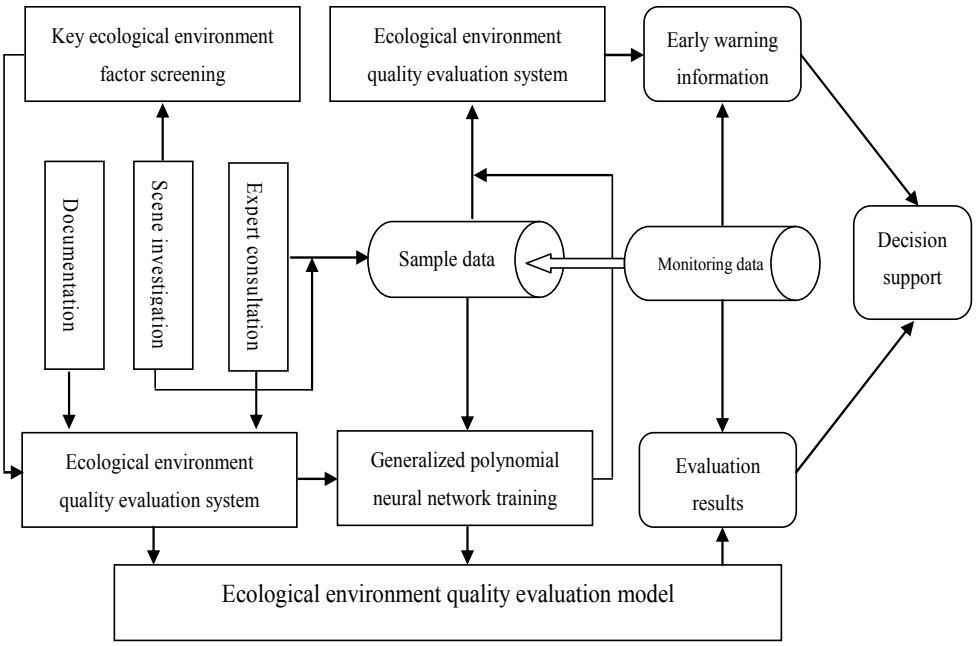

Fig. 1. Technical route flow chart.

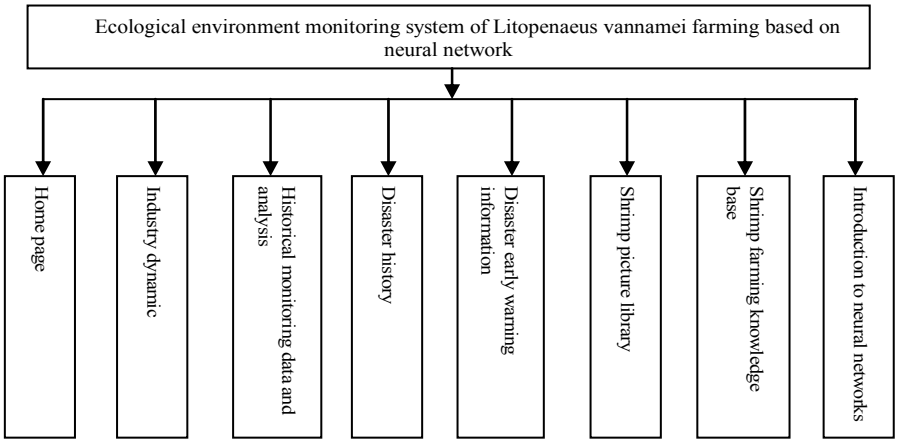

Fig. 2. Main interface of system.

Table 1. Warning (warning information).

No.	Name	Data Type	Length	Deci-mals	Identifi-cation	Primary Key	Allowed Empty	Default	Introductions
1.	id	int	4	0	Yes	Yes	No		
2.	Data Item Id	int	4	0			Yes		Generated warning information data item id (Monitoring Data_id)
3.	Title	nvarchar	100	0			Yes		Information title
4.	Warning Message	nvarchar	400	0			Yes		Warning information content
5.	Create_User	nvarchar	50	0			Yes		
6.	Create_Time	datetime	8	3			Yes		
7.	Update_User	nvarchar	50	0			Yes		
8.	Update_Time	datetime	8	3			Yes		
9.	Record_Sta	int	4	0			Yes	((0))	Record status (0: effective, 1: invalid)

5. Implementing the Monitoring Functions of Ecological Environment

Improving the success rate of shrimp farming is system engineering and needs a series of technical research and development and integration. The effective early warning of ecological environment deterioration of shrimp farming is the most important part of this R & D project, and the system uses the prediction model of generalized polynomial neural network to achieve the early warning function of ecological environment factor changes of Litopenaeus vannamei farming.

5.1. Generalized Polynomial Model of Neural Network and Forecasting Principles

The related literature established a generalized polynomial model of neural network (Fig. 3) [8].

Network output is:

$$y = \sum_{i=1}^{n} w_i p_i(x_1, x_2, \cdots, x_m), \qquad (1)$$

Sample set is set up as $\{((x_1(t), x_2(t), ..., x_m(t), y(t)), t = 1, 2, \cdots, l$ (where the sampling value is $y(t)$, and the number of samples is l) for m element objective function $f(x_1, x_2, ..., x_m)$. The output vectors of all samples in sample set and neural network weight vector are ordered as

$$\gamma = \begin{bmatrix} y_1 & y_2 & \cdots & y_d \end{bmatrix}^T \in R^l$$

and

$$w = \begin{bmatrix} w_1 & w_2 & \cdots & w_n \end{bmatrix}^T \in R^n,$$

respectively. The excitation function of hidden layer neuron is set up as $p_i(x_1, x_2, \cdots, x_m)$. The excitation response of the i-th hidden neuron to the t-th sample is $q_i^{(t)} = p_i(x_1, x_2, \cdots; x_m)$ where

$t = 1, 2, \cdots, l; i = 1, 2, \cdots, n$ The excitation-response vector of hidden layer to the t-th sample is $q^{(t)} = [q_1^{(t)} \quad q_2^{(t)} \quad \ldots \quad q_n^{(t)}]^T \in R^n$. Then, the excitation response matrix of hidden layer to all samples is

$$Q = \begin{bmatrix} q_1^{(1)} & q_2^{(1)} & \cdots & q_n^{(1)} \\ q_1^{(2)} & q_2^{(2)} & \cdots & q_n^{(2)} \\ \vdots & \vdots & \ddots & \vdots \\ q_1^{(l)} & q_2^{(l)} & \cdots & q_n^{(l)} \end{bmatrix} \in R^{l \times n},$$

and thus, the optimum weight of neural network can be obtained:

$$w = Q^{+}\gamma, \qquad (2)$$

The ecological environment factor changes of Litopenaeus vannamei farming are set up as a nonlinear system:

$$y(k) = F[y(k-1), \cdots, y(k-n)], \qquad (3)$$

without loss of generality, after the simulation models of ecological environment factors of Litopenaeus vannamei farming were built using the above method. Where, $y(k) \quad (k = 2, 3 \cdots, N, n << N)$ is the given sample collection data, and $F(\bullet)$ is the unknown nonlinear dynamic function of Litopenaeus-vannamei farming ecological environment. Thus, the forecasting principles [10] of generalized polynomial neural network are shown in Fig. 4.

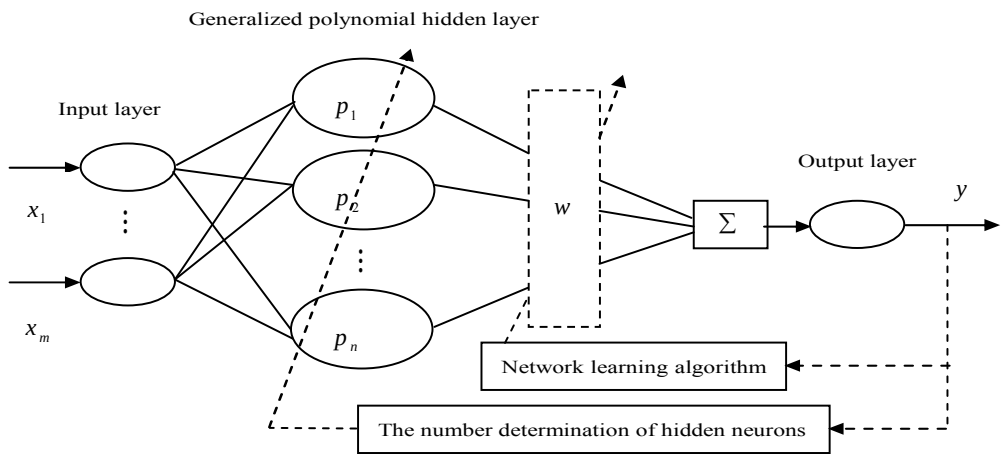

Fig. 3. Generalized polynomial model of neural network.

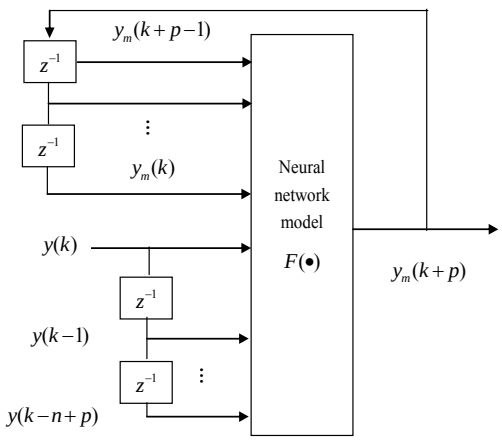

Fig. 4. Drawing of neural network forecasting principles.

The implementation process is as follows: First, the measured data of the dynamic changes in the ecological environment factors is collected in Litopenaeus vannamei farming process. Then, the data is as the training samples of generalized polynomial neural network shown in Fig. 3, and the trained neural network is the simulation model of ecological environment factors of Litopenaeus vannamei farming. Again then, the dynamic change prediction model of ecological environment factors of Litopenaeus vannamei farming was established according to Fig. 4 to generate real-time alarm information.

5.2. Pond Environmental Monitoring

The pond information list (see Fig. 5) is entered into by clicking the "pond environmental monitoring" link of back-stage management so as to perform the operations to add, modify, delete or query pond as well as view or manage monitoring data corresponding to each pond.

5.3. Monitoring Factors

The monitoring factor management interface is entered into by clicking the "monitoring factor management" link on the left of back-stage management to look the monitoring factor list up (see Fig. 6).

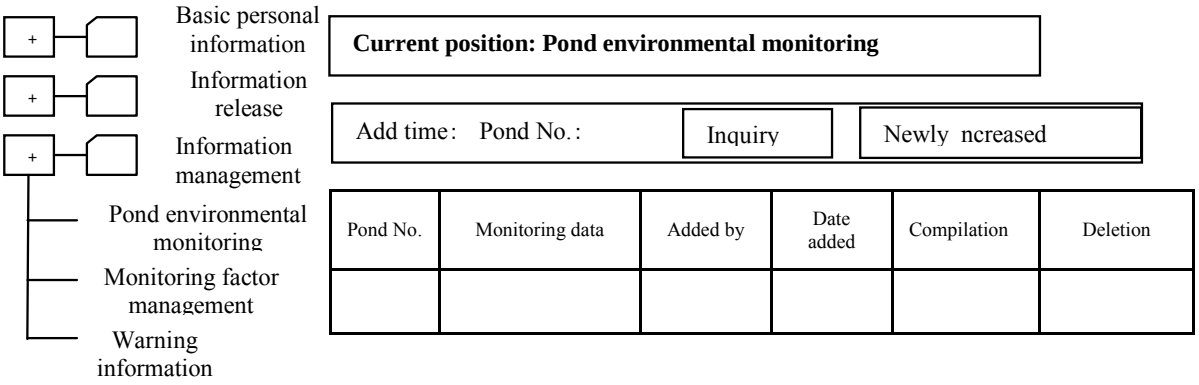

Fig. 5. Pond information

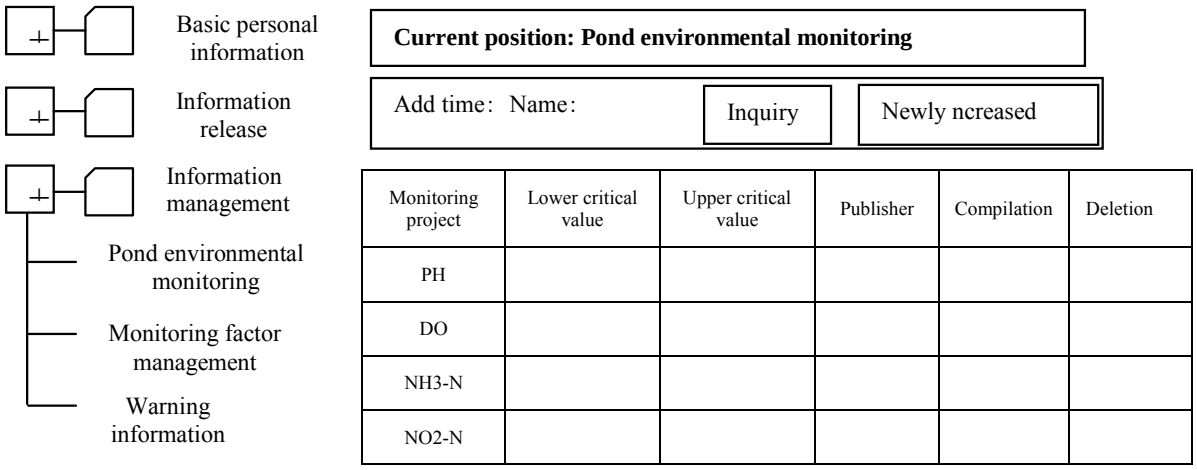

Fig. 6. Monitoring factor list.

5.4. Historical Monitoring Data and Neural Network Prediction

The "historical monitoring data and analysis" in the navigation bar is clicked to access this column page. Query date, pond number and item are input in the query conditions (see Fig. 7), and then the query results are displayed.

The interface of warning information list is entered into by clicking the "warning information" link on the left of back-stage management to generate warning information after the deterioration of each ecological environment factor. For example: Fig. 8 is the alarm content generated by system.

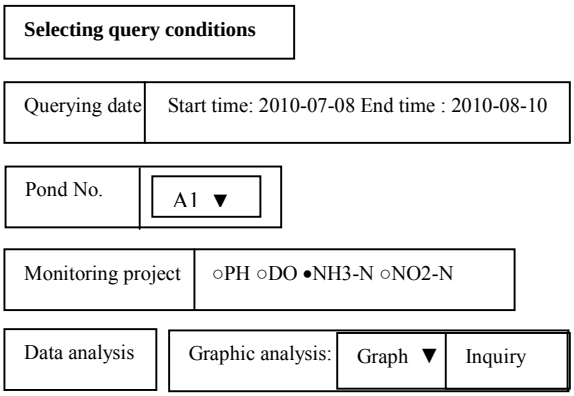

Fig. 7. Historical monitoring query.

The NO2-N monitoring value of A1 pond is too high.

Alarm content	The upper limiting standard value of monitoring item (NO2-N) is 0.15. The current monitoring value of A1 pond is 2.420, so it is too high. Suggested solutions: □ Cleaning up pond silt □ Oxygenation □ Adjusting PH value Monitoring reporter: admin Reporting time: 2010-8-7 0:00:00

Fig. 8. Warning information.

6. Conclusions

The system interface is friendly and easy to operate so that farmers can visually understand the changes in the environment of Litopenaeus vannamei farming. The system can prompt the user to timely take effective measures and adjust the ecological indicators to help to improve shrimp production for deterioration of ecological indicators so as to effectively improve the success rate of shrimp farming. The popularization and application of research achievements is meaningful to enhance the reasonable farming and scientific management of Litopenaeus vannamei.

Acknowledgements

This work was supported by the Guangdong Provincial Natural Science Foundation (S2012010009976), the Guangdong Provincial Oceanic Fisheries Special Research and Development Project of Technology Promotion for Science and Technology Development (A201008B05), the Guangdong Provincial Science and Technology Plan Project (2011B020313021, 2011B040200074), and the Zhanjiang Municipal Plan Project for Science and Technology Development (2011C3105001).

References

[1]. Zhang Heng, Liu Li-He, He Guo-Long, Liu Jun, Huang Feng, Proper Proportion of Rapeseed Meal Substitution for Fish Meal in Diet of Pacific White Leg Shrimp Litopenaeus vannamei, *Fisheries Science*, Vol. 30, Issue 10, 2011, pp. 591-596.

[2]. Technology Department of Beijing Zhishui Biological Technology Co., LTD, Key Points of Penaeus vannamei Boone Brackish Water Aquaculture, *Scientific Fish Farming*, Issue 2, 2011, pp. 84-84.

[3]. Tang Yuan-Yuan, Chen Xi-Fei, Ai Chun-Xiang, Research Progress of Vitamins and Minerals Nutritional Needs of Litopenaeus vannamei Boone, *Feed Industry*, Vol. 33, Issue 12, 2012, pp. 23-29.

[4]. Yang Fu-Yi, Li Xiu-Jun, Tian Ming-Zeng, Yang Xin-Qiao, Correlation between Growth of Litopenaeus vannamei and Environmental Factors in Saline-Alkali Waters, *Chinese Agricultural Science Bulletin*, Vol. 24, Issue 1, 2008, pp. 520-526.

[5]. Zhang Te, Sun Cheng-Bo, Guang Ren-Lei, Effect of Multi-factors on Energy Metabolism of Juvenile Litopenaeus vanname, *Journal of Tropical Organisms*, Vol. 3, Issue 1, 2012, pp. 11-15.

[6]. Shui Bo-Nian, Research on the Adaptability of Young Litopenaeus vanamei to Several Environmental Factors, *Journal of Aquacultur*, Vol. 26, Issue 1, 2005, pp. 8-13.

[7]. Zha Guang-Cai, Mai Xiong-Wei, Zhou Chang-Qing, He Jian-Guo, Aquatic Ecological Characteristics of Litopenaeus vannamei in Intensive Desalination Culture Ponds, *Marine Sciences*, Vol. 30, Issue 9, 2006, pp. 58-62.

[8]. Xiao Xiu-Chun, Zhang Yu-Nong, Jiang Xiao-Hua, MISO Multivariate Generalized Polynomials Neural Network and its Weights-Direct-Determination, *ACTA Scientiarum Naturalium Universitatis Sunyatseni*, Vol. 48, Issue 4, 2009, pp. 42-46, 56.

[9]. Zou A-Jin, Zhang Yu-Nong, Sieve-decrease Algorithms of Polynomial Neural Networks, in *Proceedings of the World Congress on Computer Science and Information Engineering (CSIE'2009)'*, Vol. 5, Los Angeles/Anaheim, USA, March 31 to April 2, 2009, pp. 564-569.

[10]. Zou A-Jin, Zhang Yu-Nong, Basis Function Neural Network and Application, *Sun Yat-sen University Press*, Guangzhou, 2009.

Sensors & Transducers, Vol. 21, Special Issue, May 2013, pp. 188-192

Sensors & Transducers

http://www.sensorsportal.com

Application of Elliptic Curve Cryptography in ZigBee Wireless Sensor Network

[1,2] Feng Xu, [3] Xuan Zhou, [1] Dan Zhou, [1*] Shusheng Peng

[1] Nanjing Univ. of Sci. & Techn., Nanjing, 210094, P. R. China

[2]Nanjing Military Region 73033 Troops, Nanjing, 211132, P. R. China

[3]Nanjing Feiteng Technological Development Co., Ltd, Nanjing, 210094, P. R. China

[1] E-mail: p3tzdhz@163.com, [*] njustpss@163.com

Received: 30 March 2013 /Accepted: 14 May 2013 /Published: 30 May 2013

Abstract: An encryption algorithm is the core of network security, but for ZigBee wireless sensor network (WSN), the complexity of this algorithm directly affects the cost and energy consumption in MCU hardware storage resources, which results in confliction between data protection and overhead. In this paper, a contradiction simple elliptic curve cryptosystem (ECC) is proposed to use for terminal nodes and host computer for data encryption and authentication, the purpose is to save the hardware cost and enhanced data security.

Keywords: Network security, ZigBee, WSN, ECC.

1. Introduction

1.1. ZigBee Technology and its Security Issues

ZigBee is a short-range communications technology, it has a low power consumption, low rate, small size, and low cost [1-2]. The short-range wireless communication technology along with integrated circuits and computer technologies mature and get a wider range of applications, the main short-range communication technology such as ZigBee technology, Bluetooth technology, and RFID, etc.

As a wireless transmission network system, ZigBee network faces many security issues, such as completeness, legality, availability, message authentication, intrusion detection, access control, and confidentiality. Wireless communication transmission is opened by the air, so as long as the same frequency are likely to become vandals or steal information, at the same time, can not be stored within the node network dynamics, changing topology and network resources makes network topology information. The safety mechanism includes a key establishment, transmission frame protection, and device management. A security framework is shown as Fig. 1.

The ZigBee Alliance integrates the elements of the IEEE802.15.4 standard of safety, and security class and software based 128-bit AES algorithm [1, 3, 5]. ZigBee protocol stack defines the security attributes, for the link layer, network layer and application layer, and equipment sharing by the Trust Center security key. Security mechanisms for the protection of the network are not the same, however, this will lead to memory resource consumption increases, therefore, the need to weigh the contradiction between data protection and overhead applied at different levels. AES standard to the attacker brought a great amount of computation, and its main function is information encryption, but it also brings the huge overhead of energy consumption and storage resources, using symmetric cryptosystem

is quite upset. Therefore, ZigBee single symmetric encryption algorithm, data encryption and key exchange may be a security risk, AES encryption and decryption operations to the ZigBee end hardware overhead also brings a certain burden. The main role of the public-key cryptosystem, including encryption and authentication without key exchange, simplified key distribution workload. This article uses a public key algorithm to encrypt and decrypt the data in the terminal node and host computer, to improve security at the same time to reduce the amount of affordable computing network.

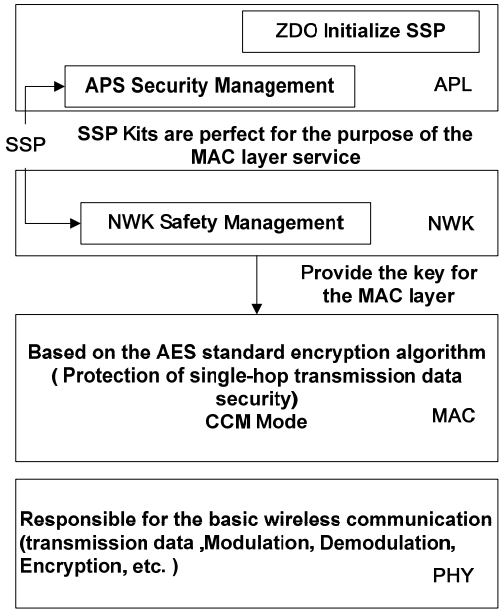

Fig. 1. ZigBee Security Framework.

1.2. Common Public-Key Encryption System

Public key cryptosystem basic idea is that the public key is used to encrypt and the private key is used to decrypt and the encryption and decryption keys are different. From a mathematical point of view, the design of public key cryptosystem is based on the difficulty of the math problems, in use, original parameters based on positive operator can easily get the results, the inverse operation by the results, it is difficult to infer the original parameters, that is, anyone can use the public key encryption, but to decrypt secret data and deduce the private key value is very difficult.

Famous public key cryptosystem backpack institutional the Williams system, EGamal system, RSA system, elliptic curve cryptosystem (ECC), and recently have the braid group public key cryptography system and NTRU, and is currently the most widely used is RSA public key cryptography authentication system [4, 6], the algorithm is a first not only encryption but also at the same time the digital signature algorithm, public key algorithm is also been widely studied, and is considered to be the best public key scheme in the current one.

But the speed is the biggest drawback of the RSA algorithm, the main reason is the key generated by the prime number generator algorithm restrictions makes it difficult to do the one-time pad, in order to ensure there is security packet length or at least 600 bit that is too large to consume computing resources.

Elliptic curve cryptosystem (ECC) is a public key cryptosystem public key cryptosystem bit high strength, the essence is elliptic curve discrete logarithm (ECDLP), which is an elliptic curve cryptosystem security infrastructure [7]. Relatively RSA, its advantages are mainly reflected in three aspects: first, using the general number field sieve (NFS) method of attacking it, its strength is higher, achieve exponentially, while RSA algorithm only achieve subexponential class; Second, equal security under the conditions of the key length is short, but this advantage is very suitable for use in low storage conditions; Third, password storage space consumed by the small, low bandwidth requirements, it is also very suitable for storing restricted environment uses; Fourth computing speed is much higher than the RSA algorithm, to improve the efficiency of the service.

2. System Architecture

A sensor module is connected with ZigBee terminal nodes, or routing nodes, via RS485 line, and data are encrypted/deencrypted/authenticated in the terminal node and deencrypted or encrypted/authenticated in the host computer. In a ZigBee network, a separate security system is adopted, in which ECC encryption and authentication system are designed, namely processing hardware nodes and host computer sensor module data. This method is able to guarantee the security of the network data and less consumption of network resources. The system design architecture is shown as Fig. 2.

3. Elliptic Curve Encryption Algorithm Design

Define abbreviations and acronyms the first time they are used in the text, even after they have been defined in the abstract. Abbreviations such as IEEE, IFSA, ac, dc, ms, etc. do not have to be defined. Do not use abbreviations in the title or heads unless they are unavoidable.

Elliptic curve cryptosystem has become the hotspot of the field of security research direction with a high-strength security, the fastest processing speed and lowest cost [4], For now, the elliptic curve encryption algorithm key length is shorter, generally about 30 to 60, which is determined by the execution rate of the software implementation. And a key length is relatively large in the hardware implementation of elliptic curve. The encryption algorithm will need a lot of hardware resources.

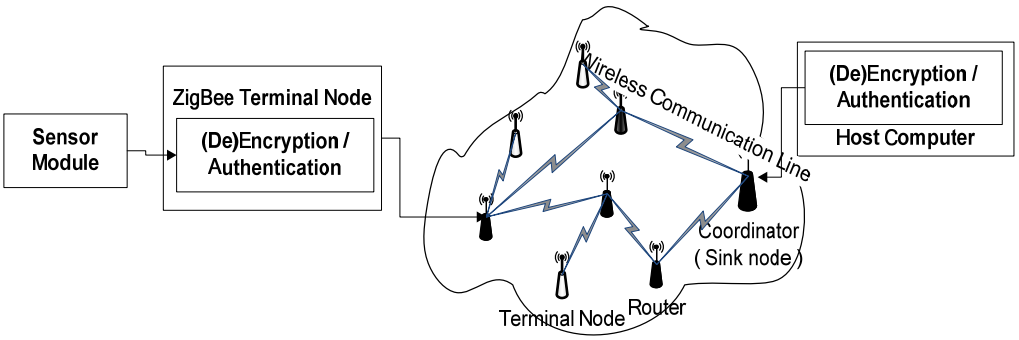

Fig. 2. System Design Architecture.

Elliptic curve refers to the curve plane defined by the Weierstrass equation, as shown by Eq. 1.

$$Y^2Z + a_1XYZ + a_3YZ^2 = X^3 + a_2X^2Z + a_4XZ^2 + a_6Z^3, \quad (1)$$

Elliptic curve for normal point (X:Y:Z) (Z ≠ 0) and the infinite point O (Z=0) sets defined in the photography coordinate system, each point on the curve is non-singular point, curve is smooth. Coefficient a_i (i=1,2,3,…,6) is defined in the base field K, K is the field of rational numbers, real numbers, complex domain, or a finite field. And elliptic curves in cryptography are defined over finite field which is studied in this paper for the prime field.

To extend photography coordinate system to the rectangular coordinate system, sets x=X/Z, y=Y/Z (Z ≠ 0), then Eq.1 can be converted into Eq. 2.

$$y^2 + a_1xy + a_3y = x^3 + a_2x^2 + a_4x + a_6, \quad (2)$$

As shown in Fig. 3 and Fig. 4, $y^2=x^3-x$ and $y^2=x^3+x+1$ are two elliptic curve on a rectangular coordinate. For these two elliptic curves and two arbitrary points P and Q (do the tangent at the point P if two points P and Q coincide) ,draws a linear and gets its intersect-point R' with the elliptic curve. Through the point R' a y-axis parallel line is drawn to get another intersect-point R. Set P+Q=R, in which the sum of infinity point O and the point P still get the P, Added to the point P k times, referred to as kP, point addition is equivalent as P * Q = R. The elliptic curve defined in the base field K of the point and infinite point is composed of a set of E(K), Execution point addition in E(K) collection for this addition, E(K) form a commutative group, this exchange group called elliptic curve group, that is, the set of points on elliptic curve addition operation constitutes elliptic curve group. Its general form is shown as Eq. 3.

$$y^2 = x^3 + ax + b \ \ (4a^3 + 27b^2 \neq 0), \quad (3)$$

ECC is a password system built on the finite field on the elliptic curve group, and all coefficients of the elliptic curve are certain elements of the finite field GF(p), where p is a large prime number. One of the most commonly used is the curve defined by the equation. p is a prime number, and {0,1, ..., p-1} is the exchange group of modulo p plus (Abelian); and {1, ..., p-1} is the commutative group of modulo p multiplication. The present study is relatively mature finite field, there are two, one for the GF(p), and one for $GF(p^m)$. This paper describes the GF(p).Refer with: Eq. 4 [7-9].

$$\begin{gathered} y^2 \equiv x^3 + ax + b \bmod p \\ (a, b \in GF(p), \\ 4a^3 + 27b^2 \bmod p \neq 0), \end{gathered} \quad (4)$$

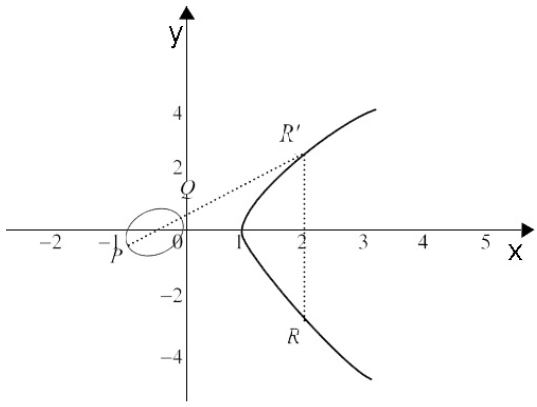

Fig. 3. $y^2=x^3-x$.

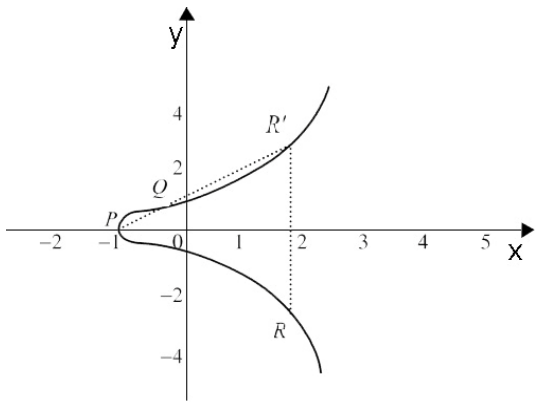

Fig. 4. $y^2=x^3+x+1$.

GF(p) on the elliptic curve group E(GF(p)) is the point p(x,y)∈(GF(p)×GF(p)) to satisfy the equation and its infinity point O. For points $p(x_1,y_1)\in E(GF(p))$, $Q(x_2,y_2)\in E(GF(p))$, the Eq. 5 and Eq. 6 for both point to add the calculation method. Arbitrary point p(x,y)∈E(GF(p)) , there are P+O=P, and the inverse element of P is expressed as the -P=(x,-y).

$$\begin{cases} \lambda = (y_1 - y_2)/(x_1 - x_2) \bmod p \\ x_3 = \lambda^2 - x_1 - x_2 \bmod p \\ y_3 = \lambda(x_1 - x_3) - y_1 \bmod p \end{cases} \quad (5)$$

$$\left(P \neq Q, P + Q = (x_3, y_3) \right),$$

Or,

$$\begin{cases} \lambda = (3x_1^2 + a)/2y_1 \bmod p \\ x_3 = \lambda^2 - 2x_1 \bmod p \\ y_3 = \lambda(x_1 - x_3) - y_1 \bmod p \end{cases} \quad (6)$$

$$\left(P = Q, P + Q = 2P = (x_3, y_3) \right),$$

Support a point P on an elliptic curve and let k an integer, define the scalar multiplication as Eq. 7.

$$kP = \underbrace{P + P + \cdots + P}_{k}, \quad (7)$$

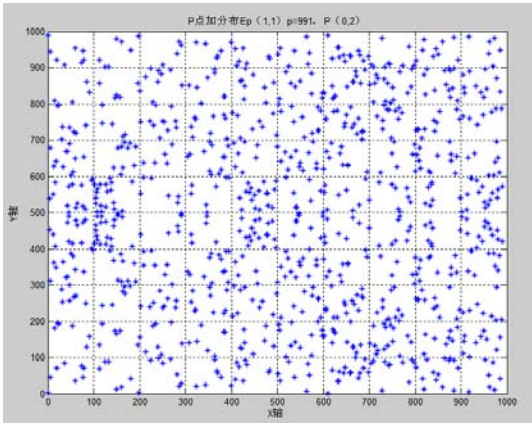

Fig. 5. $E_{991}(1,1)$ Scalar Multiplication Point P(0,2), Rank is 955.

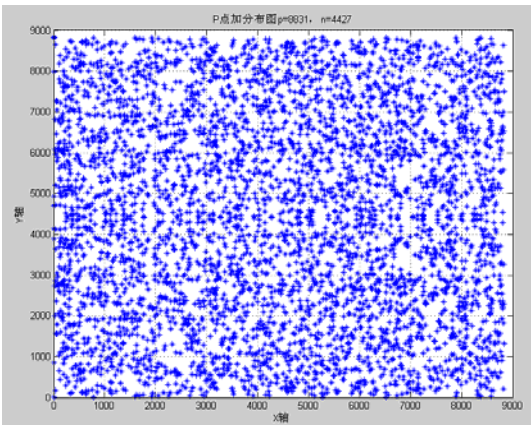

Fig. 6. $E_{8831}(3,45)$ Scalar Multiplication Point P(4,11), Rank is 4427.

Referenced as Eq. 7, if k < 0, then kP=(-k)(-P).When k is increased to a certain value, n = k_{max} is the rank of the point P. The problem of ECDLP is, for a k and the base point P, when known scalar multiplication kP and P, seeking the value of k, Time to solve this problem exponentially. ECC public key cryptosystem is built at the top of this problem [8, 10].

As shown in Fig. 5, an access point P (0,2) on the in $E_{991}(1,1)$, its rank can be calculated as n=955. With m=8831, the elliptic curve E_{8831} (3,45) point are distributed in Fig. 6. With an access point P(4, 11), the distribution of kP points will be more intensive, the rank of this point P is 4427. In actual condition, a suitable base point P would be chosen, so that the rank 's value is as large as possible firstly.

ECC calculation contains four key steps, such as operations over finite field, point operation, scalar multiplication and ECC application algorithms. Encryption and decryption calculation step is following as:

Step 1: A appropriate basic point G (x,y) and an elliptic curve equation $E_P(a,b)$ selection such as Eq. 3.

Step 2: Private key k selection and the public K_p calculation.

The order of the point G is calculated as n, and in the open interval (0,n), a random number k is adopted to calculate K_p=kG.

Step 3: Plaintext data encoding.

The collected information data is encoded in accordance with the form of the coordinates (x,y) to get plaintext P_m= (x_m,y_m).

Step 4: Plaintext data encryption.

A random positive integer r is selected to calculate rG and P_m+rK_p, and to generate ciphertext. Ciphertext data, the base point G, the public key K_p are sent to a trusted party.

Step 5: Ciphertext data decryption.

The receiving party decrypts the ciphertext data with the private key k and a formula C_{my}-kK_p to get the plaintext data encoding.

Encryption and decryption processes are shown in Fig. 7.

ECC is adopted for encryption, decryption and authentication of sensors' data, concrete steps are following as:

Step1: Chooses the elliptic curve $E_{8831}(3,45)$, i.e.

Step2: Selects the basic point G=(4,11) on the curve, and calculate the rank of the point, n=4427.

Step3: From the interval (0,4427), selects the private key, sets k=200, and calculates the public key, K_p=kG= (3536,1563).

Step4: Extracts data from a sensor at the transmitter, such as 0xFFAB28954AB1. The data in each of the three as a group are encoded, a zero is added before the highest bit, finally get the new data, 0x0FFA0B2809540AB1.

Step5: The sensor data to code according to each of the four as a group are grouped, and encoded in Cartesian coordinate data format, P_{m1}= (40902856) and P_{m2}= (23882737).

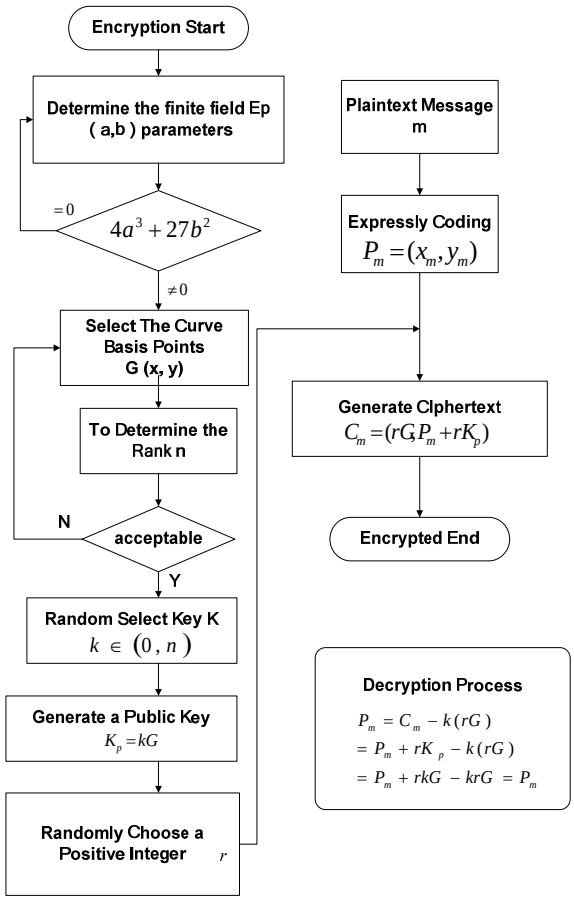

Fig. 7. Elliptic Curve Encryption and Decryption Process.

Step6: Encrypt P_{m1} and P_{m2}, randomly generated integer r ∈ (04427), of which, r_1=125, r_2=137. The following results were obtained by calculation.

r_1K_p = (4642, 6242), r_1G = (5000, 267), r_2K_p = (4385, 8355), r_2G = (3051, 3946);$P_{m1}+r_1K_p$ = (3239, 3100), $P_{m2}+ r_2K_p$ = (6487, 674).

Through calculation of the ciphertext data to obtain the plaintext encrypted for 0x0FFA0B2809540 AB1:0x1388010B0CA70C1C0BEB0F6A195702A2.

Step7: Decrypt the encrypted data.

At the receiving terminal, the ciphertext is converted to Cartesian coordinates format. For the C_m = (rG, P_m+rK_p), first isolated longitudinal coordinate C_{my}, using the private key k, by computing the C_{my}-kK_p, C_m corresponding to the plaintext P_m, after calculation, then obtain the original plaintext.

4. Conclusions

In this paper, a simple ECC encryption and authentication technology is presented between terminal node and host computer in a ZigBee wireless sensor network. Most security technologies are hardware-based encryption, which requires additional hardware resources. In order to reduce hardware overhead, data format and encapsulation are unified from a sensor modular and (de) encryption and authentication are completed in the host computer and terminal nodes. This method not only saves energy and storage overhead and reduces the amount of network computing burden, but also enhances data security and reduces security risks in data encryption and key distribution and exchange.

References

[1]. L. Subramanian, R. H. Katz, An Architecture for Building. Self Configurable Systems, in *Proceedings of the IEEE/AC M Workshop on Mobile Ad Hoc Networking and Computing*, Boston, MA, 2000, pp. 63-73.

[2]. Limin Sun, Jianzhong Li, Chen Yu, Hongsong Zhu, Wireless Sensor Network, *Tsinghua University Press*, Beijing, 2005 (in Chinese).

[3]. Jiang Ting, Chenglin Zhao, ZigBee Technology and Application, *Beijing University of Posts and Telecommunications press*, Beijing, 2006 (in Chinese).

[4]. A. R. Masoleh, Efficient algorighms and architectures for field multiplication using Gaussian normal bases, *IEEE Transactions on Computers*, 55, 1, 2006, pp. 34-47.

[5]. Peng J., Chengdong W., Yun Z. Z., et al., Research of an energyaware MAC protocol in Wireless Sensor Network, in *Proceedings of the Control and Decision Conference (CCDC' 08)*, Chinese, 2008, pp. 4686-4690.

[6]. Koblitz, N., Elliptic curve cryptosystems, *Mathematics of Computation*, Vol. 48, 1987, pp. 204-209.

[7]. Miller, V., Uses of elliptic curve in cryptography, in CRYPTO Lecture Notes in Computer 85, Science, LNCS218, pp. 417-426, *Springer-Verlag*, 1986.

[8]. Koblitz, N., Elliptic curve cryptosystems, *Mathematics of Computation*, Vol. 48, 1987, pp. 204-209.

[9]. Miller, V., Uses of elliptic curve in cryptography, In *CRYPTO'85*, Lecture Notes in Computer Science, LNCS218, pp. 417-426, *Springer-Verlag*, 1986.

[10]. J. Silverman, The Arithmetic of Elliptic Curves, *Springer-Verlag*, New York, 1986.

Sensors & Transducers, Vol. 21, Special Issue, May 2013, pp. 193-198

Sensors & Transducers

http://www.sensorsportal.com

The Analysis and Measurement for Three-port Scatter Parameters of Substructure in Multimode Feed Network

[1*] Huawei Zhan, [1,2] Haigang Yang, [1] Fei Han, [1] Yu Zhang, [1] Yufeng Peng

[1] College of Physics and Electronic Engineering, Henan Normal University, Xinxiang, 453007, China

[2] Renewable Energy School, North China Electric Power University, Beijing 102206, China

[1] E-mail: huaweizhan@yeah.net

Received: 30 March 2013 /Accepted: 14 May 2013 /Published: 30 May 2013

Abstract: In opinion of substructure cascade, multimode feed network is composed of impedance transforming substructure and isolating substructure. Starting from the characteristic of the substructure in multimode feed network, a method of measurement for its three-port scatter parameters of substructure is presented, based on the applying of the available two-port vector network analyzer (VNA), considering the port impedance matching, the three-port scatter parameters of substructure in multimode feed network are researched, the mixed-mode S-parameters of three-port networks are used to verify the actual measured data. All those provide a favorable base for the optimizing design of the entire multimode multi-feed antenna system. *Copyright © 2013 IFSA.*

Keywords: Multimode feed network, Substructure, Three-port, Scatter parameters.

1. Introduction

The multimode feed network of multi-mode multi-feed shortwave antenna is composed of impedance convertor and isolator [1], the equivalent circuits are shown in Fig. 1, both the two substructures are based on the transmission-line transformer. It is the key to the short-wave multi-mode multi-feed antenna and complicated in structure. The function of impedance convertor in multi-mode feed network is for impedance match. The function of isolator in multi-mode feed network is to divide (or synthesize) power and isolate the signal. In opinion of substructure cascade, the characteristic of feed network can gain through the characteristic of impedance transforming substructure and isolating substructure. To give an effective and convenient analysis for substructures will provide the foundation for the design and optimization of multi-mode feed network and be of great applied value for the design, analysis of transmission-line transformer, isolator on short-wave and microwave.

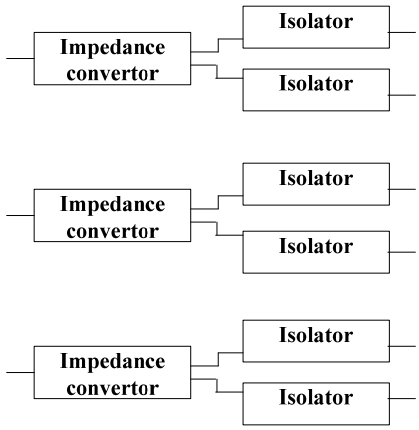

Fig. 1. The Feed Network Configuration.

For the convenient cascade of the multimode feed network, the two-port network is not only inadequate for the characteristic of substructure, but also not precise enough. Analyzing by three-port network is aptitude. So, the three-port network parameters are derived.

In this paper, from the passive network characteristic of substructure in the multimode feed network, considering the port impedance matching, the three-port scatter parameters(S-parameters) of substructure in multimode feed network are researched, the mixed-mode S-parameters of three-port networks are used to verify the actual measured data. Those not only are used to examine the results, but also can help to the optimize goal. These theoretical results provide the effective foundation for the device, modeling and optimize of the multimode feed network.

2. Overview of the Substructure Analyzing Method of Interconnect-net

With the progress of software and hardware of computer, the combination of numerical method using high-speed computer technology and Electromagnetism resolution method has solved a great deal of questions of the application domain, especially in the analyzing and designing of electromagnetic components. Several years ago, we brought forward the substructure analyzing method of interconnect-net [2], based on great capacity database, to settle the question that we encountered while researching, for example the difficulty in analyzing and optimizing the complex electromagnetic structure, the certain blindness in designing and machining.

Microwave net analyzing method has been developing rapidly. Recently, as a result of the progress of information and electronics, especially using of computer widely, microwave network is advancing more quickly than ever and appearing many new concept, theory and method. The substructure analyzing method of interconnect-net is on the base of our microwave engineering experience, technology of software and hardware of computer and microwave auto highly precise measure, it analyzes net using substructure idea, the outline of this method as follow:

1. Treat the complex net as the cascading of a set of substructures;
2. With the substructure database model, use multiple methods to character the net property of substructures. Database is a basic method here;
3. Using the net cascading method to get the overall net parameters;
4. With the direct use of the database data and the use of some technologies such as data lookup, data interpolation, database self-completeness, data pre-compute and data visualization, the net analyzing will be performed effectively;
5. Based on the analysis, optimization design can be achieved with the use of complex optimization method and the tact-select method, process trace technology.

The basic goal of the substructure analyzing method of interconnect-net is to resolve the question of analyzing and microwave net, and it also can settle the question of analyzing and optimizing design of analogy physical net, for example:

1. The analyzing and optimizing design of net which has some complex substructure.
2. Improving the calculate speed of substructure cascade of some certain model.

Substructure can be basic net unit or a set of net unit due to different objects. The aim is to make analyze more quickly and calculate more precise, for the convenience of debug, design and the optimization of system performance. The mainly point is which of definite electronic-magnetism characteristic or net parameter. For the multimode feed network usually, we use the S-parameters to describe the port characteristic of a certain substructure [3], for it has some merits as follow:

1. Easy to measure and use.
2. S-parameters can calculate circuit with Smith chart.
3. When preference plane moving, the change of S-parameters is reflected on phase only.
4. It is easy to deduce the S-parameters of multiple ports network.

3. Substructure in Multimode Feed Network

The substructure network S-parameters can be measured easily by Vector Network Analyzer (VNA).

Impedance convertor and isolator can be abstracted as three-port networks having the function of impedance transforming, see Fig. 2. BALUNS usually is used when these three ports networks are measured with two ports VNA. Balanced port 2 and 3 can be converted to unbalanced ports and impedance transforming is finished to match reference impedances of VNA.S-parameters of balanced ports and unbalanced ports can be gained with BALUNS. But substructure cascade need all 9 S-parameters of three ports networks [4]. So it is unsuited to measure S-parameters of substructure with BALUNS.

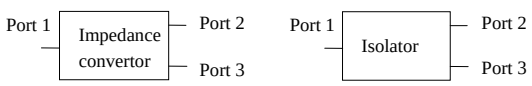

Fig. 2. The feed network substructure.

By the notion of substructure cascade, impedance convertor and isolator are looked on as substructures

of multimode feed network. Impedance convertor and isolator are composed of windings, which is coiled with high permeability cores.

When signals are input from port 2 and port 3 which are same amplitude and phase, magnetic-flux which has inverse direction in cores is quit each other. Two signals are added.

When signals are input from port 2 and port 3 which are same amplitude and out-of-phase, 180 degrees, magnetic-flux which has same direction in cores is added each other. Inductive reactance which is produced by winding will reject signals to pass.

When arbitrary signals are input from port 2 and port 3, these two signals can be decomposed to common mode signal and differential mode signal. According to the same methods as above, the characteristic of substructure can be analyzed. So the transmission parameters of substructure networks when arbitrary signals pass networks can be got from the transmission parameters of networks when common mode signals pass networks whichever stare networks work in.

Otherwise, in the model of substructure at Fig. 2, the connecting way of port 2 and port 3 can influence the transmission parameters measured. So in each state, only a part of S-parameters of substructure networks can be gained when the S-parameters of networks are measured and transformed in this state.

When signals are input from port 1, the methods of analyzing are same to above.

In terms of the definition of S-parameters of multi-ports,

$$S_{ij} = \left.\frac{b_i}{a_j}\right|_{a_j=0,\quad when\quad i\neq j} \tag{1}$$

S-parameters can be gained through all ports are matched except for port j. But usually the reference impedances of two ports VNA are 50 ohms or 75 ohms and the reference impedances at two ports are uniform. For example, Agilent 4395A VNA has two kinds of reference impedances to select [5], 50 ohms and 75 ohms. So it is also difficult to measure this kind of three ports network which having the function of impedance transforming by definition through impedance match.

Applying knowledge about arbitrary impedance transformations, indefinite admittance matrix and mixed-mode S-parameters of three ports networks [6], this paper presents a method of measuring and analyzing [S] of substructure in multimode feed network at low frequency. As an example, isolating substructure is measured and its [S] is gained by this method. To verify test results, the measuring result of [S] is transformed to mixed-mode [S]. The curves of mixed mode [S] are in good agreement with theoretic results.

4. Measuring of Substructure in Multimode Feed Network

Through above analyze to substructure in multimode feed network, the following measurement method can be applied at low frequency.

Port 3 at Fig. 2 of substructure is grounded, see Fig. 3. Then three-port networks are transformed to two-port networks.

Fig. 3. The two-port substructure.

4.1. Transforming of S-parameters at Different Reference Impedance

It is assumed that ports reference impedance of two ports VNA is Z0 and the calibration can be done in a Z0 ohms environment. The networks will be measured with this VNA.S-parameters matrix will be gained and it is signed as

$$\left[S^{Z_0-Z_0}\right] = \begin{bmatrix} S_{11}^m & S_{12}^m \\ S_{21}^m & S_{22}^m \end{bmatrix} \tag{2}$$

$\left[S^{Z_0-Z_0}\right]$ can be transformed to $\left[R^{Z_0-Z_0}\right]$ according to the relationships of S-parameters matrix and R-parameters matrix of two ports networks. $\left[R^{Z_0-Z_0}\right]$ can be signed as:

$$\left[R^{Z_0-Z_0}\right] = \begin{bmatrix} R_{11}^m & R_{12}^m \\ R_{21}^m & R_{22}^m \end{bmatrix} = \frac{1}{S_{21}^m}\begin{bmatrix} S_{12}^m S_{21}^m - S_{11}^m S_{22}^m & S_{11}^m \\ -S_{22}^m & 1 \end{bmatrix} \tag{3}$$

It is assumed that the matching impedance at port 1 is Z_1 and it is Z_2 at port 2 in the two ports networks[7].The R-parameters matrix of this network can be got from $\left[R^{Z_0-Z_0}\right]$ according to the transforming rules of R-parameters matrix in different reference impedance environment. It is signed as

$$\left[R^{Z_1-Z_2}\right] = \begin{bmatrix} R_{11}^{Z_1-Z_2} & R_{12}^{Z_1-Z_2} \\ R_{21}^{Z_1-Z_2} & R_{22}^{Z_1-Z_2} \end{bmatrix} = Q^{Z_1-Z_0} R^{Z_0-Z_0} Q^{Z_0-Z_2} \tag{4}$$

where

$$Q^{Z_1-Z_0} = \frac{1}{2\left|N_{Z_1-Z_0}\right|^2}\sqrt{\frac{R_e(Z_1)}{R_e(Z_0)}}\begin{bmatrix} 1+N_{Z_1-Z_0}^2 & 1-N_{Z_1-Z_0}^2 \\ 1-N_{Z_1-Z_0}^2 & 1+N_{Z_1-Z_0}^2 \end{bmatrix} \tag{5}$$

$$N_{Z_1-Z_0} = \sqrt{\frac{Z_1}{Z_0}} \tag{6}$$

$$Q^{Z_0-Z2} = \frac{1}{2\left|N_{Z_0-Z_2}\right|^2}\sqrt{\frac{R_e(Z_0)}{R_e(Z_2)}}\begin{bmatrix} 1+N^2_{Z_0-Z_2} & 1-N^2_{Z_0-Z_2} \\ 1-N^2_{Z_0-Z_2} & 1+N^2_{Z_0-Z_2} \end{bmatrix} \tag{7}$$

$$N_{Z_0-Z2} = \sqrt{\frac{Z_0}{Z_2}} \tag{8}$$

$\left[R^{Z_1-Z_2}\right]$ is transformed to $\left[S^{Z_1-Z_2}\right]$ according to the relationships between R-parameters matrix and S-parameters matrix of two ports networks.

$$\left[S^{Z_1-Z_2}\right] = \begin{bmatrix} S^{Z_1-Z_2}_{11} & S^{Z_1-Z_2}_{12} \\ S^{Z_1-Z_2}_{21} & S^{Z_1-Z_2}_{22} \end{bmatrix} = \frac{1}{R^{Z_1-Z_2}_{22}}\begin{bmatrix} R^{Z_1-Z_2}_{12} & R^{Z_1-Z_2}_{11}R^{Z_1-Z_2}_{22} - R^{Z_1-Z_2}_{12}R^{Z_1-Z_2}_{21} \\ 1 & -R^{Z_1-Z_2}_{21} \end{bmatrix} \tag{9}$$

$\left[S^{Z_1-Z_2}\right]$ is the S-parameters matrix of the two ports network when it has the function of impedance transforming from Z_1 to Z_2.

4.2. S-parameters Matrix Transformation From Two-port to Three-port

$\left[S^{Z_1-Z_2}\right]$ at (9) is transformed to Y-parameters matrix according to the relationships between S-parameters matrix and Y-parameters matrix of two ports networks.

$$[Y] = \begin{bmatrix} Y_{11} & Y_{12} \\ Y_{21} & Y_{22} \end{bmatrix} = \left([I]-\left[S^{Z_1-Z_2}\right]\right)\left([I]+\left[S^{Z_1-Z_2}\right]\right)^{-1} \tag{10}$$

where [I] is the identity matrix.

The Y-parameters matrix of three ports network can be gained according to knowledge about indefinite admittance matrix when network is in the state of that port 3 is grounded.

$$\left[Y^{3g}\right] = \begin{bmatrix} Y^{3g}_{11} & Y^{3g}_{12} & Y^{3g}_{13} \\ Y^{3g}_{21} & Y^{3g}_{22} & Y^{3g}_{23} \\ Y^{3g}_{31} & Y^{3g}_{32} & Y^{3g}_{33} \end{bmatrix} = \begin{bmatrix} Y_{11} & Y_{12} & -Y_{11}-Y_{12} \\ Y_{21} & Y_{22} & -Y_{21}-Y_{22} \\ -Y_{11}-Y_{21} & -Y_{12}-Y_{22} & Y_{11}+Y_{21}+Y_{12}+Y_{22} \end{bmatrix} \tag{11}$$

Y-parameters matrix can be got according to the relationships between Y-parameters and S-parameters of three ports networks.

$$\left[S^{3g}\right] = \begin{bmatrix} S^{3g}_{11} & S^{3g}_{12} & S^{3g}_{13} \\ S^{3g}_{21} & S^{3g}_{22} & S^{3g}_{23} \\ S^{3g}_{31} & S^{3g}_{32} & S^{3g}_{33} \end{bmatrix} = \left([I]-\left[Y^{3g}\right]\right)\left([I]+\left[Y^{3g}\right]\right)^{-1} \tag{12}$$

where [I] is the identity matrix.

4.3. Transformation from $[S^{3g}]$ to Common and Differential Mode Transmission Parameters

Mixed-mode S-parameters matrix of three ports network can be gained from $[S^{3g}]$ according to the relationships between mixed-mode S-parameters and single-ended S-parameters matrix. It is

$$S^{M3} = \begin{bmatrix} S^3_{11} & S^3_{1C} & S^3_{1D} \\ S^3_{C1} & S^3_{CC} & S^3_{CD} \\ S^3_{D1} & S^3_{DC} & S^3_{DD} \end{bmatrix} = MS^{3g}M^{-1} \tag{13}$$

where $M = \begin{bmatrix} 1 & 0 & 0 \\ 0 & 1/\sqrt{2} & 1/\sqrt{2} \\ 0 & 1/\sqrt{2} & -1/\sqrt{2} \end{bmatrix}$

4.4 S-parameters of Substructure

It is assumed that S-parameters matrix of substructure is [S].That is

$$S = \begin{bmatrix} S_{11} & S_{12} & S_{13} \\ S_{21} & S_{22} & S_{23} \\ S_{31} & S_{32} & S_{33} \end{bmatrix}$$

According to power relationships, a part of S-parameters can be gained from (13).They are

$$S_{12} = \sqrt{2}S^3_{1C} \quad S_{21} = \sqrt{2}S^3_{C1}$$
$$S_{22} = S^3_{CC} \quad S_{32} = S^3_{DC} \tag{14}$$

Mixed-mode S-parameters matrix of two ports network can be gained according to the same method when port 2 is grounded [8]. It is

$$S^{M2} = \begin{bmatrix} S^2_{11} & S^2_{1C} & S^2_{1D} \\ S^2_{C1} & S^2_{CC} & S^2_{CD} \\ S^2_{D1} & S^2_{DC} & S^2_{DD} \end{bmatrix}$$

A part of S-parameters of substructure can be got by the same method. They are

$$S_{13} = \sqrt{2}S^2_{1C} \quad S_{31} = \sqrt{2}S^2_{C1}$$
$$S_{33} = S^2_{CC} \quad S_{23} = S^2_{DC} \tag{15}$$

To S_{11}, it is can be got from

$$S_{11} = \frac{S_{11}^3 + S_{11}^2}{2} \tag{16}$$

Then S-parameters matrix of substructure is gained.

5. Application, Analysis and Example

Because of the different function, the two substructures have the different ends connected together [9], the different input port and the different output port. In this paper, an isolator is taken as example.

Example: Isolator to be exampled consists of six tunes of coaxial-line (characteristic impedance is 50 ohm) wound on a ferrite core, with outer and inner dimensions of $0.061m$ and $0.025m$ respectively. The core thickness is $0.015m$.

Where: ε_{eff} = the effective dielectric constant of the media inside the coil [10] (ε_{eff} of coaxial-line to be used in this example is 2.1).

S-parameter can be measured with Agilent 4395A, measuring frequency from 0MHz to 80MHz, Ports impedance of isolator are $Z_1 = 200\Omega$, $Z_2 = Z_3 = 400\Omega$. The $\left[Q^{Z_0 - Z_1}\right]$ can be gained from (5) and (7).Then

$$Q^{200-50} = \begin{bmatrix} 5/4 & -3/4 \\ -3/4 & 5/4 \end{bmatrix} Q^{50-400} = \sqrt{2}\begin{bmatrix} 9/8 & 7/8 \\ 7/8 & 9/8 \end{bmatrix}$$

S-parameters matrix can be got by programming. To verify data, isolator is analyzed with mixed-mode S-parameters [11]. It is

$$S^M = \begin{bmatrix} \overline{S_{11}} & \overline{S_{1C}} & \overline{S_{1D}} \\ \overline{S_{C1}} & \overline{S_{CC}} & \overline{S_{CD}} \\ \overline{S_{D1}} & \overline{S_{DC}} & \overline{S_{DD}} \end{bmatrix}$$

In ideal instances, a part of mixed-mode S-parameters of isolator can be got by analyzing and calculating. That is

$$\begin{aligned} &\left|\overline{S_{1D}}\right| = 0 \quad \left|\overline{S_{1C}}\right| = 1 \quad \left|\overline{S_{CD}}\right| = 0 \\ &\left|\overline{S_{D1}}\right| = 0 \quad \left|\overline{S_{C1}}\right| = 1 \quad \left|\overline{S_{DC}}\right| = 0 \end{aligned} \tag{17}$$

S-parameters matrix of isolator measured is transformed to mixed-mode S-parameters according to the following formula: $S^M = MSM^{-1}$

where $M = \begin{bmatrix} 1 & 0 & 0 \\ 0 & 1/\sqrt{2} & 1/\sqrt{2} \\ 0 & 1/\sqrt{2} & -1/\sqrt{2} \end{bmatrix}$.

The corresponding mixed-mode S-parameters are compared with those in (17). The following is the comparative curves.

They are in good agreement at Fig. 4. So this method can be used to measure three-port Scatter Parameters of Substructure in multimode feed network at low frequency.

6. Conclusions

In opinion of substructure cascade, multimode feed network is composed of impedance transforming substructure and isolating substructure. Impedance transformer and isolator can be abstracted as three-port networks having the function of impedance transforming.

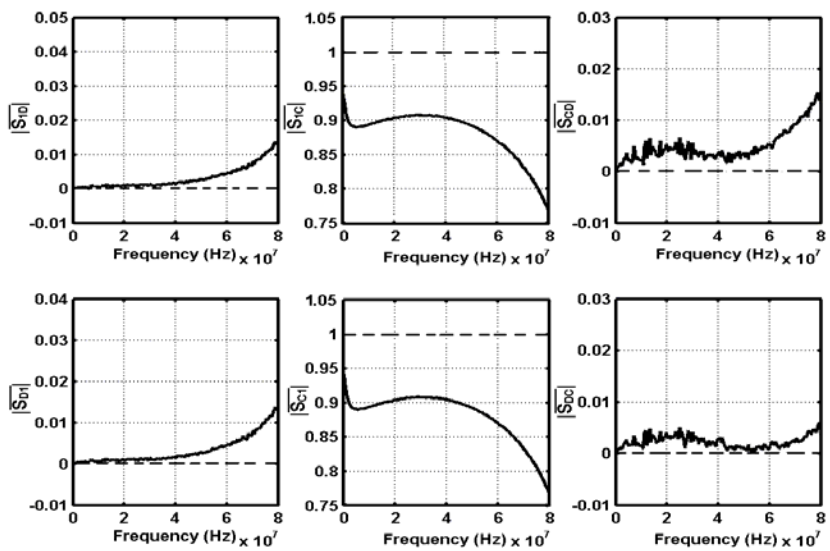

Fig. 4. The comparison of metrical and theoretic result.

This paper presents a method of measuring and analyzing [S] of this kind of three-port networks at low frequency with two ports VNA which has arbitrary reference impedances. the three-port scatter parameters of substructure in multimode feed network are researched, the mixed-mode S-parameters of three-port networks are used to verify the actual measured data. The proposed method also can provide a favorable base for the optimizing design of the entire multimode multi-feed antenna system.

Acknowledgements

This work is supported by National Natural Science Foundation of China (61077037), Key Scientific and Technological Project of Henan Province (102102210033), Science and Technology Research Project of The Education Department of Henan Province (12B510014), National Training Programs of Innovation and Entrepreneurship for Undergraduates, Henan Normal University (201210476075).

References

[1]. Enzo Carpentieri, Model characterizes transmission-line transformers, *Microwaves&RF*, Vol. 35, Issue 11, 1996, pp. 73-80.

[2]. Zhan Huawei, Zhou Yun, Zhang Yu, Property analysis of the usage in NiZn ferrite of broadband transmission-line transformer, *High Power Laser and Particle Beams*, Vol. 22, Issue 2, 2010, pp. 443-446.

[3]. Du Xiaoyan, Lei Xue, Niu Zhongxia, Obtaining of network parameters of impedance converter in multimode feed network, *Journal of Information Engineering University*. Vol. 9, Issue 1, 2008, pp. 54-58.

[4]. Dong Zhang, Ping Li, Visual Odometry in Dynamical Scenes, *Sensors & Transducers*, Vol. 147, Issue 12, December 2012, pp. 78-86.

[5]. Wang Liqiu, Wei Huancai, Zhou Xuesheng, Data analysis in engineering, *Publishing Company of Shan Dong University*, China, 2002.

[6]. Mark Cameron, Ibrahim Al-Bahadly, Visual Odometry in Dynamical Scenes, *Sensors & Transducers*, Vol. 140, Issue 5, May 2012, pp. 65-73.

[7]. Ding Weiping, Li Hongbin, Yu Tongbin, A design of two element microstrip antenna array with broad bandwidth, *Chinese Journal of Ratio Science*, Vol. 26, Issue 5, 2011, pp. 979-982.

[8]. Zhan Huawei, Niu Zhongxia, Du Xiaoyan, The theory research and design of feed network based on measurement database, in *Proceedings of the ISTM Symposium (Conference) on Test and Measurement*, DaLian, China, 01-04 June 2005, pp. 7428-7431.

[9]. Zhang Xiaolei, Research on Improved Minimal Probability Distance and Image Registration, *Journal of Convergence Information Technology*, Vol. 7, Issue 16, 2012, pp. 508 -514.

[10]. Smith P W, Transient electronics, *Wiley*, London, UK, 2002.

[11]. Zhang Jigang, Broadband Ferrite Elements of Radiofrequency, *Science Press*, China, 1986.

Sensors & Transducers, Vol. 21, Special Issue, May 2013, pp. 199-204

Sensors & Transducers

http://www.sensorsportal.com

Numerical Simulation of Gas-Solid Two-Phase Flow for Four-Channels Pulverized Swirling Burner

[1] Defu LI, Maozhao XIE, Chunyan SHEN, [*] Hongchao YIN, Hong LIU

[1, 2] Energy and Power Engineering, Dalian University of Technology, Liaoning, 116024, China

[*] E-mail: hcyin@dlut.edu.cn

Received: 9 April 2013 /Accepted: 14 May 2013 /Published: 30 May 2013

Abstract: This article presents a mathematical model of cold gas-solid two-phase flow which is based on the cement rotary kiln in service. By altering the parameters of air supply system of four- channels pulverized burner, investigations are taken of that motion trajectory and particle distributions in the very turbulent field. The results show that motion trail of most particles in rotary kiln is a combination process of gradual diffusion and slow sedimentation; increasing internal flow velocity would aggravate coal particles to diffuse; external flow velocity should be controlled in a reasonable range. *Copyright © 2013 IFSA.*

Keywords: Two-phase flow, Four- channels pulverized burner, Particle-trajectory model.

1. Introduction

Burner is a key component of combustion systems, by which air flow and fuel are blown to rotary kiln and form a specific flow structure that will contribute to rapid ignition and stable combustion. Hence, to achieve an excellent performance, the design and operation of burner is conclusive to economical efficiency and reliability for rotary kiln [1].

A good burner ensure rotary kiln operating in the most suitable thermotechnical condition for the cement production, which will obtain high grade, high efficient, low cost and long-term production, also meet the environmental requirement [2]. Therefore, the study on burner character is critical to cement industry development [3-6]. This article applies CFD to simulate 3-D four-channels pulverized burner by creating a cold model to simulate flow motion driven by multi-tunnel burner and particle distributions influenced by turbulent field. This is an attempt to provide theoretical basis to hot model combustion research.

2. Two-phase Flow Model Description

It is well known that the numerical model for simulating two-phase flow model can be described in two major methods [7-10]. One is two- fluid model, also named as EULERIAN-EULERIAN model in which particle is regarded as fluid. Particle and gas together are considered as in a coexisting and interpenetrating continuum model. The other is dispersed phase model, also called as EULERIAN-LAGRANGIAN model in which particle is considered discrete and gas is considered as continuum model. The interaction between each particle and ambient gas is calculated as well. In the paper, numerical investigation of particle motion trail is simulated by applying dispersed phase model, and two phases are coupled by interactive force, where particle phase is calculated in LAGRANGIAN coordinate, while continuous gas phase is calculated in EULERIAN coordinate.

Regardless of the pulsation from gas density and phase transition, and resistance, gas phase

conservation equation can be written in a general form as [11]:

$$\frac{\partial}{\partial t}(\rho\phi)+\frac{\partial}{\partial x_j}(\rho v_j\phi)=\frac{\partial}{\partial x_j}(\Gamma_\phi\frac{\partial\phi}{\partial x_j})+S_\phi+S_{\rho\phi} \quad (1)$$

where S_ϕ is the origin of gas phase; $S_{\rho\phi}$ is the origin of the interaction between gas phase and particle phase; ϕ, Γ_ϕ, S_ϕ and $S_{\rho\phi}$ are the usual source term, which are listed in [12].

3. Physical Model and Numerical Method

3.1. Physical Model

According to the reference [13], numerical investigations on coal particle was burned in cement rotary kiln, four-channel swirling burner was numerically built up to analyze ambient aerodynamic field character and unburned coal particle distributions in that field. The inner diameter of the investigated rotary kiln was 3.5 m, and the length was 20 m. As shown in Fig. 1, primary air is blown from the four tunnels of burner, while secondary air is blown from outer space in rotary kiln.

Grid is integrated with few partitioned regions; denser mesh is placed locally where needs extra care. The calculated domain is divided into two regions, for the near hood region, structural tetrahedral mesh is used; as for the rest region; structural non-uniform hexahedral mesh is used.

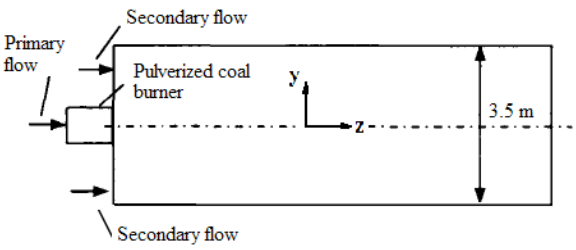

Fig. 1. Computational domain.

3.2. Numerical Method and Boundary Conditions

In the paper, particle-trajectory is taken to resolve two-phase flow, and *k-ε* turbulent model is used. Considering the field of gravity, trajectory of particle motion and particle distributions in the turbulent field which driven by four-channels swirling burner is intently focused to provide a theoretical basis on combustion research in the industrial rotary kiln.

Both primary and secondary airs are set as velocity -inlet and pressure-outlet. 5 sets of operating condition are indicated in Table 1, comparison with condition 1 by varying pulverized coal particle diameters, swirling angle, inner and external flow blowing speed, etc., respectively.

Table 1. Initial velocity of the air duct inlets under different working conditions.

Conditions	Primary airflow				V_{ecf}
	V_{zxf}	V_{mf}	V_{nf}	V_{wf}	
Units	m/s	m/s	m/s	m/s	m/s
1	116	25.25	71.575	310.18	13.085
2	116	25.25	60	310.18	13.085
3	116	25.25	85	310.18	13.085
4	116	25.25	71.575	260	13.085
5	116	25.25	71.575	360	13.085

4. Characteristics of Motion Trail and Distributions of Coal Particles

4.1. Two-phase Turbulence Features

Fig. 2 indicates that, from burner tunnel, swirling flow is spread into the space at a proper angle. During this process, the primary air decreases to 0 gradually, and then even reaches to negative (minimum at -22.2 m/s). Meanwhile, asymmetric heart-shape central backflow is formed and bringing more coal particles into central backflow field under the force of gravity. It extends residence time of particles in the backflow, which could promote particles mixed and enhance combustion efficiency.

Mass distributions on the longitudinal section and cross section are shown in Fig. 3. It can be found that, the barycenter of coal particles move slowly toward negative direction of y axis and, observed from cross section, the region occupied by coal particles gradually expends. This indicates that, particles diffuse gradually and settled down slowly.

Fig. 4 shows the distributions of coal particle when they are just spread into the kiln by annular tunnel. In this figuration, it is clearly observed that, the shape of particle distributions is like asymmetric 'pommel horse' at z = 0.5 m. The reason for asymmetric is that particles are blown in through 10 tunnels, then distributed in random trajectory. Therefore, central backflow region is shaped into an asymmetric domain from observation of transverse section. In addition, the region occupied by denser particles is surely with less air flow. That provides an explanation for the vector distribution character in the centre of kiln in Fig. 2 At z = 2 m, particle distributed shape, from unimodal, becomes to bimodal, because particle start to concentrate into beam under the motion of central backflow. And, at z = 6 m, particles are about to diffuse and mostly distributed under y axis due to gravity begins to play a dominant role.

Fig. 5 is observed in different axis. At z = 2~6 m, coal mass are mainly centralized on and around central axis (y=0) indicating coal particles are mainly distributed in the central region of kiln; while, the mass located at y = -0.1 m is larger than at y = 0.1 m,

and at z = 7 m, coal mass is almost as the same as at y = 0. Because, particles settle down acted by gravity. At y = -2 m and y = -5 m, mass located is gradually reducing, meanwhile, at y = -5 m, particles begin to distribute locally after z = 3 m. This illustrates that, after spread into kiln, particles are blown straightly in the first 3 m, after that, they begin to diffuse into the space between y = ±5 m (cross section).

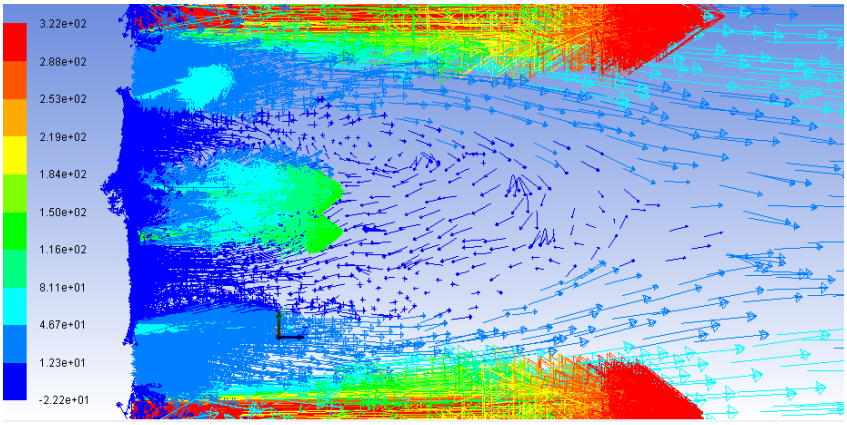

Fig. 2. Velocity vectors in the vertical section.

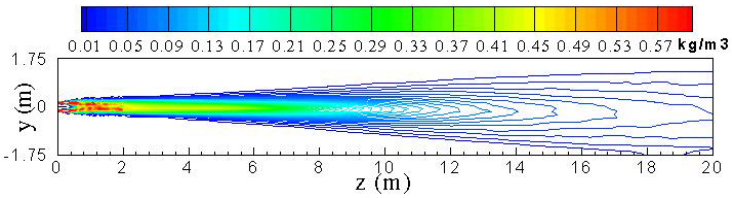

(a)

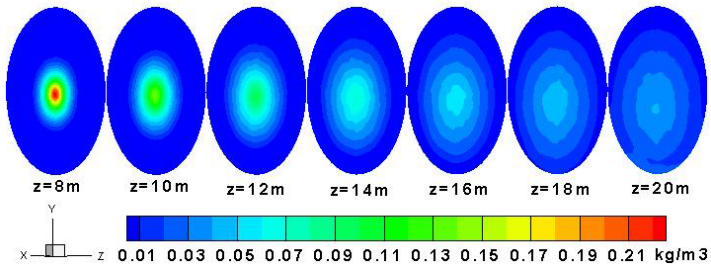

(b)

Fig. 3. Particle distributions in (a) longitudinal section and (b) cross section of kiln.

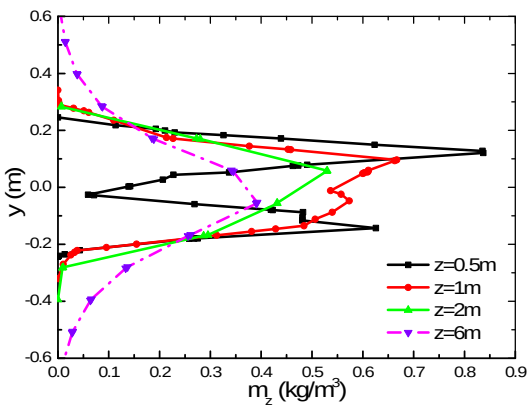

Fig. 4. Coal particle distributions near nozzle.

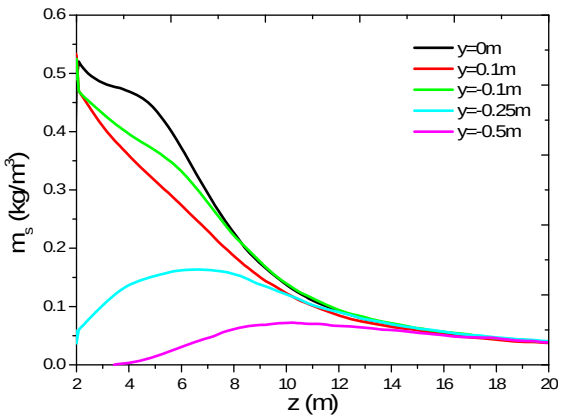

Fig. 5. Coal particle distributions in different axis

4.2. The Influence of Particle Size on Coal Distributions

A comparison is made to research the relationship between particle size and distributions on the operating condition 1, in which 3 sets particle of different diameters (60, 86.4, 120 μm) are chosen. Fig. 6 shows the mass distribution along the central axis of rotary kiln. This curve also indicates the extent of particle diffusion. It is obvious that, after blown from the flow inlet, particles gather at by the suction of central backflow at z = 2 m where reach to the highest mass. Then, diffusion occurs, at z = 12 m, diffusion retards, finally spread to the whole space.

In addition, from the comparison mentioned above, it is found that, in the range z = 2 m ~ 6 m, the smaller of particle size, the larger mass, hence, the slope of curve increases. It seems that smaller particles diffuse easily than larger ones. When turbulent intensity grows, diffusion aggravates too; with smaller size, particles more likely go by airflow.

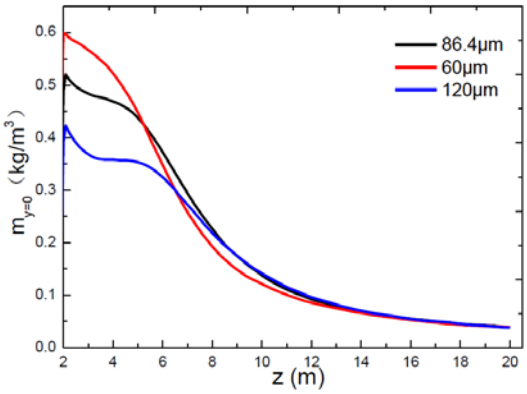

Fig. 6. Particle distributions along central axis.

4.3. The Influence of Internal Flow on Coal Distributions

The following is the research focused on the effect of internal flow velocity. A comparison has been done by employing three internal flow velocities which are 71.575 m/s, 60 m/s and 85 m/s respectively. Fig. 7 shows that the tangential velocity definitely increase with larger internal flow velocity. In Fig. 8, from the coal particle distribution curves in the three conditions, the comparison is obvious. It validates the strong effect on particle motion brought by internal flow velocity, in other word, it can be considered as larger tangential velocity acts obviously. Through the comparison, it is known that, smaller internal velocity leads to smaller tangential velocity, but larger coal particle mass and more concentrated particles. This helps to form long and slender shaped flame.

In above, internal flow velocity should be controlled in proper range. When it cooperates with central flow and external flow in the appropriate behavior, well shaped flame and high combustion intensity are easily obtained.

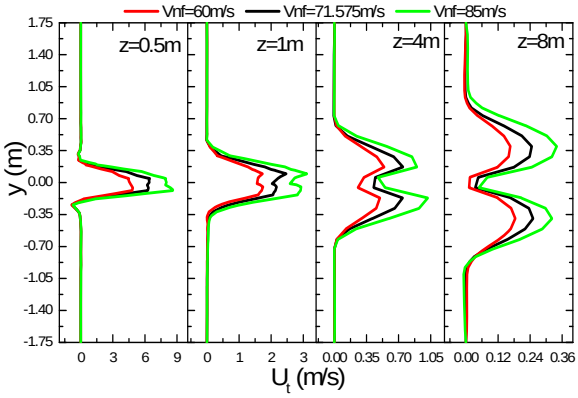

Fig. 7. Tangential velocity distributions along radial direction.

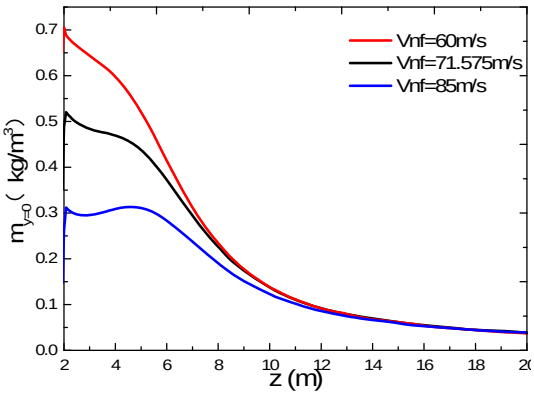

Fig. 8. Particle distributions along central axis.

4.4. The Influence of External Flow on Coal Distributions

High velocity external flow plays an important part in turbulent flow, which is adjacent to both secondary airflow and internal swirling flow, and critical to form central backflow and outer backflow. In Fig. 9, radial velocity is enhanced with the growth of external flow velocity. As external flow velocity is reaching 360 m/s, radial velocity tends to be more symmetrically distributed, leading to particles well-distributed and stable combustion.

With the alternating external flow, particle movements change accordingly. In Fig. 10, it validates the effect on particle motion brought by external flow velocity. Through the comparison, it is known that, larger external velocity leads to more stable distribution of radial velocity, coal particles tend to gathering rapidly. So, the coal has the largest mass at the 360 m/s external velocity. However, in the case, coal particles diffuse fast, till occupy full space of the rotary kiln.

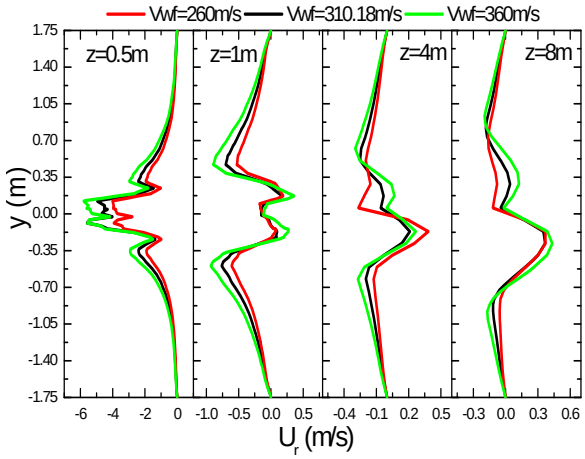

Fig. 9. Radial velocity distributions.

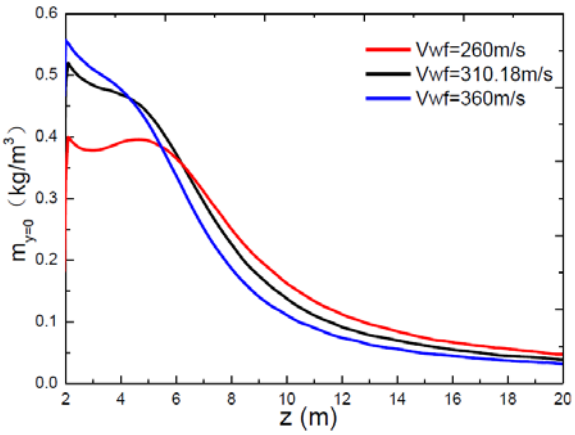

Fig. 10. Particle distributions along central axis.

In above, external flow velocity should be controlled in proper range. When it cooperates with central flow and internal flow in the appropriate behavior, well shaped flame and high combustion intensity are easily obtained.

5. Conclusion

The paper builds up a numerical model of cold solid-gas two-phase flow based on the kiln and four-channel burner. The results are shown below:

(1) The smaller pulverized coal particle size is, the less affected by gravity, the more affected by turbulence flow, more evenly distributed in kiln.

(2) With increasing velocity of internal flow, the degree of disturbance and diffusion raises, while tangential velocity boosts as internal flow velocity increases, which will be adverse to achieve long-slender shaped flame and converge particles.

(3) Improvement on external flow velocity leads to activate particles to converge into a bundle faster. However, out of central backflow region, particles are easily to blown away and diffusion aggravates.

Nomenclature

m_s	coal particle mass located at certain axis, kg/m^3
m_y	coal particle mass located on radial direction, kg/m^3
$m_{y=0}$	coal particle mass located at y=0 (central axis) , kg/m^3
U_r	radial velocity, m/s
U_s	longitudinal velocity, m/s
U_t	tangential velocity, m/s
V_{mf}	coal spread airflow velocity, m/s
V_{nf}	internal swirling flow velocity, m/s
V_{wf}	external flow velocity, m/s
V_{zxf}	central flow velocity, m/s
V_{ecf}	secondary airflow, m/s

References

[1]. Andrzej Smolarz, Andrzej Kotyra, Waldemar Wojcik, Javier Ballester, Advanced diagnostics of industrial pulverized coal burner using optical methods and artificial intelligence, *Experimental Thermal and Fluid Science*, Vol. 43, 2012, pp. 82-89.

[2]. E. Mastorakos, A. Massias, C. D. Tsakiroglou, D. A. Goussis, V. N. Burganos, A. C. Payatakes, CFD predictions for cement kilns including flame modeling, heat transfer and clinker chemistry, *Applied Mathematical Modeling*, Vol. 23, 1999, pp. 55-76.

[3]. Kaustubh S. Mujumdar, Vivek V. Ranade, CFD modeling of rotary cement kilns, *Asia-Pacific Journal of Chemical Engineering*, Vol. 3, 2008, pp. 106-118.

[4]. Jianping Jing, Zhengqi Li, Qunyi Zhu, Zhichao Chen, Lin Wang, Lizhe Chen, Influence of the outer secondary air vane angle on the gas/particle flow characteristics near the double swirl flow burner region, *Energy*, Vol. 36, 2011, pp. 258-267.

[5]. Cristian H. Birzer, Peter A. M. Kalt, Graham J. Nathan, The influences of particle mass loading on mean and instaneous particle distributions in processing jet flows, *International Journal of Multiphase Flow*, Vol. 41, 2012, pp. 13-22.

[6]. Hao Zhou, Guiyuan Mo, Jiapei Zhao, Kefa Cen, DEM-CFD simulation of the particle dispersion in a two-phase flow for a fuel-rich/lean burner, *Fuel*, Vol. 90, 2011, pp. 1584-1590.

[7]. M. S. Manju, S. Sacithri, Three dimensional CFD simulation of pheumatic coal injection in a direct reduction rotary kiln, *Fuel*, Vol. 102, 2012, pp. 54-64.

[8]. A. Bermudez, J. L. Ferrin, A. Linan, L. Saavedra, Numerical simulation of group combustion of pulverized coal. *Combustion and Flame*, Vol. 158, 2011, pp. 1852-1865.

[9]. Federico Cangialosi, Francesco Di Canio, Gianluca Intini, Michele Notarnicola, Lorenzo Liberti, Giulio Belz, Pompilio Caramuscio, Experimental and theoretical investigation on unburned coal char burnout in a pilot-scale rotary kiln, *Fuel*, Vol. 85, 2006, pp. 2294-2300.

[10]. G. J. Nathan, J. Mi, Z. T. Alwahabi, G. J. R. Newbold, D. S. Nobes, Impacts of a jet's exit flow pattern on mixing and combustion performance, *Progress in Energy and Combustion Science*, Vol. 32, 2006, pp. 496-538.

[11]. T. P. Bhad, S. Sarkar, A. Kaushik, S. V. Herwadkar, Kiln with multi-channel burner for optimization of

flame profile, in *Proceedings of the 7th International Conference on CFD in the Minerals and Process Industries*, CSIRO, Melbourne, Australia, 2009, pp. 9-11.

[12]. Zhou Jiemin, Zhu Zaixin, Ma Aichun, Numerical simulation research on coal combustion in rotary kiln with multi-air channel coal burner, in *Proceedings of the International Conference on Intelligent Systems Design and Engineering Application*, 2012, pp. 1070-1073.

[13]. Ma Aichun, Zhou Jiemin, Li Wang Xing, CFD prediction of cold airflow field for multi-air channel pulverized coal burner in rotary kiln, in *Proceedings of the 37th Intersociety Energy Conversion Engineering Conference*, 2002, pp. 418-421.

Sensors & Transducers, Vol. 21, Special Issue, May 2013, pp. 205-210

Sensors & Transducers

http://www.sensorsportal.com

Improved Optical Flow Algorithm for an Intelligent Traffic Tracking System

[1] Xia Yupeng, [2] Hu Feng

[1] School of Mechanical and Electrical Engineering, Shenzhen Polytechnic,
Xili Lake, Shenzhen, Guangdong, 518055, China
[2] Shenzhen Graduate School, Harbin Institution and Technology,
Xili Lake, Shenzhen, Guangdong 518055, China
[1] E-mail: xiayupeng2013@163.com

Received: 9 April 2013 /Accepted: 14 May 2013 /Published: 30 May 2013

Abstract: It is known that to get the contours and segmentations of moving cars is the essential step of image processing in intelligent traffic tracking systems. As an effective way, the optical flow algorithm is widely used for this kind of applications. But in traditional gradient-based approaches, in order to make the data responding to the edges of moving objects expand to the area, which gray level is flat, it needs to keep the iteration times large enough. It takes a large amount of calculation time, and the accuracy of the result is not as good as expected. In order to improve the numerical reliability of image gradient data, Hessian matrix distinguishing, Gaussian filtering standard deviation amending, mean model amending and multi-image comparing, the four algorithms were investigated by applying them to track moving objects. From the experimental results, it is shown that both the calculation convergence speed and accuracy of our methods have greatly improved comparing with traditional algorithms, the feasibility and validity of those methods were confirmed.

Keywords: Computer vision, Image processing, Optical flow, Image grads, Hessian matrix, Gaussian filtering, Mean model.

1. Introduction

Since the conception, optical flow, was first raised, there are a lot of successful applications of it. We call that apparent motion caused by image brightness patterns, Optical Flow Field, who reflects velocity vectors distribution, which three-dimensional objects project to two-dimensional image plane. Then, optical flow field provides us with a lot of very useful information about velocity and three-dimensional motion structure of moving objects and spatial arrangements of the environment. Up to now, optical flow calculation methods are gradient method, regional method, energy method and phase method. In 1981, Horn and his partners [1] brought forward optical flow constraint equation based on gradient. Since then, various advanced ideas and improved versions have emerged. Nagel [2] used weighted matrix to control gradient data for different smooth handling result, and it improved Horn's global smoothness approach. Lucas and Kanade [3] proposed that optical flow is local smoothness. Their method provides an accurate solution for motion estimation, but it requires large searching window to handle large motions. Juan L et al. [4] take 3D Sobel operator instead of normal Sobel operator, which is in common use for computing image gradient. This method improved result accuracy, but increased large calculation. Thus, maybe it is useful in static scene. Shi Rong [5] proposed a method to eliminate errors

caused by high-speed motion analysis. Clearly, it is necessary to repair results, when moving object's velocity is too high.

In this paper, the research on the accuracy and reliability of the gradient data during calculation of the optical flow was preformed, based on Horn's global smoothness method primarily. First, the principle of optical flow and its iterative formula were investigated. Then, the reasons of low accuracy and large calculation burden for the calculation results due to the optical flow algorithm were analyzed. Aiming at current existing shortcomings and problems about the gradient method, some approaches were performed to optimize the image gradient data, when calculating optical flow field. Finally, applying these methods to moving vehicles automatically tracking system, the validity of those methods was confirmed.

2. Horn-Schunck Constraints

Suppose that intensity of a point $p(x, y)$ on an image is $f(x, y, t)$ at time t, and when it arrives at a new position, its intensity turns to $f(x+\Delta x, y+\Delta y, t+\Delta t)$ at time $t+\Delta t$. Without regards to light changing, if $\Delta t \to 0$, we get

$$f(x, y, t) = f(x+\Delta x, y+\Delta y, t+\Delta t) \tag{1}$$

Easily, a dynamic image can be represented as a function of position and time permits it to be expressed as a Taylor series. Ignoring high-order terms, it is easily to get

$$\nabla f \bullet (u, v, 1) = 0 \tag{2}$$

where $u=dx/dt$, $v=dy/dt$. The u and v are horizontal and vertical optical flow vectors, and $\nabla f=(\partial f/\partial x, \partial f/\partial y, \partial f/\partial t)$ is gradient vector along x, y and t. Obviously, it is impossible to determinate optical flow field depending on Eq. (2) only, due to the lack of another constraint. Horn and others' optical flow constraint is based on hypothesis, which is intensity unchangeable and global smoothness. Thus, optical flow must meet the following requirements

$$\min\{E = \iint [u_x^2 + u_y^2 + v_x^2 + v_y^2 + \lambda(f_x u + f_y v + f_t)^2] dxdy\} \tag{3}$$

where λ is weighted coefficient, which reflects that how calculation depend on the quality of image data, and can be decided by image noise. Associating Eq. (2) with (3), analyzing Euler equation and dispersing them, we can get

$$u^{n+1} = \overline{u}^n - \frac{f_x \overline{u}^n + f_y \overline{v}^n + f_t}{\lambda + f_x^2 + f_y^2} f_x, \tag{4}$$

where $\overline{u}$, $\overline{v}$ denote average value of neighborhood, which is decided by the case of application. n denotes iteration times, which is decided by required accuracy. When circulation cannot terminate, it must be set a maximal iterative time.

Usually, the flow chart of optical flow calculation is shown by Fig. 1. There are mostly 3 blocks in the chart, which is image preprocessing, parameters initialization and iterative calculation. In this paper, we amend image gradient data before and during iterative calculation, for the sake of computing optical flow as accurate as possible. For requirement of image segmentation, the iterative results were described by a 256 gray-level bitmap.

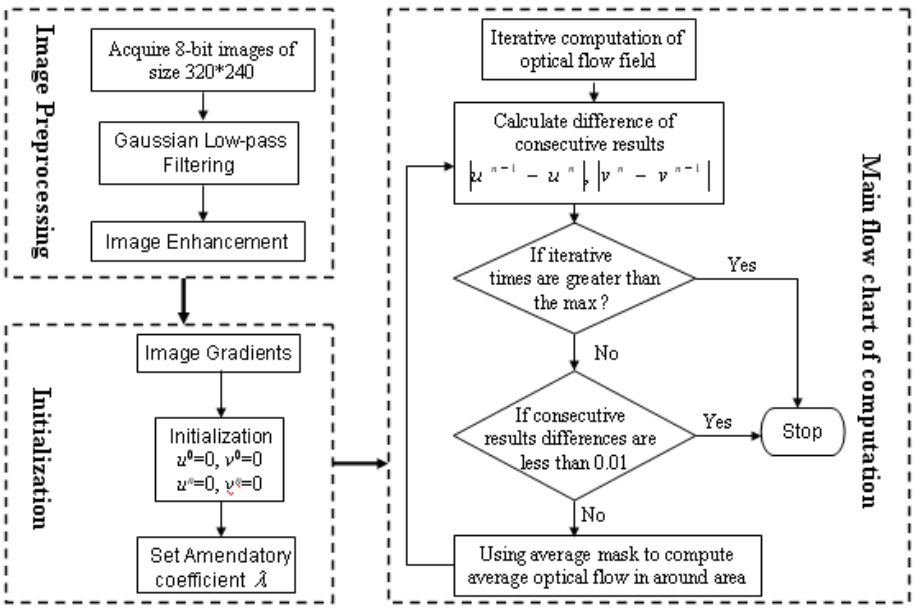

Fig. 1. The flow chart of calculation of optical flow.

The gradient is almost few in the flat area of moving object's gray on image plane. Those can be estimated by computing average value of its bonder data. But this needs a large number of iterative times to keep bonder motion data penetrate to a whole object area. From Eq. (4), we can see that image gradient accuracy and reliability will affect the final accuracy and convergence speed during progress of iterative computation. Hence, we supervise and repair image gradient matrix before and during iterative process, for the sake of getting more accurate optical flow field. In order to illuminate importance of image gradient data, we also compute non-enhancement image, including filtering and sharpening.

2. Methods of Improving Image Gradient Numerical Reliability

3.1. Hessian Matrix

In Yang Chunle's [6] method, they used Hessian matrix to filter image gradient data before calculating optical flow field by using weighted windows local smooth method. Then, they applied Least-squares method for computing optical flow. In this paper, we attempt to use this method in our system for optimizing image gradient data. According to smoothness hypothesis, we can easily obtain the following equation from Eq. (2).

$$\begin{aligned} f_{xx}u + f_{yx}v + f_{tx} &= 0, \\ f_{xy}u + f_{yy}v + f_{ty} &= 0 \end{aligned} \tag{5}$$

And it also can be shown as following

$$\begin{Bmatrix} f_{xx} & f_{yx} \\ f_{xy} & f_{yy} \end{Bmatrix} \begin{pmatrix} u \\ v \end{pmatrix} = -\begin{pmatrix} f_{tx} \\ f_{ty} \end{pmatrix}, \tag{6}$$

Denote $H = \begin{Bmatrix} f_{xx} & f_{yx} \\ f_{xy} & f_{yy} \end{Bmatrix}$, where $\boldsymbol{H}$ is a Hessian matrix of function $f(x, y, t)$. Then, we can eliminate unreliable gradient constraint before optical flow iterative calculation in flow chart 1. The method mainly solves the problem lies in conventional optical flow methods where inaccurate optical flow estimation would always be resulted when unreliable or unreliable gradient constraints exist. From the experimental result, we can see that iterative time is almost cut off 50 %.

3.2. Standard Deviation of Gaussian Curve

There are a lot of noises in images, which is acquired from digital camera by image acquisition. Gaussian filter operator is an effective means to wipe off noises when image processes. Images data are more numerical reliability by filtering. The form of these filters in two dimensions is given by

$$G(x, y, \sigma) = \frac{1}{2\pi\sigma^2} \exp\{-\frac{1}{2}(\frac{x^2 + y^2}{\sigma^2})\} \tag{7}$$

where σ is the standard deviation of Gaussian curve. When σ approaches infinity, G tends towards a constant function. Usually, σ=1. Bartolini and Pica [7] decided it according to the calculation results of optical flow field as

$$\sigma^2 = \sum_{i=1}^{n} f_i^2 / n - \left(\sum_{i=1}^{n} f_i \right)^2 / n^2, \tag{8}$$

In our methods, we calculate optical flow by comparing frame k with frame k-1 and k-2. Because σ is larger, and motion data of moving object border diffuse more enough in images, we hold optical flow results which σ are larger. Flag the method algorithm ***B***.

3.3. Optical Flow Constraint and Smoothness Constraint

It requires optical flow itself as smooth as possible in Horn's smoothness constraint. In Eq. (2), we have ignored high-order Infinitesimal of Taylor expansion. Then, we can define a judgment rule for reliability as following

$$r = \lambda \left| f_x u + f_y v + f_t \right| + u_x^2 + u_y^2 + v_x^2 + v_y^2 \tag{9}$$

where λ is the same as Eq. (3), and u_x, u_y, v_x, v_y are partial differential along x and y of the last time optical flow. As regards this method, in order to obtain more accurate optical flow field, it is possible to validate contentment tolerance of optical flow over again. Acquire 3 consecutive frame images k-2, k-1, k, and separately associate frame k with frame k-1, and k-2 to calculate optical flow. For each pixel of frame k, we calculate optical flow two times on every iterative processing. If ($r_1 \leq r_2$), we set $(u, v)=(u_1, v_1)$, or else $(u, v)=(u_2, v_2)$. This approach is similar to algorithm ***B***. Differently, This approach selects and set the best result into formula during every iterative process. For low-speed moving object and ambiguous border image, relative displace position of moving object is less on image plane. It is possible to get good result by using it. Flag it algorithm ***C***.

3.4. Weighted Coefficient

It is obvious that optical flow on edges cannot be decided when objects move along edges, and because gradient changes faster on image corner, there are large errors [8]. When calculating average optical

flow in neighborhood area for each pixel, the following usual mask is used.

$$\begin{aligned} \bar{u}^n &= (u_{i,j-1}^{n-1} + u_{i,j+1}^{n-1} + u_{i-1,j}^{n-1} + u_{i+1,j}^{n-1})/4, \\ \bar{v}^n &= (v_{i,j-1}^{n-1} + v_{i,j+1}^{n-1} + v_{i-1,j}^{n-1} + v_{i+1,j}^{n-1})/4 \end{aligned} \quad (10)$$

Besides, Horn mask is another one in common use. In fact, Image gradient data should be paid more attention to, when calculating corner and edge of images.

Here, we use an advance approach to acquire average value of neighborhood for each pixel, which is focused on edge feature when calculating. On the edge of moving object, we limit that image gradient data should not penetrate from moving object area to background. Thus, we set exponential function e^x as weighted coefficient for each pixel. Of course, in accordance with the actual speed of moving objects and images gradient, we can also choose other functions based of other numbers.

$$\begin{aligned} \bar{u}^n &= \frac{(e^{-d_{i,j-1}} u_{i,j-1}^{n-1} + e^{-d_{i,j+1}} u_{i,j+1}^{n-1} + e^{-d_{i-1,j}} u_{i-1,j}^{n-1} + e^{-d_{i+1,j}} u_{i+1,j}^{n-1})}{4(e^{-d_{i,j-1}} + e^{-d_{i,j+1}} + e^{-d_{i-1,j}} + e^{-d_{i+1,j}})}, \\ \bar{v}^n &= \frac{(e^{-d_{i,j-1}} v_{i,j-1}^{n-1} + e^{-d_{i,j+1}} v_{i,j+1}^{n-1} + e^{-d_{i-1,j}} v_{i-1,j}^{n-1} + e^{-d_{i+1,j}} v_{i+1,j}^{n-1})}{4(e^{-d_{i,j-1}} + e^{-d_{i,j+1}} + e^{-d_{i-1,j}} + e^{-d_{i+1,j}})} \end{aligned} \quad (11)$$

where $d_{(\cdot,\cdot)}$ is gray-level difference absolute value along x and y of each pixel. Table 1 shows the typical average value template which is obtained by Eq. (11). We take the one above instead of average mask for optical flow of each pixel, to effectively prevent the indiscriminate spread of gradient data. Flag it algorithm *D*.

Table 1. Typical average value template.

0	1/4	0
1/4	1	1/4
0	1/4	0

4. Experimental Result and Discussion

In order to make sure that above approaches are effective, we use several series images of cars about traffic scene to estimate motion parameter and to test system's performance. On our system, we acquire series motion images from a camera, and use above approaches to compute optical flow field for distilling moving objects' contour, and, then, control step-motors to track moving objects on real-time. The image sizes are all 320×240. Images must be preprocessed, such as Gaussian low-pass filtering and Laplace sharpening, before being calculated.

If the calculation error is two times continuous less than 0.01 during iteration, then the results are judged as converge, and calculation would be stopped. The final result is shown with a 256 bitmap. Usually, there are two criterions for estimating computation error of optical flow, which is angle error average value and magnitude error average value, whose definition is as following

$$\begin{aligned} f &= \|\vec{u} - \tilde{\vec{u}}\| \\ \theta &= \arccos\left(\frac{<\vec{u}, \tilde{\vec{u}}>}{\|\vec{u}\| \bullet \|\tilde{\vec{u}}\|}\right) \end{aligned}, \quad (12)$$

where $\vec{u} = (u, v)$ is real velocity of moving object in image, and $\tilde{\vec{u}} = (\tilde{u}, \tilde{v})$ is optical flow velocity vector. But, in fact, because it is difficult to count the real velocity of vehicles in traffic scene, we used PNSR and iterative times and converge time to evaluate above algorithm. The PSNR is given by

$$\sum_{x=0,y=0}^{w,h} (f_1(x,y) - f_2(x + u(x,y), y + v(x,y))^2 / (wh))], \quad (13)$$

where w, h are image's width and height.

In Table 2, the data of the column "non-preprocess image" are results calculated according to Horn method from source images without enhancing.

Table 2. Calculation results.

	PSNR/dB	Iteration times	Converge time
Non-preprocessing	4.48	171	5.65
Horn	24.09	68	2.47
A	26.83	48	1.66
B	25.04	31	2.03
C	24.62	22	1.9
D	24.74	6	1.34

From iterative times and convergence hours in table, we can see that enhancement is very necessary for optical flow calculation. But, the item "PNSR" is meaningless, because the final optical flow results were standardized and shown in a 256 bitmap. Algorithm ***A*** can advance accuracy and computation time, and not only improve PNSR, but also reduce the iteration times and converge time. Algorithm *D* can improve PNRS a little, and reduces both iteration times and convergence time. Algorithm *B* and *C* are similar, the calculation results of them are also almost the same, but the judgment of them are different. Therefore, their results are close. Because it filters reliable image gradient data before circulating in algorithm ***A***, diffusing velocity of moving object's border data advanced. Of course, convergence speed improved. But, we found that filtering threshold is not easy to choose in experiment. If it is not appropriate, on the contrary, real objects will lose. In future, we will do research on it furthermore, and look for a better approach. It needs a few iterative times, but iterative period is long. This method limits

moving object border data to disperse to background, and avoid shortcomings about which traditional method average blindfold. It got good results. According to comparing two iterative results of σ, we choose the better after computing optical flow every time using algorithm *B*. In fact, it is possible to limit error when repeatedly computing, and to improve result accuracy. Based on Horn optical flow smoothness constraint hypothesis, algorithm *D* amends image gradient data, and choose one whose error is less. So, optical flow field improved. Obviously, this method loses meaning when acquisition hours are too large.

The source image is shown in Fig. 2, and there are two moving cars in the photograph.

The non-enhanced image's result is shown in Fig. 3(f), the car on the right-up corner in the source image almost disappeared. Compared to Horn method, image data diffuse more averagely. On Fig. 3(b), we can see that some more brighter white points are averagely around with some less brighter points, which means that image data diffuse enough locally. It reflects that data diffuse directly in Fig. 3(e). In motion region, white points distribute uniformly along moving direction. Principles of algorithm in Fig. 3(c) and Fig. 3(d) are similar. Comparing to Horn's method, image data diffuse more enough globally.

Fig. 2. Source image of a moving car.

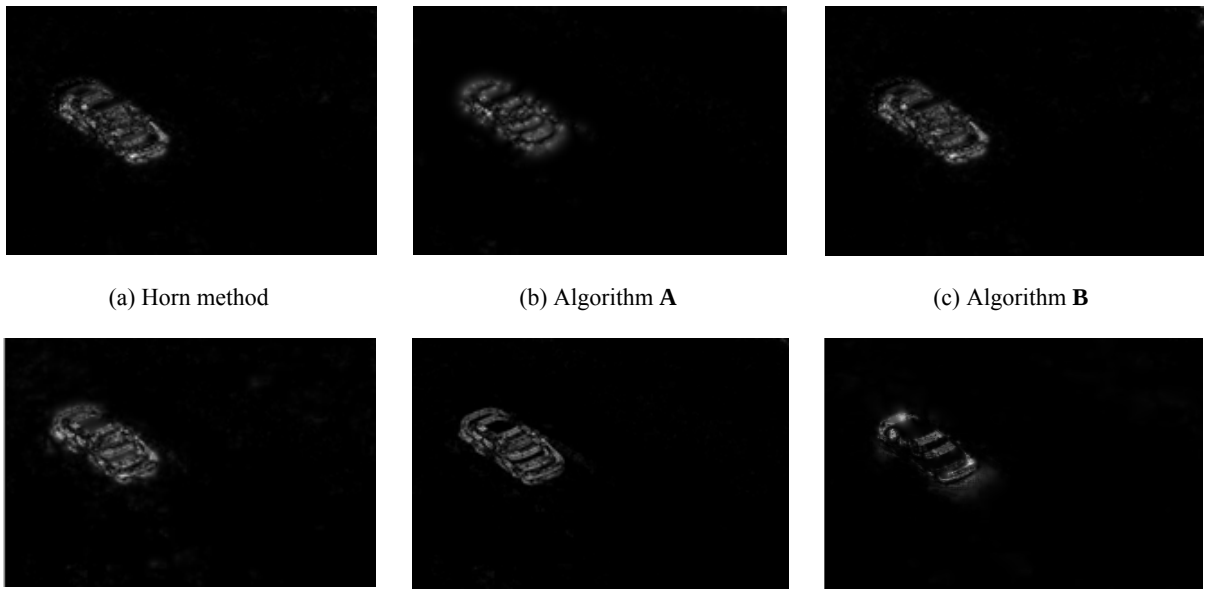

(a) Horn method (b) Algorithm **A** (c) Algorithm **B**

(d) Algorithm **C** (e) Algorithm **D** (f) The final image whose source

Fig. 3. Image processing results for different algorithm.

5. Conclusions

In this paper, we emphasize weightiness of image gradient data for optical flow field calculation based on gradient method through analyzing Horn method, and raise several approaches to improving image gradient data. From the experiment results, these approaches all improved optical flow field accuracy and computing speed with different degree, and they show validity of approaches. But, these approaches to improving optical flow calculating speed and accuracy just all confine to methods based on gradient. In fact, on one hand, Horn's global smoothness constraint has localization; on the other hand, more accurate calculation methods lay hope on new methods and advanced thought, for example, never dynamics method [9], and so on. For the future, we will try other approaches, for the sake of calculating much faster and more accurately.

References

[1]. B. K. P. Horn and B. G. Schunck, Determing optical flow, *Artificial Intelligence*, 17, 1981, pp. 185-203.

[2]. H. H. Nagel, W. Enkelmann, An Investigation of Smoothness Constraints for the Estimation of

Displacement Vector Field from Image Sequences, *IEEE Trans. Pattern Analyze and Machine Intelligence,* 1986, 8, pp. 565-593.

[3]. Lucas B., Kanade T, An interactive image registration technique with an application to stereo vision, in *Proceedings of the 7th International Joint Conference on Artificial Intelligence*, 1981, 2, pp. 121-130.

[4]. J. Uan L., Mattthew M., Naveed S., Performance of passive ranging form image flow, *IEEE, ICIP,* 9, 2003, pp. 929 -932.

[5]. Shi Rong, and Li Zaiming, The Optical Flow Estimation with Displacement Compensation for High-speed, *IEEE, 2002*, pp. 595-599.

[6]. Yang Chunle and Shunichiro Oe, A New Gradient-based Optical Flow Method and Its Application to Motion Segmentation, *IEEE,* 2000, pp. 1225-1230.

[7]. F. Bartolini and A. Pica, Enhancement of Horn and Schunck optical flow algorithm by means of median filters, in *Proceedings of the 13th International Conference on Digital Signal Processing*, Vol. 2, 1997, pp. 503-506.

[8]. Chen Xilin, Computer Vision-Algorithm and system theory, *Tsinghua Press,* Beijing, *Guangxi Science Press,* Guilin, 1999, pp. 81-92.

[9]. Liu Guofeng, Zhu Changling, Optical flow calculation technique, *Southwest Jiaotong University Transaction,* 32, 6, 1997, pp. 656-662.

Sensors & Transducers, Vol. 21, Special Issue, May 2013, pp. 211-217

Sensors & Transducers

http://www.sensorsportal.com

Research on Soft Sensing Modeling Method Based on the Algorithm of Adaptive Affinity Propagation Clustering and Bayesian Theory

[1,2] LIU Ranran, [1*] LI Zhengming, [1] PAN Tianhong

[1] School of Electrical and Information Engineering, Jiangsu University, Zhenjiang 212013, China
[2] Changzhou Liu Guojun Vocational Technology College, Changzhou 213004, China
[1] Tel.: 0511-88790618, fax: 0511-88791245
[1] E-mail: lzming@ujs.edu.cn

Received: 9 April 2013 /Accepted: 14 May 2013 /Published: 30 May 2013

Abstract: The industrial data has the characteristic of clustering and migrating with the operating point. The accuracy and generalization ability of the single-model prediction are poor because of the large amount of information lost in single-model modeling. In order to overcome these problems, a modeling method of multi-model soft sensor was proposed based on adaptive affinity propagation clustering (ADAP) and Bayesian filtering. ADAP algorithm was utilized in this method to realize the clustering and tracking of multiple operating points. The sub-models of various types of samples were established utilizing Bayesian filtering method, and the joint output and estimation were carried out based on the model of the subclass of current working point. The soft sensor models of CO and CO_2 in PX oxidation side reaction were utilized in the method. The simulation results show that the estimation and generalization ability of soft sensing model is significantly improved by the method. *Copyright © 2013 IFSA.*

Keywords: Adaptive affinity propagation clustering algorithm, Bayesian filtering, Soft sensor, Multi-model.

1. Introduction

In practical production process, the manipulated variables of each device are controlled around the given values. These given values of the operating point often need to be changed to meet the production requirement, which leads to a problem that the production data cluster and migrate with the working point. Single model has problems like long studying time, low accuracy, poor process characteristic match and poor generalization ability. Therefore, the multi-model modeling method was proposed [1-3]. The basic idea of this modeling method is to cluster the training samples by clustering algorithm and establish the soft sensor sub-model for different types of samples. When the process operating point changes in a wide range, the model can identify this change, and the prediction and output could be conducted in accordance with the model of the corresponding operating point.

The common clustering algorithms are K-means clustering and fuzzy clustering, etc. The initial cluster centers and the number of clusters are determined based on prior knowledge. However, prior knowledge is generally unknown for the operation data of actual production. Affinity propagation clustering algorithm, a new clustering algorithm [4] proposed in recent years, could determine the centers and the number of clusters according to the characteristics of the data. This method has been widely applied so far

[5-7]. A multi-model modeling algorithm of support vector machine based on affinity propagation clustering algorithm (ADAP) was proposed for the modeling of arachidonic acid fermentation process in literature [5]. A multi-model soft-sensing modeling method based on online clustering and association vector machine was proposed in literature [8] which has achieved good results in the final-boiling-point prediction system of light naphtha in hydrocracking unit fractionator. A multi-model algorithm of affinity propagation clustering with supervision was proposed in literature [6] to circularly adjust the clustering based on the output errors, and this method was better than traditional multi-modeling methods in term of modeling effect.

Affinity propagation clustering algorithm, however, is difficult in determining the values of key parameters for the optimal clustering results, and the concussion of the cluster number generated in the iterative process does not automatically disappear to make algorithm converged [9-13]. In allusion to these problems, a soft-sensing modeling method based on Bayesian filtering and adaptive affinity propagation clustering was proposed in the study. The ADAP algorithm was utilized for the classification of training samples in this method; Bayesian estimation method was utilized to create the sub-models of the small classified sample and carry out global output in accordance with the model of the belonging subclass of current operating point. The effectiveness of this method was proved by the CO and CO2 soft-sensing model in PX oxidation side reaction.

2. Algorithm of Adaptive Affinity Propagation Clustering

2.1. Affinity Propagation Clustering Algorithm

Affinity propagation clustering is a new fast and effective clustering method proposed in literature [4]. First, all sample points are regarded as potential cluster centers, and each sample point competes for the cluster center in the iteration loop. So there is no need to determine the number of clusters in advance.

A given sample set $\{x_i, y_i\}, i=1,2,...,N, x_i \in R^m$ is the input of m-dimension sample; $y_i \in R^m$ is the output of the sample. Negative Euclidean distance is utilized to measure the similarity of x_i and x_j, which is $S(i,j) = -\|x_i - x_j\|$., Samples are standardized before solving the similarity to eliminate the effect of dimension. $R(i,k)$ is defined as the attraction degree that x_k is suit for the cluster center of x_i; $A(i,k)$ is defined as the membership degree that x_k is chosen as the cluster center of x_i. AP algorithm continuously collects the evidences ($R(i,k)$ and $A(i,k)$) from data samples. The iteration formula of $R(i,k)$ is shown in formula 1:

$$\begin{aligned} R^{old}(i,k) &= R(i,k), \\ R^{new}(i,k) &= S(i,k) - \max\left[A(i,j) + S(i,j)\right], \\ R(i,k) &= (1-\lambda)R^{new}(i,k) + \lambda R^{old}(i,k) \end{aligned} \tag{1}$$

The iteration formula of $A(i,k)$ is shown in formula 2:

$$\begin{aligned} A^{old}(i,k) &= A(i,k), \\ A^{new}(k,k) &= \sum \max\left[0 + R(j,k)\right], \\ A^{new}(i,k) &= \min(0, R(k,k) - \sum \max\left[0 + R(j,k)\right] \\ A(i,k) &= (1-\lambda)A^{new}(i,k) + \lambda A^{old}(i,k) \end{aligned} \tag{2}$$

If $R(i,k) + A(i,k) = \max\{R(i,j) + A(i,j)\}, j = 1,2,...,n$, data point x_k is the cluster center of x_i. The update speed of the iteration could be changed by the adjustment of damping factor λ, λ=0~1. The element on the diagonal of similarity matrix is a bias parameter P which meets.

$$R(k,k) = p(k) - \max_{j \neq k}\left[A(k,j) + S(k,j)\right]$$

The bigger $p(k)$ is, the bigger $R(k,k)$ and $A(k,j)$ are. So cluster head x_k has the biggest chance of becoming the cluster center. The more and bigger $p(k)$ means that the more cluster heads could finally become the cluster center. Thus the change of P could affect the cluster number of AP. When prior knowledge is unknown, the value of $p(k)$ is the median of S, which is

$$p(k) = p_m = \frac{\sum_{i,j=1}^{n} S(i,j)}{n^2}, k = 1,...,n \tag{3}$$

An indicator Silhouette, introduced to achieve the effect of evaluation cluster, indicates the inner-cluster tightness and inter-cluster separability of cluster structure. Assume that the data set is divided into k cluster subset $C_i (i = 1,2,...,k)$, the indicator Silhouette of a sample t is

$$Sil(t) = \frac{\min\{d(t,C_j)\} - a(t)}{\max\{a(t), \min\{d(t,C_j)\}\}}, \tag{4}$$

where in $d(t, C_j)$ is the average Euclidean distance from t to another cluster C_j; *a(t)* is the average Euclidean distance from t to the cluster C_i. The average value of the indicator Silhouette of all the samples in a sample set is $S_{il-av} = mean[sum(Sil(t))]$. S_{il-av} can reflect the quality of all the data and clusters. A bigger S_{il-av} means better cluster effect, and the corresponding cluster number of the maximum is the optimal cluster number. If S_{il-av} is bigger than 0.5, each cluster could be apparently separated; if S_{il-av} is smaller than 0.2, then, a relevant cluster structure is needed.

2.2. Clustering Algorithm of Adaptive Affinity Propagation

AP algorithm can determine the clustering results based on the characteristics of the data with a fast arithmetic rate. But the algorithm has the following problems: the increase or decrease of the bias parameter p can increase or decrease the cluster number of AP algorithm, so it is difficult to determine the value of P to generate the optimal clustering results of algorithm; algorithm cannot automatically eliminate the concussion and converge. In order to solve the above problems, the clustering algorithm of adaptive affine propagation was proposed in literature [9].

The iteration steps of the clustering algorithm of adaptive affine propagation are:

Step 1: initialize S and P and start the algorithm with a relative big P. The initial value of P in this paper is $p=0.5\times p_m$ (the element in S is negative, so p_m is negative);

Step 2: execute AP algorithm once, then K cluster heads and the types of each sample are generated, wherein $\lambda=0.5$;

Step 3: examine whether the K cluster heads are converged (the convergence condition is to meet the preset continuous constant frequency $\omega=0.5$); if they are converged, evaluate the clustering results with effectiveness indicator S_{il-av} and reduce P with a step of

$$p_{step} = \frac{0.01 p_m}{0.1\sqrt{K+50}},$$

if they are not converged, increase λ with a step of $\lambda_{step} = 0.05$; if they are not converged when $\lambda \geq \lambda_{max}$ (λ_{max} is 0.85), the concussion of P is obstinate, and a relatively big λ could not restrain the concussion. This P needs to be abandoned. Reduce P with a step of

$$p_{step} = \frac{0.01 p_m}{0.1\sqrt{K+50}}.$$

Step 4: determine whether the algorithm meets the termination condition, which is to meet that the maximum number of loop iteration or the number of clusters reaches 2. Terminate the iteration if the condition is met; otherwise, go to step 2. ADAP algorithm searches for the number of clusters space to find the optimal clustering results by adaptive scanning bias parameter space. Adaptively adjust the damping factor to eliminate the concussion in the iterative process and reduce the value of P to get rid of the concussion when the damping factor adjustment method fails.

3. Establishment of Soft Sensing Multi-model

In order to overcome the problems of single-model modeling, the structure of soft sensing multi-model based on Bayesian theory is shown in Fig. 1. Firstly, cluster the training samples and find the optimal clustering results utilizing ADAP algorithm. Secondly, establish the sub-models of each sample utilizing Bayesian theory. Lastly, predict the output based on the corresponding sub-model of current operating point in the process. Its structure is shown in Fig. 1.

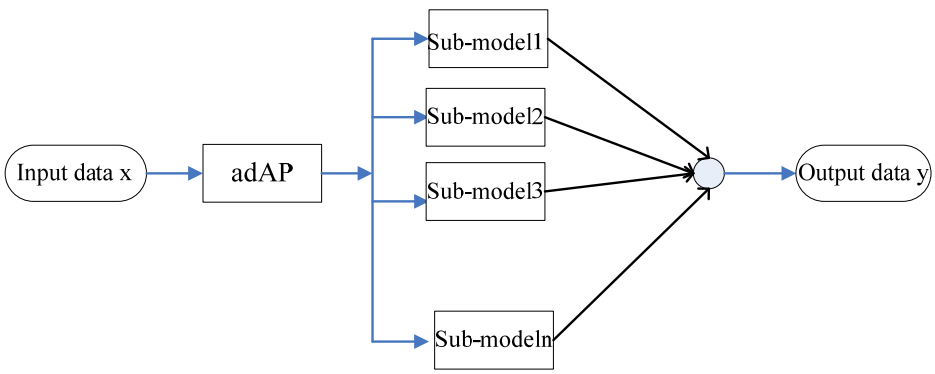

Fig. 1. Structure of multiple models soft-sensing method.

3.1. Bayesian Estimation

In this research, the content of CO and CO2 was thought as a state estimation problem. The state-space model was utilized to describe this problem. Assume that the position state of the target is $(x_t \mid t = 1,...,N)$, and the collection for each moment observation is $(x_t \mid t = 1,...,N)$. Then the state of the target can be described by the motion equation and observation equation in formula 5:

$$\begin{cases} x_t = F(x_{t-1}) + \omega_t \\ z_t = H(x_t) + \upsilon_t \end{cases} \quad (5)$$

where F is the impact parametric equation describing the model input;

H is the observation model which describes the relationship between the observed quantity and model output;

ω_t is the noise, which is utilized to describe the uncertainty of movement;

υ_t is the observed noise, which is utilized to describe the uncertainty caused by outside interference and the noise of the detecting element.

Bayesian estimation is a state estimation method utilizing state priori distribution and the observation of likelihood function to determine the posterior probability distribution. For a first-order Markov process, assume that the observation of each moment is mutually independent. If the posterior distribution at time t-1 is $p(x_{t-1} \mid z_{t-1})$, the prior distribution at time t can be expressed as shown in formula 6:

$$p(x_t \mid z_{t-1}) = \int p(x_{t-1} \mid z_{t-1}) p(x_t \mid z_{t-1}) dx_{t-1} \quad (6)$$

where $p(x_t \mid z_{t-1})$ is the transition probability density function, which is determined by F and the probability distribution of the noise ω_t ($p(\omega_t)$) in motion equation 5. The definition is:

$$p(x_t \mid x_{t-1}) = \int p(\omega_t) \delta(x_t - F(x_{t-1})) d\omega_t \quad (7)$$

where in $\delta()$ is the Dirac function. After the prior distribution $p(x_t \mid z_{t-1})$ is obtained, the state posterior distribution $p(x_t \mid z_t)$ could be expressed as:

$$p(x_t \mid z_t) = \frac{p(z_t \mid x_t) p(x_t \mid z_{t-1})}{\int p(z_t \mid x_t) p(x_t \mid z_{t-1}) dx_t} \quad (8)$$

where $p(z_t \mid x_t)$ is the observation likelihood function, which is determined by H and the probability distribution of the noise υ_t ($p(\upsilon_t)$). The definition is:

$$p(z_t \mid x_t) = \int p(\upsilon_t) \delta(z_t - H(x_t)) d\upsilon_t \quad (9)$$

The above formula 6 and 7 constitute the prediction process of Bayesian estimation; formula 8 and 9 constitute the update process of Bayesian estimation. The two processes are determined by the equation and observation equation of state space model parameters in formula 5, respectively. The tracking of the posterior distribution of state x_t could be achieved through the iterative and recursive solution of above prediction and update process.

3.2. Simulation Study

The source of our data was the PTA production process data in a chemical plant. The model of paraxylene (PX) oxidation side reaction through soft sensor model provided the basis for production optimization of operating parameters and the transformation of the production process. The main factors that will affect the combustion side reaction are: the reaction temperature (x_1, °C), solvent ratio (x_2, Kg. HAc/Kg. PX), the concentration of cobalt catalyst (x_3, wt%), the concentration of manganese catalyst (x_4, wt%), the concentration of bromine accelerator (x_5, wt%) and the residence time (x_6, S). Regard these main factors after data preprocessing as the input data; the total content of CO and CO_2 (ΦCOX) of the reactor exhaust gas as the output data y. Generally 250 sets of data were obtained. 170 sets of data are the training data, and the remaining 80 sets of data are the current running data in the process, which were utilized to test the generalization capability of the model.

Fig. 2 is the cluster number of ADAP clustering algorithm and the corresponding indicator of effectiveness S_{il-av}. Fig. 2 shows the ADAP algorithm was started with a large value of P to obtain several clustering results. The optimal clustering results could be selected according to the indicator S_{il-av}. The indicator S_{il-av} was the largest when the training samples were divided into two clusters in terms of the data utilized in this study. Therefore, the training samples were divided into two clusters.

Further simulation analysis on the training results and the linear regression analysis of the output and target output of network simulation are shown in Fig. 3. The figure shows that the correlation coeffi-

cient is 0.99, which means that the performance of the network is satisfying.

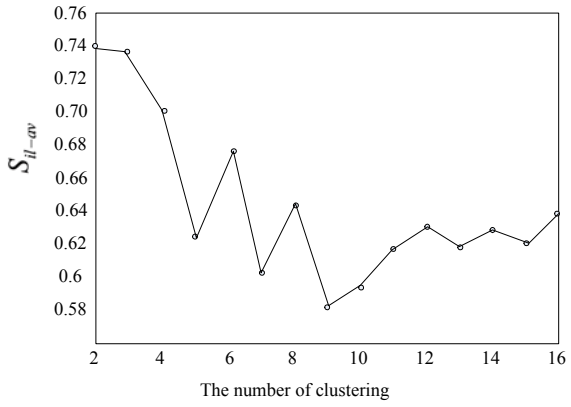

Fig. 2. The effective index of clustering algorithm.

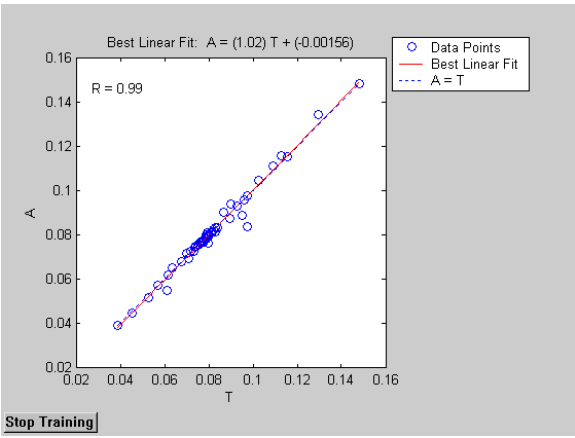

Fig. 3. The analysis result of network output.

3.3. The Combustion Loss Model of Acetic Acid and Xylene

Establish the combustion loss model of acetic acid and PX based on the determined generation model of CO_x. The combustion loss model of acetic acid:

$$m_{HAc}^{consume} = \frac{m_{gas} \times x_{CO_x} \times \frac{x_{HAc}}{100} \times \frac{60}{1000}}{2 \times \frac{m_{HAc}^{CO_x}}{100} \times m_{CTA}}$$

The combustion loss model of PX is:

$$m_{PX}^{consume} = \frac{m_{gas} \times x_{CO_x} \times \frac{x_{PX}}{100} \times \frac{106}{1000}}{8 \times \frac{m_{PX}^{CO_x}}{100} \times m_{CTA}}$$

x_{CO_x} : the total content of generated CO and CO_2 of the exhaust gas;

x_{HAc} : the percentage of CO_x generated by acetic acid (%);

$m_{HAc}^{CO_x}$: the percentage of CO_x accounting for the combustion product of acetic acid side reaction (%);

m_{gas} : the flow of exhaust gas from the reactor (ft3/hr);

m_{CTA} : CTA product yield (tons / Hr);

The molecular weight of acetic acid: 60 (g / mol);

$m_{HAc}^{consume}$: the amount of acetic acid loss (Kg / ton. CTA);

x_{PX} : the percentage of CO_x generated by PX (%);

$m_{PX}^{CO_x}$: the percentage of CO_x accounting for the combustion product of PX side reaction (%);

The molecular weight of PX: 106 (g / mol);

$m_{PX}^{consume}$: the amount of PX loss (Kg / ton CTA);

From the above text, the value of x_{HAc}, $m_{HAc}^{CO_x}$, x_{PX} and $m_{PX}^{CO_x}$ are known as 60 %, 75 %, 40 % and 60 %, respectively; m_{gas} and m_{CTA} were obtained through the actual production data.

4. Analysis of the Effect on Process Operating Parameters on Combustion Loss

Establish a model to reflect the effect of operating parameters on the HAC and PX combustion loss in PX oxidation reaction process. Then, analyze the effect of various operating parameters on HAC and PX combustion loss in the reaction process. Thereafter, analyze the effect of residence time, reaction temperature, solvent ratio, the concentration of catalyst like cobalt, manganese, bromine and other operating parameters on the HAC and PX combustion loss through the model, respectively. The results are shown in Figs. 4-8.

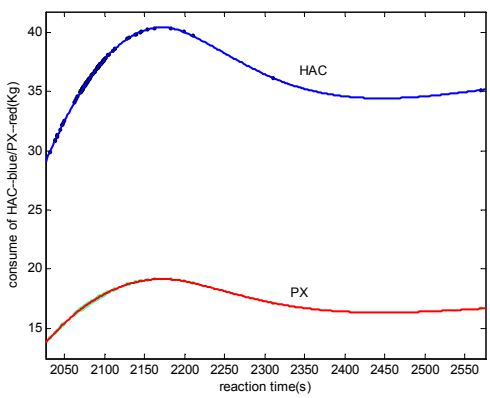

Fig. 4. Effect of reaction time on oxidative side-reaction.

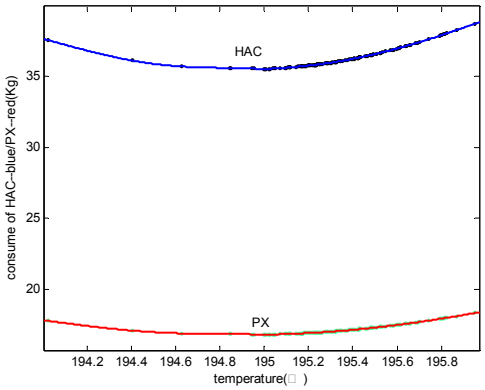

Fig. 5. Effect of reaction temperature on oxidative side-reaction.

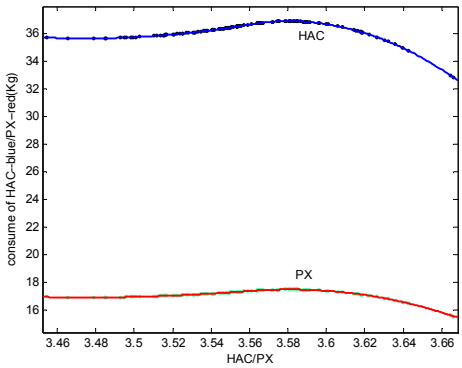

Fig. 6. Effect of HAC/PX on oxidative side-reaction.

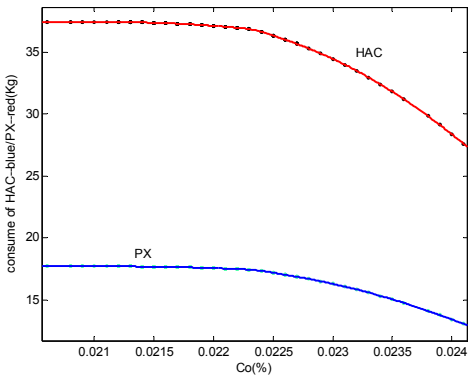

Fig. 7. Effect of Co concentration on oxidative side-reaction.

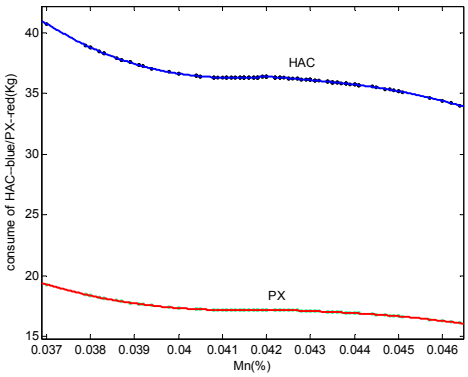

Fig. 8. Effect of Mn concentration on oxidative side-reaction.

Fig. 4-9: reaction residence time has a great effect on the combustion loss; the effects of reaction temperature and the concentration of Co, Mn, Br are small, but the effect of reaction temperature is slightly bigger. The effects of each operating parameter on the combustion loss can be quantitatively analyzed from these curves to provide guidance for the adjustment and optimization of operating parameters in practical production process.

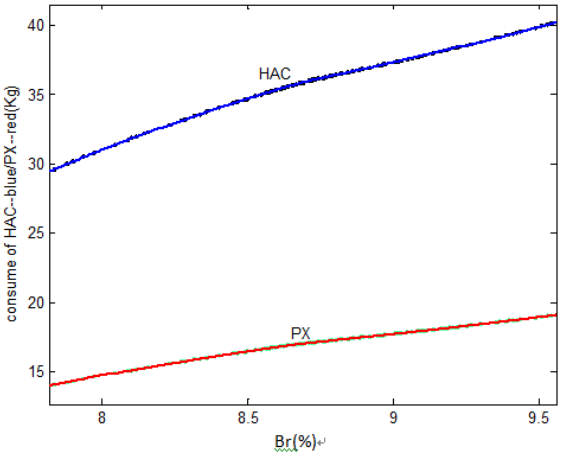

Fig. 9. Effect of Br concentration on oxidative side-reaction.

5. Conclusions

Utilize the algorithm of adaptive affine propagation clustering to divide the field data into two categories. The combustion loss model of HAC and PX was established based on Bayesian filtering. And this neural network model regarded the main adjustable process parameters (residence time, the concentration of Co, Mn, Br, reaction temperature and solvent ratio) as the independent variables and the total content of CO and CO2 as the dependent variable. The simulation results show that the network is well performed. The effects of process operating parameters on HAC and PX combustion loss are analyzed based on the model. Wherein, the effects of residence time, reaction temperature on the combustion loss are bigger, while the effects of other factors are relatively small.

Acknowledgement

The authors would like to thank the financial support provided by Research and Innovation Project for College Graduates of Jiangsu Province of China under Grant CXLX12_0648, National Natural Science Foundation under Grant 61273142 and Priority Academic Program Development of Jiangsu Higher Education Institutions (PAPD).

References

[1]. Li Wei, Yang Yupu, Wang Na, LSSVM multi-model regression modeling based on the fuzzy kernel clustering, *Control and Decision*, Vol. 23, Issue 5, 2008, pp. 560-562.

[2]. Suo Xingyi, Shi Hongbo, The soft sensor modeling of sewage treatment process based on multi-model fuzzy kernel clustering algorithm, *East China University of Technology: Natural Science*, Issue 5, 2010, pp. 732-736.

[3]. Petr K., Bogdan G., Sibylle S., Data-driven soft sensors in the process industry, *Computers and Chemical Engineering*, Vol. 33, Issue 4, 2009, pp. 795-814.

[4]. Frey B. J., Dueck D., Clustering by passing messages between data points, *Science*, Vol. 315, Issue 5814, 2007, pp. 972-976.

[5]. Li Lijuan, Song Kun, Zhao Yingkai, ARA fermentation process modeling based on affinity propagation clustering, *Journal of Chemical Industry and Engineering,* Vol. 62, Issue 8, 2011, pp. 2116-2121.

[6]. Deng Weiwei, Yang Hui, A supervision multi-modeling method of affinity propagation clustering, *Shanghai Jiao Tong University*, Vol. 45, Issue 8, 2011, pp. 1172-1175.

[7]. Li X., Su H., Chu J., Multiple Model Soft Sensor Based on Affinity Propagation, Gaussian Process and Bayesian Committee Machine, *Chinese Journal of Chemical Engineering*, Vol. 17, Issue 1, 2009, pp. 95-99.

[8]. Liu Xiuliang, Su Hongye, Chu Jian, Multiple model soft sensor based on online clustering and relevance vector machine, *Control and Instruments in Chemical Industry,* Vol. 35, Issue 3, 2008, pp. 34-37.

[9]. Wang KaiJun, Zhang Junying, Li Dan, Adaptive Affinity Propagation Clustering, *AAS*, Vol. 33, Issue 8, 2007, pp. 1242-1246.

[10]. Shang F., Jiao L. C., Shi J., et al., Fast affinity clustering: a multilevel approach, *Pattern Recognition*, Vol. 45, Issue 1, 2012, pp. 474-486.

[11]. Su Z., Wang P., Shen J., et al., Multi-model strategy based evidential soft sensor model for predicting evaluation of variables with uncertainty, *Applied Soft Computing*, Vol. 11, Issue 2, 2011, pp. 2595-2610.

[12]. Tan S., An effective refinement strategy for KNN text clusterifier, *Export Systems with Applications,* Vol. 30, Issue 2, 2006, pp. 290-298.

[13]. Ge Z., Song Z., A comparative study of just-in-time-learning based methods for online soft sensor modeling, *Chemometrics and Intelligent Laboratory Systems*, Vol. 104, Issue 2, 2010, pp. 306-317.

Sensors & Transducers, Vol. 21, Special Issue, May 2013, pp. 218-222

Sensors & Transducers

http://www.sensorsportal.com

Multifunctional Simulation Instrument for Control Systems Based on MATLAB GUI

[1] XING XUENING

[1] School of Electrical and Electronic Engineering, Shandong University of Technology, 255049, China

[1] E-mail: xingxuening@yeah.net

Received: 12 April 2013 /Accepted: 14 May 2013 /Published: 30 May 2013

Abstract: In the automatic control principle course teaching, the experiment is a kind of important teaching methods used to help students understand and grasp what they learned in class. MATLAB GUI is used to design a kind of multifunctional control system simulation. When input the zero pole parameters of transfer function, and the open loop transfer function of the corresponding control system can be got the bode diagram and Nyquist diagram, the root locus diagram and the unit step response curve. The simulator can make up for the deficiency of the traditional laboratory, moreover it can increase the students' interest in learning about the course. Students are the biggest beneficiaries. *Copyright © 2013 IFSA.*

Keywords: MATLAB GUI, Simulation instrument, Automatic control, Transfer function, Root locus.

1. Introduction [1-3]

Principle of automatic control technology is the study of automatic control theory, which is one of the main courses of professional. In the automatic control principle of the course, we must learn the control system's basic theory, the basic concept and the analysis and the design method. In the automatic control principle course teaching, the experiment is a kind of important teaching methods used to help students understand and grasp what they learned in class. In the traditional hardware experimental platform, you must change or adjust the corresponding components in the experimental stage if you want to change the parameters of the system and structure more often and sometimes it is difficult to achieve due to various reasons. In recent years, with the wide application of MATLAB in automatic control theory and the use of MATLAB to assist teaching, which has played a good role in the process of teaching. But simply use MATLAB to the simulation needs certain programming basis. With the emergence of virtual instrument technology and the development of computer technology, using the virtual experiment system developed by MATLAB GUI can do virtual experiments.

GUIDE from the Graphical User Interface Development Environment, it is short for MATLAB Graphical User Interface Development Environment, it can provide the GUI with a series of tools, which greatly simplifies the design and the process of creating a GUI. Using GUI editor to edit needs to editing respectively two files: A FIG file (FIG), containing the attribute set of GUI objects and layout information; the other one is M file. (M), containing the control GUI objects implement the callback function.

In this paper, a control system analysis and design of simulation software based on MATLAB GUI platform was designed, combined with control system basic theory and MATLAB control system toolbox. And the bode diagram, the step response

curve, Nyquist diagram and the root locus diagram according to the given transfer function can be plotted.

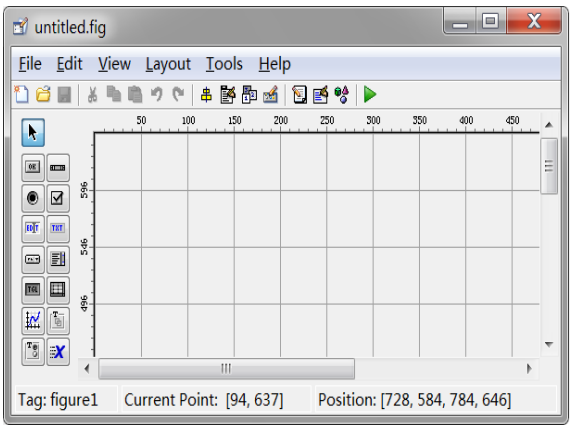

Fig. 1. GUI editor interface.

2. Classical Control Theory and Simulation [4-6]

System's transfer function is the basis of the classical control theory, mainly studies the analysis and design problems of single input and single output of the linear time-invariant systems with frequency domain method .In constant value system and servo system, the theory has more extensive application, lying a solid foundation for the further study of the intelligent control theory and the modern control theory [4-6].

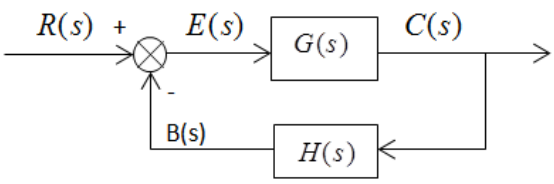

Fig. 2. Typical structure of control system.

2.1. Transfer Function and Simulation

Transfer function is a mathematical model for describing the dynamic characteristics of linear systems, but is only applicable to linear time-invariant system and initial conditions are zero.

A linear time-invariant system consists of the following n order linear ordinary differential equations.

$$a_0\frac{d^n}{dt^n}y(t)+a_1\frac{d^{n-1}}{dt^{n-1}}y(t)+\cdots+a_{n-1}\frac{d}{dt}y(t)+a_ny(t)$$
$$=b_0\frac{d^m}{dt^m}u(t)+b_1\frac{d^{m-1}}{dt^{m-1}}u(t)+\cdots+b_{m-1}\frac{d}{dt}u(t)+b_mu(t) \quad (1)$$

In this type, $y(t)$ it is the output of the system; $u(t)$ is the system input; $a_i(i=0,1,2,\cdots,n)$ and $b_j(j=0,1,2,\cdots,m)$ is associated with the system structure and parameters of constant coefficient.

Set $u(t)$, $y(t)$ and each derivative are all zero when $t=0$, i.e. zero initial conditions, in the type of the Lap lace transform, respectively, set $Y(s)=\lambda[y(t)]$ and $U(s)=\lambda[u(t)]$, s available for algebraic equation.

Then, the system transfer is defined as

$$G(s)=\frac{Y(s)}{U(s)}=\frac{b_0s^m+b_1s^{m-1}+\cdots+b_{m-1}s+b_m}{a_0s^n+a_1s^{n-1}+\cdots+a_{n-1}s+a_n} \quad (2)$$

$b_j(j=0,1,2,\cdots,m)$

$a_i(i=0,1,2,\cdots,n)$

Therefore, molecules can be used in MATLAB, the denominator coefficient vectors num and den to represent the transfer function $G(s)$, realizing the function of tf(), it calls the format is as follows:

num = [b_0, b_1,…, b_{m-1}, b_m]

den = [a_0, a_1,…, a_{n-1}, a_n]

sys = tf (num，den)

2.2. The Unit Step Response and Simulation

For the unit step input r (t) = 1 (t), r (s) = $\frac{1}{s}$, and so

$$C(s)=\frac{1}{s(Ts+1)}=\frac{1}{s}-\frac{1}{s+\frac{1}{T}} \quad (3)$$

Therefore,

$$c(t)=c_{ss}(t)-c_t(t)=1-e^{-\frac{t}{T}} \quad (4)$$

$c_{ss}(t)$ for steady state component, $c_{ss}(t)=1$; $c_t(t)$ As the transient component, $c_t(t)=e^{-\frac{t}{T}}$.

step(sys)
step(sys,tfinal)
step(sys,t)
step(sys1,sys2,…,t)
[n, d]=step(sys)
[n,d,x]=step(sys)

The t final as a response to a termination time variables; T for a given time variables, such as: t = 0:0.01:10; Return variable, y for the response vector, vector t is time, as the state vector x.

2.3. Bode Diagram and Simulation

The performance of the control system with time domain measurement is intuitive, but a high order control system characteristics in time domain, it is difficult to determine with the analytical method, we usually use frequency domain method to solve. Frequency domain method is a graphical method, mainly includes three kinds of methods: Bode (amplitude / phase frequency characteristic curve), Nyquist curve and Nichole diagram. Bode diagram is the logarithmic frequency characteristic curve. A known system transfer

$$H(s) = \frac{b_1 s^m + b_2 s^{m-1} + \cdots + b_{m+1}}{a_1 s^n + a_2 s^{n-1} + \cdots + a_{n+1}} \qquad (5)$$

The frequency response of the system can be directly calculated

$$H(jw) = \frac{b_1 (j\omega)^m + b_2 (j\omega)^{m-1} + \cdots + b_{m+1}}{a_1 (j\omega)^n + a_2 (j\omega)^{n-1} + \cdots + a_{n+1}} \qquad (6)$$

Bode diagrams of the system is H ($j\omega$) of rendering, so it is also called the amplitude frequency and phase frequency characteristic curve. Abscissa is angular frequency w, is commonly used in logarithmic scale, namely unit is rad/s. The ordinate is the logarithmic phase frequency characteristics $\varphi(\omega)$ and the unit for Angle; Ordinate is logarithmic amplitude-frequency characteristics $L(\omega) = 20\log A(\omega)$ and the unit is decibels (dB).

Bode diagram drawing function of MATLAB for Bode(), which calls the format is as follows:

bode(sys)
bode(sys, w)
[mag, phase, w]=bode(sys)

Among them: artificial give the frequency of the input vector for the vector; mag for the returned amplitude vector; phase to return to the phase Angle of the vector. In addition, MATLAB provides a very convenient computing system function of the amplitude and phase Angle margin, which calls the format is as follows:

margin(sys)
[gm, pm, wg, wp]=margin(sys)
[gm, pm, wg, wp]=margin(mag, phase, w)

Among them: gm for the returned vector amplitude margin; pm as the phase Angle margin; wg for phase through frequency; wp for the cutoff frequency.

2.4. Nyquist Curve and the Simulation

Nyquist curve is based on open loop frequency characteristic in the complex plane on the amplitude and phase trajectory of the paint. According to the Nyquist curve of open loop, it can judge the stability of the closed-loop system.

Feedback control is necessary and sufficient conditions for system stability, Nyquist curve counterclockwise around the critical point (-1, j0) circle number P is equal to the open-loop transfer function poles book in right half of s plane, otherwise the closed-loop system instability. When the open-loop transfer function contains the poles on the imaginary axis of closed curves, should be from the right side of the semicircle around the pole. This is the Nyquist criterion.

MATLAB Nyquist frequency curve drawing function Nyquist(), which calls the format is as follows:

nyquist(sys)
nyquist(sys,w)
[re,im,w]=nyquist(sys)

2.5. Root Locus and Simulation

The basic performance of the closed loop system transient response is composed of closed-loop poles distribution in root plane more determined. The closed-loop poles are the roots of the characteristic equation. The root locus is when a variable parameter system by, the closed-loop poles are portrayed in the S plane trajectory.

Set up control system of the open loop transfer function can be expressed as:

$$G(s)H(s) = K^* \frac{(s-z_1)(s-z_2)\cdots(s-z_m)}{(s-p_1)(s-p_2)\cdots(s-p_n)} = K^* \frac{\prod_{j=1}^{m}(s-z_j)}{\prod_{i=1}^{n}(s-p_i)} \qquad (7)$$

In the formula, K* as the root locus gain open-loop system; Z_j for the system open loop zero (j=1,2,... , m); P_i for the system open loop poles (i=1,2,... , n). The closed-loop characteristic equation of system is:

$$1 + G(s)H(s) = 0 \qquad (8)$$

The formula is called the root locus equation. It can be drawn when K changed from zero to infinity, continuous root locus system.

Using root locus function provided by the MATLAB can be conveniently and accurately plot the root locus of control system, and can use the root locus diagram of control system are analyzed.

Used to map the root locus of system, its call format is as follows:

rlocus(sys)
rlocus(sys,k)
r=rlocus(sys,k)
[r,k]=rlocus(sys)

3. Simulation Instrument Design [7-10]

Main parts include start, exit button, input parameters and graphic display. Which use the GUI static text in the selection area, editable text, touch button and axes. The designed simulator is only applicable to the system transfer function is zero pole models:

$$G(s) = \frac{K(s - z_1)}{(s - p_1)(s - p_2)(s - p_3)} \qquad (9)$$

In the simulation instrument panel plot the Bode graph, the system step response curve, Nyquist diagram and root locus diagram at the same time, this provides great convenience for system research.

Design and Simulation of instrument is divided into design and software programming of the control panel. According to the idea of publishing on the control panel in the GUI interface, modify each text box or button, and then write the program of the multi-function control system simulation instrument in the callback function, repeated debugging and modification, until it reaches the expected goal.

3.1. Layout of GUI Objects

According to their overall conception of multifunctional control system simulation, the simulation instrument panel consists of three parts.

The first part is the parameter input, on the left side of the object and selects the Static Text zone (static text); it is often used to display other objects, such as numerical state. Drag the mouse to determine the size of the text box in the GUI layout area of the properties dialog box, double-click the text box pops up Static Text, modify the text box static text in String. If you want to enter the numbers in the text box in the corresponding parameters, you need to select the object selection in Edit Text (editable text); it allows the user to modify the text content, used for data input and display. Drag the mouse to determine the size of the text box, and then click the text box to modify its properties. Delete the contents of the String correspond to change the color to white and its interface is shown in Fig. 3.

The second part is the beginning, exit Button, choose the Push Button object selection area on the left (touch Button), drag the mouse in the GUI layout area to determine the size of the Button, double-click the Button pop-up Push Button in the properties dialog box, and amend the content in the String to start or exit.

The third part is the graphical display, select the axes (axis) on the left side of the object, drag the mouse to determine the coordinate axis size, double-click the coordinate axis modify its properties. You can use the GUI menu bar tool will these axes alignment.

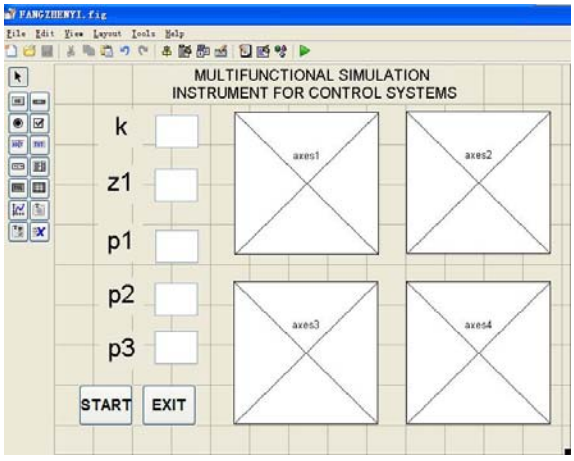

Fig. 3. Simulator interface editor.

3.2. Callback Function

Right click on the interface of Fig. 3 in the start button, select View Callbacks callback; in the popup editor page in the function pushbutton1_Callback :(hObject, eventdate, handles) enter the following procedures:

```
K =str2double(get(handles.edit1,'String'));
z1=str2double(get(handles.edit2,'String'));
p1=str2double(get(handles.edit3,'String'));
p2=str2double(get(handles.edit4,'String'));
p3=str2double(get(handles.edit5,'String'));
k=k;
z=[z1];
p=[p1,p2,p3];
y=zpk(z,p,k);
axes(handles.axes1);
bode(y)
grid on
axes(handles.axes2);
y1=feedback(y,1)
step(y1)
grid on
axes(handles.axes3);
nyquist(y)
grid on
axes(handles.axes4);
rlocus(y)
grid on
```

Right click the exit button interface as shown in Fig. 3, select the callback in the View Callbacks , in the popup editor page in the function pushbutton2_Callback (hObject, eventdate, handles) enter the close, point to save. Click the toolbar in the Run Figure, run the program, get the control panel of multifunctional control system simulation instrument.

4 The Use of the Simulator

The system model has been built, you can start the simulation. In the simulation, you should set the simulation parameters. The simulation system is

designed in this paper is based on pole-zero system model design, so the zero and pole of the system should be calculated before the simulation.

Sets the transfer function:

$$G(s) = \frac{100s + 300}{s^3 + 11s^2 + 10s}.$$

(1) Start MATLAB, at the MATLAB command window, type the following sequence Program:

num=[100,300];

den=[1,11,10,0]; [z,p,k]=tf2zp(num,den)

sys=zpk(z,p,k)

Press the Enter key, getting the pole zero negative feedback system

```
Zero/pole/gain:
  100 (s+3)
--------------
s (s+10) (s+1)
```

(2) Operating system, as shown in Fig. 4.

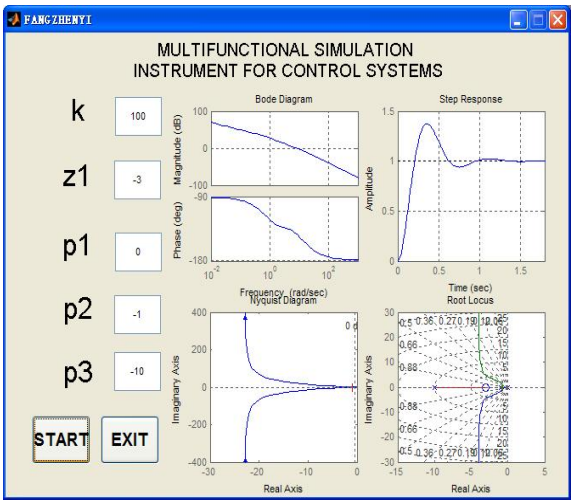

Fig.4. Test Result.

Input the pole-zero transfer function parameters in the parameter input control panel on the left side of the simulation system, we can get the corresponding control system open-loop transfer function of the Bode diagram, Nyquist diagram, and the root locus diagram and unit step response curve. Fig. 4 shows an open-loop gain of 100, zero - 3, pole respectively, 1, 0-10 to the simulation of the system. From this interface can obtain some parameters of system dynamic performance and steady-state performance, and through parameter controls the system, make the system stable, accurate and fast running. After the analysis of system press the exit button to end.

5 Conclusions

The simulator put bode diagram, unit step response curve, Nyquist diagram and the root locus diagram which are commonly used in control system in the same control panel, can more convenient to study the stability, accuracy and rapidity of the control system. Curve has the characteristics of intuitive; it is very convenient to study the steady-state performance and dynamic performance of the control system used by curve. The instrument also has some shortcomings, such as the control system to study the model is the best model of zero-pole, if not zero pole model and using MATLAB language into pole-zero model and then use the simulation instrument simulation; transfer function of control system simulation number order is relatively low, and form a fixed. Also can be used for further modification and perfection of the simulation system, it can simulate order transfer function better, but at this time of the MATLAB programming requirements will be higher.

Reference

[1]. Dub, Michal, Brotan, Lukas, MATLAB GUI for DC drive parameter identification, *Mechatronika*, 2012, 2012.

[2]. Mitchell, R. J. Using MATLAB GUIs to improve the learning of frequency response methods, *Control*, 2012, 2012.

[3]. Elmagroud, Bachir, Educational software for wave propagation phenomena using MATLAB GUIs and FDTD method, *EDUCON 2012*, 2012.

[4]. Li Suling, Automatic Control Theory (3rd Edition) *Machinery Industry Press*, 2012.

[5]. Zhang Defeng, MATLAB and automatic control system design, *Machinery Industry Press*, 2010.

[6]. Zhang Jing, Application of MATLAB in control systems, *Publishing House of Electronics Industry*, 2007.

[7]. Chen Chao, MATLAB application examples succinctly -- image processing and GUI design, *Publishing House of Electronics Industry*, 2011.

[8]. Huang Wenmei, Yang Yong, System simulation analysis and Design - MATLAB application, *National University of Defense Technology Press*, 2001.

[9]. Wang Zhenglin, MATLAB/Simulink and Control System Simulation (2nd Edition), *Electronic Industry Press*, 2008.

[10]. Sun Liang, MATLAB simulation and control system, *Beijing University of Technology Press*, 2006.

Sensors & Transducers, Vol. 21, Special Issue, May 2013, pp. 223-227

Sensors & Transducers

http://www.sensorsportal.com

Research on the Electrical Characteristics of Photovoltaic Arrays and Corresponding MPPT Simulation

[1] Shengming Li, [2] Yinqiao Liang, [2,*] Xiaobing Zhang

[1] Electrical and Electronic Training Center, Harbin University of Science and Technology, Harbin, Heilongjiang, 150080, P. R. China

[2] College Measurement Control Technology and Communication Engineering, Harbin University of Science and Technology, Harbin, Heilongjiang, 150080, P. R. China

[1] E-mail: xiaobingzhangmail@163.com

Received: 12 April 2013 /Accepted: 14 May 2013 /Published: 30 May 2013

Abstract: Photovoltaic cells, as the primary part of a solar photovoltaic system, are a nonlinear DC power supply related to multiple parameters. The demand of increasing the generating efficiency of photovoltaic cells requires having a good understanding of their electrical characteristics. In this study, the mathematical and physical model of the photovoltaic cells was built by the means of Matlab and Simulink based on the internal principles and equivalent circuits of the photovoltaic cells. After the simulation of such practical and versatile model, it's found that the nonlinear P-V and I-V characteristics of the photovoltaic cells, with the change of sunlight intensity and temperature, could be accurately reflected by this high simulation precision model. Furthermore, the Maximum Power Point Tracking method was proposed using the logical formula dP/dI=0 of the maximum power point of photovoltaic cells. This method can simply and fast implement the tracking for the maximum power point. *Copyright © 2013 IFSA.*

Keywords: Photovoltaic cell, Electrical characteristic, Maximum power point tracking.

1. Introduction

Solar photovoltaic systems have earned more attention with the aggravation of the world's energy crisis, and the solar energy is a kind of clean energy which is pollution-free, noiseless, widely distributed and without region limit. Therefore, the solar photovoltaic technology, compared to other new energy technologies, is a renewable energy technology for sustainable development. The critical part of a solar photovoltaic system is the photovoltaic array whose generating efficiency has an effect on the stability and feasibility of the entire system. Nevertheless, affected by sunlight intensity, temperature and raw materials, etc., the electrical characteristics of the photovoltaic array assume nonlinearity. The voltage across the photovoltaic array varies with the change of sunlight intensity and ambient temperature, and so is its output power. In other words, the photovoltaic cells provide unstable power supply. MPPT (Maximum Power Point Tracking) is a process of adjusting the operating point of the photovoltaic cells in real time to keep it near the maximum power point for the purpose of improving the overall efficiency of the solar photovoltaic system [1-2].

Currently, there are many MPPT algorithms for photovoltaic cells, such as the voltage feedback method, power feedback method, perturbation and observation method, incremental conductance method and actual measurement method. All these methods take voltage as the reference value to

perform adjustment in order to track and control the maximum power point of a solar photovoltaic system. However, there are some shortcomings unavoidably like complexity and rapidity owing to the nonlinear relationship between P and V. The disturbance attributed to these shortcomings inevitably causes power fluctuations and consequently generates extra losses. As a result, this study presents a straight-line approximation method based on many MPPT methods to avoid such shortcomings. This MPPT method is simple, easy to track and relatively accurate [3-4].

The mathematical simulation model of the photovoltaic array in the early research was built to reduce cost. The dynamic simulation of the photovoltaic array was implemented using this simulation platform, which is beneficial to fully study the characteristics of the photovoltaic array. In addition, it can either increase the utilization efficiency of the photovoltaic cells or shorten the research cycle of the solar photovoltaic system considerably.

2. Establishment of the Photovoltaic Cell Models

2.1. Mathematical-physical Model of a Single Photovoltaic Cell

A photovoltaic cell is a device directly converting light energy into electric energy through the photovoltaic effect. When a photovoltaic cell exposed to sunlight connects to a load, the photo current flows through the load and creates terminal voltage at the both ends of the load. At this time, an equivalent circuit model can be used for the current working status of the photovoltaic cell. Fig. 1 shows the photovoltaic cell can be considered as an ideal current source that stably generates the photo current I_{ph}[5].

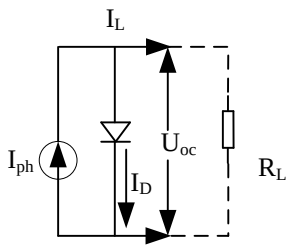

Fig. 1. Ideal equivalent circuit of the photovoltaic cell.

Considering the effects of the photovoltaic cell resistance on the photovoltaic cell's properties, the actual equivalent circuit is shown in Fig. 2. R_s is the series resistance composed of the internal resistance of silicon wafers and electrode resistance. It primarily consists of body resistance, surface resistance, electrode conductor resistance, and the contact resistance between electrodes and silicon surface. R_{sh} is bypass resistance resulting from the unclean edges of silicon wafers and inherent defects. The circuit models can help to have an insight into the working principle and electrical characteristics of the photovoltaic cell.

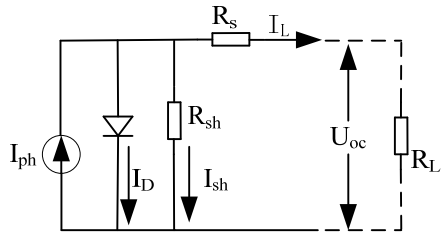

Fig. 2. Actual equivalent circuit of the photovoltaic cell.

According to the equivalent circuits in Figs. 1 and 2, the equations of output characteristics variables of the photovoltaic cell can be given as:

$$I_D = I_0[\exp(\frac{qU_D}{AkT}) - 1] \tag{1}$$

$$I_L = I_{ph} - I_0[\exp(\frac{q(U_{oc} + I_L R_s)}{AkT}) - 1] - \frac{U_D}{R_{sh}} \tag{2}$$

$$I_{sc} = I_{ph} - I_D - \frac{U_D}{R_{sh}} - \frac{U_D}{R_s}, \tag{3}$$

where

$$I_{ph} = I_{sc}[1 + a(T - 298)]\frac{G}{1000} \tag{4}$$

$$I_0 = I_{or}[\frac{T}{T_r}]\exp[\frac{qE_G}{Bk}(\frac{1}{T_r} - \frac{1}{T})] \tag{5}$$

The parallel resistance R_{sh} can be ignored, since it can generally reach several thousand ohms and its current value is far less than the photo current's. So we can simplify the output characteristic equation of the photovoltaic cell as:

$$I_L = I_{ph} - I_0[\exp(\frac{q(U_{oc} + I_L R_s)}{AkT}) - 1] \tag{6}$$

In case of the short circuit of the external load, $U_{oc} = 0$, all the photovoltaic current I_{ph} flows into the shorted external load, and the short circuit current I_{sc} is almost equal to the photo current, $I_{ph} = I_{sc}$. In case of the open circuit, I = 0, all the photo current flows through the diode D, and the open circuit voltage is:

$$U_{oc} = \frac{AKT}{q}\ln(\frac{I_{ph}}{I_0} + 1) \tag{7}$$

According to Equation (7), the short circuit current I_{sc} varies with the change of temperature and sunlight intensity and is proportional to the sunlight intensity, when the output current and voltage of the photovoltaic cell are affected by these external factors. At the same time, the open circuit voltage is also tightly related to the above two factors [6], as shown in Equation (8), (see Table 1) is the parameters of any of the above formula.

$$U_{oc} = U_{ocs}[1 + b(T - T_r)] \tag{8}$$

Table 1. Parameter list of the equivalent circuit of the photovoltaic cell.

Parameter	Description	Type
I_o	The reverse saturation current of the photovoltaic cell	Variables
T	The temperature of the photovoltaic cell	Constant
K	Boltzmann constant	Constant (1.38×10^{-23}J/K)
G	Sunlight intensity	Variables
q	Electron charge	Constant (1.6×10^{-19} C)
I_{or}	The reverse saturation current of the diode	Constant
T_r	Reference temperature under standard test conditions	Constant (298 K)
E_G	The band gap of the semiconductor material	Constant
a	Short circuit current temperature coefficient	Constant
A, B	The curve constant of the P-N junction	Constant (from 1 to 5)
b	Open circuit voltage temperature coefficient	Constant

2.2. Establishment of the Photovoltaic Array Model

A silicon photo cell has the open circuit voltage of 0.45–0.6 V and the short circuit current density of 20–25 mA/m^2. However, instead of a photovoltaic cell which is rarely used individually in actual lives, the form of many series-parallel photovoltaic cells is the common selection. These photovoltaic cells form a photovoltaic module, with a certain degree of impact and corrosion resistance, which increases the voltage through series connection and the current through parallel connection to provide a load with the larger power. Based on the fact that the series-parallel combination of photovoltaic cells can provide the expected DC voltage or current, the output characteristic equation of the photovoltaic cell module group can be obtained as:

$$I_L = n_p I_{ph} - n_p I_o \left\{ \exp\left[\frac{q(U_{oc} + I_L R_s)}{n_s AkT} \right] - 1 \right\}, \tag{9}$$

where n_p is the parallel connection number of the photovoltaic cells in the module group; n_s is the series connection number of the photovoltaic cells in the module group.

3. Electrical Characteristic Simulation and Analysis for the Photovoltaic Cells

Based on the above mathematical equivalent model, the physical mechanism-based mathematical simulation model of the photovoltaic array is directly built based on the existing math operations by means of Simulink in the Matlab environment [7-8]. We set the photovoltaic array parameters in the above model for simulation based on the technical parameters of the 60 W photovoltaic cell panel of our laboratory (see Table 2).

Table 2. Electrical specification parameters of XMT-U60 panel (1000 W/m ^{2}, 25 °C).

Maximum power (W)	60
Maximum working voltage (V)	18 V
Maximum working currency (A)	3.3
Open circuit voltage (V)	22.5
Short circuit current (A)	3.5
Photovoltaic cell number	36 (4)
Short circuit current temperature coefficient	0.065 /°C
Open circuit voltage temperature coefficient	-2.23 mV/°C

When the sunlight intensity is 1000 W/m^2, the I-V and P-V curves of the photovoltaic array are obtained through measurement at 5 °C, 25 °C and 50 °C. The results are shown in Figs. 3 and 4, respectively.

At the fixed temperature of 25 °C, the I-V and P-V curves of the photovoltaic array are obtained through measurement with the sunlight intensity of 1000 W/m^2, 800 W/m^2 and 600 W/m^2. The results are shown in Figs. 5 and 6.

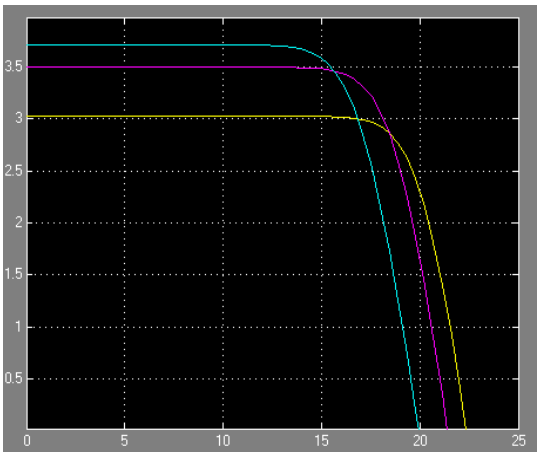

Fig. 3. Photovoltaic array I-V curve based on the change of temperature.

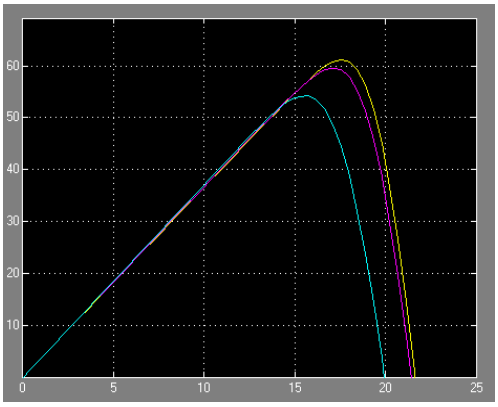

Fig. 4. Photovoltaic array P-V curve based on the change of temperature.

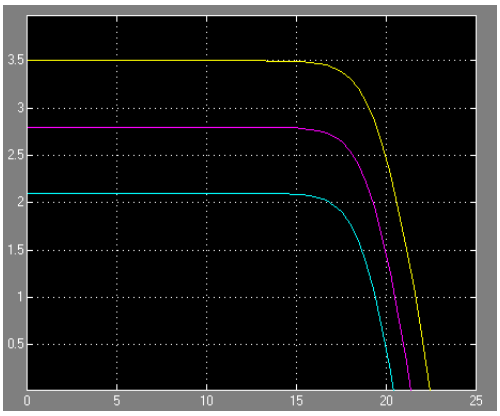

Fig. 5. Photovoltaic array I-V curve based on the change of sunlight intensity.

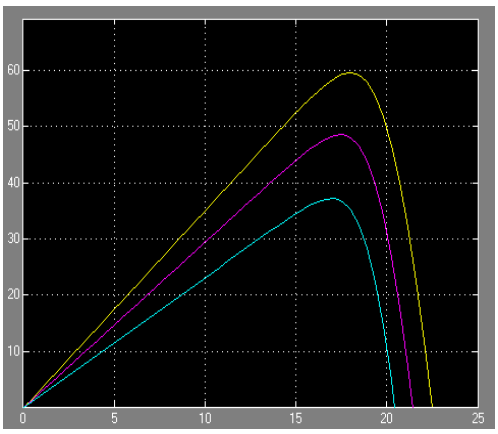

Fig. 6. Photovoltaic array P-V curve based on the change of sunlight intensity.

Figs. 3, 4 indicates that the short circuit current I_{sc} of the photovoltaic array slightly increases but the open circuit voltage U_{oc} rapidly decreases with the temperature rise at the fixed sunlight intensity, which leads to the general coastdown of output power of the photovoltaic array. Fig. 5, 6 indicates that the open circuit voltage U_{oc} of the photovoltaic array slightly changes and the short circuit current I_{sc} obviously increases at the fixed ambient temperature when the sunlight intensity rises, which leads to the increase of the maximum output power. It can be seen that the working environment temperature and sunlight intensity are the critical factors affecting the output characteristics of the photovoltaic array. However, the frequent change of the temperature and sunlight intensity may cause the photovoltaic array to fail in providing adequate energy to the load and even zero voltage which induces application losses. As a result, the MPPT method is capable of seeking the best operating point of a photovoltaic array by controlling an external load to avoid these disadvantages wherever possible and obtain optimum power.

4. MPPT Algorithm Simulation of the Photovoltaic Array

The fundamental concept of the straight line approximation method is to make use of the logical formula dP/dI=0. A straight line is applied for approximating the maximum power points under different sunlight intensity at a certain temperature. Only if controlling the output current to be on this straight line, MPPT can be easily implemented [9].

For the abovementioned equivalent model of the photovoltaic array, if n_s=36 and n_p=1, and in addition the equivalent series resistance is not ignored, Equation (9) can be rewritten as:

$$V = \frac{36kTA}{q}\ln[\frac{(I_{ph}+I_0-I)}{I_0}]-IR_s \qquad (10)$$

Then based on Equation (9) and (10), we can obtain:

$$P = IV = \frac{36kTA}{q} I \ln[\frac{(I_{ph}+I_0-I)}{I_0}]-I^2R_s \qquad (11)$$

Because the maximum power point is required to satisfy *dP/dI*=0, the differential of I is performed with Equation (11) and we make it equal to zero:

$$\frac{36kTA}{q}\ln[\frac{(I_{ph}+I_0-I)}{I_0}-\frac{I}{I_{ph}+I_0-I}]-2IR_s=0 \qquad (12)$$

Based on Equation (10), (11), and (12), the relationship of the output power P_1 and the output current I_1 at the maximum power point can be obtained as:

$$P_1 = \frac{36kTA}{q} I_1 \ln[\frac{36kTAI_1^2}{(P_1-I_1^2R_s)I_0}]-I_1^2R_s \qquad (13)$$

Finally, based on the above algorithms, we acquire the P_1-I_1 curve, as shown in Fig. 7, by solving Equation (10-13) with Matlab. It can be seen from

the figure that there is a linear relationship between the maximum power point and the output current under different sunlight intensity at the same temperature [10-11].

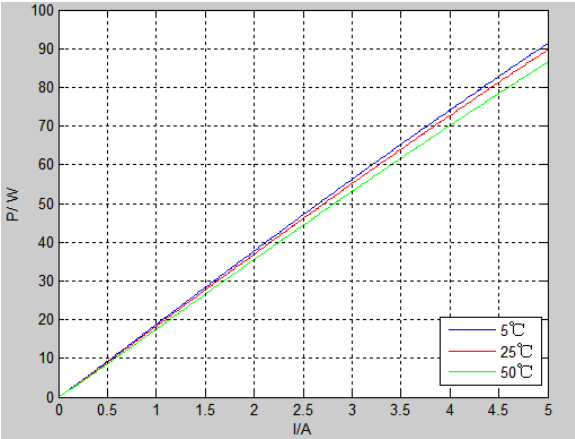

Fig. 7. Relationship of the maximum power point and the output current.

5. Conclusion

The mathematical expression of output I-V characteristics of the photovoltaic array composed of series-parallel photovoltaic cells is solved based on the equivalent circuit model of the photovoltaic cells. The simulation experiment results show the nonlinear P-V and I-V characteristics of photovoltaic cells with the change of sunlight intensity and temperature, and the photovoltaic cells output is a random and unstable power supply system. When the photovoltaic cells are used, their output characteristics often substantially change under the effects of load states, sunshine amount and ambient temperature, etc. The short circuit current is almost proportional to the sunshine amount, and the open circuit voltage is greatly affected by the temperature change. Therefore, the output power has a great change, in other words, the maximum power point is changing. In this study, new algorithms were used to deduce the approximate linear relationship of the maximum power point and the output current, and the MPPT control algorithm, based on current control, was proposed. The MPPT method, simple, easy to track and relatively accurate, is suitable for the simulation studies of complex solar photovoltaic systems.

References

[1]. He Renwang, Qiu Wanying, Wu Xun, MPPT Simulation Research Based on the PSIM Perturbation and Observation Method, *Power System Protection and Control*, 7, 2012, pp. 56-59.

[2]. Abd Kadir Mahammad, Sharifah Saon, Wong Swee Chee, Development of Optimum Controller based on MPPT for Photovoltaic System during Shading Condition, *Procedia Engineering*, 53, 2013, pp. 337-346.

[3]. Pin-Chun Chou, Hsin Chen, An Adaptive, Linear-line Approximation Method and its VLSI Implementation for Maximum Power Control of Photovoltaic System, *Control and Modeling for Power Electronics (COMPEL)*, Kyoto, 10-13 June 2012. pp. 1-5.

[4]. A. López Ríos, A. R. Messina, An optimal modal approximation method for model reduction of linear power system models, *International Journal of Electrical Power & Energy Systems*, 44, 1, 2013, pp. 293-300.

[5]. Zhao Zhengming, Liu Jianzheng, Sun Xiaoying, Yuan Lijiang, Solar Photovoltaic and Its Application, *Science Press*, Beijing, 2009, pp. 26-29.

[6]. Wang Xianan, Independent Solar Photovoltaic System and the Corresponding MPPT research, *Nanjing University of Aeronautics and Astronautics*, 2008, pp. 8-17.

[7]. Isiam M. A., Mohammad N., Khan P. K. S., Modeling and performance analysis of a generalized photovoltaic array in Matlab, *PEDES*, 2010, pp, 1-5.

[8]. Jama Assi A., Kathairi K. M. Al., MATLAB based modeling tool for designing predicting and analyzing grid tied photovoltaic systems, *ACTEA*, 2009, pp, 508-513.

[9]. Wu Caifu, Zhang Jianxuan, Chen Yukai, Grid-connected Photovoltaic Generation and Illuminating System, *Science Press*, Beijing, 2009, pp. 14-23.

[10]. Chih-Lung Shen, Yu-En Wu, Fang-Shiang Liu, A Double-Linear Approximation Algorithm to Achieve Maximum-Power-Poin Tracking for PV Arrays, *Power Electronics and Drive Systems*, 2, 2009, pp. 758-763.

[11]. Moon Gil Yoon, Hwi Young Lee, Yoon Sook Songc, Linear approximation approach for a stochastic seat allocation problem with cancellation & refund policy in airlines, *Journal of Air Transport Management*, 23, 2012, pp. 41-46.

The Fourth International Conference on Sensor Device Technologies and Applications

SENSORDEVICES 2013

25 - 31 August 2013 - Barcelona, Spain

Tracks: Sensor devices - Ultrasonic and Piezosensors - Photonics - Infrared - Gas Sensors - Geosensors - Sensor device technologies - Sensors signal conditioning and interfacing circuits - Medical devices and sensors applications - Sensors domain-oriented devices, technologies, and applications - Sensor-based localization and tracking technologies - Sensors and Transducers for Non-Destructive Testing

Deadline for papers: 30 March 2013

http://www.iaria.org/conferences2013/SENSORDEVICES13.html

The Seventh International Conference on Sensor Technologies and Applications

Deadline for papers: 30 March 2013

SENSORCOMM 2013

25 - 31 August 2013 - Barcelona, Spain

Tracks: Architectures, protocols and algorithms of sensor networks - Energy, management and control of sensor networks - Resource allocation, services, QoS and fault tolerance in sensor networks - Performance, simulation and modelling of sensor networks - Security and monitoring of sensor networks - Sensor circuits and sensor devices - Radio issues in wireless sensor networks - Software, applications and programming of sensor networks - Data allocation and information in sensor networks - Deployments and implementations of sensor networks - Under water sensors and systems - Energy optimization in wireless sensor networks

http://www.iaria.org/conferences2013/SENSORCOMM13.html

The Sixth International Conference on Advances in Circuits, Electronics and Micro-electronics

CENICS 2013

25 - 31 August 2013 - Barcelona, Spain

Deadline for papers: 30 March 2013

Tracks: Semiconductors and applications - Design, models and languages - Signal processing circuits - Arithmetic computational circuits - Microelectronics - Electronics technologies - Special circuits - Consumer electronics - Application-oriented electronics

http://www.iaria.org/conferences2013/CENICS13.html

Aims and Scope

Sensors & Transducers is a peer reviewed international, interdisciplinary journal that provides an advanced forum for the science and technology of physical, chemical sensors and biosensors. It publishes original research articles, timely state-of-the-art reviews and application specific articles with the following devices areas:

- Physical, chemical and biosensors;
- Digital, frequency, period, duty-cycle, time interval, PWM, pulse number output sensors and transducers;
- Theory, principles, effects, design, standardization and modeling;
- Smart sensors and systems;
- Sensor instrumentation;
- Virtual instruments;
- Sensors interfaces, buses and networks;
- Signal processing and interfacing;
- Frequency (period, duty-cycle)-to-code converters, ADC;
- Technologies and materials;
- Nanosensors;
- Microsystems;
- Applications.

Further information on this journal is available from the Publisher's web site:
http://www.sensorsportal.com/HTML/DIGEST/Submission.htm

Subscriptions

An annual subscription includes 12 regular issues and some special issues. Annual subscription rates for 2013 are the following:

Electronic version (in printable pdf format): 400.00 EUR
Printed with b/w illustrations: 640.00 EUR
Printed full color version: 760.00 EUR

40 % discount is available for IFSA Members.

Prices include shipping costs by mail. Further information about subscription is available through IFSA Publishing's web site: http://www.sensorsportal.com/HTML/DIGEST/Journal_Subscription.htm

Advertising Information

If you are interested in advertising or other commercial opportunities please e-mail sales@sensorsportal.com and your enquiry will be passed to the correct person who will respond to you within 24 hours. Please download also our Media Planner 2013: http://www.sensorsportal.com/DOWNLOADS/Media_Planner_2013.pdf

Books for Review

Publications should be sent to the IFSA Publishing Office: Ronda de Ramon Otero Pedrayo, 42C, 1-5, 08860, Castelldefels, Barcelona, Spain.

Abstracting Services

This journal is cited, indexed and abstracted by Chemical Abstracts, EBSCO Publishing, IndexCopernicus Journals Master List, ProQuest Science Journals, CAS Source Index (CASSI), Ulrich's Periodicals Directory, Scirus, Google Scholar, etc. Since 2011 *Sensors & Transducers* journal is covered and indexed by EI Compendex index (including a Scopus, Embase, Engineering Village and Reaxys) in *Elsevier* products.

Instructions for Authors

Please visit the journal web page http://www.sensorsportal.com/HTML/DIGEST/Submission.htm Authors must follow the instructions very carefully when submitting their manuscripts. Manuscript must be send electronically in both: MS Word 2003 for Windows (doc) and Acrobat (pdf) formats by e-mail: editor@sensorsportal.com

International Frequency Sensor Association Publishing

ADVANCES IN SENSORS: REVIEWS 2

Sergey Y. Yurish
Editor

Sensors and Biosensors, MEMS Technologies and its Applications

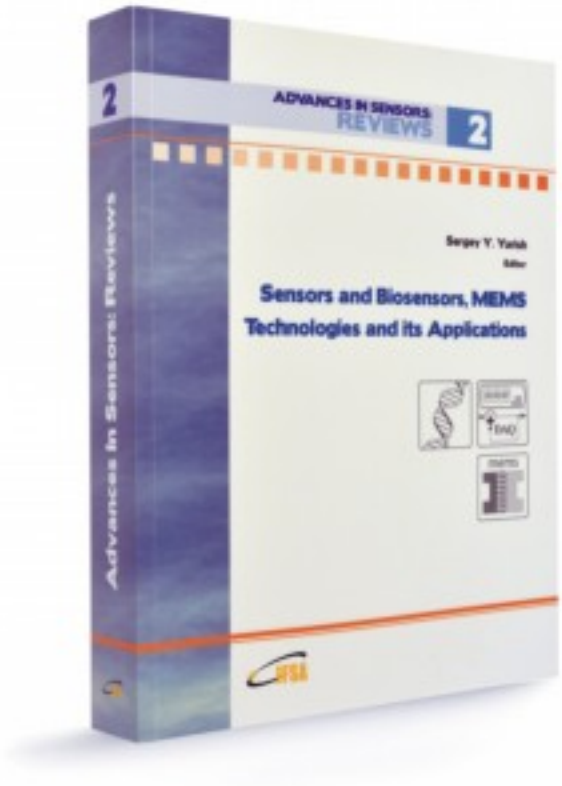

The second volume titled *'Sensors and Biosensors, MEMS Technologies and its Applications'* from the *'Advances in Sensors: Review'* Book Series contains eighteen chapters with sensor related state-of-the-art reviews and descriptions of the latest achievements written by experts from academia and industry from 12 countries: China, India, Iran, Malaysia, Poland, Singapore, Spain, Taiwan, Thailand, UK, Ukraine and USA.

This book ensures that our readers will stay at the cutting edge of the field and get the right and effective start point and road map for the further researches and developments. By this way, they will be able to save more time for productive research activity and eliminate routine work.

Built upon the series *Advances in Sensors: Reviews* - a premier sensor review source, it presents an overview of highlights in the field and becomes. This volume is divided into three main parts: physical sensors, biosensors, nanoparticles, MEMS technologies and applications. With this unique combination of information in each volume, the *Advances in Sensors: Reviews* Book Series will be of value for scientists and engineers in industry and at universities, to sensors developers, distributors, and users.

Like the first volume of this Book Series, the second volume also has been organized by topics of high interest. In order to offer a fast and easy reading of the state of the art of each topic, every chapter in this book is independent and self-contained. The eighteen chapters have the similar structure: first an introduction to specific topic under study; second particular field description including sensing applications.

Order online:
http://sensorsportal.com/HTML/BOOKSTORE/Advance_in_Sensors_Vol_2.htm

www.sensorsportal.com

ISSN 1726- 5479
9 771726 547001